Cryopreservation of Induced Pluripotent Stem Cell Derived Neurons and Primary T-Cells and Natural Killer Cells Using Ice Recrystallization Inhibitor Technology

Salma Alasmar

B. Sc. Honours Biopharmaceutical Science,
Medicinal Chemistry- University of Ottawa (2018)

Thesis submitted to the University of Ottawa
in partial fulfillment of the requirements for the
Doctorate in Philosophy degree in Chemistry

Department of Chemistry and Biomolecular Sciences
Faculty of Science
University of Ottawa

Candidate	Supervisor
Salma Alasmar	Robert N. Ben

Abstract

Given the rising demand for diverse cell types in regenerative and transfusion medicines, such as human induced pluripotent stem cell-derived neurons (iPSC-Ns), human T/chimeric antigen receptor (CAR) T cells, and human natural killer (NK) cells, the ability to cryopreserve cells has become increasingly important. In regenerative medicine, iPSC-Ns are powerful tools for treating and modelling neurodegenerative diseases. Moreover, transplants/transfusions of T/CAR T cells or NK cells offer promising treatment for numerous types of tumors, such as leukemia and multiple myeloma. Cryopreservation of cells at sub-zero temperatures (-80 to -196 °C) allows for the development of master cell banks that can be used for clinical applications. Conventional cryoprotective agents (CPAs), such as dimethylsulfoxide (DMSO) and glycerol, are utilized to protect cells from cryoinjuries associated with the freezing process. However, the use of high concentrations of DMSO (i.e., 10 to 20%) has been shown to be accompanied with toxic effects on patients receiving cell therapies if it is not removed or diluted prior to transfusion. Moreover, DMSO does not prevent the occurrence of the cryoinjury associated with ice recrystallization, which is one of the major causes of cell death/damage during cryopreservation. As a result, there is a surge of attention toward developing new non-toxic cryo-additives that inhibit ice recrystallization during cryopreservation to permit future advancement in regenerative and transfusion medicines. Moreover, the use of ice recrystallization inhibitors (IRIs) as novel CPAs has become a promising strategy to improve cell viability and function post-thaw.

The Ben laboratory heavily invested in synthesizing several classes of carbohydrate-based small molecule IRIs (i.e., *O*-linked alkyl and aryl glycosides, and *N*-

aryl-D-gluconamides), and studying the correlation between their IRI activity and molecular properties, such as polar surface area to molecular surface area (PSA/MSA) ratio. Moreover, compounds that belong to the *O*-linked aryl glycosides and *N*-aryl-D-gluconamides classes of IRIs have been shown to enhance the viability and functionality of red blood cells (RBCs), hematopoietic stem cells (HSCs), and induced pluripotent stem cells (iPSCs) after thawing.

Part of the research presented throughout this thesis focuses on structure-activity relationship (SAR) studies of alkyl pyranoses with modified alkyl chain lengths to explore any correlations between the IRI activity and the net polarity (i.e., PSA/MSA ratio) of the IRI candidates. *O*- and *C*-linked alkyl pyranose derivatives with different alkyl chain lengths were synthesized and their IRI activity was assessed using the modified splat cooling assay. While the IRI activity of the *O*- and *C*-linked alkyl glucosides did differ as the length of the alkyl chain increased, no correlation between the PSA/MSA ratios and their IRI activity was observed. In addition, this work allowed for investigation into the effect of the type of the glycosidic bond (i.e., *C*-*O* and *C*-*C* bonds) at the anomeric position, on the IRI activity of the different compounds. The *O*-linked alkyl glucosides appeared to be more IRI active than the *C*-linked compounds, suggesting the nature of the glycosidic bond is important for IRI activity.

The second part of the research presented in this thesis focuses on examining the potential for IRIs to cryopreserve iPSC-Ns, T/CAR T cells, and NK cells. 2-fluorophenyl-D-gluconamides (2FA), which is one of the most active IRIs from the *N*-aryl-D-gluconamides, has shown promising results in maintaining a high number of viable and functional HSCs and iPSCs post-thaw, and therefore it was employed in the

cryopreservation protocol of iPSC-Ns, human-derived T/CAR T cells, and human-derived NK cells. The efficacy of the cryopreservation protocol being constructed was evaluated by assessing the post-thaw viability and recovery rate, as well as the functionality of iPSC-Ns, T/CAR T cells, and NK cells post-thaw. These studies showed that protecting against ice recrystallization during cryopreservation with IRIs increases the number of viable and functional iPSC-Ns, and T/CAR T cells. It was also observed that employing IRI technology in the cryopreservation protocol of NK cells does not compromise their functionality compared to fresh, non-frozen NK cells. Overall, inhibition of ice recrystallization using IRIs appeared to enhance the cryopreservation outcomes of the different cell types, which will allow for the development of off-the-shelf cell therapy products and improvement of the delivery of efficacious cell products to clinics and hospitals.

Dedications

Dedicated to
My husband, Georges Tony Abdou
My father, Eng. Riad Mikhael Alasmar
My mother, Mayada Ibrahim Haddad
My brother, Mikhael Riad Alasmar

"Do not be anxious about anything, but in every situation, by prayer and petition, with thanksgiving, present your requests to God. And the peace of God, which transcends all understanding, will guard your hearts and your minds in Christ Jesus."
- Philippians 4:6-7, NIV

Acknowledgments

I owe a debt of gratitude to so many people for their infinite encouragement and support throughout my graduate studies. Firstly, I want to express my sincere gratitude to the almighty God whose grace guided me from the very inception to the completion of my PhD studies.

I also would like to express my appreciation to my supervisor, Dr. Robert N. Ben, for giving me the opportunity to work in his laboratory. I sincerely thank you for your guidance, support, and assistance throughout my graduate school journey. I am extremely grateful for all the discussions and suggestions regarding all projects I was part of. Thank you for teaching me to think outside the box in research. I also thank you for all the work opportunities you have given me through my PhD journey.

I would also like to thank all the past and present members of the Ben laboratory for their support, help, and friendship. Anna Ampaw has been an amazing deskmate and "bay buddy". Thank you for being a true friend inside and outside the lab. I also thank you for all the support and help in the lab, you definitely made this journey pleasant. I would also like to thank Karishma Chopra for being a great lab partner and friend. I appreciate your help and support in some of the experiments we conducted together at NRC. Thank you to Marcus Diamante for all the discussions and suggestions he offered whether for chemistry experiments or for editing presentations, abstracts, and some of my thesis chapters. To other past and present Ben lab members that I had the pleasure to work with or alongside Madeleine Adam, Julia Meyer, Jessica Poisson, Sandra El-Gazal, Stephanie Bogdan, Jatinder Singh, Thomas Charlton, Odile Pressoir, Romeo El-Issa, and Elly Walsh. Thank you to Sophia Mangan for her feedbacks on the first version of my thesis chapters.

I would also like to express my appreciation to Leah McMunn for offering her editing expertise and for all the comments and feedbacks she gave while editing my thesis.

I would like to extend my sincere thanks to the members of the Department of Chemistry and Biomolecular Sciences, Dr. Christopher Boddy, Dr. Adam Shuhendler, Dr. Maria Musgaard, and Dr. Francois-Xavier Campbell-Valois for their suggestions and contributions when reading and evaluating my comprehensive exam, research proposal, seminar, and doctoral dissertation. I would like to thank Dr. James Benson from the University of Saskatchewan for reading and evaluating my doctoral dissertation.

I would also like to thank my co-supervisor, Dr. Anna Jezierski, for all your guidance, support, and encouragement throughout my PhD journey. I appreciate all the discussions and suggestions you offered for editing presentations, abstracts, and my thesis. I am grateful for all the experience you gave me during my work period at NRC. I would also like to express my gratitude to her laboratory team members, Ewa Baumann, Junzhuo Huang, Claudie Charlebois, Caroline Sodja, Dr. Betty Li, and Dr. Will Costain at the Human Health Therapeutic Department at National Research Council Canada. I would like to thank Dr. Joe Tauskela and Amy Aylsworth for their help in training me on MEAs and in analyzing the functionality data. I would also like to thank Dr. Scott McComb and his research team, especially Tina Nguyen, Ahmed Zafer, for their help and guidance in the T-cell project. I appreciate all the discussions we had regarding all presentations and abstracts I submitted for the T-cell work. I would also like to acknowledge all of the other collaborators that I have worked with, including Dr. Seung-Hwan Lee at the University of Ottawa, Department of Biochemistry, Microbiology, Immunology, and his research team,

Bryan Marr, Darren Jo, and Shelby Kaczmarek, who helped me with my NK cell project. I gratefully acknowledge the funding received during my PhD from GlycoNet.

I am also appreciative to the loving, supportive, and caring family that I have. I am grateful for the constant love and support that my mom, dad, and brother gave me throughout my education journey. Thank you for encouraging me in all of my pursuits and inspiring me to follow my dreams. To my mom, Mayada, I always knew that you believed in me and wanted the best for me. Thank you for teaching me that my job in life was to learn, to be happy, and to know and understand myself; only then could I know and understand others. To my dad, Riad, I am especially grateful for your support emotionally, socially, and financially. To my brother, Mikhael, thank you for the encouragement and support you give me in life.

Thank you to my friends, Joelle Chalhoub, Salma Hammoud, and Nour Antoun, for your support throughout my studies. I will always be thankful for our study sessions. I would also like to thank my close friends Marilyn El-Khoury, Dajana Pavic, and Theresa Saliba for all for all the laughs, the good memories, the cottage trips, and for cheering me on throughout my thesis writing process.

I would like to devote the last part of my acknowledgements to the love of my life, my husband, Georges. I thank you for your endless love, support, and encouragement during all the challenges I have faced throughout my studies, and life, in general. Thank you for always showing how proud you are of me, you helped in shaping the woman I have become. Thank you for all that you have done and still do for us. I am so lucky to have such courageous and loving husband in my life forever.

Table of Contents

Table of Contents

List of Figures

List of Tables

List of Schemes

List of Abbreviations

α	Alpha
β	Beta
δ	Delta
γ	Gamma
σ	sigma
^{1}H	Proton
^{13}C	Carbon
Å	Angstrom
°C	Celsius degree
2FA	*N*-(2-fluorophenyl)-D-gluconamide
2,6-DFB	*N*-(2,6-diflurobenzyl)-D-gluconamide
4ClA	*N*-(4-chlorophenyl)-D-gluconamide
4AP	4-Aminopyridine
7-AAD	7-Aminoactinomycin D
aa	Amino acid
Ac	Acetyl
Ac_2O	Acetic anhydride
ACT	Adoptive T cell therapy
AFPs	Antifreeze proteins
AFGPs	Antifreeze glycoproteins
Ag_2CO_3	Silver carbonate
AD	Alzheimer's disease

AML	Acute myeloid leukemia
ANOVA	Analysis of variance
Ar	Argon
BAs	Biological antifreezes
Bn	Benzyl
BCMA	B cell maturation antigen
BDNF	Brain-derived neurotrophic factor
BF_3•OEt_2	Boron trifluoride diethyl etherate
br	broad
C	Cytosine
Ca^{2+}	Calcium
CAR-NK	Chimeric antigen receptor natural killer cells
CAR-NK92	Chimeric antigen receptor natural killer 92 cell line
CAR-T	Chimeric antigen receptor T-cells
CB	Cord blood
CCRM	Center for commercialization of regenerative medicine
CD19	Cluster of differentiation 19
$CDCl_3$	Deuterated chloroform
ChAT	Choline Acetyltransferase
CH_2Cl_2	Dichloromethane
CMC	Critical micellization concentration
CNS	Central nervous system
c-Myc	Cellular-myelocytomatosis transcription factor

CPAs	Cryoprotective Agents
CS5	Cryostor®5%DMSO
CS10	Cryostor®10%DMSO
d	Doublet
D_2O	Deuterated water
dd	Doublet of doublet
DCM	Dichloromethane
dbcAMP	Dibutyryl cyclic adenosine monophosphate
DIS	Dynamic ice shaping
DMEM	Dulbecco's modifies eagle medium
DMSO	Dimethyl sulfoxide
DOCD	Delayed onset cell death
dt	Doublet of triplet
EGFR	Epidermal growth factor receptor
ESCs	Embryonic stem cells
ESI	Electrospray ionization
EtOAc	Ethyl acetate
Et_3SiH	Triethyl silane
FBS	Fetal bovine serum
FBS10	FBS + 10% DMSO
FC	Flowcytometry
G	Guanine
GABA	Gamma aminobutyric acid

GAD	Glutamic acid decarboxylase
GBM	Glioblastoma multiform
GDNF	Glial cell line-derived neurotrophic factor
GFs	Growth factors
GFAP	Glial fibrillary acidic protein
H_2O	Water
HBr in ACOH	Hydrogen bromide in Acetic acid
HepG2	Human liver hepatocellular carcinoma cells
HES	Hydroxyethyl starch
HSCs	Hematopoietic stem cells
Hz	Hertz
I_h	Hexagonal ice
I_c	Cubic ice
I_{sd}	Stacking-disordered ice
IC_{50}	Half maximal inhibitory concentration
IFN-γ	Interferon-γ
IL2	Interleukin 2
IIF	Intracellular ice formation
iPSCs	Induced pluripotent stem cells
iPSC-CART	Induced pluripotent stem cell-derived chimeric antigen receptor T cells
iPSC-Ns	Induced pluripotent stem cell-derived neurons
iPSC-NPCs	Induced pluripotent stem cell-derived neural progenitor cells

iPSC-ML	Induced pluripotent stem cell-derived myeloid lineage
IRI	Ice recrystallization inhibition
IRI(s)	Ice recrystallization inhibitor(s)
K	Kelvin
K^+	Potassium
K562	Human erythroleukemic cell line
LD_{50}	Half maximal lethal dose
LRMS	Low resolution mass spectrometry
M	Molar
m	Multiplet
m-	*Meta*-
MAP-2	Microtubule-associated protein-2
MEAs	Microelectrode arrays
MeOD	Deuterated methanol
MeOH	Methanol
MGS	Mean grain size
MHz	Megahertz
$MgSO_4$	Magnesium sulfate
mM	Millimolar
μM	Micromolar
mmol	Millimole
MS	Molecular sieves
MS	Mass spectrometry

MSA	Molecular surface area
MW	Molecular weight
Na^+	Sodium
NaCl	Brine
$NaHCO_3$	Sodium bicarbonate
NaOMe	Sodium methoxide
NBQX	2,3-Dioxo-6-nitro-7-sulfamoyl-benzo[f]quinoxaline
NDs	Neurodegenerative diseases
nm	Nanometer
Nestin	Neuroepithelial stem cell protein
NeuN	Neuronal nuclear proteins
NK	Natural Killer
NKSF	Natural killer cell stimulatory factor
NMDAR	*N*-methyl-D-aspartate receptor
NMR	Nuclear magnetic resonance
o-	*Ortho*-
OCT3/4	Octamer-binding transcription factor3/4
p-	*Para*-
PBMCs	Peripheral blood mononuclear cells
pBrPh	*para*-bromophenol
PBS	Phosphate buffer solution
PD	Parkinson's diseases
Pd/C	Palladium on carbon

PEG	Polyethylene Glycol
PLO	Poly-L-orthenine
PMA	*N*-(4-methoxyphenyl)-D-gluconamide
PMP	*para*-methoxyphenyl
pNK	Primary natural killer cells
ppm	Parts per million
PSA	Polar surface area
PSA/MSA	Polar surface area to molecular surface area ratio
PVA	Polyvinyl alcohol
PVP	Polyvinylpyrrolidone
q	Quartet
QLL	Quasi-liquid layer
RBCs	Red blood cells
RM	Regenerative medicine
RMgCl	Magnesium chloride
ROCK	Rho-associated, coiled-coil containing protein kinase
RP5	RPMI + 20% albumin + 25% dextran + 5% DMSO
RP10	RPMI + 10% DMSO
RPMI	Roswell park memorial institute medium
RT	Room temperature
s	Singlet
SAR	Structure activity relationship
SEM	Standard error of mean

SOX2	SRY-Box transcription factor
Syp	Synaptophysin
Syts	Synaptotagmins
t	Triplet
TB	Trypan blue
TCR	T cell receptor
TES	Triethyl silane
TNF-α	Tumor necrosis factor-α
TLC	Thin layer chromatography
TH	Thermal hysteresis
THF	Tetrahydrofuran
TTX	Tetrodotoxin
v_{norm}	Normalized ice crystal growth rate
VGlut	Vesicular glutamate transporter
WBCs	White blood cells
Wt-NK92	Wildtype natural killer 92 cell line

Chapter 1: Introduction - Cryopreservation of Cellular Therapy Products Using Ice Recrystallization Inhibitor Technology

1.1 Regenerative Medicine, Cell-Based Therapy, and Cryopreservation Fundamentals

Regenerative medicine (RM) and cell-based therapy refer to the regeneration or replacement of human cells, tissues, or organs to repair or establish normal function.[1-2] The principle of cell-based therapy relies on the injection and application of cell cultures, stem cells or immunotherapeutic cell products, into pathological tissues or organs to restore their function.[1] The ability to generate therapeutic cellular products from different cell types has led to the significant advancement of the RM and cell-based therapy fields.[1,3-5] As the application of cell-based therapy in clinics continues to rise, the demand for an optimized methodology to preserve biological samples for long-term is warranted.[3,5-6]

Cryopreservation is commonly used to increase the shelf-life of cellular products, and to develop master cell banks which allows for easier distribution of cell products to clinics and hospitals.[5-6] Cryopreservation is the process by which biological samples are cooled to sub-zero temperature (e.g. -78 °C or -196 °C, depending on the cell type) at a controlled rate.[6-7] However, the protocols for cryopreserving clinically relevant cell types, such as human induced pluripotent stem cells (iPSCs), human T-cells, chimeric antigen receptor (CAR)-T cells, and natural killer (NK) cells, are not optimized and result in low cell viability and expansion rates.[8] Thus, it is important to discover effective cryopreservation protocols that produce improved outcomes where the number and functionality of cells are not affected post-thaw to work toward delivery of a higher quality,

safer, and more efficacious cellular product.[9-10] The continued development of cell-based therapies for the treatment of chronic diseases necessitates improved cryopreservation of different cellular products, which will allow for easier access to cells for both research and therapy applications.[10-12]

1.1.1 Importance of Cryopreservation

The rising demand for clinically relevant cell types has rapidly increased the requirement to preserve these cells, and thus, the field of cryobiology has risen in tandem. Cryobiology is an interdisciplinary field which examines the survival of biological material, such as cells and tissues, at low temperatures by assessing how cryopreservation techniques affect the viability and functionality of cell products after cryopreservation.[13-14] During cryopreservation, biological processes such as proliferation and metabolism are slowed or halted, elongating the shelf-life of cell products.[15] Cryopreservation of neuronal stem cells allows for the preservation of the neuronal functional properties, including neural regeneration and restoration of neural networks, which will help patients suffering from different neurodegenerative diseases and spinal cord injuries.[15-17] Moreover, the ability to freeze and store different types of immune-cell therapy products, such as T-cells and NK cells, without compromising their functional properties will assist in treating patients suffering from cancer and other immune diseases.[18-24] Long-term cryopreservation of therapeutic cells is vital for further development of cell therapy products since the capacity to properly store and distribute these products is critical to their widespread transportation and usage.

1.1.2 Preservation Strategies for Cellular Therapy Products and their Limitations

Hypothermic storage, vitrification, and cryopreservation are the three fundamental methods utilized to preserve cellular therapy products, each with its own set of benefits and drawbacks.[25] The preservation method used depends on the storage duration as well as the cell type.[25] Hypothermic storage is the process of preserving cells at temperatures between 4 and 10 °C, and is often utilized for short-term storage of biological samples, with a shelf-life ranging between days to weeks.[25] Lowering the temperatures of samples to 4 - 10 °C inhibits the degradation of key cellular metabolites as the biological processes are significantly reduced.[6,13,25-27] Some of the disadvantages associated with hypothermic storage include the short shelf-life of preserved cells, as well as the induction of a stress response leading to low number of viable and functional cells/organs upon re-warming.[25,28] The process of vitrification is used to preserve cell products in a glass-like state at cryogenic temperatures, avoiding ice nucleation.[29] During vitrification, it is necessary to supply the cryomedia with high concentration of CPAs and to use fast cooling rates.[29-30] Some of the limitations associated with vitrification are cytotoxicity, as a result of the high concentrations of CPA, and cellular torsion or shearing that is caused during warming cycles (devitrification).[30-32]

Cryopreservation is defined as a long-term preservation process where cells and tissues are stored at sub-zero temperatures (-78 °C to -196 °C), halting biological processes in living cells.[6,25] Long-term preservation methods have enabled the development of biobanks and subsequent wide-spread distribution of cellular products.[11] However, the occurrence of cryoinjury, such as osmotic stress, and the formation of extra- and intra-cellular ice, is still a major challenge associated with cryopreservation.[27] The challenges

are mitigated through the addition of cryoprotective agents (CPAs) to cryo-solutions, which will be discussed further in **section 1.1.4**. Many CPAs, such as dimethyl sulfoxide (DMSO) and glycerol, have been described as effective agents for controlling the harmful effects of physiochemical stressors associated with osmotic changes.[25,33-37] However, it is necessary to remove DMSO-containing cryo-solutions prior to clinical use as the solution itself can have cytotoxic effects, depending on the DMSO concentration and cell type being frozen.[25,33-37] Ultimately, the difficulties and consequences of present preservation strategies highlight the need to overcome cryoinjuries caused by freezing and warming cycles (i.e., ice formation and cellular torsion), and to mitigate the toxic effects associated with CPAs, and in order to satisfy the growing demands of cellular therapy.

1.1.3 Cellular Injury Associated with Cryopreservation and the Impact of Ice Crystallization

There are several modes of cell death that can occur during cryopreservation such as chilling injury (cold shock), physical cell rupture, necrosis, and apoptosis, with physical cell rupture and apoptosis being the two most common cryopreservation-related cell death mechanisms, as shown in **Figure 1.1**.[38-39] It has been well-documented that cell rupture is a result of the extreme volumetric fluctuations associated with freezing and thawing cycles, where ice crystals form intracellularly, disrupting the integrity of cell membrane (also known as the osmometric balance effect).[39] Moreover, gene-regulated cell death or apoptosis is another form of cryoinjury that is triggered by cold-induced changes in the cellular components.[38] Apoptosis is an energy-dependent mechanism associated with the maintenance of physiological and biochemical events of cells. Some of the characteristics

identified for apoptosis are cell shrinkage, nuclear fragmentation, and cellular fragmentation into apoptotic bodies.[28,39-40]

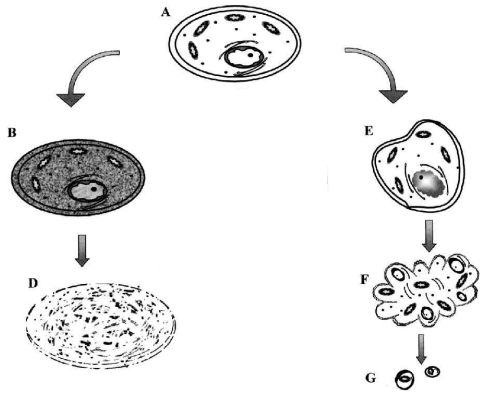

Figure 1.1 Schematic graph of the proposed mechanisms of cell death during freezing and thawing processes. Physical ice rupture is illustrated in diagrams A, B, and D. Diagrams A, E, F, G describe the different characteristics of apoptosis cell death mode.39 Figure adapted from Cell Preservation Technology. 1 (1), J.M. Baust, Molecular Mechanisms of Cellular Demise Associated with Cryopreservation Failure, 17-31, 2003, with permission from Mary Ann Liebert.

It has been well-documented that cooling rates have a substantial effect on cell survival during cryopreservation.[20,40-41,] As described by Mazur, plotting the percentage of cell survival versus cooling rates generated inverted U-shaped curves, demonstrating that for different cell types, there is an optimal cooling rate to enable maximum cell survival, represented in **Figure 1.2**.[41] The inverted U-shaped curve demonstrates a direct relationship between the slow/fast cooling rates and cell death.[40,41-42]

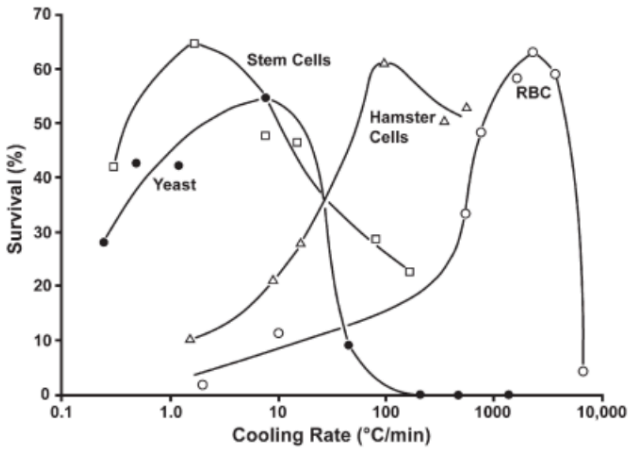

Figure 1.2 The inverted U-shaped curve representing the survival of cell (%) depending on the cooling rate (°C/min) in the absence of IRIs.[41] Figure adapted from Science, 138 (3934), P. Mazur, Cryobiology; The Freezing of Biological Systems, 939-949, 1970, with permission from American Association for the Advancement.

The finding of optimum cooling rates for each cell leads to the two-factor hypothesis, proposed by Mazur.[43] When cells are cryopreserved at sub-zero temperatures, they are subjected to ice nucleation (formation of ice), which subsequently, causes significant changes in the physical and chemical components of the cells. As depicted in **Figure 1.3**, the extracellular and intracellular components of the cell are supercooled (chilled below its freezing point without recrystallization) when cells are held at -5 °C. Lowering the temperature further (-10 °C to -15 °C) results in extracellular ice nucleation while the intracellular content remains supercooled and unfrozen. The formation of extracellular ice creates an osmotic pressure gradient across the cell membrane.[42] The ensuing osmotic pressure gradient across the plasma membrane acts as a driving factor for water efflux from cells, with the rate of efflux being restricted by the plasma membrane's water permeability.[42,44] With slow cooling rates, the intracellular water travels to the outside of the cell in response to osmotic pressure gradient, resulting in a decrease in intracellular volume and prolonged exposure to high electrolyte concentration. The cells get extremely dehydrated and suffer dramatic volume shrinkage, as shown in **Figure 1.3**. During this time, solutes are concentrated inside the cell ("solute effect") which is toxic and ultimately decreases the viability rate of the cells significantly.[42,44-45] On the other hand, when cells are subjected to rapid or fast cooling rate, intracellular freezing, also known as intracellular ice formation (IIF), can occur.[44,46] When cooling rates are high enough to induce a large departure from osmotic equilibrium, cells do not have time to dehydrate as water is retained inside the cells, and therefore, ice will form intra- and

extracellularly, which is a damaging effect that causes cell rupture (**Figure 1.3)**.[43] To maximize post-thaw viability and recovery, each cell type must be cooled at its optimum rate.[41]

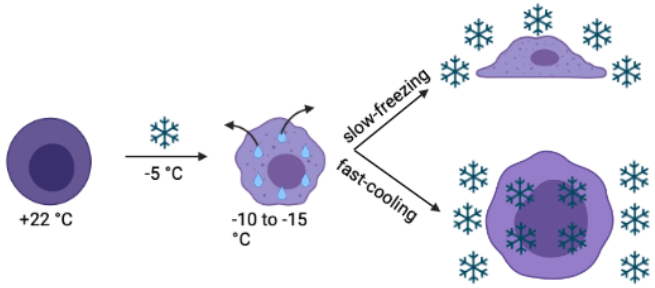

Figure 1.3 Schematic illustration of the physical changes occurring during freezing.[43] Figure created using free licence from BioRender.

Intracellular ice formation (IIF) is directly proportional to the amount of water in the cell during freezing as a result of membrane permeability, and therefore, the cooling rates that result in IIF vary substantially between cell types.[45] While it is commonly known that the production of intracellular ice is harmful to cell survival, new research has demonstrated that IIF is not always damaging. The detrimental effect of IIF is mainly related to the size of ice crystals that forms during freezing process where large ice crystals increase the risk of cell rupture.[45] However, research has shown that post-cryopreservation cell viability does not only rely on the freezing rate; it also depends on the rate at which cells are warmed.[31,47-48] As previously indicated, the size of ice crystals is associated with several downstream, uncontrolled cellular damage mechanisms, and therefore, the formation of large ice crystals (ice recrystallization) during thawing process has a negative impact on the cell.[31,47-48] While cryoinjuries associated with slow and fast cooling rates have been controlled by the utilization of chemical agents that protect cells from ice formation during freezing process. The cellular damages caused by ice recrystallization during warming process are not fully controlled, and therefore, control of ice

recrystallization becomes an important consideration when designing cryopreservation protocols.

1.1.4 Conventional Cryoprotective Agents (CPAs)

1.1.4.1 Classes of CPAs

Though the rate at which a sample is frozen or warmed is crucial to cell survival post-cryopreservation, further reduction of cryoinjury associated with freezing and thawing cycles can be achieved by formulating cryoprotective agents in the freezing medium. Cryoprotective agents (CPAs) are chemical additives that are formulated with the cell solution before freezing to mitigate the cellular damage caused by ice formation and to improve cell survival post-cryopreservation. There are two categories of CPAs: permeating and nonpermeating.[48-49] Dimethyl sulfoxide (DMSO) and glycerol are the two most common penetrating CPAs. They can easily permeate the cell membrane and protect cells from any detrimental effects associated with slow freezing rates.[48-52] Permeating CPAs minimize cryoinjuries by buffering the increase in solute concentration as ice nucleation occurs. The main mechanism of protection of permeating CPAs is that they maintain the solute concentration during freezing by replacing intracellular water, limiting the effect of osmotic shrinkage (i.e., loss of water and the reduction in cell volume) at lower temperatures.[20,41,51-54] One of the drawbacks to using permeating CPAs is the cytotoxic effect on patients which requires their removal or dilution prior to cell injection.[55-57] On the other hand, non-permeating CPAs are restricted to the extracellular environment as they cannot pass through cell membranes. They range from high molecular weight cryoprotectants such as polyvinylpyrrolidone (PVP), hydroxyethyl starch (HES), dextran 40, and polyethylene glycol (PEG) to low molecular weight additives such as sucrose and

trehalose.[58-64] This class of CPAs concentrates in the extracellular environment which raises the osmolality, inducing cell dehydration .[41,49-50] The increase in the extracellular osmolar concentration will result in a decrease in the freezing rate of the extracellular environment, promoting cell dehydration which, in turn, reduces the formation of intracellular ice formation (IIF).[61-63,65-67] Although non-penetrating CPAs are less toxic than other CPAs and they do not necessarily need to be removed following cryopreservation, cell survival post-thaw is often lower when utilizing non-permeating CPAs compared to permeating CPAs.[66] To achieve higher protection and therefore improved cell survival during cryopreservation, permeating CPAs are often used, however, their toxicity on cellular signaling and other biological activities must be mitigated.[56-57]

1.1.4.2 DMSO-Associated Toxicity

DMSO is formulated in multiple solutions that are used for the cryopreservation of various cell types and tissues, including hematopoietic stem cell (HSCs), iPSCs, neurons, T-cells, and NK cells.[68-74] Much research has reported the damaging toxic effect of DMSO, such as protein unfolding,[57] decreasing cell membrane thickness,[75] induction of stress protein,[56] reduction in cell viability and changes in the morphological properties of primary neurons,[68,70] functionality impairment of $CD34^+$ cells,[69] decrease in natural killer (NK) cell functionality,[71] and inhibition in the metabolic activity of $CD4^+$ T cells.[72] There is also evidence that injection of 10% DMSO-cryopreserved bone marrow and engraftment of hematopoietic stem cell (HSCs) results in various unpleasant reactions in patients.[73-74,76] Due to the cytotoxic effects imposed by CPAs on cells, many studies have been conducted to optimize the concentrations, as well as the length of exposure, of different CPAs. Reduction of DMSO concentrations in cryo-solutions, or co-formulation of DMSO with

other non-permeating CPAs (i.e., DMSO + Dextran), has shown to result in increased cell survival.[77-78] Despite the multiple attempts to explore methods to reduce permeating CPA concentrations, these cryopreservation protocols fail to protect against cellular damage that is associated with ice recrystallization, growth of large ice crystals at the expense of small ones. Therefore, it is of great interest to discover compounds that help to mitigate the cellular injury that is caused by ice recrystallization to improve cryopreservation protocols.

1.2 Regulating Ice Recrystallization: Biological Antifreeze and Ice Recrystallization Inhibitors

Recrystallization of ice is a thermodynamically driven process whereby large ice crystals grow at the expense of smaller ones and is the primary cause of cellular injury/death during cryopreservation; it occurs primarily during the thawing cycles.[79] This phenomenon is also described in other scientific areas and the frozen food industry, where the recrystallization of ice, and its associated morphological changes that occur during freezing and thawing cycles, have been linked to reduced quality of frozen food products.[80-81] Consequently, controlling the damage caused by ice recrystallization is key to optimizing cryopreservation protocols for different technologies (i.e., the food industry and biological samples). This can be done by developing molecules that inhibit ice recrystallization. Prior to this, it is necessary to learn more about the structure of ice, the mechanism of ice nucleation and recrystallization.

1.2.1 Ice Structure and the Mechanism of Ice Nucleation

The transition of water into its solid form (ice) is a common occurrence, and therefore, much research has been conducted to study structural properties of ice and its nucleation mechanisms.[82-85] Numerous morphological forms of ice exist depending on the

temperature and pressure.[82-83,86] Two of the most common crystalline forms of ice that occur naturally are stable hexagonal ice (I_h) and metastable cubic ice (I_c). Both crystalline structures of ice are composed of hydrogen-bonded water molecules ordered in layers of six-membered rings; the difference between the two forms lies in the stacking of the layers.[82,87] Moreover, experiments and dynamic stimulations imply that another form of ice structure, meta-stable stacking-disordered ice (I_{sd}) which is a combination of I_c and I_h stacking sequences, is formed by either recrystallization at high pressures or warming of glassy aqueous solutions.[87-92] However, at ambient pressure and high temperature, I_{sd} polymorph transform into the stable thermodynamic ice crystalline form, I_h.[87] In the I_h lattice, there exist four axes (a_1, a_2, a_3, c) that confine eight faces and four planes (basal plane, primary prism plane, secondary prism plane and pyramidal plane), as shown in **Figure 1.4**.[93-97] The hexagonal ice form is a result of highly ordered water molecules bound to each other through hydrogen bonds (H-bonds) whereby each oxygen atom binds two neighboring hydrogen atoms.[95-97] A hexagonal ice crystal can develop in any orientation after ice nucleation, however, the temperature of the surrounding water and the level of hydration determine the rate at which ice crystals grow.[98] Generally, the hexagonal ice shape is developed due to the rapid growth along the a-axis (prism plane) and due to slow growth along the c-axis (basal plane).[93-94,96,99]

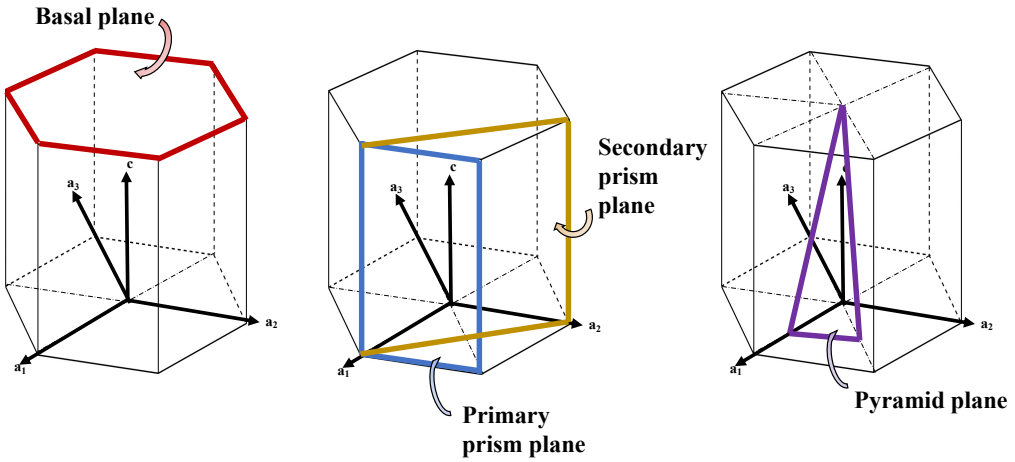

Figure 1.4 A depicted diagram of the different axes and planes in the hexagonal ice form (I_h).[94] Figure created using free licence from BioRender.

The mechanism by which ice nucleates is a three-step process, including transportation of water, generation of hydrogen bonds (surface kinetic stage), and production of heat. Nucleation is known to be the initial and important event in recrystallization process.[100] In the initial phases of freezing where ice formation has occurred (temperatures below 0 °C), a transitional surface layer starts to form, known as the quasi-liquid later (QLL). The QLL acts as an interface between the disordered liquid phase of bulk water and the ordered ice crystalline phase of ice.[101] The thickness of the QLL is temperature-dependent, where it increases as the melting temperature approaches.[100-103] The geometrical morphology and molecular dynamics of the QLL have been studied extensively, and it was found that the QLL gives indications of adhesion events and reactions that occur on the ice surface.[100-103] Light scattering studies have reported that the QLL is thicker on the basal and primary prism faces rather than secondary prism and pyramidal plane, in addition, more ice crystals grow into the QLL than the bulk water layer.[103-105] There are an appreciable number of studies on the characteristics of the QLL, however, they vary from one another in the description of the QLL's structure, thickness, water or ice-properties and diffusion constants.[98,104-116] Despite the various

reports on the exact nature of the QLL, it has been recognized as a significant physical state of water molecule organization, which in turn, can play a significant role in the outcome of ice recrystallization on cryopreservation.

1.2.2 Mechanism of Ice Recrystallization

Ice recrystallization, as defined previously, is a thermodynamic phenomenon that takes place through two proposed mechanisms: grain boundary migration and Ostwald ripening. [117-118] The arrangement of water molecules in its solid phase (ice) is called an ice grain, where the ice is found in its thermodynamically favoured form, hexagonal ice (I_h). Thus, grain boundaries are the points where different oriented ice grains meet.[117-118] Grain boundary migration is influenced by interfacial energy and stress; the migration of adversely oriented ice grains to a more favourably oriented one causes grain boundary migration.[117-119] Ice grains differ in size and their degree of boundary curvature, where smaller ice grain boundaries tend to be more curved than larger ones, rendering them more convex (bulging outward) and so contain more surface energy.[119] The morphological shape of larger ice grains appears more concave (less curved), and thus contain less surface energy. In order to reduce the energy of the system, grain boundary migration occurs where the border of ice grains migrate to the center of the curve to decrease the degree of curvature.[119] This migration event, illustrated in **Figure 1.5**, causes smaller ice grains to decrease in size (concave shape migrates inward) while large ice grains grow larger (concave shape migrates outward).[119] It is important to note that, the grain boundary migration is limited to temperatures below -10 °C and it is proposed that water molecules move directly between small ice grains that are decreasing in size to the growing ice

grains.[119] This assumption of direct movement ignores the presence of the bulk-water layer, as well as the QLL, present between each ice grain.[119]

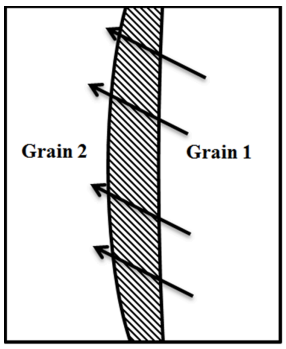

Figure 1.5 A pictorial illustration of the grain boundary migration mechanism adapted from. *Wilson, P., Ed.; InTech Open, Ltd. London, UK* **2013**, 177–224. Copyright © 2013 InTechOpen.[79] The shaded area represents the liquid layer between two curved ice grains. Movement of the interface grain boundary is referred to as arrows where large ice grains (Grain 2) grow larger at the expense of small ice grains (Grain 1) which decrease in size. Grain boundary migration reduces the energy of the system by decreasing the curvature of grain boundaries.

Ostwald ripening of polycrystalline ice in an aqueous solution, on the other hand, takes into account the entire ice grain and liquid water combination.[120] The mechanism of Ostwald ripening occurs as two crystals merge together to form a large ice grain, while a constant ice volume is maintained.[120] This process leads to a reduction in the total energy of the ice crystal and the bulk water interface by way of an increase in the mean size of ice crystals and a decrease in the total number of ice crystals.[120-124] As described previously, at low temperatures, hydrogen bonds form between water molecules resulting in a highly ordered and stable hexagonal ice form.[94-97] However, water molecules present at the bulk-water/ice interface are less ordered. Therefore, the presence of water molecules on the surface, rather than within the ice lattice, leads to a high surface free energy. Smaller ice crystals have a high surface area to volume ratio which implies a higher surface free energy, and thus are less stable. Whereas larger ice crystals have a greater volume to surface area ratio, resulting in a lower surface energy and comparably more stable ice crystals. As ice

recrystallizes via the Ostwald ripening process, water molecules migrate from the surface of smaller ice grains to the surface of larger ones through the QLL and bulk-water layers to decrease the total surface free energy.[123-126] The ice recrystallization phenomenon is an inevitable process that occurs during the freezing and thawing stages of cryopreservation and is a major contributor to cellular injury. Therefore, it is of great interest to control the recrystallization of ice to ensure high quality biological samples upon thawing post-preservation.

1.2.3 Biological Antifreezes (BAs) Activities: Thermal Hysteresis and Ice Recrystallization Inhibition

Species that live in sub-zero temperature environments, such as arctic fish and the *Lobelia telekii* plant, adopt a variety of mechanisms to prevent the damage caused by the nucleation and recrystallization processes of ice.[127-130] For example, some organisms inhibit ice formation by raising the solute concentration in their body fluids, which in turn, decreases the freezing point of water, or by removing molecules that induce ice nucleation (such organisms are called freeze-avoiding species).[120,128] Other species protect themselves against freezing injuries associated with freezing by producing special proteins that inhibit the growth of ice. These proteins were initially observed in teleost fish and are termed antifreeze proteins (AFPs) and antifreeze glycoproteins (AFGPs), also known as biological antifreezes (BAs).[93,96-97,127,131-133] While the exact mechanism by which BAs inhibit the growth of ice crystals is still debated, the adsorption-inhibition model has been the most accepted theory to explain the protective properties of BAs against freeze-associated damage. In this model, AFPs and AFGPs are known for their ability to adsorb and bind irreversibly onto the non-basal planes of ice crystals, therefore inhibiting ice growth and

recrystallization as temperatures are lowered.[133-137] This phenomenon can be explained by the Kelvin effect, whereby the adsorption of BAs onto the surface of ice increases the surface area and the degree of curvature of ice grains, raising the surface free energy which makes the adsorption of water molecules onto ice unfavorable, and consequently lowering the freezing point.[134,138-140] Moreover, the activity of AFPs and AFGPs is proposed to be governed by their affinity to bind to ice through specific ice-binding sites on the proteins themselves.[141-148] Many driving forces have been found to influence the binding of BAs to ice, including the generation of a network of ordered water molecules, the formation of hydrogen bonds between amino acid (aa) side chains and water molecules, as well as the formation of hydrophobic and Van der Waals interactions with ice.[144-145,149-156]

Two of the main antifreeze mechanisms associated with BAs have been recognized as **thermal hysteresis (TH)** and **ice recrystallization inhibition (IRI).**[118,132,138] Thermal hysteresis (TH) is referred to as the gap between the melting and freezing temperatures of a solution. During this phenomenon, ice crystals cannot grow or melt due to the adsorption of the AF(G)Ps to the ice surface. AF(G)Ps bind to the prism plane of the hexagonal ice crystal lattice blocking the addition of water molecules which will bind to the non-basal planes resulting in a burst of ice growth occurring on the c-axis (basal plane) giving rise to bipyramidal crystals (dynamic ice shaping, DIS).[138,157-160] When AF(G)Ps adsorb on the ice crystal, water molecules cannot bind resulting in the growth of the frontal edge of the ice to between neighbouring AF(G)Ps which increases the radius of curvature. As a consequence, addition of more water to the curved ice lattice is energetically undesirable which results in a freezing point depression (Kelvin effect). [138,157-160] Two mechanisms have been proposed to explain the activity of BAs within the TH window: the step-pinning

mechanism and the three-dimensional mattress model.[118,138,145] In the first one, the step pinning model, AF(G)Ps allow the growth of ice crystals at sites along the same plane where proteins are not bound,[138,145] whereas the second model (three-dimensional mattress model) assumes that the growth of ice grains happens perpendicularly to specific ice surface.[145] Nanoliter osmometry is utilized as method to assess TH activity for BAs. In this method, ice crystal morphology changes are observed, and the temperature at which solutions freeze and thaw are measured, as shown in **Figure 1.6**. The resulting difference between freezing and melting temperatures represents the TH activity expressed in Kelvin (K) or °C.[159-163]

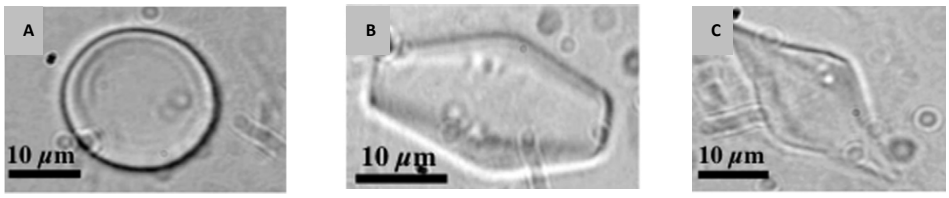

Figure 1.6 The different morphological adaptions of ice crystals in the presence of (A) water, (B) AFP-8 and (C) WT *Lp*AFP. Image A represents no TH activity in the absence of AF(G)P. Images B-C represent TH activity (changes in the ice crystal dynamics) in the presence of two different AF(G)Ps.[163] Images are adapted from Cryobiology, 70 (2), C. Capicciotti, Modulation of Antifreeze Activity and the Effect upon Post-Thaw HepG2 Cell Viability after Cryopreservation, 79-89, 2015, with permission from Elsevier.

Not only do AF(G)Ps inhibit ice growth (as a result of their TH activity), but they also prevent the recrystallization of ice. Ice recrystallization inhibition by AF(G)Ps is regulated by ions and hydrocolloids in solutions different ions adsorb on the surface of recrystallized ice, decreasing its size, and thus inhibiting recrystallization.[164-168] The ice recrystallization inhibition property of BAs is intriguing for cryopreservation technologies; however, the associated TH activity has been recognized as a process that significantly damages the cells (because of DIS). [169-171] Therefore, over the past several years, there has been considerable effort to synthesize AF(G)P analogues that have only IRI activity and to

test the ability for these analogues to enhance the outcomes of cryopreservation protocols for different cell types.

1.2.4 Ice Recrystallization Inhibitors (IRIs): from Synthetic Macromolecule AF(G)P Analogues to Small Molecule IRIs

Several studies of structure-activity relationship (SAR) of AF(G)Ps have been conducted to reveal key structural features that control ice formation and growth, toward the design of safe ice recrystallization inhibitors (IRIs). Using specific AF(G)P scaffolds, numerous *"custom tailored"* derivatives have been synthesized and assessed for their ability to inhibit ice recrystallization. [140,172] These AF(G)P analogues have a greater potential to successfully cryopreserve biological samples without causing TH and DIS, enhancing the efficacy of these cryopreservation technologies.

1.2.4.1 Structural Characteristics for AF(G)P Analogues

Various studies have been conducted to identify key structural features that are associated with AF(G)P functional activity.[142-143,150-155] One of the proposed theories to explain the function of BAs is their ability to bind to ice by either forming hydrogen bonds between the hydrophilic groups (hydroxyl groups) or the amino acid residues of AF(G)Ps and water molecules in the ice lattice, generating a network of ordered water, or through hydrophobic and Van der Waals interactions with ice binding.[144-145,149-156,173] Another proposed feature is the size of glycoprotein moiety attached to the AF(G)P, in addition to the glycosidic bond configuration and its secondary structural arrangement, have been found to play a significant role in controlling ice growth.[140,172] Further SAR studies have used different analysis strategies (i.e., conformational analysis, click chemistry, and polymerization studies) to determine the most significant characteristics linked to AF(G)P

activity. For instance, polymerization studies have revealed the importance of the distance between the AFGP backbone and water hydroxyl groups for the IRI activity of AFGP mimetics.[172,174-175] From this work, numerous polymer analogues have been identified as AF(G)P analogues with a wide range of antifreeze activity.[176-179] In addition, *C*-linked glycoconjugate derivatives are one of the first synthesized analogues that exhibit IRI activity without TH activity.[172,174-183] Synthesis of macromolecule AF(G)P mimetics are typically both lengthy and costly,[118,184] and this discovery has fueled the search for more synthetically accessible small molecules that display IRI activity with no TH.[173,185-191]

1.2.4.2 Synthetic Polymers and Glycopeptides as BA Analogues

Because large scale production of naturally occurring AF(G)Ps is costly and time-consuming, efforts have been diverted into synthesizing BA analogues such as polymers. It was discovered in late 20th century that polyvinyl alcohol (PVA) inhibits the growth of ice crystals.[118] Further research by Inada *et al.* revealed that increasing the molecular weight (MW) of PVA polymers resulted in enhanced IRI activity, proportional to type I AFP.[152,176-177,192] Further testing on PVA has shown that its antifreeze activity is also attributed to its ability to adsorb onto ice surface, suggesting an ice binding activity, which in turn, results in DIS and TH activity.[176-177,148,192] It was hypothesized that the different linkage length between hydroxyl groups in PVA structures allows for the adsorption onto different prism planes of ice grains.[178-179,192] More studies have since been conducted to synthesize polymers and glycopolymers that display ice recrystallization inhibition without any TH activity.[193] Gibson *et al*. reported their success in developing new antifreeze macromolecule glycopolymers, such as poly L-glutamate, poly L-lysine, and poly(methyl-6-O-methacryloyl-α-D-glucopyranoside), as well as polyols such as polyethylene glycol

(PEG).[194-196] As the efforts to synthesize AF(G)P polymer mimetics and identify their mechanism of action continues, ongoing research has identified that smaller carbohydrate molecules can display IRI activity. Small molecule IRIs are appealing alternatives to high molecular weight polymer because of their ease of synthesis, allowing them to be prepared in large quantities for a variety of applications.

1.2.4.3 Discovery of Novel Small Molecule IRIs

As described previously, ice recrystallization is a cause of cellular damage and death during freezing and thawing processes which needs to be mediated.[79] Conventional CPAs fail to protect cellular products from ice recrystallization, and thus, the development of ice recrystallization inhibitors as cryoprotective additives has become an attractive prospect.[79,189,197] The Ben laboratory has been investigating antifreeze properties, especially IRI activity associated with AF(G)Ps and incorporating some of these features (i.e., a tripeptide unit and the linker portion of the glycopeptide) into other synthetically accessible molecules to develop different classes of IRIs.[79,189,197]

1.2.4.3.1 Early Discovery of IRI Active Compounds and their Structural Features: C-linked AF(G)P Analogues

The first class of IRIs discovered and assessed for their IRI activity by the Ben laboratory are *carbon*-linked or *C*-linked AFGP analogues, as shown in **Figure 1.7**.[197] In this class of IRIs, the carbohydrate component is substituted for mono-α-D-galactose and the AAs are substituted for L-lysine and L-glycine (compared to the naturally occurring AF(G)Ps), as shown in **Figure 1.7 A-B**, to bypass any racemization may occur during solid phase synthesis.[197-198] Altering the length of the polypeptide chain (n = 2, 6 or 9) resulted in compounds either bearing moderate IRI activity and small TH activity (n = 6 or 9) or

weak IRI activity and low degree of TH activity when n = 2. Increasing the number of polypeptide repeats appeared to contribute to increasing the IRI activity of the C-linked analogues.[174,199] Further research by the Ben laboratory has resulted in the discovery of IRI-active *C*-linked mimetics without TH activity. These mimetics contained four repeats of L-serine (**Figure 1.7**, **C**) or tripeptide chain (**Figure 1.7 D**). These results suggest that the length of the linker chain, as well as the presence of an amide bond, play a significant role in displaying IRI activity without exhibiting TH activity.[175,197-198]

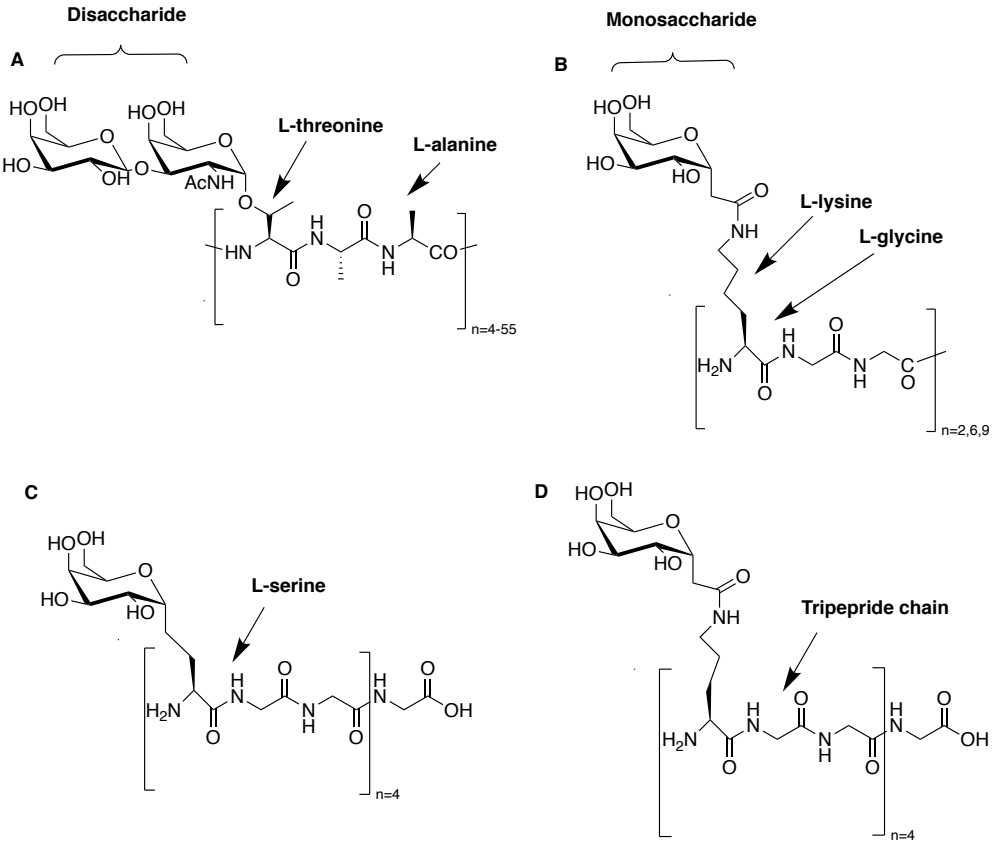

Figure 1.7 An illustration of the general structures and modifications of AFGPs **(A)** and C-linked AFGP analogues **(B-D)**.

Further SAR studies have revealed that alterations to the carbohydrate component of the AF(G)P also affect the IRI activity. For example, changing the D-galactose sugar to a configuration such as D-glucose, D-mannoses, or D-talose sugar is found to show a correlation between IRI activity and the hydration index of the carbohydrate, where a more

hydrated carbohydrate has greater IRI activity, depicted in **Figure 1.8**.[200] Several disaccharides have also been assessed for their IRI activity and have been correlated with their hydration index, where melibiose displayed the greatest IRI activity, followed by lactose, then sucrose and maltose with very little IRI activity (**Figure 1.8**).[200] The hydration index refers to the quantity of water molecules tightly bound to carbohydrates per molar volume of the carbohydrate.[173,199-202] The experimental results drawn from the correlation between the hydration index and IRI activity demonstrated that the higher the hydration index, the greater the IRI activity. [173,178-179,192-196, 198-210]

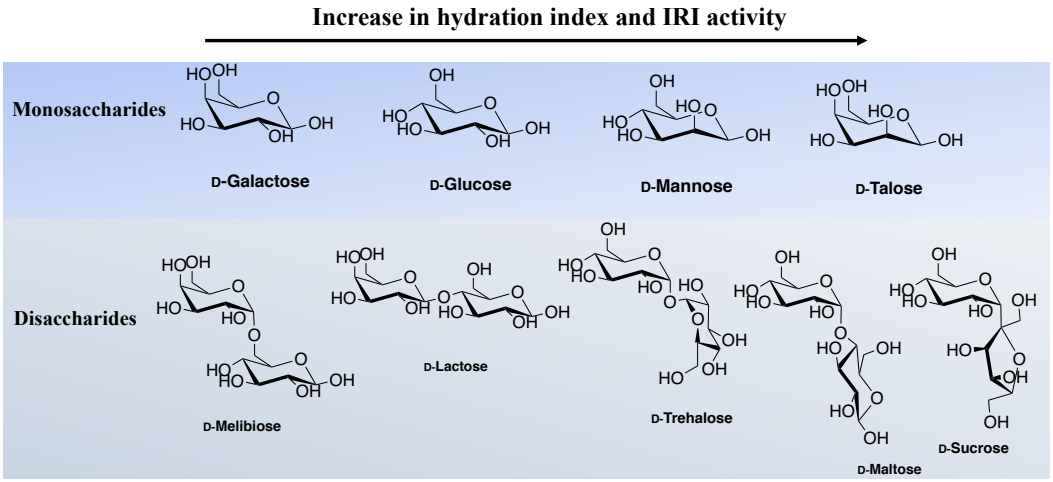

Figure 1.8 Structures of the different mono- and disaccharides that have been assessed for IRI activity. The hydration index and IRI activity increase from left to right.

Since small carbohydrate molecules (i.e., monosaccharides) exert ice recrystallization inhibition activity with no TH activity, the Ben laboratory has been invested in synthesizing novel carbohydrate-based ice recrystallization inhibitors, which are less complex and easier to synthesize than AF(G)P analogues.

1.2.4.3.2 Small Molecule IRIs: Alkyl/Aryl Pyranoses and Aryl Aldonamides

As mentioned in section 1.2.4.4.1, the discovery of low molecular weight compounds possessing IRI activity has led the Ben laboratory to investigate small-

molecule carbohydrate derivatives as ice recrystallization inhibitors. The first class of small molecule IRIs found to be active are pyranose-based surfactant and hydrogelators, shown in **Figure 1.9**.[211] This class of IRIs is characterized by its amphiphilic nature (carbohydrate portion and alkyl chain).[211-213] The surfactant properties of these molecules can cause cell membrane solubilization making them not suitable for use as cryo-additives.[211] As a result, through further SAR studies the Ben laboratory has developed a class of IRIs, known as aryl-linked pyranoses. In this class of IRIs, the alkyl chain at the anomeric carbon is substituted for an aryl component.[163,184,187] SAR studies on this group of compounds showed that occupying different substituents on the aryl ring, such as *p*-bromophenyl-β-D-glucoside and *p*-methoxyphenyl-β-D-glucoside (**Figure 1.9**), has resulted in a wide library of compounds that possess a range of IRI activity without TH activity.[163,184,187,190-191,214] Moreover, some of the IRI active aryl-linked glucosides have been found to be successful candidates for enhanced cryopreservation outcomes of red blood cells (RBCs) showing the promise of these small molecules as potential cryo-additives.[214]

Further manipulation to the carbohydrate-based surfactant has led to the discovery of open-chain carbohydrates, *N*-alkyl-D-gluconamides (**Figure 1.9**), that have displayed a wide range of IRI activity depending on the length of the alkyl chains.[211] As these molecules also suffer from the detrimental surfactant-like properties, the alkyl chains are further modified and are substituted with aryl components.[178-179,189-191] Several of the *N*-aryl-D-gluconamides (**Figure 1.9**) are active IRI and have been shown to improve the viability and functionality of multiple cellular therapy products such as HSCs and iPSCs.[178-179,189-191,195-215]

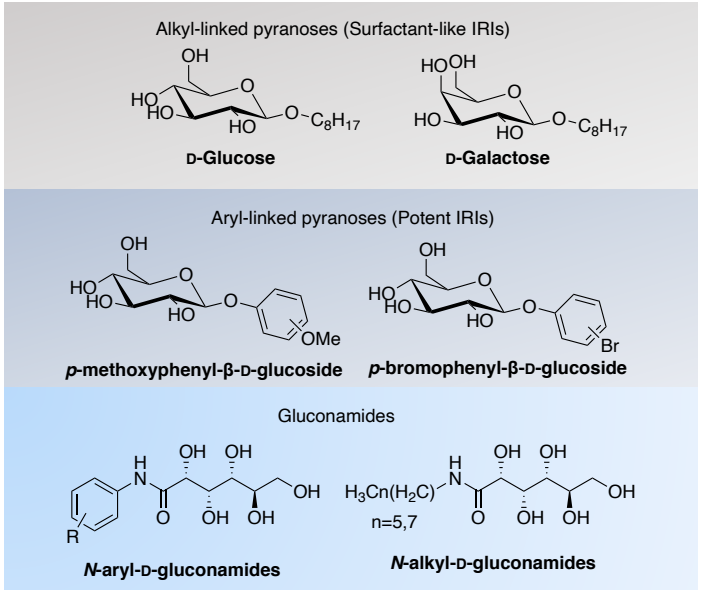

Figure 1.9 Structures of different classes of small-molecule IRIs.

Development of different small-molecule ice recrystallization inhibitors is undoubtedly more efficient and less expensive compared to the complex AF(G)P macromolecule analogues. Moreover, the capability of carbohydrate-based small molecules to display IRI activity without the presence of TH activity permit them to be more widely applicable to the cryopreservation of biological samples.

1.2.4.4 Methods for Measuring IRI Activity

To successfully apply IRI candidates in the cryopreservation protocol of different cellular products, it is significant to measure their activity and to determine detailed kinetic parameters of their IRI activity, such as the half maximal inhibitory concentration (IC_{50}). Multiple strategies have been proposed for the assessment of IRI activity such as the capillary assay, the sucrose sandwich assay, and the splat cooling assay.[163,216-222] In the capillary assay, a series of diluted solution of the AF(G)P analogue is prepared and loaded into 10 μL glass capillaries, which are then sealed and snap-frozen to -78 °C. Snap-freezing the samples results in a chevron pattern of multi-crystalline ice. The samples are then left to anneal at -6 °C overnight (~16 hours). The disappearance of chevron patterns from some

capillaries indicates the concentration at which AF(G)P analogues can no longer inhibit ice recrystallization (no IRI activity).[216]

The sucrose sandwich splat assay entails a 30 to 40% (w/w) of sucrose is employed and a 2 μL of the diluted sample is sandwiched between two coverslips. The sample is then frozen to -78 °C and then annealed at -6 °C for 30-90 minutes. Images of the ice crystals are then taken to monitor the growth of ice crystals which can be further analyzed to determine the concentration at which AF(G)P analogues can no longer inhibit ice recrystallization.[222]

The modified splat cooling assay is another method that is utilized by the Ben laboratory to assess IRI activity where a 10 μL droplet of the diluted solution is frozen to -78 °C using dry ice, then allowed to anneal at -6.4 °C for 5 minutes, as shown in **Figure 1.10**.[163,220] Images of the ice wafer are then taken using a microscope-fitted camera. In this protocol, ice crystals are analyzed at different concentrations where three pictures of each concentration can be used to determine the rate of ice crystal growth for the given concertation; plotting the rate of ice recrystallization against the concentrations (logarithm transformed) tested allows for the generation of a dose-response curve by which an IC_{50} value can be determined.[163,184,220-223] Active IRIs can undergo further testing, including cytotoxicity screening on route to functional cryopreservation applications.[184,220-223] Cytotoxicity of IRIs is measured using resazurin assay which quantifies the number of live cells in a sample and monitor cell viability/cytotoxicity. It is cheap, non-toxic to cells at low concentrations, and only requires a short incubation time (~4 hours). However, the reliability of the calculated number of live cells relies on cell density, the metabolic activity across the cell population which can vary from one cell culture to another.[220-223]

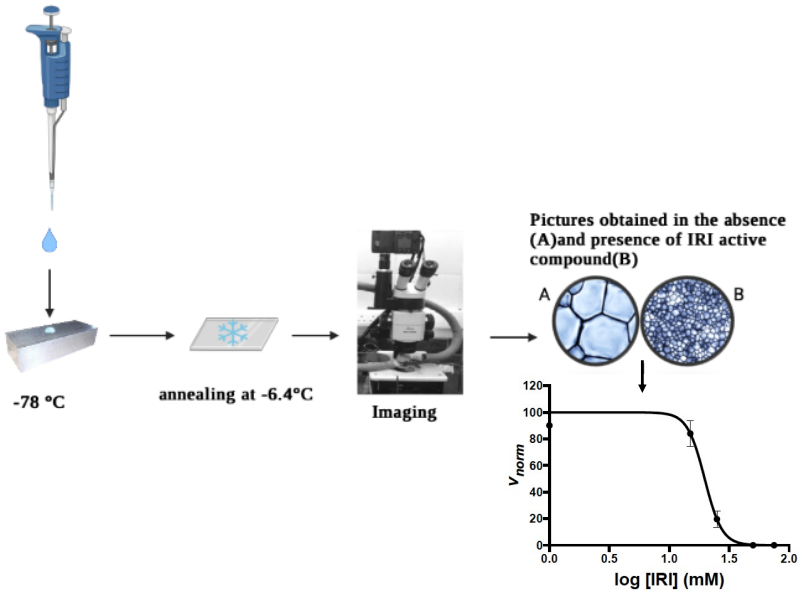

Figure 1.10 Graphical representation of the splat cooling assay. Figure created using free licence from BioRender.[184]

1.3 Cryopreservation Strategies of Different Cell Types

As discussed in **sections 1.1.2** and **1.1.3**, there are different preservation strategies used depending on the cellular therapy products. In addition, different CPAs can be used to prevent cryoinjury during freezing and thawing cycles (**section 1.1.4**). However, ice recrystallization contributes to major cellular death/injury and conventional CPAs often do not protect the cells from this injury. Developing compounds that are active IRIs serves as potential improvement to conventional cryo-solutions as a solution additive. Different classes of IRIs have been synthesized and evaluated in several cell types including RBCs and HSCs.[187,189] However, IRIs have yet to be tested on primary immunological cell-based products (i.e., T cells and NK cells), and on stem cell-derived neurons (i.e., iPSC-Ns). Conventional cryo-solution media for the different cell types comprise of dimethyl sulfoxide (DMSO) at varying concentrations. Using the conventional cryo-solutions, cell viability is often decreased, while functionality is either delayed or disrupted. [224-225] By

formulating IRIs into cryo-solutions, it is thought that they will be able to mitigate some of the detrimental cryopreservation outcomes.

1.3.1 The Significance of iPSC-Derived Neurons (iPSC-Ns) in Cell-Based Therapy

Diseases of the central nervous system (CNS) that cause progressive loss of neurons are referred to as neurodegenerative diseases (NDs).[8,226] Neurodegenerative diseases occur in different regions of the brain and spinal cord such as Alzheimer's disease (AD) and Parkinson disease (PD); NDs are the fourth most common cause of death in developed world after cardiovascular diseases, cancer and stroke.[226-229] Due to the prevalence and severity of NDs, interest in modeling and curing these NDs using cellular therapy products, such as embryonic stem cells (ESCs) and induced pluripotent stem cells (iPSCs), has risen significantly.[230-232] While ESCs impose some ethical and legal challenges that limit neuroscience research, iPSCs are easier to generate and are not ethically restricted, and thus, they are a better alternative source of cell-based therapy.[233] iPSCs can proliferate to give more of the same cell type (self-renewal) or can differentiate to generate other cell types (pluripotency).[233-236] Therefore, Human induced pluripotent stem cells (iPSCs) and their derivatives, such as iPSC-derived neurons (iPSC-Ns), are a distinct approach to generating new cell-based therapeutics for regenerative medicine and cell-based therapy.[233-236] iPSC-Ns have proven to be extremely useful in modelling and understanding the aetiologies of neurological diseases. Preclinical studies have revealed that iPSC-Ns have the potential as a cell replacement therapy for individuals with AD and other neurological diseases.[237-243] For example, grafting iPSC-Ns has shown to enhance cognition in AD-modeled mice by reducing β amyloid oligomers in the culture medium.[242]

1.3.2 Current State of Art in the Cryopreservation of iPSC-Ns

Differentiating iPSCs into iPSC-Ns is a lengthy process; requiring between 2 to 6 months, depending on the type of neurons required.[244-246] This poses a major challenge for the clinical translation of iPSC-Ns since large-scale manufacturing will necessitate downstream cryopreservation that can retain high viability and recovery, differentiation fidelity and functionality post-thaw. The currently proposed cryo-solutions used to preserve iPSC-Ns contain 10% of DMSO to prevent cryoinjuries associated with slow freezing.[66,244,247] However, DMSO does not protect the cells from the detrimental effects imposed by ice recrystallization during cryopreservation. iPSC-Ns hardly survive cryopreservation which is implied by the low recovery rate and the delay in establishing functionality post-thaw.[224] In addition, using DMSO at this concentration has been reported to cause neurotoxic effects if it is not washed or diluted prior to any clinical application.[224-225] Thus, developing cryopreservation additives (i.e., IRIs) that account for the cryoinjuries associated with ice recrystallization will assist in establishing an effective cryopreservation protocol for iPSC-Ns. This will allow for longer-term storage of iPSC-Ns, overcoming the lengthy and costly differentiation processes, and thus, permitting the delivery of successful iPSC-derived therapies to clinics.

1.3.3 T Cells and NK Cells for Cancer Immunotherapy and their Cryopreservation Protocol

An immunotherapy revolution has resulted from a greater understanding of the immune system's role in cancer treatment, delivering effective and long-lasting treatments to patients with previously incurable tumors.[248] Manipulations of the immune system response using different immunotherapies (T cells or NK cells) result in a redirection of

the immune cells to fight various kinds of malignancies. For example, T cell- and NK cell-based immunotherapies have been used to treat blood malignancies as well as solid tumors.[250-254] Moreover, the ability to genetically modify these immune system cells by expressing different cancer antigens has resulted in the establishment of diverse chimeric antigen receptor (CAR) T/NK cells, such as CD19 and epidermal growth factor receptor (EGFR) CAR- T/NK cells.[250-255] However, the successful application of immunotherapy products in clinics for an effective cryopreservation protocol that results in viable and functional CAR-T or CAR-NK cells.[256-257]

Conventional cryo-solutions containing 10 or 20% of DMSO allow long-term preservation of the different immunotherapies, however, post-thaw viability and functionality of these cellular products are lowered.[18,23-24,78,257-261] The reduction in cell viability, proliferation rate and killing functionality of the cells after cryopreservation can be linked to cryoinjuries associated with ice recrystallization process, as discussed in **section 1.2.2**. Therefore, effort toward developing cryo-additives (i.e., IRIs) that protect immunotherapies from cellular injury during freezing and thawing cycles has risen to facilitate the production of master immune cell banks and the delivery of T/NK cell products to clinics.

1.4 Chapter Summary

Cryopreservation has emerged as a powerful method for extending the shelf-life of cells by storing cellular therapy products, such as iPSC-Ns, T cells, and NK cells at low sub-zero temperatures. Conventional CPAs such as DMSO are used to protect cells from any cellular damages associated with freezing (slow or fast cooling rates). However, conventional CPAs are not capable of preventing the cryoinjury associated with ice

recrystallization, which is a major contributor to cellular injury and death during cryopreservation. Therefore, alternative CPAs that have the ability to inhibit ice recrystallization are very appealing additives to cryo-solutions. SAR studies on various BAs have facilitated the discovery of key structural features for IRI activity, which in turn, have allowed the synthesis of several classes of small molecule carbohydrate-based IRIs. *O*-alkyl glucosides have been demonstrated to be excellent ice recrystallization inhibitors; however, their surfactant-like features have limited their application. Substituting the long alkyl chain moiety with aryl groups has led to the development of aryl-linked glycosides which have been shown to improve the cryopreservation outcomes of RBCs. Further investigations led to the discovery of *N*-aryl-D-gluconamide that have been shown to preserve stem cells such as HSCs and iPSCs. Continued SAR studies of IRI-active compounds will aid in the identification of additional structural properties required for IRI activity and will help in understanding the mechanism of action by which IRIs inhibit the ice recrystallization process. Ultimately, the development of small molecule IRIs that protect cellular therapy products from the cryoinjury associated with ice recrystallization will help to improve current cryopreservation protocols and assist in developing master cell banks for different cellular therapies.

1.5 References

(1) Sampogna, G.; Guraya, S. Y.; Forgione, A. Regenerative Medicine: Historical Roots and Potential Strategies in Modern Medicine. *J. Microsc. Ultrastruct.* **2015**, *3* (3), 101–107. https://doi.org/10.1016/j.jmau.2015.05.002.

(2) Mason, C.; Manzotti, E. Editorial: Regenerative Medicine Cell Therapies: Numbers of Units Manufactured and Patients Treated between 1988 and 2010. *Regen. Med.* **2010**, *5* (3), 307–313. https://doi.org/10.2217/rme.10.37.

(3) Edwards, J.; Thomas, R.; Guilliatt, R. Regenerative Medicine: From the Laboratory

Looking Out. *Palgrave Commun.* **2017**, *3* (1). https://doi.org/10.1057/s41599-017-0036-x.

(4) Gage, F. H.; Temple, S. Neural Stem Cells: Generating and Regenerating the Brain. *Neuron* **2013**, *80* (3), 588–601. https://doi.org/10.1016/j.neuron.2013.10.037.

(5) Ratcliffe, E.; Thomas, R. J.; Williams, D. J. Current Understanding and Challenges in Bioprocessing of Stem Cell-Based Therapies for Regenerative Medicine. *Br. Med. Bull.* **2011**, *100* (1), 137–155. https://doi.org/10.1093/bmb/ldr037.

(6) Hainaut, P.; Vaught, J.; Zatloukal, K.; Pasterk, M. *Biobanking of Human Biospecimens: Principles and Practice*; 2017. https://doi.org/10.1007/978-3-319-55120-3.

(7) Asghar, W.; El Assal, R.; Shafiee, H.; Anchan, R. M.; Demirci, U. Preserving Human Cells for Regenerative, Reproductive, and Transfusion Medicine. *Biotechnol. J.* **2014**, *9* (7), 895–903. https://doi.org/10.1002/biot.201300074.

(8) Volkman, R.; Offen, D. Concise Review: Mesenchymal Stem Cells in Neurodegenerative Diseases. *Stem Cells* **2017**, *35* (8), 1867–1880. https://doi.org/10.1002/stem.2651.

(9) John, H.; Gerald, H. Alzheimer' s Disease : The Amyloid Cascade Hypothesis. *Science (80).* **1992**, *256*, 184–185.

(10) Woods, E. J.; Thirumala, S.; Badhe-Buchanan, S. S.; Clarke, D.; Mathew, A. J. Off the Shelf Cellular Therapeutics: Factors to Consider during Cryopreservation and Storage of Human Cells for Clinical Use. *Cytotherapy* **2016**, *18* (6), 697–711. https://doi.org/10.1016/j.jcyt.2016.03.295.

(11) Giwa, S.; Lewis, J. K.; Alvarez, L.; Langer, R.; Roth, A. E.; Church, G. M.; Markmann, J. F.; Sachs, D. H.; Chandraker, A.; Wertheim, J. A.; Rothblatt, M.; Boyden, E. S.; Eidbo, E.; Lee, W. P. A.; Pomahac, B.; Brandacher, G.; Weinstock, D. M.; Elliott, G.; Nelson, D.; Acker, J. P.; Uygun, K.; Schmalz, B.; Weegman, B. P.; Tocchio, A.; Fahy, G. M.; Storey, K. B.; Rubinsky, B.; Bischof, J.; Elliott, J. A. W.; Woodruff, T. K.; Morris, G. J.; Demirci, U.; Brockbank, K. G. M.; Woods, E. J.; Ben, R. N.; Baust, J. G.; Gao, D.; Fuller, B.; Rabin, Y.; Kravitz, D. C.; Taylor, M. J.; Toner, M. The Promise of Organ and Tissue Preservation to Transform Medicine. *Nat. Biotechnol.* **2017**, *35* (6), 530–542.

https://doi.org/10.1038/nbt.3889.

(12) Stacey, G. N.; Masters, J. R. Cryopreservation and Banking of Mammalian Cell Lines. *Nat. Protoc.* **2008**, *3* (12), 1981–1989. https://doi.org/10.1038/nprot.2008.190.

(13) Baust, J. G.; Gao, D.; Baust, J. M. Cryopreservation: An Emerging Paradigm Change. *Organogenesis* **2009**, *5* (3), 90–96. https://doi.org/10.4161/org.5.3.10021.

(14) Zhang, C.-L.; Huang, T.; Wu, B.-L.; He, W.-X.; Liu, D. Stem Cells in Cancer Therapy: Opportunities and Challenges. *Oncotarget* **2017**, *8* (43), 75756–75766. https://doi.org/10.18632/oncotarget.20798.

(15) Jang, T. H.; Park, S. C.; Yang, J. H.; Kin, J. Y.; Seok, J. H.; Park, U. S.; Choi, C. W.; Lee, S. R.; Han, J. Cryopreservation and Its Clinical Applications. *Integr. Med. Res.* **2017**, *6* (1), 12–18. https://doi.org/10.1016/j.imr.2016.12.001.

(16) Seggio, A. M.; Ellison, K. S.; Hynd, M. R.; Shainc, W.; Thompson, D. M. Cryopreservation of Transfected Primary Dorsal Root Ganglia Neurons. *J. Neurosci. Methods* **2008**, *173* (1), 67–73. https://doi.org/10.1016/j.jneumeth.2008.05.017.

(17) Robert, M. C.; Juan de Paz, L.; Graf, D. A.; Gazzin, S.; Tiribelli, C.; Bottai, H.; Rodriguez, J. V. Cryopreservation by Slow Cooling of Rat Neuronal Cells. *Cryobiology* **2016**, *72* (3), 191–197. https://doi.org/10.1016/j.cryobiol.2016.05.003.

(18) Angel, S.; von Briesen, H.; Oh, Y.-J.; Baller, M. K.; Zimmermann, H.; Germann, A. Toward Optimal Cryopreservation and Storage for Achievement of High Cell Recovery and Maintenance of Cell Viability and T Cell Functionality. *Biopreserv. Biobank.* **2016**, *14* (6), 539–547. https://doi.org/10.1089/bio.2016.0046.

(19) Schmidt-Wolf, I. G. H.; Aihara, M.; Negrin, R. S.; Blume, K. G.; Chao, N. J. Lymphokine-Activated Killer Cell Activity after Cryopreservation. *J. Immunol. Methods* **1989**, *125* (1–2), 185–189. https://doi.org/10.1016/0022-1759(89)90092-6.

(20) Gao, D.; Critser, J. K. Mechanisms of Cryoinjury in Living Cells. *ILAR J.* **2000**, *41* (4), 187–196. https://doi.org/10.1093/ilar.41.4.187.

(21) Mata, M. M.; Mahmood, F.; Sowell, R. T.; Baum, L. L. Effects of Cryopreservation

on Effector Cells for Antibody Dependent Cell-Mediated Cytotoxicity (ADCC) and Natural Killer (NK) Cell Activity in 51Cr-Release and CD107a Assays. *J. Immunol. Methods* **2014**, *406*, 1–9. https://doi.org/10.1016/j.jim.2014.01.017.

(22) Domogala, A.; Alejandro Madrigal, J.; Saudemont, A. Cryopreservation Has No Effect on Function of Natural Killer Cells Differentiated in Vitro from Umbilical Cord Blood CD34+ Cells. *Cytotherapy* **2016**, *18* (6), 754–759. https://doi.org/10.1016/j.jcyt.2016.02.008.

(23) Weinberg, A.; Song, L. Y.; Wilkening, C.; Sevin, A.; Blais, B.; Louzao, R.; Stein, D.; Defechereux, P.; Durand, D.; Riedel, E.; Raftery, N.; Jesser, R.; Brown, B.; Keller, M. F.; Dickover, R.; McFarland, E.; Fenton, T. Optimization and Limitations of Use of Cryopreserved Peripheral Blood Mononuclear Cells for Functional and Phenotypic T-Cell Characterization. *Clin. Vaccine Immunol.* **2009**, *16* (8), 1176–1186. https://doi.org/10.1128/CVI.00342-08.

(24) Wang, S. Y.; Hsu, M. L.; Tzeng, C. H.; Hsu, H. C.; Ho, C. K. The Influence of Cryopreservation on Cytokine Production by Human T Lymphocytes. *Cryobiology* **1998**, *37* (1), 22–29. https://doi.org/10.1006/cryo.1998.2094.

(25) Buskirk, R. G. Van; Baust, J. M.; Snyder, K. K.; Mathew, A. J.; Baust, J. G. Hypothermic Storage and Cryopreservation. *Bioprocess Int.* **2004**, 42–49.

(26) Holovati, J. L.; Hannon, J. L.; Gyongyossy-Issa, M. I. C.; Acker, J. P. Blood Preservation Workshop: New and Emerging Trends in Research and Clinical Practice. *Transfus. Med. Rev.* **2009**, *23* (1), 25–41. https://doi.org/10.1016/j.tmrv.2008.09.003.

(27) Scott, K. L.; Lecak, J.; Acker, J. P. Biopreservation of Red Blood Cells: Past, Present, and Future. *Transfus. Med. Rev.* **2005**, *19* (2), 127–142. https://doi.org/10.1016/j.tmrv.2004.11.004.

(28) Baust, J. M.; Van Buskirk, R.; Baust, J. G. Gene Activation of the Apoptotic Caspase Cascade Following Cryogenic Storage. *Cell Preserv. Technol.* **2003**, *1* (1), 63–80. https://doi.org/10.1089/15383440260073301.

(29) Brockbank, K. G. An Alternative Strategy for Reducing Tissue Immunogenicity Using Ice-Free Cryopreservation. *MOJ Cell Sci. Rep.* **2016**, *3* (3), 76–79. https://doi.org/10.15406/mojcsr.2016.03.00058.

(30) G.M, F.; Wowk, B. Principles of Cryopreservation by Vitrification. *Methods Mol. Biol.* **2015**, 21–82. https://doi.org/10.1007/978-1-4939-2193-5_24.

(31) Kasai, M.; Mukaida, T. Cryopreservation of Animal and Human Embryos by Vitrification. *Reprod. Biomed. Online* **2004**, *9* (2), 164–170. https://doi.org/10.1016/S1472-6483(10)62125-6.

(32) Barry J. Fuller, Nick Lane, and Erica E. Benson, E. Life in the Frozen State. Boca. *Boca Raton, Florida CRC Press* **2004**, *83* (3), 696. https://doi.org/10.1016/j.fertnstert.2004.10.025.

(33) Fuller, B. J.; Petrenko, A. Y.; Rodriguez, J. V.; Somov, A. Y.; Balaban, C. L.; Guibert, E. E. Biopreservation of Hepatocytes: Current Concepts on Hypothermic Preservation, Cryopreservation, and Vitrification. *Cryo-Letters* **2016**, *37* (4), 432–452.

(34) Baust, J. M. Advances in Media for Cryopreservation and Hypothermic Storage. *BioProcess Int* **2005**, *3* (6), 46–56.

(35) Rubinsky, B. Principles of Low Temperature Cell Preservation. *Heart Fail. Rev.* **2003**, *8*, 277–284. https://doi.org/10.1023/A.

(36) CORREIA, C.; KOSHKIN, A.; CARIDO, M.; ESPINHA, N.; SARIC, T.; LIMA, P. A.; SERRA, M.; ALVES, P. M. Effective Hypothermic Storage of Human Pluripotent Stem Cell-Derived Cardiomyocytes Compatible With Global Distribution of Cells for Clinical Applications and Toxicology Testing. *Stem Cells Transl. Med.* **2016**, *5*, 658–669.

(37) Zenhäusern, R.; Tobler, A.; Leoncini, L.; Hess, O. M.; Ferrari, P. Fatal Cardiac Arrhythmia after Infusion of Dimethyl Sulfoxide-Cryopreserved Hematopoietic Stem Cells in a Patient with Severe Primary Cardiac Amyloidosis and End-Stage Renal Failure. *Ann. Hematol.* **2000**, *79* (9), 523–526. https://doi.org/10.1007/s002770000186.

(38) Fahy, G. M.; Mouta, C. da; Tsonev, L.; Khirabadi, B. S.; Mehl, P.; Meryman, H. T. Cellular Injury Associated with Organ Cryopreservation: Chemical Toxicity and Cooling Injury. In *Cell Biology of Trauma*; 1995; pp 333–356. https://doi.org/10.1201/9781003067801-25.

(39) Baust, J. M. Molecular Mechanisms of Cellular Demise Associated with

Cryopreservation Failure. *Cell Preserv. Technol.* **2003**, *1* (1), 17–31. https://doi.org/10.1089/15383440260073266.

(40) Jurisicova, A. Involvement of Programmed Cell Death in Preimplantation Embryo Demise. *Hum. Reprod. Update* **1995**, *1* (6), 558–566. https://doi.org/10.1093/humupd/1.6.558.

(41) Mazur, P. Cryobiology : The Freezing of Biological Systems. *Am. Assoc. Adv. Sci.* **1970**, *168* (3934), 939–949.

(42) Fowler, A.; Toner, M. Cryo-Injury and Biopreservation. *Ann. N. Y. Acad. Sci.* **2006**, *1066*, 119–135. https://doi.org/10.1196/annals.1363.010.

(43) Mazur, P.; Leibo, S. P.; Chu, E. H. Y. A Two-Factor Hypothesis of Freezing Injury. Evidence from Chinese Hamster Tissue-Culture Cells. *Exp. Cell Res.* **1972**, *71* (2), 345–355. https://doi.org/10.1016/0014-4827(72)90303-5.

(44) Mullen, S. F.; Critser, J. K. The Science of Cryobiology. *Cancer Treat Res* **2007**, *138*, 83.

(45) Mazur, P. Kinetics of Water Loss From Cells At Subzero Temperatures and the Likelihood of Intracellular Freezing. *J. Gen. Physiol.* **1963**, *47*, 347–369. https://doi.org/10.1085/jgp.47.2.347.

(46) Lovelock, J. E. The Denaturation of Lipid-Protein Complexes as a Cause of Damage by Freezing. *R. Soc. London. Ser. B, Biol. Sci.* **1957**, *147* (929), 427–433.

(47) Shimada, K.; Asahina, E. Visualization of Intracellular Ice Crystals Formed in Very Rapidly Frozen Cells at -27 °C. *Cryobiology* **1975**, *12* (3), 209–218. https://doi.org/10.1016/0011-2240(75)90019-X.

(48) Bank, H. Visualization of Freezing Damage. II. Structural Alterations during Warming. *Cryobiology* **1973**, *10* (2), 157–170. https://doi.org/10.1016/0011-2240(73)90023-0.

(49) Meryman, H. T. Cryoprotective Agents. *Cryobiology* **1971**, *8* (2), 173–183.

(50) McGann, L. E. Differing Actions of Penetrating and Nonpenetrating Cryoprotective Agents. *Cryobiology* **1978**, *15* (4), 382–390. https://doi.org/10.1016/0011-2240(78)90056-1.

(51) Lovelock, J. E. The Mechanism of the Protective Action of Glycerol against Haemolysis by Freezing and Thawing. *BBA - Biochim. Biophys. Acta* **1953**, *11* (C),

28–36. https://doi.org/10.1016/0006-3002(53)90005-5.

(52) LOVELOCK, J. E. The Protective Action of Neutral Solutes against Haemolysis by Freezing and Thawing. *Biochem. J.* **1954**, *56* (2), 265–270. https://doi.org/10.1042/bj0560265.

(53) Lovelock, J. E.; Bishop, M. W. . Prevention of Freezing Damage to Living Cells by Dimethyl Sulphoxide. *Nature* **1959**, *183* (1), 1394–1395.

(54) Meryman, H. T. Freezing Injury and Its Prevention in Living Cells. *Annu. Rev. Biophys. Bioeng.* **1974**, *3* (0), 341–363. https://doi.org/10.1146/annurev.bb.03.060174.002013.

(55) Elliott, G. D.; Wang, S.; Fuller, B. J.; Charlotte, C. CRYOPROTECTANTS : A REVIEW OF THE ACTIONS AND APPLICATIONS OF CRYOPROTECTIVE SOLUTES THAT MODULATE CELL RECOVERY FROM ULTRA-LOW TEMPERATURES of Mechanical Engineering and Engineering Science , University of North Carolina at Charlotte , Charlotte , USA ; **2017**, *1* (704), 1–78.

(56) Hallare, A. V.; Köhler, H. R.; Triebskorn, R. Developmental Toxicity and Stress Protein Responses in Zebrafish Embryos after Exposure to Diclofenac and Its Solvent, DMSO. *Chemosphere* **2004**, *56* (7), 659–666. https://doi.org/10.1016/j.chemosphere.2004.04.007.

(57) Best, B. P. Cryoprotectant Toxicity: Facts, Issues, and Questions. *Rejuvenation Res.* **2015**, *18* (5), 422–436. https://doi.org/10.1089/rej.2014.1656.

(58) Fuller, B. J. Cryoprotectants: The Essential Antifreezes to Protect Life in the Frozen State. *Cryo-Letters* **2004**, *25* (6), 375–388.

(59) Sasnoor, L. M.; Kale, V. P.; Limaye, L. S. Supplementation of Conventional Freezing Medium with a Combination of Catalase and Trehalose Results in Better Protection of Surface Molecules and Functionality of Hematopoietic Cells. *J. Hematotherapy Stem Cell Res.* **2003**, *12* (5), 553–564. https://doi.org/10.1089/152581603322448268.

(60) Svalgaard, J. D.; Haastrup, E. K.; Reckzeh, K.; Holst, B.; Glovinski, P. V.; Gørløv, J. S.; Hansen, M. B.; Moench, K. T.; Clausen, C.; Fischer-Nielsen, A. Low-Molecular-Weight Carbohydrate Pentaisomaltose May Replace Dimethyl Sulfoxide as a Safer Cryoprotectant for Cryopreservation of Peripheral Blood Stem

Cells. *Transfusion* **2016**, *56* (5), 1088–1095. https://doi.org/10.1111/trf.13543.

(61) Svalgaard, J. D.; Talkhoncheh, M. S.; Haastrup, E. K.; Munthe-Fog, L.; Clausen, C.; Hansen, M. B.; Andersen, P.; Gørløv, J. S.; Larsson, J.; Fischer-Nielsen, A. Pentaisomaltose, an Alternative to DMSO. Engraftment of Cryopreserved Human CD34+ Cells in Immunodeficient NSG Mice. *Cell Transplant.* **2018**, *27* (9), 1407–1412. https://doi.org/10.1177/0963689718786226.

(62) Xian, M.; Fatima, Z.; Zhang, W.; Fang, J.; Li, H.; Pei, D.; Loo, J.; Stevenson, T.; Wang, P. G. Identification of α-Galactosyl Epitope Mimetics through Rapid Generation and Screening of C-Linked Glycopeptide Library. *J. Comb. Chem.* **2004**, *6* (1), 126–134. https://doi.org/10.1021/cc030042u.

(63) Motta, J. P. R.; Paraguassú-Braga, F. H.; Bouzas, L. F.; Porto, L. C. Evaluation of Intracellular and Extracellular Trehalose as a Cryoprotectant of Stem Cells Obtained from Umbilical Cord Blood. *Cryobiology* **2014**, *68* (3), 343–348. https://doi.org/10.1016/j.cryobiol.2014.04.007.

(62) Poisson, J.; Briard, J.; Turner, T.; Acker, J.; Ben, R. Hydroxyethyl Starch Supplemented with Ice Recrystallization Inhibitors Greatly Improves Cryopreservation of Human Red Blood Cells. *Bioprocess. J.* **2017**, *15* (4), 16–21. https://doi.org/10.12665/j154.ben.

(63) Arakawa, T.; Carpenter, J. F.; Kita, Y. A.; Crowe, J. H. The Basis for Toxicity of Certain Cryoprotectants: A Hypothesis. *Cryobiology* **1990**, *27* (4), 401–415. https://doi.org/10.1016/0011-2240(90)90017-X.

(64) Ohboshi, S.; Fujihara, N.; Yoshida, T.; Tomogane, H. Usefulness of Polyethylene Glycol for Cryopreservation by Vitrification of in Vitro-Derived Bovine Blastocysts. *Anim. Reprod. Sci.* **1997**, *48* (1), 27–36. https://doi.org/10.1016/S0378-4320(97)00034-1.

(65) Anchordoguy, T. J.; Rudolph, A. S.; Carpenter, J. F.; Crowe, J. H. Modes of Interaction of Cryoprotectants with Membrane Phospholipids during Freezing. *Cryobiology* **1987**, *24* (4), 324–331. https://doi.org/10.1016/0011-2240(87)90036-8.

(66) Crowe, J. H.; Crowe, L. M.; Carpenter, J. F.; Rudolph, A. S.; Wistrom, C. A.; Spargo, B. J.; Anchordoguy, T. J. Interactions of Sugars with Membranes. *BBA* -

Rev. Biomembr. **1988**, *947* (2), 367–384. https://doi.org/10.1016/0304-4157(88)90015-9.

(67) Rudolph, A. S.; Crowe, J. H. Membrane Stabilization during Freezing: The Role of Two Natural Cryoprotectants, Trehalose and Proline. *Cryobiology* **1985**, *22* (4), 367–377. https://doi.org/10.1016/0011-2240(85)90184-1.

(68) Zhang, C.; Deng, Y.; Dai, H.; Zhou, W.; Tian, J.; Bing, G.; Zhao, L. Effects of Dimethyl Sulfoxide on the Morphology and Viability of Primary Cultured Neurons and Astrocytes. *Brain Res. Bull.* **2017**, *128*, 34–39. https://doi.org/10.1016/j.brainresbull.2016.11.004.

(69) Yang, H.; Zhao, H.; Acker, J. P.; Liu, J. Z.; Akabutu, J.; McGann, L. E. Effect of Dimethyl Sulfoxide on Post-Thaw Viability Assessment of CD45 + and CD34+ Cells of Umbilical Cord Blood and Mobilized Peripheral Blood. *Cryobiology* **2005**, *51* (2), 165–175. https://doi.org/10.1016/j.cryobiol.2005.06.003.

(70) Tamagnini, F.; Scullion, S.; Brown, J. T.; Randall, A. D. Low Concentrations of the Solvent Dimethyl Sulphoxide Alter Intrinsic Excitability Properties of Cortical and Hippocampal Pyramidal Cells. *PLoS One* **2014**, *9* (3). https://doi.org/10.1371/journal.pone.0092557.

(71) Dominguez, E.; Lowdell, M. W.; Perez-Cruz, I.; Madrigal, A.; Cohen, S. B. A. Natural Killer Cell Function Is Altered by Freezing in DMSO. *Biochem. Soc. Trans.* **1997**, *25* (2), 997. https://doi.org/10.1042/bst025175s.

(72) Holthaus, L.; Lamp, D.; Gavrisan, A.; Sharma, V.; Ziegler, A. G.; Jastroch, M.; Bonifacio, E. CD4+ T Cell Activation, Function, and Metabolism Are Inhibited by Low Concentrations of DMSO. *J. Immunol. Methods* **2018**, *463* (June), 54–60. https://doi.org/10.1016/j.jim.2018.09.004.

(73) Stroncek, D.; Fautsch, S.; Lasky, L.; Hurd, D.; Ramsay, N.; McCullough, J. Adverse Reactions in Patients Transfused with Cryopreserved Marrow. *Transfusion* **1991**, *31* (6), 521–526. https://doi.org/10.1046/j.1537-2995.1991.31691306250.x.

(74) Shu, Z.; Heimfeld, S.; Gao, D. Hematopoietic SCT with Cryopreserved Grafts: Adverse Reactions after Transplantation and Cryoprotectant Removal before Infusion. *Bone Marrow Transplant.* **2014**, *49* (4), 469–476.

https://doi.org/10.1038/bmt.2013.152.

(75) Wang, X.; Hua, T. C.; Sun, D. W.; Liu, B.; Yang, G.; Cao, Y. Cryopreservation of Tissue-Engineered Dermal Replacement in Me2SO: Toxicity Study and Effects of Concentration and Cooling Rates on Cell Viability. *Cryobiology* **2007**, *55* (1), 60–65. https://doi.org/10.1016/j.cryobiol.2007.05.006.

(76) Khawandanah, M.; Hopps, S.; Nabeel, S.; Ahmad, B.; Weiss, S.; Holter Charkrabarty, J.; Yuen, C.; Selby, G. DMSO Induced Myocardial Infarction during Allogeneic Cryopreserved Bone Marrow Transplant. *Ann. Hematol.* **2015**, *94* (3), 511–513. https://doi.org/10.1007/s00277-014-2181-2.

(77) Mitrus, I.; Smagur, A.; Fidyk, W.; Czech, M.; Prokop, M.; Chwieduk, A.; Glowala-Kosinska, M.; Czerw, T.; Sobczyk-Kruszelnicka, M.; Mendrek, W.; Michalak, K.; Sadus-Wojciechowska, M.; Najda, J.; Holowiecki, J.; Giebel, S. Reduction of DMSO Concentration in Cryopreservation Mixture from 10% to 7.5% and 5% Has No Impact on Engraftment after Autologous Peripheral Blood Stem Cell Transplantation: Results of a Prospective, Randomized Study. *Bone Marrow Transplant.* **2018**, *53* (3), 274–280. https://doi.org/10.1038/s41409-017-0056-6.

(78) Min, B.; Choi, H.; Her, J. H.; Jung, M. Y.; Kim, H. J.; Jung, M. Y.; Lee, E. K.; Cho, S. Y.; Hwang, Y. K.; Shin, E. C. Optimization of Large-Scale Expansion and Cryopreservation of Human Natural Killer Cells for Anti-Tumor Therapy. *Immune Netw.* **2018**, *18* (4), 1–13. https://doi.org/10.4110/in.2018.18.e31.

(79) Capicciotti, C. J.; ;Doshi, M. .; Ben, R. N. Ice Recrystallization Inhibitors: From Biological Antifreezes to Small Molecules. *Recent Dev. Study Recryst. Wilson, P., Ed.; InTech Open, Ltd. London, UK* **2013**, 177–224. https://doi.org/10.5772/54992.

(80) Venketesh, S.; Dayananda, C. Properties, Potentials, and Prospects of Antifreeze Proteins. *Crit. Rev. Biotechnol.* **2008**, *28* (1), 57–82. https://doi.org/10.1080/07388550801891152.

(81) Petzold, G.; Aguilera, J. M. Ice Morphology: Fundamentals and Technological Applications in Foods. *Food Biophys.* **2009**, *4* (4), 378–396. https://doi.org/10.1007/s11483-009-9136-5.

(82) Thurmer, K.; Nie, S. Formation of Hexagonal and Cubic Ice during Low-Temperature Growth. *Proc. Natl. Acad. Sci. U. S. A.* **2013**, *110* (29), 11757–11762.

https://doi.org/10.1073/pnas.1303001110.

(83) Fletcher, N. H. The Chemical Physics of Ice. *Am. Assoc. Adv. Sci.* **1970**, *169* (3947), 756.

(84) Hobbs, P. V. Ice Physics. *J. Glaciol. Oxford, Clarendon Press* **1976**, *17* (75), 155–156.

(85) Petrenko, V.; Whithworth, R. The Physics of Ice. *J. ofGlaciology, Oxford Univ. Press* **2000**, *46* (153), 384.

(86) Shultz, M. J. Ice Surfaces. *Annu. Rev. Phys. Chem.* **2017**, *68* (March), 285–304. https://doi.org/10.1146/annurev-physchem-052516-044813.

(87) Malkin, T. L.; Murray, B. J.; Salzmann, C. G.; Molinero, V.; Pickering, S. J.; Whale, T. F. Stacking Disorder in Ice I. *Phys. Chem. Chem. Phys.* **2015**, *17* (1), 60–76. https://doi.org/10.1039/c4cp02893g.

(88) Malkin, T. L.; Murray, B. J.; Brukhno, A. V.; Anwar, J.; Salzmann, C. G. Structure of Ice Crystallized from Supercooled Water. *Proc. Natl. Acad. Sci. U. S. A.* **2012**, *109* (4), 1041–1045. https://doi.org/10.1073/pnas.1113059109.

(89) Li, T.; Donadio, D.; Russo, G.; Galli, G. Homogeneous Ice Nucleation from Supercooled Water. *Phys. Chem. Chem. Phys.* **2011**, *13* (44), 19807–19813. https://doi.org/10.1039/c1cp22167a.

(90) Haji-Akbari, A.; Debenedetti, P. G. Direct Calculation of Ice Homogeneous Nucleation Rate for a Molecular Model of Water. *Proc. Natl. Acad. Sci. U. S. A.* **2015**, *112* (34), 10582–10588. https://doi.org/10.1073/pnas.1509267112.

(91) Lupi, L.; Hudait, A.; Peters, B.; Grünwald, M.; Gotchy Mullen, R.; Nguyen, A. H.; Molinero, V. Role of Stacking Disorder in Ice Nucleation. *Nature* **2017**, *551* (7679), 218–222. https://doi.org/10.1038/nature24279.

(92) Moore, E. B.; Molinero, V. Is It Cubic? Ice Crystallization from Deeply Supercooled Water. *Phys. Chem. Chem. Phys.* **2011**, *13* (44), 20008–20016. https://doi.org/10.1039/c1cp22022e.

(93) Devries, A. L.; Lin, Y. Structure of a Peptide Antifreeze and Mechanism of Adsorption to Ice. *Biochim. Biophys. Acta - Protein Struct.* **1977**, *495* (2), 388–392. https://doi.org/10.1016/0005-2795(77)90395-6.

(94) Olijve, L. L. C.; Meister, K.; DeVries, A. L.; Duman, J. G.; Guo, S.; Bakker, H. J.;

Voetsa, I. K. Blocking Rapid Ice Crystal Growth through Nonbasal Plane Adsorption of Antifreeze Proteins. *Proc. Natl. Acad. Sci. U. S. A.* **2016**, *113* (14), 3740–3745. https://doi.org/10.1073/pnas.1524109113.

(95) Nenow, D. Surface Premelting. *Prog. Cryst. Growth Charact.* **1984**, *9* (3–4), 185–225. https://doi.org/10.1016/0146-3535(84)90081-9.

(96) Harding, M. M.; Ward, L. G.; Haymet, A. D. J. Type I 'Antifreeze'Proteins. *Eur. J. Biochem* **1999**, *264*, 653–665.

(97) Hayward, J. A.; Haymet, A. D. J. Ice/Water Interface: Molecular Dynamics Simulations of the Basal, Prism, {20$\bar{2}$1}, and {2$\bar{1}\bar{1}$0} Interfaces of Ice Ih. *J. Chem. Phys.* **2001**, *114* (8), 3713–3726. https://doi.org/10.1063/1.1333680.

(98) Karim, O. A.; Kay, P. A.; Haymet, A. D. J. The Ice/Water Interface: A Molecular Dynamics Simulation Using the Simple Point Charge Model. *J. Chem. Phys.* **1990**, *92* (7), 4634–4635. https://doi.org/10.1063/1.457730.

(99) Harding, M. M.; Anderberg, P. I.; Haymet, A. D. J. "Antifreeze" Glycoproteins from Polar Fish. *Eur. J. Biochem.* **2003**, *270* (7), 1381–1392. https://doi.org/10.1046/j.1432-1033.2003.03488.x.

(100) Furukawa, Y.; Ishikawa, I. Direct Evidence for Melting Transition at Interface between Ice Crystal and Glass Substrate. *J. Cryst. Growth* **1993**, *128* (1-4 PART 2), 1137–1142. https://doi.org/10.1016/S0022-0248(07)80112-6.

(101) Fletcher, N. H. Surface Structure of Water and Ice. *Philos. Mag.* **1968**, *18* (156), 1287–1300. https://doi.org/10.1080/14786436808227758.

(102) Beaglehole, D.; Nason, D. Transition Layer on the Surface on Ice. *Surf. Sci.* **1980**, *96* (1–3), 357–363. https://doi.org/10.1016/0039-6028(80)90313-1.

(103) Faraday, P. X. On Regelation, and on the Conservation of Force. *London, Edinburgh, Dublin Philos. Mag. J. Sci.* **1858**, *17* (113), 162–169.

(104) Bilgram, J. H. The Structure and Properties of Melt and Concentrated Solutions. *Prog. Cryst. Growth Charact. Mater.* **1993**, *26* (C), 99–119. https://doi.org/10.1016/0960-8974(93)90012-S.

(105) Halter, P. U.; Bilgram, J. H.; Känzig, W. Properties of the Solid-Liquid Interface Layer of Growing Ice Crystals: A Raman and Rayleigh Scattering Study. *J. Chem. Phys.* **1988**, *89* (5), 2622–2629. https://doi.org/10.1063/1.455011.

(106) Björneholm, O.; Hansen, M. H.; Hodgson, A.; Liu, L. M.; Limmer, D. T.; Michaelides, A.; Pedevilla, P.; Rossmeisl, J.; Shen, H.; Tocci, G.; Tyrode, E.; Walz, M. M.; Werner, J.; Bluhm, H. Water at Interfaces. *Chem. Rev.* **2016**, *116* (13), 7698–7726. https://doi.org/10.1021/acs.chemrev.6b00045.

(107) Goertz, M. P.; Zhu, X. Y.; Houston, J. E. Exploring the Liquid-like Layer on the Ice Surface. *Langmuir* **2009**, *25* (12), 6905–6908. https://doi.org/10.1021/la9001994.

(108) Henson, B. F.; Voss, L. F.; Wilson, K. R.; Robinson, J. M. Thermodynamic Model of Quasiliquid Formation on H 2O Ice: Comparison with Experiment. *J. Chem. Phys.* **2005**, *123* (14). https://doi.org/10.1063/1.2056541.

(109) Furukawa, Y.; Yamamoto, M.; Kuroda, T. Ellipsometric Study of the Transition Layer on the Surface of an Ice Crystal. *J. Cryst. Growth* **1987**, *82* (4), 665–677. https://doi.org/10.1016/S0022-0248(87)80012-X.

(110) Döppenschmidt, A.; Kappl, M.; Butt, H. J. Surface Properties of Ice Studied by Atomic Force Microscopy. *J. Phys. Chem. B* **1998**, *102* (40), 7813–7819. https://doi.org/10.1021/jp981396s.

(111) Bluhm, H.; Ogletree, D. F.; Fadley, C. S.; Hussain, Z.; Salmeron, M. The Premelting of Ice Studied with Photoelectron Spectroscopy. *J. Phys. Condens. Matter* **2002**, *14* (8). https://doi.org/10.1088/0953-8984/14/8/108.

(112) Beaglehole, D.; Wilson, P. Thickness and Anisotropy of the Ice-Water Interface. *J. Phys. Chem.* **1993**, *97* (42), 11053–11055. https://doi.org/10.1021/j100144a025.

(113) Fitzner, M.; Sosso, G. C.; Cox, S. J.; Michaelides, A. Ice Is Born in Low-Mobility Regions of Supercooled Liquid Water. *Proc. Natl. Acad. Sci. U. S. A.* **2019**, *116* (6), 2009–2014. https://doi.org/10.1073/pnas.1817135116.

(114) Elbaum, M.; Lipson, S. G.; Dash, J. G. Optical Study of Surface Melting on Ice. *J. Cryst. Growth* **1993**, *129* (3–4), 491–505. https://doi.org/10.1016/0022-0248(93)90483-D.

(115) Dosch, H.; Lied, A.; Bilgram, J. H. Disruption of the Hydrogen-Bonding Network at the Surface of Ih Ice near Surface Premelting. *Surf. Sci.* **1996**, *366* (1), 43–50. https://doi.org/10.1016/0039-6028(96)00805-9.

(116) Golecki, I.; Jaccard, C. Journal of Physics C : Solid State Physics Related Content

Intrinsic Surface Disorder in Ice near the Melting Point. *J. Phys. C Solid State Phys.* **1978**, *11*, 4229–4237.

(117) Knight, C. A. Grain Boundary Migration and Other Processes in the Formation of Ice Sheets on Water. *J. Appl. Phys.* **1966**, *37* (2), 568–574. https://doi.org/10.1063/1.1708217.

(118) Knight, C. A.; Wen, D.; Laursen, R. A. Nonequilibrium Antifreeze Peptides and the Recrystallization of Ice. *Cryobiology*. 1995, pp 23–34. https://doi.org/10.1006/cryo.1995.1002.

(119) Alley, R. B.; Perepezko, J. H.; Bentley, C. R. Grain Growth in Polar Ice: II. Application. *J. Glaciol.* **1986**, *32* (112), 425–433. https://doi.org/10.3189/s0022143000012132.

(120) Budke, C.; Heggemann, C.; Koch, M.; Sewald, N.; Koop, T. Ice Recrystallization Kinetics in the Presence of Synthetic Antifreeze Glycoprotein Analogues Using the Framework of LSW Theory. *J. Phys. Chem. B* **2009**, *113* (9), 2865–2873. https://doi.org/10.1021/jp805726e.

(121) Sutton, R. L.; Lips, A.; Piccirillo, G.; Sztehlo, A. Kinetics of Ice Recrystallization in Aqueous Fructose Solutions. *J. Food Sci.* **1996**, *61* (4), 741–745. https://doi.org/10.1111/j.1365-2621.1996.tb12194.x.

(122) Cook, K. L. K.; Hartel, R. W. Mechanisms of Ice Crystallization in Ice Cream Production. *Compr. Rev. Food Sci. Food Saf.* **2010**, *9* (2), 213–222. https://doi.org/10.1111/j.1541-4337.2009.00101.x.

(123) Van Westen, T.; Groot, R. D. Predicting the Kinetics of Ice Recrystallization in Aqueous Sugar Solutions. *Cryst. Growth Des.* **2018**, *18* (4), 2405–2416. https://doi.org/10.1021/acs.cgd.8b00038.

(124) Dalvi-Isfahan, M.; Jha, P. K.; Tavakoli, J.; Daraei-Garmakhany, A.; Xanthakis, E.; Le-Bail, A. Review on Identification, Underlying Mechanisms and Evaluation of Freezing Damage. *J. Food Eng.* **2019**, *255* (March), 50–60. https://doi.org/10.1016/j.jfoodeng.2019.03.011.

(125) Alley, R. B.; Perepezko, J. H.; Bentley, C. R. Grain Growth in Polar Ice: I. Application. *J. Glaciol.* **1986**, *32* (112), 425–433. https://doi.org/10.3189/s0022143000012132.

(126) Van Westen, T.; Groot, R. D. Effect of Temperature Cycling on Ostwald Ripening. *Cryst. Growth Des.* **2018**, *18* (9), 4952–4962. https://doi.org/10.1021/acs.cgd.8b00267.

(127) Scholander, P. F.; van Dam, L.; Kanwisher, J. W.; Hammel, H. T.; Gordon, M. S. Supercooling and Osmoregulation in Arctic Fish. *J. Cell. Comp. Physiol.* **1957**, *49* (1), 5–24. https://doi.org/10.1002/jcp.1030490103.

(128) Zachariassen, K. E.; Kristiansen, E. Ice Nucleation and Antinucleation in Nature. *Cryobiology* **2000**, *41* (4), 257–279. https://doi.org/10.1006/cryo.2000.2289.

(129) Franks, F.; Mathias, S. F.; Hatley, R. H. M. Water, Temperature and Life. *Philos. Trans. - R. Soc. London, B* **1990**, *326* (1237), 517–533. https://doi.org/10.1098/rstb.1990.0029.

(130) Smallwood, M.; Bowles, D. J.; Gerday, C.; Marahiel, M. A.; Davies, P. L.; Bradbeer, W.; Warren, G. Plants in a Cold Climate. *Philos. Trans. R. Soc. B Biol. Sci.* **2002**, *357* (1423), 831–847. https://doi.org/10.1098/rstb.2002.1073.

(131) Davies, P. L.; Baardsnes, J.; Kuiper, M. J.; Walker, V. K.; Hall, D.; Marahiel, M. A.; Smallwood, M.; Smith, D.; Haymet, T.; Knight, C. Structure and Function of Antifreeze Proteins. *Philos. Trans. R. Soc. B Biol. Sci.* **2002**, *357* (1423), 927–935. https://doi.org/10.1098/rstb.2002.1081.

(132) Knight, C. A.; De Vries, A. L.; Oolman, L. D. Fish Antifreeze Protein and the Freezing and Recrystallization of Ice. *Nature* **1988**, *308* (5956), 295–296. https://doi.org/10.1038/308295a0.

(133) Yeh, Y.; Feeney, R. E. Antifreeze Proteins: Structures and Mechanisms of Function. *Chem. Rev.* **1996**, *96* (2). https://doi.org/10.1021/cr950260c.

(134) Lin, Y.; Duman, J. G.; DeVries, A. L. Studies on the Structure and Activity of Low Molecular Weight Glycoproteins from an Antarctic Fish. *Biochem. Biophys. Res. Commun.* **1972**, *46* (1), 87–92. https://doi.org/10.1016/0006-291X(72)90633-X.

(135) Feeney, R. E.; Yeh, Y. Antifreeze Proteins from Fish Bloods. *Adv. Protein Chem.* **1978**, *32* (C), 191–282. https://doi.org/10.1016/S0065-3233(08)60576-8.

(136) Janech, M. G.; Krell, A.; Mock, T.; Kang, J. S.; Raymond, J. A. Ice-Binding Proteins from Sea Ice Diatoms (Bacillariophyceae). *J. Phycol.* **2006**, *42* (2), 410–416. https://doi.org/10.1111/j.1529-8817.2006.00208.x.

(137) Jung, W.; Gwak, Y.; Davies, P. L.; Kim, H. J.; Jin, E. S. Isolation and Characterization of Antifreeze Proteins from the Antarctic Marine Microalga Pyramimonas Gelidicola. *Mar. Biotechnol.* **2014**, *16* (5), 502–512. https://doi.org/10.1007/s10126-014-9567-y.

(138) Raymond, J. A.; DeVries, A. L. Adsorption Inhibition as a Mechanism of Freezing Resistance in Polar Fishes. *Proc. Natl. Acad. Sci. U. S. A.* **1977**, *74* (6), 2589–2593. https://doi.org/10.1073/pnas.74.6.2589.

(139) Wöhrmann, A. P. A. Antifreeze Glycopeptides and Peptides in Antarctic Fish Species from the Weddell Sea and the Lazarev Sea. *Mar. Ecol. Prog. Ser.* **1996**, *130* (1–3), 47–59. https://doi.org/10.3354/meps130047.

(140) Wilkinson, B. L.; Stone, R. S.; Capicciotti, C. J.; Thaysen-Andersen, M.; Matthews, J. M.; Packer, N. H.; Ben, R. N.; Payne, R. J. Total Synthesis of Homogeneous Antifreeze Glycopeptides and Glycoproteins. *Angew. Chemie - Int. Ed.* **2012**, *51* (15), 3606–3610. https://doi.org/10.1002/anie.201108682.

(141) Garnham, C. P.; Natarajan, A.; Middleton, A. J.; Kuiper, M. J.; Braslavsky, I.; Davies, P. L. Compound Ice-Binding Site of an Antifreeze Protein Revealed by Mutagenesis and Fluorescent Tagging. *Biochemistry* **2010**, *49* (42), 9063–9071. https://doi.org/10.1021/bi100516e.

(142) Liu, Y.; Li, Z.; Lin, Q.; Kosinski, J.; Seetharaman, J.; Bujnicki, J. M.; Sivaraman, J.; Hew, C. L. Structure and Evolutionary Origin of Ca2+-Dependent Herring Type II Antifreeze Protein. *PLoS One* **2007**, *2* (6). https://doi.org/10.1371/journal.pone.0000548.

(143) SCOTT, G. K.; DAVIES, P. L.; SHEARS, M. A.; FLETCHER, G. L. Structural Variations in the Alanine-rich Antifreeze Proteins of the Pleuronectinae. *Eur. J. Biochem.* **1987**, *168* (3), 629–633. https://doi.org/10.1111/j.1432-1033.1987.tb13462.x.

(144) Sun, T.; Lin, F. H.; Robert, L.; Campbell; Allingham, J. S.; Davies, P. L. An Antifreeze Protein Folds with an Interior Network of More than 400 Semi-Clathrate Waters. *Science (80).* **2014**, *343* (6172), 795–798. https://doi.org/10.1126/science.1247407.

(145) Knight, C. A.; Cheng, C. C.; DeVries, A. L. Adsorption of Alpha-Helical

Antifreeze Peptides on Specific Ice Crystal Surface Planes. *Biophys. J.* **1991**, *59* (2), 409–418. https://doi.org/10.1016/S0006-3495(91)82234-2.

(146) Wathen, B.; Kuiper, M.; Walker, V.; Jia, Z. A New Model for Simulating 3-D Crystal Growth and Its Application to the Study of Antifreeze Proteins. *J. Am. Chem. Soc.* **2003**, *125* (3), 729–737. https://doi.org/10.1021/ja0267932.

(147) Strom, C. S.; Liu, X. Y.; Jia, Z. Antifreeze Protein-Induced Morphological Modification Mechanisms Linked to Ice Binding Surface. *J. Biol. Chem.* **2004**, *279* (31), 32407–32417. https://doi.org/10.1074/jbc.M401712200.

(148) Budke, C.; Dreyer, A.; Jaeger, J.; Gimpel, K.; Berkemeier, T.; Bonin, A. S.; Nagel, L.; Plattner, C.; Devries, A. L.; Sewald, N.; Koop, T. Quantitative Efficacy Classification of Ice Recrystallization Inhibition Agents. *Cryst. Growth Des.* **2014**, *14* (9), 4285–4294. https://doi.org/10.1021/cg5003308.

(149) Meister, K.; Strazdaite, S.; DeVries, A. L.; Lotze, S.; Olijve, L. L. C.; Voets, I. K.; Bakker, H. J. Observation of Ice-like Water Layers at an Aqueous Protein Surface. *Proc. Natl. Acad. Sci. U. S. A.* **2014**, *111* (50), 17732–17736. https://doi.org/10.1073/pnas.1414188111.

(150) Garnham, C. P.; Campbell, R. L.; Davies, P. L. Anchored Clathrate Waters Bind Antifreeze Proteins to Ice. *Proc. Natl. Acad. Sci. U. S. A.* **2011**, *108* (18), 7363–7367. https://doi.org/10.1073/pnas.1100429108.

(151) Howard, E. I.; Blakeley, M. P.; Haertlein, M.; Haertlein, I. P.; Mitschler, A.; Fisher, S. J.; Siah, A. C.; Salvay, A. G.; Popov, A.; Dieckmann, C. M.; Petrova, T.; Podjarny, A. Neutron Structure of Type-III Antifreeze Protein Allows the Reconstruction of AFP-Ice Interface. *J. Mol. Recognit.* **2011**, *24* (4), 724–732. https://doi.org/10.1002/jmr.1130.

(152) Fairley, K.; Westman, B. J.; Pham, L. H.; Haymet, A. D. J.; Harding, M. M.; Mackay, J. P. Type I Shorthorn Sculpin Antifreeze Protein: Recombinant Synthesis, Solution Conformation, and Ice Growth Inhibition Studies. *J. Biol. Chem.* **2002**, *277* (27), 24073–24080. https://doi.org/10.1074/jbc.M200307200.

(153) Haymet, A. D. J.; Ward, L. G.; Harding, M. M. Winter Flounder "antifreeze" Proteins: Synthesis and Ice Growth Inhibition of Analogues That Probe the Relative Importance of Hydrophobic and Hydrogen-Bonding Interactions. *J. Am. Chem.*

Soc. **1999**, *121* (5), 941–948. https://doi.org/10.1021/ja9801341.

(154) Davies, P. L. Ice-Binding Proteins: A Remarkable Diversity of Structures for Stopping and Starting Ice Growth. *Trends Biochem. Sci.* **2014**, *39* (11), 548–555. https://doi.org/10.1016/j.tibs.2014.09.005.

(155) Gwak, Y.; Jung, W.; Lee, Y.; Kim, J. S.; Kim, C. G.; Ju, J. H.; Song, C.; Hyun, J. K.; Jin, E. An Intracellular Antifreeze Protein from an Antarctic Microalga That Responds to Various Environmental Stresses. *FASEB J.* **2014**, *28* (11), 4924–4935. https://doi.org/10.1096/fj.14-256388.

(156) Yang, D. S. C.; Hon, W. C.; Bubanko, S.; Xue, Y.; Seetharaman, J.; Hew, C. L.; Sicheri, F. Identification of the Ice-Binding Surface on a Type III Antifreeze Protein with a "flatness Function" Algorithm. *Biophys. J.* **1998**, *74* (5), 2142–2151. https://doi.org/10.1016/S0006-3495(98)77923-8.

(157) Kristiansen, E.; Zachariassen, K. E. The Mechanism by Which Fish Antifreeze Proteins Cause Thermal Hysteresis. *Cryobiology* **2005**, *51* (3), 262–280. https://doi.org/10.1016/j.cryobiol.2005.07.007.

(158) Cziko, P. A.; DeVries, A. L.; Evans, C. W.; Christina Cheng, C. H. Antifreeze Protein-Induced Superheating of Ice inside Antarctic Notothenioid Fishes Inhibits Melting during Summer Warming. *Proc. Natl. Acad. Sci. U. S. A.* **2014**, *111* (40), 14583–14588. https://doi.org/10.1073/pnas.1410256111.

(159) DeVries, A. L.; Komatsu, S. K.; Feeney, R. E. Chemical and Physical Properties of Freezing Point-Depressing Glycoproteins from Antarctic Fishes. *J. Biol. Chem.* **1970**, *245* (11), 2901–2908. https://doi.org/10.1016/s0021-9258(18)63073-x.

(160) DeVries, a. Glycoproteins as Biological Antifreeze Agents in Antarctic Fishes. *Science (80).* **1971**, *172* (3988), 1152–1155.

(161) CHAKRABARTTY, A.; HEW, C. L. The Effect of Enhanced A-helicity on the Activity of a Winter Flounder Antifreeze Polypeptide. *Eur. J. Biochem.* **1991**, *202* (3), 1057–1063. https://doi.org/10.1111/j.1432-1033.1991.tb16470.x.

(162) Knight, C. A.; Driggers, E.; DeVries, A. L. Adsorption to Ice of Fish Antifreeze Glycopeptides 7 and 8. *Biophys. J.* **1993**, *64* (1), 252–259. https://doi.org/10.1016/S0006-3495(93)81361-4.

(163) Capicciotti, C. J.; Poisson, J. S.; Boddy, C. N.; Ben, R. N. Modulation of Antifreeze

Activity and the Effect upon Post-Thaw HepG2 Cell Viability after Cryopreservation. *Cryobiology* **2015**, *70* (2), 79–89. https://doi.org/10.1016/j.cryobiol.2015.01.002.

(164) Gaukel, V.; Leiter, A.; Spieß, W. E. L. Synergism of Different Fish Antifreeze Proteins and Hydrocolloids on Recrystallization Inhibition of Ice in Sucrose Solutions. *J. Food Eng.* **2014**, *141*, 44–50. https://doi.org/10.1016/j.jfoodeng.2014.05.016.

(165) Leiter, A.; Rau, S.; Winger, S.; Muhle-Goll, C.; Luy, B.; Gaukel, V. Influence of Heating Temperature, Pressure and PH on Recrystallization Inhibition Activity of Antifreeze Protein Type III. *J. Food Eng.* **2016**, *187*, 53–61. https://doi.org/10.1016/j.jfoodeng.2016.04.019.

(166) Hassas-Roudsari, M.; Goff, H. D. Ice Structuring Proteins from Plants: Mechanism of Action and Food Application. *Food Res. Int.* **2012**, *46* (1), 425–436. https://doi.org/10.1016/j.foodres.2011.12.018.

(167) DeVries, A. L. The Role of Antifreeze Glycopeptides and Peptides in the Freezing Avoidance of Antarctic Fishes. *Comp. Biochem. Physiol. -- Part B Biochem.* **1988**, *90* (3), 611–621. https://doi.org/10.1016/0305-0491(88)90302-1.

(168) Wierzbicki, A.; Taylor, M. S.; Knight, C. A.; Madura, J. D.; Harrington, J. P.; Sikes, C. S. Analysis of Shorthorn Sculpin Antifreeze Protein Stereospecific Binding to (2 -1 0) Faces of Ice. *Biophys. J.* **1996**, *71* (1), 8–18. https://doi.org/10.1016/S0006-3495(96)79204-4.

(169) Wang, T.; Zhu, Q.; Yang, X.; Layne, J. R.; Devries, A. L. Antifreeze Glycoproteins from Antarctic Notothenioid Fishes Fail to Protect the Rat Cardiac Explant during Hypothermic and Freezing Preservation. *Cryobiology*. 1994, pp 185–192. https://doi.org/10.1006/cryo.1994.1022.

(170) Carpenter, J. F.; Hansen, T. N. Antifreeze Protein Modulates Cell Survival during Cryopreservation: Mediation through Influence on Ice Crystal Growth. *Proc. Natl. Acad. Sci. U. S. A.* **1992**, *89* (19), 8953–8957. https://doi.org/10.1073/pnas.89.19.8953.

(171) Rubinsky, B.; Arav, A.; Devries, A. L. The Cryoprotective Effect of Antifreeze Glycopeptides from Antarctic Fishes. *Cryobiology* **1992**, *29* (1), 69–79.

https://doi.org/10.1016/0011-2240(92)90006-N.

(172) Tachibana, Y.; Fletcher, G. L.; Fujitani, N.; Tsuda, S.; Monde, K.; Nishimura, S.-I. Antifreeze Glycoproteins: Elucidation of the Structural Motifs That Are Essential for Antifreeze Activity. *Angew. Chemie* **2004**, *116* (7), 874–880. https://doi.org/10.1002/ange.200353110.

(173) Czechura, P.; Tam, R. Y.; dimitrijevic, E.; Murphy, A.; Ben, R. N. The Importance of Hydration for Inhibiting Ice Recrystallization With. *J. Am. Chem. Soc.* **2008**, *130*, 2928–2929.

(174) Garner, J.; Harding, M. M. Design and Synthesis of Antifreeze Glycoproteins and Mimics. *ChemBioChem* **2010**, *11* (18), 2489–2498. https://doi.org/10.1002/cbic.201000509.

(175) Capicciotti, C. J.; Trant, J. F.; Leclère, M.; Ben, R. N. Synthesis of C -Linked Triazole-Containing Afgp Analogues and Their Ability to Inhibit Ice Recrystallization. *Bioconjug. Chem.* **2011**, *22* (4), 605–616. https://doi.org/10.1021/bc100394k.

(176) Inada, T.; Lu, S. S. Thermal Hysteresis Caused by Non-Equilibrium Antifreeze Activity of Poly(Vinyl Alcohol). *Chem. Phys. Lett.* **2004**, *394* (4–6), 361–365. https://doi.org/10.1016/j.cplett.2004.07.021.

(177) Inada, T.; Lu, S.-S. Inhibition of Recrystallization of Ice Grains by Adsorption of Poly (Vinyl Alcohol) onto Ice Surfaces. *Cryst. Growth Des.* **2003**, *3* (5), 747–752.

(178) Budke, C.; Koop, T. Ice Recrystallization Inhibition and Molecular Recognition of Ice Faces by Poly(Vinyl Alcohol). *ChemPhysChem* **2006**, *7* (12), 2601–2606. https://doi.org/10.1002/cphc.200600533.

(179) Olijve, L. L. C.; Hendrix, M. M. R. M.; Voets, I. K. Influence of Polymer Chain Architecture of Poly(Vinyl Alcohol) on the Inhibition of Ice Recrystallization. *Macromol. Chem. Phys.* **2016**, *217* (8), 951–958. https://doi.org/10.1002/macp.201500497.

(180) Miller, N.; Williams, G. M.; Brimble, M. A. Synthesis of Fish Antifreeze Neoglycopeptides Using Microwave-Assisted "Click Chemistry." *Org. Lett.* **2009**, *11* (11), 2409–2412. https://doi.org/10.1021/ol9005536.

(181) Peltier, R.; Evans, C. W.; Devries, A. L.; Brimble, M. A.; Dingley, A. J.; Williams,

D. E. Growth Habit Modification of Ice Crystals Using Antifreeze Glycoprotein (AFGP) Analogues. *Cryst. Growth Des.* **2010**, *10* (12), 5066–5077. https://doi.org/10.1021/cg1005083.

(182) Heggemann, C.; Budke, C.; Schomburg, B.; Majer, Z.; Wibrock, M.; Koop, T.; Sewald, N. Antifreeze Glycopeptide Analogues: Microwave-Enhanced Synthesis and Functional Studies. *Amino Acids* **2010**, *38* (1), 213–222. https://doi.org/10.1007/s00726-008-0229-0.

(183) Norgren, A. S.; Budke, C.; Majer, Z.; Heggemann, C.; Koop, T.; Sewald, N. On-Resin Click-Glycoconjugation of Peptoids. *Synthesis (Stuttg).* **2009**, No. 3, 488–494. https://doi.org/10.1055/s-0028-1083302.

(184) Abraham, S.; Keillor, K.; Capicciotti, C. J.; Perley-Robertson, G. E.; Keillor, J. W.; Ben, R. N. Quantitative Analysis of the Efficacy and Potency of Novel Small Molecule Ice Recrystallization Inhibitors. *Cryst. Growth Des.* **2015**, *15* (10), 5034–5039. https://doi.org/10.1021/acs.cgd.5b00995.

(185) Liu, S.; Ben, R. N. C-Linked Galactosyl Serine AFGP Analogues as Potent Recrystallization Inhibitors. *Org. Lett.* **2005**, *7* (12), 2385–2388. https://doi.org/10.1021/ol050677x.

(186) Tam, R. Y.; Rowley, C. N.; Petrov, I.; Zhang, T.; Afagh, N. A.; Woo, T. K.; Ben, R. N. Solution Conformation of C-Linked Antifreeze Glycoprotein Analogues and Modulation of Ice Recrystallization. *J. Am. Chem. Soc.* **2009**, *131* (43), 15745–15753. https://doi.org/10.1021/ja904169a.

(187) Capicciotti, C. J.; Kurach, J. D. R.; Turner, T. R.; Mancini, R. S.; Acker, J. P.; Ben, R. N. Small Molecule Ice Recrystallization Inhibitors Enable Freezing of Human Red Blood Cells with Reduced Glycerol Concentrations. *Sci. Rep.* **2015**, *5*, 1–10. https://doi.org/10.1038/srep09692.

(188) Ghobadloo, S. M.; Balcerzak, A. K.; Gargaun, A.; Muharemagic, D.; Mironov, G. G.; Capicciotti, C. J.; Briard, J. G.; Ben, R. N.; Berezovski, M. V. Carbohydrate-Based Ice Recrystallization Inhibitors Increase Infectivity and Thermostability of Viral Vectors. *Sci. Rep.* **2014**, *4*, 1–6. https://doi.org/10.1038/srep05903.

(189) Briard, J. G.; Jahan, S.; Chandran, P.; Allan, D.; Pineault, N.; Ben, R. N. Small-Molecule Ice Recrystallization Inhibitors Improve the Post-Thaw Function of

Hematopoietic Stem and Progenitor Cells. *ACS Omega* **2016**, *1* (5), 1010–1018. https://doi.org/10.1021/acsomega.6b00178.

(190) Capicciotti, C. J.; Mancini, R. S.; Turner, T. R.; Koyama, T.; Alteen, M. G.; Doshi, M.; Inada, T.; Acker, J. P.; Ben, R. N. O-Aryl-Glycoside Ice Recrystallization Inhibitors as Novel Cryoprotectants: A Structure-Function Study. *ACS Omega* **2016**, *1* (4), 656–662. https://doi.org/10.1021/acsomega.6b00163.

(191) Balcerzak, A. K.; Capicciotti, C. J.; Briard, J. G.; Ben, R. N. Designing Ice Recrystallization Inhibitors: From Antifreeze (Glyco)Proteins to Small Molecules. *RSC Adv.* **2014**, *4* (80), 42682–42696. https://doi.org/10.1039/c4ra06893a.

(192) Congdon, T.; Notman, R.; Gibson, M. I. Antifreeze (Glyco)Protein Mimetic Behavior of Poly(Vinyl Alcohol): Detailed Structure Ice Recrystallization Inhibition Activity Study. *Biomacromolecules* **2013**, *14* (5), 1578–1586. https://doi.org/10.1021/bm400217j.

(193) Peltier, R.; Brimble, M. A.; Wojnar, J. M.; Williams, D. E.; Evans, C. W.; Devries, A. L. Synthesis and Antifreeze Activity of Fish Antifreeze Glycoproteins and Their Analogues. *Chem. Sci.* **2010**, *1* (5), 538–551. https://doi.org/10.1039/c0sc00194e.

(194) Gibson, M. I.; Barker, C. A.; Spain, S. G.; Albertin, L.; Cameron, N. R. Inhibition of Ice Crystal Growth by Synthetic Glycopolymers: Implications for the Rational Design of Antifreeze Glycoprotein Mimics. *Biomacromolecules* **2009**, *10* (2), 328–333. https://doi.org/10.1021/bm801069x.

(195) Gibson, M. I. Slowing the Growth of Ice with Synthetic Macromolecules: Beyond Antifreeze(Glyco) Proteins. *Polym. Chem.* **2010**, *1* (8), 1141–1152. https://doi.org/10.1039/c0py00089b.

(196) Deller, R. C.; Congdon, T.; Sahid, M. A.; Morgan, M.; Vatish, M.; Mitchell, D. A.; Notman, R.; Gibson, M. I. Ice Recrystallisation Inhibition by Polyols: Comparison of Molecular and Macromolecular Inhibitors and Role of Hydrophobic Units. *Biomater. Sci.* **2013**, *1* (5), 478–485. https://doi.org/10.1039/c3bm00194f.

(197) Eniade, A.; Purushotham, M.; Ben, R. N.; Wang, J. B.; Horwath, K. A Serendipitous Discovery of Antifreeze Protein-Specific Activity in C-Linked Antifreeze Glycoprotein Analogs. *Cell Biochem. Biophys.* **2003**, *38* (2), 115–124. https://doi.org/10.1385/CBB:38:2:115.

(198) Ben, R. N.; Eniade, A. A.; Hauer, L. Synthesis of a C-Linked Antifreeze Glycoprotein (AFGP) Mimic: Probes for Investigating the Mechanism of Action. *Org. Lett.* **1999**, *1* (11), 1759–1762. https://doi.org/10.1021/ol991025+.

(199) Trant, J. F.; Biggs, R. A.; Capicciotti, C. J.; Ben, R. N. Developing Highly Active Small Molecule Ice Recrystallization Inhibitors Based upon C-Linked Antifreeze Glycoprotein Analogues. *RSC Adv.* **2013**, *3* (48), 26005–26009. https://doi.org/10.1039/c3ra43835j.

(200) Tam, R. Y.; Ferreira, S. S.; Czechura, P.; Ben, R. N.; Chaytor, J. L. Hydration Index-a Better Parameter for Explaining Small Molecule Hydration in Inhibition of Ice Recrystallization. *J. Am. Chem. Soc.* **2008**, *130* (51), 17494–17501. https://doi.org/10.1021/ja806284x.

(201) Galema, S. A.; Howard, E.; Engberts, J. B. F. N.; Grigera, J. R. The Effect of Stereochemistry upon Carbohydrate Hydration. A Molecular Dynamics Simulation of β-d-Galactopyranose and (α,β)-d-Talopyranose. *Carbohydr. Res.* **1994**, *265* (2), 215–225. https://doi.org/10.1016/0008-6215(94)00241-X.

(202) Suggett, A. Molecular Motion and Interactions in Aqueous Carbohydrate Solutions. III. A Combined Nuclear Magnetic and Dielectric-Relaxation Strategy. *J. Solution Chem.* **1976**, *5* (1), 33–46. https://doi.org/10.1007/BF00647179.

(203) Kabayama, M. A.; Patterson, D.; Piche, L. The Thermodynamics of Mutarotation of Some Sugars. *Can. J. Chem.* **1958**, *36* (1658), 557–562.

(204) Suggett, A. Molecular Motion and Interactions in Aqueous Carbohydrate Solutions. III. A Combined Nuclear Magnetic and Dielectric-Relaxation Strategy. *J. Solution Chem.* **1976**, *5* (1), 33–46. https://doi.org/10.1007/BF00647179.

(205) Franks, F. Solute-Water Interactions: Do Polyhydroxy Compounds Alter the Properties of Water? *Cryobiology* **1983**, *20* (3), 335–345. https://doi.org/10.1016/0011-2240(83)90022-6.

(206) Painter, T. J. Effect of Axial Hydroxyl Groups upon the Hydration of Glycopyranosides: Evidence from Mechanistic Studies of Acid Hydrolysis. *Carbohydr. Res.* **1980**, *82* (2), 362–365. https://doi.org/10.1016/S0008-6215(00)85711-0.

(207) Stokes, R. H.; Robinson, R. A. Interactions in Aqueous Nonelectrolyte Solutions.

I. Solute-Solvent Equilibria. *J. Phys. Chem.* **1966**, *70* (7), 2126–2131. https://doi.org/10.1021/j100879a010.

(208) Tait, M. J.; Suggett, A.; Franks, F.; Ablett, S.; Quickenden, P. A. Hydration of Monosaccharides: A Study by Dielectric and Nuclear Magnetic Relaxation. *J. Solution Chem.* **1972**, *1* (2), 131–151. https://doi.org/10.1007/BF01028450.

(209) Uedaira, H., Uedaira, H. Sugar-Water Interaction from Diffusion Measurements. *J. Solution Chem.* **1985**, *14* (1), 27–34.

(210) Walkinshaw, M. D. Variation in the Hydrophilicity of Hexapyranose Sugars Explains Features of the Anomeric Effect. *J. Chem. Soc. Perkin Trans. 2* **1987**, No. 12, 1903–1906. https://doi.org/10.1039/p29870001903.

(211) Capicciotti, C. J.; Leclère, M.; Perras, F. A.; Bryce, D. L.; Paulin, H.; Harden, J.; Liu, Y.; Ben, R. N. Potent Inhibition of Ice Recrystallization by Low Molecular Weight Carbohydrate-Based Surfactants and Hydrogelators. *Chem. Sci.* **2012**, *3* (5), 1408–1416. https://doi.org/10.1039/c2sc00885h.

(212) Estroff, L. A.; Hamilton, A. D. Water Gelation by Small Organic Molecules. *Chem. Rev.* **2004**, *104* (3), 1201–1217. https://doi.org/10.1021/cr0302049.

(213) De Loos, M.; Feringa, B. L.; Van Esch, J. H. Design and Application of Self-Assembled Low Molecular Weight Hydrogels. *European J. Org. Chem.* **2005**, No. 17, 3615–3631. https://doi.org/10.1002/ejoc.200400723.

(214) Briard, J. G.; Poisson, J. S.; Turner, T. R.; Capicciotti, C. J.; Acker, J. P.; Ben, R. N. Small Molecule Ice Recrystallization Inhibitors Mitigate Red Blood Cell Lysis during Freezing, Transient Warming and Thawing. *Sci. Rep.* **2016**, *6* (November 2015), 2–11. https://doi.org/10.1038/srep23619

(215) Chopra, K. Improved Cryopreservation of Induced Pluripotent Stem Cells Using N-Aryl Glycosidic Small Molecule Ice Recrystallization Inhibitors. (Master's Dissertation, Universit d'Ottawa/University of Ottawa),. **2020**.

(216) Tomczak, M. M.; Marshall, C. B.; Gilbert, J. A.; Davies, P. L. A Facile Method for Determining Ice Recrystallization Inhibition by Antifreeze Proteins. *Biochem. Biophys. Res. Commun.* **2003**, *311* (4), 1041–1046. https://doi.org/10.1016/j.bbrc.2003.10.106.

(217) Yu, S. O.; Brown, A.; Middleton, A. J.; Tomczak, M. M.; Walker, V. K.; Davies,

P. L. Ice Restructuring Inhibition Activities in Antifreeze Proteins with Distinct Differences in Thermal Hysteresis. *Cryobiology* **2010**, *61* (3), 327–334. https://doi.org/10.1016/J.CRYOBIOL.2010.10.158.

(218) Surís-Valls, R.; Voets, I. K. The Impact of Salts on the Ice Recrystallization Inhibition Activity of Antifreeze (Glyco)Proteins. *Biomolecules* **2019**, *9* (8). https://doi.org/10.3390/biom9080347.

(219) Graham, L. A.; Agrawal, P.; Oleschuk, R. D.; Davies, P. L. High-Capacity Ice-Recrystallization Endpoint Assay Employing Superhydrophobic Coatings That Is Equivalent to the 'Splat' Assay. *Cryobiology* **2018**, *81* (January), 138–144. https://doi.org/10.1016/j.cryobiol.2018.01.011.

(220) Knight, C. A.; Hallett, J.; DeVries, A. L. Solute Effects on Ice Recrystallization: An Assessment Technique. *Cryobiology* **1988**, *25* (1), 55–60. https://doi.org/10.1016/0011-2240(88)90020-X.

(221) Sharma, B.; Deswal, R. Antifreeze Proteins in Plants: An Overview with an Insight into the Detection Techniques Including Nanobiotechnology. *J. Proteins Proteomics* **2014**, *5* (8), 89–107.

(222) Smallwood, M.; Worrall, D.; Byass, L.; Elias, L.; Ashford, D.; Doucet, C. J.; Holt, C.; Telford, J.; Lillford, P.; Bowles, D. J. Isolation and Characterization of a Novel Antifreeze Protein from Carrot (Daucus Carota). *Biochem. J.* **1999**, *340* (2), 385–391. https://doi.org/10.1042/0264-6021:3400385

(223) Jackman, J.; Noestheden, M.; Moffat, D.; Pezacki, J. P.; Findlay, S.; Ben, R. N. Assessing Antifreeze Activity of AFGP 8 Using Domain Recognition Software. *Biochem. Biophys. Res. Commun.* **2007**, *354* (2), 340–344. https://doi.org/10.1016/j.bbrc.2006.12.225.

(224) Fahy, G. M.; Lilley, T. H.; Linsdell, H.; Douglas, M. S. J.; Meryman, H. T. Cryoprotectant Toxicity and Cryoprotectant Toxicity Reduction: In Search of Molecular Mechanisms. *Cryobiology* **1990**, *27* (3), 247–268. https://doi.org/10.1016/0011-2240(90)90025-Y.

(225) Mueller, L. P.; Theurich, S.; Christopeit, M.; Grothe, W.; Muetherig, A.; Weber, T.; Guenther, S.; Behre, G. Neurotoxicity upon Infusion of Dimethylsulfoxide-Cryopreserved Peripheral Blood Stem Cells in Patients with and without Pre-

Existing Cerebral Disease. *Eur. J. Haematol.* **2007**, *78* (6), 527–531. https://doi.org/10.1111/j.1600-0609.2007.00851.x.

(226) Goldman, S. Stem and Progenitor Cell-Based Therapy of the Human Central Nervous System. *Nat. Biotechnol.* **2005**, *23* (7), 862–871. https://doi.org/10.1038/nbt1119.

(227) Frega, M. *In Vitro Neuronal Networks*; 2016. https://doi.org/10.1007/978-3-319-30237-9_3.

(228) Oecd. *Health at a Glance 2011: OECD Indicators*; 2013. https://doi.org/10.1787/health_glance-2013-en.

(229) Spuch, C.; Navarro, C. Liposomes for Targeted Delivery of Active Agents against Neurodegenerative Diseases (Alzheimer's Disease and Parkinson's Disease). *J. Drug Deliv.* **2011**, *2011*, 1–12. https://doi.org/10.1155/2011/469679.

(230) Dauer, W.; Przedborski, S. Parkinson's Diseases: Mechanisms and Models. *cell Press* **2003**, *39*, 889–909. https://doi.org/10.1017/CCOL9780521851282.008.

(231) Muchowski, P. J. Protein Misfolding, Amyloid Formation, and Neurodegeneration. *Neuron* **2002**, *35* (1), 9–12. https://doi.org/10.1016/s0896-6273(02)00761-4.

(232) Morizane, A.; Li, J. Y.; Brundin, P. From Bench to Bed: The Potential of Stem Cells for the Treatment of Parkinson's Disease. *Cell Tissue Res.* **2008**, *331* (1), 323–336. https://doi.org/10.1007/s00441-007-0541-0.

(233) Takahashi, K.; Tanabe, K.; Ohnuki, M.; Narita, M.; Ichisaka, T.; Tomoda, K.; Yamanaka, S. Induction of Pluripotent Stem Cells from Adult Human Fibroblasts by Defined Factors. *Cell* **2007**, *131* (5), 861–872. https://doi.org/10.1016/j.cell.2007.11.019.

(234) Yu, J.; Thomson, J. A. *Induced Pluripotent Stem Cells*, Fourth Edition.; Elsevier, 2013. https://doi.org/10.1016/B978-0-12-398358-9.00030-6.

(235) Seymour, T.; Twigger, A. J.; Kakulas, F. Pluripotency Genes and Their Functions in the Normal and Aberrant Breast and Brain. *Int. J. Mol. Sci.* **2015**, *16* (11), 27288–27301. https://doi.org/10.3390/ijms161126024.

(236) Robinton, D. A.; Daley, G. Q. The Promise of Induced Pluripotent Stem Cells in Research and Therapy. *Nature* **2012**, *481* (7381), 295–305. https://doi.org/10.1038/nature10761.

(237) Jakeman, L. B.; Reier, P. J. Axonal Projections between Fetal Spinal Cord Transplants and the Adult Rat Spinal Cord: A Neuroanatomical Tracing Study of Local Interactions. *J. Comp. Neurol.* **1991**, *307* (2), 311–334. https://doi.org/10.1002/cne.903070211.

(238) Reier, P. J.; Stokes, B. T.; Thompson, F. J.; Anderson, D. K. Fetal Cell Grafts into Resection and Contusion/Compression Injuries of the Rat and Cat Spinal Cord. *Exp. Neurol.* **1992**, *115* (1), 177–188. https://doi.org/10.1016/0014-4886(92)90245-L.

(239) Wictorin, K.; Bjorklund, A. Axon Outgrowth from Grafts of Human Embryonic Spinal Cord in the Lesioned Adult Rat Spinal Cord. *NeuroReport*. 1992, pp 1045–1048. https://doi.org/10.1097/00001756-199212000-00003.

(240) Coumans, J. V.; Lin, T. T. S.; Hai Ning Dai; MacArthur, L.; McAtee, M.; Nash, C.; Bregman, B. S. Axonal Regeneration and Functional Recovery after Complete Spinal Cord Transection in Rats by Delayed Treatment with Transplants and Neurotrophins. *J. Neurosci.* **2001**, *21* (23), 9334–9344. https://doi.org/10.1523/jneurosci.21-23-09334.2001.

(241) Ager, R. R.; Davis, J. L.; Agazaryan, A.; Benavente, F.; Poon, W. W.; Laferla, F. M.; Blurton-Jones, M. Human Neural Stem Cells Improve Cognition and Promote Synaptic Growth in Two Complementary Transgenic Models of Alzheimer's Disease and Neuronal Loss. *Hippocampus* **2015**, *25* (7), 813–826. https://doi.org/10.1002/hipo.22405.

(242) Takamatsu, K.; Ikeda, T.; Haruta, M.; Matsumura, K.; Ogi, Y.; Nakagata, N.; Uchino, M.; Ando, Y.; Nishimura, Y.; Senju, S. Degradation of Amyloid Beta by Human Induced Pluripotent Stem Cell-Derived Macrophages Expressing Neprilysin-2. *Stem Cell Res.* **2014**, *13* (3), 442–453. https://doi.org/10.1016/j.scr.2014.10.001.

(243) Kim, J. H.; Auerbach, J. M.; Rodríguez-Gómez, J. A.; Velasco, I.; Gavin, D.; Lumelsky, N.; Lee, S. H.; Nguyen, J.; Sánchez-Pernaute, R.; Bankiewicz, K.; McKay, R. Dopamine Neurons Derived from Embryonic Stem Cells Function in an Animal Model of Parkinson's Disease. *Nature* **2002**, *418* (6893), 50–56. https://doi.org/10.1038/nature00900.

(244) Nishiyama, Y.; Iwanami, A.; Kohyama, J.; Itakura, G.; Kawabata, S.; Sugai, K.; Nishimura, S.; Kashiwagi, R.; Yasutake, K.; Isoda, M.; Matsumoto, M.; Nakamura, M.; Okano, H. Safe and Efficient Method for Cryopreservation of Human Induced Pluripotent Stem Cell-Derived Neural Stem and Progenitor Cells by a Programmed Freezer with a Magnetic Field. *Neurosci. Res.* **2016**, *107*, 20–29. https://doi.org/10.1016/j.neures.2015.11.011.

(245) Kobayashi, Y.; Okada, Y.; Itakura, G.; Iwai, H.; Nishimura, S.; Yasuda, A.; Nori, S.; Hikishima, K.; Konomi, T.; Fujiyoshi, K.; Tsuji, O.; Toyama, Y.; Yamanaka, S.; Nakamura, M.; Okano, H. Pre-Evaluated Safe Human IPSC-Derived Neural Stem Cells Promote Functional Recovery after Spinal Cord Injury in Common Marmoset without Tumorigenicity. *PLoS One* **2012**, *7* (12), 1–13. https://doi.org/10.1371/journal.pone.0052787.

(246) Pei, Y.; Peng, J.; Behl, M.; Sipes, N. S.; Shockley, K. R.; Rao, M. S.; Tice, R. R.; Zeng, X. Comparative Neurotoxicity Screening in Human IPSC-Derived Neural Stem Cells, Neurons and Astrocytes. *Brain Res.* **2016**, *1638*, 57–73. https://doi.org/10.1016/j.brainres.2015.07.048.

(247) Imaizumi, K.; Nishishita, N.; Muramatsu, M.; Yamamoto, T.; Takenaka, C.; Kawamata, S.; Kobayashi, K.; Nishikawa, S. I.; Akuta, T. A Simple and Highly Effective Method for Slow-Freezing Human Pluripotent Stem Cells Using Dimethyl Sulfoxide, Hydroxyethyl Starch and Ethylene Glycol. *PLoS One* **2014**, *9* (2), 1–11. https://doi.org/10.1371/journal.pone.0088696.

(248) Majzner, R. G.; Mackall, C. L. Clinical Lessons Learned from the First Leg of the CAR T Cell Journey. *Nat. Med.* **2019**, *25* (9), 1341–1355. https://doi.org/10.1038/s41591-019-0564-6.

(249) Zhu, H.; Kaufman, D. S. An Improved Method to Produce Clinical-Scale Natural Killer Cells from Human Pluripotent Stem Cells. *Methods Mol. Biol.* **2019**, *2048*, 107–119. https://doi.org/10.1007/978-1-4939-9728-2_12.

(250) Bloemberg, D.; Nguyen, T.; Maclean, S.; Zafer, A.; Gadoury, C.; Gurnani, K.; Chattopadhyay, A.; Ash, J.; Lippens, J.; Harcus, D.; Pagé, M.; Pon, R. A.; Gilbert, R.; Marcil, A.; Weeratna, R. D.; Mccomb, S.; Mccomb, S. A Modular High-Throughput Screening Platform for Chimeric Antigen Receptor (CAR)

Development.

(251) Calmels, B.; Mfarrej, B.; Chabannon, C. From Clinical Proof-of-Concept to Commercialization of CAR T Cells. *Drug Discov. Today* **2018**, *23* (4), 758–762. https://doi.org/10.1016/j.drudis.2018.01.024.

(252) Fang, F.; Wang, W.; Chen, M.; Tian, Z.; Xiao, W. Technical Advances in NK Cell-Based Cellular Immunotherapy. *Cancer Biol. Med.* **2019**, *16* (4), 647–654. https://doi.org/10.20892/j.issn.2095-3941.2019.0187.

(253) Melero, I.; Rouzaut, A.; Motz, G. T.; Coukos, G. T-Cell and NK-Cell Infiltration into Solid Tumors: A Key Limiting Factor for Efficacious Cancer Immunotherapy. *Cancer Discov.* **2014**, *4* (5), 522–526. https://doi.org/10.1158/2159-8290.CD-13-0985.

(254) Turtle, C. J.; Hanafi, L.; Berger, C.; Riddell, S. R.; Maloney, D. G.; Turtle, C. J.; Gooley, T. A.; Cherian, S.; Hudecek, M.; Sommermeyer, D.; Melville, K.; Pender, B.; Budiarto, T. M.; Robinson, E.; Steevens, N. N.; Chaney, C.; Soma, L.; Chen, X.; Yeung, C.; Wood, B.; Li, D.; Cao, J.; Heimfeld, S.; Jensen, M. C.; Riddell, S. R.; Maloney, D. G. CD19 CAR – T Cells of Defined CD4 + : CD8 + Composition in Adult B Cell ALL Patients Find the Latest Version : CD19 CAR – T Cells of Defined CD4 + : CD8 + Composition in Adult B Cell ALL Patients. *J. Clin. Invest.* **2016**, *126* (6), 2123–2138. https://doi.org/10.1172/JCI85309.modified.

(255) Rosenberg, J.; Huang, J. CD8+ T Cells and NK Cells: Parallel and Complementary Soldiers of Immunotherapy. *Curr. Opin. Chem. Eng.* **2018**, *19*, 9–20. https://doi.org/10.1016/j.coche.2017.11.006.

(256) Meneghel, J.; Kilbride, P.; Morris, J. G.; Fonseca, F. Physical Events Occurring during the Cryopreservation of Immortalized Human T Cells. *PLoS One* **2019**, *14* (5), 1–14. https://doi.org/10.1371/journal.pone.0217304.

(257) Lee, J. S.; Yi, K.; Ju, Y. S.; Shin, E. C. Effects of Cryopreservation and Thawing on Single-Cell Transcriptomes of Human T Cells. *Immune Netw.* **2020**, *20* (4), 1–8. https://doi.org/10.4110/in.2020.20.e34

(258) Xu, H.; Cao, W.; Huang, L.; Xiao, M.; Cao, Y.; Zhao, L.; Wang, N.; Zhou, J. Effects of Cryopreservation on Chimeric Antigen Receptor T Cell Functions. *Cryobiology* **2018**, *83* (1095), 40–47. https://doi.org/10.1016/j.cryobiol.2018.06.007.

(259) Hanley, P. J. Fresh versus Frozen: Effects of Cryopreservation on CAR T Cells. *Mol. Ther.* **2019**, *27* (7), 1213–1214. https://doi.org/10.1016/j.ymthe.2019.06.001.

(260) Golab, K.; Leveson-Gower, D.; Wang, X. J.; Grzanka, J.; Marek-Trzonkowska, N.; Krzystyniak, A.; Millis, J. M.; Trzonkowski, P.; Witkowski, P. Challenges in Cryopreservation of Regulatory T Cells (Tregs) for Clinical Therapeutic Applications. *Int. Immunopharmacol.* **2013**, *16* (3), 371–375. https://doi.org/10.1016/j.intimp.2013.02.001.

(261) El Assal, R.; Abou-Elkacem, L.; Tocchio, A.; Pasley, S.; Matosevic, S.; Kaplan, D. L.; Zylberberg, C.; Demirci, U. Bioinspired Preservation of Natural Killer Cells for Cancer Immunotherapy. *Adv. Sci.* **2019**, *6* (6). https://doi.org/10.1002/advs.201802045

Chapter 2: Goals and Objectives

2.1 Introduction

Regenerative medicine (RM) and cell-based therapy represent a promising path toward healing or replacing damaged cells, tissues, and organs.[1-3] However, successful application of cell-based therapies is dependent on optimizing bio-preservation protocols to ensure safe storage, transport, and banking of cell-based therapy products.[1-3] Moreover, advancements in the field of RM have been made directly due to the increased demand to retain biospecimen samples at ultra-low temperatures; these include biorelevant cell types such as hematopoietic stem and progenitor cells (HSPCs), red blood cells (RBCs), and induced-pluripotent stem cells-derived neurons (iPSC-Ns).[4-9] Cryopreservation is one of the bio-preservation methods utilized for preserving cellular.[10-11] The main consideration with this method is the incidence of cryoinjury such as membrane breakdown, as a result of extra- and intra-cellular ice formation following freezing and thawing cycles.[12] Therefore, cryoprotective agents (CPAs), such as dimethylsulfoxide (DMSO), have been employed as key agents for mitigating the detrimental effects associated with cryopreservation protocols.[13-17] The use of common CPAs is often associated with toxicity effects on cellular signaling and other biological activities, prompting the need for their removal prior to clinical use of cellular products.[17-20] The removal of CPAs itself, however, imposes detrimental consequences on cellular functionality and is time-consuming.[21-23] For example, DMSO is one the most common permeating CPAs which can easily penetrate the cell membrane and protect the cells from damaging effects associated with slow freezing rate.[13-17] However, toxic effects associated with DMSO are inevitable, for instance, DMSO has been reported to cause protein unfolding[84] and to decrease cell membrane thickness.[85]

Therefore, it is pertinent to develop a safe cryomedium containing nontoxic cryo-additives that prevent cell death associated with ice formation that occurs during freezing and thawing.

Ice recrystallization is a thermodynamic phenomenon where ice crystals grow larger at the expense of small one during thawing cycles and is one of the major causes of cell death during cryopreservation.[86] Thus, compounds that can inhibit the recrystallization of ice, also called ice recrystallization inhibitors (IRIs), are promising potential additives for future cryopreservation applications.[24] The Ben laboratory has been heavily invested in the generation and testing of several novel classes of IRIs to help mediate the issue of ice recrystallization during ice recrystallization.[24,29-31] Structure-activity relationship (SAR) studies from naturally occurring antifreeze glycoproteins (AF(G)Ps) allowed for the discovery of small molecule IRI candidates, such as alkyl/aryl pyranoses and *N*-alkyl/aryl-D-gluconamides.[25-31] Alkyl pyranoses such as *n*-octyl-β-D-glucose are referred to as pyranose-based surfactants and hydrogelators and are known for their amphiphilic nature. However, due to their membrane solubilizing property, they are not amenable for the cryopreservation of biological samples.[29,32-33] Despite the fact that alkyl-pyranose derivatives cannot be employed to preserve cellular products, they are nevertheless interesting due to their IRI activity. Thus, conducting SAR studies on this class of IRIs will allow to learn about the structural features correlated to IRI activity. Previous research conducted by the Ben lab has introduced *n*-octyl-β-D-glucose as an active IRI without comprehending its mechanism of action. The first goal of this thesis is to study the relationship between IRI activity of alkyl pyranoses and the length of alkyl chain (hydrophobic component) to better comprehend the importance of

hydrophobic/hydrophilic balance for the activity of IRI candidates. This was conducted by examining how incremental changes to the length of the hydrophobic component of the alkyl pyranoses affect IRI activity.

Another class of IRI, *N*-aryl-D-gluconamides, has been shown to be active IRIs and to enhance the cryopreservation outcome of different cell types, especially HSPCs.[30] One of the IRIs in this class, *N*-2-fluorphenyl-D-gluconamide (2FA), has been shown to increase post-thaw functionality and viability of HSPCs which allows the availability and delivery of such cellular products into clinics.[30,34-35] Similar to HSPCs, induced-pluripotent stem cells (iPSCs) and their derivatives (i.e., iPSC-derived neurons, iPSC-Ns) are powerful tools in cell-based therapy for modeling different neurodegenerative diseases (NDs) and for enhancing cognition in Alzheimer's patients.[36-38] 2FA has shown to successfully maintain higher number of iPSCs post-thaw without compromising their pluripotency properties nor their proliferation activity.[87] Therefore, the second goal of this thesis focuses on exploring the potential advantage of employing 2FA to cryopreserve iPSC-Ns, which are very sensitive toward cryopreservation due to their post mitotic nature.

Cell-based immunotherapies have revolutionized the treatment of numerous tumors.[88] For example, human-derived T cells, and human chimeric antigen receptor (CAR)-T cells have been shown to effectively treat tumors such as hematopoietic malignancies and solid tumors.[39-40] Moreover, human-derived primary natural killer cells (pNKs) are key revolutionary elements in immunotherapy due to their cytotoxic characteristics against numerous kinds of tumor cells;[41] a further benefit is the lack of graft-versus-host reactions in patients receiving allogenic NK cell transfusions.[41-43] Both T cells and pNK cells are extremely sensitive to freezing and thawing processes, and therefore, the

third and fourth objectives of this thesis are to explore the application of IRIs to the cryopreservation protocol of T and pNK cells, with an aim to enhance the post-thaw viability, recovery rates, as well as functionality of the cells.

The overall goals of this thesis are to conduct SAR studies on IRI candidates to better understand their activity, and to investigate the novel applications of IRIs in cryopreservation protocols to optimize freezing media for biorelevant cell types. The preliminary results of *in vitro* functionality assays presented in this thesis are essential for future *in vivo* studies, and eventually for the translation of IRI technology into clinical applications.

2.2 Objective 1: Determining the Effect of Alkyl Chain Length and Glycosidic Linkage on IRI Activity

The Ben laboratory has conducted multiple SAR studies to develop different classes of IRIs and to comprehend key structural features that are significant for IRI activity. A library of various IRIs has been produced including high molecular weight compounds such as *C*-linked AF(G)Ps and small molecular compounds such as alkyl pyranoses, presented in **Figure 2.1**.[24,29,44] Alkyl pyranoses (**Figure 2.1**) are characterized by their amphiphilic nature because of the hydrophobic (alkyl chain) and hydrophilic (carbohydrate) structural components.[33,45-47]

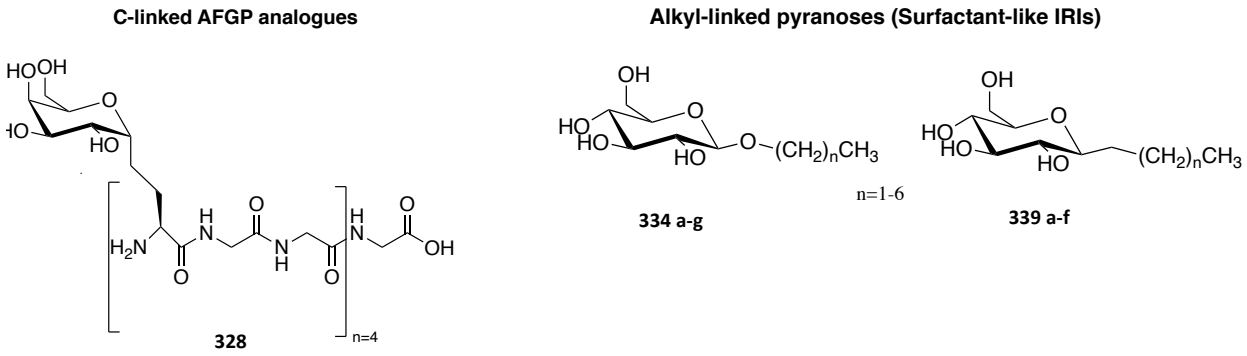

Figure 2.1 Examples of high molecular weight IRIs (AFGPs) and small molecular weight IRIs (alkyl pyranoses)

Previous research has revealed that compounds bearing a long alkyl chain (i.e., an octyl chain) at the β position of the anomeric carbon (C_1) of glucose display IRI activity.[24,29] Several SAR studies have been conducted to correlate the IRI activity of the *n*-octyl-β-D-glucoside with its structural features, for example, hydration index has been well correlated with the IRI activity of glucose.[45] However, no correlations can be made between the hydration index and IRI activity of *n*-octyl-β-D-glucose since the hydration parameters are currently unknown.[24]

Moreover, it has been established that there is no correlation between critical micellization concentrations (CMC) and the IRI activity of *n*-octyl-β-D-glucose, implying that formation of micelles in solution does not contribute to inhibition of ice crystal growth.[24,29] Nonetheless, the counterbalance between hydrophobic and hydrophilic moieties of *n*-octyl-D-glycosides appears to be foundational to IRI activity.[48] Further SAR studies on a broader scope of *N*-alkyl-D-gluconamides have confirmed the correlation between hydrophobic/hydrophilic moieties and IRI activity.[49] In order to study the relationship between active IRIs and their amphiphilic nature, the ratio of polar surface area to molecular surface area (PSA/MSA) of different derivatives was used as a metric, and was correlated with the %MGS of the different *N*-alkyl-D-aldonamide derivatives.[49]

Moreover, previous Ben lab member, Dr. Jennie Briard, has discovered that increasing the length of the alkyl chain linked to the aldonamide structure improves IRI activity, suggesting that changing the net polarity of IRI candidates (i.e., increasing PSA/MSA ratio) influences its activity.[49] Therefore, we seek to conduct similar SAR studies on alkyl pyranose derivatives to examine any relationship between PSA/MSA ratios and IRI activity. These correlations will assist in determining key structural properties required for IRI activity. This objective focuses on **(1)** studying the relationship between hydrophobic moieties at the anomeric position (C_1) and the PSA/MSA ratio of different *O*- or *C*-linked alkyl pyranose derivatives, and **(2)** on exploring the impact of different glycosidic linkages (*C-O vs C-C*) on IRI activity.

Initially, the hydrophobic component of *O*- or *C*-linked alkyl glucosides, presented in **Figure 2.2**, is studied. Different lengths of alkyl chains are installed at the anomeric carbon of glucose and are subjected to kinetic analysis of IRI activity to determine the concentration of inhibitor that results in 50% inhibition of ice growth (IC_{50}). Kinetic analysis of IRIs using a modified splat cooling assay involves evaluating various concentration of IRI candidates to obtain a normalized rate for inhibition activity, as mentioned in the introduction chapter. PSA and MSA values of **334 a-g** and **339 a-f** are calculated using Marvin Sketch software (ChemAxon) [83] and are further correlated with the log transformed IC_{50} values to examine potential trends between IRI activity and the size of the hydrophobic component. We hypothesize that the lower the PSA/MSA ratio, the more active the compound will be, and therefore, the longer the alkyl chain is, the more IRI active the compound should be.

The second part of the first objective investigates the effect of the glycosidic bond on IRI activity. *N*-octyl-β-D-glycoside, with an oxygen-linked glycosidic bond, have been previously reported as an active IRI.[48] However, *O*-glycosidic bond is known for its reactivity and instability as the exocyclic alkoxy group that can be metabolized by various hydrolase enzymes.[50] Interest in synthesizing more stable alternatives has arisen, where the *O*-glycosidic bond could be exchanged for a *C*-glycosidic bond.[50] Thus, the *C*-linked alkyl pyranoses (**339 a-f**) are synthesized and assessed for IRI activity using the modified splat cooling assay. IC_{50} values of the *C*-linked derivatives are then compared with those of the *O*-linked parent compounds to examine any significant changes in inhibiting ice recrystallization upon the alteration of the glycosidic linkage at C_1. The two aspects of this objective will help comprehend important structural aspects of carbohydrate-based IRIs and their activity.

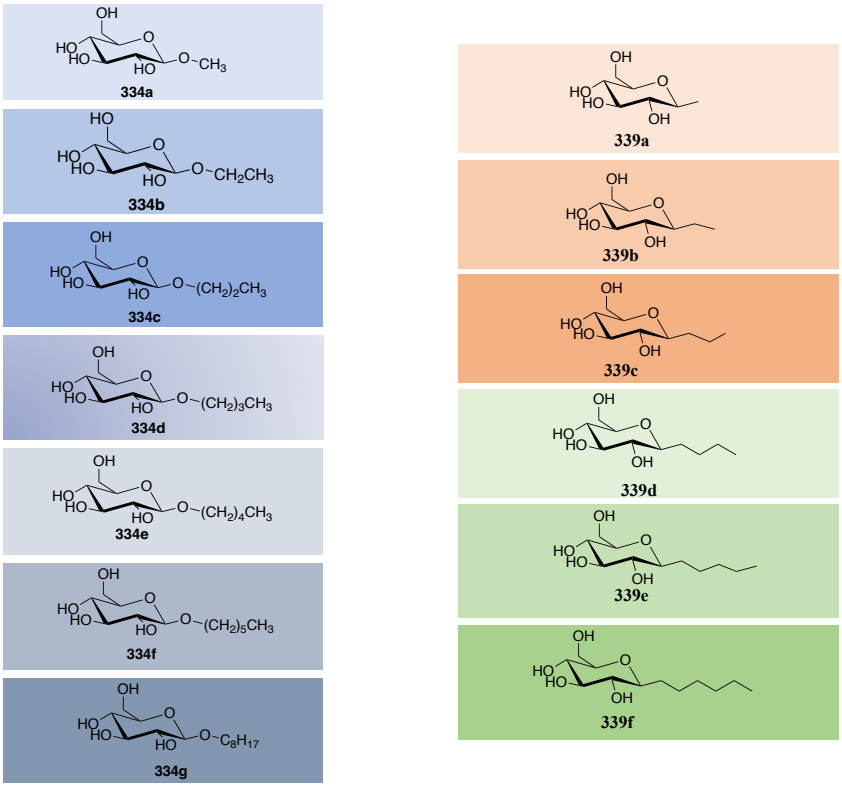

Figure 2.2 Chemical structures of the different *O*- and *C*- alkyl linked pyranose derivatives.

2.3 Objective 2: Assessing the Potential of Small Molecule Ice Recrystallization Inhibitors (IRIs) to Cryopreserve Induced Pluripotent Stem Cell-Derived Neurons (iPSC-Ns)

iPSCs and their derivatives, such as iPSC-Ns, are powerful tools in the RM and cell-based therapy fields because they can be used to study the cause and aetiology of different neurological diseases, and to develop potential cellular therapy products.[51] iPSCs are somatic stem cells which are reprogrammed by overexpressing the pluripotency-specific transcription factors: SOX2, OCT3/4 and c-MYC.[52-54] iPSCs represent a differentiated modality toward producing other cell types, which makes them useful in modelling and understanding the mechanisms of different diseases, such as Alzheimer's and Parkinson diseases.[55-57] The grafting of iPSC-derived myeloid lineage (iPSC-ML) has been found to improve cognition in Alzheimer's-modeled mice.[58-59] The growing applications of stem-cell based therapies necessitates a large supply of quality-controlled working and master cell banks; this, in turn, facilitates the need for efficient and effective protocols for the cryopreservation of iPSCs and their derivatives. The sensitivity of iPSCs and iPSC-Ns results in low yield and in disrupted functionality following cryopreservation.[60-61] Conventional cryopreservation protocols suggest freezing iPSCs prior to differentiation into iPSC-Ns because the post-mitotic nature of the terminally differentiated iPSC-Ns renders them extremely susceptible to cryoinjuries associated with the freezing and thawing processes. Moreover, generating iPSC-Ns from iPSCs is a costly and lengthy process, taking between 2 and 6 months, depending on the specific type of

neurons required.[62-63] Therefore, a viable cryopreservation regimen, utilized for freezing and thawing iPSC-Ns directly, is paramount for their therapeutic application in clinics.

In collaboration with Dr. Anna Jezierski and her laboratory (NRC, Human Health Therapeutic Department, Ottawa), the supplementation of cryomedia with IRIs is examined as an avenue for improved iPSC-Ns cryopreservation. The use of *N*-2-fluorophenyl-D-gluconamide (2FA) has been found to enhance the post-thaw viability and functionality outcomes of HSPCs and iPSCs.[30,64] With this work as a baseline, this thesis seeks to investigate whether 2FA may increase the yield of cells post-thaw and shorten the timeline required for the re-establishment of synaptic activity of iPSC-Ns post preservation. iPSCs are differentiated into iPSC-Ns according to STEMCELL Technologies' protocol (**Figure 2.3**) to yield post-mitotic neurons.[51] iPSC-Ns are then frozen in a commercially available, GMP-compatible, cryomedium, Cryostor®10 (CS10), in the presence (10 mM, 5 mM, 2.5 mM) or absence of 2FA. The efficacy of the cryopreservation protocol of iPSC-Ns is assessed by analyzing the post-thaw viability and recovery rate, as well as the firing activity post cryopreservation. The post-thaw functionality is determined by monitoring the firing activity and network re-establishment of the cryopreserved iPSC-Ns using a microelectrode array system (**Figure 2.3)**. Viable and functional iPSC-Ns express key neuronal, membrane- or synaptic-associated markers, therefore, iPSC-Ns are also subjected to immunostaining to ensure that the cryopreservation protocol does not compromise the expression of fundamental neuronal receptors/channels post-thaw. Moreover, the functionality of the different channels and receptors is examined via neuropharmacological responses. The cryopreserved iPSC-Ns are subjected to a panel of neuroactive drugs to measure the change in the firing activity of

neurons and maturity of the different channels/receptors found in iPSC-N culture (**Figure 2.3**). The data from this objective will help establish the importance of an IRI active component toward an optimized cryopreservation protocol for iPSC-Ns, a highly sensitive and clinically relevant cell type.

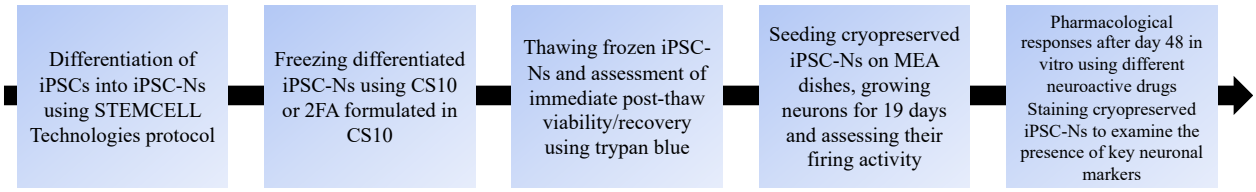

Figure 2.3 Workflow diagram illustrating the different steps done to characterize the efficacy of the proposed cryopreservation protocol.

2.4 Objective 3: Evaluating the Capacity of IRIs to Cryopreserve Jurkat Cell Line and Primary T Cells

Adoptive T-cell therapy (ACT), a type of immunotherapy, is a promising treatment option for a variety of cancers.[65-67] ACT enhances antigen-specific immunity in cancer patients through the introduction of modified T cells with specific antigens/receptors to selectively target tumor antigens.[68-69] Some of the cellular products produced for ACT include chimeric antigen receptor T cell (CAR-T cells) and T cell receptor (TCR) engineering.[69] T cell therapy products have proven to be effective treatments for different tumors, such as B-cell malignancies and acute myeloid leukemia (AML).[70-72] One of the major challenges for these therapies lies in retaining a high yield of functional T cell products.[73-75] Conventional cryopreservation media currently proposed for freezing T cell products result in low recovery rate and loss of functionality post-thaw,[73-75] generating the need to develop an optimized cryopreservation protocol for these products.

The third objective of this thesis is to develop IRIs for use in the cryopreservation protocol T cell-based therapy products. Initially, two IRIs, 2FA and *N*-4-chlorophenyl-D-

gluconamide (4ClA), are compared for T cell preservation in collaboration with Dr. Scott McComb and his laboratory (NRC, Human Health Therapeutics Department, Ottawa). Jurkat cells (an immortalized line of human-derived primary T cells), as well as primary T cells and human CD19 CAR-T cells are first tested where they are frozen with CS10 in the presence and absence of 2FA or 4ClA to establish which compound best improves the post-thaw viability and recovery rate. After the establishment that 2FA yields higher number of viable cells, it is further examined on primary T cells obtained at different stages (pre-activation, day 1 or day 9 post-activation) to further confirm its capacity in preserving high numbers of live cells post-thaw.

The effect of cryopreservation on the cytotoxic killing functionality of activated-T cells (MOCK) and epidermal growth factor receptor (EGFR) CAR-T cells post-thaw is then assessed. Delayed onset cell death (DOCD) is one of the cryopreservation-induced stressors that affects the recovery and functionality of T cell products. Therefore, MOCK T cells and EGFR CAR-T cells are frozen with CS10 in the presence and absence of 2FA to investigate any changes in the presence of IRIs. Cryopreserved MOCK T cells and EGFR CAR-T cells are then seeded in the presence of tumor cells (SKOV3) and the IncuCyte live cell imaging system (Sartorius) is utilized to measure the killing activity of the cryopreserved cells. Ultimately, the data obtained from this chapter will assist in optimizing the cryopreservation protocol for T cell products to ensure the delivery of safe and efficacious T cell therapy products to clinics.

2.5 Objective 4: Optimizing the Freezing Solution Used for Cryopreserving Primary Natural Killer (pNK) Cells

Human-derived natural killer (NK) cells are one of the most powerful tools in immunotherapy due to their cytotoxic nature toward various tumor cells.[41] Moreover, NK cell-based therapy has been shown to be highly efficacious and avoids causing graft-versus-host reactions post engraftment in cancer patients.[41-43,76] Therefore, production of clinical scale NK cells from different cell sources such as iPSCs and peripheral blood mononuclear cells (PBMCs) has increased significantly.[77-79] The successful application of NK-based therapy relies on the availability and delivery of NK cellular products to patients, thus, establishing improved cryopreservation protocols is vital to meet the rising demand for NK cell therapy.

One of the major challenges in cryopreserving NK cells is that they are highly susceptible to cellular damage caused by cycles of freezing and thawing, which necessities the investigation of several modified cryomedia formulations.[80-81] To date, none of the conventionally proposed cryomedia solutions protect NK cells from ice recrystallization which is one of the main contributors to cryoinjury associated with cryopreservation.[30-31,82] Consequently, the fourth objective of this thesis investigates the potential for IRIs to enhance the yield of NK cells post-thaw, as well as their cytotoxic activity against tumors.

Four different literature-proposed cryomedia formulations are examined and their cryopreservation outcomes are compared with a commercially available, GMP-compatible cryo-solution, Cryostore®10 (CS10). The NK92 cell line and pNK cells are frozen in four different cryomedia to evaluate the effectiveness of each cryo-solution. DOCD is further

monitored by analyzing the 48-hr post-thaw viability and recovery rate to ensure that the proposed cryomedia protect cells from any delayed cryoinjuries.

Given the success of 2FA in our studies on iPSC-Ns and T cells, it is further tested as a cryo-additive for pNK cells, to investigate any changes in cell survival and functionality. The killing activity of CS10- or 2FA-frozen pNK cells is also assessed and compared to the cytotoxic killing functionality of unfrozen pNK cells by co-culturing frozen and unfrozen pNK cells with K562 tumor cells. Overall, the preliminary results presented in this chapter will determine whether integrating IRIs into current protocols enhances the cryopreservation outcomes and allows the delivery of safe and effective NK cell products.

2.6 Chapter Summary

The overall goal of this thesis is to study the structural features of IRI candidates to assist in future IRI development, and to discover the applicability of IRIs in the cryopreservation protocol of several types of cells (iPSC-Ns, T cells, and NK cells). The investigation of the overall goal follows the objectives mentioned below:

1- Investigation of the influence of alkyl chain length and glycosidic linkage on the IRI activity of *O*-linked and *C*-linked alkyl pyranose derivatives (chapter 3).

2- Assessing the ability to cryopreserve induced pluripotent stem cell-derived neurons (iPSC-Ns) using small molecule ice recrystallization inhibitors (IRIs) (chapter 4).

3- Determination of the ability of *N*-aryl-D-gluconamide derivatives to cryopreserve Jurkat cell line and primary T cells (chapter 5).

4- Evaluation of the conventional cryomedia proposed to preserve primary natural killer (pNK) cells, as well as the assessment of an IRI active molecule to enhance the cryopreservation outcome of pNK cells (chapter 6).

2.7 References

(1) Sampogna, G.; Guraya, S. Y.; Forgione, A. Regenerative Medicine: Historical Roots and Potential Strategies in Modern Medicine. *J. Microsc. Ultrastruct.* **2015**, *3* (3), 101–107. https://doi.org/10.1016/j.jmau.2015.05.002.

(2) Edwards, J.; Thomas, R.; Guilliatt, R. Regenerative Medicine: From the Laboratory Looking Out. *Palgrave Commun.* **2017**, *3* (1). https://doi.org/10.1057/s41599-017-0036-x.

(3) Gage, F. H.; Temple, S. Neural Stem Cells: Generating and Regenerating the Brain. *Neuron* **2013**, *80* (3), 588–601. https://doi.org/10.1016/j.neuron.2013.10.037.

(4) Yang, H.; Zhao, H.; Acker, J. P.; Liu, J. Z.; Akabutu, J.; McGann, L. E. Effect of Dimethyl Sulfoxide on Post-Thaw Viability Assessment of CD45 + and CD34+ Cells of Umbilical Cord Blood and Mobilized Peripheral Blood. *Cryobiology* **2005**, *51* (2), 165–175. https://doi.org/10.1016/j.cryobiol.2005.06.003.

(5) Tamagnini, F.; Scullion, S.; Brown, J. T.; Randall, A. D. Low Concentrations of the Solvent Dimethyl Sulphoxide Alter Intrinsic Excitability Properties of Cortical and Hippocampal Pyramidal Cells. *PLoS One* **2014**, *9* (3). https://doi.org/10.1371/journal.pone.0092557.

(6) Stroncek, D.; Fautsch, S.; Lasky, L.; Hurd, D.; Ramsay, N.; McCullough, J. Adverse Reactions in Patients Transfused with Cryopreserved Marrow. *Transfusion* **1991**, *31* (6), 521–526. https://doi.org/10.1046/j.1537-2995.1991.31691306250.x.

(7) Shu, Z.; Heimfeld, S.; Gao, D. Hematopoietic SCT with Cryopreserved Grafts: Adverse Reactions after Transplantation and Cryoprotectant Removal before Infusion. *Bone Marrow Transplant.* **2014**, *49* (4), 469–476. https://doi.org/10.1038/bmt.2013.152.

(8) Negishi, T.; Ishii, Y.; Kawamura, S.; Kuroda, Y.; Yoshikawa, Y. Cryopreservation and Primary Culture of Cerebral Neurons from Cynomolgus Monkeys (Macaca

Fascicularis). *Neurosci. Lett.* **2002**, *328* (1), 21–24. https://doi.org/10.1016/S0304-3940(02)00433-0.

(9) Nishigaki, T.; Teramura, Y.; Nasu, A.; Takada, K.; Toguchida, J.; Iwata, H. Highly Efficient Cryopreservation of Human Induced Pluripotent Stem Cells Using a Dimethyl Sulfoxide-Free Solution. *Int. J. Dev. Biol.* **2011**, *55* (3), 305–311. https://doi.org/10.1387/ijdb.103145tn.

(10) Buskirk, R. G. Van; Baust, J. M.; Snyder, K. K.; Mathew, A. J.; Baust, J. G. Hypothermic Storage and Cryopreservation. *Bioprocess Int.* **2004**, 42–49.

(11) Hainaut, P.; Vaught, J.; Zatloukal, K.; Pasterk, M. *Biobanking of Human Biospecimens: Principles and Practice*; 2017. https://doi.org/10.1007/978-3-319-55120-3.

(12) Scott, K. L.; Lecak, J.; Acker, J. P. Biopreservation of Red Blood Cells: Past, Present, and Future. *Transfus. Med. Rev.* **2005**, *19* (2), 127–142. https://doi.org/10.1016/j.tmrv.2004.11.004.

(13) Fuller, B. J.; Petrenko, A. Y.; Rodriguez, J. V.; Somov, A. Y.; Balaban, C. L.; Guibert, E. E. Biopreservation of Hepatocytes: Current Concepts on Hypothermic Preservation, Cryopreservation, and Vitrification. *Cryo-Letters* **2016**, *37* (4), 432–452.

(14) Baust, J. M. Advances in Media for Cryopreservation and Hypothermic Storage. *BioProcess Int* **2005**, *3* (6), 46–56.

(15) Rubinsky, B. Principles of Low Temperature Cell Preservation. *Heart Fail. Rev.* **2003**, *8*, 277–284. https://doi.org/10.1023/A.

(16) Correia, C. .; Koshkin, A. .; Carido, M. .; Espinha, N. .; Saric, T. .; Lima, P. .; Serra, M. .; Alves, P. Effective Hypothermic Storage of Human Pluripotent Stem Cell-Derived Cardiomyocytes Compatible With Global Distribution of Cells for Clinical Applications and Toxicology Testing. *Stem Cells Transl. Med* **2016**, *5*, 658.

(17) Zenhäusern, R.; Tobler, A.; Leoncini, L.; Hess, O. M.; Ferrari, P. Fatal Cardiac Arrhythmia after Infusion of Dimethyl Sulfoxide-Cryopreserved Hematopoietic Stem Cells in a Patient with Severe Primary Cardiac Amyloidosis and End-Stage Renal Failure. *Ann. Hematol.* **2000**, *79* (9), 523–526. https://doi.org/10.1007/s002770000186.

(18) Wakeman, D. R.; Hiller, B. M.; Marmion, D. J.; McMahon, C. W.; Corbett, G. T.; Mangan, K. P.; Ma, J.; Little, L. E.; Xie, Z.; Perez-Rosello, T.; Guzman, J. N.; Surmeier, D. J.; Kordower, J. H. Cryopreservation Maintains Functionality of Human IPSC Dopamine Neurons and Rescues Parkinsonian Phenotypes In Vivo. *Stem Cell Reports* **2017**, *9* (1), 149–161. https://doi.org/10.1016/j.stemcr.2017.04.033.

(19) Bakar, B.; Kose, E. A.; Sonal, S.; Alhan, A.; Kilinc, K.; Keskil, I. S. Evaluation of the Neurotoxicity of DMSO Infused into the Carotid Artery of Rat. *Injury* **2012**, *43* (3), 315–322. https://doi.org/10.1016/j.injury.2011.08.021.

(20) Cavaletti, G.; Oggioni, N.; Sala, F.; Pezzoni, G.; Cavalletti, E.; Marmiroli, P.; Petruccioli, M. G.; Frattola, L.; Tredici, G. Effect on the Peripheral Nervous System of Systemically Administered Dimethylsulfoxide in the Rat: A Neurophysiological and Pathological Study. *Toxicol. Lett.* **2000**, *118* (1–2), 103–107. https://doi.org/10.1016/S0378-4274(00)00269-1.

(21) Hess, J. R. Red Cell Freezing and Its Impact on the Supply Chain. *Transfus. Med.* **2004**, *14* (1), 1–8. https://doi.org/10.1111/j.0958-7578.2004.00472.x.

(22) Meryman, H. T.; Hornblower, M. A Method for Freezing and Washing Red Blood Cells Using a High Glycerol Concentration. *Transfusion* **1972**, *12* (3), 145–156. https://doi.org/10.1111/j.1537-2995.1972.tb00001.x.

(23) Valeri, C. R.; Ragno, G.; Pivacek, L. In Vivo Survival of Apheresis RBCs, Frozen with 40-Percent (Wt/Vol) Glycerol, Deglycerolized in the ACP 215, and Stored at 4°C in AS-3 for up to 21 Days. *Transfusion* **2001**, *41* (7), 928–932.

(24) Capicciotti, C. J.; Doshi, M.; Ben, R. N. Ice Recrystallization Inhibitors: From Biological Antifreezes to Small Molecules. *Recent Dev. Study Recryst.* **2013**. https://doi.org/10.5772/54992.

(25) Devries, A. L.; Lin, Y. Structure of a Peptide Antifreeze and Mechanism of Adsorption to Ice. *Biochim. Biophys. Acta - Protein Struct.* **1977**, *495* (2), 388–392. https://doi.org/10.1016/0005-2795(77)90395-6.

(26) Harding, M. M.; Ward, L. G.; Haymet, A. D. J. Type I 'Antifreeze'Proteins. *Eur. J. Biochem* **1999**, *264*, 653–665.

(27) Hayward, J. A.; Haymet, A. D. J. Ice/Water Interface: Molecular Dynamics

Simulations of the Basal, Prism, {20$\bar{2}$1}, and {21$\bar{1}$0} Interfaces of Ice Ih. *J. Chem. Phys.* **2001**, *114* (8), 3713–3726. https://doi.org/10.1063/1.1333680.

(28) Scholander, P. F.; van Dam, L.; Kanwisher, J. W.; Hammel, H. T.; Gordon, M. S. Supercooling and Osmoregulation in Arctic Fish. *J. Cell. Comp. Physiol.* **1957**, *49* (1), 5–24. https://doi.org/10.1002/jcp.1030490103.

(29) Capicciotti, C. J.; Leclère, M.; Perras, F. A.; Bryce, D. L.; Paulin, H.; Harden, J.; Liu, Y.; Ben, R. N. Potent Inhibition of Ice Recrystallization by Low Molecular Weight Carbohydrate-Based Surfactants and Hydrogelators. *Chem. Sci.* **2012**, *3* (5), 1408–1416. https://doi.org/10.1039/c2sc00885h.

(30) Briard, J. G.; Jahan, S.; Chandran, P.; Allan, D.; Pineault, N.; Ben, R. N. Small-Molecule Ice Recrystallization Inhibitors Improve the Post-Thaw Function of Hematopoietic Stem and Progenitor Cells. *ACS Omega* **2016**, *1* (5), 1010–1018. https://doi.org/10.1021/acsomega.6b00178.

(31) Capicciotti, C. J.; Mancini, R. S.; Turner, T. R.; Koyama, T.; Alteen, M. G.; Doshi, M.; Inada, T.; Acker, J. P.; Ben, R. N. O-Aryl-Glycoside Ice Recrystallization Inhibitors as Novel Cryoprotectants: A Structure-Function Study. *ACS Omega* **2016**, *1* (4), 656–662. https://doi.org/10.1021/acsomega.6b00163.

(32) Estroff, L. A.; Hamilton, A. D. Water Gelation by Small Organic Molecules. *Chem. Rev.* **2004**, *104* (3), 1201–1217. https://doi.org/10.1021/cr0302049.

(33) De Loos, M.; Feringa, B. L.; Van Esch, J. H. Design and Application of Self-Assembled Low Molecular Weight Hydrogels. *European J. Org. Chem.* **2005**, No. 17, 3615–3631. https://doi.org/10.1002/ejoc.200400723.

(34) Woods, E. J.; Thirumala, S.; Badhe-Buchanan, S. S.; Clarke, D.; Mathew, A. J. Off the Shelf Cellular Therapeutics: Factors to Consider during Cryopreservation and Storage of Human Cells for Clinical Use. *Cytotherapy* **2016**, *18* (6), 697–711. https://doi.org/10.1016/j.jcyt.2016.03.295.

(35) Hunt, C. J. Cryopreservation of Human Stem Cells for Clinical Application: A Review. *Transfus. Med. Hemotherapy* **2011**, *38* (2), 107–123. https://doi.org/10.1159/000326623.

(36) Jakeman, L. B.; Reier, P. J. Axonal Projections between Fetal Spinal Cord Transplants and the Adult Rat Spinal Cord: A Neuroanatomical Tracing Study of

Local Interactions. *J. Comp. Neurol.* **1991**, *307* (2), 311–334. https://doi.org/10.1002/cne.903070211.

(37) Coumans, J. V.; Lin, T. T. S.; Hai Ning Dai; MacArthur, L.; McAtee, M.; Nash, C.; Bregman, B. S. Axonal Regeneration and Functional Recovery after Complete Spinal Cord Transection in Rats by Delayed Treatment with Transplants and Neurotrophins. *J. Neurosci.* **2001**, *21* (23), 9334–9344. https://doi.org/10.1523/jneurosci.21-23-09334.2001.

(38) Takamatsu, K.; Ikeda, T.; Haruta, M.; Matsumura, K.; Ogi, Y.; Nakagata, N.; Uchino, M.; Ando, Y.; Nishimura, Y.; Senju, S. Degradation of Amyloid Beta by Human Induced Pluripotent Stem Cell-Derived Macrophages Expressing Neprilysin-2. *Stem Cell Res.* **2014**, *13* (3), 442–453. https://doi.org/10.1016/j.scr.2014.10.001.

(39) Bloemberg, D.; Nguyen, T.; Maclean, S.; Zafer, A.; Gadoury, C.; Gurnani, K.; Chattopadhyay, A.; Ash, J.; Lippens, J.; Harcus, D.; Pagé, M.; Pon, R. A.; Gilbert, R.; Marcil, A.; Weeratna, R. D.; Mccomb, S. A Modular High-Throughput Screening Platform for Chimeric Antigen Receptor (CAR) Development.

(40) Majzner, R. G.; Mackall, C. L. Clinical Lessons Learned from the First Leg of the CAR T Cell Journey. *Nat. Med.* **2019**, *25* (9), 1341–1355. https://doi.org/10.1038/s41591-019-0564-6.

(41) Mehta, R. S.; Randolph, B.; Daher, M.; Rezvani, K. NK Cell Therapy for Hematologic Malignancies. *Int. J. Hematol.* **2018**, *107* (3), 262–270. https://doi.org/10.1007/s12185-018-2407-5.

(42) Melaiu, O.; Chierici, M.; Lucarini, V.; Jurman, G.; Conti, L. A.; De Vito, R.; Boldrini, R.; Cifaldi, L.; Castellano, A.; Furlanello, C.; Barnaba, V.; Locatelli, F.; Fruci, D. Cellular and Gene Signatures of Tumor-Infiltrating Dendritic Cells and Natural-Killer Cells Predict Prognosis of Neuroblastoma. *Nat. Commun.* **2020**, *11* (1), 1–15. https://doi.org/10.1038/s41467-020-19781-y.

(43) Xie, G.; Dong, H.; Liang, Y.; Ham, J. D.; Rizwan, R.; Chen, J. CAR-NK Cells: A Promising Cellular Immunotherapy for Cancer. *EBioMedicine* **2020**, *59*. https://doi.org/10.1016/j.ebiom.2020.102975.

(44) Ben, R. N.; Eniade, A. A.; Hauer, L. Synthesis of a C-Linked Antifreeze

Glycoprotein (AFGP) Mimic: Probes for Investigating the Mechanism of Action. *Org. Lett.* **1999**, *1* (11), 1759–1762. https://doi.org/10.1021/ol991025+.

(45) Tam, R. Y.; Ferreira, S. S.; Czechura, P.; Ben, R. N.; Chaytor, J. L. Hydration Index-a Better Parameter for Explaining Small Molecule Hydration in Inhibition of Ice Recrystallization. *J. Am. Chem. Soc.* **2008**, *130* (51), 17494–17501. https://doi.org/10.1021/ja806284x.

(46) Wong, F. M. P.; Reimer, D. L.; Bally, M. B. Cationic Lipid Binding to DNA: Characterization of Complex Formation. *Biochemistry* **1996**, *35* (18), 5756–5763. https://doi.org/10.1021/bi952847r.

(47) Lehanine, Z.; Badache, L. Effect of the Molecular Structure on the Adsorption Properties of Cationic Surfactants at the Air-Water Interface. *J. Surfactants Deterg.* **2016**, *19* (2), 289–295. https://doi.org/10.1007/s11743-015-1772-9.

(48) Balcerzak, A. K.; Febbraro, M.; Ben, R. N. The Importance of Hydrophobic Moieties in Ice Recrystallization Inhibitors. *RSC Adv.* **2013**, *3* (10), 3232–3236. https://doi.org/10.1039/c3ra23220d.

(49) Ampaw, A.; Charlton, T. A.; Briard, J. G.; Ben, R. N. Designing the next Generation of Cryoprotectants – from Proteins to Small Molecules. *Pept. Sci.* **2019**, *111* (e24086), 1–12. https://doi.org/10.1002/pep2.24086.

(50) Brenna, E.; Fuganti, C.; Grasselli, P.; Serra, S.; Zambotti, S. A Novel General Route for the Synthesis of C-Glycosyl Tyrosine Analogues. *Chem. - A Eur. J.* **2002**, *8* (8), 1872–1878. https://doi.org/10.1002/1521-3765(20020415)8:8<1872::AID-CHEM1872>3.0.CO;2-A.

(51) Jezierski, A.; Baumann, E.; Aylsworth, A.; Costain, W. J.; Corluka, S.; Banderali, U.; Sodja, C.; Ribecco-Lutkiewicz, M.; Salma, A.; Marzia, M.; Joseph, T. Electrophysiological- and Neuropharmacological-Based Benchmarking of Human Induced Pluripotent Stem Cell-Derived and Primary Rodent Neurons. *Stem Cell Rev. Reports* **2021**, No. 0123456789.

(52) Scudellari, M. A Decade of : IPS Cells. *Nature* **2016**, *534* (7607), 310–312. https://doi.org/10.1038/534310a.

(53) Wu, S. M.; Hochedlinger, K. Harnessing the Potential of Induced Pluripotent Stem Cells for Regenerative Medicine. *Nat. Publ. Gr.* **2011**, *13* (5), 497–505.

https://doi.org/10.1038/ncb0511-497.

(54) Takahashi, K.; Tanabe, K.; Ohnuki, M.; Narita, M.; Ichisaka, T.; Tomoda, K.; Yamanaka, S. Induction of Pluripotent Stem Cells from Adult Human Fibroblasts by Defined Factors. *Cell* **2007**, *131* (5), 861–872. https://doi.org/10.1016/j.cell.2007.11.019.

(55) Meijer, M.; Rehbach, K.; Brunner, J. W.; Classen, J. A.; Lammertse, H. C. A.; van Linge, L. A.; Schut, D.; Krutenko, T.; Hebisch, M.; Cornelisse, L. N.; Sullivan, P. F.; Peitz, M.; Toonen, R. F.; Brüstle, O.; Verhage, M. A Single-Cell Model for Synaptic Transmission and Plasticity in Human IPSC-Derived Neurons. *Cell Rep.* **2019**, *27* (7), 2199-2211.e6. https://doi.org/10.1016/j.celrep.2019.04.058.

(56) Penney, J.; Ralvenius, W. T.; Tsai, L. H. Modeling Alzheimer's Disease with IPSC-Derived Brain Cells. *Mol. Psychiatry* **2020**, *25* (1), 148–167. https://doi.org/10.1038/s41380-019-0468-3.

(57) Schöndorf, D. C.; Aureli, M.; McAllister, F. E.; Hindley, C. J.; Mayer, F.; Schmid, B.; Sardi, S. P.; Valsecchi, M.; Hoffmann, S.; Schwarz, L. K.; Hedrich, U.; Berg, D.; Shihabuddin, L. S.; Hu, J.; Pruszak, J.; Gygi, S. P.; Sonnino, S.; Gasser, T.; Deleidi, M. IPSC-Derived Neurons from GBA1-Associated Parkinson's Disease Patients Show Autophagic Defects and Impaired Calcium Homeostasis. *Nat. Commun.* **2014**, *5* (May). https://doi.org/10.1038/ncomms5028.

(58) Ager, R. R.; Davis, J. L.; Agazaryan, A.; Benavente, F.; Poon, W. W.; Laferla, F. M.; Blurton-Jones, M. Human Neural Stem Cells Improve Cognition and Promote Synaptic Growth in Two Complementary Transgenic Models of Alzheimer's Disease and Neuronal Loss. *Hippocampus* **2015**, *25* (7), 813–826. https://doi.org/10.1002/hipo.22405.

(59) Rosenzweig, E. S.; Brock, J. H.; Lu, P.; Kumamaru, H.; Salegio, E. A.; Kadoya, K.; Weber, J. L.; Liang, J. J.; Moseanko, R.; Hawbecker, S.; Huie, J. R.; Havton, L. A.; Nout-Lomas, Y. S.; Ferguson, A. R.; Beattie, M. S.; Bresnahan, J. C.; Tuszynski, M. H. Restorative Effects of Human Neural Stem Cell Grafts on the Primate Spinal Cord. *Nat. Med.* **2018**. https://doi.org/10.1038/nm.4502.

(60) Crook, J. M.; Tomaskovic-Crook, E.; Ludwig, T. Cryobanking Pluripotent Stem Cells. In *Methods Mol Biol*; 2017; Vol. 1590, pp 151–164.

https://doi.org/10.1007/978-1-4939-6921-0.

(61) Martn-Ibez, R.; Hovatta, O.; M., J. Cryopreservation of Human Pluripotent Stem Cells: Are We Going in the Right Direction? *Curr. Front. Cryobiol.* **2012**. https://doi.org/10.5772/34853.

(62) Lee, S.; Huang, E. J. Modeling ALS and FTD with IPSC-Derived Neurons. *Brain Res.* **2017**, *1656*, 88–97. https://doi.org/10.1016/j.brainres.2015.10.003.

(63) Kobayashi, Y.; Okada, Y.; Itakura, G.; Iwai, H.; Nishimura, S.; Yasuda, A.; Nori, S.; Hikishima, K.; Konomi, T.; Fujiyoshi, K.; Tsuji, O.; Toyama, Y.; Yamanaka, S.; Nakamura, M.; Okano, H. Pre-Evaluated Safe Human IPSC-Derived Neural Stem Cells Promote Functional Recovery after Spinal Cord Injury in Common Marmoset without Tumorigenicity. *PLoS One* **2012**, *7* (12), 1–13. https://doi.org/10.1371/journal.pone.0052787.

(64) Chopra, K. Improved Cryopreservation of Induced Pluripotent Stem Cells Using N-Aryl Glycosidic Small Molecule Ice Recrystallization Inhibitors. *(Master's Diss. Univ. d'Ottawa/University Ottawa* **2020**.

(65) Fridman, W. .; Galon, J.; Dieu-Nosjean, M. C.; Cremer, I.; Fisson, S.; Damotte, D.; Page`s, F.; Tartour, E.; Saute`s-Fridman, C.; Contents. *Immune Infiltration in Human Cancer: Prognostic Significance and Disease Control*; 1977; Vol. 344. https://doi.org/10.1016/0026-265x(77)90137-0.

(66) Yee, C.; Thompson, J. A.; Byrd, D.; Riddell, S. R.; Roche, P.; Celis, E.; Greenberg, P. D. Adoptive T Cell Therapy Using Antigen-Specific CD8+ T Cell Clones for the Treatment of Patients with Metastatic Melanoma: In Vivo Persistence, Migration, and Antitumor Effect of Transferred T Cells. *Proc. Natl. Acad. Sci. U. S. A.* **2002**, *99* (25), 16168–16173. https://doi.org/10.1073/pnas.242600099.

(67) Walsh, S. R.; Simovic, B.; Chen, L.; Bastin, D.; Nguyen, A.; Stephenson, K.; Mandur, T. S.; Bramson, J. L.; Lichty, B. D.; Wan, Y. Endogenous T Cells Prevent Tumor Immune Escape Following Adoptive T Cell Therapy. *J. Clin. Invest.* **2019**, *129* (12), 5400–5410. https://doi.org/10.1172/JCI126199.

(68) Fesnak, A. D.; June, C. H.; Levine, B. L. Engineered T Cells: The Promise and Challenges of Cancer Immunotherapy. *Nat. Rev. Cancer* **2016**, *16* (9), 566–581. https://doi.org/10.1038/nrc.2016.97.

(69) Payne, K. K.; Bear, H. D.; Manjili, M. H. Adoptive Cellular Therapy of Cancer: Exploring Innate and Adaptive Cellular Crosstalk to Improve Anti-Tumor Efficacy. *Futur. Oncol.* **2014**, *10* (10), 1779–1794. https://doi.org/10.2217/fon.14.0.

(70) Gill, S.; Maus, M. V.; Porter, D. L. Chimeric Antigen Receptor T Cell Therapy: 25 Years in the Making. *Blood Rev.* **2016**, *30* (3), 157–167. https://doi.org/10.1016/j.blre.2015.10.003.

(71) Cappell, K. M.; Sherry, R. M.; Yang, J. C.; Goff, S. L.; Vanasse, D. A.; McIntyre, L.; Rosenberg, S. A.; Kochenderfer, J. N. Long-Term Follow-Up of Anti-CD19 Chimeric Antigen Receptor T-Cell Therapy. *J. Clin. Oncol.* **2020**, *38* (32), 3805–3815. https://doi.org/10.1200/JCO.20.01467.

(72) Kochenderfer, J. N.; Somerville, R. P. T.; Lu, T.; Yang, J. C.; Sherry, R. M.; Feldman, S. A.; McIntyre, L.; Bot, A.; Rossi, J.; Lam, N.; Rosenberg, S. A. Long-Duration Complete Remissions of Diffuse Large B Cell Lymphoma after Anti-CD19 Chimeric Antigen Receptor T Cell Therapy. *Mol. Ther.* **2017**, *25* (10), 2245–2253. https://doi.org/10.1016/j.ymthe.2017.07.004.

(73) Owen, R. E.; Sinclair, E.; Emu, B.; Heitman, J. W.; Hirschkorn, D. F.; Epling, C. L.; Tan, Q. X.; Custer, B.; Harris, J. M.; Jacobson, M. A.; McCune, J. M.; Martin, J. N.; Hecht, F. M.; Deeks, S. G.; Norris, P. J. Loss of T Cell Responses Following Long-Term Cryopreservation. *J. Immunol. Methods* **2007**, *326* (1–2), 93–115. https://doi.org/10.1016/j.jim.2007.07.012.

(74) Baboo, J.; Kilbride, P.; Delahaye, M.; Milne, S.; Fonseca, F.; Blanco, M.; Meneghel, J.; Nancekievill, A.; Gaddum, N.; Morris, G. J. The Impact of Varying Cooling and Thawing Rates on the Quality of Cryopreserved Human Peripheral Blood T Cells. *Sci. Rep.* **2019**, *9* (1), 1–13. https://doi.org/10.1038/s41598-019-39957-x.

(75) Weinberg, A.; Song, L. Y.; Wilkening, C.; Sevin, A.; Blais, B.; Louzao, R.; Stein, D.; Defechereux, P.; Durand, D.; Riedel, E.; Raftery, N.; Jesser, R.; Brown, B.; Keller, M. F.; Dickover, R.; McFarland, E.; Fenton, T. Optimization and Limitations of Use of Cryopreserved Peripheral Blood Mononuclear Cells for Functional and Phenotypic T-Cell Characterization. *Clin. Vaccine Immunol.* **2009**, *16* (8), 1176–1186. https://doi.org/10.1128/CVI.00342-08.

(76) Gurney, M.; O'Dwyer, M. Realizing Innate Potential : CAR-NK Cell Therapies for

Acute Myeloid Leukemia. *Cancers (Basel).* **2021**, *13*, 1568. https://doi.org//doi.org/10.3390/cancers 13071568 Academic.

(77) Zhu, H.; Kaufman, D. S. An Improved Method to Produce Clinical-Scale Natural Killer Cells from Human Pluripotent Stem Cells. *Methods Mol. Biol.* **2019**, *2048*, 107–119. https://doi.org/10.1007/978-1-4939-9728-2_12.

(78) Shankar, K.; Capitini, C. M.; Capitini, C. M.; Saha, K.; Saha, K.; Saha, K. Genome Engineering of Induced Pluripotent Stem Cells to Manufacture Natural Killer Cell Therapies. *Stem Cell Res. Ther.* **2020**, *11* (1), 1–14. https://doi.org/10.1186/s13287-020-01741-4.

(79) Dalle, J. H.; Menezes, J.; Wagner, É.; Blagdon, M.; Champagne, J.; Champagne, M. A.; Duval, M. Characterization of Cord Blood Natural Killer Cells: Implications for Transplantation and Neonatal Infections. *Pediatr. Res.* **2005**, *57* (5 I), 649–655. https://doi.org/10.1203/01.PDR.0000156501.55431.20.

(80) Mata, M. M.; Mahmood, F.; Sowell, R. T.; Baum, L. L. Effects of Cryopreservation on Effector Cells for Antibody Dependent Cell-Mediated Cytotoxicity (ADCC) and Natural Killer (NK) Cell Activity in 51Cr-Release and CD107a Assays. *J. Immunol. Methods* **2014**, *406*, 1–9. https://doi.org/10.1016/j.jim.2014.01.017.

(81) Cells, N. K.; Antitumor, E.; Yang, B.; Cho, S. Y.; Hwang, Y. K.; Yun, C. Erratum: Cryopreserved Human Natural Killer Cells Exhibit Potent Antitumor Efficacy against Orthotopic Pancreatic Cancer through Efficient Tumor-Homing and Cytolytic Ability (Running Title: Cryopreserved NK Cells Exhibit Antitumor Effect) (Cancers 2019, 1. *Cancers (Basel).* **2020**, *12* (11), 1–2. https://doi.org/10.3390/cancers12113255.

(82) Matsumoto, S.; Matsusita, M.; Morita, T.; Kamachi, H.; Tsukiyama, S.; Furukawa, Y.; Koshida, S.; Tachibana, Y.; Nishimura, S. I.; Todo, S. Effects of Synthetic Antifreeze Glycoprotein Analogue on Islet Cell Survival and Function during Cryopreservation. *Cryobiology* **2006**, *52* (1), 90–98. https://doi.org/10.1016/j.cryobiol.2005.10.010.

(83) Marvin was used for drawing, displaying and characterizing chemical structures, substructures and reactions, Marvin 21.14, 2021, ChemAxon (http://www.chemaxon.com)

(84) Best, B. P. Cryoprotectant Toxicity: Facts, Issues, and Questions. *Rejuvenation Res.* **2015**, *18* (5), 422–436. https://doi.org/10.1089/rej.2014.1656.

(85) Wang, X.; Hua, T. C.; Sun, D. W.; Liu, B.; Yang, G.; Cao, Y. Cryopreservation of Tissue-Engineered Dermal Replacement in Me2SO: Toxicity Study and Effects of Concentration and Cooling Rates on Cell Viability. *Cryobiology* **2007**, *55* (1), 60–65. https://doi.org/10.1016/j.cryobiol.2007.05.006.

(86) Capicciotti, C. J.; ;Doshi, M. .; Ben, R. N. Ice Recrystallization Inhibitors: From Biological Antifreezes to Small Molecules. *Recent Dev. Study Recryst. Wilson, P., Ed.; InTech Open, Ltd. London, UK* **2013**, 177–224. https://doi.org/10.5772/54992.

(87) Chopra, K. Improved Cryopreservation of Induced Pluripotent Stem Cells Using N-Aryl Glycosidic Small Molecule Ice Recrystallization Inhibitors. (Master's Dissertation, Universit d'Ottawa/University of Ottawa),. **2020**.

(88) Majzner, R. G.; Mackall, C. L. Clinical Lessons Learned from the First Leg of the CAR T Cell Journey. *Nat. Med.* **2019**, *25* (9), 1341–1355. https://doi.org/10.1038/s41591-019-0564-6.

Chapter 3: Structure-Activity Relationship Studies on *O*- and *C*-Alkyl Glucosides

3.1 Introduction

3.1.1 Types of Glycosidic Linkages at the Anomeric Carbon in Antifreeze Glycoproteins (AF(G)Ps): O- and C-Glycosidic Bonds

Several creatures in nature, such as arctic fish and the *Lobelia telekii* plant, can survive in sub-zero temperatures and protect themselves from cryoinjury due to the presence of naturally occurring antifreeze (glyco)proteins (AF(G)Ps).[1-11] AF(G)Ps are known for their capacity to bind to ice crystals, preventing ice formation and recrystallization when temperatures are reduced.[9-11] AF(G)Ps have attracted considerable interest in the cryobiology field because of their capacity to prevent cryoinjury when exposed to cold temperatures.[8-10] For example, research has shown that AF(G)Ps enhance the viability of various cell types, such as oocytes and spermatozoa, post cryopreservation.[12] There exist two naturally found types of AF(G)Ps: *O*-linked or *C*-linked AF(G)Ps, shown in **Figure 3.1**.[6-10,12-13] *O*-linked AF(G)Ps refer to the glycosidic bond that is formed between the anomeric carbon of the carbohydrate moiety and the hydroxyl group of the peptide chain (**Figure 3.1**).[12-13] Moreover, the linkage between the anomeric carbon with the peptide chain via a carbon atom results in the formation of a *C*-glycosidic bond, referred to as *C*-linked AF(G)Ps (**Figure 3.1**).[12,14]

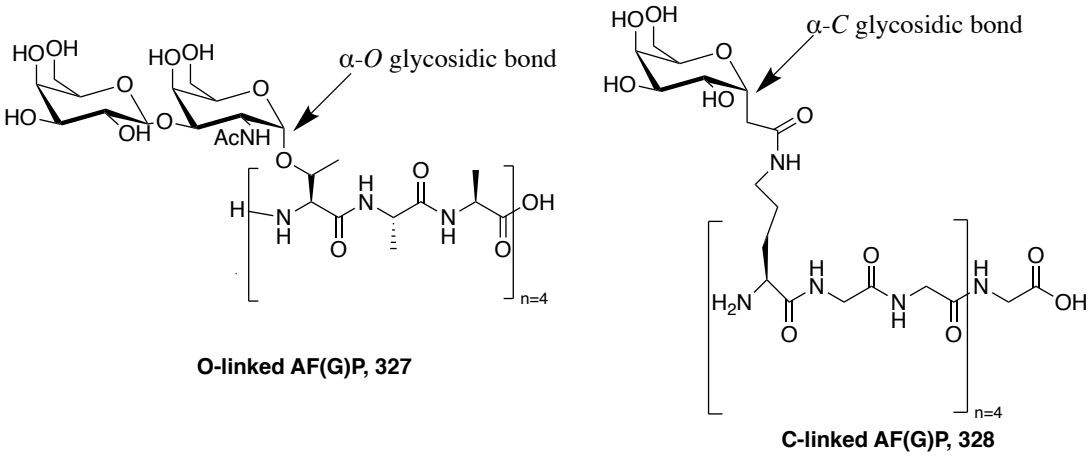

Figure 3.1 Chemical structures of *O*-linked and *C*-linked AF(G)Ps.[12]

The antifreeze properties of AF(G)Ps gave rise to many synthetic *O*- and *C*-linked glycosides (**Figure 3.2**) after several years of development and optimization, that have also been utilized as ice recrystallization inhibitors (IRIs) for the cryopreservation of several cell types, such as red blood cells (RBCs) and hematopoietic stem cells (HSCs).[1,12,15-17] While *O*-linked AF(G)Ps/glycosides are known for their reactivity and the instability of their exocyclic alkoxy group, *C*-linked alternatives are considerably more stable.[12] Carbon-oxygen bonds can be cleaved under acid/base conditions, and can be identified and metabolized by several *in vivo* hydrolase enzymes.[12,18-19] On the other hand, the presence of the *C*-*C* bond in *C*-linked AF(G)Ps/glycosides results in more stable compounds that withstand enzymatic or acid/base hydrolysis, expanding their *in vivo* applicability.[18-19] In this chapter, we compare the ice recrystallization inhibition (IRI) activity of *O*- and *C*-linked alkyl glucoside compounds, where the peptide component of AF(G)Ps is substituted for an alkyl chain, to further understand the effect of the glycosidic bond on IRI activity.

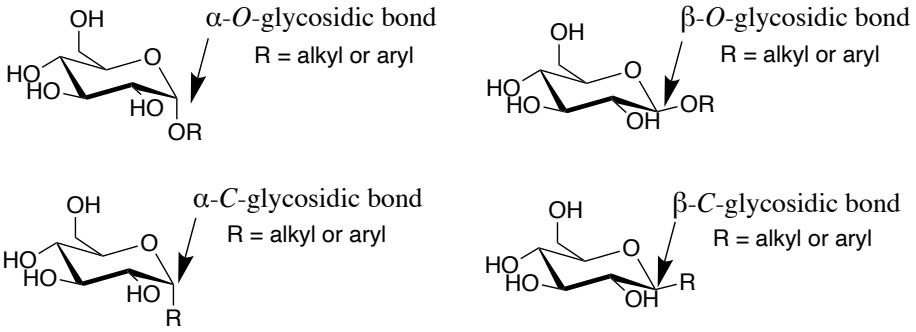

Figure 3.2 General structures of α/β-*O*-, and α/β-*C*-glycosidic bonds.

3.1.1.1 The Impact of Different Glycosidic Linkages at the Anomeric Carbon on the IRI Activity of O- and C-Linked Alkyl Glucosides

Several structure-function studies conducted by the Ben laboratory have identified key properties that impact the activity of different classes of IRI candidates, such as the configuration of the C_4 hydroxyl group, as well as the configuration and nature of the glycosidic bond (α or β and *O*- or *C*- linkages).[1,16-17,20-22] A glycosidic bond is defined as the covalent bond that forms upon the linkage between the anomeric carbon (C_1) of carbohydrates and a nucleophilic group of another organic compound (i.e., alcohol or nucleophilic alkyl).[23] It has been reported that several *O*-linked glucosides, such as *n*-octyl-β-D-glucose and 4-bromophenyl-β-D-glucopyranoside, are active IRIs in which the latter has been used as a cryoprotectant additive for the cryopreservation of RBCs.[1,20]

The Ben laboratory has previously reported that changing the linkage at the anomeric carbon of AF(G)Ps from oxygen to carbon bond either maintains or increases IRI activity.[20,24-26] Consequently, we sought to synthesize different *O*- and *C*-linked-β-alkyl-glucopyranosides and assess their IRI activity to examine any potential relationship between the type of glycosidic bond and IRI activity.

3.1.2 Previous SAR Studies Highlighting Structural Properties Important for IRI Activity

As discussed previously in **Chapter 1**, AF(G)Ps have two antifreeze properties: thermal hysteresis (TH) and ice recrystallization inhibition (IRI) activity.[6-10] Nonetheless, TH activity of AF(G)Ps is not compatible for the cryopreservation of cellular products due to the often associated phenomenon of dynamic ice shaping (DIS),[17] which has been recognized as a contributor to cell damage post cryopreservation.[27] The Ben laboratory conducted several SAR studies to discover key structural characteristics that are linked to displaying IRI activity without exhibiting TH activity.[1,15,24] As a result, different classes of IRIs have been synthesized, ranging from large IRIs, such as *C*-linked AFGP analogues (**Figure 3.3**), to small-molecule IRIs, such as *n*-octyl-β-D-glucose and 4-bromophenyl-β-D-glucopyranoside (**Figure 3.3**).[15,20,24-25]

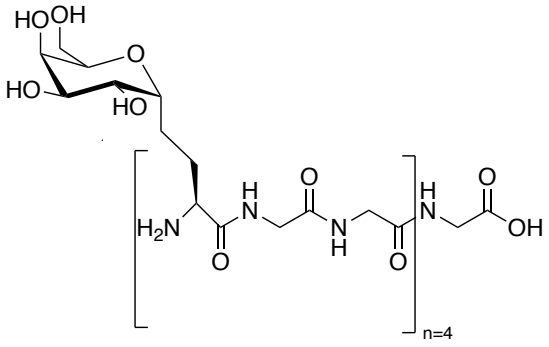

C-linked AFGPs, 328

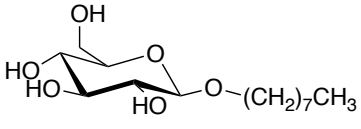

***n*-Octyl-β-D-glucoside, 334g**

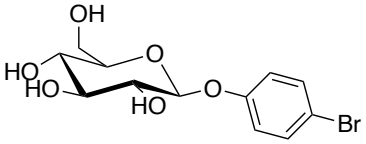

4-Bromophenyl-β-D-glucopyranoside, 329

Figure 3.3 Structures of *C*-linked AFGP analogue, *n*-octyl-β-D-glucose and 4-bromophenyl-β-D-glucopyranoside

Some of the SAR studies that have been demonstrated by the Ben laboratory examined the relationship between the activity of IRI candidates and their critical

micellization concentration (CMC) value,[20] or polar surface area to molecular surface area ratio (PSA/MSA) value,[28-29] to better understand the mechanism by which IRIs inhibit the growth of ice crystals.

3.1.2.1 Relationship Between the CMC and IRI Activity

n-Octyl-β-D-glucose has been demonstrated to be effective in the investigation of hydrophobic proteins throughout the last two decades.[30] It solubilizes most membrane proteins effectively and affects the activity of hydrolytic enzymes.[30] Moreover, the amphiphilic nature of *n*-Octyl-β-D-glucose can result in the formation of micelles in aqueous solutions above a certain concentration.[30-31] The concentration of surfactant above which micellization occurs (at a certain temperature and pressure) is referred to as the critical micellization concentration (CMC).[30,32-33] The CMC value of *n*-octyl-β-D-glucose in water has been reported to be 20-25 mM.[30-31] Previous work by the Ben laboratory has, therefore, attempted to correlate the IRI activity of *n*-octyl-β-D-glucose with its CMC value in an effort to understand the mechanism by which this molecule exhibits IRI activity.[20] It was hypothesized that the formation of micelles at concentrations above their CMC values may be linked to the IRI activity of *n*-octyl-β-D-glucose.[20] Despite the fact that the CMC value of *n*-octyl-β-D-glucoside is stated in water rather than PBS, it has been reported that the CMC values are marginally reduced in salt solutions.[20] It was observed that *n*-octyl-β-D-glucose exhibited no IRI activity at concentrations above its CMC value (i.e., 44 mM). This implies that there is no direct relationship between a compound's ability to inhibit ice recrystallization and its micelle formation. However, the results of this study suggest that the amphiphilic nature of *n*-octyl-β-D-glucose where long alkyl side chains are

counterbalanced by the hydrophilic moiety of carbohydrates enhances IRI activity compared to their parent sugar (i.e., glucose).[20,34]

3.1.2.2 Correlations Between the PSA/MSA ratio and IRI Activity

Another class of surfactants, *N*-alkyl-D-gluconamides (**Figure 3.4 B**), has emerged as active IRIs.[20] The capacity to aggregate and form hydrogen bonds renders this class of surfactants significant for drug delivery and tissue engineering.[35-36] Moreover, previous work conducted by the Ben laboratory revealed that *N*-alkyl-D-gluconamide analogues exhibit a range of IRI activity (%MGS varies between 3 % and 95 %) depending on the length of the alkyl chain they possess.[28-29] Notably, the IRI activity has been observed to increase as the length of the alkyl chain increases (**Figure 3.4 A**).[15,28] It was hypothesized that correlating the net polarity of *N*-alkyl-D-aldonamide derivatives with their IRI activities would assist in the discovery of key structural properties that are important for IRI activity.[15,28] The polar surface area to molecular surface area ratio (PSA/MSA) has, therefore, been utilized as a metric to measure the net polarity of the different analogues.[15,28] The PSA/MSA ratio is a significant physiochemical parameter in medicinal chemistry as it is commonly used to evaluate the bioavailability of drugs, in addition, it affects the properties of several biological assays.[37-39] Previous Ben lab member, Dr. Jennie Briard, has reported that there is a positive linear relationship between the PSA/MSA ratio and the %MGS of different *N*-alkyl-D-aldonamide derivatives, presented in **Figure 3.4 A-B**, which demonstrates that the net polarity of an IRI candidate affects its activity.[15,28]

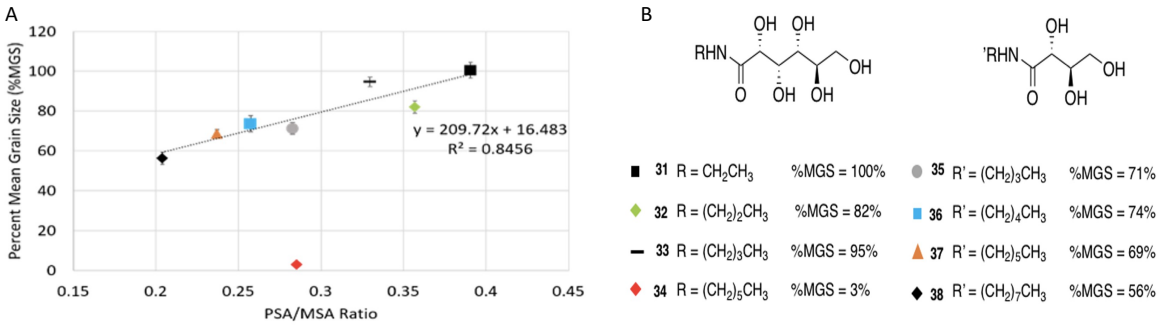

Figure 3.4 (A) Correlation between mean grain size percentage and PSA/MSA ratio of the different *N*-alkyl-D-aldonamide derivatives. **(B)** Chemical structure of *N*-alkyl-D-aldonamide derivatives.[28] Figure is adapted from Peptide Scinece, *111* (e24086), A. Ampaw, Designing the next Generation of Cryoprotectants – from Proteins to Small Molecules, 1-12, 2019, with permission from John Wiley and Sons.

While the precedent work highlighted a positive correlation between the length of the alkyl chain in *N*-alkyl-D-gluconamide analogues and their net polarity,[15,28] there were some outliers (i.e., the hexyl analogue, **Figure 3.4 A**) and the dataset was incomplete (i.e., pentyl and octyl aldonamide analogues). Consequently, we sought to occupy the anomeric position of *O*- or *C*-alkyl glucosides with different alkyl chain lengths to determine their IRI activity and study any potential relationship with their PSA/MSA ratios. The IRI activity was evaluated using the modified splat cooling assay to generate their half-maximal inhibitory concentration (IC_{50}). The calculated values of PSA/MSA ratios of the *C*- and *O*-linked compounds were then correlated with their IC_{50} values to investigate any potential relationship the net polarity of the compounds and their IRI activity, which may reveal critical structural characteristics for the development of new IRIs.

3.2 Synthesis and IRI Activity of *O*-Alkyl-β-D-Glucosides

N-octyl-β-D-glucoside (**334g**, **Figure 3.3**) has been extensively investigated for a variety of applications such as the production of DNA-lipid particles, which can be used for drug delivery *in vitro* and *in vivo*, and the solubilization of membrane proteins.[36,40] As mentioned earlier, previous research conducted by the Ben laboratory has investigated the

potential application of **334g** to inhibit ice recrystallization.[1] In this study, we occupy different alkyl chain lengths at the C_1 position of D-glucose and examine the relationship between the different lengths of alkyl chains at the anomeric carbon and the IRI activity. We hypothesize that the lower the PSA/MSA ratio, the more active the compound will be, and therefore, the longer the alkyl chain is, the more IRI active the compound should be.

3.2.1 Synthesis of O-Alkyl Glucosides

The β-anomer of the *O*-alkyl glucosides were synthesized based on either a Lewis-acid mediated glycosidation with the respective glycosyl donor,[20] or through a glycosyl bromide intermediate.[41] The length of the alkyl chain varied from one to eight carbons, presented in **Scheme 3.1**.

The alkyl chains were introduced at the anomeric carbon using conventional synthetic protocols.[20,41] A Lewis-acid mediated glycosidation was utilized to functionalize C_1 position with alkyl chains (methyl, ethyl, propyl, butyl, pentyl, hexyl and octyl groups) to afford compounds **334 a-g**.[1] However, this synthetic route resulted in both the α and β anomers of the ethyl compound which was prohibitively difficult to isolate. Therefore, an alternative synthetic protocol, utilizing a glycosyl bromide as an intermediate, was employed to generate **334 b**.

The different compounds **334 a**, and **334 c-g** were prepared staring from β-D-glucose pentaacetate (**331**), elucidated in **Scheme 3.1 A**. The Lewis acid, boron trifluoride diethyl etherate ($BF_3{\cdot}OEt_2$), allowed for activation of the β-linked anomeric acetate group, followed by glycosidation with the appropriate alkyl alcohol to provide alkyl-2,3,4,6-tetra-*O*-acetyl-β-D-glucopyranoside intermediates (**333 a**, and **333 c-g**) exclusively.[20] On the other hand, bromination of β-D-glucose pentaacetate (**331**) using 33% hydrogen bromide

(HBr) in acetic acid (AcOH) generated the α-bromo glycoside intermediate (**332**), presented in **Scheme 3.1 B**. The bromide sugar (**332**) was then treated with anhydrous ethyl alcohol to afford **333 b**.[41] Under Zemplén conditions, deacetylation of **333 a-g** intermediates produced the final compounds (alkyl-β-D-glucopyranosides, **334 a-g**), shown in **Scheme 3.1 A-B**.[20,41]

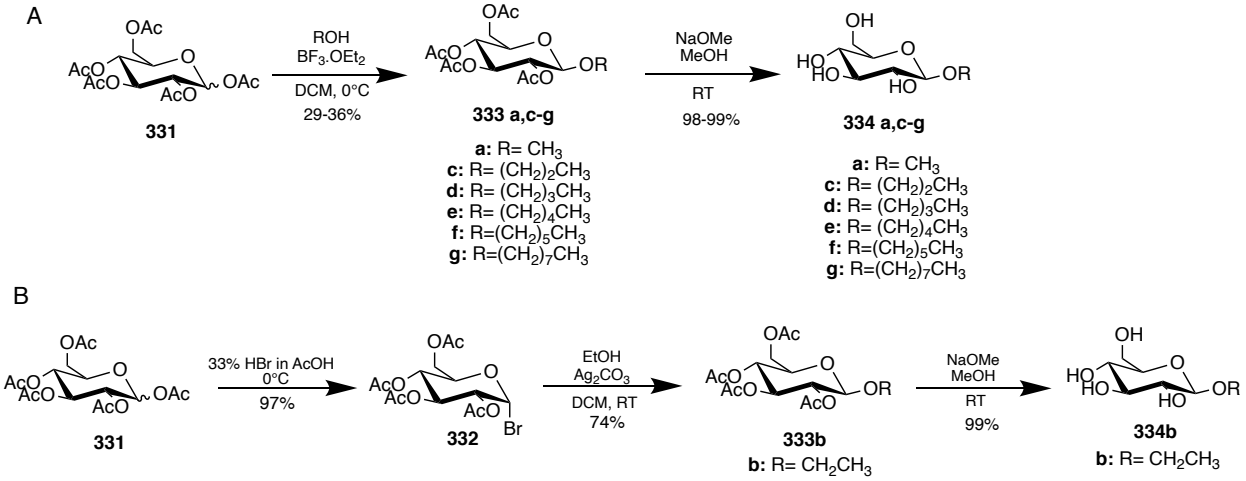

Scheme 3.1 Synthetic scheme of *O*-linked alkyl glucoside derivatives (**334 a-g**).

3.2.2 IRI Activity of O-Alkyl Glucosides

Assessment of the IRI activity of the alkyl glucoside compounds (**334 a-g**) was conducted utilizing the modified splat cooling assay.[42] Each compound generated a dose-response curve from which the IC_{50} values (the concentration of compound required to inhibit the rate of ice recrystallization by 50%) were calculated. In the modified splat cooling assay protocol, the different *O*-alkyl glucosides were dissolved in a phosphate buffer solution (PBS) at various concentrations, starting from their maximum solubility observed in PBS. The areas of ice crystals were evaluated after a 5-minute annealing time at -6.4 °C. The rate of ice recrystallization was determined for each concentration using the binning approach where ice crystals are categorized in different bins depending on their

size as a function of time.[43] The rate of ice recrystallization was then determined and normalized (v_{norm}) to the positive control (PBS) for each concentration; it was then plotted against the logarithmic values of the concentrations which yielded dose-response curves (**Figure 3.5**). The IC_{50} value of each compound was then determined using a four-parameter variable slope fitting of the data (GraphPad Prism). Comparing the IC_{50} of *n*-octyl-β-D-glucoside (**334 g**) with the other analogues (**334 a-f**), it is evident that IRIs with alkyl chains of less than 8 carbons resulted in a decrease in the IRI activity, **Table 3.1**. However, no correlation was observed between the IRI activity and the length of the alkyl chain of the different compounds (**334 a-g**)**.**

Overall, reducing the alkyl chain from 8 (**334 g**) carbons to 3-6 (**334 c-f**) carbons was found to decrease the IRI activity by 1.7- to 2.8-fold. On the other hand, bearing a methyl (**334 a**) or ethyl (**334 b**) group at the C_1 position decreased the IRI activity by 4- to 6-fold (IC_{50} = 38.9 mM and 59.6 mM, respectively) compared to **334 g** (IC_{50} = 9.7 mM). These results suggest that the IRI activity is influenced by the length of the alkyl chain present at the anomeric carbon of *O*-alkyl glucosides, however, there is no relationship between the IRI activity and the length of the alkyl chain. These preliminary data suggest that employing alkyl chains with one to eight carbons increases the IRI activity compared to D-glucose (IC_{50} = 118 mM),[44] however, the IRI activity of the octyl analogue appeared to be higher than the ones with one to six carbons. Therefore, it is pertinent to further investigate the IRI activity of *O*-alkyl glucosides bearing 9 carbons and more, which may unveil significant properties for future IRI development

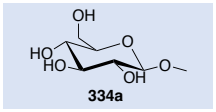

334a

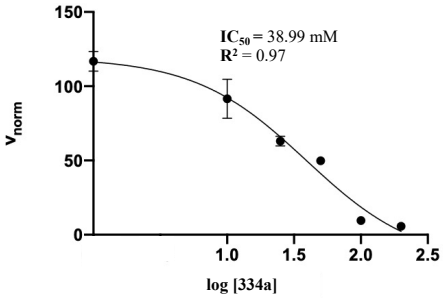

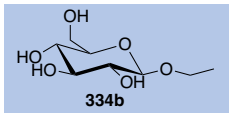

334b

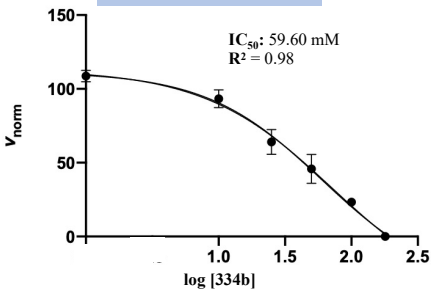

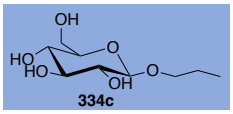

334c

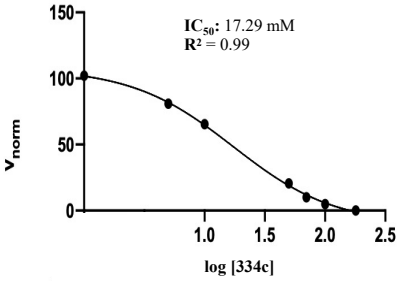

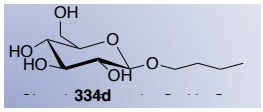

334d

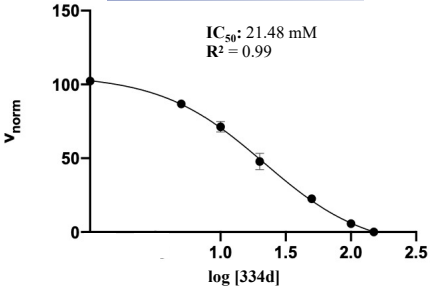

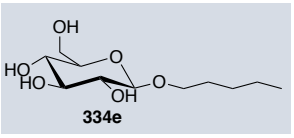

334e

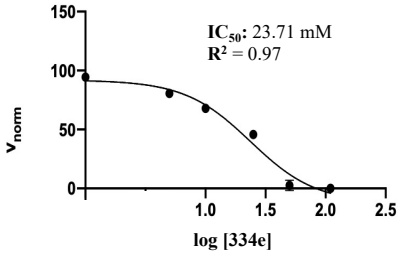

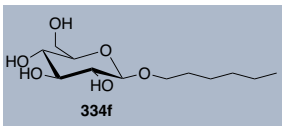

334f

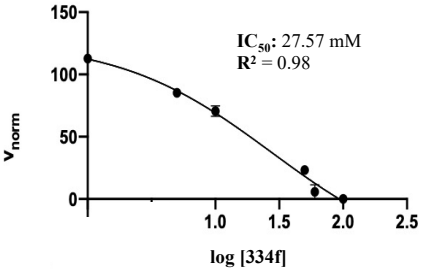

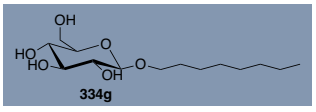

334g

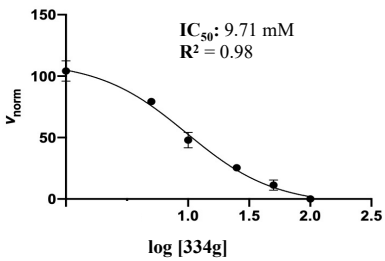

Figure 3.5 Dose-response curves for alkyl glucoside compounds (**334 a-g**). Ice crystals growth rates were normalized to PBS and measured in triplicates. Error bars correspond to the standard deviation (SD). A four-parameter variable slope sigmoidal curve was fitted to the data.

Table 3.1 Maximum solubility observed in PBS and IC_{50} values for *O*-alkyl glucoside compounds (**334 a-g**). Errors for IC_{50} values are given in standard deviation (SD).

Compound	Maximum solubility observed in PBS (mM)	IC_{50} (mM)
334a	200	38.9 ± 4.7
334b	180	59.6 ± 5.1
334c	180	17.3 ± 5.9
334d	150	21.5 ± 2.2
334e	110	23.7 ± 0.5
334f	100	27.6 ± 6.4
334g	100	9.7 ± 3.1

3.3 Synthesis and IRI Activity of *C*-Alkyl-β-D-Glucosides

The anomeric carbon-oxygen linkage in *O*-linked AF(G)Ps is susceptible to cleavage under acid/base conditions and by hydrolase enzymes, which limits their use in the cryopreservation of several types of cells (i.e., RBCs, MSCs, and HSCs).[12,18] Therefore, interest in synthesizing *C*-linked AF(G)P analogues and *C*-linked alkyl glucosides has risen due to the fact that *C*-*C* bonds resist enzymatic hydrolysis, extending the *in vivo* lifetime of these compounds.[18-19] The Ben laboratory has reported success in synthesizing *C*-linked AF(G)P mimetics that possess IRI activity and can be used in the cryopreservation protocol of cells.[12] However, the ability for *C*-linked alkyl glucopyranosides to inhibit ice recrystallization has yet to be discovered. Therefore, we sought to examine the effect of a *C*-*C* linkage of different alkyl chain lengths at C_1 on IRI activity in comparison to *O*-linked derivatives. Different lengths of alkyl chains at the anomeric position were employed with a *C*-*C* linkage and were assessed for their IRI activity. We also evaluated the presence of

any relationship between the IRI activity and PSA/MSA ratio of the different *C*-alkyl glucoside compounds. We hypothesized that as the length of the alkyl chain increased, the IRI activity of the *C*-linked compounds would increase; in other words, as the value of PSA/MSA ratio decreased, the IRI activity would increase. This will help in understanding if there is any correlation between the IRI activity and the net polarity of the *C*-linked alkyl glycosides.

3.3.1 Synthesis of C-Alkyl Glucoside Compounds

The alkyl substituents were introduced at the β position of the anomeric carbon (C_1) of glucose utilizing a literature approach by Kishi *et al*., where the perbenzylated lactone (**336**) is treated with a Grignard reagent to give a hemiketal intermediate (**337 a-f**). The intermediate is then converted to β-alkyl glucoside (**338 a-f**) exclusively using triethyl silane (Et_3SiH, TES), as presented in **Scheme 3.2**.[45-46]

In accordance with the literature procedure, 2,3,4,6-tetra-*O*-benzyl-D-glucopyranose (**335**) was oxidized using acetic anhydride (Ac_2O) and anhydrous DMSO to provide 2,3,4,6-tetra-*O*-benzyl-D-gluconolactone (**336)**, presented in **Scheme 3.2**.[46-47] The lactone intermediate was treated with a 2.0 M solution of alkyl magnesium chloride (RMgCl) in tetrahydrofuran (THF) at -78 °C for 3-4 hours, which allowed the formation of **337 a-f**.[18] Reduction of **337 a-f** intermediates using Et_3SiH in the presence of boron trifluoride diethyl etherate ($BF_3{\cdot}OEt_2$) yielded the formation of **338 a-f**.[45] Debenzylation of **338 a-f** intermediates using hydrogenolysis conditions (5% palladium on carbon, 5% Pd/C) in a solvent system of 1:1 methanol to ethyl acetate (MeOH:EtOAc) afforded the formation of the final products **339 a-f**, as shown in **Scheme 3.2**.[48]

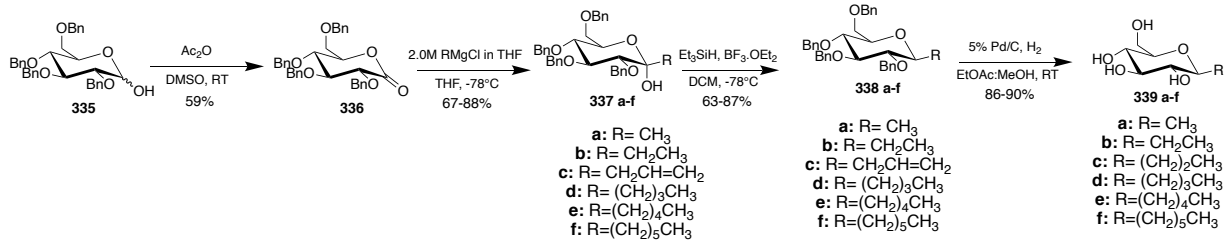

Scheme 3.2 A detailed synthetic scheme of *C*-alkyl glucoside compounds (**339 a-f**).

3.3.2 IRI Activity of C-Alkyl Glucoside compounds

The modified splat cooling assay was used to assess the IRI activity and to determine the IC_{50} value for each *C*-linked alkyl glucopyranoside compound (**339 a-f**).[13] Dose response curves were generated for the different compounds by plotting the normalized growth rate of ice crystals (v_{norm}) against the logarithmic values of the concentrations, depicted in **Figure 3.6**. The IC_{50} values of compounds **339 a-f** are presented in **Table 3.2**. Since the IRI activity of **339f** did not appear to improve when six carbons were employed in the alkyl chain with an IC_{50} of 68 mM (low IRI activity), no further compounds were synthesized (i.e., heptyl and octyl *C*-linked derivatives).

Although the IRI activity of **339 a-f** changed as the length of the alkyl chain was altered, no relationship between their IC_{50} values and the alkyl chain length was observed. The IRI activity of **339 a-f** did not increase nor decrease with increasing the length of the alkyl chain from one carbon to six carbons. This implies that there is no relationship between the alkyl chain length and the IRI activity of *C*-linked glucoside compounds. Overall, the IRI activity of the *C*-linked alkyl glucopyranose compounds, except for **339b**, appeared to be lower than the *O*-alkyl glucopyranose compounds, suggesting that exchanging the glycosidic linkage to a *C*-*C* bond decreases the IRI activity.

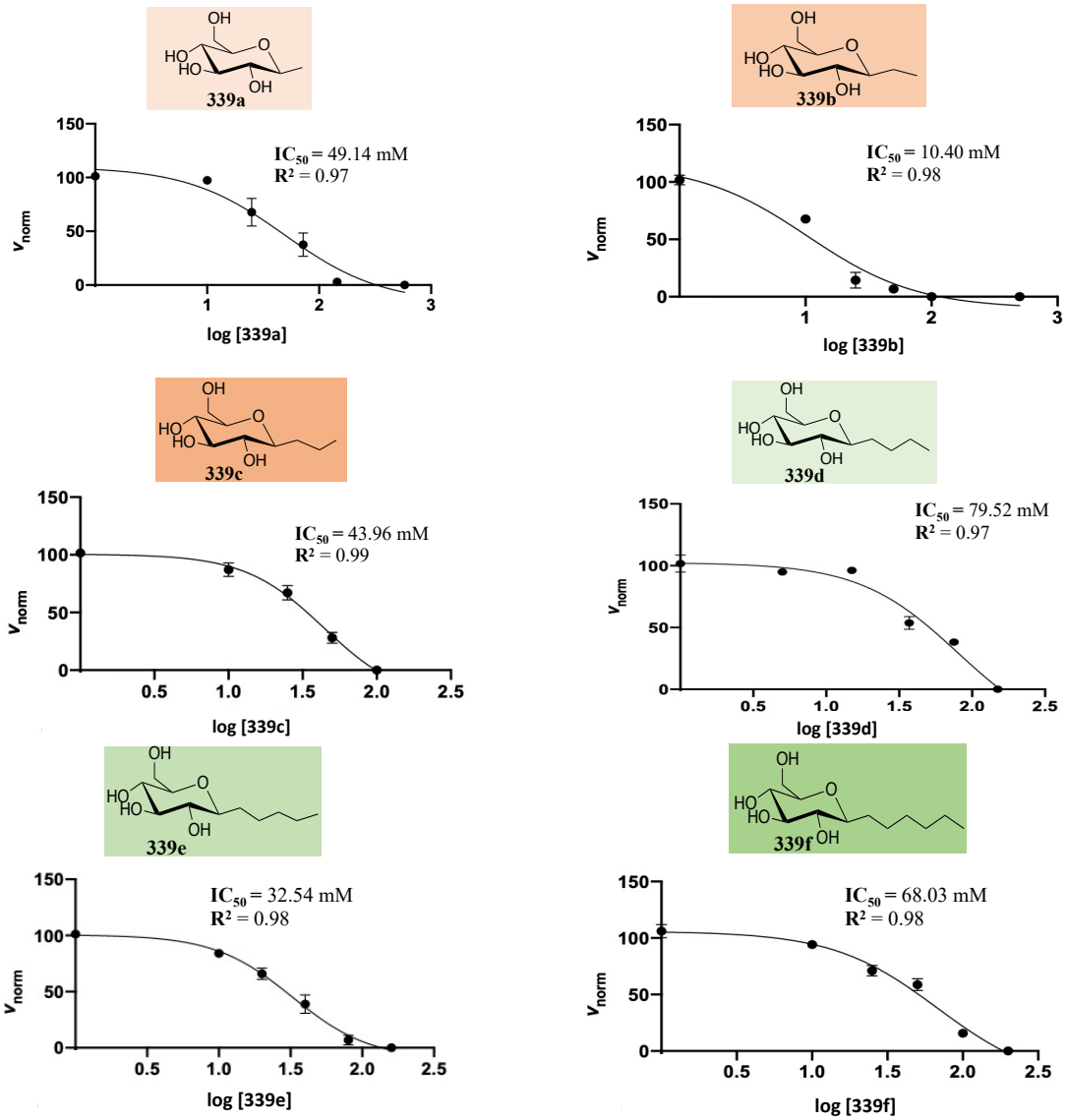

Figure 3.6 Dose-response curves for *C*-linked alkyl glucoside compounds (**339 a-f**). Ice crystals growth rates were normalized to PBS and measured in triplicates. Error bars correspond to the standard deviation (SD). A four-parameter variable slope sigmoidal curve was fitted to the data.

Table 3.2 Maximum solubility observed in PBS and IC_{50} values for *C*-linked alkyl glucoside compounds (**339 a-f**). Errors for IC_{50} values are given in standard deviation (SD).

Compound	Maximum solubility observed in PBS (mM)	IC_{50} (mM)
339a	580	49.1 ± 6.1
339b	500	10.4 ± 4.7
339c	100	43.9 ± 4.0

339d	150	79.5 ± 1.5
339e	160	32.5 ± 0.4
339f	200	68.0 ± 1.3

3.4 Investigating the Effect of Different Glycosidic Bond on IRI activity

Identification of key structural requirements for the activity of small-molecule IRIs will assist in building a larger library of active IRIs that may be applicable for the cryopreservation of cell-based therapy products. Previous SAR studies on AF(G)Ps have revealed that an α configuration of the *O*-glycosidic bond linking the disaccharide component to the peptide chain is key for their antifreeze activity.[50] Further SAR studies conducted by our laboratory have reported a variety of large and small active IRIs that possess α or β configurations.[1,16-17,20-22,49] However, the effect of the glycosidic linkage on IRI activity has yet to be fully investigated. **Sections 3.2 and 3.2** display the IRI activity of both *O*- and *C*-alkyl glucosides, respectively. Moreover, the IRI activity of most *C*-linked compounds appeared to be lower than that of *O*-linked ones. Thus, we sought to investigate the difference in IRI activity between *C*-linked-β-alkyl-D-glucopyranoside and their *O*-linked parent compounds, shown in **Figure 3.7**. This was performed by directly comparing their IC_{50} values, which may reveal new structural features necessary for IRI activity.

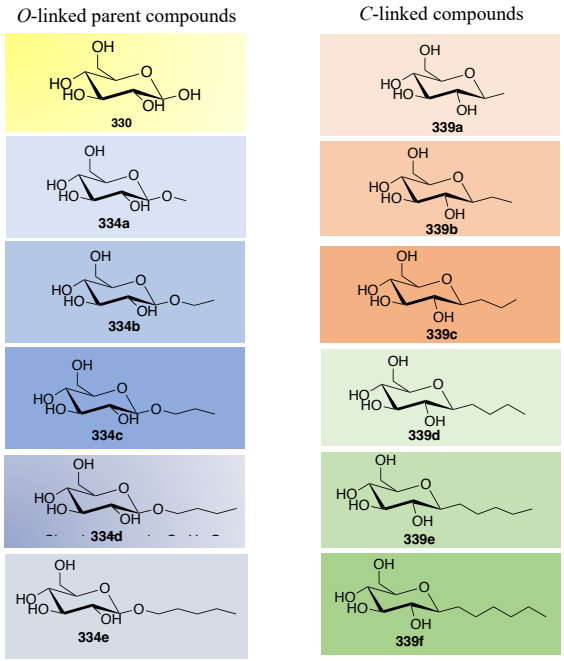

Figure 3.7 Chemical structures of *C*-linked-β-alkyl-D-glucopyranosides and their *O*-linked parent compounds.

3.4.1 The Effect of Altering the C-O Glycosidic Bond into C-C Linkage on IRI Activity Through Direct Comparison of the IC_{50} Values

The IRI activities of *O*-linked alkyl glycosides were compared with their *C*-linked analogues by directly comparing the IC_{50} values of both glycosides. From **Table 3.3**, it is evident that the IRI activity of the *O*-linked parent compounds increases when the anomeric carbon is occupied with alkyl chains, for instance, the IC_{50} of **330** is 118 mM,[44] while the IC_{50} values of **334 a-e** range between 18 mM to 60 mM, implying that occupying a functional group at the anomeric carbon (i.e., alkyl chain) is significant for the IRI activity of *O*-liked glucosides. Moreover, a direct comparison between the IC_{50} values of *O*- and *C*-linked analogues revealed that the IRI activity of *C*-linked analogues (**339 a** and **c-f**) was moderate (IC_{50} values range between 33 mM and 68 mM), except for **339 b** which appeared to be an active IRI (IC_{50} = 10 mM), presented in **Table 3.3**.

Table 3.3 IC_{50} values of *O*-linked parent compounds and their corresponding *C*-linked compounds determined by the modified splat cooling assay. Errors for IC_{50} values are given in standard deviation (SD).

***O*-linked parent compounds**	**IC_{50} (mM)**	***C*-linked compounds**	**IC_{50} (mM)**
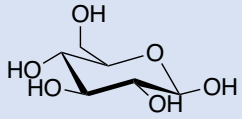 **330**	118 ± 24 [44]	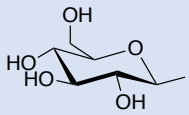 **339a**	49.1 ± 6.1
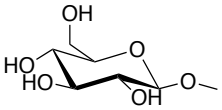 **334a**	38.9 ± 4.7	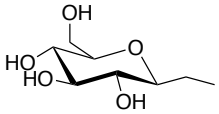 **339b**	10.4 ± 4.7
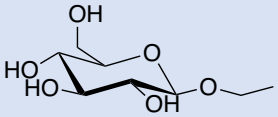 **334b**	59.6 ± 5.1	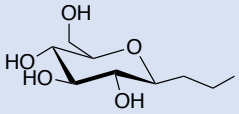 **339c**	44.0 ± 4.0
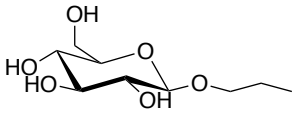 **334c**	17.3 ± 5.9	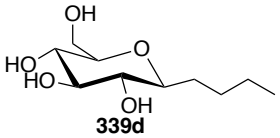 **339d**	79.5 ± 1.5
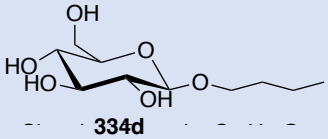 **334d**	21.5 ± 2.2	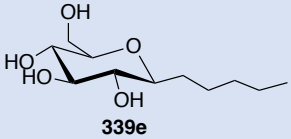 **339e**	32.5 ± 0.4
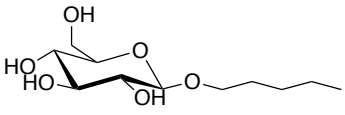 **334e**	23.7 ± 0.5	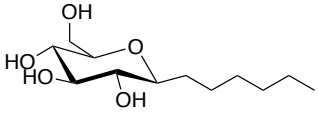 **339f**	68.0 ± 1.3

3.4.1.1 Discussion on the Effect of O-C vs C-C glycosidic bond on the IRI activity of the O-linked and C-linked Glucoside Compounds

From the results presented in **Table 3.3**, it is notable that changing the glycosidic bond from *C-O* to *C-C* influences the IRI activity of the different alkyl glucosides. Moreover, the IC_{50} values of the *O*-linked parent compounds appeared to be lower than those of *C*-linked ones, implying higher IRI activity. These findings may be due to the presence of an exo-anomeric effect in the *O*-alkyl glycoside derivatives.[51] In the exo-anomeric effect, the lone pairs on the exocyclic oxygen are delocalized to the antibonding

orbital (σ^*) of the anomeric carbon, which may contribute to having higher IRI activity compared with *C*-linked analogues, as depicted in **Figure 3.8**.[51-54] From the Newman projection shown in **Figure 3.8**, the alignment of the lone pair of the exocyclic oxygen with the antibonding orbital (σ^*) allows for delocalization of the lone pair on the exocyclic oxygen onto the σ^* orbital of the anomeric carbon. Alternatively, the *C*-linked derivatives do not have lone pairs available to delocalize onto the σ^* orbital of the anomeric carbon. The presence of the exo-anomeric effect in the β anomers of *O*-linked analogues may translate to the higher IRI activity, especially when comparing the IC_{50} of **334 c-e** vs **339 d-f**. Another reason that may explain why the *O*-linked compounds are mostly more active than the *C*-linked compounds is due to the presence of additional hydrogen bonds that can be formed between the exo-cyclic oxygen and water molecules which may affect the inhibition of ice recrystallization.

Moreover, it is evident that the length of the alkyl chain plays a role in the IRI activity, for instance, having one or two carbons linked with an exocyclic oxygen to the anomeric carbon **334 a-b** results in lower IRI activity, while their *C*-linked counterparts **339 b-c** have higher IRI activity. Notably, the IRI activity of D-glucose (**330**) appears to be much lower than the *O*-linked compounds. This can be related to the fact having an alkoxy group at the anomeric position of the *O*-linked compounds prevents the conversion of the carbohydrate ring into other confirmations (i.e., cyclic vs. linear aldoses), unlike the reducing sugar which can convert into linear aldose, which may have lower IRI activity compared to the cyclic sugar. From these preliminary data, it is evident that the nature of the glycosidic bond and the length of the alkoxy chain at the anomeric position influence the IRI activity of the different analogues. Previous study conducted in the Ben laboratory

has investigated the importance of the *N*- and *S*-linked aryl glycosides for IRI activity.[55] Therefore, it is significant to study the effect of other glycosidic bonds (i.e., *N*- or *S*-linked aryl/alkyl glycosides) to better comprehend the influence of the glycosidic linkage at the anomeric bond, which will assist in establishing key structural features for future IRI development.

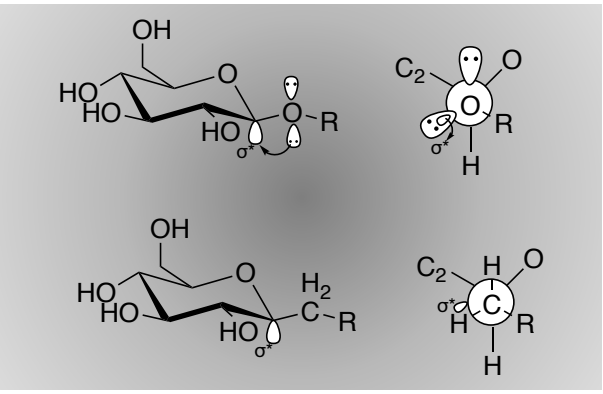

Figure 3.8 Structural illustration showing the exo-anomeric effect in *O*- and *C*-linked alkyl glycoside derivatives.

3.5 Assessing the Relationship Between the PSA/MSA Ratio and the IRI Activity of *O*- and *C*-Linked Alkyl Glucosides

Through various SAR studies, the Ben laboratory has generated a library of different classes of IRIs.[1,23,29-32] Previous SAR studies have attempted to correlate the CMC value and PSA/MSA ratio to the activity of various IRI candidates.[1,16-17,21-22,49] The PSA/MSA ratio is considered as a significant parameter during drug discovery as it can be correlated to the rate of adsorption of pharmaceutical agents by the body, which can assist in understanding structural properties (i.e., size and net polarity) that are important for future drug development.[37-39] Therefore, the PSA/MSA values of the *O*- and *C*-alkyl glucosides were correlated with their IRI activity, in an effort to understand the effect of the net polarity of IRI candidates on their activity.

3.5.1 Correlations Between the PSA/MSA Ratio and the IRI Activity of O-Alkyl Glucoside Compounds

Previous research work has demonstrated that there is a positive relationship between the percent of the mean grain size (%MGS) of ice crystals generated from the splat cooling assay and the PSA/MSA ratio of different *N*-alkyl-D-aldonamide derivatives, shown in **Figure 3.4**.[28] In this study, we investigated any correlations between the IC_{50} values of the *C*- or *O*-alkyl glucopyranoside derivatives and their calculated PSA/MSA ratio.

Several computational software programs have been designated to calculate the values of different molecular properties (i.e., log P, PSA, and MSA) of chemical molecules, such as Marvin Sketch (ChemAxon), and VCCLAB (Virtual Computational Chemistry Laboratory).[56-59] Marvin Sketch (ChemAxon) was utilized to compute the polar surface area (PSA) and molecular surface area (MSA) values of compounds **334 a-g** and **339 a-f**. The rationale for using Marvin Sketch (ChemAxon) to generate PSA and MSA values is because it is easy to utilize, and because the calculated values of molecular properties, such as the octanol-water partition coefficient (log P), are very similar to known experimental values. For instance, the experimental and calculated (Marvin Sketch) log P values of D-glucose sugar were found to be -3.10 and -2.93, respectively.[59-60] The PSA and MSA values of compounds **334 a-g** are presented in **Table 3.4**. Compounds **334 a-g** all had the same calculated PSA (99.38), whereas the MSA values of **334 a-g** increased as the length of the alkyl chain increased (ranging from 278.34 to 493.17). Because the molecular surface area rises while the polar surface area remains the same as the length of the alkyl chain increases,

the PSA/MSA ratio of the *O*-linked compounds decreased as the length of the alkyl chain increased (**Table 3.4**).

Table 3.4 The IC_{50} values of the different *O*-alkyl glucopyranosides (**334 a-g**) and PSA/MSA ratio calculated using Marvin Sketch. Errors for IC_{50} values are given in standard deviation (SD).

Compound	IC_{50} (mM)	PSA (Marvin Sketch)	MSA (Marvin Sketch)	PSA/MSA
334a	38.9 ± 4.7	99.38	278.35	0.36
334b	59.6 ± 5.1	99.38	308.90	0.32
334c	17.3 ± 5.9	99.38	340.61	0.29
334d	21.5 ± 2.2	99.38	371.22	0.27
334e	23.7 ± 0.5	99.38	401.71	0.25
334f	27.6 ± 6.4	99.38	432.30	0.23
334g	9.7 ± 3.1	99.38	493.17	0.20

As discussed in section **3.2.2**, the *O*-linked compounds bearing three to eight carbons at the anomeric position appeared to be more active than the ones bearing one or two carbons (IC_{50} = 9.7-27.5 mM vs 38.9 and 59.6 mM, respectively). However, no correlation appeared to exist between the length of the alkyl chain and the IRI activity of **334 a-g** because the IC_{50} values of **334 a-g** compounds did not increase, nor did they decrease as the number of the carbons in the alkyl chain increased. Thus, we sought to further confirm if there is a relationship between the net polarity of **334 a-g** and their IRI activity by plotting the logarithmic values of IC_{50} and their calculated PSA/MSA ratio (**Figure 3.9**). The R^2 value of the linear relationship was found to be 0.55, suggesting that the relationship between the IRI activity and PSA/MSA ratio of **334 a-g** is very weak. This further proves that there is no relationship between the length of the alkyl chain and the IRI activity of the *O*-linked compounds.

Important to note, however, there appeared to be a trend between the PSA/MSA values and the IRI activity of compounds **334 c-f**, where the IRI activity increased as the net polarity (PSA/MSA ratio) decreased. Overall, it is suggested that there is a very weak linear relationship ($R^2 = 0.55$) between the IRI activity of *O*-linked alkyl glucopyranosides and their calculated PSA/MSA ratio.

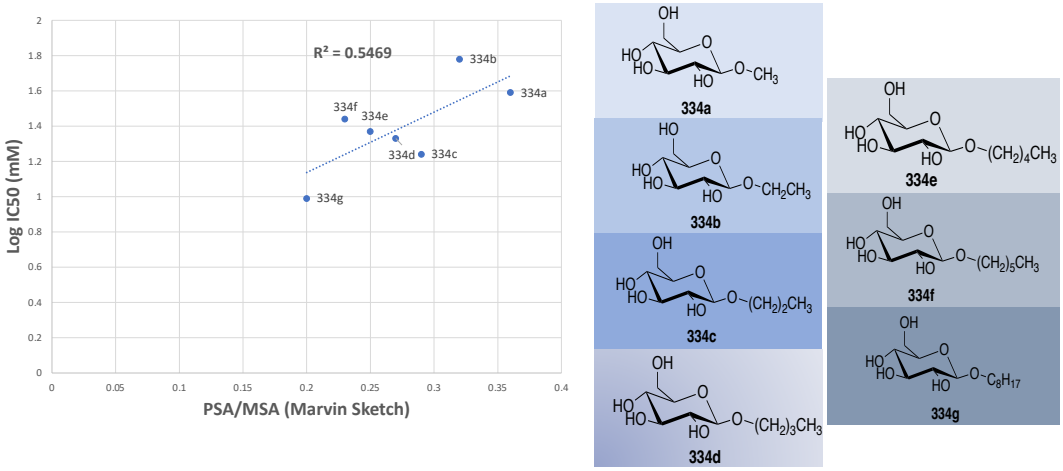

Figure 3.9 Linear correlation between the log IC_{50} values of the different *O*-alkyl glucopyranoside derivatives and their calculated PSA/MSA ratio. The R^2 value of the linear relationship is 0.55.

3.5.2 Correlations Between the PSA/MSA Ratio and the IRI Activity of C-Alkyl Glucoside Compounds

We also sought to discover any trend between the IRI activity of *C*-linked compounds and their PSA/MSA ratio. The PSA value of **339 a-f** compounds using Marvin Sketch software (ChemAxon) was found to be 90.15 (**Table 3.5**), which is lower than the *O*-linked alkyl glucoside compounds. This may be due to the loss of one oxygen atom at the anomeric position, decreasing the net polarity of *C*-linked derivatives. The MSA values of **339 a-f** compounds (ranging from 262.72 to 415.99) increased as the length of the alkyl chain increased, and as a result the PSA/MSA ratio value of the different compounds decreased accordingly (**Table 3.5**).

Table 3.5 IC_{50} values of the different *C*-linked alkyl glucopyranosides (**339 a-f**) and PSA/MSA ratio calculated using Marvin Sketch. Errors for IC_{50} values are given in standard deviation (SD).

Compound	IC_{50} (mM)	PSA (Marvin Sketch)	MSA (Marvin Sketch)	PSA/MSA
339a	49.1 ± 6.1	90.15	262.72	0.34
339b	10.4 ± 4.7	90.15	293.16	0.31
339c	43.9 ± 4.0	90.15	323.95	0.28
339d	79.5 ±1.5	90.15	354.84	0.25
339e	32.5 ± 0.4	90.15	385.87	0.23
339f	68.0 ± 1.3	90.15	415.99	0.22

As discussed in **section 3.3.2**, no trend was observed between the IRI activity of *C*-linked alkyl glucoside derivatives and the length of the alkyl chain. Furthermore, the logarithmic values of the IC_{50} of the *C*-linked compounds were plotted against their calculated values of PSA/MSA ratio to investigate the presence of any linear correlation (**Figure 3.10)**. The R^2 value of the linear correlation was found to be 0.17, indicating no linear relationship between PSA/MSA ratio and the IC_{50} values of the different *C*-linked alkyl glucosides.

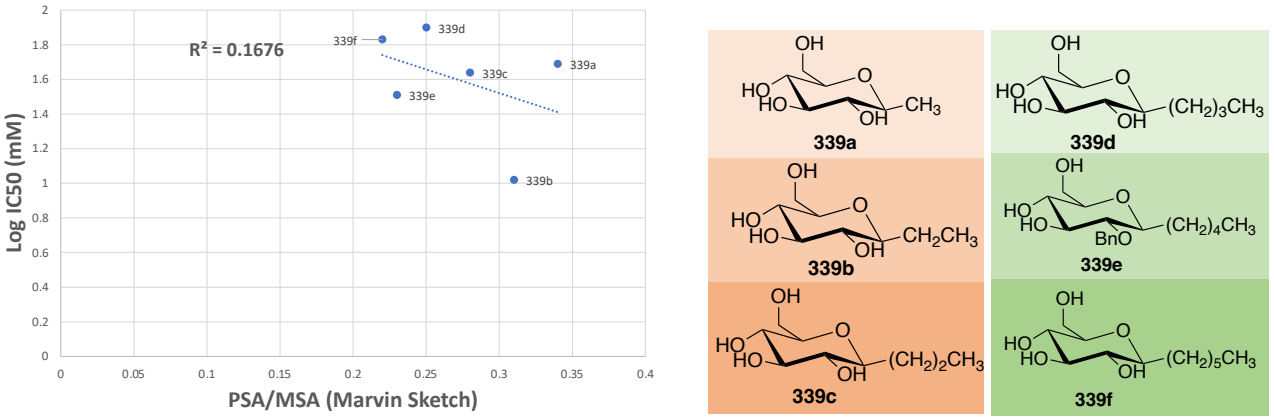

Figure 3.10 Linear correlation between the log IC_{50} values of the different *C*-linked alkyl glucopyranoside derivatives and their calculated PSA/MSA ratio. The R^2 value of the linear relationship is 0.17.

3.5.3 Discussion on the Correlation Between the PSA/MSA and IC_{50} Values of O- and C-Alkyl Glucoside Compounds

The IRI activities of compounds **334 a-f** and **339 a-f** were correlated with their PSA/MSA ratios that were computed using Marvin Sketch software (ChemAxon) to investigate any relationship between their IRI activities and the length of the hydrophobic moiety (alkyl chain) linked to the anomeric carbon. It was hypothesized that increasing the alkyl chain length will result in increasing the IRI activity of both *O*- and *C*-linked derivatives. However, **Figures 3.9** and **3.10** demonstrate that there is either a very weak relationship (*O*-linked compounds) or no relationship (*C*-linked compounds) between the PSA/MSA ratio and the IRI activity of **334 a-g** and **339 a-f** derivatives, respectively. The R^2 values were found to be 0.55 and 0.17 for *O*- and *C*-linked derivatives, respectively. These preliminary data suggest that altering the length of the alkyl chain at the anomeric carbon of glucoside compounds may result in an increase or a decrease in the IRI activity. However, there appears to be no linear relationship between the net polarity (PSA/MSA ratio) and IRI activity independent on the nature of the glycosidic linkage (*C*-*C* or *C*-*O*) at the anomeric position. Important to note, however, even though no relationship was observed between the IRI activity of the synthesized *O*- and *C*-linked compounds and their PSA/MSA ratio, there could be a special correlation between the log IC_{50} values of these compounds and the values of their net polarity which can be investigated using other types of statistical tests (i.e., Spearman's rank correlation), which should be further examined.

Although previous research revealed the presence of a positive linear relationship between the PSA/MSA ratio and the IRI activity of *N*-alkyl-D-aldonamide derivatives,[15,28] no relationship was observed for the *C*- and *O*-alkyl glucoside derivatives. This may be

due to the difference in the assay utilized to measure the IRI activity. The IRI activity of *N*-alkyl-D-aldonamide compounds was assessed by the conventional splat cooling assay which generates the measure of IRI activity as %MGS (**Figure 3.3**).[30] In the past few years, a modified version of the splat cooling assay was discovered as a better alternative of the conventional one, where the rate of ice recrystallization can be measured using the "binning process".[43] The IC_{50} value of IRI candidates can also be determined by the modified splat cooling assay (**Figures 3.5** and **3.6**). The %MGS value measures the IRI activity of a compound by a direct comparison between the grain size of the compound and the PBS control at a single concentration.[15,28] On the other hand, the modified splat cooling assay allows for a more accurate measurement where the rate of ice recrystallization and the IC_{50} values can be determined from several tested concentrations.[43] Therefore, the modified splat cooling assay was utilized to measure the IRI activity of the *O*- and *C*-linked compounds. Based upon chapter 3 data, it implies that the nature of the assay utilized for assessing the IRI activity results in different measurements of the IRI activity (i.e., %MGS and IC_{50} value). %MGS and IC_{50} values may also differ in the way they correlate to the molecular properties of the IRI candidates (i.e., PSA/MSA ratio). Therefore, future studies must be conducted to reveal the difference in the correlations between the %MGS or IC_{50} values and the molecular properties of the IRI candidates.

3.6 Chapter Summary

Several classes of IRIs have been discovered and reported by the Ben laboratory. Moreover, SAR studies have been conducted to establish key structural features that cause a compound to be an active IRI. Previous studies conducted in our lab have shown that there is a positive linear correlation between the IRI activity of *N*-alkyl-D-aldonamide

derivatives and their PSA/MSA ratio. In this study, two classes of alkyl glucoside derivatives, *C*-linked and *O*-linked alkyl glucopyranosides, were synthesized and evaluated by the modified splat cooling assay to investigate any correlations between the length of the alkyl chain at the anomeric position and the IRI activity. We hypothesized that increasing the alkyl chain length will increase the IRI activity of the compound.

Amongst the seven *O*-linked alkyl glucopyranosides (**334 a-g**), *n*-Octyl-β-D-glucosides (**334 g**) demonstrated the lowest IC_{50} value, and hence, it was the most active IRI. Employing a methyl group at the anomeric position (**334 a**) resulted in increasing the IC_{50} value by 4-fold compared to **334 g**. Moreover, reducing the length of the alkyl chain from 8 carbons to 2-6 carbons was also found to increase the IC_{50} value of 1.7- to 2.8-fold. To better understand whether the length of the alkyl chain affects the IRI activity of this class of IRI candidates, the PSA/MSA ratio of **334 a-g** was calculated using Marvin Sketch (ChemAxon) and was plotted against the logarithmic value of their IC_{50}. The R^2 value of the linear relationship was found to be 0.55, meaning the activity by which these compounds (**334 a-g**) inhibit ice recrystallization is weakly correlated to the length of the hydrophobic moiety (alkyl chain).

Six new compounds were synthesized (**339 a-f**) by altering the glycosidic linkage at the anomeric position to *C*-*C*. The IC_{50} values of the different *C*-linked compounds did not appear to decrease as the length of the alkyl chain increased, indicating no correlation between the IRI activity of this class of IRI and the length of the alkyl chain (**Table 3.2**). This was further confirmed by plotting the logarithmic values of IC_{50} of the different *C*-linked compounds and their calculated PSA/MSA ratio. The value of R^2 of the linear

correlation was found to be 0.17, representing no linear relationship between the length of the alkyl chain and the IRI activity of *C*-linked compounds.

Comparing the findings from this study with a previous work where a positive correlation was observed between the length of the alkyl chain and the IRI activity of *N*-alkyl aldonamides, it is suggested that the measurement of the IRI activity (i.e., %MGS vs IC_{50} values) that is utilized to correlate to the molecular properties of IRI candidates (i.e., PSA/MSA ratio) may yield different observations in the linear relationship between the IRI activity and their PSA/MSA ratio.

Lastly, most of the *O*-alkyl glucosides were effective IRIs (IC_{50} < 20 mM), unlike *C*-linked alkyl glucosides (IC_{50} > 20mM). This indicates that the nature of the glycosidic bond at the anomeric position may also influence the IRI activity. Therefore, further investigations to study the IRI activity of candidate with other glycosidic bonds (i.e., *C*-*S* or *C*-*N* bond) are required.

3.7 Experimental Procedures and NMR Characterization

All reactions were performed under anhydrous conditions, using flame-dried glassware and a positive pressure of dry argon. Air or moisture-sensitive reagents and anhydrous solvents were transferred with oven-dried syringes or cannulae. Reactions were monitored using analytical thin layer chromatography (TLC) with 0.2 mm pre-coated silica gel aluminum plates (60 F_{254}, E. Merck). Components were visualized by illumination with a short-wavelength (254 nm) ultra-violet light and/or by staining (p-anisaldehyde or orcinol/sulphuric acid stain solution). Flash chromatography was performed using SiliCycle (QC) or E. Merck silica gel 60 (230-400 mesh). DCM and THF solvents used for anhydrous reactions were dispensed from a benchtop solvent purifier (SPBT-1, LC

Technology Solutions Inc, Salisbury, MA) or purchased and stored over activated 4 Å molecular sieves. All anhydrous alkyl alcohol reagents and Grignard reagents were purchased from Sigma Aldrich without further purifications unless indicated.

Nuclear magnetic resonance (NMR) spectroscopy, ^{1}H (300 or 400 MHz) and ^{13}C (100 or 125 MHz) spectra, were recorded at ambient temperature on a Bruker Avance 300 or Bruker Avance 400 (Bruker, Madison, WI). Deuterated chloroform ($CDCl_3$), water (D_2O) or methanol (MeOD) were used as NMR solvents, unless otherwise stated. Chemical shifts were reported in ppm using the solvent residual peak as an internal standard. Splitting patterns were designated as follows: s, singlet; d, doublet; t, triplet; q, quartet; quint, quintet; m, multiplet; br, broad; dd, doublet of doublets; ddd, doublet of doublet; dt, doublet of triplet. Low resolution mass spectrometry (LRMS) was performed on a Micromass Quatro-TOF mass spectrometer (Waters Corporation, Milford, MA) with a positive electrospray ionization mode (ESI+) at John L. Holmes Mass Spectrometry Facility at the University of Ottawa.

3.7.1 General Procedure for Preparing Alkyl-2,3,4,6-tetra-O-acetyl-β-D-glucopyranoside Compounds (333 a, and 333 c-g).[16]

1,2,3,4,6-penta-*O*-acetyl-β-D-glucopyranose (**331**) (1 equivalent) and anhydrous alcohol (2 equivalents) were dissolved in anhydrous CH_2Cl_2 (0.12 M) in the presence of 4 Å MS. The mixture was stirred at 0 °C under argon, and boron trifluoride diethyl ether (4 equivalents) was then added slowly. The reaction mixture was stirred overnight, then diluted with CH_2Cl_2 and quenched with a saturated solution of sodium bicarbonate in water. The solution was filtered through Celite® and then extracted with CH_2Cl_2. The organic layer was washed with saturated $NaHCO_3$, H_2O, saturated brine, then dried over $MgSO_4$ and

concentrated. Column chromatography (6:4 Hexanes/EtOAc) afforded *n*-alkyl-2,3,4,6-tetra-*O*-acetyl-β-D-glucopyranoside (**333 a, and 333 c-g**) as white solids.

3.7.2 General Procedure for Preparing Ethyl-2,3,4,6-tetra-O-acetyl-β-D glucopyranoside derivative (333 b).[41,61]

1,2,3,4,6-penta-*O*-acetyl-β-D-glucopyranose (**331**) (2.0 g, 5.1 mmol) was cooled to 0°C in an ice bath and HBr (13 mL, 33% in AcOH) was added. The solution was stirred for 3 hours, and then diluted with CH_2Cl_2 (15.7 mL). The product was washed several times with H_2O (20 mL) until pH 7 was reached, and then washed with brine (2 x 50 mL). The organic layers were dried with $MgSO_4$, filtered, and concentrated to give 2,3,4,6-tetra-*O*-acetyl-α-D-glucopyranosyl bromide (**332**) as a white powder that was stored in the freezer under argon overnight and used directly for the next reaction. Glycosyl bromide (**332**) (0.5 g, 1.2 mmol) was dissolved in anhydrous CH_2Cl_2 (7.6 mL). Anhydrous ethanol (0.95 mL, 16.2 mmol) and Ag_2CO_3 (0.33 g, 1.2 mmol) were then added. The reaction mixture was stirred for 24 hours, diluted with CH_2Cl_2 (16 mL), filtered through Celite®, washed consecutively with saturated $NaHCO_3$ (10 mL) and brine (10 mL), and concentrated under vacuum. Column chromatography (6:4 Hexanes/EtOAc) afforded Ethyl-2,3,4,6-tetra-*O*-acetyl-β-D-glucopyranoside **(333 b**) as a white solid.

3.7.3 General Procedure for Preparing 1-hydroxy-1-(2,3,4,6-tetra-O-benzyl-β-D-glucopyranosyl)-alkane (337 a-f).[18]

2,3,4,6-Tetra-O-benzyl-β-D-gluconolactone (**336**) (1 equivalent) was dissolved in anhydrous THF (0.36 M). A 2.0 M solution of alkylmagnesium chloride solution in THF (2 equivalents) was added at -78 °C and the reaction mixture was stirred for 2 hours. The

reaction was then treated with 5% NH_4Cl solution and extracted with ethyl acetate which afforded compounds (**337 a-f**) exclusively as white oils.

3.7.4 General Procedure for Preparing (2,3,4,6-tetra-O-benzyl-β-D-glucopyranosyl)-alkane (338 a-f).[18]

1-hydroxy-1-(2,3,4,6-Tetra-O-benzyl-β-D-glucopyranosyl)-alkane derivatives (**337 a-f**, 1 equivalent) were dissolved in anhydrous DCM (0.21 M). Et_3SiH (3 equivalents) and $BF_3.OEt_2$ (2 equivalents) were then added to the reaction mixture at -78 °C. The reaction was stirred for 18 hours. The reaction mixture was then treated with saturated $NaHCO_3$ and extracted with DCM. The organic layer was then dried over $MgSO_4$ and concentrated. Column chromatography (6:4 Hexanes/EtOAc) afforded intermediates (**338 a-f**) as white solids.

2,3,4,6-tetra-*O*-acetyl-α-D-glucopyranosyl bromide

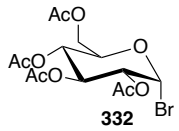

332

Using the general procedure for preparing *E*thyl-2,3,4,6-tetra-O-acetyl-β-D-glucopyranoside afforded **332** as white powder (2.1 g, 97%). Characterization data was consistent with that previously reported in literature.[72] ^1H NMR (400 MHz, $CDCl_3$): δ 6.61 (d, J = 4.3 Hz, 1H), 5.56 (t, J = 9.8 Hz, 1H), 5.16 (t, J = 9.8 Hz, 1H), 4.84 (dd, J = 4.3, 10.5 Hz, 1H), 4.35-4.28 (m, 2H), 4.13 (dd, J = 1.8, 12.3 Hz,1H), 2.10 (s, 3H), 2.09 (s, 3H), 2.,05 (s, 3H), 2.03 (s, 3H). ^{13}C NMR (100 MHz, $CDCl_3$): δ 170.5, 169.9, 169.8, 169.5, 85.55, 72.1, 70.6, 70.2, 67.2, 60.9, 20.7, 20.67, 20.6, 20.5. LRMS (ESI) m/z calcd. for $C_{14}H_{19}O_9Br$ $[M+Na]^+$ 433.0; found 433.1.

Methyl-2,3,4,6-tetra-*O*-acetyl-β-D-glucopyranoside (333 a)

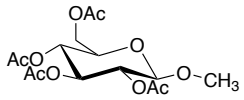

333a

Using the general procedure for preparing Alkyl-2,3,4,6-tetra-*O*-acetyl-β-D-glucopyranoside derivatives with anhydrous methanol yielded (0.55 g, 30%). Characterization data was consistent with that previously reported in literature.[75] ^{1}H NMR (400 MHz, $CDCl_3$): δ 5.21 (t, *J* = 9.5 Hz, 1H), 5.10 (t, *J* = 10.0 Hz, 1H), 4.99 (dd, *J* = 7.9, 9.5 Hz, 1H), 4.44 (d, *J* = 7.9 Hz, 1H), 4.27 (dd, *J* = 4.5, 12.4 Hz, 2H), 4.16 (dd, *J* = 2.4, 12.4 Hz, 1H), 3.72-3.68 (m, 1H), 3.51 (s, 3H), 2.10 (s, 3H), 2.06 (s, 3H), 2.03 (s, 3H), 2.01 (s, 3H).

Ethyl-2,3,4,6-tetra-*O*-acetyl-β-D-glucopyranoside (333 b)

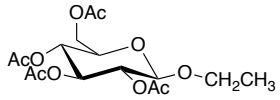

333b

Using the general procedure for preparing Ethyl-2,3,4,6-tetra-O-acetyl-β-D-glucopyranoside yielded (0.34 g, 74%). Characterization data was consistent with that previously reported in literature.[53] ^{1}H NMR (400 MHz, $CDCl_3$): δ 5.18 (t, *J* = 9.5 Hz, 1H), 5.06 (t, *J* = 9.8 Hz, 1H), 4.95 (dd, *J* = 7.9, 9.5 Hz, 1H), 4.49 (d, *J* = 7.9 Hz, 1H), 4.25 (dd, *J* = 4.6, 12.3 Hz, 1H), 4.11 (dd, *J* = 2.4, 12.3 Hz, 1H) 3.88 (dq, *J* = 7.1, 9.6 Hz, 1H) 3.70-3.64(m, 1H), 3.56 (dq, *J* = 7.1, 9.6 Hz, 1H) , 2.06 (s, 3H), 2.02 (s, 3H), 2.00 (s, 3H), 1.98 (s, 3H), 1.18 (t, *J* = 7.2 Hz, 3H).

Propyl -2,3,4,6-tetra-*O*-acetyl-β-D-glucopyranoside (333 c)

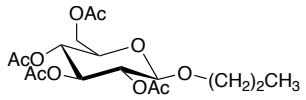

333c

Using the general procedure for preparing Alkyl-2,3,4,6-tetra-O-acetyl-β-D-glucopyranoside derivatives with anhydrous propanol yielded (0.58 g, 29%). Characterization data was consistent with that previously reported in literature.[73] ^{1}H NMR (400 MHz, $CDCl_3$): δ 5.21 (t, *J* = 9.4 Hz, 1H), 5.10 (t, *J* = 9.6 Hz, 1H), 5.01 (dd, *J* = 7.8, 9.6 Hz, 1H), 4.50 (d, *J* = 8.1 Hz, 1H), 4.27 (dd, *J* = 4.5, 12.0 Hz, 2H), 4.16 (dd, *J* = 2.6, 12.0Hz, 1H), 3.85 (dt, *J* = 6.2, 9.6 Hz, 1H), 3.71-3.67 (m, 1H), 3.43 (dt, *J* = 6.2, 9.6 HZ, 1H), 2.10 (s, 3H), 2.05 (s, 3H), 2.03 (s, 3H), 2.01 (s, 3H), 1.62-1.58 (m, 2H), 0.90 (t, *J* = 7.3 Hz, 3H).

Butyl-2,3,4,6-tetra-*O*-acetyl-β-D-glucopyranoside (333 d)

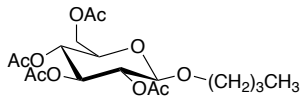

333d

Using the general procedure for preparing Alkyl-2,3,4,6-tetra-O-acetyl-β-D-glucopyranoside derivatives with anhydrous butanol yielded (0.58 g, 29%). Characterization data was consistent with that previously reported in literature.[76] ^{1}H NMR (400 MHz, CDCl3): δ 5.17 (t, *J* = 9.9 Hz, 1H), 5.06 (t, *J* = 9.7 Hz, 1H), 4.96 (dd, *J* = 7.9, 9.6 Hz, 1H), 4.46 (d, *J* = 8.3 Hz, 1H), 4.24 (dd, *J* = 4.6, 12.2 Hz, 1H), 4.11 (dd, *J* = 2.1, 12.3 Hz, 1H), 3.85 (dt, *J* = 6.2, 9.6 Hz, 1H), 3.68-3.64 (m, 1H), 3.45 (dt, *J* = 6.5, 9.6 HZ, 1H), 2.06 (s, 3H), 2.01 (s, 3H), 2.00 (s, 3H), 1.97 (s, 3H), 1.55-1.49 (m, 2H), 1.35-1.29(m, 2H), 0.87 (t, *J* = 7.5 Hz, 3H).

Pentyl-2,3,4,6-tetra-*O*-acetyl-β-D-glucopyranoside (333 e)

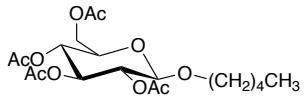

333e

Using the general procedure for preparing Alkyl-2,3,4,6-tetra-O-acetyl-β-D-glucopyranoside derivatives with anhydrous pentanol yielded (0.70 g, 33%). Characterization data was consistent with that previously reported in literature.[73] ^{1}H NMR (400 MHz, $CDCl_3$): δ 5.16 (t, *J* = 9.5 Hz, 1H), 5.04 (t, *J* = 9.7 Hz, 1H), 4.94 (dd, *J* = 7.3, 9.6 Hz, 1H), 4.45 (d, *J* = 8.0 Hz, 1H), 4.18 (dd, *J* = 4.7, 12.3 Hz, 1H), 4.09 (dd, *J* = 2.3, 12.3 Hz, 1H), 3.83 (dt, *J* = 6.3, 9.6 Hz, 1H), 3.67-3.63 (m, 1H), 3.43 (dt, *J* = 6.6, 9.5 HZ, 1H), 2.04 (s, 3H), 2.00 (s, 3H), 1.98 (s, 3H), 1.96 (s, 3H), 1.57-1.49 (m, 2H), 1.29-1.21(m, 4H), 0.84 (t, *J* = 7.1 Hz, 3H).

Hexyl-2,3,4,6 -tetra-*O*-acetyl-β-D-glucopyranoside (333 f)

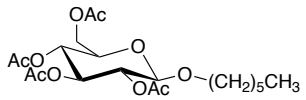

333f

Using the general procedure for preparing Alkyl-2,3,4,6-tetra-O-acetyl-β-D-glucopyranoside derivatives with anhydrous hexanol yielded (0.77 g, 35%). Characterization data was consistent with that previously reported in literature.[76] ^{1}H NMR (400 MHz, CDCl3): δ 5.20 (t, *J* = 9.6 Hz, 1H), 5.08 (t, *J* = 9.6 Hz, 1H), 4.98 (dd, *J* = 7.9, 9.6 Hz, 1H), 4.48 (d, *J* = 7.9 Hz, 1H), 4.26 (dd, *J* = 4.7, 12.2 Hz, 1H), 4.13 (dd, *J* = 2.3, 12.2 Hz, 1H), 3.87 (dt, *J* = 6.6, 9.4 Hz, 1H), 3.70-3.66 (m, 1H), 3.46 (dt, *J* = 7.0, 9.8 Hz, 1H), 2.08 (s, 3H), 2.03 (s, 3H), 2.02 (s, 3H), 2.00 (s, 3H), 1.58-1.53 (m, 2H), 1.31-1.27 (m, 6H), 0.87 (t, *J* = 6.7 Hz, 3H).

Octyl-2,3,4,6-tetra-*O*-acetyl-β-D-glucopyranoside (333 g)

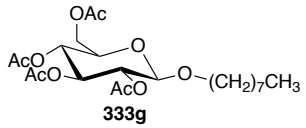

333g

Using the general procedure for preparing Alkyl-2,3,4,6-tetra-O-acetyl-β-D-glucopyranoside derivatives with 1-anhydrous octanol yielded (0.84g, 36%). Characterization data was consistent with that previously reported in literature.[29] ^{1}H NMR (400 MHz, $CDCl_3$): δ 5.21 (t, *J* = 9.9 Hz, 1H), 5.09 (t, *J* = 9.9 Hz, 1H), 4.99 (dd, *J* = 8.0, 9.9 Hz, 1H), 4.49 (d, *J* = 8.0 Hz, 1H), 4.26 (dd, *J* = 4.3, 12.3 Hz, 1H), 4.14 (dd, *J* = 2.5, 12.3 Hz, 1H), 3.87 (dt, *J* = 6.8, 9.9 Hz, 1H), 3.71-3.64 (m, 1H), 3.47 (dt, *J* = 6.9, 9.9 HZ, 1H), 2.09 (s, 3H), 2.04 (s, 3H), 2.02 (s, 3H), 2.01 (s, 3H), 1.56 (br, 2H), 1.27 (br, 10H), 0.87 (t, *J* = 6.6 Hz, 3H).

Methyl-β-D-glucopyranoside (334 a)

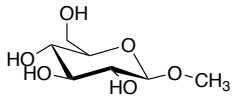

334a

Compound **333 a** (0.55 g, 1.5 mmol) was dissolved in a solution of 1 M sodium methoxide in methanol (16 mL) and stirred at room temperature until the disappearance of starting material (monitored by TLC). The solution was then neutralized with Amberlite® IR-120 (H^+) ion-exchange resin, filtered and concentrated. The product was purified by column chromatography (9:1 CH_2Cl_2/MeOH) to afford **334 a** as a white powder (0.29 g, 99%). Characterization data was consistent with that previously reported in literature.[78] ^{1}H NMR (400 MHz, D_2O) δ 4.38 (d, *J* = 7.9 Hz, 1H), 3.93 (dd, *J* = 2.4, 12.4 Hz, 1H), 3.72 (dd, *J* = 6.2, 12.4 Hz, 1H), 3.57 (s, 3H), 3.52-3.45 (m, 2H), 3.38 (t, *J* = 9.2 Hz, 1H), 3.26 (dd, *J*

=8.0, 9.1 Hz, 1H). ^{13}C NMR (100 MHz, D_2O): δ 103.2, 75.9, 75.8, 73.1, 69.7, 60.8, 57.2. LRMS (ESI) *m/z* calcd. for $C_7H_{14}O_6$ $[M+Na]^+$ 217.1 ; found 217.1.

Ethyl-β-D-glucopyranoside (334 b)

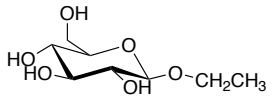

334b

Compound **333 b** (0.34 g, 0.90 mmol) was dissolved in a solution of 1 M sodium methoxide in methanol (9 mL) and stirred at room temperature until the disappearance of starting material (monitored by TLC). The solution was then neutralized with Amberlite® IR-120 (H^+) ion-exchange resin, filtered and concentrated. The product was purified by column chromatography (9:1 CH_2Cl_2/MeOH) to afford **334 b** as a white powder (0.23 g, 98%). Characterization data was consistent with that previously reported in literature.[78] ^{1}H NMR (400 MHz, D_2O) δ 4.44 (d, *J* = 8.2 Hz, 1H), 3.96-3.92 (m, 2H), 3.88 (dd, *J* = 2.3, 10.2 Hz, 1H), 3.72-3.66 (m, 2H), 3.45-3.40 (m, 2H), 3.33 (t, *J* = 9.2 Hz, 1H), 3.22 (dd, *J* = 5.7, 8.0 Hz, 1H), 1.20 (t, *J* = 7.1 Hz, 3H). ^{13}C NMR (100 MHz, D_2O): 101.8, 75.8, 75.6, 73.1, 69.6, 66.1, 60.7, 22.1, 14.2. LRMS (ESI) *m/z* calcd. for $C_9H_{18}O_6$ $[M+Na]^+$ 231.1; found 231.2.

Propyl-β-D-glucopyranoside (334 c)

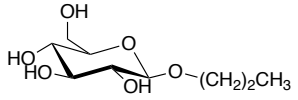

334c

Compound **333 c** (0.58 g, 1.5 mmol) was dissolved in a solution of 1 M sodium methoxide in methanol (15.8 mL) and stirred at room temperature until the disappearance of starting material (monitored by TLC). The solution was then neutralized with Amberlite® IR-120 (H^+) ion-exchange resin, filtered and concentrated. The product was purified by column chromatography (9:1 CH_2Cl_2/MeOH) to afford **334 c** as a white powder (0.33 g, 99%).

Characterization data was consistent with that previously reported in literature.[79] ^{1}H NMR (400 MHz, D_2O) δ 4.43 (d, *J* = 7.9 Hz, 1H), 3.90-3.81 (m, 2H), 3.68 (dd, *J* = 6.0, 12.4 Hz, 1H), 3.60 (dt, *J* = 6.7, 9.8 Hz, 1H), 3.47-3.39 (m, 2H), 3.35 (d, *J* = 9.0 Hz, 1H), 3.22 (dd, *J* = 7.9, 9.4 Hz, 1H), 1.62-1.55 (m, 2H), 0.88 (t, *J* = 7.5 Hz, 3H). ^{13}C NMR (100 MHz, D_2O): 102.1, 75.9, 75.8, 73.1, 72.2, 69.6, 60.7, 22.1, 9.5. LRMS (ESI) *m/z* calcd. for $C_9H_{18}O_6$ $[M+Na]^+$ 245.1; found 245.2.

Butyl-β-D-glucopyranoside (334 d)

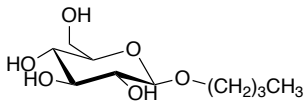

334d

Compound **333 d (**0.64 g, 1.6 mmol) was dissolved in a solution of 1 M sodium methoxide in methanol (17.5 mL) and stirred at room temperature until the disappearance of starting material (monitored by TLC). The solution was then neutralized with Amberlite® IR-120 (H^+) ion-exchange resin, filtered and concentrated. The product was purified by column chromatography (9:1 CH_2Cl_2/MeOH) to afford **334 d** as a white powder (0.41 g, 98%). Characterization data was consistent with that previously reported in literature.[79] ^{1}H NMR (400 MHz, D_2O) δ 4.43 (d, *J* = 7.9 Hz, 1H), 3.93-3.87 (m, 2H), 3.69 (dd, *J* = 5.9, 12.5 Hz, 1H), 3.64 (dt, *J* = 6.8, 9.8 Hz, 1H), 3.48-3.40 (m, 2H), 3.34 (t, *J* = 9.8 Hz, 1H), 3.22 (dd, *J* = 7.4, 9.8 Hz, 1H), 1.62-1.54 (m, 2H), 1.37-1.32(m, 2H), 0.88 (t, *J* = 7.5 Hz, 3H). ^{13}C NMR (100 MHz, D_2O): δ 102.1,75.8, 75.8, 73.1, 70.4, 69.6, 60.7, 30.8, 18.4, 13.0. LRMS (ESI) *m/z* calcd. for $C_{10}H_{20}O_6$ $[M+Na]^+$ 259.1; found 259.2.

Pentyl-β-D-glucopyranoside (334 e)

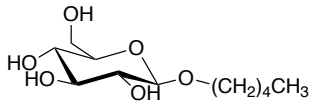

334e

Compound **333 e (**0.70 g, 1.7 mmol) was dissolved in a solution of 1 M sodium methoxide in methanol (19.1 mL) and stirred for one hour at room temperature. The solution was then neutralized with Amberlite® IR-120 (H^+) ion-exchange resin, filtered and concentrated. The product was purified by column chromatography (9:1 CH_2Cl_2/MeOH) to afford **334 e** as a white powder (0.42 g, 99%). Characterization data was consistent with that previously reported in literature.[79] ^{1}H NMR (400 MHz, D_2O) δ 4.41 (d, *J* = 7.9 Hz, 1H), 3.88 (d, *J* = 2.3 Hz, 1H), 3.86 (quint, *J* = 2.2 Hz, 1H), 370-3.60 (m, 2H), 3.46-3.39 (m, 2H), 3.33 (dd, *J* = 8.9, 9.6 Hz, 1H), 3.21 (dd, *J* = 8.1, 9.3 Hz, 1H), 1.60-1.57 (m, 2H), 1.29-1.27(m, br, 4H), 0.84 (t, *J* = 6.8 Hz, 3H). ^{13}C NMR (100 MHz, D_2O): δ 102.1,75.9, 75.8, 73.1, 70.7, 69.6, 60.7, 28.4, 27.3, 21.7, 13.2. LRMS (ESI) *m/z* calcd. for $C_{11}H_{22}O_6$ $[M+Na]^+$ 273.1; found 273.2.

Hexyl-β-D-glucopyranoside (334 f)

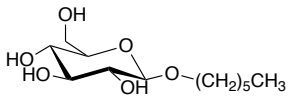

334f

Compound **333 f (**0.77 g, 1.8 mmol) was dissolved in a solution of 1 M sodium methoxide in methanol (21.0 mL) and stirred for one hour at room temperature. The solution was then neutralized with Amberlite® IR-120 (H^+) ion-exchange resin, filtered and concentrated. The product was purified by column chromatography (9:1 CH_2Cl_2/MeOH) to afford **334 f** as a white powder (0.47 g, 99%). Characterization data was consistent with that previously reported in literature.[79] ^{1}H NMR (400 MHz, D_2O) δ 4.42 (d, *J* = 8.0 Hz, 1H), 3.89 (dd, *J* = 6.8, 9.1 Hz, 1H), 3.86 (q, *J* = 2.5 Hz, 1H), 3.70-3.61 (m, 2H), 3.47-3.40 (m, 2H), 3.35 (d, *J* = 8.9 Hz, 1H), 3.22 (dd, *J* = 7.9, 9.3 Hz, 1H), 1.59 (quint, *J* = 6.9 Hz, 2H), 1.35-1.25 (m, br, 6H), 0.84 (t, *J* = 6.9 Hz, 3H). ^{13}C NMR (100 MHz, D_2O): δ 102.1, 75.9, 75.8, 73.1,

70.7, 69.6, 60.7, 48.8, 30.7, 28.7, 24.7, 21.9, 13.3. LRMS (ESI) *m/z* calcd. for $C_{12}H_{24}O_6$ $[M+Na]^+$ 287.1; found 287.3.

Octyl-β-D-glucopyranoside (334 g)

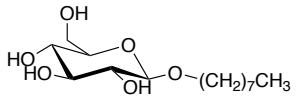

334g

Compound **333 g** (0.84 g, 1.8 mmol) was dissolved in a solution of 1 M sodium methoxide in methanol (41 mL) and stirred for one hour at room temperature. The solution was then neutralized with Amberlite® IR-120 (H^+) ion-exchange resin, filtered and concentrated. The product was purified by column chromatography (9:1 CH_2Cl_2/MeOH) to afford **334 g** as a white powder (0.52 g, 99%). Characterization data was consistent with that previously reported in literature.[29] ^{1}H NMR (400 MHz, D_2O) δ 4.45 (d, *J* = 8.2 Hz, 1H), 3.95-3.89 (m, 2H), 3.74-3.66 (m, 2H), 3.48 (t, *J* = 8.9 Hz, 1H), 3.25 (dd, *J* = 8.0. 9.1 Hz, 1H), 1.63 (quint, *J* = 6.1 Hz, 2H), 1.32-1.28 (m, br, 10H), 0.87 (t, *J* = 6.9 Hz, 3H). ^{13}C NMR (100 MHz, D_2O): δ 102.2, 75.9, 75.8, 73.2, 70.7, 69.7, 31.1, 28.7, 28.4, 28.3, 25.0, 22.0, 13.4. LRMS (ESI) *m/z* calcd. for $C_{14}H_{28}O_6$ $[M+Na]^+$ 315.2; found 315.3.

2,3,4,6-tetra-*O*-benzyl-β-D-gluconolactone (336)

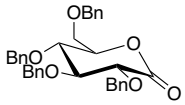

336

Acetic acid anhydride (12.0 mL) was added to a mixture of 2,3,4,6-tetra-*O*-benzyl-D-glucopyranoside (3.09 g, 5.7 mmol) in DMSO (18.1 mL). The reaction mixture was stirred overnight and then diluted with H_2O (100 mL) and extracted with EtOAc. The combined organic phase was then washed with saturated brine and dried with $MgSO_4$, filtered, and concentrated under reduced pressure. The residue was purified by column chromatography

(4:1 Hexanes:EtOAc) to give compound **336** as a colorless oil (1.82 g, 58.9%). Characterization data was consistent with that previously reported in literature.[80] ^{1}H NMR (400 MHz, $CDCl_3$): δ 7.39-7.27 (m, 18H), 7.18-7.15 (m, 2H), 4.98 (d, *J* = 11.5 Hz, 1H), 4.74-4.43 (m, 8H), 4.11 (d, *J* = 6.7 Hz, 1H), 3.96 (t, *J* = 6.8 Hz, 1H), 3.90 (t, *J* = 6.3 Hz, 1H), 3.72 (dd, *J* = 2.1, 10.5 Hz, 1H), 3.66 (dd, *J* = 3.4, 11.3 Hz, 1H). ^{13}C NMR (100 MHz, $CDCl_3$): δ 169.3, 137.6, 137.5, 137.5,136.9, 128.5, 128.4, 128.4, 128.0, 128.0, 127.8, 81.0, 78.1, 77.4, 76.1, 73.9, 73.7, 73.6, 68.3.

1-hydroxy-1-(2,3,4,6-tetra-*O*-benzyl-β-D-glucopyranosyl)-methane (337 a)

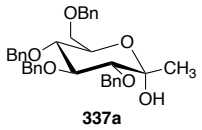

337a

Using the general procedure for preparing 1-hydroxy-1-(2,3,4,6-tetra-*O*-benzyl-β-D-glucopyranosyl)-alkane with 2.0 M methyl magnesium chloride solution in THF yielded (0.44 g, 73.8%). Characterization data was consistent with that previously reported in literature.[81] ^{1}H NMR (400 MHz, $CDCl_3$): δ 7.33-7.30 (m, 18H), 7.17-7.15 (m, 2H), 4.94 (d, *J* = 10.9 Hz, 1H), 4.89 (d, *J* = 2.6 Hz, 2H), 4.82 (d, *J* = 10.7 Hz, 1H), 4.71 (d, *J* = 11.3 Hz, 1H), 4.63 (d, *J* = 12.2 Hz, 1H), 4.55 (t, *J* = 12.2 Hz, 2H), 4.02-3.95 (m, 2H), 3.74 (dd, *J* = 4.0, 10.7 6.3 Hz, 1H), 3.70-3.63 (m, 2H), 3.37 (d, *J* = 9.4 Hz, 1H), 2.57 (br, 1H), 1.42 (s, 3H).

1-hydroxy-1-(2,3,4,6-tetra-*O*-benzyl-β-D-glucopyranosyl)-ethane (337 b)

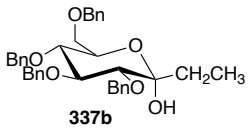

337b

Using the general procedure for preparing 1-hydroxy-1-(2,3,4,6-tetra-*O*-benzyl-β-D-glucopyranosyl)-alkane with 2.0 M ethyl magnesium chloride solution in THF yielded

(0.51 g, 83.3 %). Characterization data was consistent with that previously reported in literature.[81] ^{1}H NMR (400 MHz, $CDCl_3$): δ 7.34-7.28 (m, 18H), 7.21-7.19 (m, 2H), 4.95-4.91 (m, 2H), 4.85 (dd, *J* = 10.9, 14.4 Hz, 2H), 4.69 (d, *J* = 10.9 Hz, 1H), 4.63 (dd, *J* = 5.9, 10.7 Hz, 1H), 4.56-4.51 (m, 2H), 4.03-3.97 (m, 2H), 3.77 (dd, *J* = 3.9, 11.1 Hz, 1H), 3.67 (dd, *J* = 1.8, 10.9 Hz, 2H), 3.44 (d, *J* = 9.3 Hz, 1H), 2.53 (br, 1H), 1.74-1.71 (m, 2H), 0.90 (t, *J* = 7.4 Hz, 3H).

1-hydroxy-1-(2,3,4,6-tetra-*O*-benzyl-β-D-glucopyranos-1-yl)-2-propene (337 c)

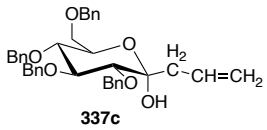

337c

Using the general procedure for preparing 1-hydroxy-1-(2,3,4,6-tetra-*O*-benzyl-β-D-glucopyranosyl)-alkane with 2.0 M allyl magnesium chloride solution in THF yielded (0.552 g, 88.9%). Characterization data was consistent with that previously reported in literature.[71] ^{1}H NMR (400 MHz, $CDCl_3$): δ 7.35-7.17 (m, 20H), 5.93-5.73 (m, 1H), 5.20-5.05 (m, 2H), 5.02-4.48 (m, 8H), 4.14-4.08 (m, 1H), 4.03-3.93 (m, 1H), 3.75 (dd, *J* = 3.7, 10.9 Hz, 1H), 3.69-3.61 (m, 2H), 3.43 (d, *J* = 9.3 Hz, 1H), 2.73 (br, 1H), 2.47-2.32 (m, 2H).

1-hydroxy-1-(2,3,4,6-tetra-*O*-benzyl-β-D-glucopyranosyl)-butane (337 d)

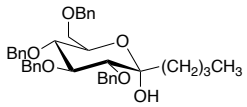

337d

Using the general procedure for preparing 1-hydroxy-1-(2,3,4,6-tetra-*O*-benzyl-β-D-glucopyranosyl)-alkane with 2.0 M butyl magnesium chloride solution in THF yielded (0.43 g, 67.5 %). Characterization data was consistent with that previously reported in literature.[82] ^{1}H NMR (400 MHz, $CDCl_3$): δ 7.33-7.26 (m, 18H), 7.21-7.19 (m, 2H), 4.93-

4.53 (m, 8H), 4.02-3.96 (m, 2H), 3.76 (dd, *J* = 4.4, 10.6 Hz, 1H), 3.66 (d, *J* = 10.6 Hz, 2H), 3.42 (d, *J* = 8.8 Hz, 1H), 2.52 (br, 1H), 1.66-1.63 (m, 2H), 1.37-1.35 (m, 1H), 1.28-1.22 (m, 3H), 0.86 (t, *J* = 7.1 Hz, 3H).

1-hydroxy-1-(2,3,4,6-tetra-*O*-benzyl-β-D-glucopyranosyl)-pentane (337 e)

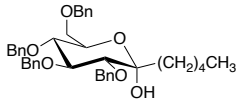

337e

Using the general procedure for preparing 1-hydroxy-1-(2,3,4,6-tetra-*O*-benzyl-β-D-glucopyranosyl)-alkane with 2.0 M pentyl magnesium chloride solution in THF yielded (0.58 g, 88.6 %). Characterization data was consistent with that previously reported in literature.[74] ^{1}H NMR (400 MHz, $CDCl_3$): δ 7.34-7.27 (m, 18H), 7.21-7.19 (m, 2H), 4.93 (d, *J* = 12.2 Hz, 2H), 4.85 (dd, *J* = 11.0, 15.3 Hz, 2H), 4.68 (d, *J* = 11.0 Hz, 1H), 4.62 (dd, *J* = 3.5, 12.4 Hz, 1H), 4.54 (d, *J* = 12.4 Hz, 1H), 4.02-3.96 (m, 2H), 4.02-3.95 (dd, *J* = 4.0, 11.0 Hz, 1H), 3.68-3.62 (m, 2H), 3.43 (d, *J* = 9.3 Hz, 1H), 2.55 (br, 1H), 1.66-1.62 (m, 2H), 1.30-1.20 (m, 6H), 0.87 (t, *J* = 6.7 Hz, 3H).

1-hydroxy-1-(2,3,4,6-tetra-*O*-benzyl-β-D-glucopyranosyl)-hexane (337 f)

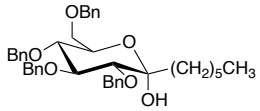

337f

Using the general procedure for preparing 1-hydroxy-1-(2,3,4,6-tetra-*O*-benzyl-β-D-glucopyranosyl)-alkane with 2.0 M hexyl magnesium chloride solution in THF yielded (0.49 g, 74.5 %). ^{1}H NMR (400 MHz, $CDCl_3$): δ 7.33-7.27 (m, 18H), 7.21-7.11 (m, 2H), 4.94-4.47 (m, 8H), 4.02-3.95 (m, 1H), 3.78-3.62 (m, 3H), 3.49-3.41 (m, 2H), 2.66 (br, 1H), 1.93-1.86 (m, 1H), 1.80-1.74 (m, 1H), 1.41-1.22 (m, 8H), 0.88 (dt, *J* = 2.6, 6.7 Hz, 3H).

(2,3,4,6-tetra-*O*-benzyl-β-D-glucopyranosyl)-methane (338 a)

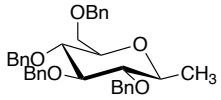

338a

Using the general procedure for preparing 1-(2,3,4,6-tetra-*O*-benzyl-β-D-glucopyranosyl)-alkane yielded **338 a** (0.32 g, 75.6%). Characterization data was consistent with that previously reported in literature.[83] ^{1}H NMR (400 MHz, $CDCl_3$): δ 7.34-7.27 (m, 18H), 7.14-7.12 (m, 2H), 4.94 (d, *J* = 10.9 Hz, 1H), 4.89-4.79 (m, 4H), 4.67-4.59 (m, 2H), 4.56-4.51 (m, 2H), 3.71 (dd, *J* = 2.1, 10.6 Hz, 1H), 3.67 (br, 1H), 3.64 (dd, *J* = 6.1, 10.6 Hz, 1H), 3.59 (t, *J* = 9.5 Hz, 1H), 3.45-3.35 (m, 2H), 3.20 (t, *J* = 9.1 Hz, 1H), 1.32 (d, *J* = 6.1 Hz, 3H).

(2,3,4,6-tetra-*O*-benzyl-β-D-glucopyranosyl)-ethane (338 b)

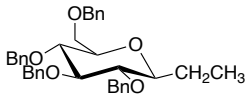

338b

Using the general procedure for preparing 1-(2,3,4,6-tetra-*O*-benzyl-β-D-glucopyranosyl)-alkane yielded **338 b** (0.43 g, 87.3%). Characterization data was consistent with that previously reported in literature.[83] ^{1}H NMR (400 MHz, $CDCl_3$) δ 7.38-7.27 (m, 18H), 7.20-7.16 (m, 2H), 4.91-4.55 (m, 8H), 3.74-3.59 (m, 4H), 3.44-3.39 (m, 1H), 3.30 (t, *J* = 8.3 Hz, 1H), 3.19 (ddd, *J* = 2.6, 8.8, 11.0 Hz, 1H), 1.95-1.87 (m, 1H), 1.58-1.45 (m, 1H), 1.01 (t, *J* = 7.4 Hz, 3H).

(2,3,4,6-tetra-*O*-benzyl-β-D-glucopyranosyl)-2-propene (338 c)

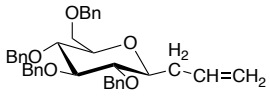

338c

Using the general procedure for preparing (2,3,4,6-tetra-*O*-benzyl-β-D-glucopyranosyl)-alkane yielded **338 c** (0.39 g, 72.1%). Characterization data was consistent with that previously reported in literature.[44] ^{1}H NMR (400 MHz, $CDCl_3$): δ 7.34-7.28 (m, 18H), 7.18-7.16 (m, 2H), 5.97-5.90 (m, 1H), 5.12-5.06 (m, 2H), 4.90-4.55 (m, 8H), 3.71-3.67 (m, 3H), 3.60 (t, *J* = 9.2 Hz, 1H), 3.42-3.40 (m, 1H), 3.34-3.32 (m, 2H), 2.62-2.57 (m, 1H), 2.34-2.28 (m, 1H).

(2,3,4,6-tetra-*O*-benzyl-β-D-glucopyranosyl)-butane (338 d)

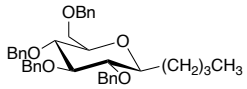

338d

Using the general procedure for preparing (2,3,4,6-tetra-*O*-benzyl-β-D-glucopyranosyl)-alkane yielded **338 d** (0.31 g, 73.7%). Characterization data was consistent with that previously reported in literature.[83] ^{1}H NMR (400 MHz, $CDCl_3$) δ 7.35-7.27 (m, 18H), 7.18-7.15 (m, 2H), 4.89-4.80 (m, 4H), 4.63 (dd, *J* = 5.7, 10.9 Hz, 2H), 4.56 (dd, *J* = 3.7, 10.8 Hz, 2H), 3.74-3.65 (m, 3H), 3.59 (t, *J* = 9.3 Hz, 1H), 3.40-3.37 (m, 1H), 3.29-3.20 (m, 1H), 1.84-1.77 (m, 1H), 1.50-1.25 (m, 5H), 0.88 (t, *J* = 7.1 Hz, 3H).

(2,3,4,6-tetra-*O*-benzyl-β-D-glucopyranosyl)-pentane (338 e)

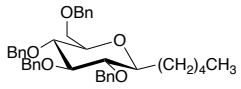

338e

Using the general procedure for preparing (2,3,4,6-tetra-*O*-benzyl-β-D-glucopyranosyl)-alkane yielded **338 e** (0.36 g, 63.3%). Characterization data was consistent with that previously reported in literature.[74] ^{1}H NMR (400 MHz, $CDCl_3$) δ 7.34-7.28 (m, 18H), 7.18-7.16 (m, 2H), 4.89-4.80 (m, 4H), 4.65-4.54 (m, 4H), 3.74-3.66 (m, 3H), 3.59 (t, *J* = 9.6 Hz,

1H), 3.41-3.37 (m, 1H), 3.27 (t, *J* = 9.3 Hz, 1H), 3.22 (dd, *J* = 2.0, 9.3 Hz, 1H), 1.83-1.77 (m, 1H), 1.29-1.25 (m, 7H), 0.88 (t, *J* = 6.7 Hz, 3H).

(2,3,4,6-Tetra-*O*-benzyl-β-D-glucopyranosyl)-hexane (338 f)

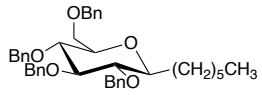

338f

Using the general procedure for preparing (2,3,4,6-tetra-*O*-benzyl-β-D-glucopyranosyl)-alkane yielded **338 f** (0.42 g, 87.4%). ^{1}H NMR (400 MHz, $CDCl_3$): δ 7.31-7.26 (m, 18H), 7.16-7.14 (m, 2H), 4.87 (s, 1H), 4.86 (d, *J* = 11.0 Hz, 1H), 4.79 (d, *J* = 11.0, 1H), 4.61 (dd, *J* = 4.8, 11.0 Hz, 2H), 4.54 (dd, *J* = 3.8, 10.8 Hz, 2H), 3.72-3.62 (m, 3H), 3.57 (t, *J* = 9.4 Hz, 1H), 3.38-3.35 (m, 1H), 3.27-3.18 (m, 2H), 1.81-1.75 (m, 1H), 1.45-1.38 (m, 1H), 1.344-1.25 (m, 8H), 0.85 (t, *J* = 6.5 Hz, 3H).

1-(β-D-glucopyranosyl)-methane (339 a)

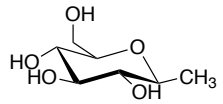

339a

A solution of MeOH:EtOAc (10 mL :10 mL) was added to a round bottom flask containing 5% Pd/C and compound **338 a** (0.32 g, 0.59 mmol).[49] The reaction mixture was stirred under H_2 gas at room temperature for 16 hours. The mixture was then filtered through celite and concentrated to give **339 a** as a white solid (0.09 g, 88.4%). ^{1}H NMR (400 MHz, D_2O). δ 3.76 (dd, *J* = 2.2, 12.2 Hz, 1H), 3.68 (dd, *J* = 5.8, 12.2 Hz, 1H), 3.48-3.36 (m, 4H), 3.14 (t, *J* = 9.3 Hz, 1H), 1.29 (d, *J* = 6.1 Hz, 3H). ^{13}C NMR (100 MHz, D_2O) δ 79.5, 77.1, 75.6, 75.0, 70.0, 60.9, 16.8. LRMS (ESI) *m/z* calcd. for $C_7H_{14}O_5$ $[M+Na]^+$ 201.1; found 201.2.

1-(β-D-glucopyranosyl)-ethane (339 b)

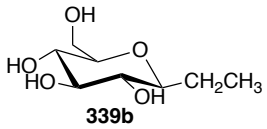

339b

A solution of MeOH:EtOAc (10 mL:10 mL) was added to a round bottom flask containing 5% Pd/C and compound **338 b** (0.43 g, 0.78 mmol).[49] The reaction mixture was stirred under H_2 gas at room temperature for 16 hours. The mixture was then filtered through celite and concentrated to give **339 b** as a white solid (0.13 g, 87.2%). ^{1}H NMR (400 MHz, D_2O): δ 3.90 (dd, *J* = 1.8, 12.1 Hz, 1H), 3.68 (dd, *J* = 5.9, 12.2 Hz, 1H), 3.48-3.45 (t, *J* = 8.5 H, 1H), 3.37-3.36 (m, 2H), 3.26-3.19 (m, 2H), 1.89-1.83 (m, 1H), 1.49-1.42 (m, 1H), 0.98 (t, *J* = 7.5 Hz, 3H). ^{13}C NMR (100 MHz, D_2O) δ 80.5, 79.6, 77.5, 73.1, 70.2, 70.0, 61.1, 23.9, 8.8. LRMS (ESI) *m/z* calcd. for $C_8H_{16}O_5$ $[M+Na]^+$ 215.1; found 215.2.

1-(β-D-glucopyranosyl)-propane (339 c)

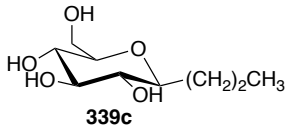

339c

A solution of MeOH:EtOAc (16.8 mL:16.8 mL) was added to a round bottom flask containing 5% Pd/C and compound **338 c** (0.39 g, 0.69 mmol).[49] The reaction mixture was stirred under H_2 gas at room temperature for 16 hours. The mixture was then filtered through celite and concentrated to give **339 c** as a white solid (0.13 g, 90.5%). ^{1}H NMR (400 MHz, MeOD): δ 3.82 (dd, *J* = 2.2, 11.8 Hz, 1H), 3.64-3.60 (m, 2H), 3.24 (t, *J* = 9.1 Hz, 1H), 3.19-3.10 (m, 2H), 3.04, (t, *J* = 8.9 Hz, 1H), 1.80 (ddd, *J* = 2.0, 7.6, 10.4 Hz, 1H), 1.61-1.59 (m, 1H), 1.42-1.37 (m, 2H), (t, *J* = 7.1 Hz, 3H). ^{13}C NMR (100 MHz, MeOD): δ 80.1, 79.2, 78.5, 74.1, 70.7, 61.7, 33.6, 29.2, 22.8, 18,2, 13.1. LRMS (ESI) *m/z* calcd. for $C_9H_{18}O_5$ $[M+Na]^+$ 228.1; found 228.3.

1-(β-D-glucopyranosyl)-butane (339 d)

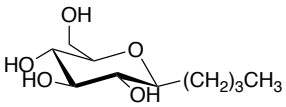

339d

A solution of MeOH:EtOAc (13.4 mL:13.4 mL) was added to a round bottom flask containing 5% Pd/C and compound **338 d** (0.31 g, 0.53 mmol).[49] The reaction mixture was stirred under H_2 gas for 16 hours. The mixture was then filtered through celite and concentrated to give **339 d** as a white solid (0.10 g, 88.3%). ^{1}H NMR (400 MHz, MeOD). δ 3.80 (dd, *J* = 2.3, 11.6 Hz, 1H), 3.60 (dd, *J* = 5.2, 11.6 Hz, 1H), 3.3 (d, *J* = 3.9 H, 1H), 3.20 (d, *J* = 8.7 Hz, 1H), 3.16-3.12 (m, 1H), 3.11-3.06 (m, 1H), 3.01 (t, *J* = 8.5 Hz, 1H), 1.85-1.79 (m, 1H), 1.56-1.52 (m, 1H), 1.37-1.26 (m, 4H), 0.89 (t, *J* = 7.2 Hz, 3H). ^{13}C NMR (100 MHz, MeOD) δ 80.2, 79.5, 78.5, 73.1, 74.1, 70.7, 61.7, 31.2, 27.3, 22.4, 12.9. LRMS (ESI) *m/z* calcd. for $C_{10}H_{20}O_5$ $[M+Na]^+$ 243.1; found 243.2.

1-(β-D-glucopyranosyl)-pentane (339 e)

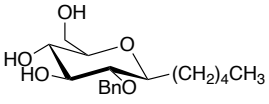

339e

A solution of MeOH:EtOAc (15.8 mL:15.8 mL) was added to a round bottom flask containing 5% Pd/C and compound **338 e** (0.36 g, 0.61 mmol).[49] The reaction mixture was stirred under H_2 gas at room temperature for 16 hours. The mixture was then filtered through celite and concentrated to give **339 e** as a white solid (0.12 g, 86.9%). ^{1}H NMR (400 MHz, MeOD). δ 3.75 (dd, *J* = 2.0, 11.7 Hz, 1H), 3.55 (dd, *J* = 5.2, 11.7 Hz, 1H), 3.20-2.94 (m, 4H), 1.79-1.71 (m, 1H), 1.56-1.50 (m, 1H), 1.34-1.20 (m, 6H), 0.84 (t, *J* = 6.9 Hz, 3H). ^{13}C NMR (100 MHz, MeOD) δ 80.2, 79.5, 78.5, 74.1, 70.7, 61.7, 31.7, 31.4, 24.8, 22.2, 13.0. LRMS (ESI) *m/z* calcd. for $C_{11}H_{22}O_5$ $[M+Na]^+$ 256.1; found 256.2.

1-(β-D-glucopyranosyl)-hexane (339 f)

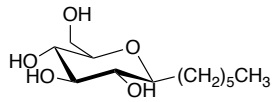

339f

A solution of MeOH:EtOAc (18.1 mL:18.1 mL) was added to a round bottom flask containing 5% Pd/C and compound **338 f** (0.42 g, 0.69 mmol).[49] The reaction mixture was stirred under H_2 gas at room temperature for 16 hours. The mixture was then filtered through celite and concentrated to give **339 f** as a white solid (0.15 g, 89.7%). ^{1}H NMR (400 MHz, MeOD). δ 3.82 (dd, *J* = 2.4, 11.8 Hz, 1H), 3.62 (dd, *J* = 5.3, 11.8 Hz, 1H), 3.27-3.00 (m, 4H), 1.87-1.80 (m, 1H), 1.59-1.55 (m, 1H), 1.42-1.30 (m, 8H), 0.89 (t, *J* = 6.5 Hz, 3H). ^{13}C NMR (100 MHz, MeOD) δ 80.2, 79.5, 78.5, 74.1, 70.7, 61.7, 31.6, 31.5, 29.2, 25.0, 22.3, 13.0. LRMS (ESI) *m/z* calcd. for $C_{12}H_{24}O_5$ $[M+Na]^+$ 271.2; found 271.3.

3.8 References

(1) Capicciotti, C. J.; ;Doshi, M. .; Ben, R. N. Ice Recrystallization Inhibitors: From Biological Antifreezes to Small Molecules. *Recent Dev. Study Recryst. Wilson, P., Ed.; InTech Open, Ltd. London, UK* **2013**, 177–224. https://doi.org/10.5772/54992.

(2) Scholander, P. F.; van Dam, L.; Kanwisher, J. W.; Hammel, H. T.; Gordon, M. S. Supercooling and Osmoregulation in Arctic Fish. *J. Cell. Comp. Physiol.* **1957**, *49* (1), 5–24. https://doi.org/10.1002/jcp.1030490103.

(3) Zachariassen, K. E.; Kristiansen, E. Ice Nucleation and Antinucleation in Nature. *Cryobiology* **2000**, *41* (4), 257–279. https://doi.org/10.1006/cryo.2000.2289.

(4) Franks, F.; Mathias, S. F.; Hatley, R. H. M. Water, Temperature and Life. *Philos. Trans. - R. Soc. London, B* **1990**, *326* (1237), 517–533. https://doi.org/10.1098/rstb.1990.0029.

(5) Smallwood, M.; Bowles, D. J.; Gerday, C.; Marahiel, M. A.; Davies, P. L.; Bradbeer, W.; Warren, G. Plants in a Cold Climate. *Philos. Trans. R. Soc. B Biol. Sci.* **2002**, *357* (1423), 831–847. https://doi.org/10.1098/rstb.2002.1073.

(6) Raymond, J. A.; DeVries, A. L. Adsorption Inhibition as a Mechanism of Freezing Resistance in Polar Fishes. *Proc. Natl. Acad. Sci. U. S. A.* **1977**, *74* (6), 2589–2593. https://doi.org/10.1073/pnas.74.6.2589.

(7) Kristiansen, E.; Zachariassen, K. E. The Mechanism by Which Fish Antifreeze Proteins Cause Thermal Hysteresis. *Cryobiology* **2005**, *51* (3), 262–280. https://doi.org/10.1016/j.cryobiol.2005.07.007.

(8) Cziko, P. A.; DeVries, A. L.; Evans, C. W.; Christina Cheng, C. H. Antifreeze Protein-Induced Superheating of Ice inside Antarctic Notothenioid Fishes Inhibits Melting during Summer Warming. *Proc. Natl. Acad. Sci. U. S. A.* **2014**, *111* (40), 14583–14588. https://doi.org/10.1073/pnas.1410256111.

(9) DeVries, A. L.; Komatsu, S. K.; Feeney, R. E. Chemical and Physical Properties of Freezing Point-Depressing Glycoproteins from Antarctic Fishes. *J. Biol. Chem.* **1970**, *245* (11), 2901–2908. https://doi.org/10.1016/s0021-9258(18)63073-x.

(10) DeVries, a. Glycoproteins as Biological Antifreeze Agents in Antarctic Fishes. *Science (80-.).* **1971**, *172* (3988), 1152–1155.

(11) Gaukel, V.; Leiter, A.; Spieß, W. E. L. Synergism of Different Fish Antifreeze Proteins and Hydrocolloids on Recrystallization Inhibition of Ice in Sucrose Solutions. *J. Food Eng.* **2014**, *141*, 44–50. https://doi.org/10.1016/j.jfoodeng.2014.05.016.

(12) Lui, S.; Wang, W.; von Moos, E.; Jackman, J.; Mealing, G.; Monette, R.; Ben, R. N. In Vitro Studies of Antifreeze Glycoprotein (AFGP) and a C-Linked AFGP Analogue. *Biomacromolecules* **2007**, *8* (5), 1456–1462. https://doi.org/10.1021/bm061044o.

(13) Abraham, S.; Keillor, K.; Capicciotti, C. J.; Perley-Robertson, G. E.; Keillor, J. W.; Ben, R. N. Quantitative Analysis of the Efficacy and Potency of Novel Small Molecule Ice Recrystallization Inhibitors. *Cryst. Growth Des.* **2015**, *15* (10), 5034–5039. https://doi.org/10.1021/acs.cgd.5b00995.

(14) Stylianopoulos, C. Carbohydrates: Chemistry and Classification. *Encycl. Hum. Nutr.* **2012**, *1–4*, 265–271. https://doi.org/10.1016/B978-0-12-375083-9.00041-6.

(15) Briard, J. G.; Jahan, S.; Chandran, P.; Allan, D.; Pineault, N.; Ben, R. N. Small-Molecule Ice Recrystallization Inhibitors Improve the Post-Thaw Function of

Hematopoietic Stem and Progenitor Cells. *ACS Omega* **2016**, *1* (5), 1010–1018. https://doi.org/10.1021/acsomega.6b00178.

(16) Capicciotti, C. J. The Rational Design of Potent Ice Recrystallization Inhibitors for Use as Novel Cryoprotectants (Doctoral Dissertation, Université d'Ottawa/University of Ottawa). **2014**.

(17) Poisson, J. S. Synthesis and In Vitro Applications of Ice Recrystallization Inhibitors (Doctoral Dissertation, Université d'Ottawa/University of Ottawa). **2019**.

(18) Brenna, E.; Fuganti, C.; Grasselli, P.; Serra, S.; Zambotti, S. A Novel General Route for the Synthesis of C-Glycosyl Tyrosine Analogues. *Chem. - A Eur. J.* **2002**, *8* (8), 1872–1878. https://doi.org/10.1002/1521-3765(20020415)8:8<1872::AID-CHEM1872>3.0.CO;2-A.

(19) Marcaurelle, L. A.; Bertozzi, C. R. New Directions in the Synthesis of Glycopeptide Mimetics. *Chem. - A Eur. J.* **1999**, *5* (5), 1384–1390. https://doi.org/10.1002/(sici)1521-3765(19990503)5:5<1384::aid-chem1384>3.3.co;2-o.

(20) Capicciotti, C. J.; Leclère, M.; Perras, F. A.; Bryce, D. L.; Paulin, H.; Harden, J.; Liu, Y.; Ben, R. N. Potent Inhibition of Ice Recrystallization by Low Molecular Weight Carbohydrate-Based Surfactants and Hydrogelators. *Chem. Sci.* **2012**, *3* (5), 1408–1416. https://doi.org/10.1039/c2sc00885h.

(21) Tam, R. Y.; Ferreira, S. S.; Czechura, P.; Ben, R. N.; Chaytor, J. L. Hydration Index-a Better Parameter for Explaining Small Molecule Hydration in Inhibition of Ice Recrystallization. *J. Am. Chem. Soc.* **2008**, *130* (51), 17494–17501. https://doi.org/10.1021/ja806284x.

(22) Chaytor, J. L. *Examining the Role of Carbohydrate Hydration and Structure in Preventing Ice-Recrystallization (Doctoral Dissertation, Université d'Ottawa/University of Ottawa)*; **2009**.

(23) Stylianopoulos, C. L. Carbohydrates: Chemistry and Classification. In *Encyclopedia of Human Nutrition*; 2005; Vol. 2, pp 303–309. https://doi.org/10.1016/B978-0-12-375083-9.00041-6.

(24) Ben, R. N.; Eniade, A. A.; Hauer, L. Synthesis of a C-Linked Antifreeze Glycoprotein (AFGP) Mimic: Probes for Investigating the Mechanism of Action.

Org. Lett. **1999**, *1* (11), 1759–1762. https://doi.org/10.1021/ol991025+.

(25) Eniade, A.; Purushotham, M.; Ben, R. N.; Wang, J. B.; Horwath, K. A Serendipitous Discovery of Antifreeze Protein-Specific Activity in C-Linked Antifreeze Glycoprotein Analogs. *Cell Biochem. Biophys.* **2003**, *38* (2), 115–124. https://doi.org/10.1385/CBB:38:2:115.

(26) Trant, J. F.; Biggs, R. A.; Capicciotti, C. J.; Ben, R. N. Developing Highly Active Small Molecule Ice Recrystallization Inhibitors Based upon C-Linked Antifreeze Glycoprotein Analogues. *RSC Adv.* **2013**, *3* (48), 26005–26009. https://doi.org/10.1039/c3ra43835j.

(27) Wang, T.; Zhu, Q.; Yang, X.; Layne, J. R.; Devries, A. L. Antifreeze Glycoproteins from Antarctic Notothenioid Fishes Fail to Protect the Rat Cardiac Explant during Hypothermic and Freezing Preservation. *Cryobiology*. 1994, pp 185–192. https://doi.org/10.1006/cryo.1994.1022.

(28) Ampaw, A.; Charlton, T. A.; Briard, J. G.; Ben, R. N. Designing the next Generation of Cryoprotectants – from Proteins to Small Molecules. *Pept. Sci.* **2019**, *111* (e24086), 1–12. https://doi.org/10.1002/pep2.24086.

(29) Trant, J. F.; Biggs, R. A.; Capicciotti, C. J.; Ben, R. N. Developing Highly Active Small Molecule Ice Recrystallization Inhibitors Based upon C-Linked Antifreeze Glycoprotein Analogues. *RSC Adv.* **2013**, *3* (48), 26005–26009. https://doi.org/10.1039/c3ra43835j.

(30) Lorber, B.; Bishop, J. B.; DeLucas, L. J. Purification of Octyl β-d-Glucopyranoside and Re-Estimation of Its Micellar Size. *BBA - Biomembr.* **1990**, *1023* (2), 254–265. https://doi.org/10.1016/0005-2736(90)90421-J.

(31) Chong, T. T.; Hashim, R.; Bryce, R. A. Molecular Dynamics Simulation of Monoalkyl Glycoside Micelles in Aqueous Solution: Influence of Carbohydrate Headgroup Stereochemistry. *J. Phys. Chem. B* **2006**, *110* (10), 4978–4984. https://doi.org/10.1021/jp056851g.

(32) Aviles-Moreno, J. R.; Demaison, J.; Huet, T. R. Conformational Flexibility in Hydrated Sugars: The Glycolaldehyde-Water Complex. *J. Am. Chem. Soc.* **2006**, *128* (32), 10467–10473. https://doi.org/10.1021/ja062312t.

(33) Lee, K. S.; Lee, J. H. *Hybrid Chemical EOR Using Low-Salinity and Smart*

Waterflood; 2019. https://doi.org/10.1016/b978-0-12-816776-2.00004-0.

(34) Balcerzak, A. K.; Febbraro, M.; Ben, R. N. The Importance of Hydrophobic Moieties in Ice Recrystallization Inhibitors. *RSC Adv.* **2013**, *3* (10), 3232–3236. https://doi.org/10.1039/c3ra23220d.

(35) De Loos, M.; Feringa, B. L.; Van Esch, J. H. Design and Application of Self-Assembled Low Molecular Weight Hydrogels. *European J. Org. Chem.* **2005**, No. 17, 3615–3631. https://doi.org/10.1002/ejoc.200400723.

(36) Estroff, L. A.; Hamilton, A. D. Water Gelation by Small Organic Molecules. *Chem. Rev.* **2004**, *104* (3), 1201–1217. https://doi.org/10.1021/cr0302049.

(37) Bytheway, I.; Darley, M. G.; Popelier, P. L. A. The Calculation of Polar Surface Area from First Principles: An Application of Quantum Chemical Topology to Drug Design. *ChemMedChem* **2008**, *3* (3), 445–453. https://doi.org/10.1002/cmdc.200700262.

(38) Di, L.; Kerns, E. H. Effects of Properties on Biological Assays. *Drug-Like Prop.* **2016**, 487–496. https://doi.org/10.1016/b978-0-12-801076-1.00040-x.

(39) Edwards, M. P.; Price, D. A. *Role of Physicochemical Properties and Ligand Lipophilicity Efficiency in Addressing Drug Safety Risks*; Elsevier Inc., 2010; Vol. 45. https://doi.org/10.1016/S0065-7743(10)45023-X.

(40) Wong, F. M. P.; Reimer, D. L.; Bally, M. B. Cationic Lipid Binding to DNA: Characterization of Complex Formation. *Biochemistry* **1996**, *35* (18), 5756–5763. https://doi.org/10.1021/bi952847r.

(41) Randall, L. H.; Huang, H.; Wong, C. H. Solution-and Solid-Phase Synthesis of Inhibitors of H. Pylori Attachment and E-Selectin-Mediated Leukocyte Adhesion. *J. Am. Chem. Soc.* **1994**, *116* (25), 11315–11322. https://doi.org/10.1021/ja00104a011.

(42) Haller, J.; Kaatze, U. Monomer Exchange and Rotational Isomerization of Alkyl Monoglycosides in Water. *J. Phys. Chem. B* **2009**, *113* (36), 12283–12292. https://doi.org/10.1021/jp905523p.

(43) Abraham, S.; Keillor, K.; Capicciotti, C. J.; Perley-Robertson, G. E.; Keillor, J. W.; Ben, R. N. Quantitative Analysis of the Efficacy and Potency of Novel Small Molecule Ice Recrystallization Inhibitors. *Cryst. Growth Des.* **2015**, *15* (10), 5034–

5039. https://doi.org/10.1021/acs.cgd.5b00995.

(44) Ampaw, A. A. Addressing Solubility Limitations in Small-Molecule Ice Recrystallization Inhibitors and Evaluating Their Use in Hematopoietic Stem Cell and Red Blood Cell Cryopreservation (Doctoral Dissertation, Université d'Ottawa/University of Ottawa). **2022**.

(45) Lewis, M. D.; Cha, J. K.; Kishi, Y. Highly Stereoselective Approaches to α- and β-C-Glycopyranosides. *J. Am. Chem. Soc.* **1982**, *104* (18), 4976–4978. https://doi.org/10.2307/j.ctt5hjq7r.5.

(46) Yokoyama, M.; Toyoshima, H.; Shimizu, M.; Mito, J.; Togo, H. Simple Synthesis of Aromatic β-C-Nucleosides via Coupling of Aryl Grignard Reagents with Sugar Fluorides. *Synthesis (Stuttg).* **1998**, *1998* (04), 409–412. https://doi.org/10.1055/s-1998-4487.

(47) Wang, J.; Zhao, Y.; Zhao, W.; Wang, P.; Li, J. An Improved Synthetic Method for N-Butyl-1-Deoxynojirimycin. *Med. Chem. (Los. Angeles).* **2016**, *6* (7), 492–496. https://doi.org/10.4172/2161-0444.1000388.

(48) Forget, S. M.; Bhattasali, D.; Hart, V. C.; Cameron, T. S.; Syvitski, R. T.; Jakeman, D. L. Synthesis and Enzymatic Evaluation of Ketose Phosphonates: The Interplay between Mutarotation, Monofluorination and Acidity. *Chem. Sci.* **2012**, *3* (6), 1866–1878. https://doi.org/10.1039/c2sc01077a.

(49) Alteen, M. Investigating the Importance of Electronic and Hydrophobic Effects for Ice Recrystallization Inhibition Using β-O-Aryl Glycosides (Master's Dissertation, Université d'Ottawa/University of Ottawa), 2013.

(50) Tachibana, Y.; Fletcher, G. L.; Fujitani, N.; Tsuda, S.; Monde, K.; Nishimura, S.-I. Antifreeze Glycoproteins: Elucidation of the Structural Motifs That Are Essential for Antifreeze Activity. *Angew. Chemie* **2004**, *116* (7), 874–880. https://doi.org/10.1002/ange.200353110.

(51) Van Den Steen, P.; Rudd, P. M.; Dwek, R. A.; Opdenakker, G. Concepts and Principles of O-Linked Glycosylation. *Crit. Rev. Biochem. Mol. Biol.* **1998**, *33* (3), 151–208. https://doi.org/10.1080/10409239891204198.

(52) Lemieux, R. U.; Pavia, A. A.; Martin, J. C.; Watanabe, K. A. Solvation Effects on Conformational Equilibria. Studies Related to the Conformational Properties of 2-

Methoxytetrahydropyran and Related Methyl Glycopyranosides. *Can. J. Chem.* **1969**, *47* (23), 4427–4439. https://doi.org/10.1139/v69-731.

(53) Gaweda, K.; Plazinski, W. The Endo- and Exo-Anomeric Effects in Furanosides. A Computational Study. *European J. Org. Chem.* **2020**, *2020* (6), 674–679. https://doi.org/10.1002/ejoc.201901473.

(54) Kamerling, J. P. Basics Concepts and Nomenclature Recommendations in Carbohydrate Chemistry. *Compr. Glycosci. From Chem. to Syst. Biol.* **2007**, *1–4*, 1–38. https://doi.org/10.1016/B978-044451967-2/00001-5.

(55) Musca, V. Elucidating the Important Structural Features of Aryl Glycosides and Antifreeze Glycoprotein Disaccharide Analogs for Ice Recrystallization Inhibition (Master's Dissertation, Universit d'Ottawa/University of Ottawa). **2014**.

(56) Dong, J.; Cao, D. S.; Miao, H. Y.; Liu, S.; Deng, B. C.; Yun, Y. H.; Wang, N. N.; Lu, A. P.; Zeng, W. Bin; Chen, A. F. ChemDes: An Integrated Web-Based Platform for Molecular Descriptor and Fingerprint Computation. *J. Cheminform.* **2015**, *7* (1), 1–10. https://doi.org/10.1186/s13321-015-0109-z.

(57) Tetko, I. V.; Gasteiger, J.; Todeschini, R.; Mauri, A.; Livingstone, D.; Ertl, P.; Palyulin, V. A.; Radchenko, E. V.; Zefirov, N. S.; Makarenko, A. S.; Tanchuk, V. Y.; Prokopenko, V. V. Virtual computational chemistry laboratory - design and description, *J. Comput. Aid. Mol. Des.*, **2005**, 19, 453-63, *article.*

(58) VCCLAB, Virtual Computational Chemistry Laboratory, http://www.vcclab.org, 2005.

(59) Marvin was used for drawing, displaying and characterizing chemical structures, substructures and reactions, Marvin 21.14, 2021, ChemAxon (http://www.chemaxon.com)

(60) Mazzobre, M. F.; Román, M. V.; Mourelle, A. F.; Corti, H. R. Octanol-Water Partition Coefficient of Glucose, Sucrose, and Trehalose. *Carbohydr. Res.* **2005**, *340* (6), 1207–1211. https://doi.org/10.1016/j.carres.2004.12.038

(61) Rodebaugh, R.; Fraser-Reid, B. Evidence for Cyclic Bromonium Ion Transfer in Electrophilic Bromination of Alkenes: Reaction of ω-Alkenyl Glycosides with Aqueous N-Bromosuccinimide. *Tetrahedron* **1996**, *52* (22), 7663–7678. https://doi.org/10.1016/S0040-4020(96)00349-3.

(62) Czechura, P.; Tam, R. Y.; Dimitrijevic, E.; Murphy, A. V.; Ben, R. N. The Importance of Hydration for Inhibiting Ice Recrystallization with C-Linked Antifreeze Glycoproteins. *J. Am. Chem. Soc.* **2008**, *130* (10), 2928–2929. https://doi.org/10.1021/ja7103262.

(63) Okuno, Y.; Isomura, S.; Kamakura, T.; Sano, F.; Tamahori, K.; Goto, T.; Hayashida, T.; Kitagawa, Y.; Fukuhara, A.; Takeda, K. Dimethylaminopyridine-Supported Graft Polymer Catalyst and Its Flow System. *ChemSusChem* **2015**, *8* (10), 1711–1715. https://doi.org/10.1002/cssc.201500092.

(64) Pastore, A.; Adinolfi, M.; Iadonisi, A. BiBr3-Promoted Activation of Peracetylated Glycosyl Iodides: Straightforward Access to Synthetically Useful 2-O-Deprotected Allyl Glycosides. *European J. Org. Chem.* **2008**, *4* (36), 6206–6212. https://doi.org/10.1002/ejoc.200800914.

(65) Pilgrim, W.; Murphy, P. V. SnCl4- and TiCl4-Catalyzed Anomerization of Acylated O - And S -Glycosides: Analysis of Factors That Lead to Higher α: β d Reaction Rates. *J. Org. Chem.* **2010**, *75* (20), 6747–6755. https://doi.org/10.1021/jo101090f.

(66) Li, W.; Koike, K.; Asada, Y.; Yoshikawa, T.; Nikaido, T. Biotransformation of Low-Molecular-Weight Alcohols by Coleus Forskohlii Hairy Root Cultures. *Carbohydr. Res.* **2003**, *338* (8), 729–731. https://doi.org/10.1016/S0008-6215(03)00011-9.

(67) Kurashima, K.; Fujii, M.; Ida, Y.; Akita, H. Enzymatic β-Glycosidation of Primary Alcohols. *J. Mol. Catal. B Enzym.* **2003**, *26* (1–2), 87–98. https://doi.org/10.1016/S1381-1177(03)00168-1.

(68) Liu, H.; Li, X. Synthesis of Protected Sugar-Amino Acid Hybrid Molecules as Platform for Further Derivatization. *Tetrahedron Lett.* **2012**, *53* (51), 6957–6960. https://doi.org/10.1016/j.tetlet.2012.10.042.

(69) Knapp, S.; Yang, C.; Haimowitz, T. Addition of Trialkylaluminum Reagents to Glyconolactones. Synthesis of 1-C-Methyl GlcNAc Oxazoline and Thiazoline. *Tetrahedron Lett.* **2002**, *43* (39), 7101–7104. https://doi.org/10.1016/S0040-4039(02)01506-X.

(70) Oda, Y.; Yamanoi, T. Trimethylsilyl Trifluoromethanesulfonate Catalyzed Nucleophilic Substitution to Give C- and N-Glucopyranosides Derived from d-Glucopyranose. *Synthesis (Stuttg).* **2007**, No. 19, 3021–3031.

https://doi.org/10.1055/s-2007-983882.

(71) Buskas, T.; Söderberg, E.; Konradsson, P.; Fraser-Reid, B. Use of N-Pentenyl Glycosides as Precursors to Various Spacer Functionalities. *J. Org. Chem.* **2000**, *65* (4), 958–963. https://doi.org/10.1021/jo9909554

(72) Pasetto, P.; Walczak, M. C. A Mitsunobu Route to C-Glycosides. *Tetrahedron* **2009**, *65* (41), 8468–8477. https://doi.org/10.1016/j.tet.2009.08.024.

3.9 NMR Spectra of Compounds in Chapter 3

^{1}H NMR

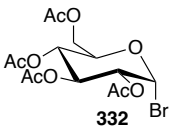

332

^{13}C NMR

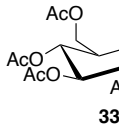

332

^{1}H NMR

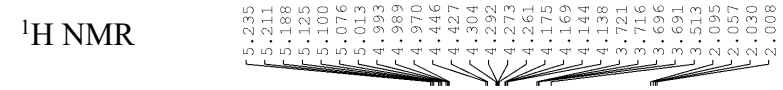

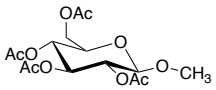

333a

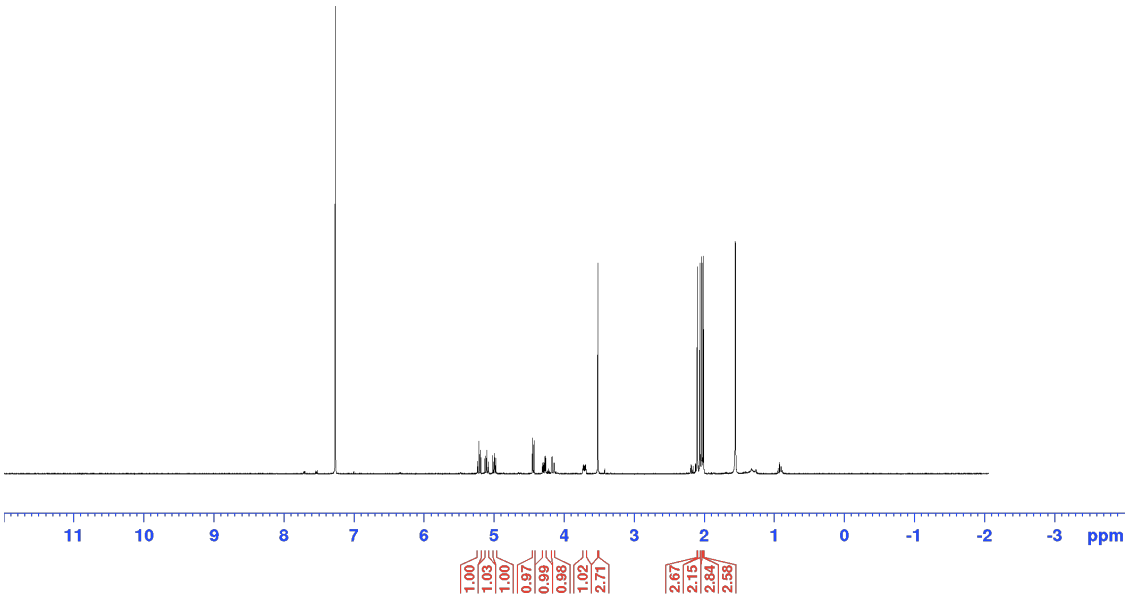

^{1}H NMR

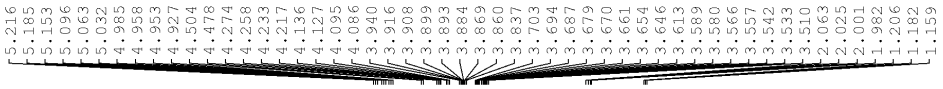

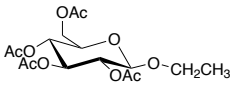

333b

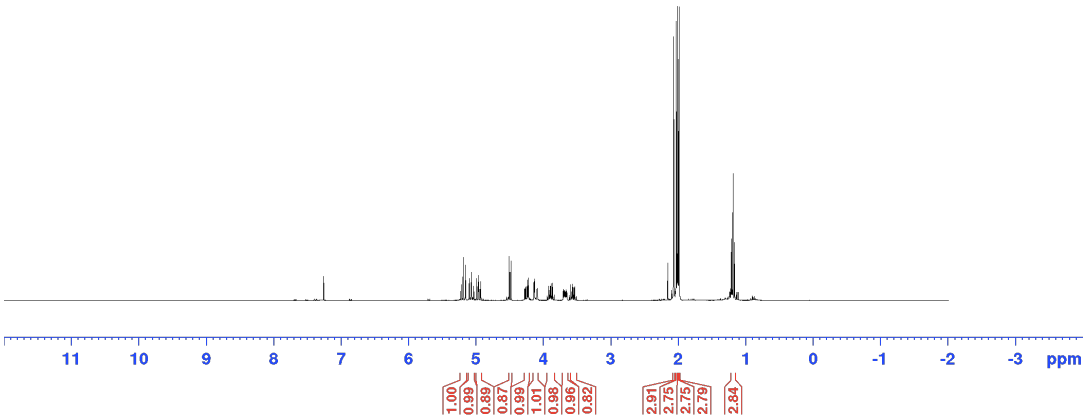

^{1}H NMR

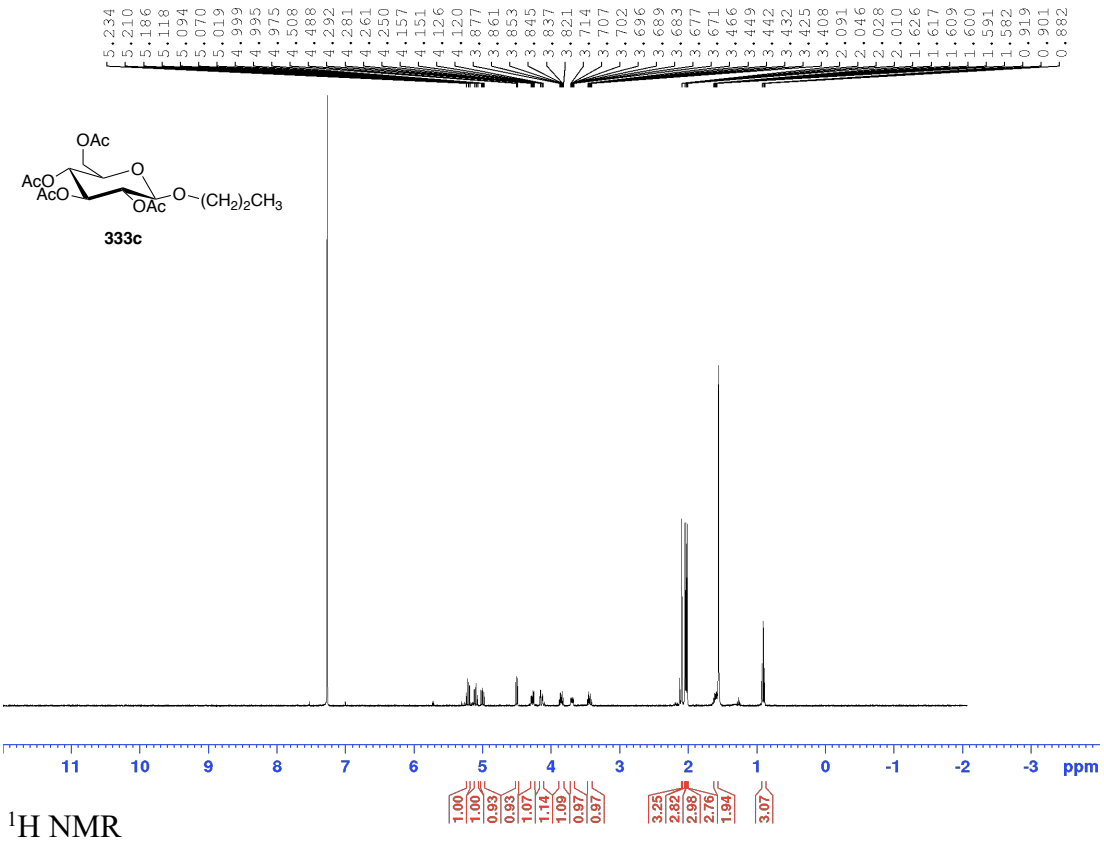
OAc
AcO
AcO
O
OAc
O(CH2)2CH3
333c
ppm

^{1}H NMR

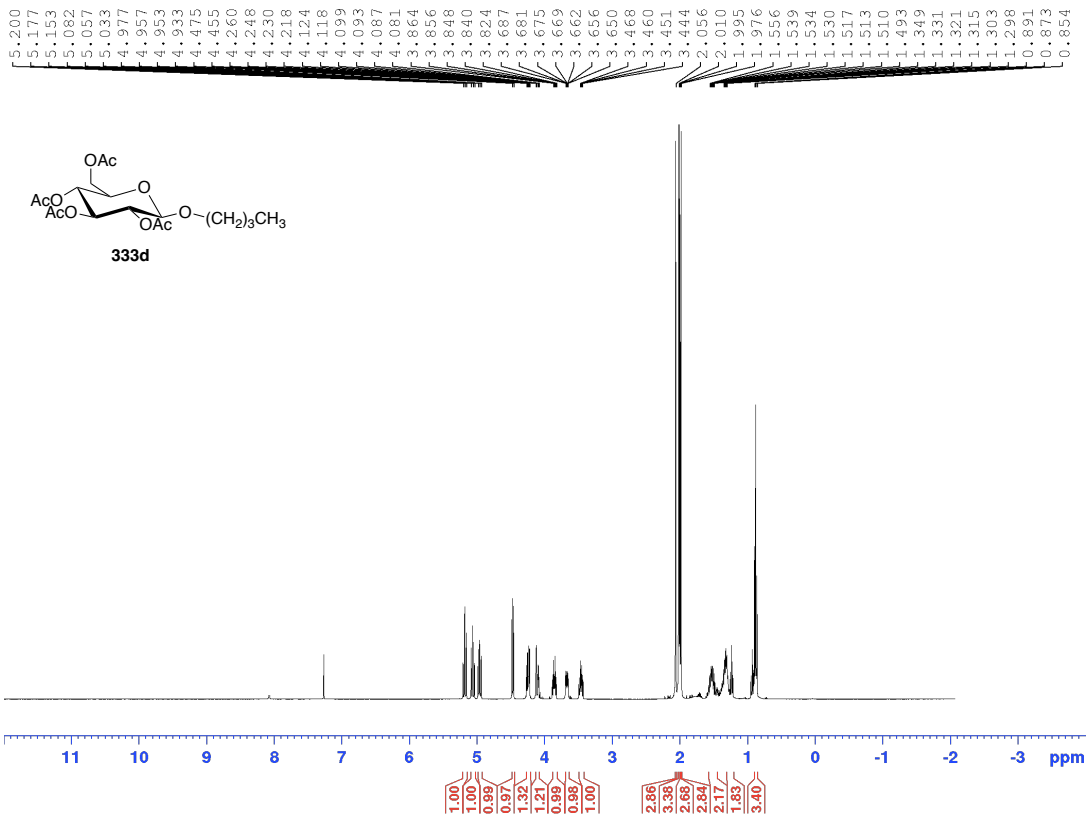
OAc
AcO
AcO
O
OAc
O(CH2)3CH3
333d
ppm

^{1}H NMR

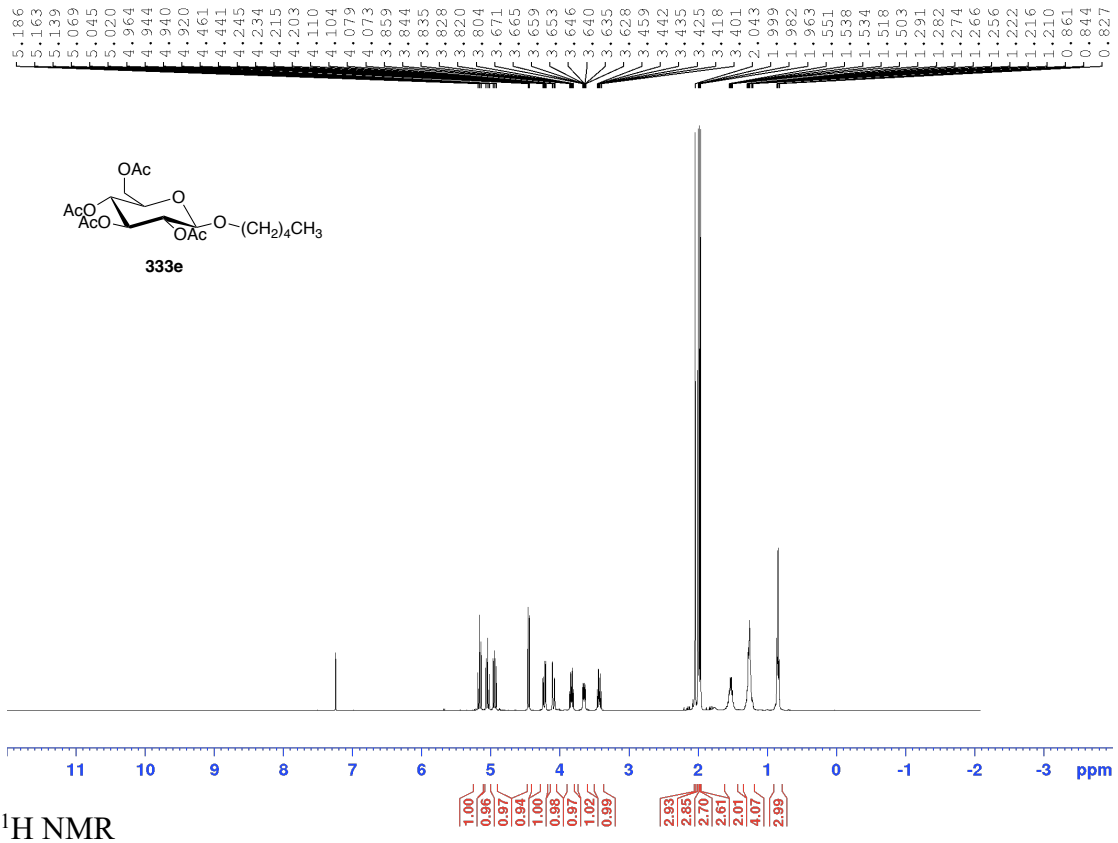
OAc
AcO
AcO
O
OAc
O(CH2)4CH3
333e
ppm

^{1}H NMR

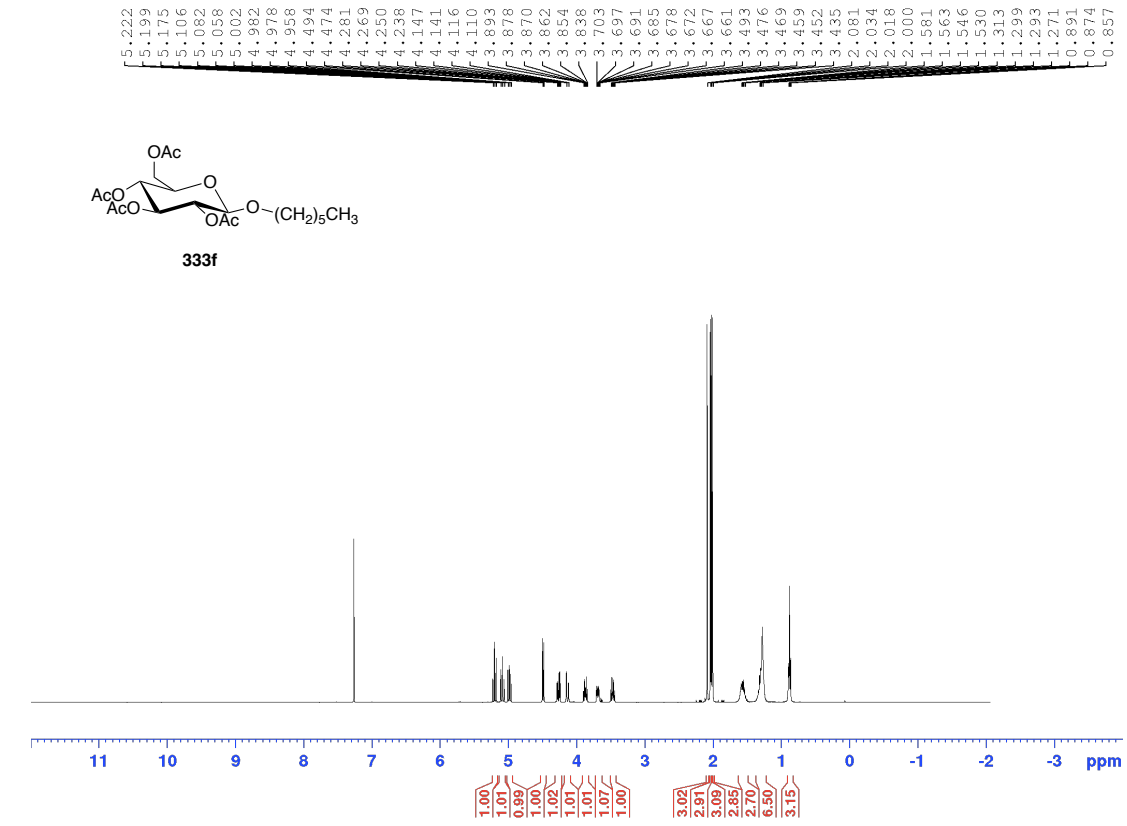
OAc
AcO
AcO
O
OAc
O(CH2)5CH3
333f
ppm

^{1}H NMR

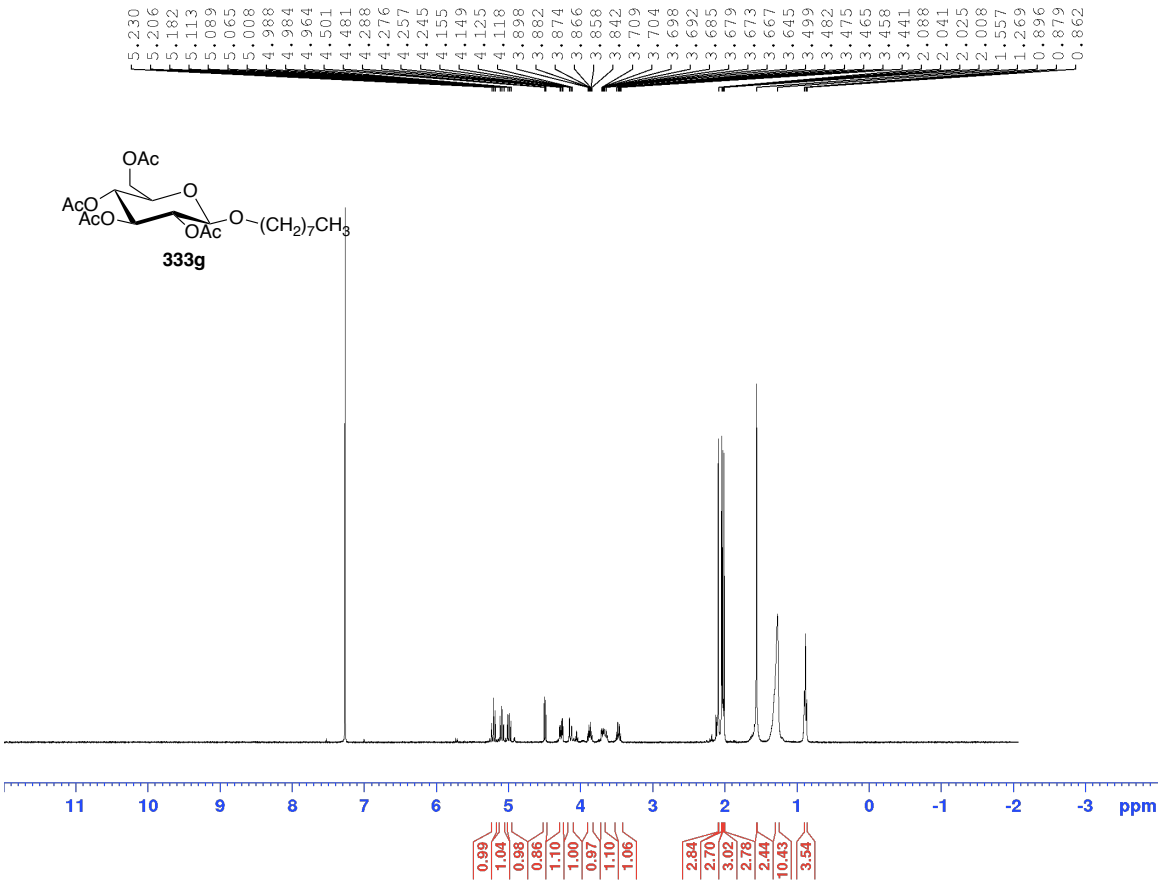
5.230
5.206
5.182
5.113
5.089
5.065
5.008
4.988
4.984
4.964
4.501
4.481
4.288
4.276
4.257
4.245
4.155
4.149
4.125
4.118
3.898
3.882
3.874
3.866
3.858
3.842
3.709
3.704
3.698
3.692
3.685
3.679
3.673
3.667
3.645
3.499
3.482
3.475
3.465
3.458
3.441
2.088
2.041
2.025
2.008
1.557
1.269
0.896
0.879
0.862
OAc
AcO
AcO
OAc
O
O
(CH2)7CH3
333g
11
10
9
8
7
6
5
4
3
2
1
0
-1
-2
-3
ppm
0.99
1.04
0.98
0.86
1.10
1.00
0.97
1.10
1.06
2.84
2.70
3.02
2.78
2.44
10.43
3.54

^{1}H NMR

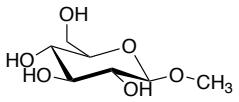

334a

^{13}C NMR

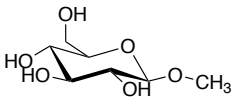

334a

^{1}H NMR

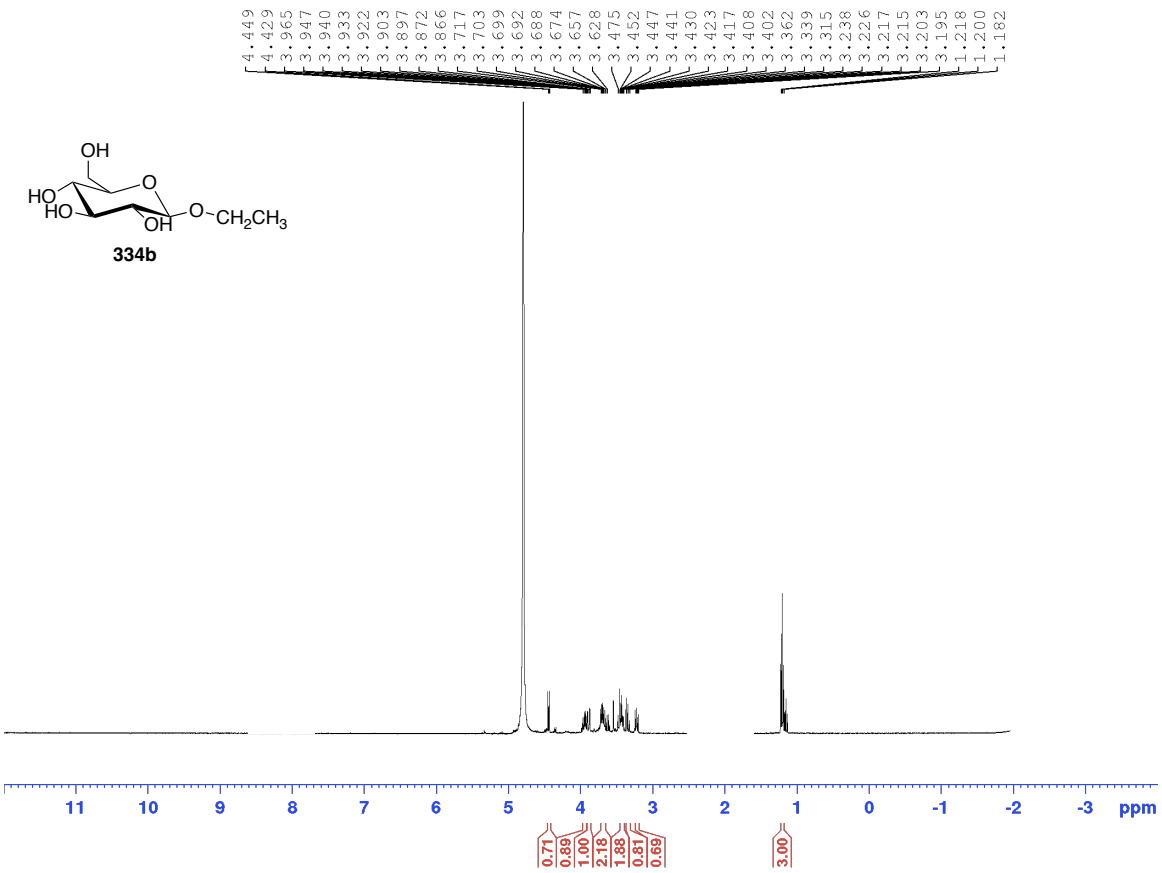

^{13}C NMR

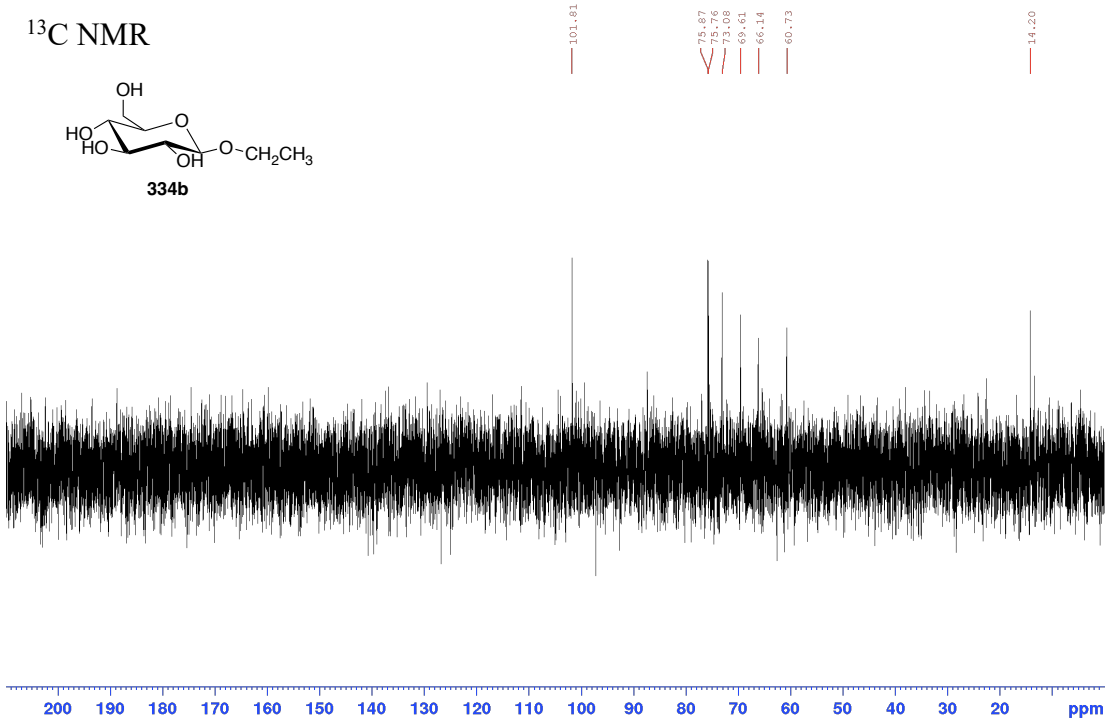

^{1}H NMR

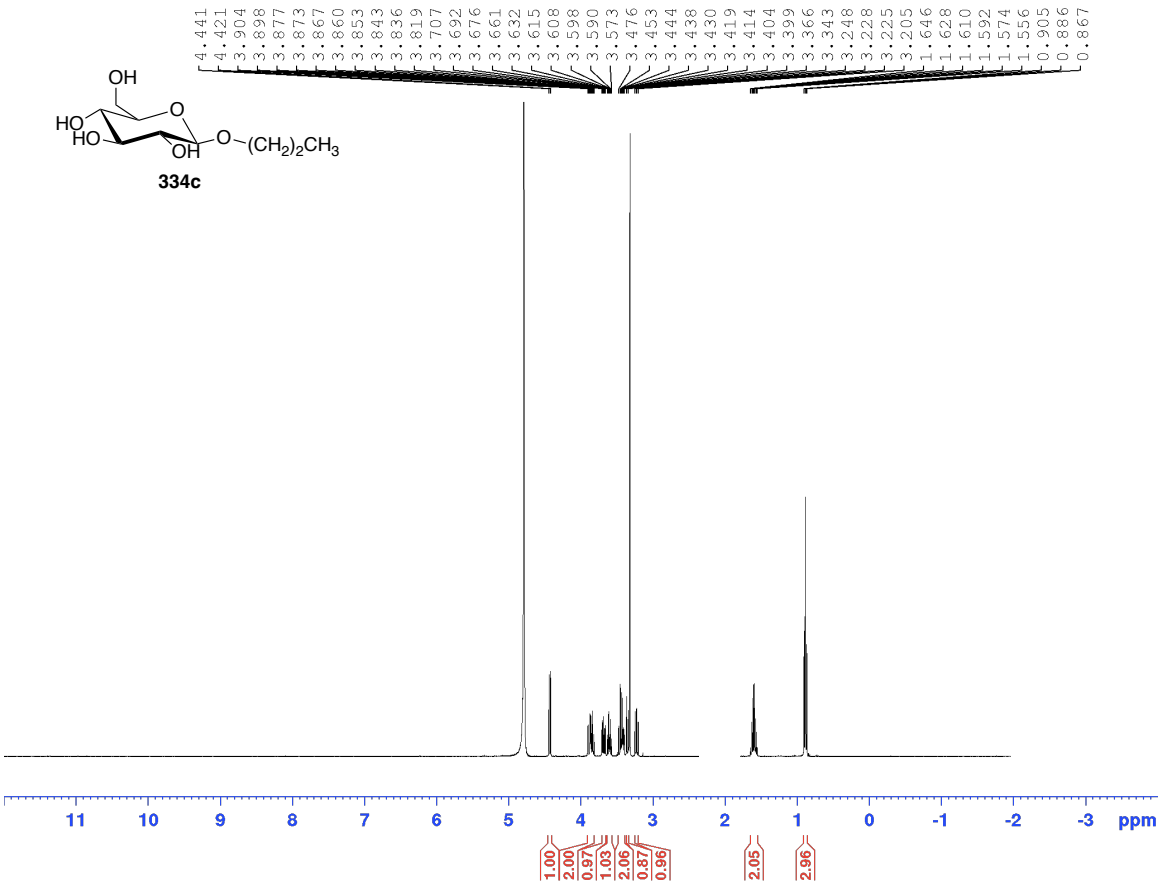

^{13}C NMR

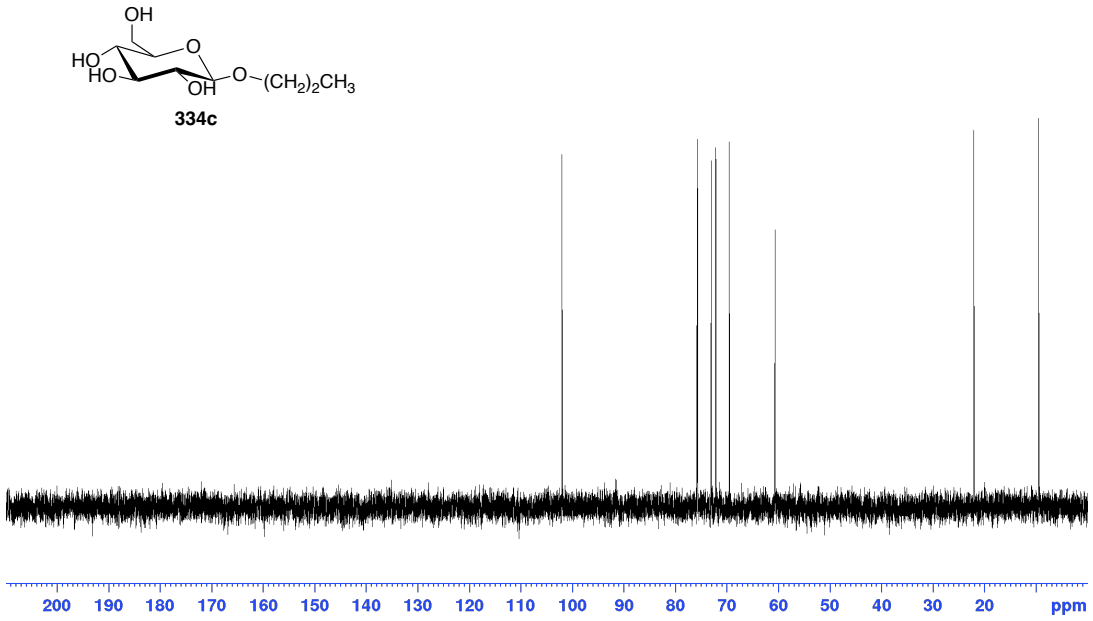

^{1}H NMR

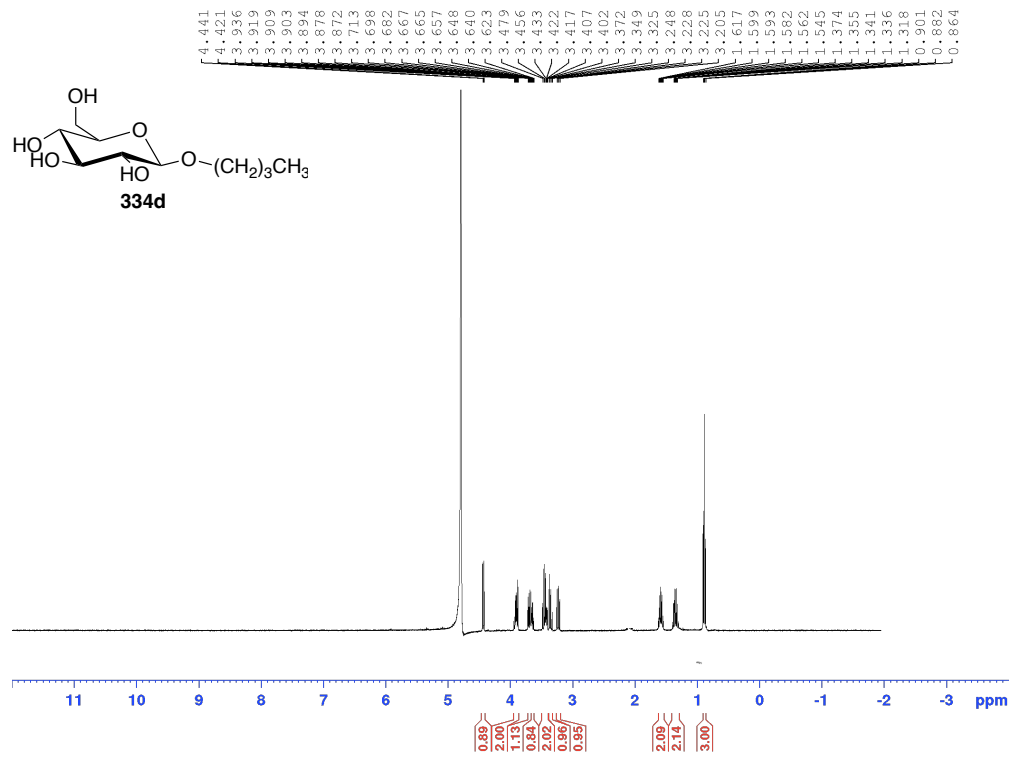

^{13}C NMR

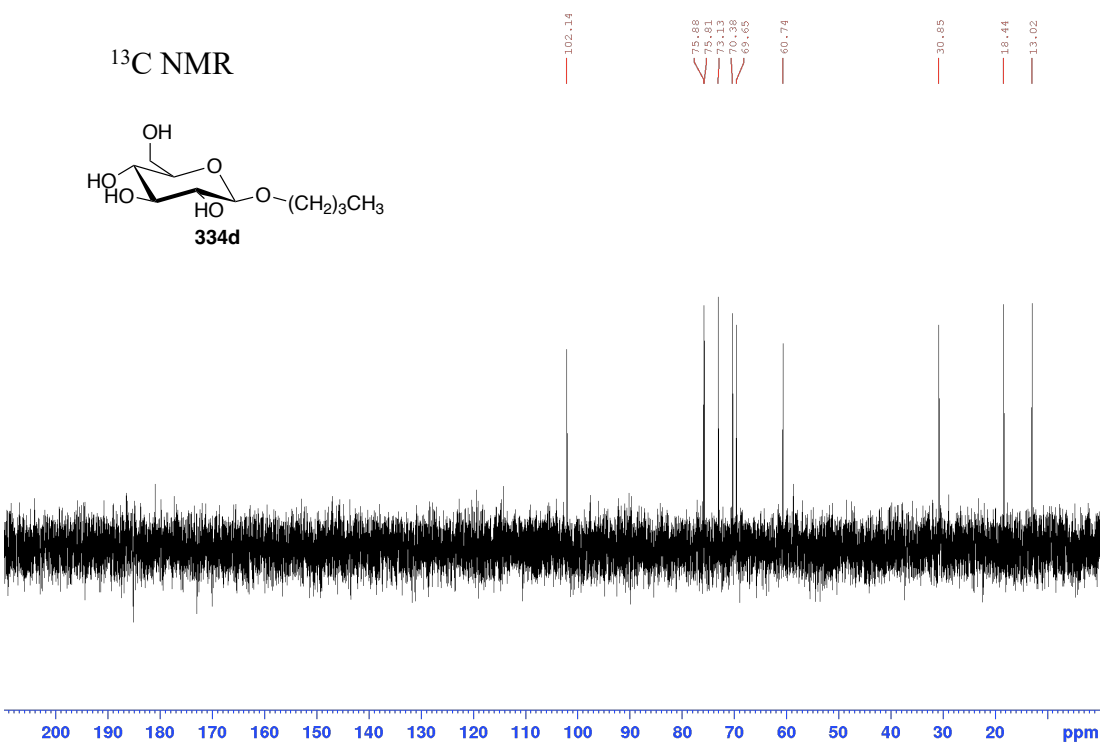

^{1}H NMR

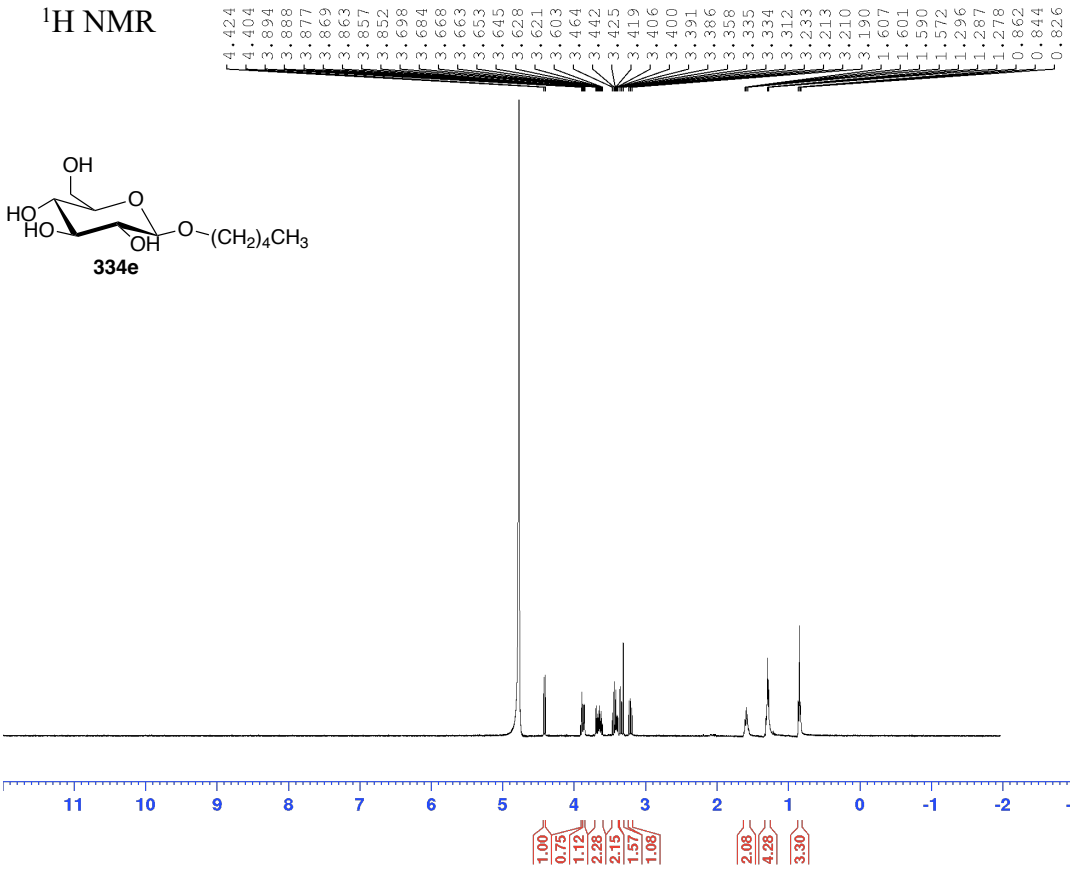

^{13}C NMR

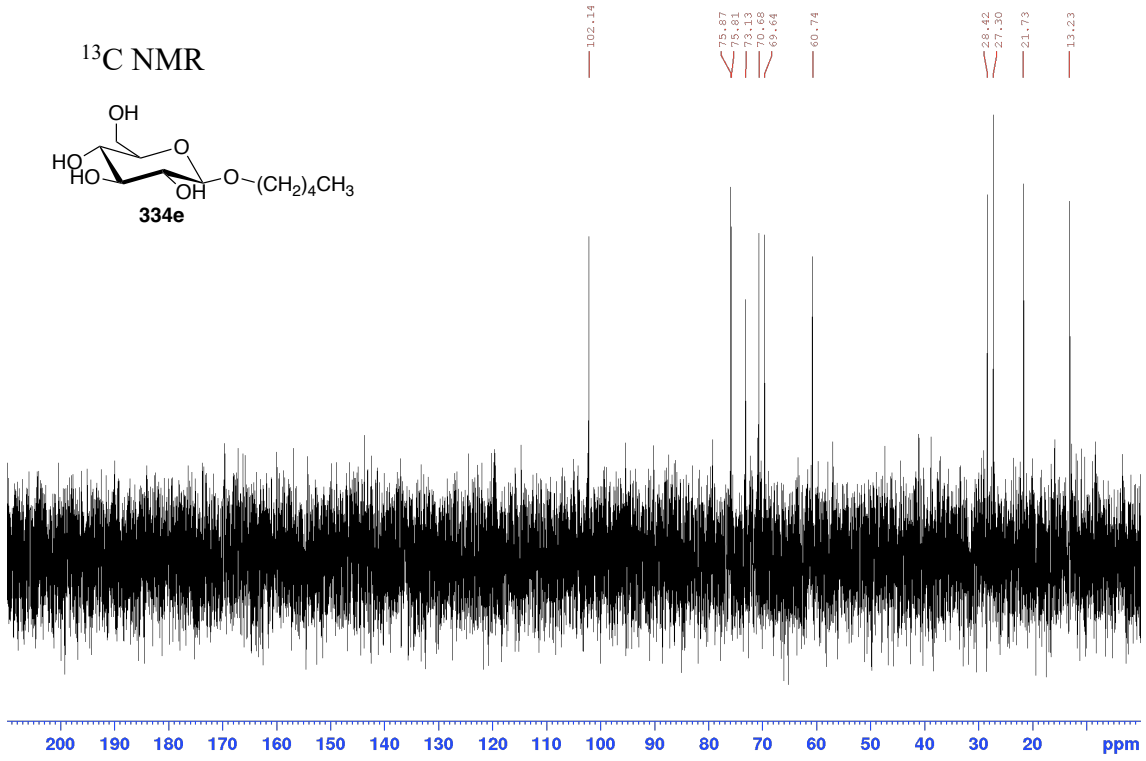

^{1}H NMR

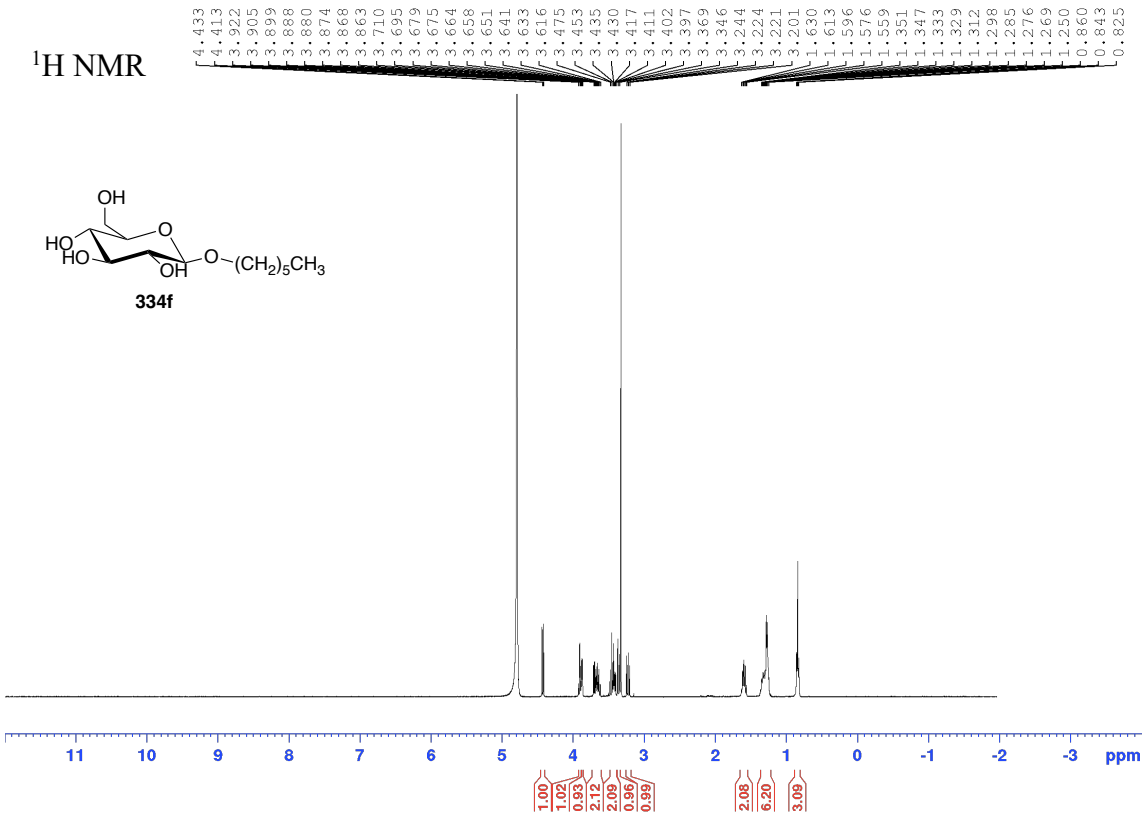

^{13}C NMR

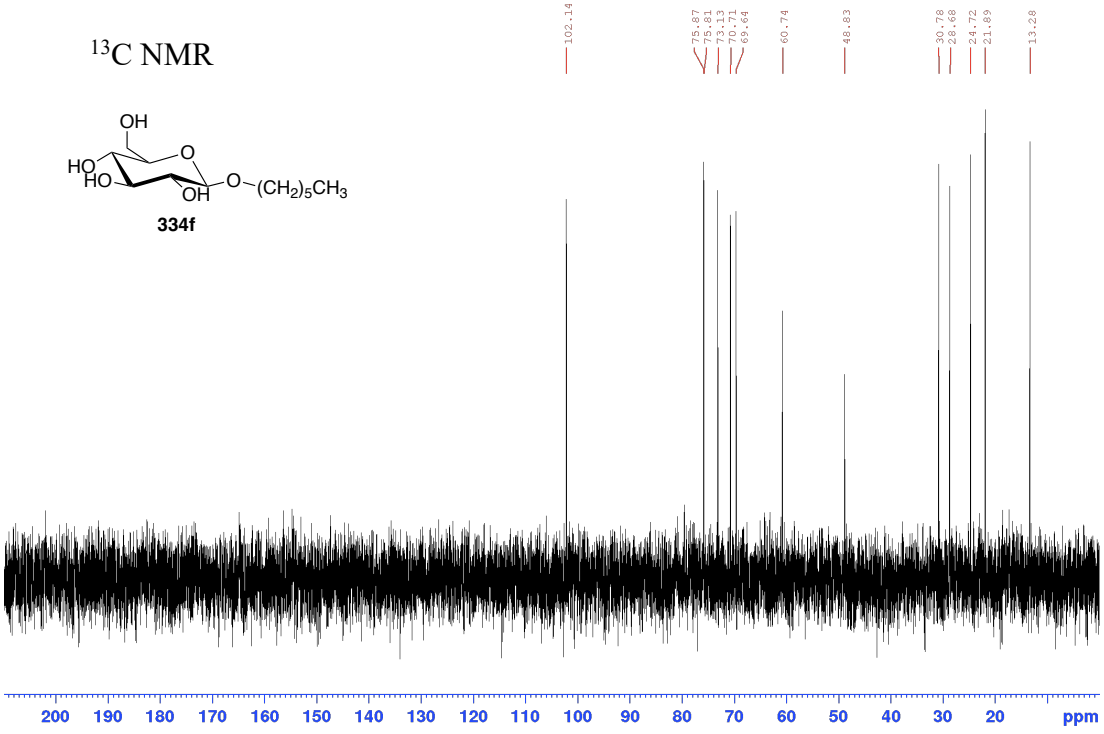

^{1}H NMR

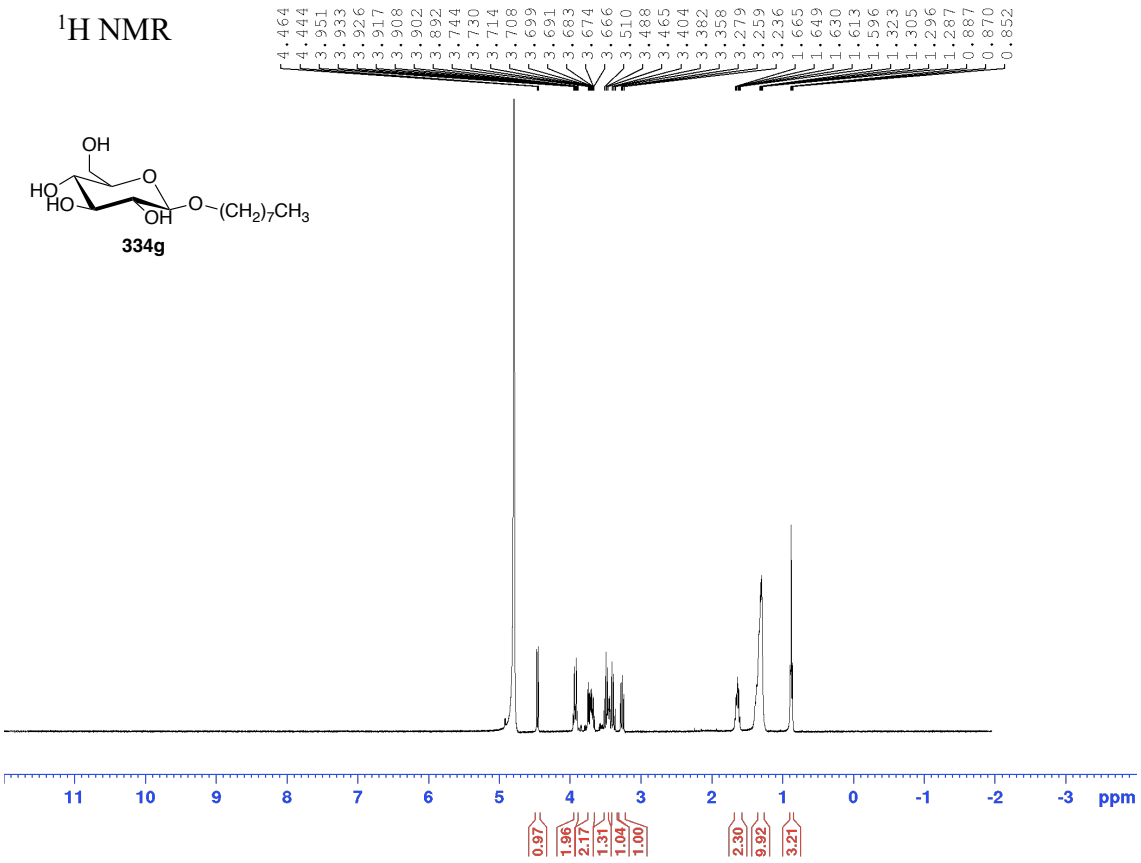

^{13}C NMR

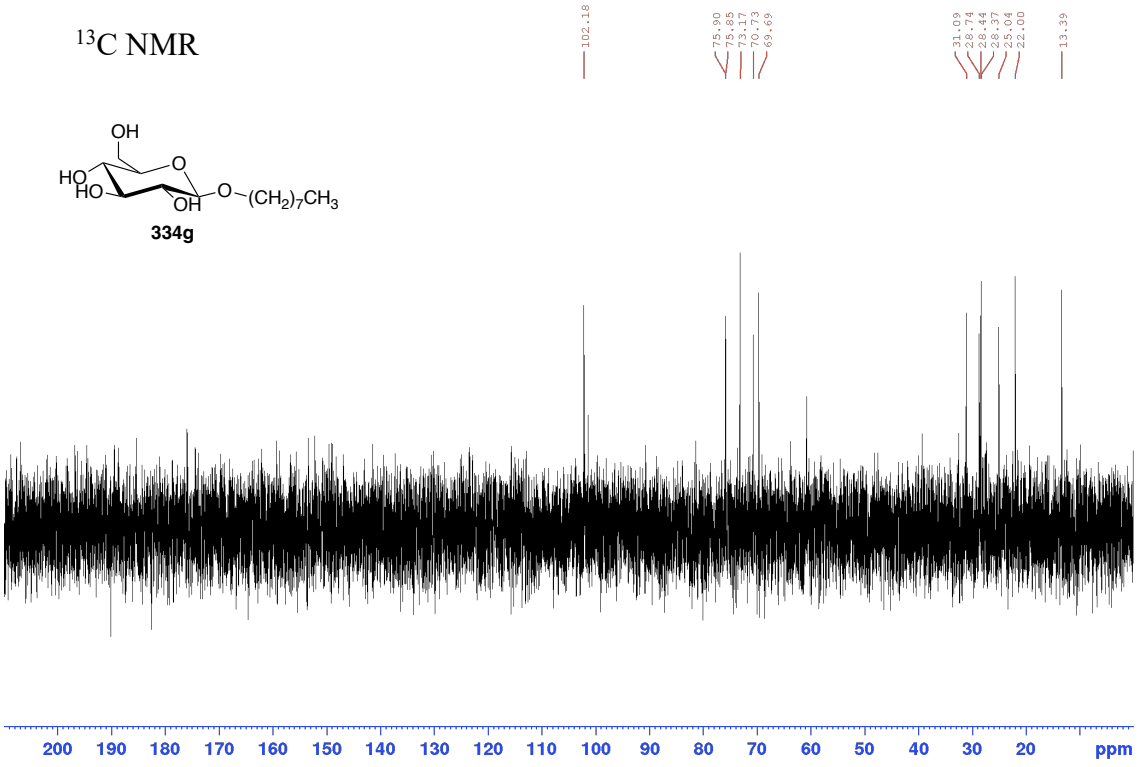

^{1}H NMR

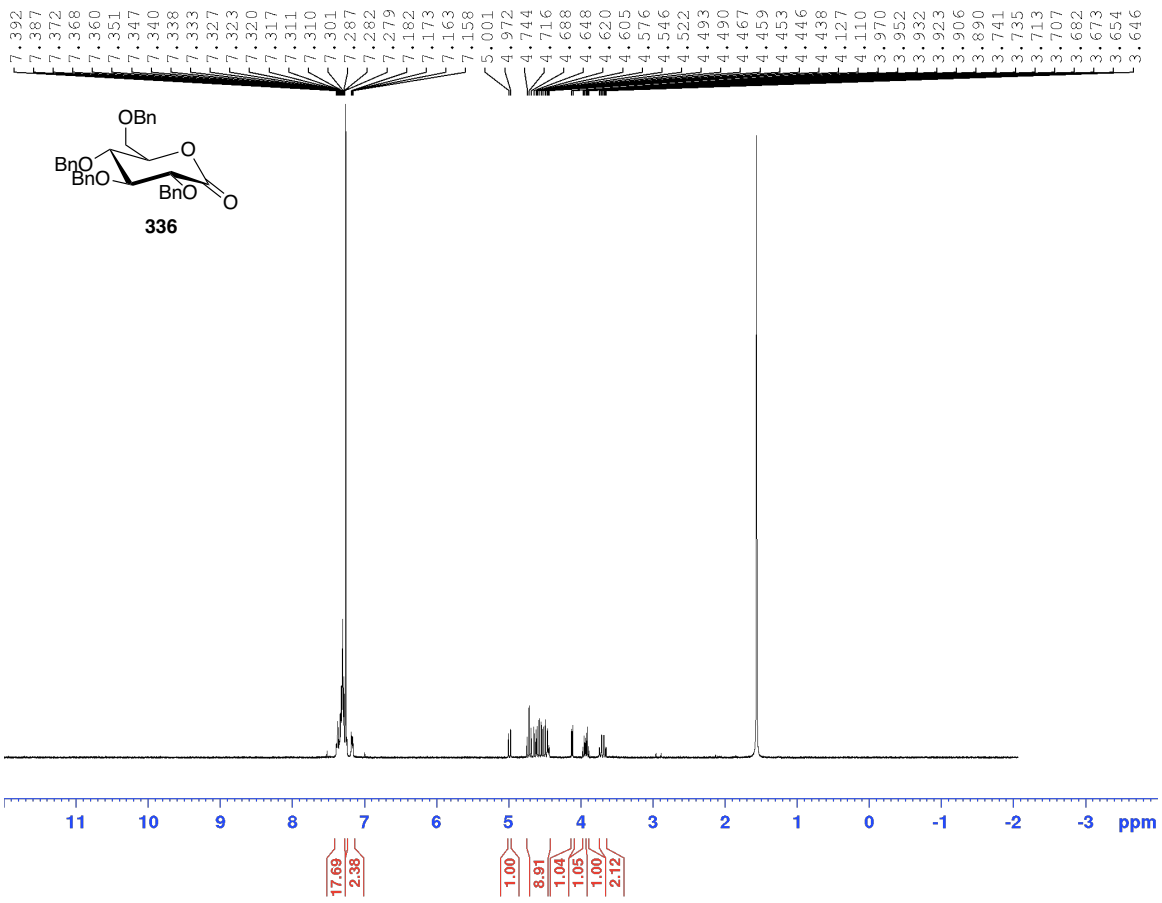

^{13}C NMR

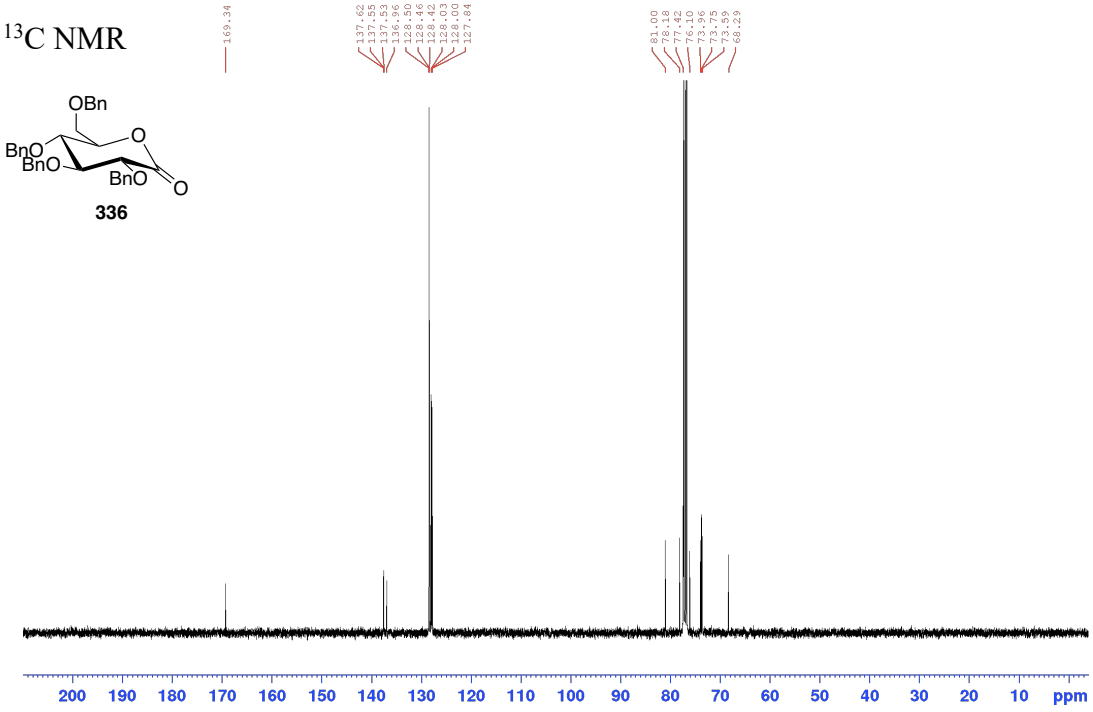

^{1}H NMR

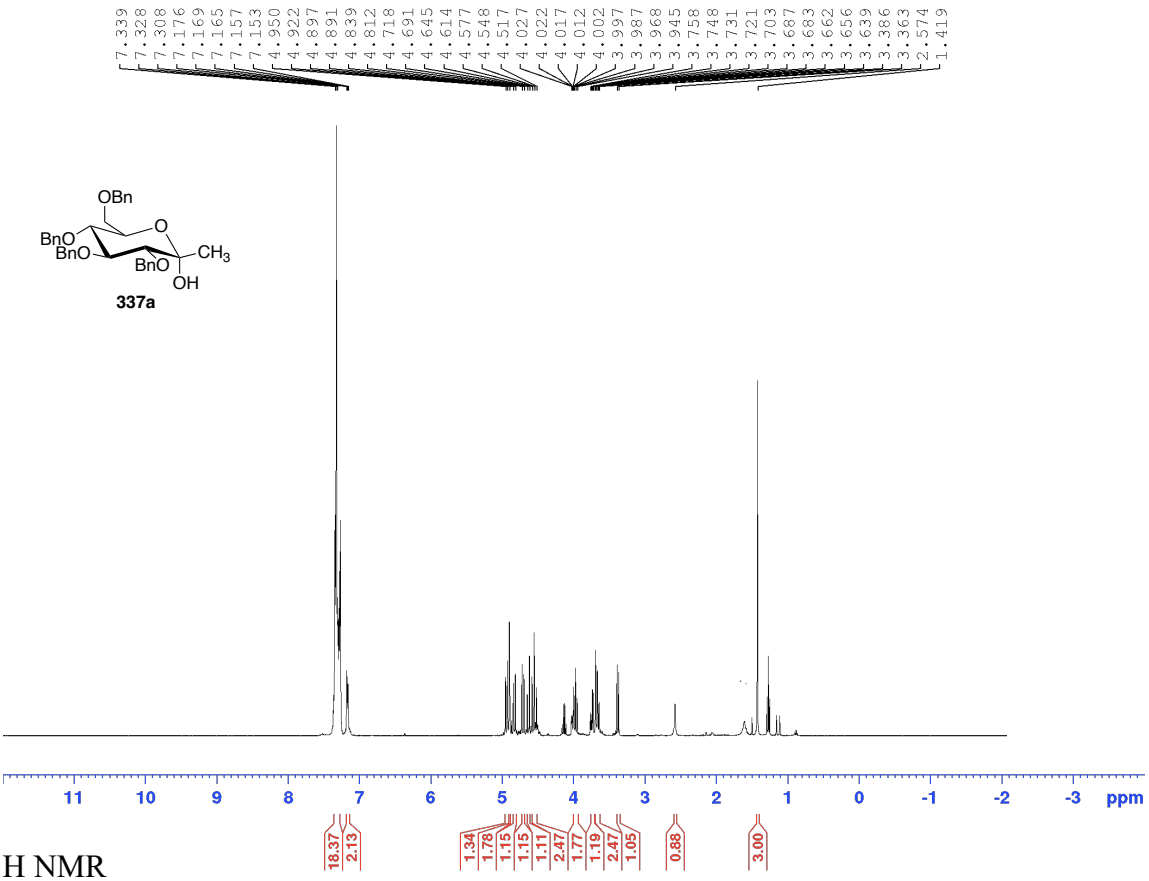
7.339
7.328
7.308
7.176
7.169
7.165
7.157
7.153
4.950
4.922
4.897
4.891
4.839
4.812
4.718
4.691
4.645
4.614
4.577
4.548
4.517
4.027
4.022
4.017
4.012
4.002
3.997
3.987
3.968
3.945
3.758
3.748
3.731
3.721
3.703
3.687
3.683
3.662
3.656
3.639
3.386
3.363
2.574
1.419
OBn
BnO
BnO
O
BnO
CH3
OH
337a
11
10
9
8
7
6
5
4
3
2
1
0
-1
-2
-3
ppm
18.37
2.13
1.34
1.78
1.15
1.15
1.11
2.47
1.77
1.19
2.47
1.05
0.88
3.00

^{1}H NMR

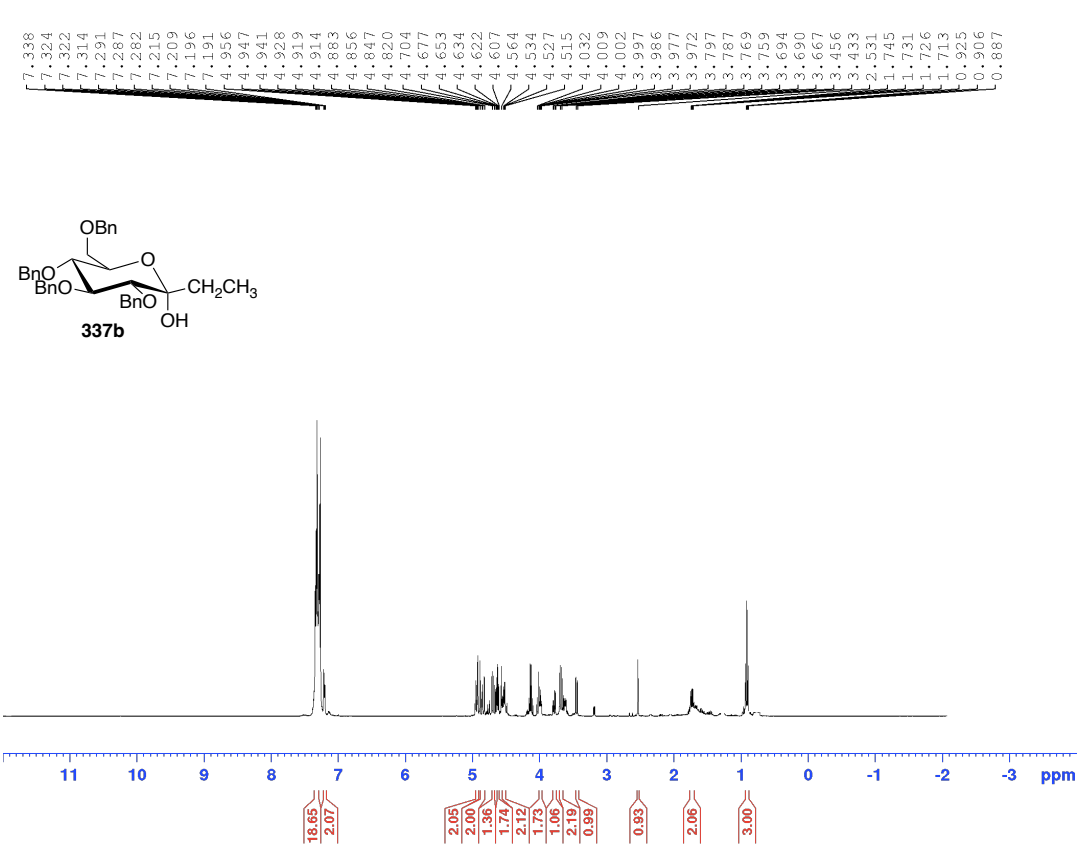
7.338
7.324
7.322
7.314
7.291
7.287
7.282
7.215
7.209
7.196
7.191
4.956
4.947
4.941
4.928
4.919
4.914
4.883
4.856
4.847
4.820
4.704
4.677
4.653
4.634
4.622
4.607
4.564
4.534
4.527
4.515
4.032
4.009
4.002
3.997
3.986
3.977
3.972
3.797
3.787
3.769
3.759
3.694
3.690
3.667
3.456
3.433
2.531
1.745
1.731
1.726
1.713
0.925
0.906
0.887
OBn
BnO
BnO
O
BnO
CH2CH3
OH
337b
11
10
9
8
7
6
5
4
3
2
1
0
-1
-2
-3
ppm
18.65
2.07
2.05
2.00
1.36
1.74
2.12
1.73
1.06
2.19
0.99
0.93
2.06
3.00

^{1}H NMR

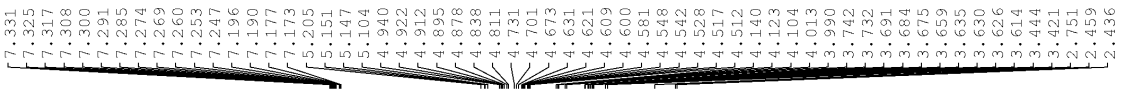

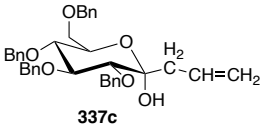

337c

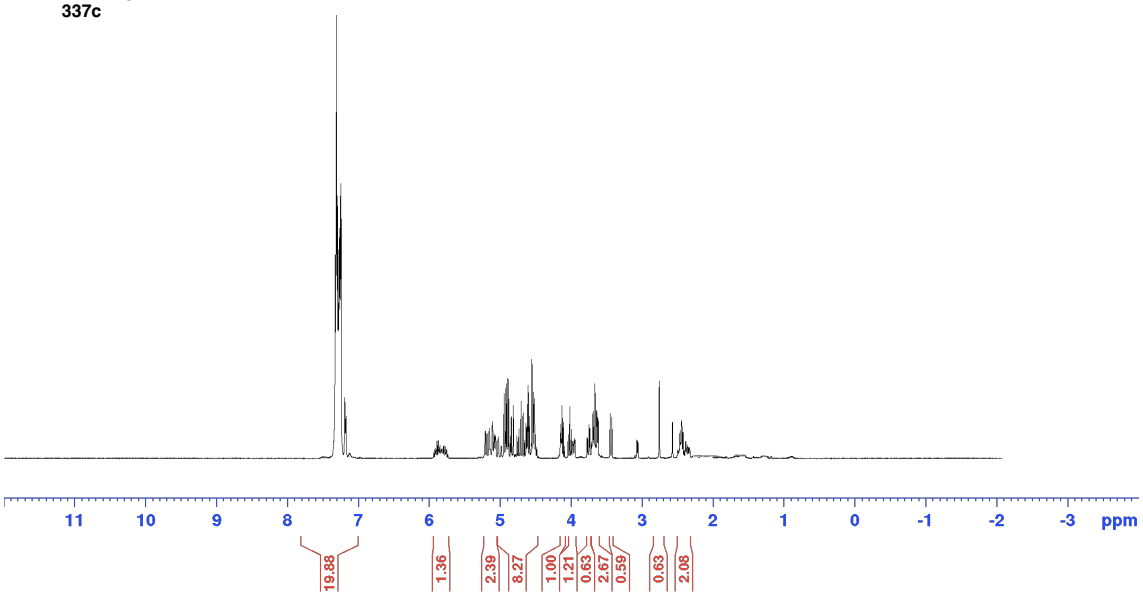

^{1}H NMR

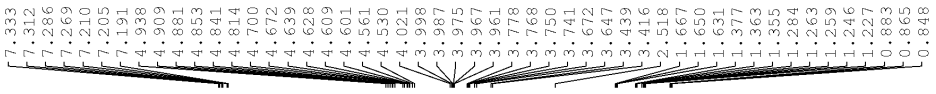

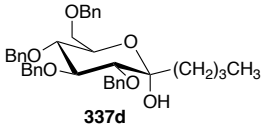

337d

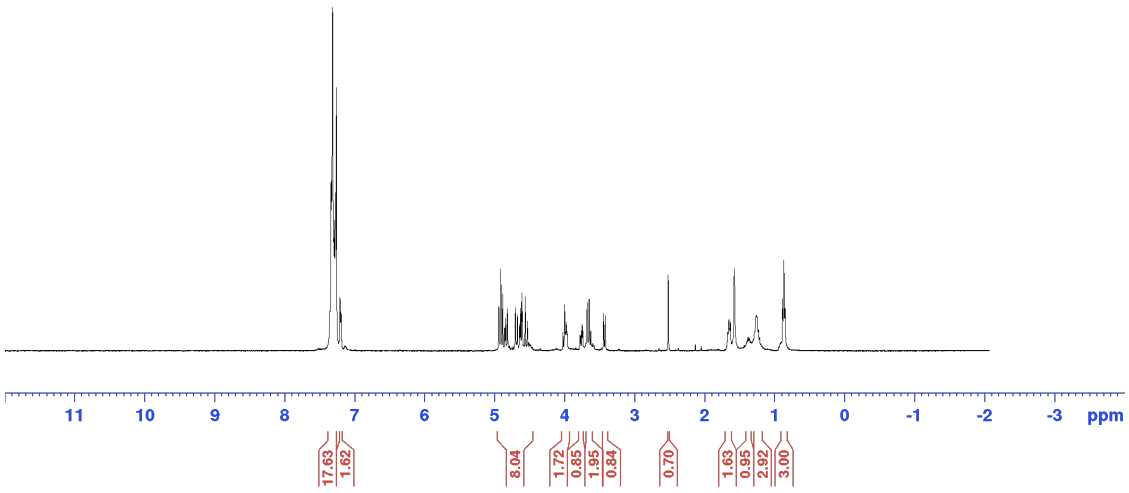

^{1}H NMR

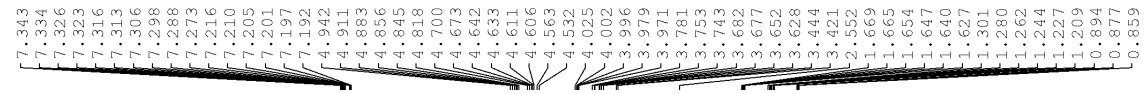

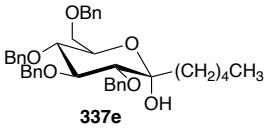

337e

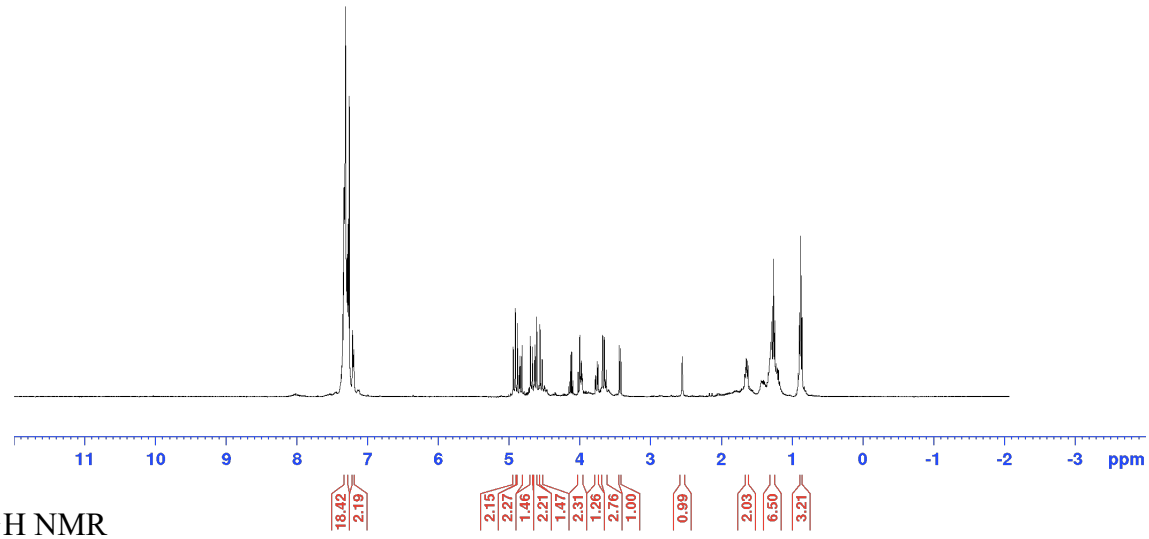

^{1}H NMR

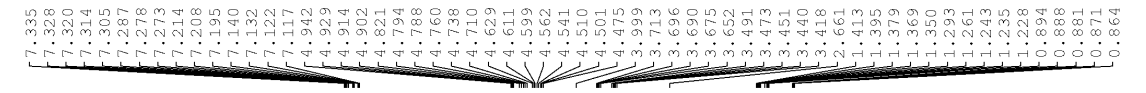

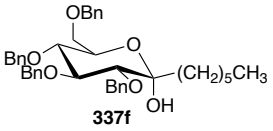

337f

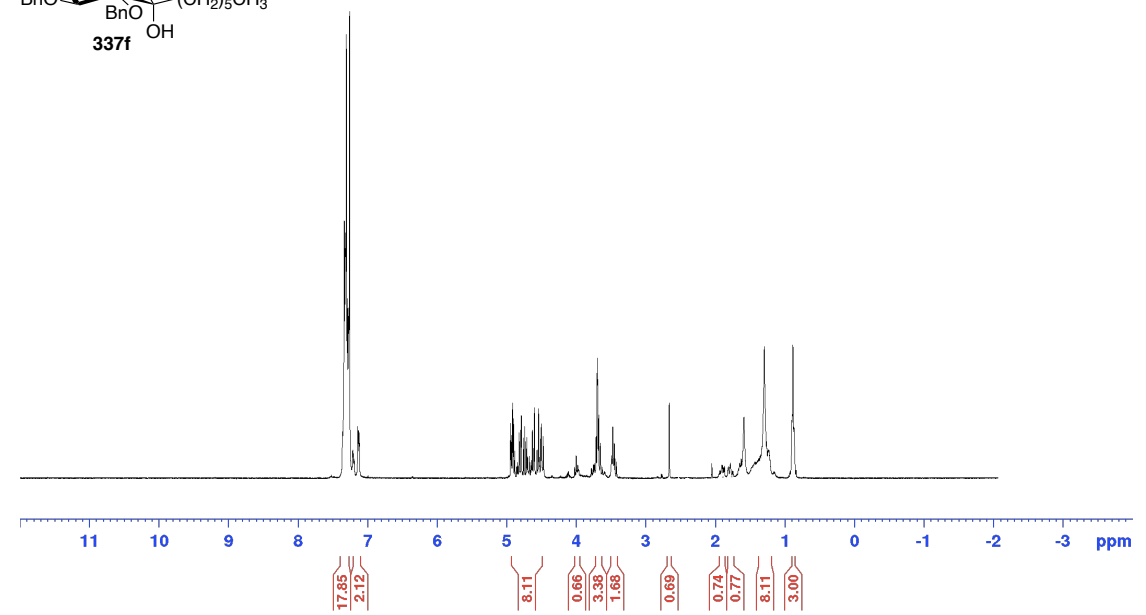

^{1}H NMR

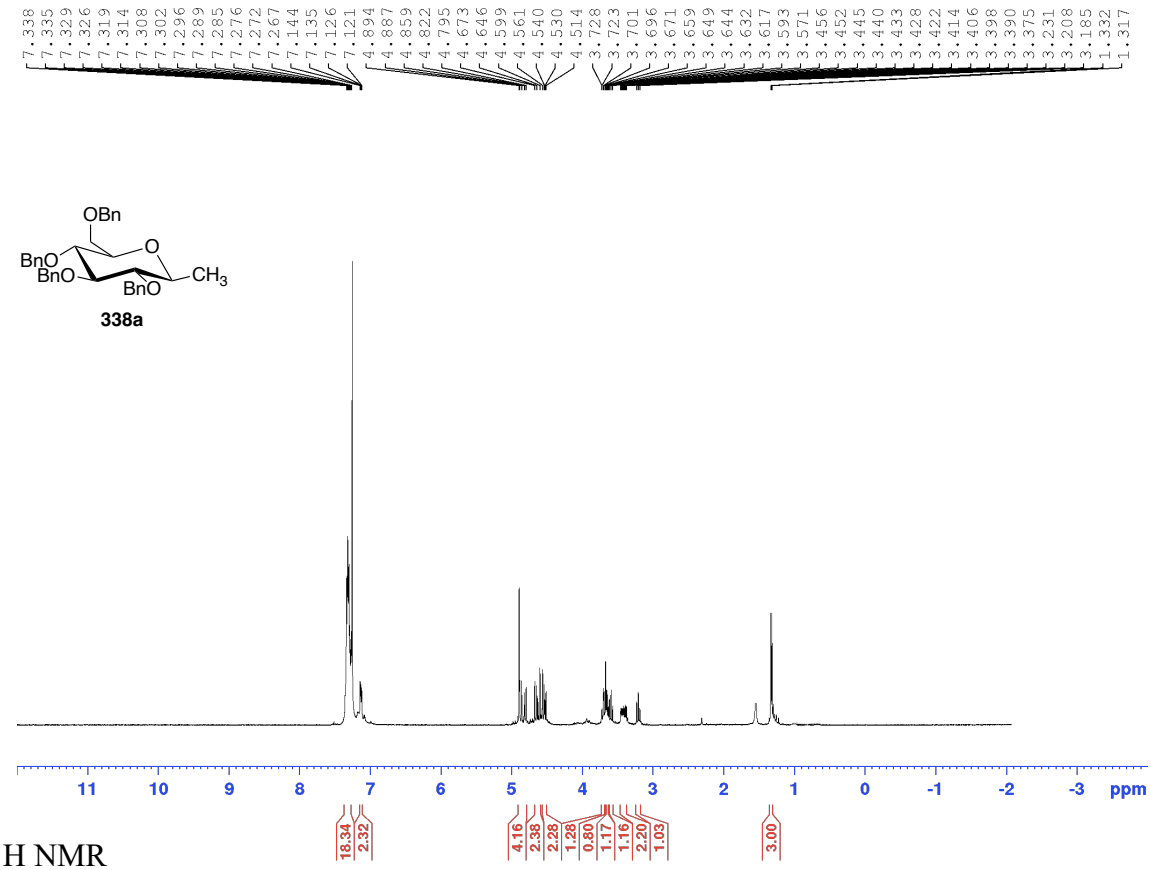
7.338
7.335
7.329
7.326
7.319
7.314
7.308
7.302
7.296
7.289
7.285
7.276
7.272
7.267
7.144
7.135
7.126
7.121
4.894
4.887
4.859
4.822
4.795
4.673
4.646
4.599
4.561
4.540
4.530
4.514
3.728
3.723
3.701
3.696
3.671
3.659
3.649
3.644
3.632
3.617
3.593
3.571
3.456
3.452
3.445
3.440
3.433
3.428
3.422
3.414
3.406
3.398
3.390
3.375
3.231
3.208
3.185
1.332
1.317
OBn
BnO
BnO
O
BnO
CH3
338a
11
10
9
8
7
6
5
4
3
2
1
0
-1
-2
-3
ppm
18.34
2.32
4.16
2.38
2.28
1.28
0.80
1.17
1.16
2.20
1.03
3.00

^{1}H NMR

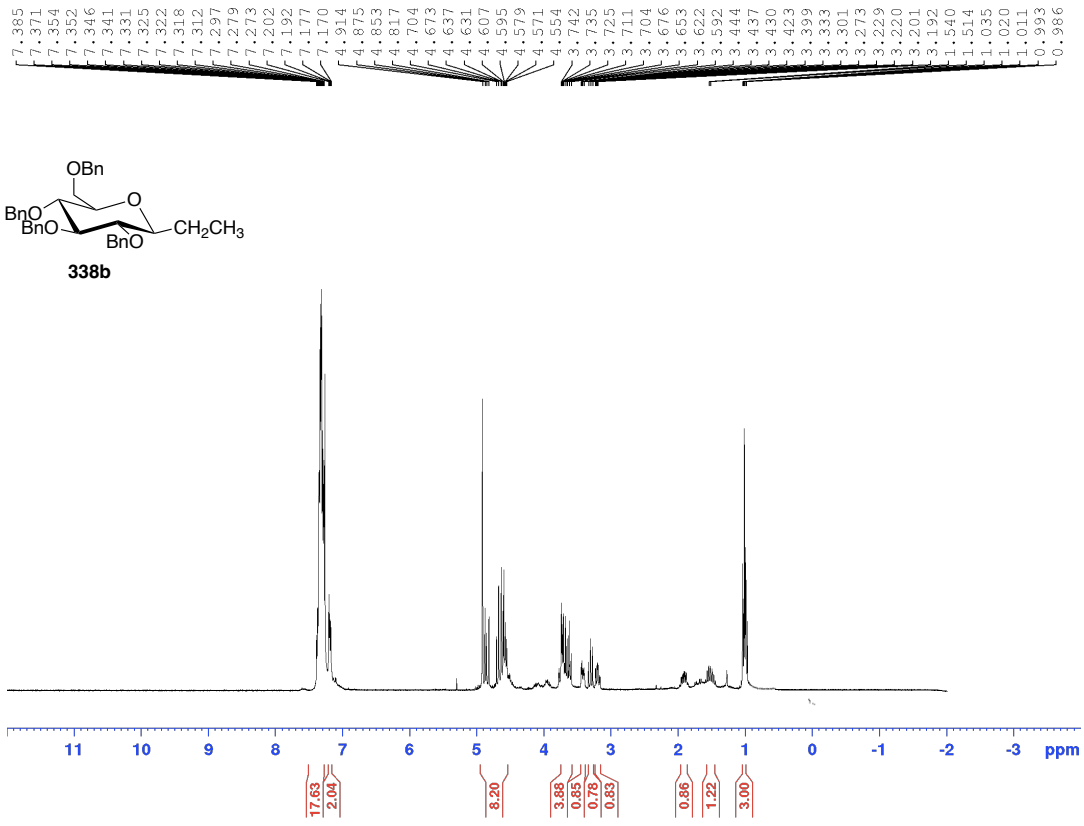
7.385
7.371
7.354
7.352
7.346
7.341
7.331
7.325
7.322
7.318
7.312
7.297
7.279
7.273
7.202
7.192
7.177
7.170
4.914
4.875
4.853
4.817
4.704
4.673
4.637
4.631
4.607
4.595
4.579
4.571
4.554
3.742
3.735
3.725
3.711
3.704
3.676
3.653
3.622
3.592
3.444
3.437
3.430
3.423
3.399
3.333
3.301
3.273
3.229
3.220
3.201
3.192
1.540
1.514
1.035
1.020
1.011
0.993
0.986
OBn
BnO
BnO
O
BnO
CH2CH3
338b
11
10
9
8
7
6
5
4
3
2
1
0
-1
-2
-3
ppm
17.63
2.04
8.20
3.88
0.85
0.78
0.83
0.86
1.22
3.00

^{1}H NMR

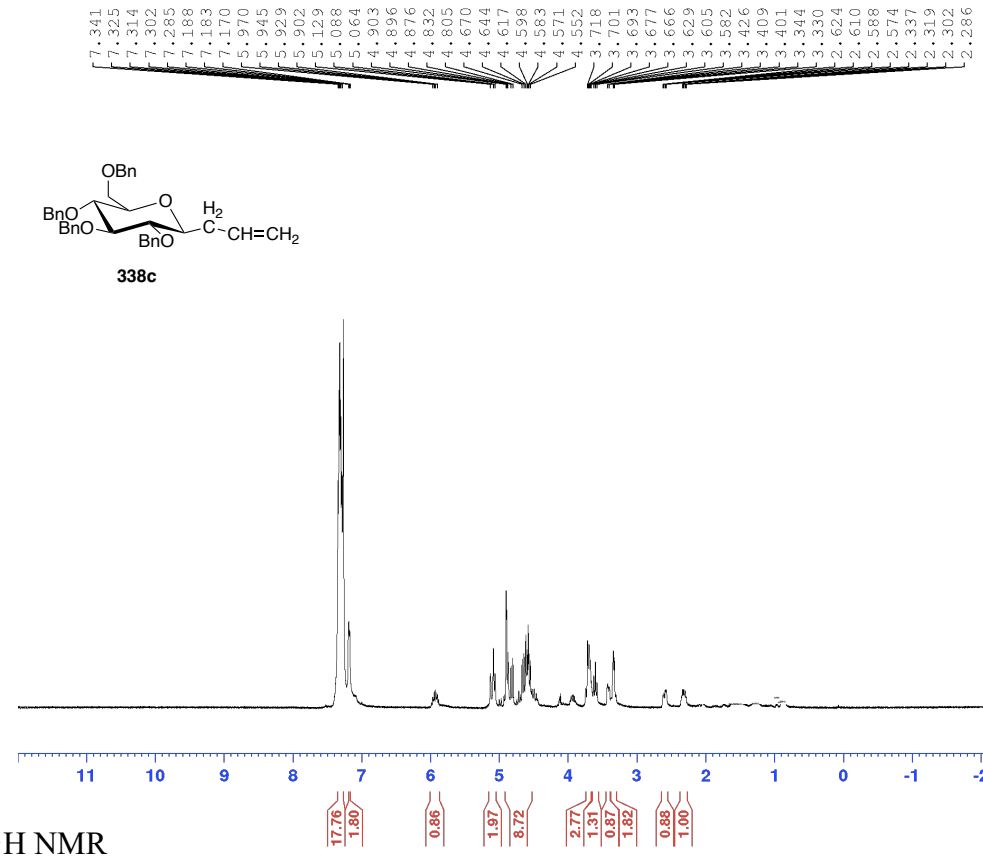

338c

^{1}H NMR

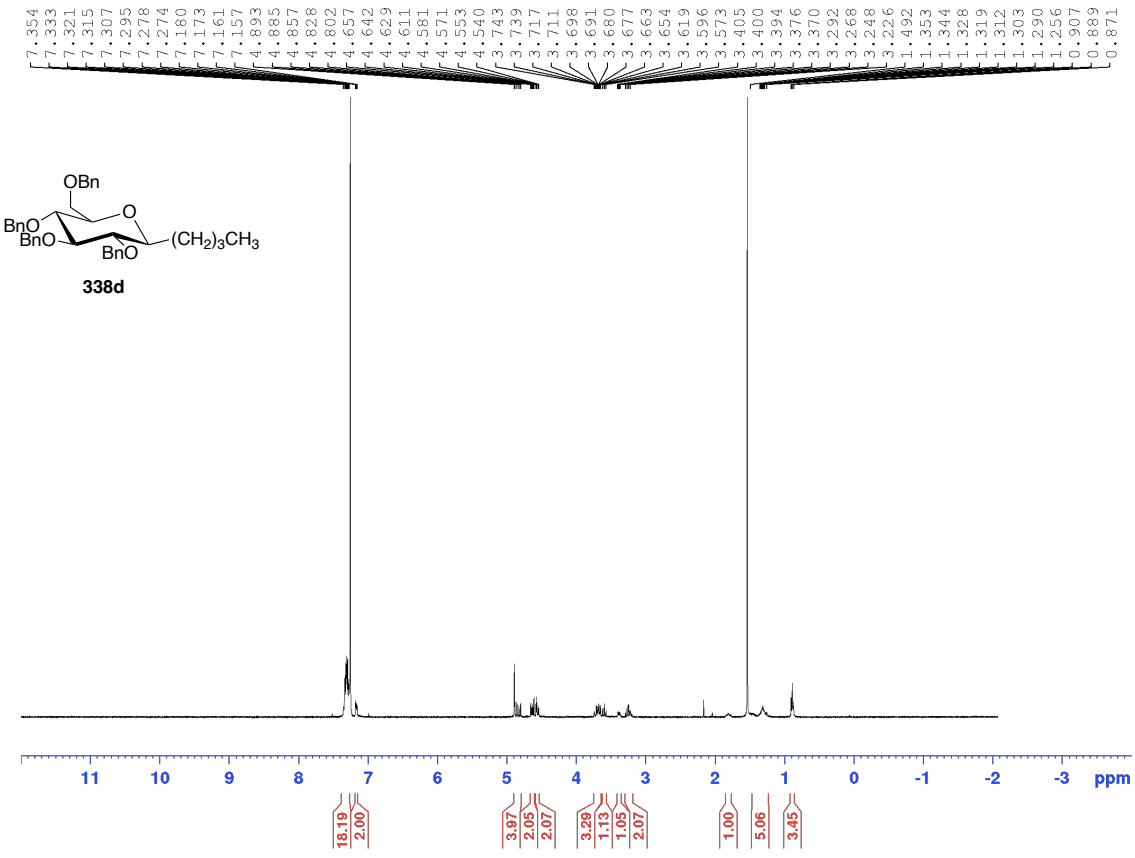

338d

^{1}H NMR

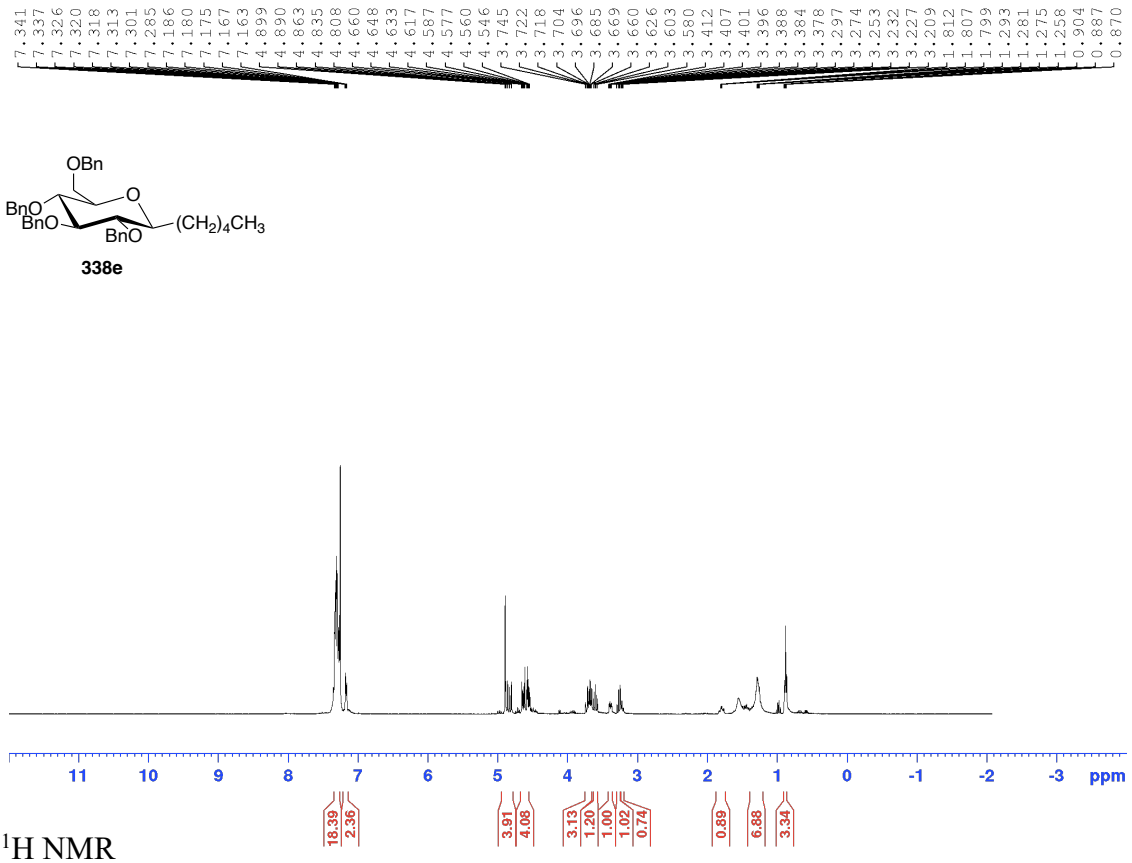
7.341 7.337 7.326 7.320 7.318 7.313 7.301 7.285 7.186 7.180 7.175 7.167 7.163 4.899 4.890 4.863 4.835 4.808 4.660 4.648 4.633 4.617 4.587 4.577 4.560 4.546 3.745 3.722 3.718 3.704 3.696 3.685 3.669 3.660 3.626 3.603 3.580 3.412 3.407 3.401 3.396 3.388 3.384 3.378 3.297 3.274 3.253 3.232 3.227 3.209 1.812 1.807 1.799 1.293 1.281 1.275 1.258 0.904 0.887 0.870
OBn
O
BnO
BnO
BnO
(CH2)4CH3
338e
11 10 9 8 7 6 5 4 3 2 1 0 -1 -2 -3 ppm
18.39 2.36 3.91 4.08 3.13 1.20 1.00 1.02 0.74 0.89 6.88 3.34

^{1}H NMR

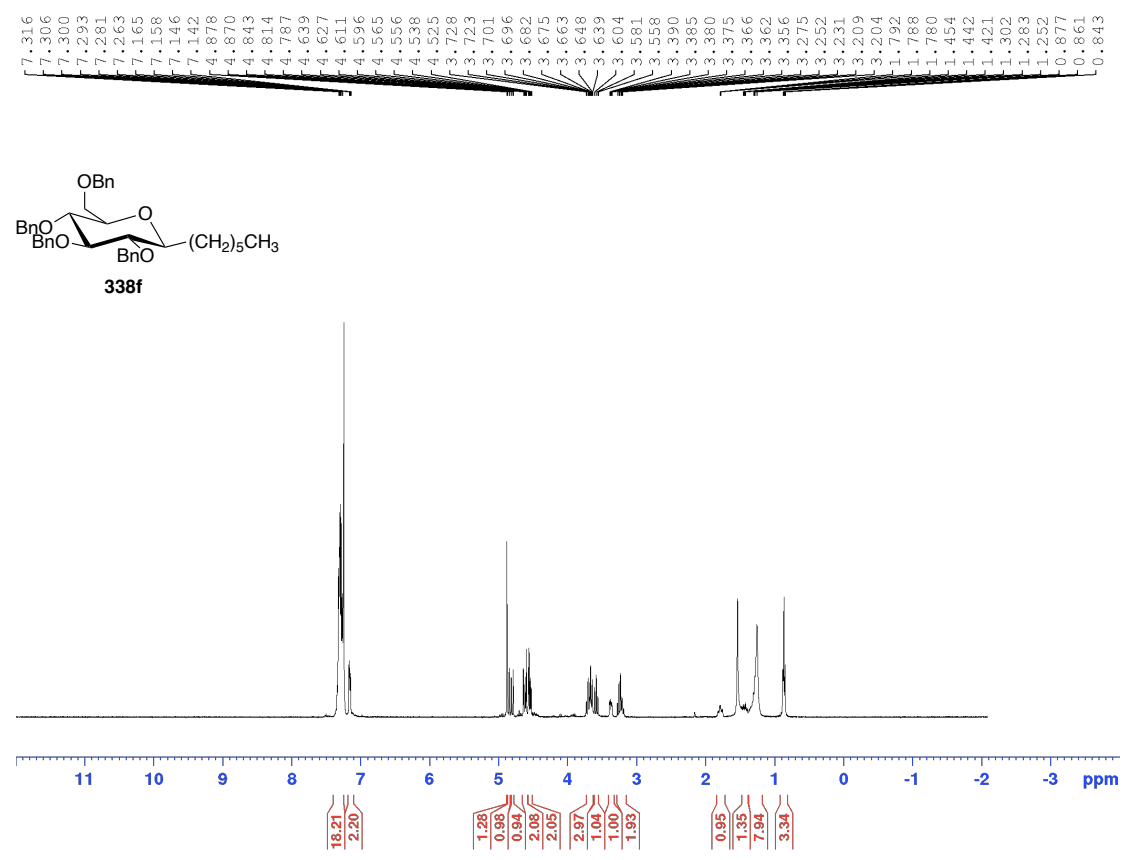
7.316 7.306 7.300 7.293 7.281 7.263 7.165 7.158 7.146 7.142 4.878 4.870 4.843 4.814 4.787 4.639 4.627 4.611 4.596 4.565 4.556 4.538 4.525 3.728 3.723 3.701 3.696 3.682 3.675 3.663 3.648 3.639 3.604 3.581 3.558 3.390 3.385 3.380 3.375 3.366 3.362 3.356 3.275 3.252 3.231 3.209 3.204 1.792 1.788 1.780 1.454 1.442 1.421 1.302 1.283 1.252 0.877 0.861 0.843
OBn
O
BnO
BnO
BnO
(CH2)5CH3
338f
11 10 9 8 7 6 5 4 3 2 1 0 -1 -2 -3 ppm
18.21 2.20 1.28 0.98 0.94 2.08 2.05 2.97 1.04 1.00 1.93 0.95 1.35 7.94 3.34

^{1}H NMR

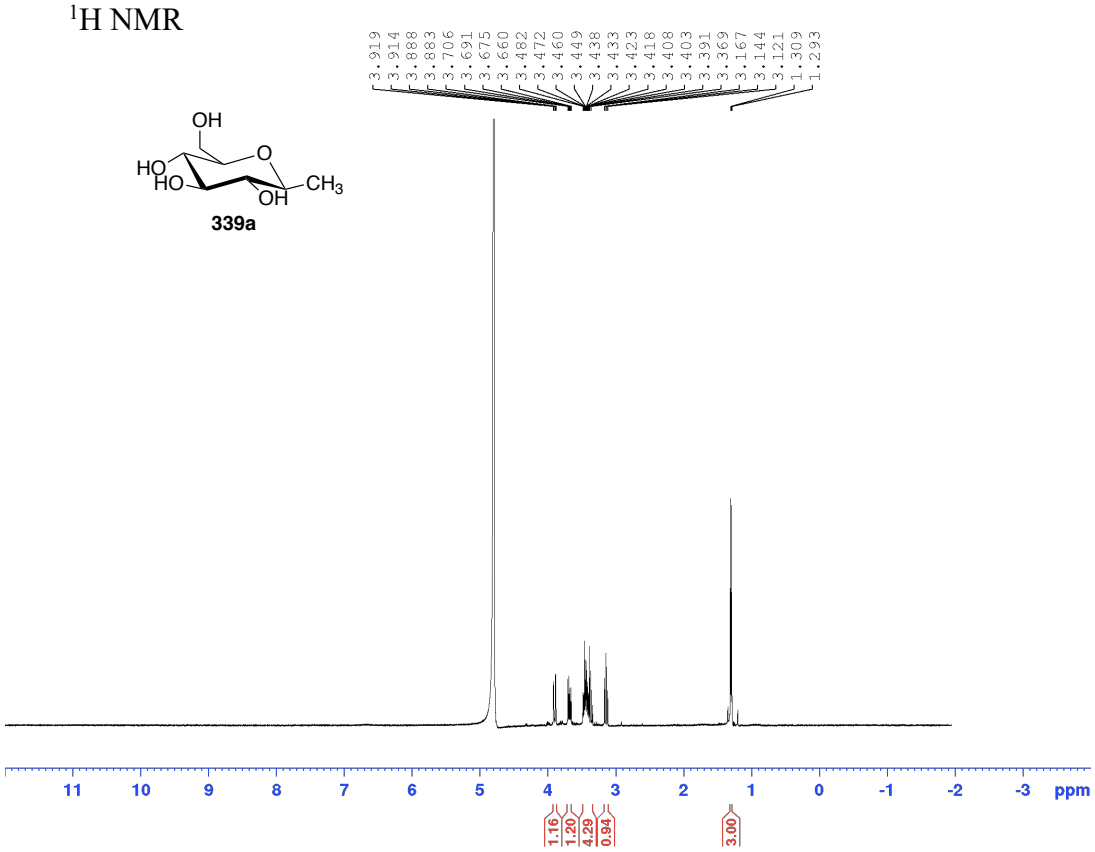

^{13}C NMR

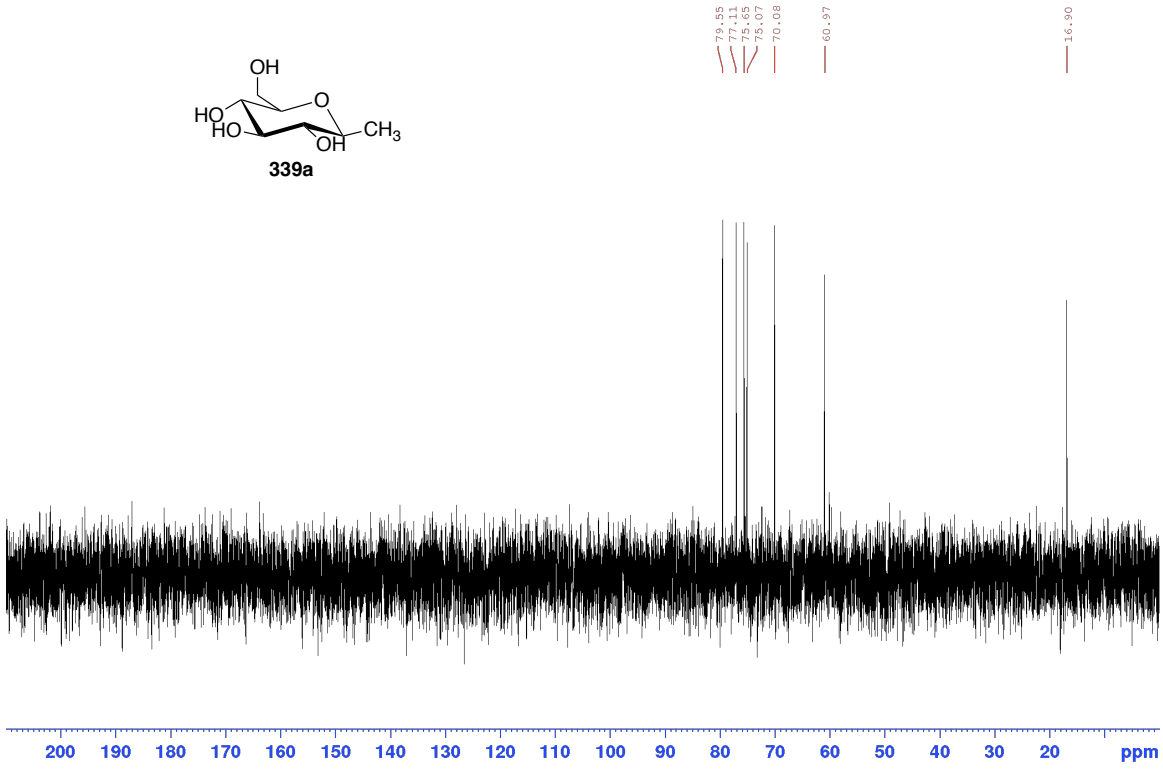

^{1}H NMR

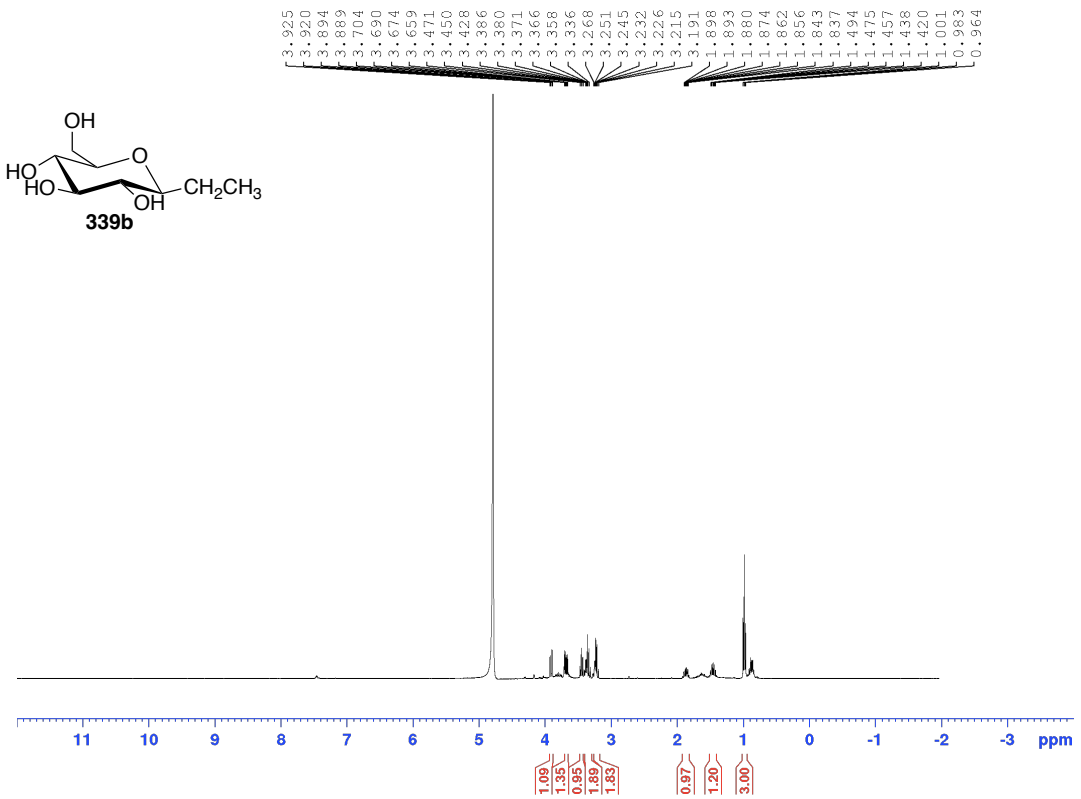

^{13}C NMR

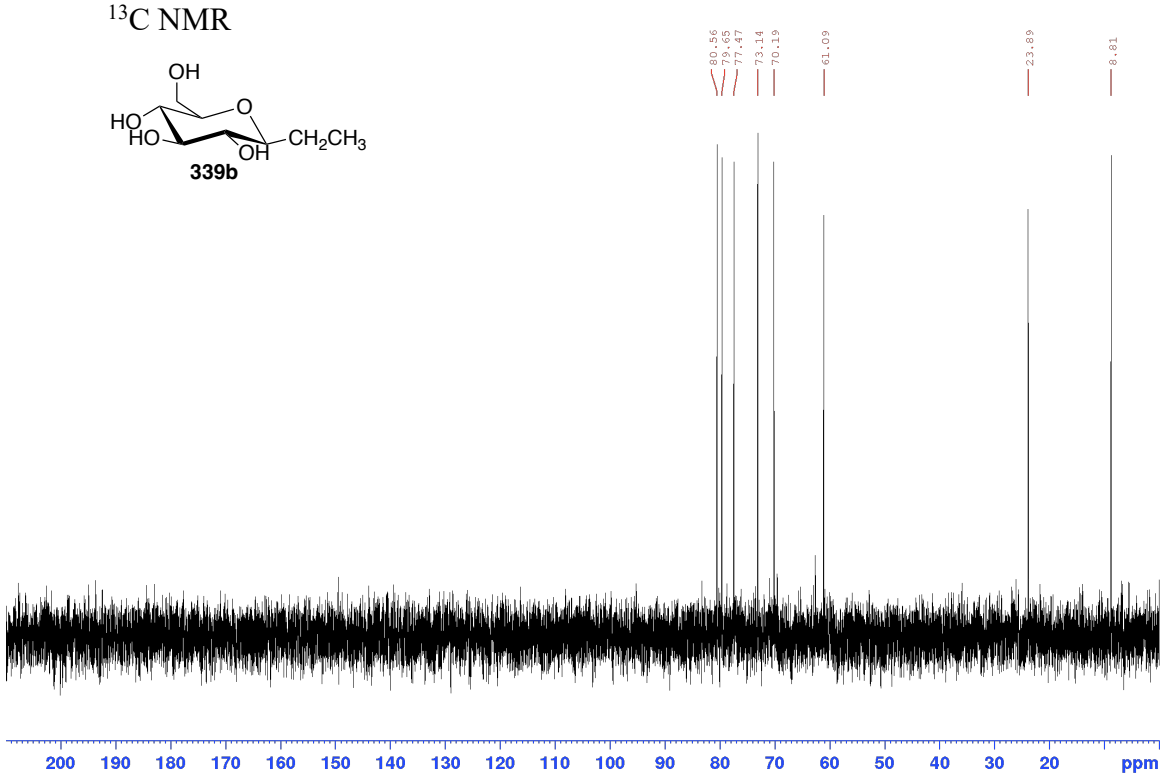

^{1}H NMR

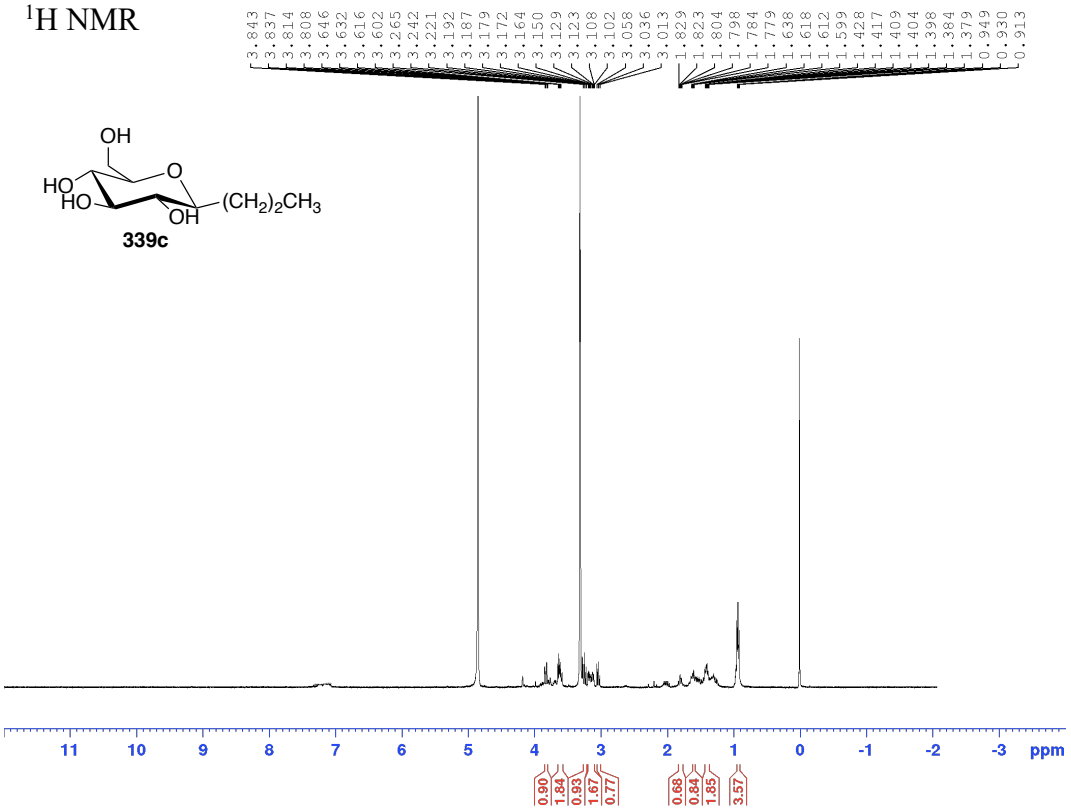

^{13}C NMR

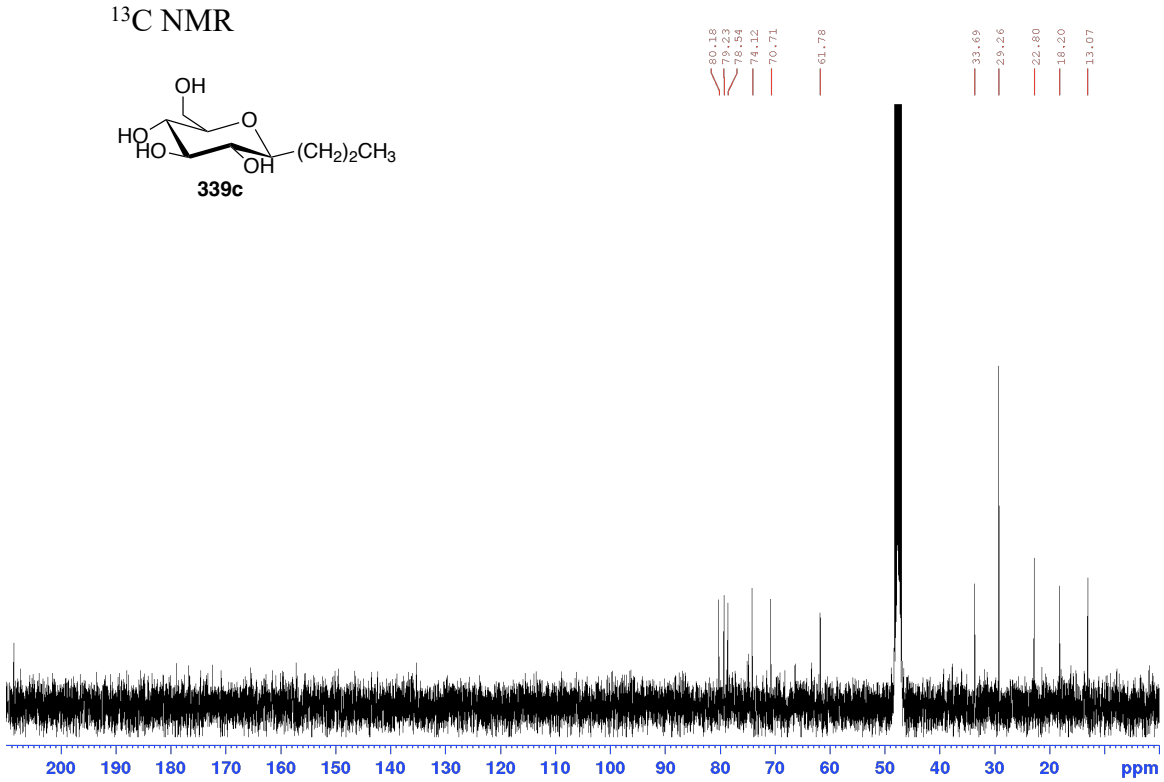

^{1}H NMR

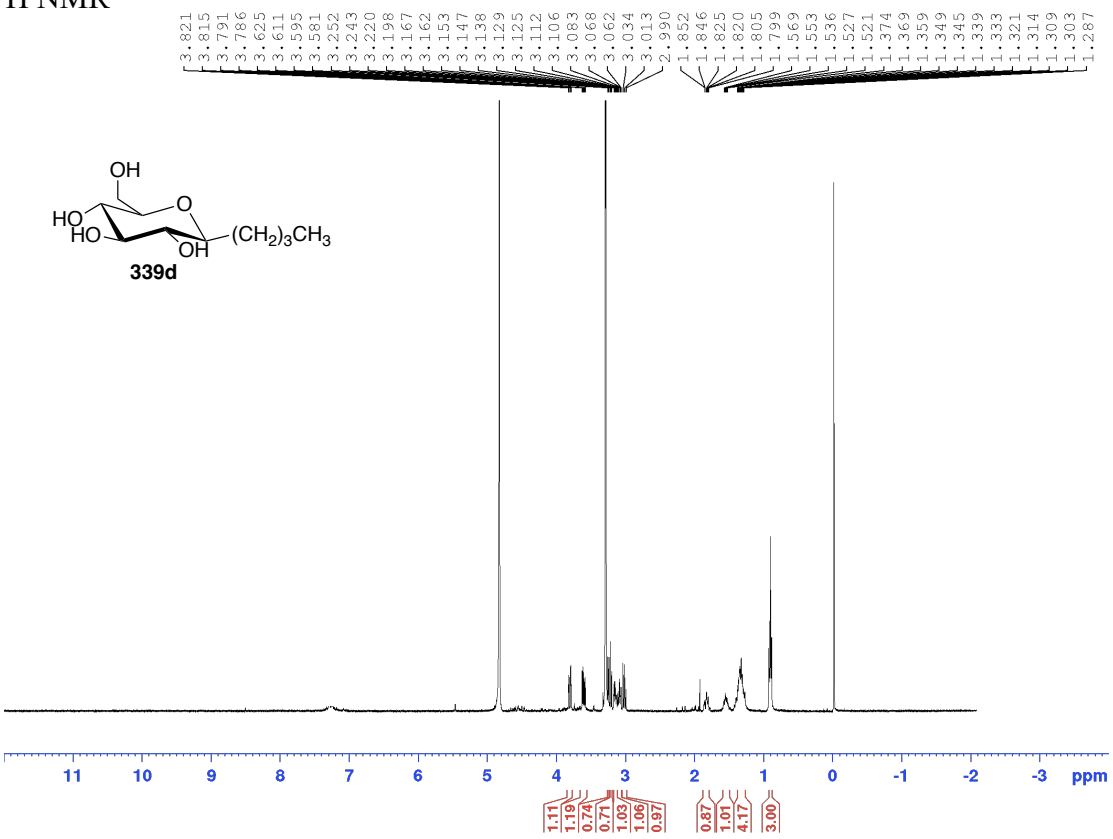

^{13}C NMR

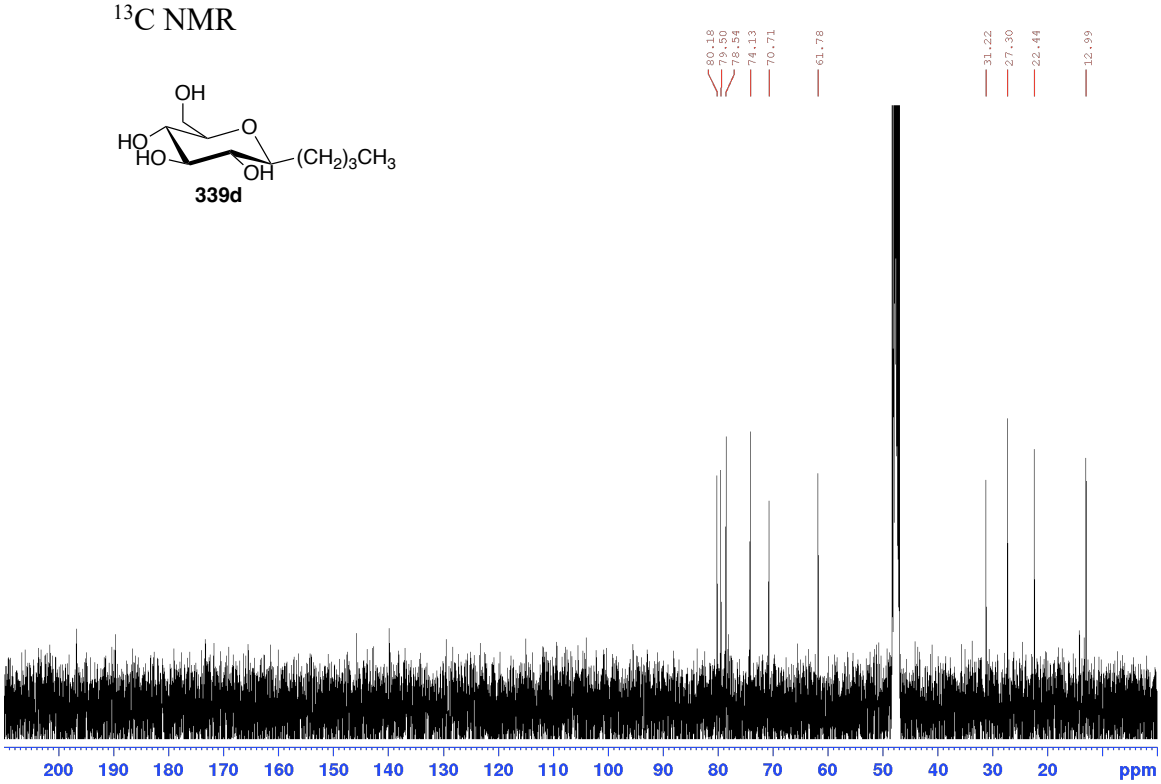

^{1}H NMR

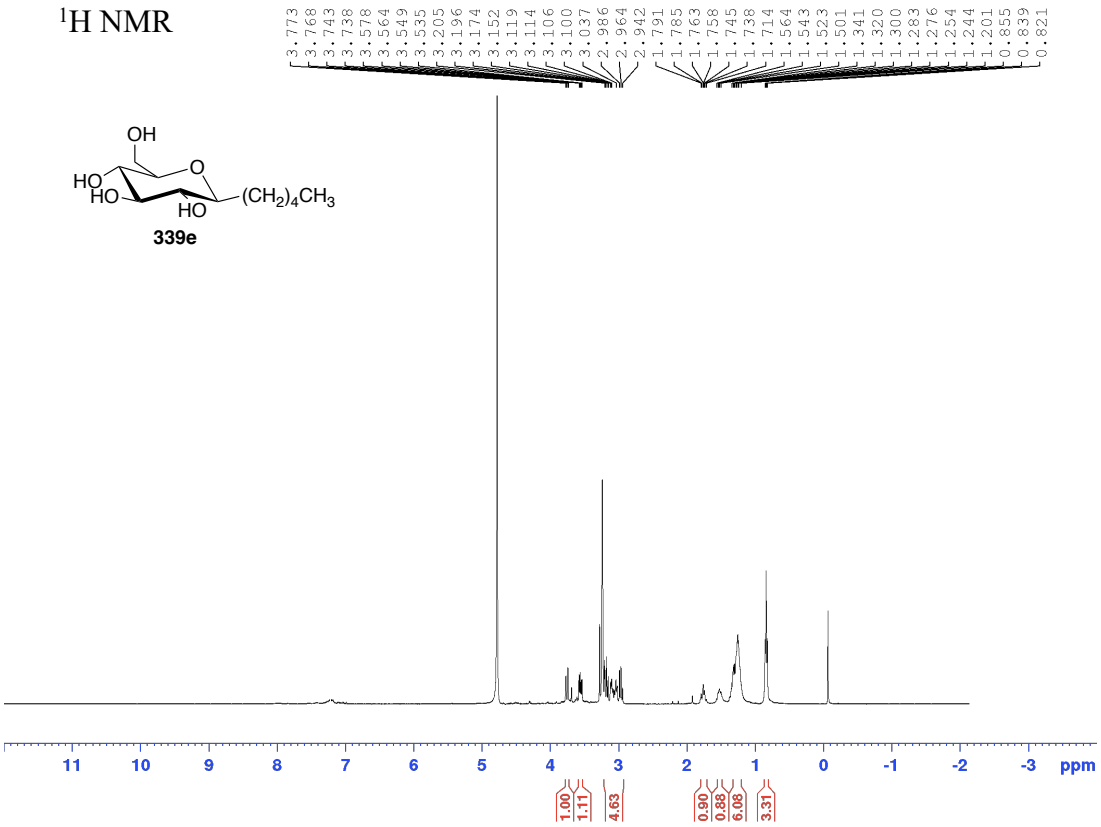

^{13}C NMR

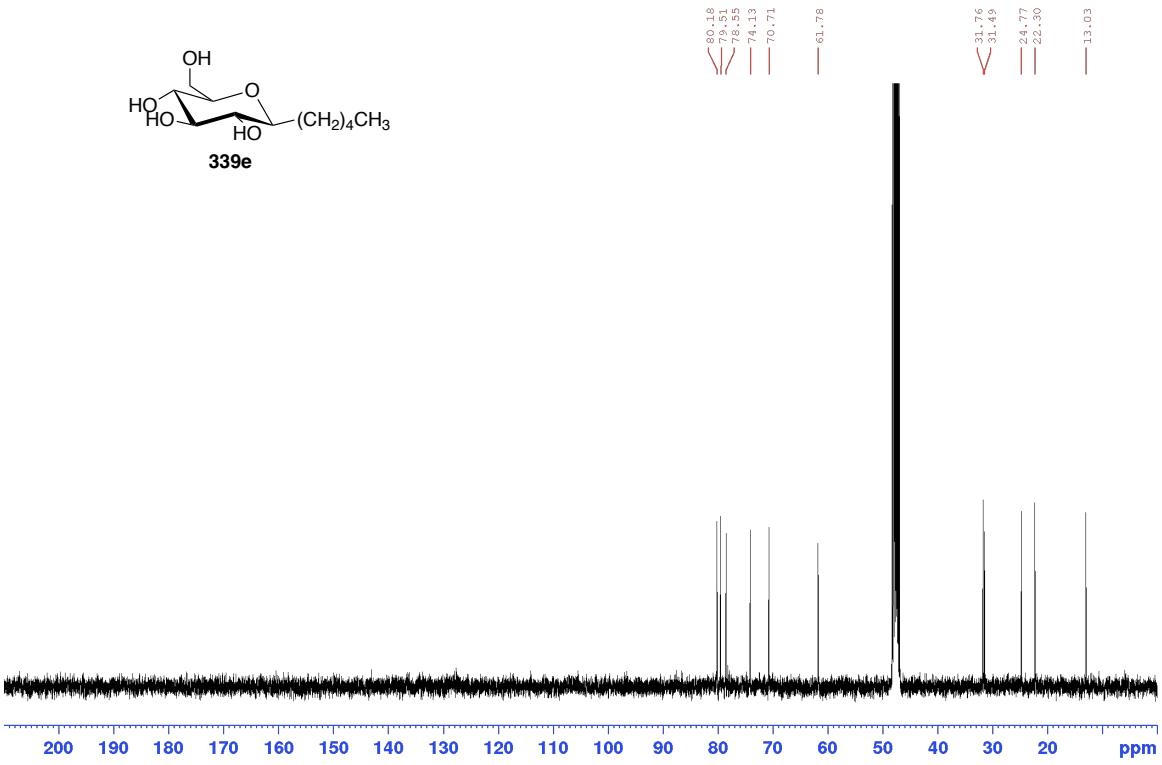

^{1}H NMR

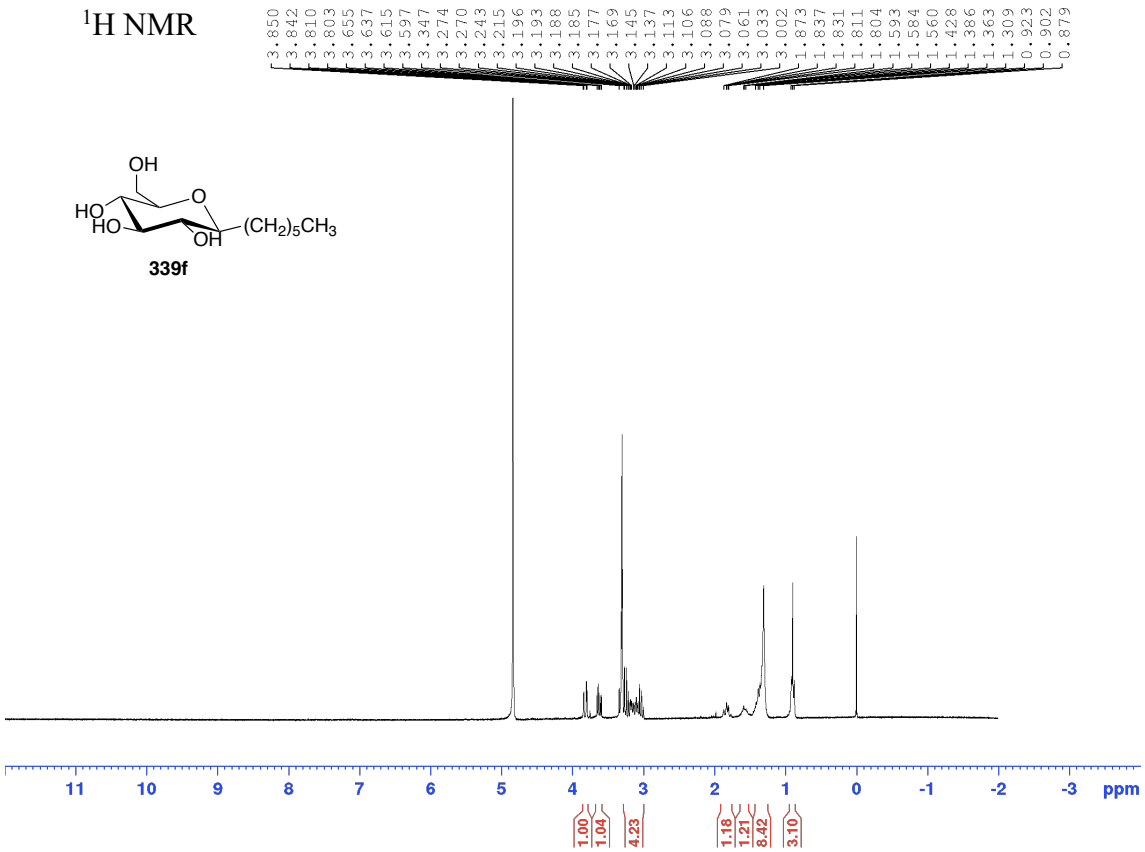

^{13}C NMR

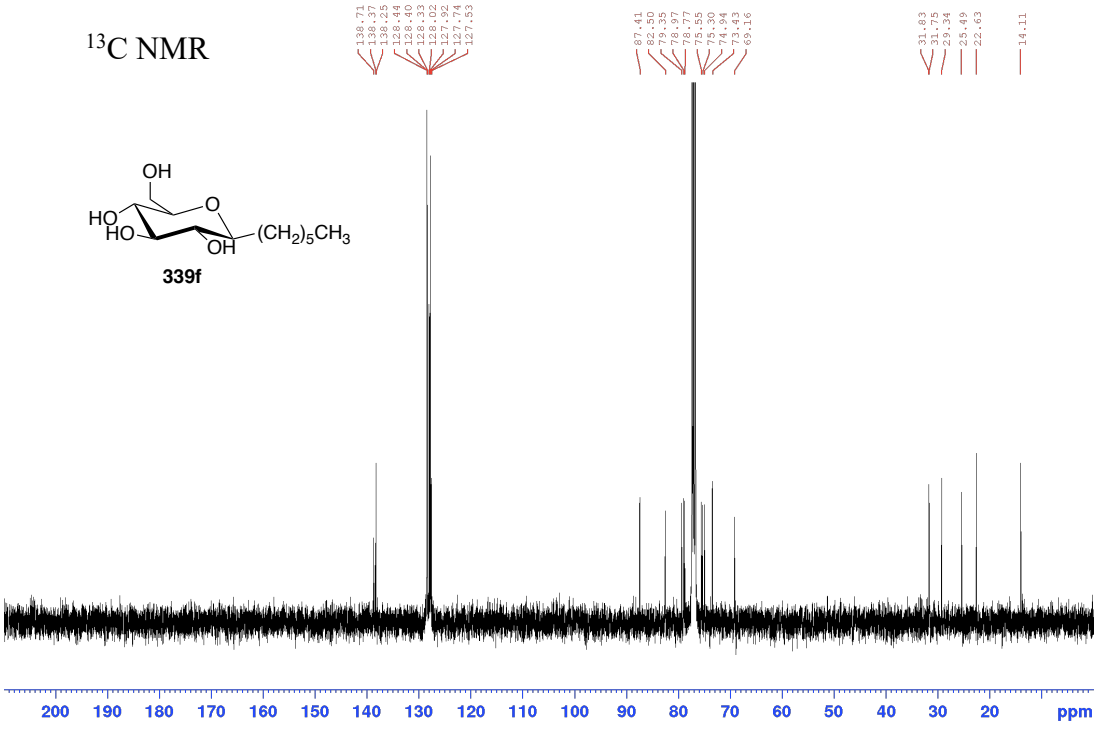

Chapter 4: Small Molecule Ice Recrystallization Inhibitors (IRIs) as Potential Cryoprotective Agents for Human Induced Pluripotent Stem Cell Derived Neurons (iPSC-Ns)

4.1 Introduction: iPSCs and iPSC-Ns as Promising Cellular Therapy Products for Neurodegenerative Diseases

Neurodegenerative disorders are diseases of the central nervous system (CNS) that involve a gradual loss of neurons, affecting different parts of the brain and spinal cord.[1-3] Alzheimer's (AD) and Parkinson's (PD) diseases are the two most common neurodegenerative diseases impacting aging populations.[1,4-6] Different mechanisms have been proposed as the leading cause of the gradual loss of neurons such as aggregation of misfolded proteins, genetic mutations, and impairment in mitochondrial function.[7-9] Although there are several food and drug administration (FDA)-approved drugs that are used to treat AD and PD, there are significant side effects and complications that are accompanied with their consumption.[10-11] Consequently, regenerative medicine has emerged as a therapeutic option for the treatment of some neurodegenerative diseases.[8,12] For example, it has been shown that transplantation of fetal neural tissues and human embryonic CNS tissues into lesions of rat spinal cord have restored axonal regeneration and neuronal functionality at the injury site.[13-16] Moreover, embryonic stem cell (ESC)-derived neurons have been used in treating PD in mice.[19] Nonetheless, ESCs encounter ethical and legal issues in neuroscience research, and therefore, human induced pluripotent stem cells (iPSCs) are a better alternative source of stem cells since they are easy to generate and are not complicated by ethical limitations.[20] iPSCs and their derivatives (i.e., iPSC-derived neurons (iPSC-Ns) have become invaluable and powerful tools for disease

modeling, drug discovery and cell replacement therapy.[20-22]

iPSCs are reprogrammed from somatic stem cells by overexpressing pluripotency-specific transcription factors, such as SOX2, OCT3/4, and c-MYC.[22-23] iPSCs can self-renew to produce more of the same cell type and differentiate to produce other cell types.[23-25] iPSCs and their derivatives are thus a unique tool that can be used to develop new cell-based treatments for regenerative medicine. iPSC-Ns have proven to be extremely useful in modelling and understanding the aetiologies of neurological disease.[23-31] For instance, iPSC-Ns assist in understanding the relationship between Parkin dysfunction in human dopaminergic neurons and the development of PD *in vitro*.[23-31] Moreover, grafting induced pluripotent stem cell-derived myeloid lineage (iPSC-ML) cells are shown to reduce β amyloid oligomers in culture medium, enhancing the cognition in Alzheimer's modeled mice.[17-18] However, future stem cell-based research and therapies will require vast numbers of quality-controlled master cell banks, hence, cryopreservation of iPSC and iPSC-Ns is required. iPSCs are extremely susceptible to the cryoinjury associated with freezing and thawing procedures, leading to significant decreases in survival and growth rates as well as spontaneous differentiation.[119-120] Not only do conventional cryopreservation regimes reduce cell viability and recovery, but they also cause phenotypic variation and/or alterations in their pluripotency properties as a result of selective genetic/epigenetic pressures on the iPSCs, which can affect the reproducibility and downstream differentiation efficiencies.[120]

The differentiation process of iPSCs into iPSC-Ns takes anywhere from 2 to 6 months, depending on the type of neurons required, which represents a major challenge for the clinical translation of iPSC-Ns.[32-33] The post-mitotic nature of terminally differentiated

iPSC-Ns renders them more sensitive to cryoinjury compared to iPSCs.[59,65] Consequently, it is necessary to develop an effective cryopreservation protocol that maintains high viability, recovery, and functionality of iPSC-Ns in order to deliver high-quality cell products to patients.[34-35]

4.2 Cryopreservation of iPSC-Ns: From Conventional Cryomedia to IRI-Formulated Cryomedia

Cryopreservation allows for the storage of cellular therapy products for months or years depending on the exact cell type.[37] However, there are different factors that must be taken into consideration with cryopreservation, such as the cooling and warming rates, to maintain high post-thaw viability and functional activity.[38-40] Recrystallization of intra- and/or extra-cellular ice is a major cause of cellular injury and death during cryopreservation.[40-43] Therefore, depending on the cell type and its required cooling rate, permeating and non-permeating cryoprotective agents (CPAs) have been employed in an attempt to mitigate cryoinjuries associated with cryopreservation.[44-46]

4.2.1 Conventional Cryopreservation Protocols for Primary Neurons and iPSC-Ns

Cryopreservation of neurons differentiated from different cell sources offers several advantages to regenerative medicine. For example, it allows the delivery of neurons for clinical applications, such as neural transplantation, providing scalable sources of cells for emerging cell replacement therapy.[47-48] Mitigation of cellular injury caused by cryopreservation has been achieved by the addition of CPAs, that are either permeating or non-permeating, to cryopreservation solutions. For example, dimethyl sulfoxide (DMSO) penetrates cell membranes and protects iPSCs when freezing with slow cooling rates.[1] The postulated mechanism of protection from cryoinjury by DMSO is that it replaces

intracellular water, minimizing the osmotic effect (i.e., water loss and cell volume reduction) at lower temperatures.[49-51] Conventional cryopreservation protocols for primary neurons, or iPSC-Ns, utilize slow cooling rates (-1 to -2 °C/min) at -80 °C overnight, followed by transfer of the cells to liquid nitrogen for several months/years.[52-64]

Numerous conventional cryomedia solutions have been proposed for the preservation of neuronal precursors (i.e., neural progenitor cells, NPCs), or primary and iPSC-derived neurons. Most of these cryomedia solutions contain DMSO, or a combination of DMSO and another non-permeating CPA such as ethylene glycol.[57,60] Supplementing Dulbecco's Modified Eagle Medium (DMEM) with 10 % DMSO results in 35-41% post-thaw viability of neurons, or 80% post-thaw viability of NPCs. [52,59,65] Another conventional cryomedium used for preserving primary and iPSC-derived neurons is fetal bovine serum (FBS) supplemented with 10% or 20% DMSO which results in 32% and 75% post-thaw viability of neurons, respectively.[1,48,56,66] NeuroB medium supplemented with 10% FBS and 10% DMSO has also been used to preserve iPSC-Ns and has shown to result in 80% post-thaw viability.[54] However, none of these cryomedia formulations can be used in clinical settings because they contain animal components (i.e., FBS). Some commercially available cryomedia, serum free cryo-solutions containing 5% or 10% DMSO have been found to enhance the cryopreservation outcomes for primary neurons and iPSC-Ns, such as Cryostor®5 or 10 (CS5 or CS10), and Neurostore, which have shown to result in post-thaw viabilities of 50%, 70%, and 90%, respectively.[53,58,62-63,67] Nonetheless, the morphology and electrophysiological functionality of iPSC-Ns appeared to decrease post-thaw,[48,56,66-67] which can be related to a secondary cryoinjury that is associated with the prolonged exposure to ice crystals post cryopreservation or to the toxic effect associated

with DMSO.[68,77] To explain, none of the proposed cryomedia contain additives that protect sensitive cells (i.e., iPSC-Ns) from the cryoinjury associated with ice recrystallization.[77] In addition, using DMSO at the higher concentrations (i.e., 10-20 %) has been reported to cause neurotoxic effects if it is not washed or diluted prior to clinical application.[68-71] Consequently, the need to improve current CPAs and cryopreservation protocols has risen to reduce or eliminate the use of DMSO.

4.2.2 N-2-Fluoropnehyl-D-Gluconamide (2FA) as a Potential Cryoprotective Agent

Given the fact that ice recrystallization results in significant cellular damage in a considerable number of cells during cryopreservation, efforts to developing ice recrystallization inhibitors for use as new CPAs has risen.[43-44] As discussed in the introduction chapter, ice recrystallization causes an increase in the average size of ice crystals in biological samples, which can cause mechanical damage to cell membranes. Slow warming of cryopreserved cells has been shown to accelerate ice recrystallization, significantly reducing cell viability.[72-73] Therefore, biological samples are often thawed rapidly (i.e., 45 °C/min and 113 °C/min) to avoid ice recrystallization.[72-73] While conventional CPAs, such as DMSO, fail to control ice recrystallization, ice recrystallization inhibitors (IRIs) can improve post-thaw viability and functionality outcomes by preventing the growth of ice crystals.[74,76] The use of IRIs can also reduce the need for DMSO,[76] limiting the undesirable cytotoxic effects imposed by DMSO which will help in establishing optimal cryopreservation protocols for different cell types.

As mentioned in the introduction chapter, small-molecule IRIs have been successfully synthesized by the Ben laboratory.[74-78] Moreover, IRIs from different classes have been shown to enhance the cryopreservation outcomes of different cell types.[74,76] For

example, some molecules from the *N*-aryl-D-gluconamide class of IRIs, presented in **Figure 4.1**, have been shown to be excellent inhibitors of ice recrystallization and can be used as effective additives to preserve different stem cell-based therapies, such as hematopoietic stem cells (HSCs) and mesenchymal stem cells (MSCs).[73-77]

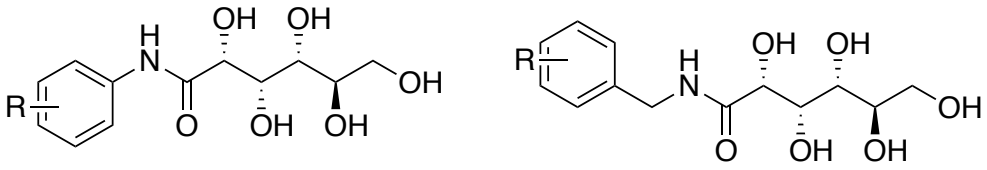

Figure 4.1 General chemical structure of *N*-aryl-D-gluconamide class of IRIs

4.2.2.1 Assessment of the Cryoprotective Feature of N-Aryl-D-Gluconamide Class of IRIs in iPSCs

A panel of *N*-aryl-D-gluconamide IRIs, presented in **Figure 4.2**, has been shown to improve the post-thaw functionality of different stem cells (i.e., HSCs and MSCs).[77-78] Because of the success in preserving the functionality of HSCs and MSCs after cryopreservation, these compounds are promising candidates for additional cryopreservation studies, and thus, they were chosen to be tested on iPSCs. These compounds were *N*-2-fluorophenyl-D-gluconamide (**2FA**, 4.1), *N*-4-methoxyphenyl-D-gluconamide (**PMA**, 4.2), *N*-4-chlorophenyl-D-gluconamide (**4ClA**, 4.3), and *N*-2,6-difluorobenzyl-D-gluconamide (**2,6 DFB**, 4.4).

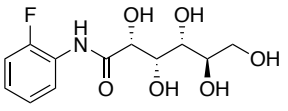

***N*-2-fluorophenyl-D-gluconamide (2FA)**

(4.1)

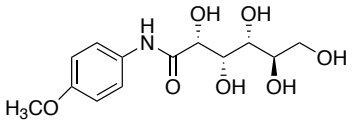

***N*-4-methoxyphenyl-D-gluconamide (PMA)**

(4.2)

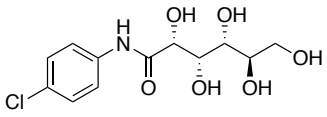

***N*-4-chlorophenyl-D-gluconamide (4ClA)**

(4.3)

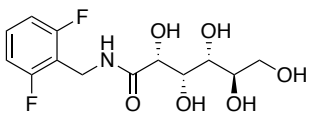

***N*-2,6-difluorobenzyl-D-gluconamide (2,6DFB)**

(4.4)

Figure 4.2 Chemical structures of the different *N*-aryl-D-gluconamide used for cryopreservation of iPSC and iPSC-Ns. [77-78]

The IRI activity of these compounds was previously examined using the modified splat cooling assay, which generates dose response curves (**Figure 4.3**), from which the IC_{50} values for each compound were determined. Previous Ben lab student, Dr. Madeline Adam, found the IC_{50} values of 2FA, PMA, 4ClA, and 2,6 DFB to be 4.1 mM, 5.1 mM, 12.0 mM, and 10.8 mM, respectively.[77-78]

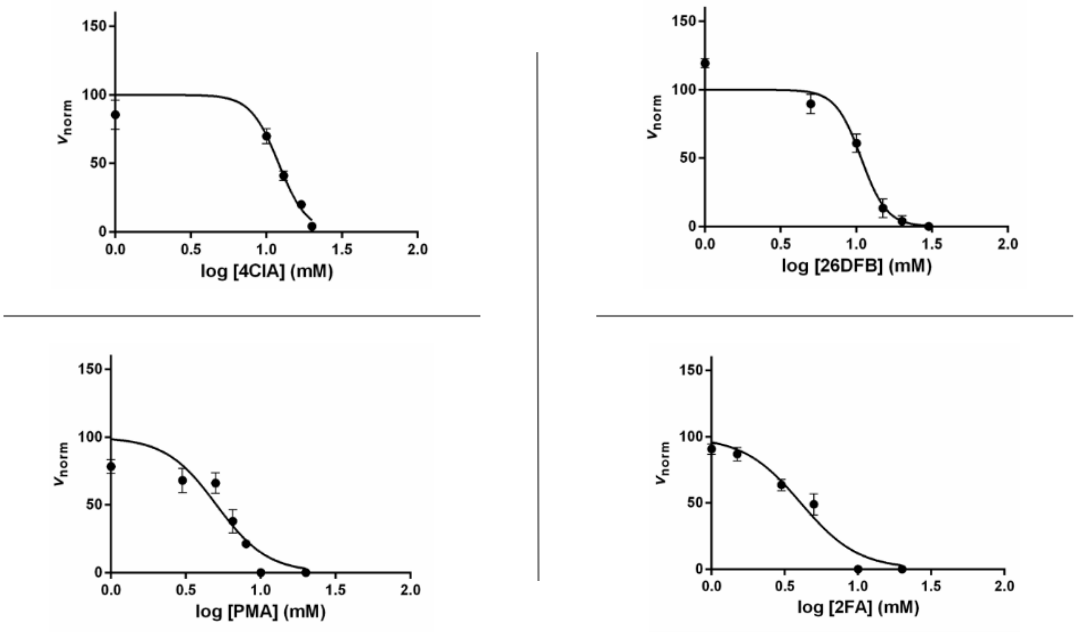

Figure 4.3 Dose response curves for 4ClA, 2,6 DFB, PMA, and 2FA generated by the modified splat cooling assay. IC_{50} curves were adapted from Dr. Madeline Adam's doctoral disseration.[78]

A previous work conducted by a former master's student at the Ben laboratory, Karishma Chopra, aimed to examine the ability for the four selected IRIs (2FA, PMA, 4ClA, and 2,6 DFB) formulated in a commercially available cryomedium, mFreSR™ (STEMCELL Technologies), to improve the post-thaw viability and functionality of iPSCs.[84] According to Karishma Chopra, formulating 0.5 mM of 4ClA, 5 mM and 10 mM of 2FA, and 15 mM of PMA in mFreSR™ resulted in a 20% increase in the immediate

post-thaw viability compared to iPSCs frozen with mFreSR™ alone (control), **S. Figure 4.1 A**.[84] Moreover, 48-hour post-thaw toxicity of the four different IRIs was assessed using the BioRad Zoe™ imaging system by comparing cell density and morphology between the different conditions and the control (mFreSR™), as shown in **S. Figure 4.1 B**.[84] It is evident that the formulation of 10 mM 2FA in mFreSR™ did not alter the colony size and morphology compared to mFreSR culture. Wherease 4ClA, PMA and 2,6 DFB cultures had a delayed cytotoxicity effect, as suggested from the change in the colony size and morphology compared to control (mFreSR™). This suggests that supplementing 10 mM 2FA in mFreSR may enhance the cryopreservation outcomes (i.e., higher viability and no toxicity effects) post-thaw.[84]

Chopra also assessed of the post-thaw functionality of 2FA-frozen iPSCs using an *in vivo* xenograft teratoma assay to confirm the ability of iPSCs to generate three germ layers (the ectoderm, endoderm, and mesoderm layers).[84-85] As shown in **S. Figure 4.2**, iPSCs frozen with 10 mM 2FA supplemented in mFreSR™ did not alter the capability of iPSCs to generate the three germ layers compared to cultures that were frozen with mFreSR™ alone.

Overall, formulation of 10 mM 2FA in mFreSR™ (STEMCELL Technologies) resulted in a higher post-thaw viability compared to mFreSR™ alone. 2FA-frozen iPSCs also retained their pluripotency features (assessed by a teratoma assay).[84] Therefore, we sought to discover whether 2FA could enhance the cryopreservation outcomes of iPSC-Ns which are more sensitive to freezing and thawing processes.

4.2.2.2 Differentiation of iPSCs into iPSC-Ns and the Evaluation of IRIs to Enhance Cryopreservation Outcomes of iPSC-Ns

As mentioned in **section 4.1**, given the length of time required to differentiate iPSCs into functionally mature neurons and the post-mitotic nature of iPSC-Ns, cryopreservation of these cells remains key to support research and development as well as clinical applications.[32-33] In this project, STEMCELL Technologies' protocol for differentiating iPSCs into iPSC-Ns was used to generate a mixed population of forebrain neurons.[121] As shown in **Figure 4.4**, iPSCs were thawed and cultured in mTeSR1 media (STEMCELL Technologies) for 5 days. Induction and expansion of iPSCs into iPSC-NPCs were initiated using directed monolayer SMAD inhibition-mediated differentiation medium (STEMCELL Technologies), which took 14 days to fully obtain iPSC-NPCs. iPSC-NPCs were then differentiated into neurons by transitioning to BrainPhys Neuronal Medium supplemented with SM1 (STEMCELL Technologies), followed by the addition of neurotrophic growth factors which are the glial cell line-derived neurotrophic factor (GDNF), the brain-derived neurotrophic factor (BDNF), dibutyryl cyclic adenosine monophosphate (dbcAMP), and ascorbic acid, to assist the maturation of iPSC-Ns.[121]

The generation of fully differentiated and mature iPSC-Ns from iPSC-NPCs required 49 days. Once the iPSC-Ns were fully matured, they were frozen in duplicates in a GMP-compatible cryo-solution that contains 10% of DMSO, Cryostor®10 (CS10, STEMCELL Technologies), or in CS10 supplemented with different concentrations of 2FA (10 mM, 5 mM, and 2.5 mM). Frozen iPSC-Ns were allowed to cool to -80 °C using a Mr. Frosty rate-controlled freezing container (-1 °C/min) overnight. iPSC-Ns were then transferred to a liquid nitrogen dewar for long-term storage. iPSC-Ns were thawed two

months after cryopreservation. The post-thaw viability as well as the electrophysiological firing activity were assessed using the Trypan blue exclusion assay and microelectrode array (MEA), respectively.

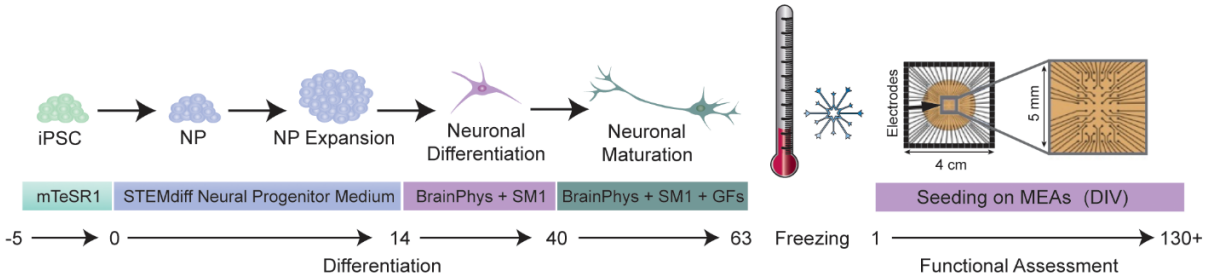

Figure 4.4 A schematic diagram of the iPSC-Ns differentiation protocol. Human iPSCs were cultured in mTeSR1 for 5 days. The medium was switched to STEMdiff neural progenitor medium (14 days) to stimulate the differentiation into neural progenitor cells (iPSC-NPCs). After the expansion of iNPCs, the medium was switched into BrainPhys, containing SM1, for 26 days to drive the differentiation into iPSC-Ns. The neurotrophic factors BDNF and GDNF, as well as dbcAMP and ascorbic acid were then added to the medium to induce neuronal maturation and specification (10-12 days). At day 63, the cells were lifted and counted for cryopreservation (control cryo-solution medium: Cryostor®10, or 2FA-formulated in Cryostor®10). Live and dead cells were counted immediately upon thawing using Trypan Blue exclusion assay. The thawed iPSC-Ns were also plated on microelectrode array plates (MEAs) to assess post-thaw functionality. Figure created using a free license from BioRender.

4.3 Post-Thaw Viability and Recovery Rate of 2FA-Frozen iPSC-Ns

Cellular injuries associated with cryopreservation often alter cell membrane integrity, exposing cellular components such as the cytoplasm and nucleus.[86] Many dye-exclusion tests, such as with Trypan blue, allow for the measurement of post-thaw viability and recovery, relying on the fact that viable cells have intact cell membrane, and thus, they are not permeable unlike a dead cell with a damaged cell membrane that is permeable and can absorb the dye.[86] In the Trypan blue exclusion assay, the dye permeates the cell membrane and binds to intracellular proteins, which causes the staining and the blue colouring of the dead cells.[86]

Two of the initial parameters to consider when evaluating cryopreservation procedures are post-thaw viability and recovery rates.[127] Viability refers to the number of live cells over the total number of cells (both live and dead cells) counted post-thaw, whereas recovery rate (percent yield) takes into consideration the number of cells that were frozen initially, in other words, it represents the percentage of viable cells over the total quantity of frozen cells.[127]

4.3.1 Cryoprotective Capacity of 2FA in iPSCs

Previously, Chopra reported that formulation of 10 mM 2FA in a commercially available cryomedium (mFreSR™) resulted in an increase in the post-thaw viability (~20% fold) and the proliferation rate of iPSCs (~ 2-fold increase) in comparison to mFreSR™-frozen iPSCs.[84] In addition, cryopreservation of iPSCs in the presence 2FA did not alter their functionality which was confirmed by xenograft teratoma assay.[84] Therefore, 2FA was further tested on iPSC-Ns.

4.3.2 Potential IRIs for the Cryopreservation of iPSC-Ns

Fully matured neurons were reached on day 63; they were then dissociated and frozen at a concentration of 1E6 cells in 1 mL of CS10 cryomedia in the presence or absence of 2.5 mM, 5 mM, or 10 mM 2FA. The iPSC-Ns were thawed approximately two months after cryopreservation utilizing a fast rate of thawing by submerging the cryovials in a 37 °C waterbath. Frozen iPSC-Ns were cultured in BrainPhys Neuronal Medium supplemented with SM1, growth factors, and ROCK inhibitor (Y-27632), also known as Rho-associated, coiled-coil containing protein kinase inhibitor, which are important component for the maturation of neurons and the formation of neurites.[122-123] The presence of ROCK inhibitor (Y-27632) in iPSC-Ns culture within 24 hours post-thaw is vital to

prevent cell death associated with the loss of E-cadherin and to assist in the establishment of neural networks.[79,124-126] Since neurite branching is regulated, in part, by the rho kinase pathway, ROCK inhibitor treatment has been shown to increase neurite formation (within 24 hours) without any adverse effects on neuronal maturity or electrophysiological properties in iPSC-Ns as well as other neuronal cell types.[124-126] Therefore, cryopreserved iPSC-Ns were seeded in the presence of 10 μM of ROCK inhibitor.

Immediate post-thaw viability and recovery rates were quantified using the Trypan blue exclusion assay. As shown in the bar graph in **Figure 4.5 A**, it is evident that mean post-thaw viability of iPSC-Ns frozen with 5 mM and 2.5 mM 2FA in CS10 increased compared to CS10 alone: (65.3% ± 5%), and (67.2% ± 6%) vs (54% ± 1%), respectively. The mean post-thaw viability of 10 mM 2FA-frozen iPSC-Ns was similar to that of CS10, which was found to be 56.7% ± 1%. The post-thaw viability of CS10-frozen iPSC-Ns is consistent with CS10 viability statistics that were published previously for other iPSC-N subtypes (~70%).[67] Moreover, a one-way ANOVA test with Dunnett's multiple comparisons suggests that there is no trend in the number of viable cells vs formulations of 2FA in CS10, where the number of viable 2FA-frozen iPSC-Ns did not increase (P value > 0.1, n = 2) compared to CS10-frozen ones.

The mean recovery rate of iPSC-Ns frozen with 2.5 mM 2FA was found to be lower than that of CS10 (**Figure 4.5 B**). Whereas the recovery rate of 10 mM and 5 mM 2FA-frozen iPSC-Ns were found to be higher than CS10-frozen cells (~ 1.5-fold increase, **Figure 4.5 B**). The percentage mean recovery for CS10 was 32.2% ± 1%, 10 mM 2FA was 45.0% ± 0.7%, 5 mM 2FA was 50.3% ± 2%, and 2.5 mM 2FA was 35.0% ± 6%. A one-way ANOVA test where the recovery of 2FA-frozen iPSC-Ns were compared to the CS10-

frozen ones suggest that there is an increase in the average percent yields for both 10 mM and 5 mM 2FA cultures compared to CS10 alone (P value < 0.1, n = 2), emphasizing the necessity of evaluating the post-thaw recovery rate in addition to viability when analyzing the efficacy of cryopreservation protocols.[127] These preliminary results suggest that controlling ice growth and recrystallization during cryopreservation is valuable. This was implied by the capacity of an IRI, 2FA, to maintain a high number of viable and mature iPSC-Ns.

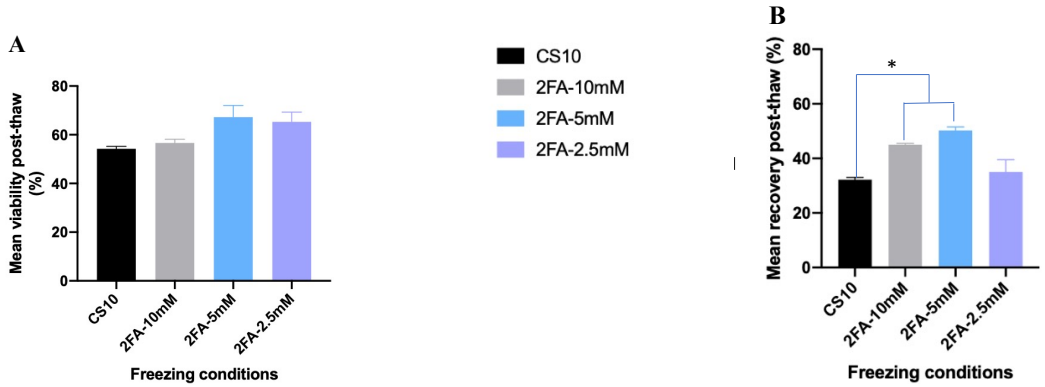

Figure 4.5 (A) The mean post-thaw viability of iPSC-Ns and **(B)** the mean post-thaw recovery of the different freezing conditions. iPSC-Ns were cryopreserved in duplicates in CS10 in the presence or absence of 2FA (10 mM, 5 mM, and 2.5 mM). iPSC-Ns were thawed in a 37 °C water bath after two months and the immediate post-thaw viability and recovery were assessed using the Trypan blue exclusion assay. Error bars are presented as the standard error of mean (SEM). One-way ANOVA test was performed where the 2FA-frozen iPSC-Ns were compared to the CS10-frozen ones. Immediate post-thaw recovery rate of iPSC-Ns frozen with 10 mM and 5 mM 2FA significantly increased in comparison with CS10-frozen iPSC-Ns (* = P value < 0.1, n = 2).

4.4 Elucidating the Effect of 2FA on the Morphology of the Cryopreserved iPSC-N Cultures

Neurons are specialized cells that can send and receive electrical impulses and neurochemical signals to process information in the CNS.[67] The transmission of electrical signals and neurotransmitters is done via synaptic- or membrane-associated receptors/channels, such as gamma aminobutyric acid (GABA) receptor and

synaptotagmin.[67,87-101] iPSC-Ns can also be differentiated into different kinds of neurons, such as dopaminergic or GABAergic neurons.[54,67] Nonetheless, cryopreservation of iPSC-Ns can result in detrimental effects on the morphology of the cells as well as the expression of the receptors and channels. Therefore, we sought to examine whether employing IRIs in the cryopreservation protocol of iPSC-Ns would maintain the morphology of the cells as well as the expression of significant synaptic and membrane-associated receptors.

4.4.1 Synaptic and Membrane-Associated Neuronal Markers

Cryopreserved iPSC-Ns were subjected to immunostaining to identify any variation in the expression of important neural markers. The neural markers that were stained for were: β tubulin III, GFAP, MAP2, NeuN, NMDAR, GABA, synaptotagmin, GAD, VGlut, ChaT, Synaptophysin, and Nestin. The primary and secondary antibodies utilized to stain for the different markers/receptors are described in **Supplementary Tables (S. Tables) 4.2-4.3**.

A. *β tubulin III*

General tubulins play a wide range of roles in the cellular processes such as mitosis and motility, however, beta (β) tubulin III is specifically localized in neurons. β tubulin III belongs to the tubulin protein family that form the microtubule network.[87-88] β tubulin III compromises the major components of microtubules in neurons, and therefore, it has been used as a marker to identify neurons that are differentiated from stem cells.[121]

B. *GFAP*

Glial fibrillary acidic protein, GFAP, is a type III intermediate filament protein that is expressed in the cytoskeleton of different types of CNS cells, such as astrocytes and ependymal cells. GFAP plays role in cell communication and function with blood brain

barrier.[89-90] Staining for GFAP allows for differentiation between astrocytes and neurons in a mixed population.[121]

C. *MAP-2*

Microtubule-associated proteins (MAPs) are diverse proteins that conjugate to tubulins and promote the assembly of microtubules. MAP-2 is a heat-stable, phosphoprotein and is specifically found in the dendrites of neurons, which are important for transmitting electrical information to the cell body.[91] Staining for MAP-2 permits the identification of mature neurons in a mixed population.[121]

D. *NeuN*

Neuronal nuclear protein (NeuN) is a specific neuronal marker because it is only found in the nuclei and perinuclear cytoplasm of post-mitotic neurons.[92] Therefore, immunocytochemistry analysis of a mixed population of iPSC-Ns by staining for NeuN allows for the identification of differentiating and terminally differentiated neurons.[121]

E. *NMDAR*

N-methyl-D-aspartate receptors (NMDARs) are glutamate-specific receptors that are significant for higher functions in the CNS, such as learning and memory.[93] NMDARs are ligand-gated ion channels which cause an influx of cations, initiating signal transduction.[93] Staining for NMDARs confirms the presence of glutaminergic neurons in an iPSC-N population.[121]

F. *GABA*

Gamma aminobutyric acid (GABA) is an inhibitory neurotransmitter that is produced by GABAergic neurons.[94,121] The inhibitory mechanism of action is related to chloride or potassium efflux which reduces the action potential and inhibits synaptic

function.[94] $GABA_B$ receptors are G-protein linked and transmembrane receptors that are found in the neuronal membrane.[94] Immunocytochemistry analysis helps to identify GABAergic neurons in a mixed population of iPSC-Ns.[121]

G. *Synaptotagmin*

Synaptotagmins (Syts) are proteins that are found on synaptic vesicles and allow fast synaptic transmission.[95] They are referred to as membrane-trafficking proteins that consist of an N-terminal transmembrane region, a linker, and two C-terminal domains.[95] Synaptotagmins are found in mature neuronal networks, and therefore, they are key neural markers for identifying fully differentiated iPSC-Ns.[121]

H. *GAD 65 and 67*

Glutamic acid decarboxylase (GAD) is an enzyme that catalyzes the synthesis of the GABA neurotransmitter.[96] It exists in two isoforms GAD 65, which is expressed in CNS and pancreas, and GAD 67, which is CNS-specific.[96] Immunostaining for GAD 65 and 67 identifies mature GABAergic neurons.[121]

I. *VGlut2*

Vesicular glutamate transporter 2 (VGlut2) is a protein that is expressed in the synapses of neuron-rich regions for transporting the excitatory glutamate neurotransmitter.[97] VGlut2 function is highly dependent on the concentration of extravesicular chloride.[97] VGlut2 exchanges chloride for glutamate when the concentration of chloride is high in the extravesicular region.[97] Staining for VGlut2 determines the presence of selective vesicles in the synapsis, allowing the identification of a mature glutaminergic neural network in an iPSC-N population.[121]

J. *ChAT*

Choline Acetyltransferase (ChAT) is an enzyme that catalyzes the synthesis of the acetylcholine neurotransmitter which is significant for signal transduction.[98] The presence of ChAT in an iPSC-N population indicates the presence of cholinergic neurons.[121]

K. *Synaptophysin*

Synaptophysin (Syp) is a calcium-binding glycoprotein that is found in the presynaptic vesicle membranes.[99] It plays a significant role in exocytosis, synapse formation and endocytosis.[99] Therefore, it is a key neuronal marker as it helps to identify mature synapses in iPSC-N cultures.[121]

L. *Nestin*

Nestin, neuroepithelial stem cell protein, belongs to type VI intermediate filament protein category. It is specifically found in neural progenitor cells (NPCs).[100] NPCs give rise to neurons following differentiation process, and thus, nestin is replaced by neural-specific proteins.[100] Staining for nestin allows for the identification of undifferentiated neurons, specifically iPSC-NPCs.[121]

4.4.2 2FA Does Not Compromise the Expression of Key Neural Markers

Immunofluorescence staining for different neural markers was done on cryopreserved iPSC-Ns to identify any changes in the morphology of the cells and the expression of key neuronal receptors/channels post-thaw. CS10- and 2FA-frozen iPSC-Ns were plated and matured for 28 days on 12-well plates with 15 mm round coverslips that were coated with Matrigel in growth medium. The cells were then incubated with primary and secondary antibodies (**S. Tables 4.2 and 4.3**) to stain for the different markers and receptors: β tubulin III, GFAP, MAP2, NeuN, NMDAR, GABA, synaptotagmin, GAD, VGlut2, ChaT, synaptophysin, and nestin.

As depicted in **Figure 4.6**, immunostaining was conducted on all cryopreserved iPSC-Ns to verify the expression of neural markers. The iPSC-Ns frozen in 2FA and CS10 had a neuronal morphology with distinct cell bodies and neurite extensions, as well as the expression of key neural markers such as β III tubulin (a microtubule element exclusive for neurons, **S. Figure 4.3**), MAP2 (an excellent marker of neuronal cells, **S. Figure 4.4**) and NeuN (neuronal nuclei, stains mature neurons, **S. Figure 4.4**). The presence of synapses was assessed by the expression and localization of synaptic proteins, such as synaptotagmin (**S. Figure 4.6**) and synaptophysin (**S. Figure 4.7**). Staining for some of the iPSC-N channels and receptors (i.e., $GABA_A$ receptor and NMDAR, **S. Figure 4.5**) allowed for the identification of the specific type of neurons present in the cryopreserved iPSC-N cultures (i.e., GABAergic and glutaminergic neurons). Furthermore, staining of the different neural markers and receptors in the cryopreserved cultures of iPSC-Ns was compared to the unfrozen cultures of iPSC-Ns that was reported by Jezierski *et al* (**S. Figure 4.9**).[121] Comparing **Figure 4.6** with **S. Figure 4.9** confirmed that employing IRIs in the cryopreservation protocol of iPSC-Ns did not change their morphology, nor did it compromise the development of key neural receptors/channels.

Quantification of GABA and glutamine receptors using $GABA_A$ (**S. Figure 4.5**), GAD 65 + 67 (**S. Figure 4.7**), VGLUT2 (**S. Figure 4.8**), and NMDAR (**S. Figure 4.5)** pictures revealed the presence of ~65% GABAergic neurons and ~35% glutaminergic neurons. Jezierski *et al.* previously reported that using STEMCELL Technologies' protocol for differentiating iPSCs into iPSC-Ns results in a mixed population of GABAergic and glutaminergic (65% and 35%, respectively) neurons in non-frozen cultures of iPSC-Ns [121] which was in agreement with that of the iPSC-N cultures that were frozen in the presence

or absence of 2FA. This confirmed that CS10 and formulations of 2FA in CS10 did not alter the expression of the different inhibitory and excitatory receptors on iPSC-Ns post-thaw.[121]

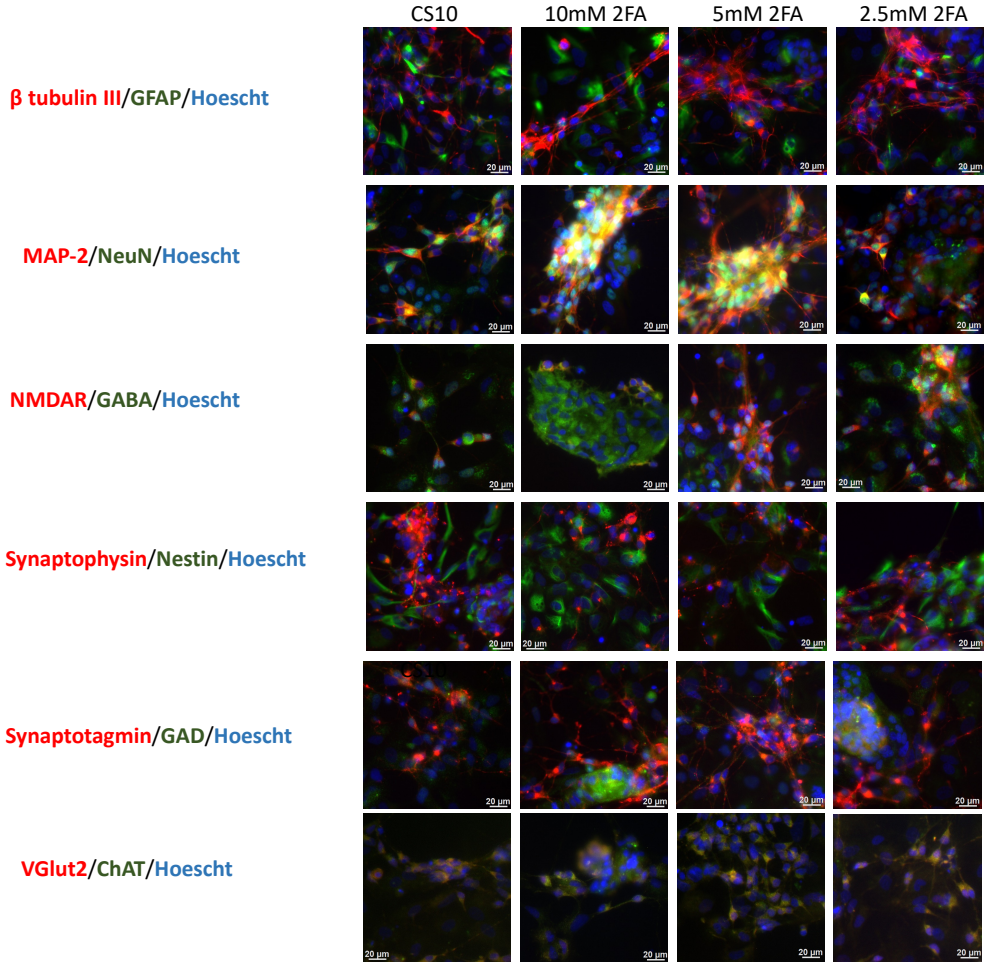

Figure 4.6 Pictures of immunofluorescence staining for the cryopreserved iPSC-Ns markers at day 28 post-thaw. Cryopreserved iPSC-Ns were plated on coverslips and grown for 28 days, followed by fixing the cells in 10% formalin and staining with different neuronal markers: β III tubulin, GFAP, MAP2, NeuN, NMDAR, GABA, synaptotagmin, GAD, VGlut2, ChaT, Synaptophysin, Nestin. Cells were counter stained with Hoechst (blue). Scale bar = 20 µm.

From immunocytochemistry analyses, it is evident that 2FA-frozen iPSC-Ns retained the expression of key neural markers, confirming the maintenance of mature neurons after cryopreservation. The efficacy of the cryopreservation protocol was further assessed by examining the firing activity of the frozen iPSC-Ns in the presence or absence

of neuroactive drugs. The functionality of the cryopreserved iPSC-Ns was also compared to that of the non-frozen cultures to confirm whether incorporating IRIs in the cryopreservation protocol of iPSC-Ns alters their post-thaw functionality.

4.5 Assessment of the Capacity of 2FA to Maintain Functional iPSC-Ns Post-Thaw

Given that CS10- and 2FA-frozen iPSC-Ns retained the expression of key neural receptors and channels, suggested by immunofluorescence staining, we then analyzed their functional output using a microelectrode array (MEA) system to assess their electrophysiological activities.[67] Mature, and functional neural networks produce spontaneous electrical activity which can be translated into action potential spikes and synchronized patterns of action potential bursts.[102,105] An MEA monitors the activity patterns of neural networks, allowing for a better understanding of the effect of cellular damage associated with cryopreservation on iPSC-Ns.[102-107] Therefore, we sought to evaluate the post-thaw functionality of the cryopreserved iPSC-Ns by assessing the firing activity between neural networks and the pharmacological responses upon treatment with a panel of neuroactive drugs.

4.5.1 Microelectrode Array (MEA) Methodology for Recording iPSC-Ns Activity

iPSC-Ns have been employed as effective *in vitro* model systems for disease modelling and drug discovery research.[107] They are projected to reproduce human neural networks more accurately than rodent neurons.[107,121] Therefore, it is significant to establish an optimized cryopreservation protocol to maintain viable and functional iPSC-Ns. From **sections 4.3.2** and **4.4.2**, we observed that 2FA-frozen iPSC-Ns had higher recovery rate compared to cells frozen with CS10 alone, and that cryopreservation of iPSC-Ns with 2FA

did not compromise the expression of key neural markers and receptors. However, a key characteristic of a successful cryopreservation procedure is to have neurons that can produce electrical signals post-thaw. Therefore, we evaluated the electrophysiological activity of cryopreserved iPSC-Ns by microelectrode array (MEA).[67] MEA is a non-invasive methodology for recording neuronal activity because it depends on the extracellular activity of neuronal networks. MEAs were first discovered by Thomas *et al.* in 1972 and are described as small glass plates containing multiple microelectrodes that can detect the neural signals produced by fully mature, differentiated iPSC-Ns, as shown in **Figure 4.7**.[4,108]

Different aspects of *in vitro* network activity, such as bursting and spike count, can be monitored and measured using the raw data generated from recordings of the electrical activity of neurons cultured on MEAs.[121] Many computational toolboxes such as MatLab and Neuroexplorer have been used to extract neural activity parameters (i.e., the number of active electrodes as a function of time, presented as a raster plot in **Figure 4.7**).[4,109] Viable and functional cryopreserved iPSC-Ns can establish synaptic connections and display synchronous electrophysiological activity patterns that can be recorded using MEA.[4,102-108] Functional alterations detected by MEA recordings, such as a decreased number of spikes, implies an impaired neuronal network.[4,102-108] Therefore, MEA technology can help detect malfunctioning neuronal networks resulting from any delayed effects of cryopreservation on iPSC-Ns.

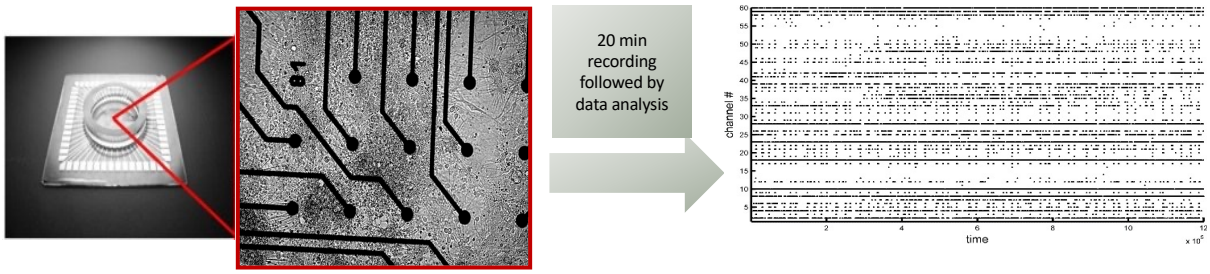

Figure 4.7 A figure representing the microelectrode array (MEA) methodology utilized to measure neural activity. Cryopreserved iPSC-Ns are plated on MEAs and grown for 19 days before recording. 20-minute recording of iPSC-Ns network activity allowed for the extraction of multiple parameters, such as the number of active electrodes as a function of time (raster plot).

4.5.2 Enhanced Synaptic Activities of 2FA-Frozen iPSC-Ns

CS10- and 2FA-cryopreserved iPSC-Ns were plated on poly-L-orthenine (PLO) coated MEA dishes at a density of 12E3 cell/mL and grown for 19 days prior to recording to give the neurons enough time to adhere to the MEA surface and to form synaptic connections, as shown in **Figure 4.8**.

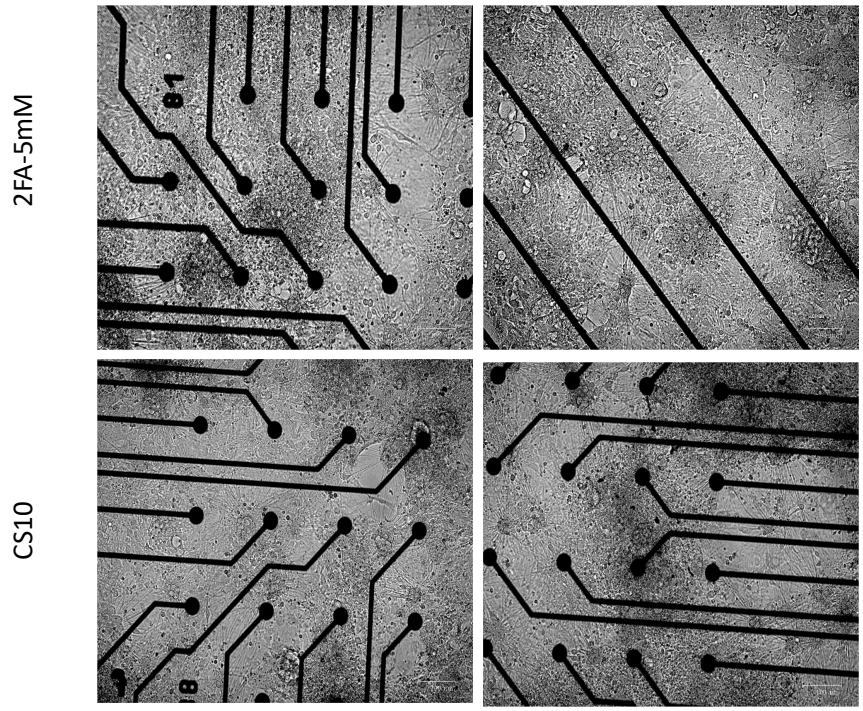

Figure 4.8 Pictures of the cryopreserved iPSC-Ns plated on PLO-coated MEA dishes. CS10- and 2FA-iPSC-Ns were plated and grown on MEA dishes for 19 days prior to recording. A routinely change of media was performed twice a week where half of the

media is drawn and replaced with a fresh complete media (BrainPhys+SM1+ Growth factors). Scale bar: 50 μm.

The development of spontaneous neuronal activity and bursting behavior of iPSC-Ns was assessed by recording the electrophysiological activity of the neuronal networks of each MEA dish for 20 minutes. MatLab software was used to process the data and to generate raster plots, which present the number of active electrodes (y-axis) as a function of time (x-axis), shown in **Figure 4.9**. At 20 days *in vitro* (DIV), the iPSC-Ns started to generate some sporadic electrical activity in a few electrodes but minor activity overall for all cryomedia conditions. From the developmental raster plots of iPSC-Ns frozen with CS10 alone (**Figure 4.9 A**), it is apparent that there was a significant delay in establishing neuronal network activity when compared to 5 mM and 2.5 mM 2FA cultures, with a robust synchronous firing activity being observed only after 130 DIV (**S. Figure 4.10**: representative developmental raster plots of CS10 culture).

Although formulation of 10 mM 2FA in CS10 significantly increased the post-thaw recovery rate in comparison to CS10 frozen cells (**Figure 4.5**), the number of active electrodes in 10 mM 2FA-frozen cultures appeared to be similar to that of CS10-frozen iPSC-Ns (**Figures 4.9 A vs B, 27 and 48 DIV**). 10 mM 2FA-frozen iPSC-Ns started to develop some activity at 27 DIV, however, there exist to be a delay in the establishing neuronal networks with synchronous firing activity where the number of active electrodes appeared to increase only after 130 DIV (**Figure 4.9 B**). The complete developmental recordings of 10 mM 2FA cultures are shown in **S. Figure 4.11**. After 27 DIV, the iPSC-Ns that were cryopreserved in 5 mM 2FA, started to show robust synchronous electrical activity, and an increase in the number of electrodes with robust bursting behavior developing by 48, 130, 156, and 190 DIV (**Figure 4.9 C**) with sustained activity over the

course of 236 days in culture (**S. Figure 4.12:** representative developmental raster plots of 5 mM 2FA culture). A similar trend was observed for 2.5 mM 2FA-frozen iPSC-Ns where the number of active electrodes with robust and synchronous electrical activity at 27 DIV was higher than that of CS10-frozen ones as shown in **Figure 4.9 A vs D**. From **Figures 4.9 C** and **D**, it is evident that supplementing 5 mM or 2.5 mM of 2FA in CS10 assists in re-establishing the functional synaptic connections between the neural networks of the cryopreserved iPSC-N cultures. The full developmental recordings of 2.5 mM 2FA cultures are presented in **S. Figure 4.13**.

The delayed response in the appearance of synchronous activity in CS10 media alone as well as 10 mM 2FA-frozen iPSC-Ns suggests that re-establishment of the neural network as well as the electrical signaling activity of iPSC-Ns is negatively affected post-thaw, compared to 2.5 mM and 5 mM 2FA-frozen cells. In addition to enhanced synaptic activity, 2FA-cryopreserved iPSC-Ns survived significantly longer on MEAs compared to CS10 cryopreserved iPSC-Ns, 236 vs 204 DIV respectively, as shown in **S. Figures 4.10-4.13**.

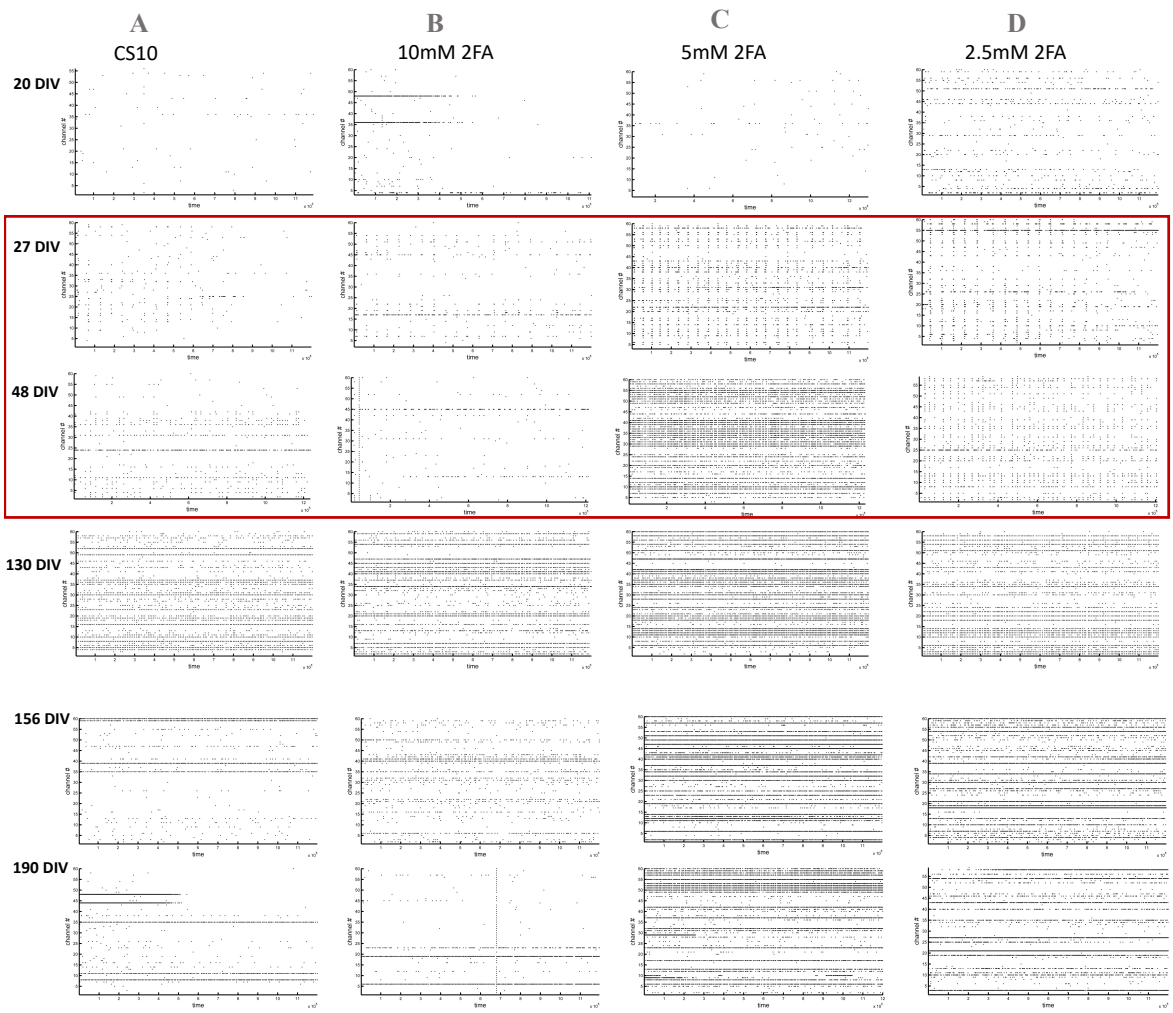

Figure 4.9 Developmental microelectrode array raster plots of cryopreserved iPSC-Ns (A: CS10, B: 10 mM 2FA, C: 5 mM 2FA, D: 2.5 mM 2FA) at 20, 27, 48, 130, 156 and 190 days *in vitro* (DIV). Microelectrode array system obtained from MultiChannel Systems (Reutlingen, Germany), with the headstage accommodating a 60-electrode MEA dish. Cryopreserved iPSC-Ns were recorded after 19 DIV. Spike analyses were performed using MatLab software. Raster plots showing developmental profile of spontaneous activity in a representative MEA of iPSC-Ns. The y axis in each plot represents the electrode or channel number (1-59) and the x-axis represents the recording time (20 min).

The developmental recordings of cryopreserved iPSC-Ns were further compared with the non-frozen cultures that were previously reported by Jezierski *et al.*[121] As shown in **S. Figure 4.14**, the non-frozen iPSC-N cultures showed robust firing activity within two weeks of plating on PLO-coated MEA dishes which can be detected by the raster plots generated from the developmental recordings.[121] Comparing the developmental raster plots

of the cryopreserved iPSC-Ns cultures with the non-frozen cultures further confirms that employing IRIs in the cryopreservation protocol of iPSC-Ns does not compromise the period at which the neural networks and synaptic activity are re-established.

4.5.3 Quantification of the Neural Activity of the Cryopreserved iPSC-Ns

The electrophysiological activity that was recorded for each culture of the cryopreserved iPSC-Ns was further quantified using NeuroExplorer (Nex technologies) software. The median number of bursts and the median number of spikes were determined to assess the functionality of the cryopreserved iPSC-Ns.[110] The number of spikes refers to the electrophysiological activity (firing activity) of each neural network detected by the MEAs. The number of bursts, on the other hand, refers to a collection of spikes within 20 minutes of recording, meaning each burst consists of multiple spikes within a time interval.

The raw voltage recordings were analyzed offline to yield multi-unit activity using NeuroExplorer (Nex technologies). Electrodes that have number of spikes (active electrodes) of less than 50 were excluded. The median number of spikes per electrode as well as the median number of bursts were obtained for each freezing condition and presented as a scatter plot (**Figure 4.10 A and B**). A generalized linear model (GLM) statistical analysis was conducted on the median number of spikes and bursts to examine any significance in the firing activity of 2FA-frozen neurons in comparison with CS10-frozen ones. GLM analysis indicates that there is a statistically significant difference in the median number of spikes ($P < 0.001$), as suggested in **Figure 4.10 A**, as well as the median number of bursts ($P < 0.001$), as depicted in **Figure 4.10 B**. The difference in the number of spikes and bursts come from 5 mM 2FA-cryopreserved iPSC-Ns which displayed a significantly higher number of active electrodes (i.e., number of spikes and

bursts) post 56 DIV compared to CS10-frozen ones It is also evident that 2.5 mM and 5 mM 2FA-frozen iPSC-Ns survived longer (236 DIV) and sustained higher numbers for firing activity, unlike CS10 cryopreserved ones which were dropped after 204 DIV due to a low number of active electrodes.

Overall, 5 mM 2FA-cryopreserved iPSC-Ns have shown earlier establishment of neural network, suggested by the higher number of spikes and bursts (56 DIV), and sustained their electrophysiological activity for longer compared to CS10-frozen ones.

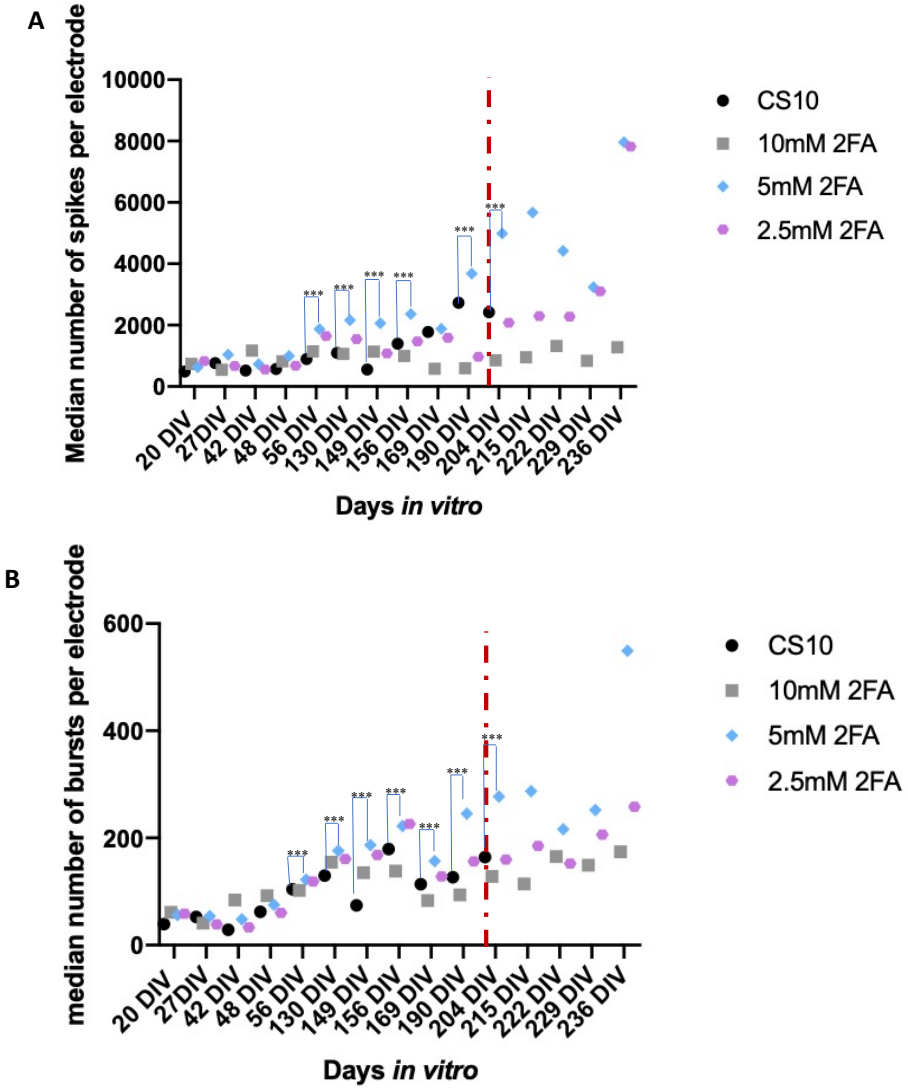

Figure 4.10 Scatter plots presenting **(A)** the median number of spikes per electrode, and **(B)** the median number of bursts per electrode assessed by MEA and quantified using

NeuroExplore. **(A)** represents the median of spikes which was determined by taking the median number of spikes per electrode per MEA dish. **(B)** corresponds to the median number of bursts which was obtained by taking the median number of bursts per electrode per MEA dish The red dashed line refers to 204 DIV, the last day where CS10 MEA dishes were recorded. A generalized linear model (GLM) analysis suggests that there is a significant difference in the median number of spikes (DIV ≥ 48) and bursts (DIV ≥ 48) between the treatments (*** = P value < 0.001, n=3).

Moreover, the mean percentage of active electrodes was quantified using NeuroExplorer (Nex technologies) and presented in **Figure 4.11**. The percent of the mean active electrodes of 5 mM 2FA-frozen iPSC-Ns was found to be ~ 30%, while the one of CS10 cultures was ~ 15%. It is evident that there was a two-fold increase in the mean percentage of active electrodes when 5 mM of 2FA was formulated in CS10, with a statistically significant difference compared to the CS10-frozen cells, suggested by a one-way ANOVA test (P value < 0.001, n = 3). This further confirmed that protection against ice recrystallization during cryopreservation using 2FA enhances the post-thaw functionality outcome of iPSC-Ns.

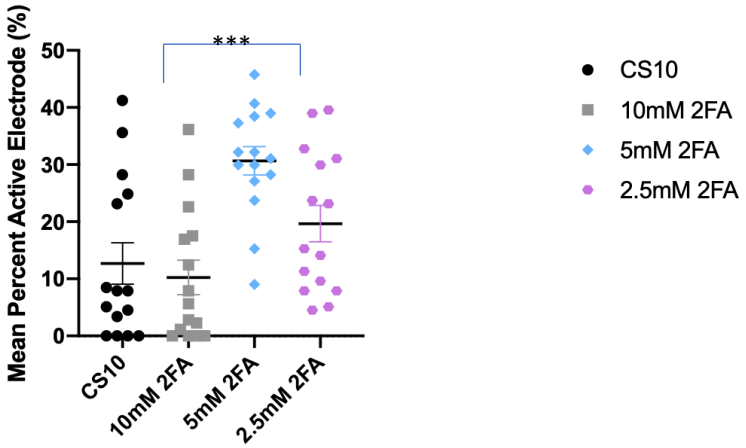

Figure 4.11 Scatter plot representing the mean percentage of active electrodes over 236 Days *in vitro* (DIV). The percentage of active electrodes was quantified using NeuroExplorer where electrodes that have less than 50 spikes were excluded. A one-way ANOVA is used to test statistical significance where *** indicates significance P value < 0.001, n = 3.

Overall, the increased recovery rate that was observed for 2FA cultures, especially for 5 mM 2FA-frozen iPSC-Ns, earlier in **section 4.3.1** can be subsequently translated to

the increased post-thaw maturation and electrophysiological activity of 2FA-cryopreserved iPSC-Ns compared to CS10-frozen iPSC-Ns. Although the cryopreserved cultures of iPSC-Ns showed a delay in establishing synchronous and spontaneous activity on MEAs compared to non-frozen iPSC-Ns (18 DIV vs 27 DIV, **S. Figure 4.14** vs. **Figure 4.9**), this delay was much shorter compared to iPSC-N cultures that were frozen with CS10 alone. To explain, Jezierski *et al.* have addressed that the number of active electrodes in non-frozen iPSC-N cultures over 11 weeks increases continuously, presented in **S. Figure 4.14 B**.[121] Similarly, the median number of spikes and bursts per electrode for 5 mM and 2.5 mM 2FA cultures increased continuously over 30 weeks (**Figure 4.10 A-B**). Ultimately, formulations of 5 mM of 2FA in CS10 did not only enhance the post-thaw recovery but also decreased the time frame required for re-establishing the firing activity of cryopreserved iPSC-Ns as suggested from the number of spikes, bursts, and percent active electrodes.

4.5.4 Assessment of the Pharmacological Responses of the Cryopreserved iPSC-Ns

Changes in the firing activity (i.e., firing rate) were examined after treatment with a panel of neuroactive drugs to verify that the functionality of the different channels and receptors present on the cryopreserved iPSC-Ns was not compromised post-thaw.[121] The concentration of each drug was chosen higher than its IC_{50} to ensure an effect on the firing activity.[111-118,121] The same panel of GABA agonists/antagonists and glutamate receptor antagonists was evaluated in CS10- and 2FA-frozen iPSC-Ns.[111-118,121] 5 mM 2FA-frozen iPSC-Ns were further treated with acetylcholine agonist, sodium channel antagonists, calcium channel antagonists and potassium channel antagonists.[121] The treatment regimen for neuropharmacological assessment is depicted in **Figure 4.12**. CS10- and 2FA- frozen

iPSC-Ns were plated and grown on MEA dishes for 47 days prior to treating them with neuroactive drugs. Before each recording, the MEAs were equilibrated for 10 minutes after transferring the MEA dish to the head-stage housed within a 37 °C incubator. Prior to treatment, a pre-drug recording was performed to acquire the mean firing rate (MFR) for each active electrode, which was then normalized to 100% to allow relative comparisons of the effect of a drug on the MFR of each electrode. Upon treatment with a neuroactive drug, the spiking frequency per electrode per MEA may increase or decrease depending on the drug's mechanism of action, as depicted in the raster plots in **Figure 4.12**.

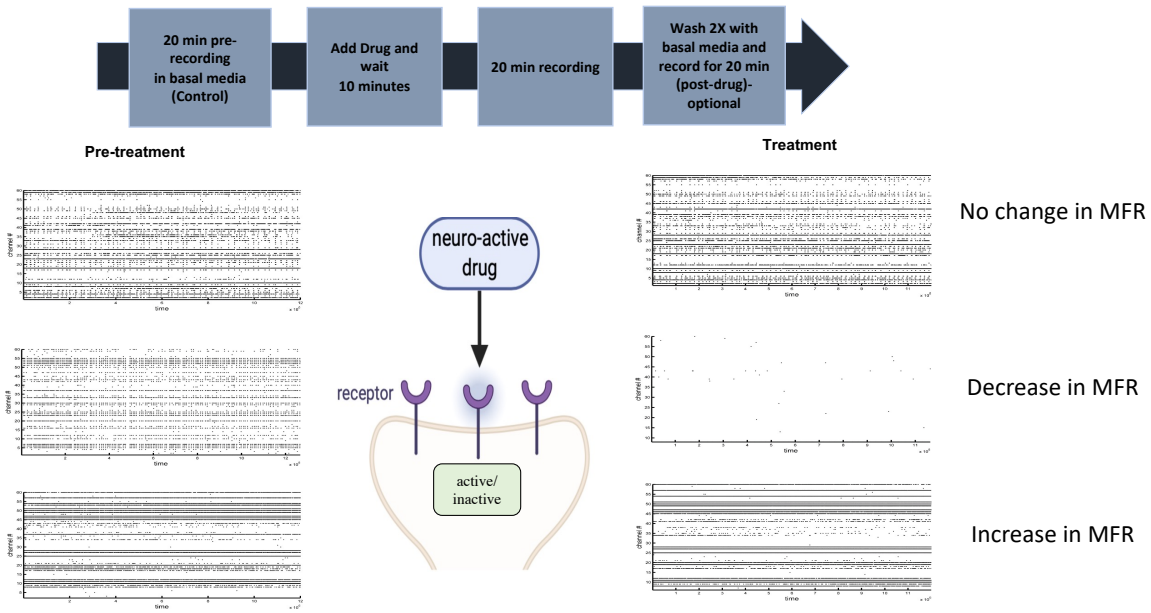

Figure 4.12 Treatment regimen for the neuropharmacological assessment of cryopreserved iPSC-Ns using MEAs. CS10- and 2FA-iPSC-Ns were plated and grown on MEA dishes for 47 days prior to treating them with neuroactive drugs. Before each recording, the MEAs were equilibrated for 10-15 minutes after transferring the MEA dish to the headstage housed within a 37 °C incubator. The cells were recorded for 20 minutes pre-drug treatment, followed by a 20-minute recording of the MEA upon the supplementation with neuroactive drug. Rastor plots generated from MEA recordings allowed for the detection of the drug effect on each MEA (activation or inactivation of neuronal receptors/channels). The drug was then washed out and the medium was restored to the MEA.

4.5.4.1 The Mechanism of Action of the Neuroactive Drugs Utilized for the Neuropharmacological Assessment

A panel of neuroactive drugs was selected to be tested on cryopreserved iPSC-Ns to measure the change in the MFR upon treatment. The effect of each drug on the cryopreserved iPSC-Ns was then compared to that of the non-frozen iPSC-N cultures.[121] Below is a description of each drug and their mechanism of action:

A. GABA Receptor Agonists/Antagonists:

From the immunocytochemistry analysis, it was observed that 65% of the mixed population of iPSC-Ns was GABAergic neurons, meaning they express GABA receptors. Therefore, the maturity and functionality of these receptor was evaluated by the treatment with GABA agonists and antagonists. GABA is an inhibitory neurotransmitter in the CNS system, and therefore, activation of GABA receptors results in a deactivation of the firing activity of neurons.[111-112]

A **GABA agonist** impacts one or more of the GABA receptors ($GABA_A$, $GABA_B$ and $GABA_C$), whereas **muscimol** is a potent $GABA_A$ receptor agonist.[111] Upon the binding of such drugs, the inhibitory GABA receptors get activated which results in the inhibition of the firing activity of iPSC-Ns.[111] On the other hand, GABA antagonist drugs such as **bicuculline** competitively bind onto GABA receptors and inhibit the action of GABA, resulting in a continuous firing activity of iPSC-Ns.[112]

B. Glutamate Receptor Antagonists:

There were ~35% of glutaminergic neurons present in the subpopulation of the cryopreserved iPSC-Ns, as discussed in **section 4.2.2**. Therefore, CS10- and 2FA-frozen

iPSC-N cultures were treated with glutamate receptor antagonists to evaluate their functionality post-thaw.

There are two main subtypes of glutamate receptors: the *N*-methyl-D-aspartate (NMDA) receptor and the α-amino-3-hydroxyl-5-methyl-4-isoxazole-propionate (AMPA) receptor.[113] Glutamate antagonists such as **memantine** (an NMDAR-specific antagonist) and 2,3-dioxo-6-nitro-7-sulfamoyl-benzo[f]quinoxaline (**NBQX**, an AMPAR-specific antagonist) work by inhibiting the excitatory activity of glutamate receptors in the brain,[113] resulting in inactivation of the firing activity of iPSC-Ns, and thus the MFR of the cryopreserved iPSC-Ns decreases.

C. Acetylcholine Receptor Agonists:

The differentiation of iPSCs into iPSC-Ns generates a mixed population of forebrain neurons.[121] Moreover, staining of the cryopreserved iPSC-Ns revealed that the iPSC-N cultures express ChAT enzyme (Choline Acetyltransferase) which catalyzes the synthesis of acetylcholine neurotransmitter (**section 4.2.2**). Therefore, the CS10- and 2FA-frozen iPSC-Ns were treated with an acetylcholine receptor agonist (i.e., nicotine) to further verify the presence of functional acetylcholine receptors.

Acetylcholine is an excitatory neurotransmitter that binds to acetylcholine receptors found in the neuromuscular junctions.[114] Nicotine is an example of an acetylcholine agonist that activates the receptor and causes depolarization of the target cells.[114] Therefore, treatment with **nicotine** can either increase or maintain the bursting activity of iPSC-Ns.

D. Calcium Channel Antagonists:

Neurons are highly polarized cells with distinct functional and morphological characteristics between dendrites and axons. The expression of voltage-gated ion channels

is a crucial determinant for the molecular and functional identity of axonal and dendritic segments.[128] Several ion channels, such as calcium channels, are distributed between dendrites and axons, therefore, the mixed population of cryopreserved iPSC-Ns was treated with a calcium channel antagonist (i.e., verapamil) to examine the integrity of their functionality post-thaw.

Blockers of calcium (Ca^{2+}) channels such as **verapamil** suppress the movement of calcium through Ca^{2+} channels, which in turn decreases the firing activity of iPSC-Ns, and therefore the MFR decreases.[115,121]

E. Potassium Channel Antagonists:

The functionality of other ion channels that may be expressed on iPSC-Ns, such as potassium (K^+) channels, was further evaluated by the treatment with a K^+ antagonist. Inhibitors of potassium channels such as **4-aminopyridine** (4AP) block the strong K^+ currents, increasing the action potential duration and firing activity of iPSC-Ns.[116] Thus, treatment with 4AP results in an increase in the MFR of the cryopreserved iPSC-Ns.

F. Sodium channel Antagonists:

The functionality of sodium (Na^+) channels was also tested by treating the cryopreserved iPSC-N cultures with Na^+ antagonists. Blockers of sodium channels such as **phenytoin** and **tetrodotoxin (TTX)** inhibit the influx of Na^+ ions which slows the rate and amplitude of depolarization and reduces the cell excitability.[117-118] This, in turn, results in a decrease in the firing activity and the MFR of iPSC-Ns.

4.5.4.2 The Effect of the Neuroactive Drugs on the MFR of the Cryopreserved iPSC-Ns

Depending on the mechanism of action of each neuroactive drug, the firing activity of the neural networks of the cryopreserved iPSC-Ns may increase or decrease. **Figures**

4.13 A-C represent raster plots of the spontaneous recordings obtained before and following the addition of GABA agonist (10 μM), muscimol (1 μM), and NBQX + memantine (10 μM + 10 μM), to assess any changes in the activity of GABA and glutamate receptors in the cryopreserved iPSC-N cultures. It is evident that the treatment of iPSC-Ns with GABA agonist drugs, such as GABA agonist and muscimol (**Figures 4.13 A-B**), resulted in a significant reduction in the firing activity, which is implied by a reduction in the number of active electrodes over the recording time (20 minutes). This confirms that cryopreservation of iPSC-Ns with CS10 and 2FA did not compromise the expression of GABA receptors nor their inhibitory activity post-thaw. Moreover, the addition of a mixture of NBQX (10 μM) and memantine (10 μM) (glutamate receptor antagonists) onto iPSC-N cultures resulted in the deactivation of the glutamate receptors which is detected by the reduction in the number of active electrodes in raster plots, presented in **Figure 4.13 C**. This indicates that incorporation of IRIs into the cryopreservation protocol of iPSC-Ns did not disrupt the activity of glutamate receptors post-thaw.

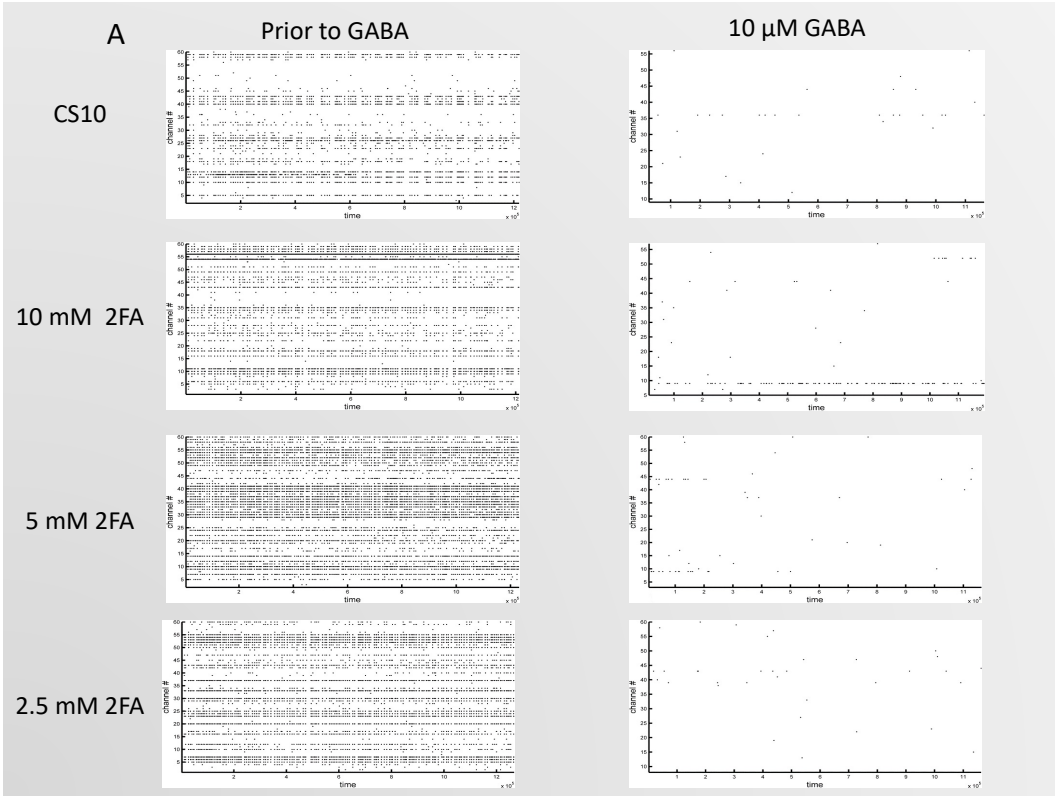
A
Prior to GABA
10 µM GABA
CS10
10 mM 2FA
5 mM 2FA
2.5 mM 2FA
channel #
time

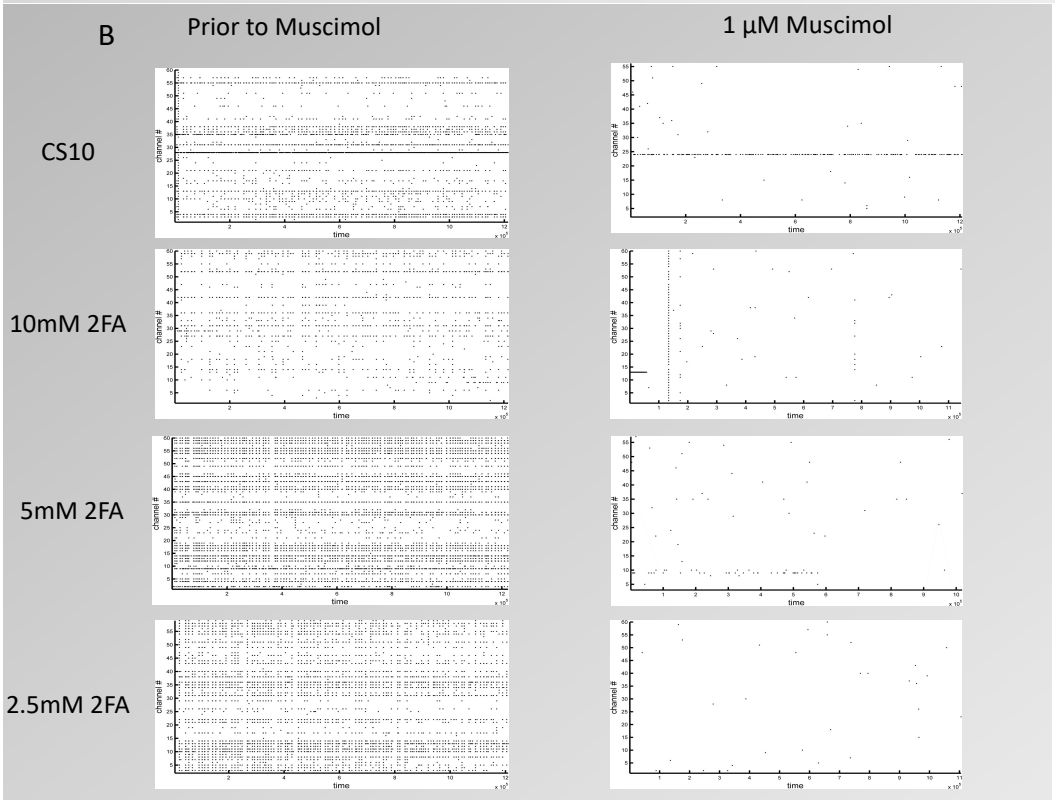
B
Prior to Muscimol
1 µM Muscimol
CS10
10mM 2FA
5mM 2FA
2.5mM 2FA
channel #
time

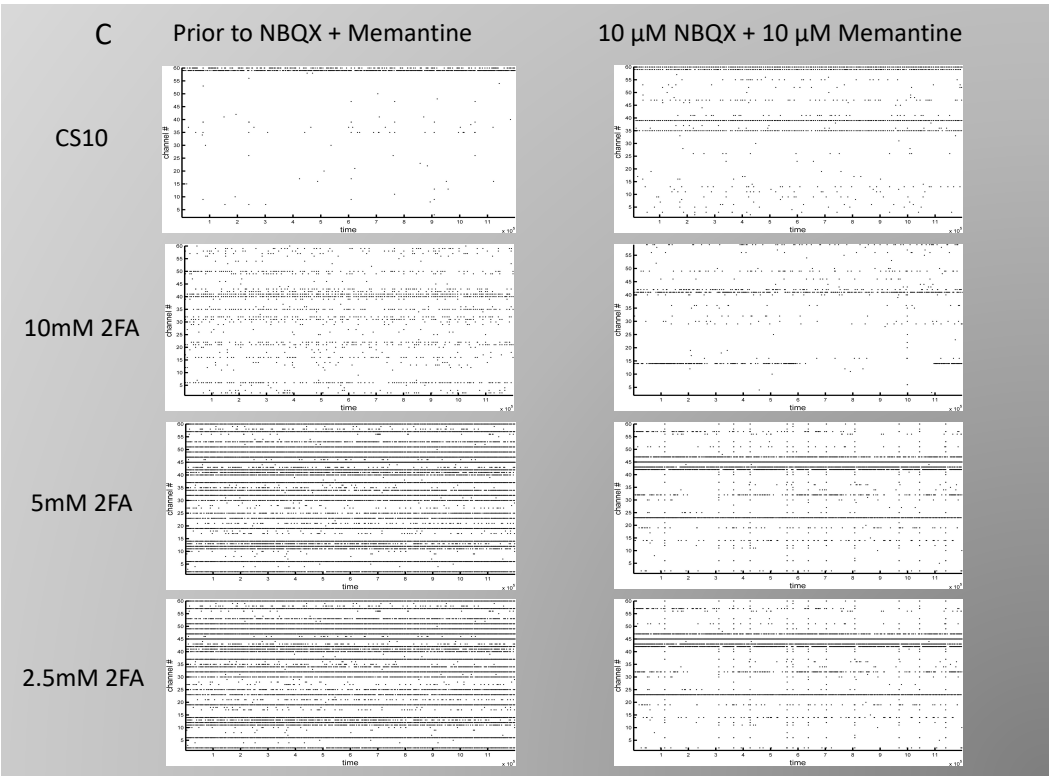

Figure 4.13 Representative raster plots of CS10- and 2FA-cryopreserved iPSC-Ns prior and post treatment with **(A)** GABA agonist **(B)** Muscimol **(C)** NBQX+Memantine.

Quantification of the difference in the MFR upon treatment was evaluated using NeuroExplorer (Nex technologies) software where the number of spikes was assessed based on all pre-drug recordings. The pre-drug recordings for each active electrode were normalized to 100% to allow for a relative assessment of the drug effect. As presented in **Table 4.1**, the number of spikes significantly decreased for all conditions upon treatment with **GABA agonist** (general GABA receptor agonist): CS10 = 1.0 ± 0.5 (P value < 0.1), 10 mM 2FA = 2.9 ± 0.9 (P value < 0.0001), 5 mM 2FA = 0.5 ± 0.2 (P value < 0.0001), and 2.5 mM 2FA = 0.5 ± 0.1 (P value < 0.0001). A similar trend was observed upon **muscimol** (specific agonist for $GABA_A$ receptors) treatment where all iPSC-N cultures had a significant decrease in the MFR: CS10 = 0.7 ± 0.3 (P value < 0.0001), 10 mM 2FA = 19.2 ± 19.0 (P value < 0.0001), 5 mM 2FA= 0.7 ± 0.2 (P value < 0.0001), and 2.5 mM 2FA = 1

± 0.6 (P value < 0.0001). Activation of GABA receptors using GABA agonist and muscimol results in inhibiting the firing activity of neurons which is implied by the decrease in the number of active electrodes (number of spikes) in all cryopreserved iPSC-N cultures. This confirms that incorporation of IRIs in the cryomedia of iPSC-Ns does not compromise the expression nor the activity of GABA receptors in the mixed population of the differentiated iPSC-Ns.

Moreover, deactivation of glutamate receptors using glutamate antagonists, such as **NBQX and memantine**, also results in a reduction in the signaling activity of neurons which, in turns, decreases the MFR of the iPSC-N cultures. As shown in **Table 4.1**, there was a significant decrease in the MFR (P value < 0.0001) for 5 mM and 2.5 mM 2FA-frozen iPSC-Ns upon treatment with the mixture of **NBQX and memantine**: 37.7 ± 4.7 and 29.0 ± 6.3, respectively. However, the MFR of the CS10- and 10 mM-2FA cryopreserved iPSC-Ns did not show in a significant decrease upon treatment with **NBQX + memantine** (P value > 0.1): 50.3 ± 27.1 and 74.7 ± 18.7, respectively. This confirms that 5 mM and 2.5 mM 2FA iPSC-N cultures consist of a higher number of active glutaminergic neurons than CS10- and 10 mM 2FA-cryopreserved iPSC-Ns.

The pharmacological responses of the cryopreserved iPSC-N cultures upon treatment with GABA agonists and glutamate antagonists were compared with that of the non-frozen iPSC-Ns that was reported previously by Jezierski *et al.*[121] As depicted in **S. Table 4.1**, treatment of the non-frozen cultures of iPSC-Ns with **GABA agonist**, **muscimol**, and **NBQX + memantine** resulted in a significant decrease in the MFR of the non-frozen iPSC-N cultures,[121] which is consistent with the pharmacological responses observed for the frozen iPSC-Ns. This further confirms that protection against ice recrystallization during

cryopreservation by employing IRIs in the cryomedia of iPSC-Ns results in a high number of viable neurons without altering the functionality of the GABA and glutamate receptors.[121]

Table 4.1 The effect of neuroactive drugs on the mean firing rate of 5 mM 2FA-cryopreserved iPSC-Ns quantified using NeuroExplorer software, where ns = P value > 0.1; * = P < 0.1, ** = P < 0.01, *** = P < 0.001; **** = P < 0.0001.

Freezing condition	Number of active electrodes	Mean Firing Rate (MFR, %)	
50 µM 4-Aminopyridine			
5mM 2FA	37	113.1 ± 48.3	****
50 µM Bicuculline			
5mM 2FA	51	154.3 ± 25.4,	**
1000 µM Nicotine			
5mM 2FA	63	130.6 ± 9.4	*
1 µM TTX			
5mM 2FA	58	0.0 ± 0.0	****
20 µM Verapamil			
5mM 2FA	88	2.1 ± 0.8	****

To confirm that the functionality of the different receptors and channels expressed in the mixed population of iPSC-Ns was not altered post-thaw, the MFR of the 5 mM 2FA-frozen iPSC-N cultures was compared with that of the non-frozen iPSC-N cultures. Jezierski *et al.* reported changes in the firing rates after treatment with a similar panel of neuroactive drugs to determine the presence of functional channels/receptors in iPSC-N

cultures, presented in **S. Table 4.1**.[121] The pharmacological responses of the non-frozen iPSC-Ns after the treatment with GABA agonist, muscimol, NBQX + memantine, TTX, and verapamil were consistent with those of the cryopreserved iPSC-Ns where the MFR decreased significantly, confirming the presence of mature and functional GABA receptors, NMDA/AMP receptors, Na^+ channels, and Ca^{2+} channels.[121] The MFR after treatment with 4AP, bicuculline, and nicotine appeared to increase in the frozen iPSC-Ns cultures (**Table 4.2**), unlike non-frozen iPSC-N cultures (**S. Table 4.1**).[121] This can be linked to an abundance of K^+ channels, $GABA_A$ receptors, and acetylcholine receptors in the cryopreserved iPSC-N cultures. The difference in the abundance of the different channels/receptors in frozen and non-frozen iPSC-N cultures is normal because the pattern of gene expression during the course of differentiation can differ from one culture to another.[129] Overall, it is evident that cryopreservation of iPSC-Ns with CS10 or 2FA formulations in CS10 did not alter the functionality of the different receptors or channels expressed on iPSC-N cultures.

4.6 Discussion

In this study, we validated whether employing IRIs in the cryopreservation protocols of iPSC-Ns would enhance the cryopreservation outcomes (i.e., recovery and functionality) post-thaw, and whether the IRI supplementation should be the standard procedure for the cryopreservation of iPSC-Ns. Recent improvements in the differentiation of iPSC-Ns have made it possible to model neurodegenerative diseases, accelerating the development of cell replacement therapies.[53,56,58-59] Despite the fact that current differentiation techniques can produce high yields of iPSC-Ns, cell line-to-cell line variations and other sources of variation persist, owing in part to the protocol's

complexity.[53] Different human iPSC lines have been shown to have varying potencies for guided differentiation into neurons and other cell types.[53] One way to address this is to create a quality-controlled cryopreserved bank of iPSC-Ns from which all research and transplants can be started. Human iPSCs and iPSC-Ns have been subjected to cryopreservation in several studies, and a number of cryo-solutions have been proposed for their cryopreservation.[53,56,58-59,61-63,102,104,121] This series of studies demonstrated that cell viability and recovery rate after the cryopreservation process vary depending on the stage at which the neurons they are frozen and the cryomedia used for freezing.[53,56,58-59,61-63,102] Moreover, the morphology and electrical activity of primary neurons and iPSC-Ns have been observed to deteriorate after thawing.[48,56,66-67] To this day, there have been no studies that directly compare freezing protocols in the presence or absence of IRIs, nor are there any guidelines governing the preservation of iPSC-Ns for clinical use.

We employed an IRI in a clinical-grade cryopreservation solution (CS10), to analyze several components of the cryopreservation process, such as the post-thaw viability, recovery rate and activity of iPSC-Ns, in an attempt to maximize the yield of viable and functional iPSC-N cells. Since there is significant cell loss associated with freezing and thawing of neurons, we hypothesize that protecting the cells against ice recrystallization will increase the cell survival rate and improve the post-thaw electrophysiological activity of iPSC-Ns.

A previous study conducted by Drummond *et al.* reported that the immediate post-thaw viability of iPSC-Ns frozen with CS10 was 70%, and the number of live iPSC-Ns appeared to decrease 24 hours post-thaw, where the cell viability was reduced to ~ 60%.[53] Through quantification of apoptosis, Drummond *et al.* revealed that the decrease in the

viability 24-hour post-thaw was due to cryopreservation-induced delayed onset of cell death.[53] One of the main causes of cryopreservation-induced cell death is the prolonged exposure to ice crystals during freezing and thawing processes,[74,77-78] and therefore, IRIs are potential cryoprotective additives that have proven to enhance the post-thaw viability and functionality of several types of stem cells, such as HSCs, MSCs, and iPSCs.[77-78,84] This study compares the efficacy of the cryopreservation solution utilized to freeze iPSC-Ns, CS10, in the absence and present of an active IRI, 2FA, by measuring the immediate post-thaw viability, recovery and neural firing activity. The increase in the number of live cells was observed to be statistically different between CS10 and the formulations of 10 mM and 5 mM 2FA in CS10 (P value < 0.1, $n = 2$) when the post-thaw recovery rate was calculated. The number of live cells appeared to increase significantly upon the addition of 10 mM or 5 mM 2FA in CS10, implying that inhibition of ice recrystallization is important to maximize the number of viable iPSC-Ns post-thaw. Moreover, 5 mM 2FA-frozen iPSC-Ns appeared to retain their neuronal networks and electrophysiological activity much earlier than CS10 (27 DIV vs 130 DIV). This suggests that the formulation of 5 mM 2FA in CS10 avoids the occurrence of delayed onset cell death that may be cause by ice recrystallization during the thawing cycles. Although the mechanism by which 2FA inhibits the growth of ice crystals is not fully understood, we postulate that inhibition of ice recrystallization using 2FA decreases the apoptotic-mediated cell death. This can be further assessed by conducting a Live Cell Event Caspase 3/7 assay to evaluate the extent of apoptosis post-thaw in the presence or absence of IRIs.[84]

Overall, this study provides the results of the first investigation of cryopreservation conditions in the presence or absence of IRIs. We found that formulations of 5 mM 2FA in

a clinical-grade cryomedium (CS10) increased the yield and enhanced the electrophysiological activity of iPSC-Ns post-thaw. These findings are similar to what was observed in the literature, where supplementation of 2FA in the freezing media of HSCs, MSCs, and iPSCs improved their post-thaw viability and functionality post-thaw.[77-78,84] However, more experiments need to be done to further validate the findings and to study the cryopreservation outcomes in the presence of IRIs when various cooling rates (i.e., -1 vs -2 °C/min) are incorporated. Cryopreserved iPSC-Ns with high post-thaw recovery rate and signaling functionality will be a significant resource for the neuroscience research and will substantially aid efforts to develop a cell replacement therapy for neurodegenerative diseases.

4.7 Chapter summary

In recent years, significant progress has been achieved in constructing neuronal differentiation techniques for a variety of central nervous system neuronal subtypes, which will help in the development of the next generation of iPSC-derived cell-based therapeutics for treating a variety of neurodegenerative diseases.[121] The generation of master cell banks of iPSCs and their derivatives (i.e., iPSC-Ns) is required for the manufacturing process of iPSC-derived cell therapies, as well as for future clinical applications. Therefore, an optimal cryopreservation protocol is necessary for the preservation of quality-controlled iPSC-N cell products.[10,50] Due to the susceptible nature of fully differentiated iPSC-Ns toward cryoinjuries associated with cryopreservation, the majority of iPSC-derived neuronal cryopreservation strategies have focused on neural precursor/progenitors cells (i.e., iPSCs or iPSC-NPCs).[10,50,68-69] These precursor cells are highly proliferative and can be differentiated into a variety of neurons, however, the differentiation process requires 2

weeks to 6 months to obtain fully differentiated and mature iPSC-Ns.[32-33,121] This limits the accessibility and availability of iPSC-N cell-based therapy to patients, thus, it is significant to develop an optimal cryopreservation protocol that maintains a high number of viability, recovery rate, and long-term electrophysiological functionality of terminally differentiated post-mitotic neurons.

Given the success of 2FA in a previous iPSC study, we sought to assess whether the formulation of 2FA in a GMP-compatible cryomedium, CS10, would enhance the cryopreservation outcomes of iPSC-Ns. Although there was an increase in the immediate post-thaw viability of 5 mM and 2.5 mM 2FA-frozen iPSC-Ns compared to CS10-frozen cells, the differences were not statistically significant (P value > 0.1, n = 2). However, analysis of the immediate post-thaw recovery rate of iPSC-Ns revealed that there was a statistically significant increase for 10 mM and 5 mM 2FA-frozen cells compared to CS10-frozen iPSC-Ns (P value > 0.1, n = 2). Both measurements (post-thaw viability and recovery rate) are critical to developing a cryopreservation protocol because they provide a preliminary indication of how different cell lines or primary cells behave to cryopreservation. The recovery rates appeared to be lower than the viability percentages because assessment of post-thaw viability only includes cells with damaged membranes that were stained with Trypan blue, while recovery rate analysis examines all cells with severe damaged membranes that were not stained with Trypan blue (i.e., cell debris). The increase in the number of viable cells in 10 mM and 5 mM iPSC-N cultures may be due to the protection against cell death caused by ice recrystallization.

Moreover, the increased recovery rate of 5 mM 2FA-frozen iPSC-Ns was subsequently translated to the increased post-thaw maturation and electrophysiological

activity on MEAs compared to CS10 (27 DIV vs 130 DIV, respectively). The increase in cell survival and the early establishment of neural network in 5 mM 2FA-frozen cultures may be due to the inhibition of ice crystal growth during cryopreservation, which masked the cells from cryoinjuries associated with ice recrystallization post-thaw. Comparison between the electrophysiological activity of the frozen iPSC-N cultures with the non-frozen cells revealed that there was a delay is establishing synchronous and spontaneous activity on MEAs compared to non-frozen iPSC-N cultures (18 DIV vs 27 DIV).[121] However, this delay was much shorter in 5 mM 2FA-frozen iPSC-Ns compared to CS10-frozen cells, which further confirms that employing IRIs in the cryopreservation protocol of iPSC-Ns may increase the availability of iPSC-N cell therapy in clinics and hospitals.

Furthermore, the 2FA cryopreserved iPSC-Ns retained expression of key neuronal specific and terminally differentiated markers and displayed functional neuropharmacological responses following treatment with a panel of neuroactive agonists and antagonists. These results confirm that cryopreservation did not negatively affect the function of these receptors and channels with similar neuropharmacological responses as observed for non-frozen iPSC-Ns.[121] Most intriguingly, 5 mM 2FA-cryopreserved neurons retained a higher spiking and bursting activity over long-term cultures (up to 236 DIV), and a higher mean percent of active electrodes than CS10-frozen iPSC-Ns. These long-term functional parameters are important considerations toward ensuring high cell quality of post-thaw cells, particularly if they are to be delivered to patients.

The application of 2FA in a GMP-compatible cryomedium (CS10) increased the post-thaw recovery rate and decreased the timeframe required to establish neural network, which demonstrates pre-clinical feasibility for clinical application in a variety of

neurodegenerative disorders. However, other variables, such as using rate-controlled freezers during freezing and lowering the DMSO concentration in the cryo-solution formulation, should be addressed to further improve the cryopreservation process. Overall, given the complexity and duration of iPSC-N differentiation strategies, optimizing cryopreservation of terminally mature and functional iPSC-Ns will revolutionize the field of cell-based therapy and will support the delivery of successful iPSC-derived therapies to the clinic.

4.8 Experimental Procedures

4.8.1 Synthesis and NMR Characterization of 2FA

D-gluconic acid-δ-lactone (2.5 g, 14.0 mmol) was dissolved in acetic acid (25 mL). 2-fluoroaniline (4 mL, 54.4 mmol) was then added and the reaction was stirred under reflux for 2 hours. Hexanes was then added to precipitate the crude product. The solid product was then recrystallized using ethanol (EtOH) to obtain white powder (84.15%). ^{1}H NMR (400 MHz, DMSO-d_6): δ 9.21 (br. s, 1H), 8.14 (td, *J* =15.9 Hz, 7.9, 1H), 7.30-7.25 (m, 1H), 7.20-7.10 (m, 2H), 5.94 (d, *J* = 4.8 Hz, 1H), 4.66 (d, *J* = 7.3 Hz, 1H), 4.61 (dd, *J* = 13.1, 5.5 Hz, 2H), 4.37 (t, *J* = 5.0 Hz, 1H), 4.24 (dd, *J* = 7.6, 3.6 Hz, 1H), 4.04-4.01 (m, 1H), 3.53-3.44 (m, 3H), 3.42-3.36 (m, 1H). ^{13}C NMR (100 MHz, DMSO-d_6) δ 172.0, 152.0, 126.4, 126.3, 125.2, 125.1, 125.0, 125.0, 122.5, 115.8, 115.6, 74.4, 72.7, 72.0, 70.7, 63.7.

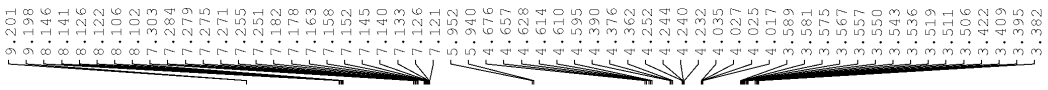

^{1}H NMR

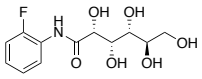

^{13}C NMR

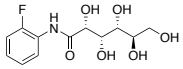

4.8.2 Differentiation of iPSC into Mixed Forebrain Neurons (iPSC-Ns)

As described in **Figure 4.7**, iPSCs that were obtained from CCRM were thawed and cultured in mTeSR1 media (STEMCELL Technologies, catalogue # 85850) on a Matrigel-coated 6-well plate (Corning) for 5 days. Neural progenitors were derived using a directed monolayer SMAD inhibition-mediated differentiation protocol (STEMCELL Technologies) by switching the medium to STEMdiff Neural Induction Medium and STEMDiff Neural Induction Supplement (STEMCELL Technologies, catalogue # 08581). Neural progenitor cells (iPSC-NPCs) were expanded in STEMDiff Neural Progenitor Medium for 1-2 passages. iPSC-NPCs were then differentiated into neurons (iPSC-Ns) by transitioning to BrainPhys Neuronal Medium supplemented with SM1 (STEMCELL Technologies, catalogue # 05792). Approximately half of media change was performed every two days as routine maintenance of the iPSC-Ns. iPSC-Ns were maintained in BrainPhys Neuronal Medium supplemented with SM1 for a minimum of three weeks, followed by the addition of maturation growth factors (20 ng/ml GDNF (STEMCELL Technologies, catalogue # 78139), 20 ng /ml BDNF (STEMCELL Technologies, catalogue # 78133), 250 µM dbcAMP (Millipore Sigma, catalogue # D0627) and 200 nM ascorbic acid (Millipore Sigma, catalogue # PHR1008) to obtain fully matured iPSC-Ns.

4.8.3 Freezing Protocol of iPSC-Ns

Once the iPSC-Ns were fully matured (Day 63), they were frozen in a control cryo-solution (Cryostor®10, CS10, STEMCELL Technologies, catalogue # 07930) in the presence or absence of 2FA. iPCS-Ns were lifted with Accutase (STEMCELL Technologies) and collected as small cell clumps by centrifugation at 300 g for 5 minutes. The iPSCs were resuspended in CS10 or CS10 supplemented with 2FA at different concentrations (2.5mM,

5mM, 10mM) at 1.0 x 10^6 cell/mL. The iPSC-Ns were transferred into 1-mL cryovials (Nunc). Cryovials were then placed in a Mr. Frosty rate-controlled freezing container, which was then placed in a −80 °C freezer for 24 hours. The cryovials were then transferred to a liquid nitrogen dewar for long-term storage (2 months).

4.8.4 Thawing *of iPSC-Ns and Assessment of Immediate Post-Thaw Viability/Recovery*

iPSC-Ns were thawed 2 months after freezing using a fast-thawing method. Cryovials were warmed in a 37 °C water bath for approximately 3 minutes. The cells were washed with 1mL of warm BrainPhys + SM1 media and spun at 300 g for 5 minutes. The cell pellets were then resuspended in 1 mL of fresh BrainPhys + SM1 + GFs and counted using Trypan blue (0.4 liquid, Millipore Sigma, catalogue # T8154) to assess immediate post-thaw viability and recovery. Immediate post-thaw viability was obtained using the formula $Number\ of\ Live\ Cells⁄Number\ of\ Live + Dead\ cells$, whereas post-thaw recovery rate was obtained using $Number\ of\ Live\ cells⁄Total\ number\ of\ frozen\ cells\ (1E6)$. Statistical analysis was completed using one-way ANOVA™ (Dunnett's multiple comparisons) in GraphPad Prism.

4.8.5 Immunocytochemistry

iPSC-Ns were plated on 12-well plates with 15 mm round coverslips that were coated with Matrigel in growth medium. The cells were fixed using 10% formalin (Fisher Scientific, catalogue # SF1004) after 28 days in maturation and stored in PBS at 4°C until use. The cells were then permeated using 0.2% Tween-20 (Millipore Sigma) for 10 minutes at room temperature, which was followed by washing with 1X PBS. Cells were then blocked with

Protein block serum free solution for an hour at room temperature and then incubated with primary antibodies (**S. Table 4.2**) for an hour. The primary antibodies were then washed two times with 1x PBS, and the cells were incubated with secondary antibodies (**S Table 4.3**) for an hour at room temperature. The cells were then washed twice with 1X PBS and mounted in DAKO fluorescent Mounting Medium (Agilent, catalogue # S302380-2) containing 5µg/mL of Hoechst 33258 (Millipore Sigma, catalogue # 94403) for the purpose of counterstaining the nuclei. Images were captured using the Axiovert 200M microscope (ZEISS), using different fluorophores (**S. Figure 4.4**). Cells were imaged using 20 X/0.4LD Archroplan Korr (DICII) objective.

To estimate the percentage of glutamatergic and GABAergic neurons in iPSC-Ns cultures, five randomly chosen immunofluorescence images were acquired. The total number of cells, and cells positive for VGLUT-2 and $GABA_A$ markers, were counted manually and percentages were determined per image. The final percentage is an average of 5 different images.

4.8.6 Microelectrode Arrays (MEAs)-Developmental Recordings

MEA systems were obtained from MultiChannel Systems (Reutlingen, Germany), with the head-stage accommodating a 60-electrode MEA dish. The thawed iPSC-Ns were plated at a density of 12E3 cells/mL in a 10 -15 µL droplet onto 0.005% PLO coated MEA plates. The iPSC-Ns were fed 2 times per week by replacing 50% of the medium with fresh BrainPhys + SM1 + GFs. The plated iPSC-Ns were grown on the MEAs for 19 days before recording. To record spontaneous activity in neurons, conditioned medium was replaced with fresh BrainPhys media + SM1 supplement and growth factors. For each recording session, a 10- to 15-minute equilibration period was allowed after transfer of the MEA dish

to the head-stage housed within a 37 ºC incubator, followed by a 20 min recording. Raw voltage recordings were analyzed offline to yield multi-unit activity using custom software written in MATLAB and NeuroExplorer (Nex technologies). Some electrodes were inactive due to lack of neuron coverage and were eliminated from analysis if they display a spike number less than 50. Statistical analysis was completed using one-way ANOVA™ (Dunnett's multiple comparisons) in GraphPad Prism.

4.8.7 Neuropharmacology Using MEAs

The thawed iPSC-Ns were also assessed for the maturity and functionality of the channels/receptors expressed on the neurons by treating them with a panel of neuro-active drugs. iPSC-Ns were fed twice a week by removing 50% of the media and replacing it with fresh growth factor-supplemented media. The neuropharmacological responses were assessed after growing the cryopreserved iPSC-Ns on MEAs for 48 days *in vitro* (DIV). A pre-drug treatment recording was first conducted by transferring the MEA dish to the head-stage housed within a 37 ºC incubator. Following a 20-minute pre-drug recording, 50% of the respective media was drawn from the MEA and replaced by 2x the final concentration of the selected neuroactive drug supplemented in fresh medium, and a 20-minute recording was performed. The drug was then washed out and the media was restored to the MEA. Raw voltage recordings were analyzed offline to yield multi-unit activity using a custom software written in MATLAB and NeuroExplorer (Nex technologies). Statistical analysis was completed using one-way ANOVA™ with Dunnett's multiple comparisons in GraphPad Prism.

4.8.8 MATLAB Analysis

Following the recording with MEA 2100-Lite, the files were converted to H5 files using Multi Channel Data Manager. The H5 files were then located and opened in the MATLAB R2014a program. Once the files were opened in the program, analysis was started, and raster plot files were generated.

4.8.9 NeuroExplorer Analysis

Following the recording with MEA 2100-Lite, the files were converted to .NEX files using Multi Channel DataManager. The NEX files were then located and opened in NeuroExplorer program using File Directory.

To obtain the number of Spikes, "detect spikes" tab was utilized and the following properties were entered: (Reference electrode, Band-pass filter, threshold, Segments before and after threshold and other variables, as shown in the figure below). Properties were selected based on a Manuscript written by Cotterill.[119] Neuron and spike waveforms were then generated. The neuron waveforms were then selected by checking the box associated with each of the electrodes-middle section of NeuroExplorer program (select 60 out of 120 electrodes). For Burst Analysis, burst analysis tab was opened and the described in Cotterill manuscript[119] were entered to conduct the analysis based on "interval specifications". A burst duration plot was generated for each electrode. To obtain numerical results, "Numerical results window" was opened from the view tab. The data were then copied to excel sheet for further manipulations. To generate raster plots, all continuous variables were deselected from the waveforms list, and "template" was selected from the top menu. Analysis was then run, which was then followed by generating raster plots by selecting

“RasterOneColumn”. Post data analysis was done in an excel sheet using established Macros to remove parameters that will not be analyzed (Ymin, Ymax, etc.).

Using the developer tab, enter an established script (below) to remove data rows that have spikes less than 50:

```
Sub DeleteRows()
   Application.ScreenUpdating = False
   Application.Calculation = xlCalculationManual
   Dim i As Long
   For i = Range("B" & Rows.Count).End(xlUp).Row To 1 Step -1
      If Not (Range("B" & i).Value > 50) Then
         Range("B" & i).EntireRow.Delete
      End If
   Next i
   Application.Calculation = xlCalculationAutomatic
   Application.ScreenUpdating = True
End Sub
```

Similarly, using the Developer Tab, enter established script (below) to remove any data rows that have ‘Bursts’ less then and equal to 20.

```
Sub DeleteRows()
```

```
    Application.ScreenUpdating = False
    Application.Calculation = xlCalculationManual
    Dim i As Long
    For i = Range("J" & Rows.Count).End(xlUp).Row To 1 Step -1
        If Not (Range("J" & i).Value > 50) Then
            Range("J" & i).EntireRow.Delete
        End If
    Next i
    Application.Calculation = xlCalculationAutomatic
    Application.ScreenUpdating = True
End Sub
```

Finally, the Average, Count, Standard Deviation and Standard Error were calculated, which can be performed by electrode-by-electrode method (each electrode counts as a data point).

4.9 Supplementary Figures and Tables

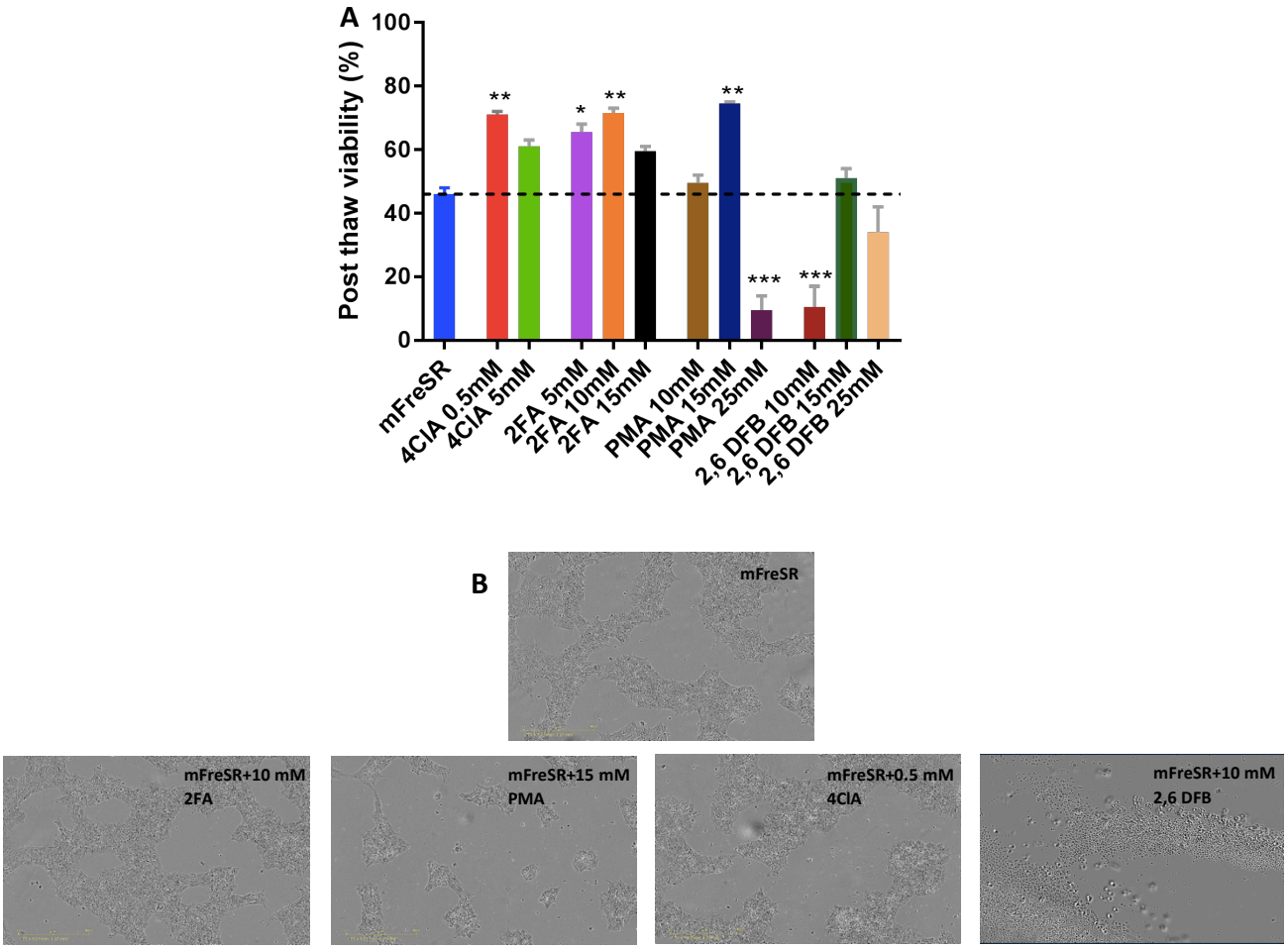

S. Figure 4.1 (A) Post-thaw viability percentage of iPSCs frozen with mFreSR and 2FA-, 4ClA-, PMA- and 2,6 DFB-supplemented in mFreSR™. Percent viability is presented as the mean and standard error of the mean (SEM). One-way analysis of variance (ANOVA) suggested statistical difference compared to mFreSR™, where * = $P \leq 0.05$, ** = $P \leq 0.01$, and *** = $P \leq 0.001$ (n=2). **(B)** Phase-contrast images of 48-hour post-thawed iPSC cultures presenting cell morphology and density. Figures were adapted from Karishma Chopra's master's dissertation.[84]

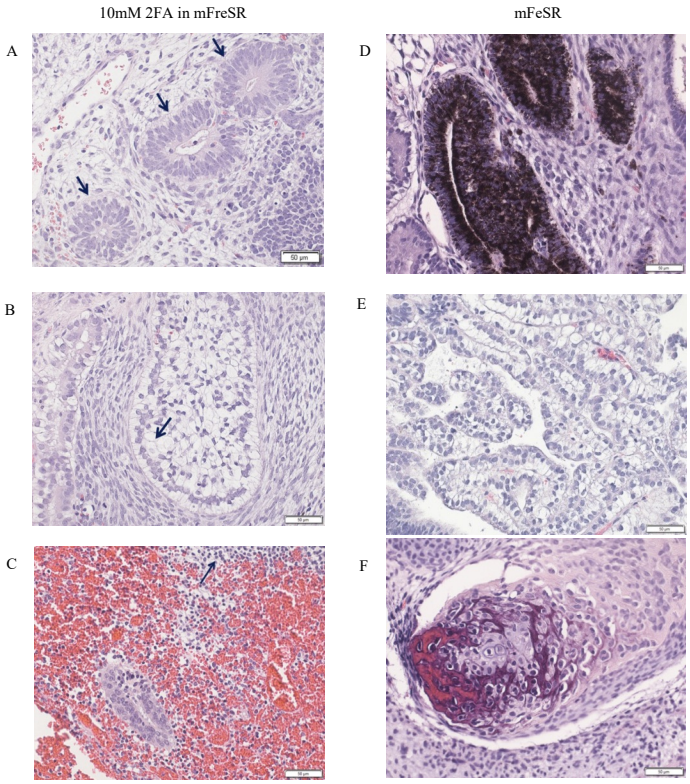

S. Figure 4.2 Pictures of the teratomas generated by 20mM 2FA- and mFreSR™-frozen iPSCs xenografted into nude or severe combined immune-deficient (SCID) mice. Pictures A and D indicate the ectoderm germ layer, while pictures B and E represent the endoderm layer, pictures C and F represent the mesoderm layer. Pictures were adapted from Chopra's master's dissertation.[84]

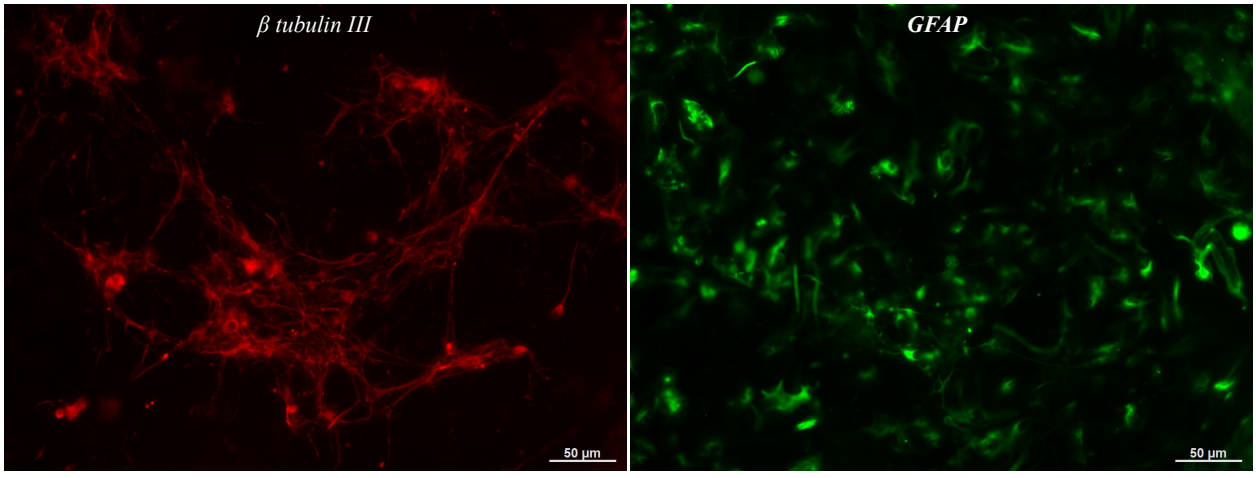

S. Figure 4.3 Pictures of immunofluorescence staining for the cryopreserved iPSC-Ns markers: β III tubulin and GFAP. Scale bar = 50µm.

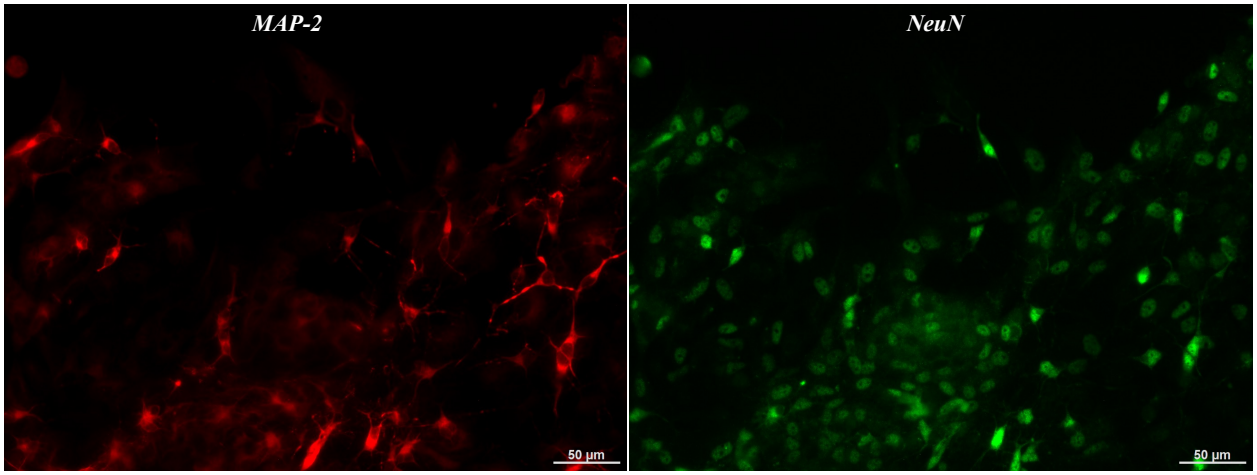

S. Figure 4.4 Pictures of immunofluorescence staining for the cryopreserved iPSC-Ns markers: MAP-2 and NeuN. Scale bar = 50µm.

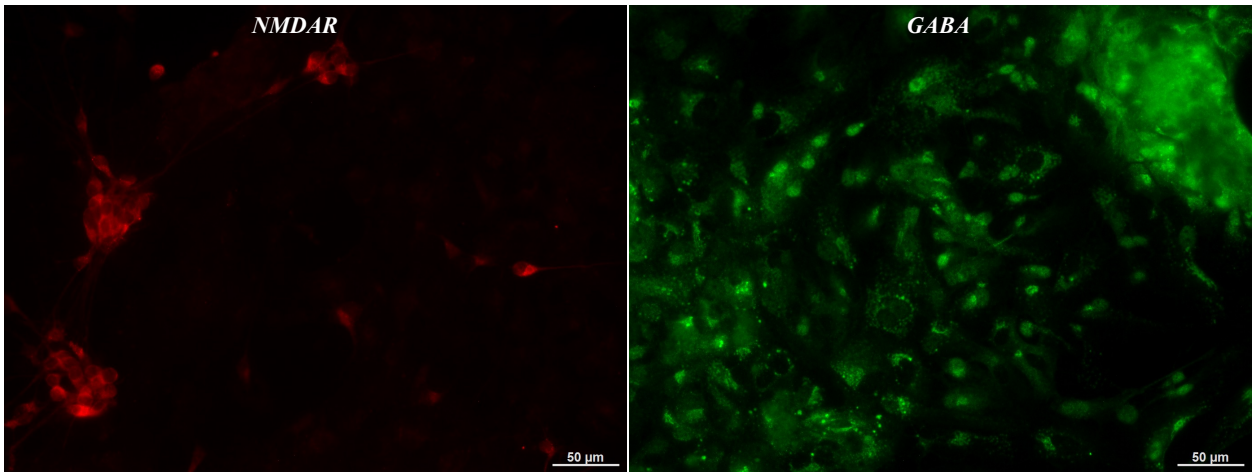

S. Figure 4.5 Pictures of immunofluorescence staining for the cryopreserved iPSC-Ns markers: NMDAR and GABA. Scale bar = 50µm.

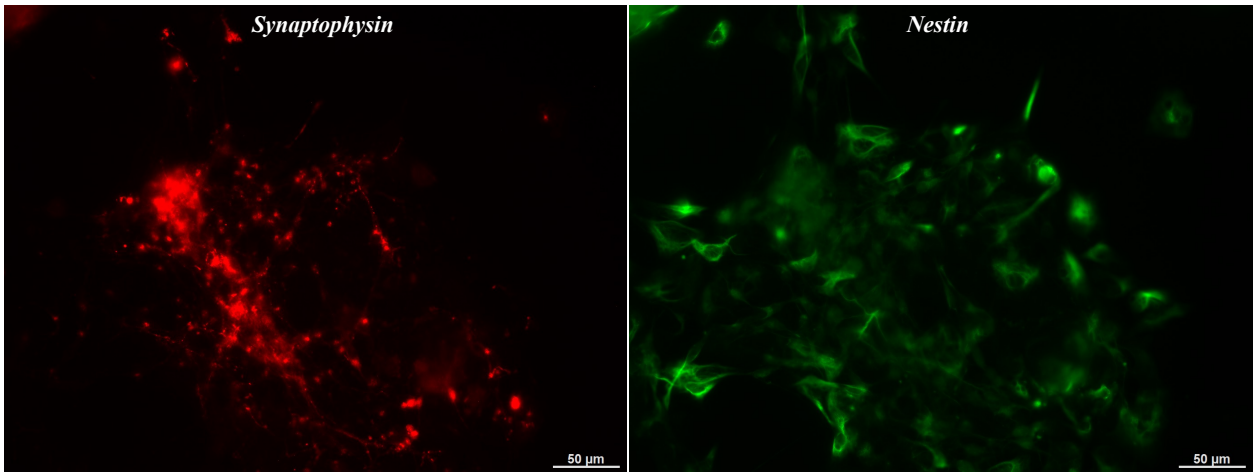

S. Figure 4.6 Pictures of immunofluorescence staining for the cryopreserved iPSC-Ns markers: synaptophysin and nestin. Scale bar = 50µm.

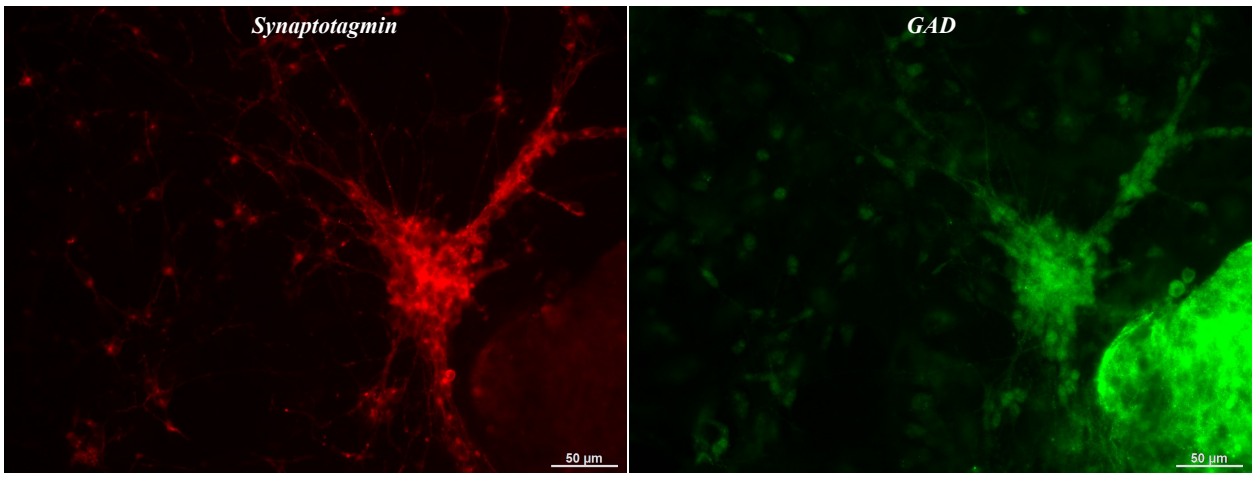

S. Figure 4.7 Pictures of immunofluorescence staining for the cryopreserved iPSC-Ns markers: synaptotagmin and GAD 65+67. Scale bar = 50µm.

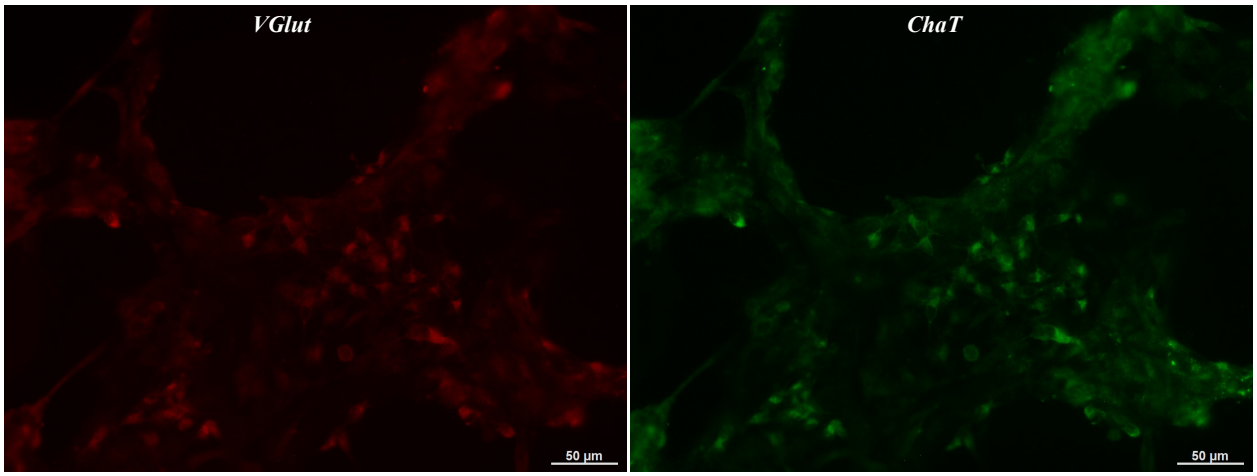

S. Figure 4.8 Pictures of immunofluorescence staining for the cryopreserved iPSC-Ns markers: VGlut2 and ChaT. Scale bar = 50µm.

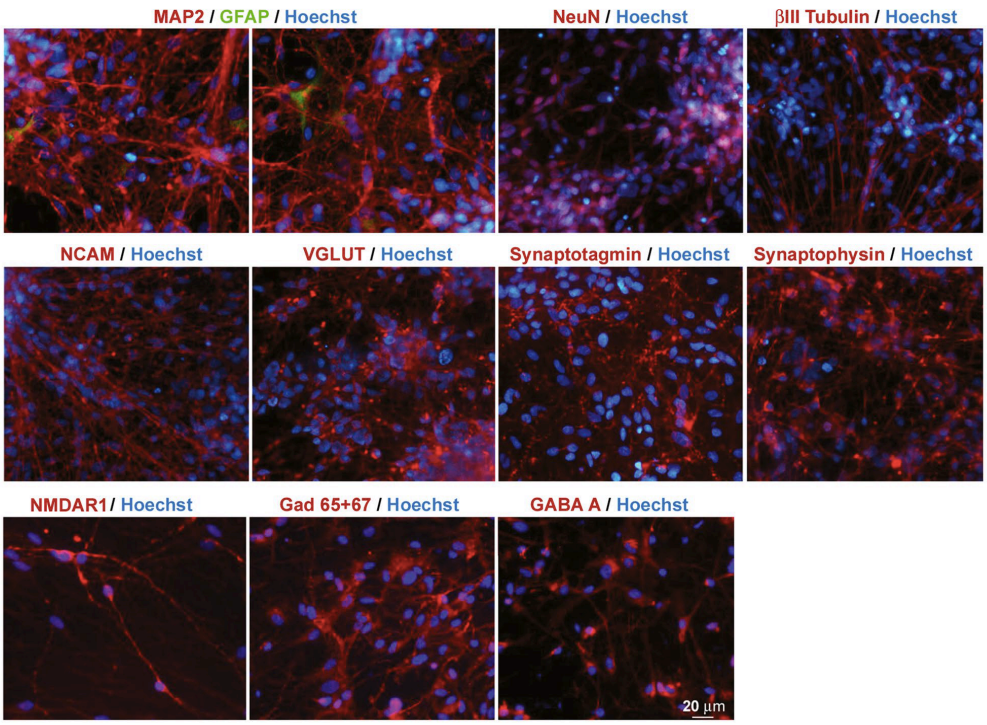

S. Figure 4.9 Pictures of immunofluorescence staining of non-frozen iPSC-Ns. The neural markers that were stained for are: MAP-2, NeuN, β-III Tubulin, NCAM, VGLUT2, Synaptophysin, Synaptotagmin NMDAR-1, GAD65 + 67, $GABA_A$ and GFAP. Hoechst (Blue) was used to counter stain the cells. Scale bare = 20 µm. Figure adapted from Stem Cell Reviews and Reports, A. Jezierski, Electrophysiological- and Neuropharmacological-Based Benchmarking of Human Induced Pluripotent Stem Cell-Derived and Primary Rodent Neurons, 2021, with permission from Springer Nature.

CS10

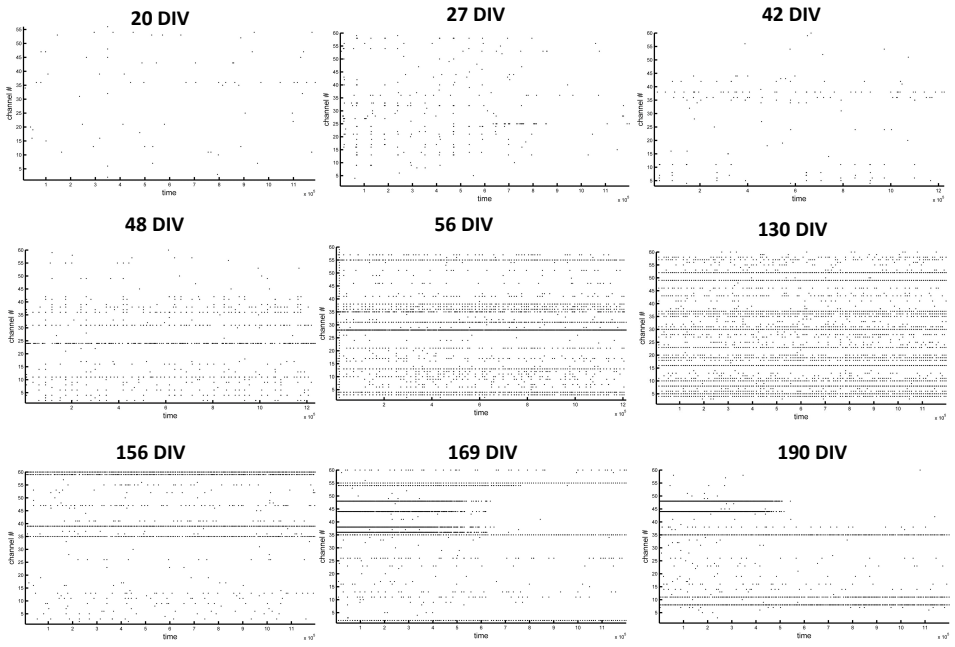

S. Figure 4.10 Developmental microelectrode arrays raster plots of CS10-cryopreserved iPSC-Ns.

10mM 2FA

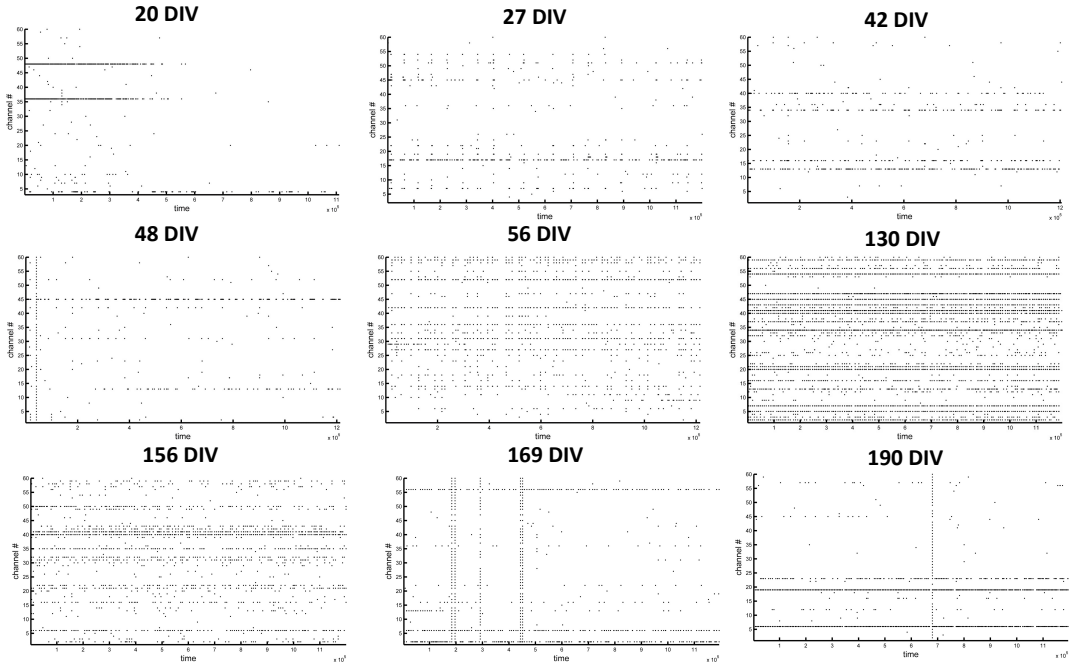

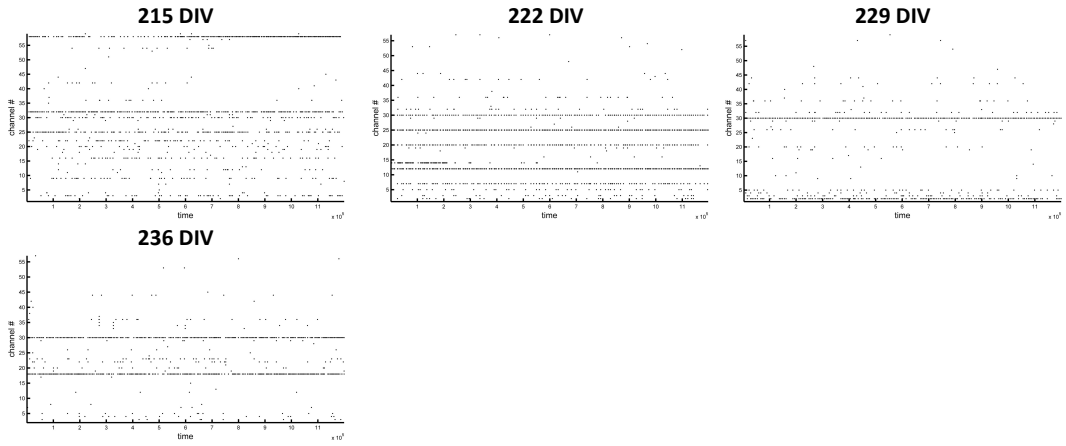

S. Figure 4.11 Developmental microelectrode arrays raster plots of 10mM 2FA-cryopreserved iPSC-Ns.

5mM 2FA

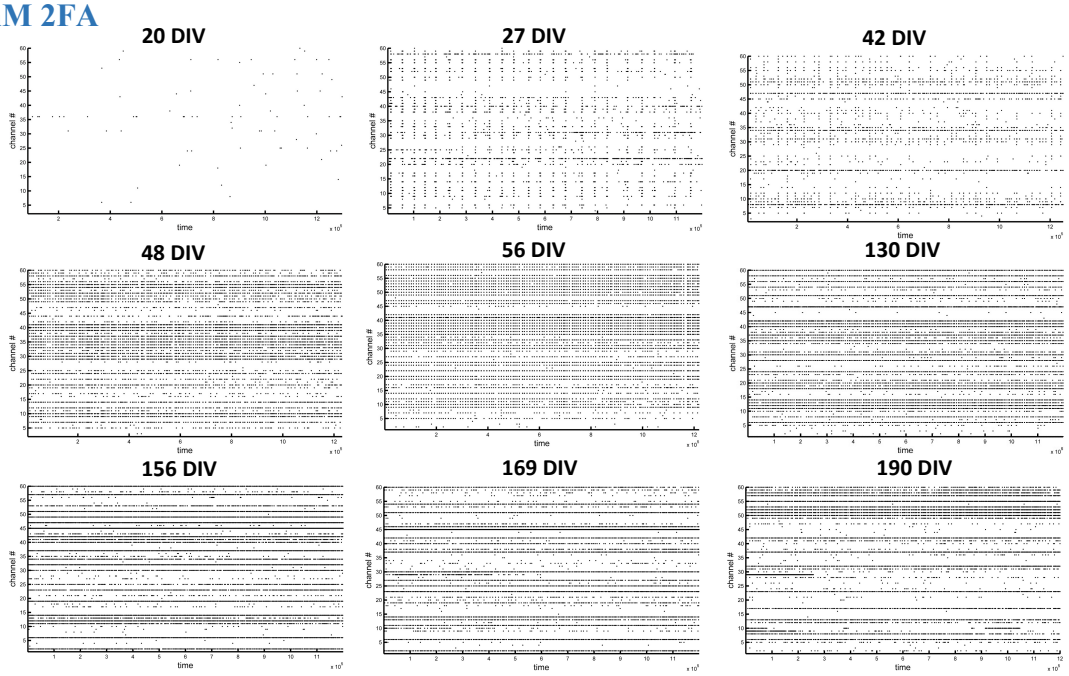

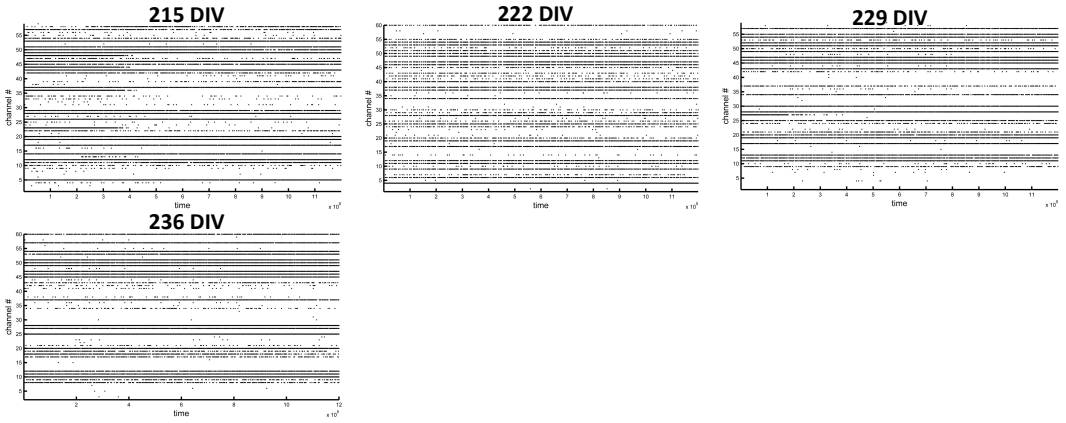

S. Figure 4.12 Developmental microelectrode arrays raster plots of 5mM 2FA-cryopreserved iPSC-Ns.

2.5mM 2FA

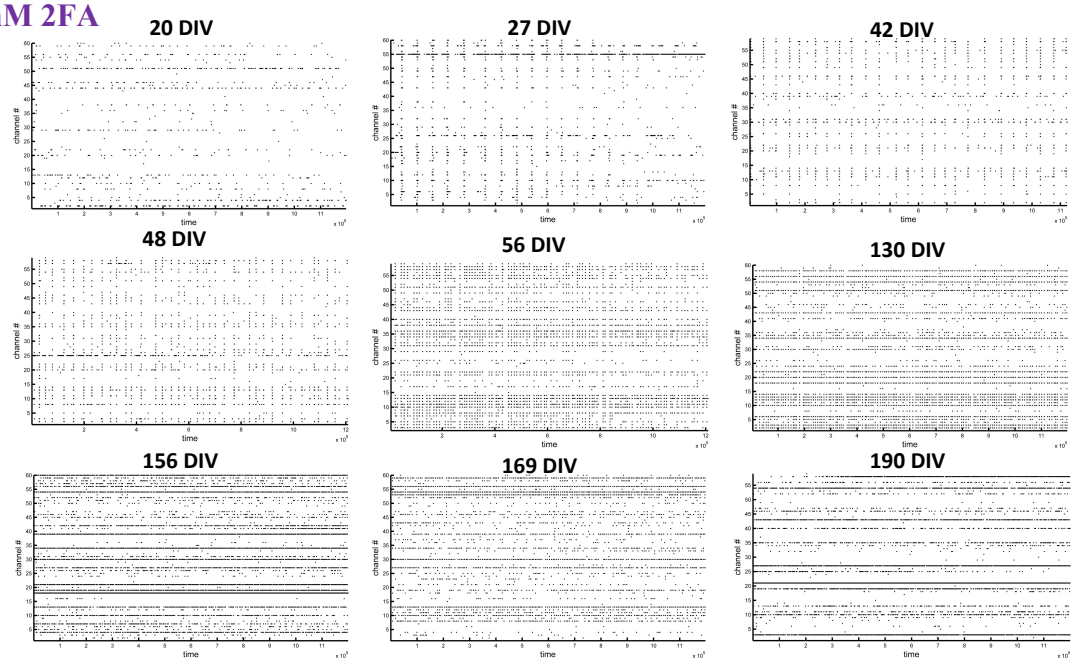

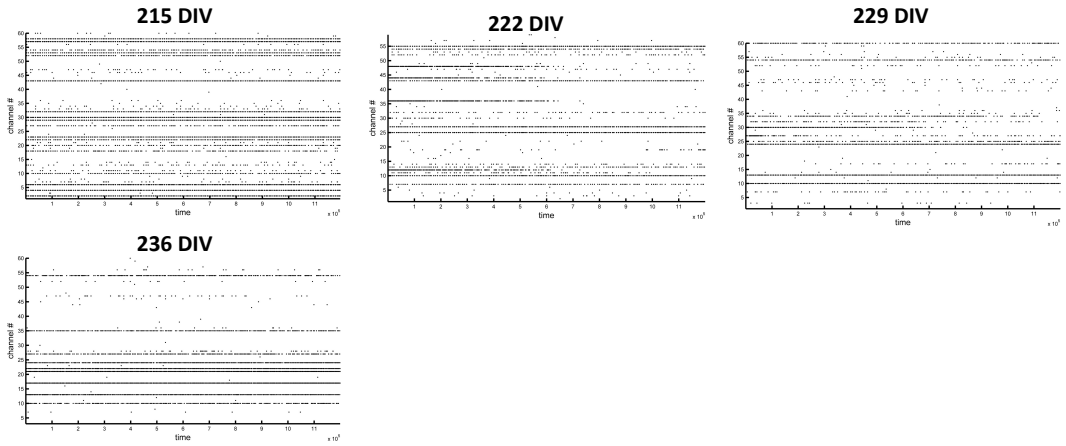

S. Figure 4.13 Developmental microelectrode arrays raster plots of 2.5mM 2FA-cryopreserved iPSC-Ns.

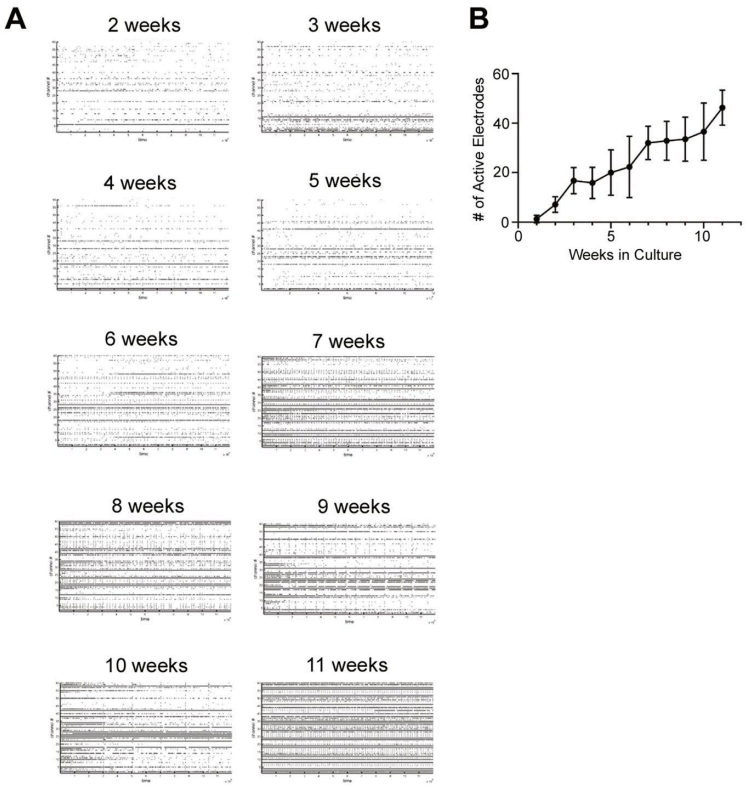

S. Figure 4.14 (A) Raster plots of non-frozen iPSC-N cultures plated on PLO-coated MEA dishes. (B) The number of active electrodes of non-frozen iPSC-Ns over 11 weeks *in vitro*.[121] Figures adapted from Stem Cell Reviews and Reports, A. Jezierski, Electrophysiological- and Neuropharmacological-Based Benchmarking of Human Induced Pluripotent Stem Cell-Derived and Primary Rodent Neurons, 2021, with permission from Springer Nature.

S. Table 4.1 Effect of drugs on mean frequency rate (MFR) of non-frozen iPSC-N cultures.[121] Table adapted from Stem Cell Reviews and Reports, A. Jezierski, Electrophysiological- and Neuropharmacological-Based Benchmarking of Human Induced Pluripotent Stem Cell-Derived and Primary Rodent Neurons, 2021, with permission from Springer Nature.

Drug	Drug Class	Conc'n (µM)	Neuron Spiking Rate (%)	
			AF-iN	
TTX	Na^+ channel antagonist	1	0.3 ± 0.1	****
Memantine/NBQX	NMDAR & AMPAR antagonist	10,10	39.4 ± 10	****
4-aminopyridine	K^+ channel agonist	50	64.8 ± 8.6	**
GABA	GABA receptor agonist	10	19 ± 5.3	****
Muscimol	$GABA_A$ receptor agonist	1	58.6 ± 4.5	****
Bicuculline	$GABA_A$ receptor antagonist	50	62.6 ± 4.8	****
Verapamil	L-type voltage-gated Ca channel antag	20	36 ± 8.3	****
Nicotine	ACh receptor agonist	1000	46.7 ± 39.4	****

S. Table 4.2 List of the primary antibodies used for immunocytochemistry experiment.

Primary antibody	Source	Dilution (in antibody diluent)
Mouse anti Oct 3/4	sc-5279/ Santa Cruz	1:100
Rabbit anti Sox2	In-house	1:5000
Goat anti Nanog	AF1997/R&D Systems	1:100
Rabbit anti Pax6	901301/ Biolegent	1:100
Rabbit anti Nestin	ABD69/ Millipore	1:500
Rabbit anti NueN	MAB377/Millipore	1:300
Mouse anti MAP-2	M1406/ Sigma	1:200
Rabbit anti GABA A	AB33299/ Abcam	1:100
Mouse anti NMDAR1	AB134308/ Abcam	1:50
Mouse anti BIII tubulin	MAB1637/ Millipore	1:300
Mouse anti Synaptotagmin	ADI-SYA-130D/Enzo	1:100
Mouse anti Synaptophysin	S5768-2mL/ Sigma	1:100
Rabbit anti GFAP	Z0334/ Dako	1:700
Mouse anti VGLUT-2	MAB5504/ Millipore	1:100
Goat anti ChaT	AB144P-200/ Chemicon	1:100
Mouse anti TH		1:100
Rabbit anti GAD65+GAD67	AB11070/Abcam	1:100
Mouse VGlut-1	MAB5502/ Millipore	1:100

S. Table 4.3 List of secondary antibodies used for immunocytochemistry experiment.

Secondary antibody	**Source**	**Dilution (in antibody diluent)**
Goat anti mouse Alexa 488	A11008/ Invitrogen	1:500 in 1XPBS
Goat anti rabbit Alexa 488	A11001/ Invitrogen	1:500 in 1XPBS
Donkey anti goat Alexa 488	A11055/ Invitrogen	1:500 in 1XPBS
Goat anti mouse Alexa 568	A11036/ Invitrogen	1:500 in 1XPBS
Goat anti rabbit Alexa 568		1:500 in 1XPBS

S. Table 4.4 List of the fluorophores used to detect the different markers using Axiovert 200M microscope (ZEISS).

Fluorophores	Fluorescent molecule	Excitation (nm)	Emission (nm)
Hoechst33342	Hoechst	350	461
Sox2, Pax6, NueN,GABA, NMDAR1, VGLUT-2, ChAT, TH, Peripherin, -ve Ctrl (2º Ab only)	Alexa 488	495	518
Nestin, MAP-2, BIII tubulin, Synaptotagmin, Synaptophysin, GFAP, GAD65+GAD67	Alexa 568	578	603

4.10 References

(1) Berz, D.; Colvin, G. Cryopreservation of Hematopoietic and Non-Hematopoietic Stem Cells – A Review for the Clinician. *Intech* **2012**, *i*, 231–266. https://doi.org/10.1016/j.colsurfa.2011.12.014.

(2) Volkman, R.; Offen, D. Concise Review: Mesenchymal Stem Cells in Neurodegenerative Diseases. *Stem Cells* **2017**, *35* (8), 1867–1880. https://doi.org/10.1002/stem.2651.

(3) Goldman, S. Stem and Progenitor Cell-Based Therapy of the Human Central Nervous System. *Nat. Biotechnol.* **2005**, *23* (7), 862–871. https://doi.org/10.1038/nbt1119.

(4) Keller, J. M.; Frega, M. *In Vitro Neuronal Networks:Past, Present, and Future of Neuronal Models*; 2019. https://doi.org/10.1007/978-3-319-30237-9_3.

(5) G7 Academies' Joint statements. The Challenge of Neurodegenerative Diseases in an Aging Population. *Trends in the Sciences*. 2017, pp 6_92-6_93. https://doi.org/10.5363/tits.22.6_92.

(6) Enciu, A. M.; Nicolescu, M. I.; Manole, C. G.; Mureşanu, D. F.; Popescu, L. M.; Popescu, B. O. Neuroregeneration in Neurodegenerative Disorders. *BMC Neurol.* **2011**, *11*, 1–7. https://doi.org/10.1186/1471-2377-11-75.

(7) Dauer, W.; Przedborski, S. Parkinson's Diseases: Mechanisms and Models. *cell Press* **2003**, *39*, 889–909. https://doi.org/10.1017/CCOL9780521851282.008.

(8) Poovaiah, N.; Davoudi, Z.; Peng, H.; Schlichtmann, B.; Mallapragada, S.; Narasimhan, B.; Wang, Q. Treatment of Neurodegenerative Disorders through the Blood-Brain Barrier Using Nanocarriers. *Nanoscale* **2018**, *10* (36), 16962–16983. https://doi.org/10.1039/c8nr04073g.

(9) Choonara, Y. E.; Kumar, P.; Modi, G.; Pillay, V. Improving Drug Delivery Technology for Treating Neurodegenerative Diseases. *Expert Opin. Drug Deliv.* **2016**, *13* (7), 1029–1043. https://doi.org/10.1517/17425247.2016.1162152.

(10) Bolshette, N. B.; Thakur, K. K.; Bidkar, A. P.; Trandafir, C.; Kumar, P.; Gogoi, R. Protein Folding and Misfolding in the Neurodegenerative Disorders: A Review. *Rev. Neurol. (Paris).* **2014**, *170* (3), 151–161. https://doi.org/10.1016/j.neurol.2013.11.002.

(11) Cummings, J. L.; Zhong, K. Treatments for Behavioural Disorders in Neurodegenerative Diseases: Drug Development Strategies. *Nat. Rev. Drug Discov.* **2006**, *5* (1), 64–74. https://doi.org/10.1038/nrd1928.

(12) Suksuphew, S. Neural Stem Cells Could Serve as a Therapeutic Material for Age-Related Neurodegenerative Diseases. *World J. Stem Cells* **2015**, *7* (2), 502. https://doi.org/10.4252/wjsc.v7.i2.502.

(13) Sampogna, G.; Guraya, S. Y.; Forgione, A. Regenerative Medicine: Historical Roots and Potential Strategies in Modern Medicine. *J. Microsc. Ultrastruct.* **2015**, *3* (3), 101–107. https://doi.org/10.1016/j.jmau.2015.05.002.

(14) Jakeman, L. B.; Reier, P. J. Axonal Projections between Fetal Spinal Cord Transplants and the Adult Rat Spinal Cord: A Neuroanatomical Tracing Study of Local Interactions. *J. Comp. Neurol.* **1991**, *307* (2), 311–334. https://doi.org/10.1002/cne.903070211.

(15) Reier, P. J.; Stokes, B. T.; Thompson, F. J.; Anderson, D. K. Fetal Cell Grafts into Resection and Contusion/Compression Injuries of the Rat and Cat Spinal Cord. *Exp. Neurol.* **1992**, *115* (1), 177–188. https://doi.org/10.1016/0014-4886(92)90245-L.

(16) Coumans, J. V.; Lin, T. T. S.; Hai Ning Dai; MacArthur, L.; McAtee, M.; Nash, C.; Bregman, B. S. Axonal Regeneration and Functional Recovery after Complete Spinal Cord Transection in Rats by Delayed Treatment with Transplants and Neurotrophins. *J. Neurosci.* **2001**, *21* (23), 9334–9344. https://doi.org/10.1523/jneurosci.21-23-09334.2001.

(17) Rosenzweig, E. S.; Brock, J. H.; Lu, P.; Kumamaru, H.; Salegio, E. A.; Kadoya, K.; Weber, J. L.; Liang, J. J.; Moseanko, R.; Hawbecker, S.; Huie, J. R.; Havton, L. A.; Nout-Lomas, Y. S.; Ferguson, A. R.; Beattie, M. S.; Bresnahan, J. C.; Tuszynski, M. H. Restorative Effects of Human Neural Stem Cell Grafts on the Primate Spinal Cord. *Nat. Med.* **2018**, *24*, 484.

(18) Ager, R. R.; Davis, J. L.; Agazaryan, A.; Benavente, F.; Poon, W. W.; Laferla, F. M.; Blurton-Jones, M. Human Neural Stem Cells Improve Cognition and Promote Synaptic Growth in Two Complementary Transgenic Models of Alzheimer's Disease and Neuronal Loss. *Hippocampus* **2015**, *25* (7), 813–826. https://doi.org/10.1002/hipo.22405.

(19) Takamatsu, K.; Ikeda, T.; Haruta, M.; Matsumura, K.; Ogi, Y.; Nakagata, N.; Uchino, M.; Ando, Y.; Nishimura, Y.; Senju, S. Degradation of Amyloid Beta by Human Induced Pluripotent Stem Cell-Derived Macrophages Expressing Neprilysin-2. *Stem Cell Res.* **2014**, *13* (3), 442–453. https://doi.org/10.1016/j.scr.2014.10.001.

(20) Kim, J. H.; Auerbach, J. M.; Rodríguez-Gómez, J. A.; Velasco, I.; Gavin, D.; Lumelsky, N.; Lee, S. H.; Nguyen, J.; Sánchez-Pernaute, R.; Bankiewicz, K.; McKay, R. Dopamine Neurons Derived from Embryonic Stem Cells Function in an Animal Model of Parkinson's Disease. *Nature* **2002**, *418* (6893), 50–56. https://doi.org/10.1038/nature00900.

(21) Takahashi, K.; Tanabe, K.; Ohnuki, M.; Narita, M.; Ichisaka, T.; Tomoda, K.; Yamanaka, S. Induction of Pluripotent Stem Cells from Adult Human Fibroblasts by Defined Factors. *Cell* **2007**, *131* (5), 861–872. https://doi.org/10.1016/j.cell.2007.11.019.

(22) Scudellari, M. A Decade of : IPS Cells. *Nature* **2016**, *534* (7607), 310–312. https://doi.org/10.1038/534310a.

(23) Wu, S. M.; Hochedlinger, K. Harnessing the Potential of Induced Pluripotent Stem Cells for Regenerative Medicine. *Nat. Publ. Gr.* **2011**, *13* (5), 497–505. https://doi.org/10.1038/ncb0511-497.

(24) Takahashi, K.; Yamanaka, S. Induction of Pluripotent Stem Cells from Mouse Embryonic and Adult Fibroblast Cultures by Defined Factors. *Cell* **2006**, *126* (4), 663–676. https://doi.org/10.1016/j.cell.2006.07.024.

(25) Meijer, M.; Rehbach, K.; Brunner, J. W.; Classen, J. A.; Lammertse, H. C. A.; van Linge, L. A.; Schut, D.; Krutenko, T.; Hebisch, M.; Cornelisse, L. N.; Sullivan, P. F.; Peitz, M.; Toonen, R. F.; Brüstle, O.; Verhage, M. A Single-Cell Model for Synaptic Transmission and Plasticity in Human IPSC-Derived Neurons. *Cell Rep.* **2019**, *27* (7), 2199-2211.e6. https://doi.org/10.1016/j.celrep.2019.04.058.

(26) Penney, J.; Ralvenius, W. T.; Tsai, L. H. Modeling Alzheimer's Disease with IPSC-Derived Brain Cells. *Mol. Psychiatry* **2020**, *25* (1), 148–167. https://doi.org/10.1038/s41380-019-0468-3.

(27) Schöndorf, D. C.; Aureli, M.; McAllister, F. E.; Hindley, C. J.; Mayer, F.; Schmid,

B.; Sardi, S. P.; Valsecchi, M.; Hoffmann, S.; Schwarz, L. K.; Hedrich, U.; Berg, D.; Shihabuddin, L. S.; Hu, J.; Pruszak, J.; Gygi, S. P.; Sonnino, S.; Gasser, T.; Deleidi, M. IPSC-Derived Neurons from GBA1-Associated Parkinson's Disease Patients Show Autophagic Defects and Impaired Calcium Homeostasis. *Nat. Commun.* **2014**, *5* (May). https://doi.org/10.1038/ncomms5028.

(28) Hernández-Sapiéns, M. A.; Reza-Zaldívar, E. E.; Cevallos, R. R.; Márquez-Aguirre, A. L.; Gazarian, K.; Canales-Aguirre, A. A. A Three-Dimensional Alzheimer's Disease Cell Culture Model Using IPSC-Derived Neurons Carrying A246E Mutation in PSEN1. *Front. Cell. Neurosci.* **2020**, *14* (June), 1–11. https://doi.org/10.3389/fncel.2020.00151.

(29) Bogetofte, H.; Jensen, P.; Ryding, M.; Schmidt, S. I.; Okarmus, J.; Ritter, L.; Worm, C. S.; Hohnholt, M. C.; Azevedo, C.; Roybon, L.; Bak, L. K.; Waagepetersen, H.; Ryan, B. J.; Wade-Martins, R.; Larsen, M. R.; Meyer, M. PARK2 Mutation Causes Metabolic Disturbances and Impaired Survival of Human IPSC-Derived Neurons. *Front. Cell. Neurosci.* **2019**, *13* (July), 1–14. https://doi.org/10.3389/fncel.2019.00297.

(30) Engle, S. J.; Blaha, L.; Kleiman, R. J. Best Practices for Translational Disease Modeling Using Human IPSC-Derived Neurons. *Neuron* **2018**, *100* (4), 783–797. https://doi.org/10.1016/j.neuron.2018.10.033.

(31) Tukker, A. M.; Wijnolts, F. M. J.; de Groot, A.; Westerink, R. H. S. Human IPSC-Derived Neuronal Models for in Vitro Neurotoxicity Assessment. *Neurotoxicology* **2018**, *67* (November 2017), 215–225. https://doi.org/10.1016/j.neuro.2018.06.007.

(32) Lee, S.; Huang, E. J. Modeling ALS and FTD with IPSC-Derived Neurons. *Brain Res.* **2017**, *1656*, 88–97. https://doi.org/10.1016/j.brainres.2015.10.003.

(33) Kobayashi, Y.; Okada, Y.; Itakura, G.; Iwai, H.; Nishimura, S.; Yasuda, A.; Nori, S.; Hikishima, K.; Konomi, T.; Fujiyoshi, K.; Tsuji, O.; Toyama, Y.; Yamanaka, S.; Nakamura, M.; Okano, H. Pre-Evaluated Safe Human IPSC-Derived Neural Stem Cells Promote Functional Recovery after Spinal Cord Injury in Common Marmoset without Tumorigenicity. *PLoS One* **2012**, *7* (12), 1–13. https://doi.org/10.1371/journal.pone.0052787.

(34) Pei, Y.; Peng, J.; Behl, M.; Sipes, N. S.; Shockley, K. R.; Rao, M. S.; Tice, R. R.;

Zeng, X. Comparative Neurotoxicity Screening in Human IPSC-Derived Neural Stem Cells, Neurons and Astrocytes. *Brain Res.* **2016**, *1638*, 57–73. https://doi.org/10.1016/j.brainres.2015.07.048.

(35) Nishiyama, Y.; Iwanami, A.; Kohyama, J.; Itakura, G.; Kawabata, S.; Sugai, K.; Nishimura, S.; Kashiwagi, R.; Yasutake, K.; Isoda, M.; Matsumoto, M.; Nakamura, M.; Okano, H. Safe and Efficient Method for Cryopreservation of Human Induced Pluripotent Stem Cell-Derived Neural Stem and Progenitor Cells by a Programmed Freezer with a Magnetic Field. *Neurosci. Res.* **2016**, *107*, 20–29. https://doi.org/10.1016/j.neures.2015.11.011.

(36) Kim, E.; Leonardo, D.; Dravinsky, A. IPSC-Derived Neurons as a Tool for Probing Molecular Pharmacology of Antipsychotic Action. *bioRxiv* **2018**.

(37) Stacey, G. N.; Masters, J. R. Cryopreservation and Banking of Mammalian Cell Lines. *Nat. Protoc.* **2008**, *3* (12), 1981–1989. https://doi.org/10.1038/nprot.2008.190.

(38) Giwa, S.; Lewis, J. K.; Alvarez, L.; Langer, R.; Roth, A. E.; Church, G. M.; Markmann, J. F.; Sachs, D. H.; Chandraker, A.; Wertheim, J. A.; Rothblatt, M.; Boyden, E. S.; Eidbo, E.; Lee, W. P. A.; Pomahac, B.; Brandacher, G.; Weinstock, D. M.; Elliott, G.; Nelson, D.; Acker, J. P.; Uygun, K.; Schmalz, B.; Weegman, B. P.; Tocchio, A.; Fahy, G. M.; Storey, K. B.; Rubinsky, B.; Bischof, J.; Elliott, J. A. W.; Woodruff, T. K.; Morris, G. J.; Demirci, U.; Brockbank, K. G. M.; Woods, E. J.; Ben, R. N.; Baust, J. G.; Gao, D.; Fuller, B.; Rabin, Y.; Kravitz, D. C.; Taylor, M. J.; Toner, M. The Promise of Organ and Tissue Preservation to Transform Medicine. *Nat. Biotechnol.* **2017**, *35* (6), 530–542. https://doi.org/10.1038/nbt.3889.

(39) Bakhach, J. The Cryopreservation of Composite Tissues: Principles and Recent Advancement on Cryopreservation of Different Type of Tissues. *Organogenesis* **2009**, *5* (3), 119–126. https://doi.org/10.4161/org.5.3.9583.

(40) Baust, J. G.; Gao, D.; Baust, J. M. Cryopreservation: An Emerging Paradigm Change. *Organogenesis* **2009**, *5* (3), 90–96. https://doi.org/10.4161/org.5.3.10021.

(41) Scott, K. L.; Lecak, J.; Acker, J. P. Biopreservation of Red Blood Cells: Past, Present, and Future. *Transfus. Med. Rev.* **2005**, *19* (2), 127–142. https://doi.org/10.1016/j.tmrv.2004.11.004.

(42) Barry J. Fuller, Nick Lane, and Erica E. Benson, E. Life in the Frozen State. Boca. *Boca Raton, Florida CRC Press* **2004**, *83* (3), 696. https://doi.org/10.1016/j.fertnstert.2004.10.025.

(43) Acker, J. P.; McGann, L. E. Innocuous Intracellular Ice Improves Survival of Frozen Cells. *Cell Transplant.* **2002**, *11* (6), 563–571. https://doi.org/10.3727/000000002783985468.

(44) Mazur, P.; Leibo, S. P.; Chu, E. H. Y. A Two-Factor Hypothesis of Freezing Injury. Evidence from Chinese Hamster Tissue-Culture Cells. *Exp. Cell Res.* **1972**, *71* (2), 345–355. https://doi.org/10.1016/0014-4827(72)90303-5.

(45) Meryman, H. T. Cryoprotective Agents. *Cryobiology* **1971**, *8* (2), 173–183.

(46) McGann, L. E. Differing Actions of Penetrating and Nonpenetrating Cryoprotective Agents. *Cryobiology* **1978**, *15* (4), 382–390. https://doi.org/10.1016/0011-2240(78)90056-1.

(47) Borlongan, C. V.; Tajima, Y.; Trojanowski, J. Q.; Lee, V. M. Y.; Sanberg, P. R. Transplantation of Cryopreserved Human Embryonal Carcinoma-Derived Neurons (NT2N Cells) Promotes Functional Recovery in Ischemic Rats. *Exp. Neurol.* **1998**, *149* (2), 310–321. https://doi.org/10.1006/exnr.1997.6730.

(48) Cano-Jaimez, M.; Tagliatti, E.; Mendonca, P. R. F.; Nicholson, E.; Vivekananda, U.; Kullmann, D. M.; Volynski, K. E. Preparation of Dissociated Mouse Primary Neuronal Cultures from Long-Term Cryopreserved Brain Tissue. *J. Neurosci. Methods* **2020**, *330* (May 2019), 108452. https://doi.org/10.1016/j.jneumeth.2019.108452.

(49) Gao, D.; Critser, J. K. Mechanisms of Cryoinjury in Living Cells. *ILAR J.* **2000**, *41* (4), 187–196. https://doi.org/10.1093/ilar.41.4.187.

(50) Mazur, P. Cryobiology : The Freezing of Biological Systems. *Am. Assoc. Adv. Sci.* **1970**, *168* (3934), 939–949.

(51) Lovelock, J. E.; Bishop, M. W. . Prevention of Freezing Damage to Living Cells by Dimethyl Sulphoxide. *Nature* **1959**, *183* (1), 1394–1395.

(52) Torregrosa, T.; Webster, S.; Aghaizu, C.; Soucy, J. R.; Bertucci, C.; Plant, L.; Koppes, A. N.; Koppes, R. A. Cryopreservation and Functional Analysis of Cardiac Autonomic Neurons. *J. Neurosci. Methods* **2020**, *341* (September 2019), 108724.

https://doi.org/10.1016/j.jneumeth.2020.108724.

(53) Drummond, N.; Dolt, K. S.; Canham, M.; Kilbride, P.; Morris, G. J.; Kunath, T. Cryopreservation of Midbrain Dopaminergic Neural Cells Differentiated from Human Embryonic Stem Cells. **2020**, 1–22. https://doi.org/10.1101/2020.02.11.944272.

(54) Grigor'eva, E. V.; Malankhanova, T. B.; Surumbayeva, A.; Pavlova, S. V.; Minina, J. M.; Kizilova, E. A.; Suldina, L. A.; Morozova, K. N.; Kiseleva, E.; Sorokoumov, E. D.; Lebedev, I. N.; Zakian, S. M.; Malakhova, A. A. Generation of GABAergic Striatal Neurons by a Novel IPSC Differentiation Protocol Enabling Scalability and Cryopreservation of Progenitor Cells. *Cytotechnology* **2020**, *7*. https://doi.org/10.1007/s10616-020-00406-7.

(55) Imaizumi, K.; Nishishita, N.; Muramatsu, M.; Yamamoto, T.; Takenaka, C.; Kawamata, S.; Kobayashi, K.; Nishikawa, S. I.; Akuta, T. A Simple and Highly Effective Method for Slow-Freezing Human Pluripotent Stem Cells Using Dimethyl Sulfoxide, Hydroxyethyl Starch and Ethylene Glycol. *PLoS One* **2014**, *9* (2), 1–11. https://doi.org/10.1371/journal.pone.0088696.

(56) Ishizuka, Y.; Bramham, C. R. A Simple DMSO-Based Method for Cryopreservation of Primary Hippocampal and Cortical Neurons. *J. Neurosci. Methods* **2020**, *333* (September 2019), 108578. https://doi.org/10.1016/j.jneumeth.2019.108578.

(57) Kaindl, J.; Meiser, I.; Majer, J.; Sommer, A.; Krach, F.; Katsen-Globa, A.; Winkler, J.; Zimmermann, H.; Neubauer, J. C.; Winner, B. Zooming in on Cryopreservation of HiPSCs and Neural Derivatives: A Dual-Center Study Using Adherent Vitrification. *Stem Cells Transl. Med.* **2019**, *8* (3), 247–259. https://doi.org/10.1002/sctm.18-0121.

(58) Milani, P.; Escalante-Chong, R.; Shelley, B. C.; Patel-Murray, N. L.; Xin, X.; Adam, M.; Mandefro, B.; Sareen, D.; Svendsen, C. N.; Fraenkel, E. Cell Freezing Protocol Suitable for ATAC-Seq on Motor Neurons Derived from Human Induced Pluripotent Stem Cells. *Sci. Rep.* **2016**, *6* (April), 1–10. https://doi.org/10.1038/srep25474.

(59) Negishi, T.; Ishii, Y.; Kawamura, S.; Kuroda, Y.; Yoshikawa, Y. Cryopreservation and Primary Culture of Cerebral Neurons from Cynomolgus Monkeys (Macaca

Fascicularis). *Neurosci. Lett.* **2002**, *328* (1), 21–24. https://doi.org/10.1016/S0304-3940(02)00433-0.

(60) Nishigaki, T.; Teramura, Y.; Nasu, A.; Takada, K.; Toguchida, J.; Iwata, H. Highly Efficient Cryopreservation of Human Induced Pluripotent Stem Cells Using a Dimethyl Sulfoxide-Free Solution. *Int. J. Dev. Biol.* **2011**, *55* (3), 305–311. https://doi.org/10.1387/ijdb.103145tn.

(61) Parker, S. S.; Moutal, A.; Cai, S.; Chandrasekaran, S.; Roman, M. R.; Koshy, A. A.; Khanna, R.; Zinsmaier, K. E.; Mouneimne, G. High Fidelity Cryopreservation and Recovery of Primary Rodent Cortical Neurons. *eNeuro* **2018**, *5* (5), 1–21. https://doi.org/10.1523/ENEURO.0135-18.2018.

(62) Pischedda, F.; Piccoli, G. Neurostore: A Novel Cryopreserving Medium for Primary Neurons. *Bio-Protocol* **2019**, *9* (12), 1–7. https://doi.org/10.21769/bioprotoc.3270.

(63) Pischedda, F.; Montani, C.; Obergasteiger, J.; Frapporti, G.; Corti, C.; Rosato Siri, M.; Volta, M.; Piccoli, G. Cryopreservation of Primary Mouse Neurons: The Benefit of Neurostore Cryoprotective Medium. *Front. Cell. Neurosci.* **2018**, *12* (March), 1–10. https://doi.org/10.3389/fncel.2018.00081.

(64) Robert, M. C.; Juan de Paz, L.; Graf, D. A.; Gazzin, S.; Tiribelli, C.; Bottai, H.; Rodriguez, J. V. Cryopreservation by Slow Cooling of Rat Neuronal Cells. *Cryobiology* **2016**, *72* (3), 191–197. https://doi.org/10.1016/j.cryobiol.2016.05.003.

(65) Rodríguez-Martínez, D.; Martínez-Losa, M. M.; Alvarez-Dolado, M. Cryopreservation of GABAergic Neuronal Precursors for Cell-Based Therapy. *PLoS One* **2017**, *12* (1), 1–17. https://doi.org/10.1371/journal.pone.0170776.

(66) Seggio, A. M.; Ellison, K. S.; Hynd, M. R.; Shainc, W.; Thompson, D. M. Cryopreservation of Transfected Primary Dorsal Root Ganglia Neurons. *J. Neurosci. Methods* **2008**, *173* (1), 67–73. https://doi.org/10.1016/j.jneumeth.2008.05.017.

(67) Wakeman, D. R.; Hiller, B. M.; Marmion, D. J.; McMahon, C. W.; Corbett, G. T.; Mangan, K. P.; Ma, J.; Little, L. E.; Xie, Z.; Perez-Rosello, T.; Guzman, J. N.; Surmeier, D. J.; Kordower, J. H. Cryopreservation Maintains Functionality of Human IPSC Dopamine Neurons and Rescues Parkinsonian Phenotypes In Vivo. *Stem Cell Reports* **2017**, *9* (1), 149–161.

https://doi.org/10.1016/j.stemcr.2017.04.033.

(68) Bakar, B.; Kose, E. A.; Sonal, S.; Alhan, A.; Kilinc, K.; Keskil, I. S. Evaluation of the Neurotoxicity of DMSO Infused into the Carotid Artery of Rat. *Injury* **2012**, *43* (3), 315–322. https://doi.org/10.1016/j.injury.2011.08.021.

(69) Cavaletti, G.; Oggioni, N.; Sala, F.; Pezzoni, G.; Cavalletti, E.; Marmiroli, P.; Petruccioli, M. G.; Frattola, L.; Tredici, G. Effect on the Peripheral Nervous System of Systemically Administered Dimethylsulfoxide in the Rat: A Neurophysiological and Pathological Study. *Toxicol. Lett.* **2000**, *118* (1–2), 103–107. https://doi.org/10.1016/S0378-4274(00)00269-1.

(70) Fahy, G. M. The Relevance of Cryoprotectant "Toxicity" to Cryobiology. *Cryobiology* **1986**, *23* (1), 1–13. https://doi.org/10.1016/0011-2240(86)90013-1.

(71) Fahy, G. M.; Lilley, T. H.; Linsdell, H.; Douglas, M. S. J.; Meryman, H. T. Cryoprotectant Toxicity and Cryoprotectant Toxicity Reduction: In Search of Molecular Mechanisms. *Cryobiology* **1990**, *27* (3), 247–268. https://doi.org/10.1016/0011-2240(90)90025-Y.

(72) Carpenter, J. F.; Hansen, T. N. Antifreeze Protein Modulates Cell Survival during Cryopreservation: Mediation through Influence on Ice Crystal Growth. *Proc. Natl. Acad. Sci. U. S. A.* **1992**, *89* (19), 8953–8957. https://doi.org/10.1073/pnas.89.19.8953.

(73) Matsumoto, S.; Matsusita, M.; Morita, T.; Kamachi, H.; Tsukiyama, S.; Furukawa, Y.; Koshida, S.; Tachibana, Y.; Nishimura, S. I.; Todo, S. Effects of Synthetic Antifreeze Glycoprotein Analogue on Islet Cell Survival and Function during Cryopreservation. *Cryobiology* **2006**, *52* (1), 90–98. https://doi.org/10.1016/j.cryobiol.2005.10.010.

(74) Capicciotti, C. J.; Mancini, R. S.; Turner, T. R.; Koyama, T.; Alteen, M. G.; Doshi, M.; Inada, T.; Acker, J. P.; Ben, R. N. O-Aryl-Glycoside Ice Recrystallization Inhibitors as Novel Cryoprotectants: A Structure-Function Study. *ACS Omega* **2016**, *1* (4), 656–662. https://doi.org/10.1021/acsomega.6b00163.

(75) Balcerzak, A. K.; Capicciotti, C. J.; Briard, J. G.; Ben, R. N. Designing Ice Recrystallization Inhibitors: From Antifreeze (Glyco)Proteins to Small Molecules. *RSC Adv.* **2014**, *4* (80), 42682–42696. https://doi.org/10.1039/c4ra06893a.

(76) Briard, J. G.; Jahan, S.; Chandran, P.; Allan, D.; Pineault, N.; Ben, R. N. Small-Molecule Ice Recrystallization Inhibitors Improve the Post-Thaw Function of Hematopoietic Stem and Progenitor Cells. *ACS Omega* **2016**, *1* (5), 1010–1018. https://doi.org/10.1021/acsomega.6b00178.

(77) Briard, J. G. The Rational Design and Use of Novel Small-Molecule Ice Recrystallization Inhibitors for the Cryopreservation of Hematopoietic Stem Cells and Red Blood Cells. *(Doctoral Diss. Univ. d'Ottawa/University Ottawa* **2016**, 235.

(78) Madeleine K., A. Improving the Engraftment Activities of Cryopreserved Human Umbilical Cord Blood Through the Development of Novel Glyco(Peptide)-Based Aryl Ice Recrystallization Inhibitors. *(Doctoral Diss. Univ. d'Ottawa/University Ottawa* **2020**.

(79) Watanabe, K.; Ueno, M.; Kamiya, D.; Nishiyama, A.; Matsumura, M.; Wataya, T.; Takahashi, J. B.; Nishikawa, S.; Nishikawa, S. I.; Muguruma, K.; Sasai, Y. A ROCK Inhibitor Permits Survival of Dissociated Human Embryonic Stem Cells. *Nat. Biotechnol.* **2007**, *25* (6), 681–686. https://doi.org/10.1038/nbt1310.

(80) Murányi, A.; Derkach, D.; Erdodi, F.; Kiss, A.; Ito, M.; Hartshorne, D. J. Phosphorylation of Thr695 and Thr850 on the Myosin Phosphatase Target Subunit: Inhibitory Effects and Occurrence in A7r5 Cells. *FEBS Lett.* **2005**, *579* (29), 6611–6615. https://doi.org/10.1016/j.febslet.2005.10.055.

(81) Riddick, N.; Ohtani, K. I.; Surks, H. K. Targeting by Myosin Phosphatase-RhoA Interacting Protein Mediates RhoA/ROCK Regulation of Myosin Phosphatase. *J. Cell. Biochem.* **2008**, *103* (4), 1158–1170. https://doi.org/10.1002/jcb.21488.

(82) Surks, H. K.; Richards, C. T.; Mendelsohn, M. E. Myosin Phosphatase-Rho Interacting Protein: A New Member of the Myosin Phosphatase Complex That Directly Binds RhoA. *J. Biol. Chem.* **2003**, *278* (51), 51484–51493. https://doi.org/10.1074/jbc.M305622200.

(83) Wang, Y.; Zheng, X. R.; Riddick, N.; Bryden, M.; Baur, W.; Zhang, X.; Surks, H. K. ROCk Isoform Regulation of Myosin Phosphatase and Contractility in Vascular Smooth Muscle Cells. *Circ. Res.* **2009**, *104* (4), 531–540. https://doi.org/10.1161/CIRCRESAHA.108.188524.

(84) Chopra, K. Improved Cryopreservation of Induced Pluripotent Stem Cells Using N-

Aryl Glycosidic Small Molecule Ice Recrystallization Inhibitors. *(Master's Diss. Univ. d'Ottawa/University Ottawa* **2020**.

(85) Nelakanti, R. V.; Kooreman, N. G.; Wu, J. C. Teratoma Formation: A Tool for Monitoring Pluripotency in Stem Cell Research. *Curr. Protoc. Stem Cell Biol.* **2015**, *2015*, 4a.8.1-4a.8.17. https://doi.org/10.1002/9780470151808.sc04a08s32.

(86) Strober, W. Trypan Blue Exclusion Test of Cell Viability. *Curr. Protoc. Immunol.* **2001**, *Appendix 3*, 2–3. https://doi.org/10.1002/0471142735.ima03bs21.

(87) Caccamo, D. V.; Herman, M. M.; Frankfurter, A.; Katsetos, C. D.; Collins, V. P.; Rubinstein, L. J. An Immunohistochemical Study of Neuropeptides and Neuronal Cytoskeletal Proteins in the Neuroepithelial Component of a Spontaneous Murine Ovarian Teratoma. Primitive Neuroepithelium Displays Immunoreactivity for Neuropeptides and Neuron-Associated β-Tubul. *Am. J. Pathol.* **1989**, *135* (5), 801–813.

(88) Sullivan, K. F.; Cleveland, D. W. Identification of Conserved Isotype-Defining Variable Region Sequences for Four Vertebrate β Tubulin Polypeptide Classes. *Proc. Natl. Acad. Sci. U. S. A.* **1986**, *83* (12), 4327–4331. https://doi.org/10.1073/pnas.83.12.4327.

(89) Jacque, C. M.; Vinner, C.; Kujas, M.; Raoul, M.; Racadot, J.; Baumann, N. A. Determination of Glial Fibrillary Acidic Protein (GFAP) in Human Brain Tumors. *J. Neurol. Sci.* **1978**, *35* (1), 147–155. https://doi.org/10.1016/0022-510X(78)90107-7.

(90) Roessmann, U.; Velasco, M. E.; Sindely, S. D.; Gambetti, P. Glial Fibrillary Acidic Protein (GFAP) in Ependymal Cells during Development. An Immunocytochemical Study. *Brain Res.* **1980**, *200* (1), 13–21. https://doi.org/10.1016/0006-8993(80)91090-2.

(91) Shafit-Zagardo, B.; Kalcheva, N. Making Sense of the Multiple MAP-2 Transcripts and Their Role in the Neuron. *Mol. Neurobiol.* **1998**, *16* (2), 149–162. https://doi.org/10.1007/BF02740642.

(92) Gusel'nikova, V. V.; Korzhevskiy, D. E. NeuN as a Neuronal Nuclear Antigen and Neuron Differentiation Marker. *Acta Naturae* **2015**, *7* (2), 42–47. https://doi.org/10.32607/20758251-2015-7-2-42-47.

(93) Furukawa, H.; Singh, S. K.; Mancusso, R.; Gouaux, E. Subunit Arrangement and Function in NMDA Receptors. *Nature* **2005**, *438* (7065), 185–192. https://doi.org/10.1038/nature04089.

(94) Johns, TheKuffler, S. W.; Edwards, C. Mechanism of Gamma Aminobutyric Acid (GABA) Action and Its Relation to Synaptic Inhibition. *J. Neurophysiol.* **1958**, *21* (6), 589–610.

(95) Dean, C.; Dunning, F. M.; Liu, H.; Bomba-Warczak, E.; Martens, H.; Bharat, V.; Ahmed, S.; Chapman, E. R. Axonal and Dendritic Synaptotagmin Isoforms Revealed by a PHluorin-Syt Functional Screen. *Mol. Biol. Cell* **2012**, *23* (9), 1715–1727. https://doi.org/10.1091/mbc.E11-08-0707.

(96) Krueger, C.; St öcker, W.; Schlosser, M. Glutamic Acid Decarboxylase Autoantibodies. *Autoantibodies* **2007**, 369–378. https://doi.org/10.1016/B978-044452763-9/50052-4.

(97) Martineau, M.; Guzman, R. E.; Fahlke, C.; Klingauf, J. VGLUT1 Functions as a Glutamate/Proton Exchanger with Chloride Channel Activity in Hippocampal Glutamatergic Synapses. *Nat. Commun.* **2017**, *8* (1). https://doi.org/10.1038/s41467-017-02367-6.

(98) Witzemann, V. Choline Acetyltransferase. *xPharm Compr. Pharmacol. Ref.* **2007**, No. 1982, 1–5. https://doi.org/10.1016/B978-008055232-3.60522-7.

(99) Bhargava, R.; Dabbs, D. J. *Immunohistology of Metastatic Carcinomas of Unknown Primary*, Third Edit.; Elsevier Inc., 2011. https://doi.org/10.1016/B978-1-4160-5766-6.00012-1.

(100) Hendrickson, M. L.; Rao, A. J.; Demerdash, O. N. A.; Kalil, R. E. Expression of Nestin by Neural Cells in the Adult Rat and Human Brain. *PLoS One* **2011**, *6* (4). https://doi.org/10.1371/journal.pone.0018535.

(101) Wharton, S. B.; Chan, K. K.; Hamilton, F. A.; Anderson, J. R. Expression of Neuronal Markers in Oligodendrogliomas: An Immunohistochemical Study. *Neuropathol. Appl. Neurobiol.* **1998**, *24* (4), 302–308. https://doi.org/10.1046/j.1365-2990.1998.00132.x.

(102) Ojima, A.; Miyamoto, N. Method for MEA Data Analysis of Drug-Treated Rat Primary Neurons and Human IPSC-Derived Neurons to Evaluate the Risk of Drug-

Induced Seizures. *Yakugaku Zasshi* **2018**, *138* (6), 823–828. https://doi.org/10.1248/yakushi.17-00213-3.

(103) Spira, M. E.; Hai, A. Multi-Electrode Array Technologies for Neuroscience and Cardiology. *Nat. Nanotechnol.* **2013**, *8* (2), 83–94. https://doi.org/10.1038/nnano.2012.265.

(104) Ronchi, S.; Buccino, A. P.; Prack, G.; Kumar, S. S.; Schröter, M.; Fiscella, M.; Hierlemann, A. Electrophysiological Phenotype Characterization of Human IPSC-Derived Neuronal Cell Lines by Means of High-Density Microelectrode Arrays. *Adv. Biol.* **2021**, *5* (3), 1–16. https://doi.org/10.1002/adbi.202000223.

(105) Asakura, K.; Hayashi, S.; Ojima, A.; Taniguchi, T.; Miyamoto, N.; Nakamori, C.; Nagasawa, C.; Kitamura, T.; Osada, T.; Honda, Y.; Kasai, C.; Ando, H.; Kanda, Y.; Sekino, Y.; Sawada, K. Improvement of Acquisition and Analysis Methods in Multi-Electrode Array Experiments with IPS Cell-Derived Cardiomyocytes. *J. Pharmacol. Toxicol. Methods* **2015**, *75*, 17–26. https://doi.org/10.1016/j.vascn.2015.04.002.

(106) Oka, H.; Shimono, K.; Ogawa, R.; Sugihara, H.; Taketani, M. A New Planar Multielectrode Array for Extracellular Recording: Application to Hippocampal Acute Slice. *J. Neurosci. Methods* **1999**, *93* (1), 61–67. https://doi.org/10.1016/S0165-0270(99)00113-2.

(107) Sasaki, T.; Suzuki, I.; Yokoi, R.; Sato, K.; Ikegaya, Y. Synchronous Spike Patterns in Differently Mixed Cultures of Human IPSC-Derived Glutamatergic and GABAergic Neurons. *Biochem. Biophys. Res. Commun.* **2019**, *513* (2), 300–305. https://doi.org/10.1016/j.bbrc.2019.03.161.

(108) Thomas, C. A.; Springer, P. A.; Loeb, G. E.; Berwald-Netter, Y.; Okun, L. M. A Miniature Microelectrode Array to Monitor the Bioelectric Activity of Cultured Cells. *Exp. Cell Res.* **1972**, *74* (1), 61–66. https://doi.org/10.1016/0014-4827(72)90481-8.

(109) Cotterill, E.; Charlesworth, P.; Thomas, C. W.; Paulsen, O.; Eglen, S. J. A Comparison of Computational Methods for Detecting Bursts in Neuronal Spike Trains and Their Application to Human Stem Cell-Derived Neuronal Networks. *J. Neurophysiol.* **2016**, *116* (2), 306–321. https://doi.org/10.1152/jn.00093.2016.

(110) Technologies, N. NeuroExplorer Manual. *NeuroExplorer Man.* 1–348.

(111) Johnston, G. A. R. Advantages of an Antagonist: Bicuculline and Other GABA Antagonists. *Br. J. Pharmacol.* **2013**, *169* (2), 328–336. https://doi.org/10.1111/bph.12127.

(112) Johnston, G. A. R. Muscimol as an Ionotropic GABA Receptor Agonist. *Neurochem. Res.* **2014**, *39* (10), 1942–1947. https://doi.org/10.1007/s11064-014-1245-y.

(113) Nourbakhsh, B.; Waubant, E. Neurodegeneration and Remyelination in Multiple Sclerosis. *Mult. Scler. A Mech. View* **2016**, 311–337. https://doi.org/10.1016/B978-0-12-800763-1.00013-0.

(114) Marx, C. E.; Trost, W. T.; Shampine, L.; Behm, F. M.; Giordano, L. A.; Massing, M. W.; Rose, J. E. Neuroactive Steroids, Negative Affect, and Nicotine Dependence Severity in Male Smokers. *Psychopharmacology (Berl).* **2006**, *186* (3), 462–472. https://doi.org/10.1007/s00213-005-0226-x.

(115) Turovaya, A. Y.; Galenko-Yaroshevskii, P. A.; Kade, A. K.; Uvarov, A. E.; Kiguradze, M. I.; Khvitiya, N. G.; Tatulashvili, D. R. Effects of Verapamil and Amiodarone on Sympathoadrenal System and Balance of Excitatory and Inhibitory Amino Acids in Rat Medulla Oblongata. *Bull. Exp. Biol. Med.* **2005**, *139* (6), 665–667. https://doi.org/10.1007/s10517-005-0372-5.

(116) Kostadinova, I.; Danchev, N. 4-Aminopyridine - the New Old Drug for the Treatment of Neurodegenerative Diseases. *Pharmacia* **2019**, *66* (2), 67–74. https://doi.org/10.3897/pharmacia.66.e35976.

(117) Esposti, F.; Signorini, M. G.; Lamanna, J.; Gullo, F.; Wanke, E. How Do TTX and AP5 Affect the Post-Recovery Neuronal Network Activity Synchronization? *Annu. Int. Conf. IEEE Eng. Med. Biol. - Proc.* **2007**, 3012–3015. https://doi.org/10.1109/IEMBS.2007.4352963.

(118) Brandão, F. P.; Rodrigues, S.; Castro, B. B.; Gonçalves, F.; Antunes, S. C.; Nunes, B. Short-Term Effects of Neuroactive Pharmaceutical Drugs on a Fish Species: Biochemical and Behavioural Effects. *Aquat. Toxicol.* **2013**, *144–145*, 218–229. https://doi.org/10.1016/j.aquatox.2013.10.005.

(119) Crook, J. M.; Tomaskovic-Crook, E.; Ludwig, T. Cryobanking Pluripotent Stem Cells. In *Methods Mol Biol*; 2017; Vol. 1590, pp 151–164.

https://doi.org/10.1007/978-1-4939-6921-0.

(120) Martn-Ibez, R.; Hovatta, O.; M., J. Cryopreservation of Human Pluripotent Stem Cells: Are We Going in the Right Direction? *Curr. Front. Cryobiol.* **2012**. https://doi.org/10.5772/34853.

(121) Jezierski, A.; Baumann, E.; Aylsworth, A.; Costain, W. J.; Corluka, S.; Banderali, U.; Sodja, C.; Ribecco-Lutkiewicz, M.; Salma, A.; Marzia, M.; Joseph, T. Electrophysiological- and Neuropharmacological-Based Benchmarking of Human Induced Pluripotent Stem Cell-Derived and Primary Rodent Neurons. *Stem Cell Rev. Reports* **2021**, No. 0123456789.

(122) Newell-Litwa, K. A.; Badoual, M.; Asmussen, H.; Patel, H.; Whitmore, L.; Horwitz, A. R. ROCK 1 and 2 Differentially Regulate Actomyosin Organization to Drive Cell and Synaptic Polarity. *J. Cell Biol.* **2015**, *210* (2), 225–242. https://doi.org/10.1083/jcb.201504046.

(123) Harbom, L. J.; Rudisill, T. L.; Michel, N.; Litwa, K. A.; Beenhakker, M. P.; McConnell, M. J. The Effect of Rho Kinase Inhibition on Morphological and Electrophysiological Maturity in IPSC-Derived Neurons. *Cell Tissue Res.* **2019**, *375* (3), 641–654. https://doi.org/10.1007/s00441-018-2942-7.

(124) Ohgushi, M.; Matsumura, M.; Eiraku, M.; Murakami, K.; Aramaki, T.; Nishiyama, A.; Muguruma, K.; Nakano, T.; Suga, H.; Ueno, M.; Ishizaki, T.; Suemori, H.; Narumiya, S.; Niwa, H.; Sasai, Y. Molecular Pathway and Cell State Responsible for Dissociation-Induced Apoptosis in Human Pluripotent Stem Cells. *Cell Stem Cell* **2010**, *7* (2), 225–239. https://doi.org/10.1016/j.stem.2010.06.018.

(125) Krawetz, R. J.; Li, X.; Rancourt, D. E. Human Embryonic Stem Cells: Caught between a ROCK Inhibitor and a Hard Place. *BioEssays* **2009**, *31* (3), 336–343. https://doi.org/10.1002/bies.200800157.

(126) Ichikawa, H.; Nakata, N.; Abo, Y.; Shirasawa, S.; Yokoyama, T.; Yoshie, S.; Yue, F.; Tomotsune, D.; Sasaki, K. Gene Pathway Analysis of the Mechanism by Which the Rho-Associated Kinase Inhibitor Y-27632 Inhibits Apoptosis in Isolated Thawed Human Embryonic Stem Cells. *Cryobiology* **2012**, *64* (1), 12–22. https://doi.org/10.1016/j.cryobiol.2011.11.005.

(127) Murray, K. A.; Gibson, M. I. Post-Thaw Culture and Measurement of Total Cell

Recovery Is Crucial in the Evaluation of New Macromolecular Cryoprotectants. *Biomacromolecules* **2020**, *21* (7), 2864–2873. https://doi.org/10.1021/acs.biomac.0c00591.

(128) Duménieu, M.; Oulé, M.; Kreutz, M. R.; Lopez-Rojas, J. The Segregated Expression of Voltage-Gated Potassium and Sodium Channels in Neuronal Membranes: Functional Implications and Regulatory Mechanisms. *Front. Cell. Neurosci.* **2017**, *11* (4), 1–19. https://doi.org/10.3389/fncel.2017.00115.

(129) Kang, S.; Chen, X.; Gong, S.; Yu, P.; Yau, S.; Su, Z.; Zhou, L.; Yu, J.; Pan, G.; Shi, L. Characteristic Analyses of a Neural Differentiation Model from IPSC-Derived Neuron According to Morphology, Physiology, and Global Gene Expression Pattern. *Sci. Rep.* **2017**, *7* (1), 1–11. https://doi.org/10.1038/s41598-017-12452-x.

Chapter 5: Cryopreservation of Primary T Cells Using Small Molecule Ice Recrystallization Inhibitors (IRIs)

5.1 Introduction: T Cells as Efficacious Cell Therapy Products for Various Tumors

In Canada, cancer is a major cause of death, accounting for 30% of all deaths; it is a serious public health issue that affects people all over the world.[1-2] A cancerous tumor develops in a microenvironment, which contains various types of immune system cells such as T lymphocytes, neutrophils, and natural killer (NK) cells.[2-3] Efforts to understand the complex interplay between tumors and their immunological microenvironment has led to the development of immunotherapies.[2,4] Research has shown that each tumor has an antigenic fingerprint that can be recognized by the human immune system, specifically by autologous T lymphocytes, which plays a vital role in directing an immune response to defeat tumor cells.[5-7] An example of immunotherapy as a promising strategy for the treatment of various cancers is adoptive T cell therapy (ACT).[4,8-9]

5.1.1 State-of-the-Art Immunotherapies

ACT relies on the augmentation of antigen-specific immunity where engineered T cells with selective antigens or receptors are introduced to a compromised immune system to target specific tumor and fight cancer cells.[8-13] One of the most effective ACT approaches is using chimeric antigen receptor T cells (CAR T cells).[12] CAR T cells are genetically modified cells that consist of a specialized tumor targeting domain.[16] The overall structure of a CAR T cell consists of four domains: the extracellular antigen binding domain, a hinge region, a transmembrane domain and an intracellular signaling domain.[95]

Engineering CAR T cells involves attaching proteins, known as chimeric antigen receptors, to patient-derived activated T cells.[16-18] These receptors have been engineered to target antigens found naturally on the surface of cancer cells, allowing the immune system of cancer patients to fight tumors on their own.[16-17] For example, epidermal growth factor receptor (EGFR) is a transmembrane protein that belongs to the receptor tyrosine kinase family, and plays a role in the development and growth of multiple cancers.[83-86] Anti EGFR-CAR T cells have been used for the treatment of gastric, lung, and colorectal carcinomas.[83-86] Another clinically-relevant CAR T cell product is CD19-transduced CAR T cells; CD19 antigen is a transmembrane glycoprotein that is expressed in B-lymphocytes.[21,75-76] Anti CD19 CAR T cells have shown promising results in the treatment of B-cell malignancies and acute lymphocytic leukemia, where the growth of tumor cells regresses significantly, and the duration of response lasts for longer than 3 years.[16-22,75-76,95]

The manufacturing process of CAR T cells starts with the extraction and isolation of T cells from a blood donor, such as healthy donors or cancer patients who did not undergo treatments such as chemotherapy or radiation. This is followed by purification, multiplication and activation using specialized beads (anti-CD3/anti-CD28). Expression of the chimeric antigen receptor is then done by either retroviral or lentiviral transduction, as shown in **Figure 5.1**.[10,17,77-78]

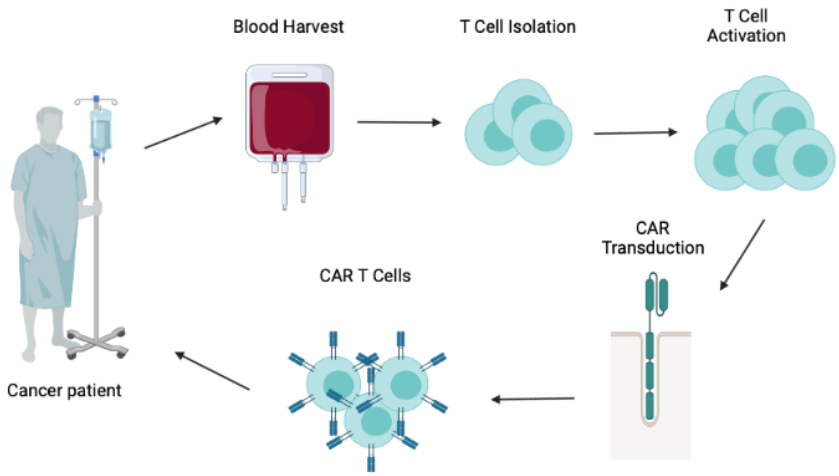

Figure 5.1 A depicted illustration of the steps required for engineering CAR T cells. Figure created using free license from BioRender.

Overall, the promise of cancer immunotherapies is becoming a prominent area of interest in the research field due to the continuous increase in the number of cancer patients.[1,58] T cells and their derivatives (i.e., CAR T cells) have emerged as effective immunotherapies for treating different kinds of tumors.[59-63] The quality of T cell products is dependent on the cell sources (i.e., cancer patients or healthy donors). Moreover, the production of engineered CAR T cells requires large numbers of healthy T cells which raises significant challenges in terms of clinical applications. The process of harvesting enough T cells to justify the manufacturing process of CAR T cells takes a considerable amount of time and money, limiting the availability of such treatment. [77-78] Moreover, the clinical process of T cell extraction, transduction, and delivery requires a good quality-controlled cryopreservation protocol that allows the transit of viable and efficacious cells throughout the manufacturing process of CAR T cell therapy products, as shown in **Figure 5.2**.[77-78] Thus, it is critical to establish an efficient cryopreservation protocol that permits T cells and CAR T cells to be stored for extended periods of time, allowing the delivery of a sufficient amount of T cell therapy products to clinics and hospitals.

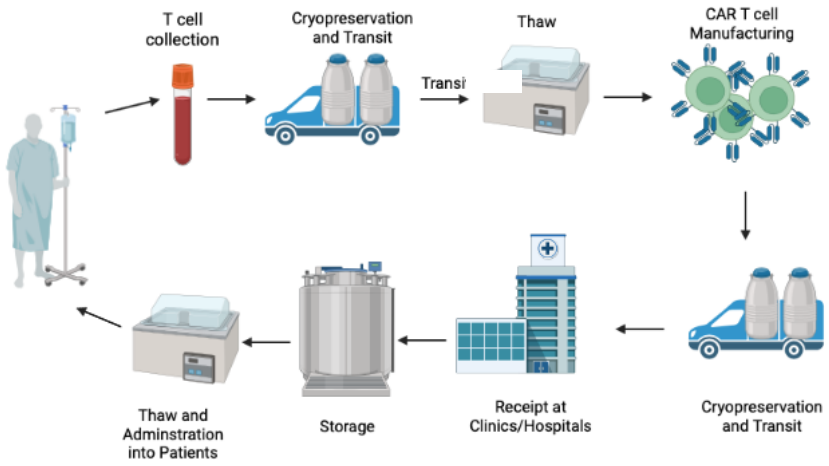

Figure 5.2 A pictorial representation of the multiple stages where cryopreservation is required throughout the manufacturing process and transit of CAR T cell therapy. Figure created using free license from BioRender.

5.2 The Optimization of the Cryopreservation Protocol of T Cell Utilizing IRIs

5.2.1 Conventional Cryopreservation Media for T cells

The success of cell-based immunotherapies is dependent on the transit of T cell products from the manufacturing site to the patient.[24,30] Current commercial designs rely on a frozen product that can be transported to clinics and stored, then thawed and infused into patients when required. However, cryopreservation-induced stressors, generally known as delayed onset cell death (DOCD), severely limit the viability and growth of T cell products after thawing.[24,30-32] The use of CPAs such as DMSO has shown to reduce the cellular damage induced by cryopreservation and to increase the viability of cells.[33-35] The conventional cryopreservation protocol for T cells and their derivatives (i.e., CAR T cells) utilizes a slow cooling rate (-1 °C/min) until - 80 °C is reached, followed by final storage in liquid nitrogen (- 196 °C) to store cells for several months/years.[30,36-37]

To successfully optimize the cryopreservation protocol and media utilized to freeze T cells and CAR T cells, an immortalized lymphocyte cell line (i.e., Jurkat cells) is typically used to measure the efficacy of the cryopreservation protocol being established.[31,39] Jurkat cells are an immortalized cell line of human acute lymphocytic leukemia cells that have been employed in numerous investigations, including the activation and cryopreservation of T cells, as well as T cell receptor signaling.[31,39] One of the primary cryomedia proposed for the preservation of the Jurkat cell line is fetal bovine serum (FBS) supplemented with 10 % or 20 % DMSO.[30,32,38-39] Some commercially available, serum-free cryomedia, such as Cryostor®5 (CS5) or Cryostor®10 (CS10), have also been proposed for the preservation of Jurkat cells.[30,32] The post-thaw viability and recovery rate of Jurkat cells vary between 50 to 90 %, depending on the cryomedium used for storage.[30,38] Moreover, CS5 has been shown to improve the proliferation activity of Jurkat cells post-thaw compared to FBS supplemented with 10 % or 20 % DMSO.[30]

In research, supplementation of FBS with 10 % DMSO has been used as the main cryomedium for the cryopreservation of human-derived T cells and CAR T cells.[40] RPMI-1640 supplemented with 10 % FBS and 10 % DMSO, phosphate-buffered saline (PBS, Dulbecco USP grade) supplemented with 50% human albumin and 10 % DMSO, Cryostor®10 (CS10), and Synth-a-Freeze™ medium are examples of other cryo-solutions that have been studied for the preservation of T cells.[40-48] The post-thaw viability of T-cells and CAR T cells range between 70 - 90 % and 40 - 60 %, respectively, depending on the cryomedium used to store T cell products.[40-49] The post-thaw viability of CAR T cells is lower than that of T cells, as they are more complex cells and behave differently compared

to non-engineered cell types, and thus, CAR T cells are more susceptible to cryoinjuries.[47,49]

Using conventional cryomedia solutions, the post-thaw functionality of T cells and CAR T cells, such as the proliferation and killing activities, have been shown to be compromised post cryopreservation.[40,43-46] For example, electroporation method is utilized to assess the transfection of T cells into CAR T cells by measuring the expression of green fluorescence protein (GFP).[45] Research has shown that the expression of GFP appears to decrease after T cells cryopreservation due to cellular damage, and therefore, T cell activation is required to increase the electro-transfection efficiency for cryopreserved T cells.[45] In addition, some cryo-solution formulations contain animal components (i.e., FBS) which limits their use in clinical settings. While other commercially available cryo-solutions (i.e., CS10 and Synth-a-Freeze™) contain high concentrations of DMSO (10 – 20 %) which has been reported to cause many neurotoxic effects if not washed or diluted prior to any clinical applications.[50-52] Furthermore, none of the conventional cryomedia account for the cryoinjuries caused by ice recrystallization, meaning, they do not contain additives (i.e., IRIs) that protect cells from the detrimental effects caused by the prolonged ice exposure or ice recrystallization. Consequently, establishing an optimized cryomedium that is clinically relevant and contains IRIs is an attractive approach for increasing the availability of T cell-based therapies in clinics and hospitals.

5.2.2 IRI-Supplemented Cryomedia for Jurkat and T Cells

Ice recrystallization is one of the major causes of cellular damage/death during freezing and thawing processes, and therefore, efforts have been guided toward the development of ice recrystallization inhibitors (IRIs) for use as novel cryoprotective

additives.[27,34,53] While conventional CPAs such as DMSO have been utilized to mitigate cellular damage during freezing,[23-24] they do not protect cells from the cryoinjury associated with ice recrystallization. The Ben laboratory has successfully synthesized a library of IRIs ranging from large to small molecules with IRI activity.[54-57] Moreover, different classes of IRIs have been found to enhance the cryopreservation outcomes of different cells. For instance, *O*-aryl glucoside IRIs (**Figure 5.3**) have been shown to increase the post-thaw viability of red blood cells (RBCs) and to maintain the membrane integrity of RBCs post-thaw.[55] Another class of IRIs, *N*-aryl gluconamide IRIs (**Figure 5.3**), have been shown to improve the post-thaw functionality of hematopoietic stem cells (HSCs) and iPSCs.[56-57] Consequently, we sought to discover the capacity of IRIs to enhance the cryopreservation outcome of T cells and CAR T cells.

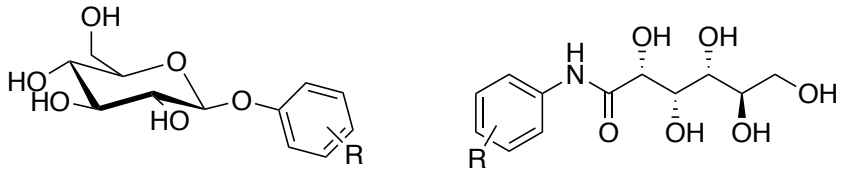

***O*-aryl-D-glucosides** ***N*-aryl-D-gluconamides**

Figure 5.3 General structures of *O*-aryl-D-glucoside and *N*-aryl-D-gluconamide IRIs.

The selection of the IRIs that were tested on Jurkat and T cells was based on a previous study where a specific class of IRIs, *N*-aryl-D-gluconamides, showed an improvement in the post-thaw recovery rate and functionality of iPSCs and iPSC-Ns (**chapter 4**), as well as HSCs.[56-57] Two active IRIs that showed an increase in the post-thaw viability of iPSCs,[93] and HSCs[56-57] were further tested on Jurkat cells and T cells.

As mentioned previously in chapter 4, the viability of iPSCs that were frozen with *N*-2-fluorophenyl-D-gluconamide (2FA, **Figure 5.4**) and *N*-4-chlorophenyl-D-gluconamide (4ClA, **Figure 5.4**) increased post-thaw. And consequently, 2FA and 4ClA were

formulated in a GMP-compatible cryomedium to further test their cryoprotective properties on T cells and CAR T cells.

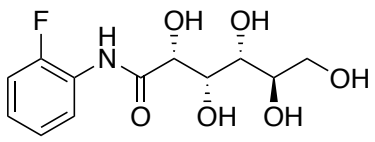

***N*-2-fluorophenyl-D-gluconamide (2FA)**

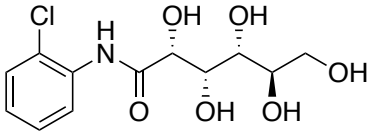

***N*-4-chlorophenyl-D-gluconamide (4ClA)**

Figure 5.4 The chemical structures of 2FA and 4ClA that were used for the cryopreservation of Jurkat cells and T cells.

To successfully optimize the concentrations of IRIs for the preservation of T and CAR T cells, IRIs were first tested on the lymphocyte cell line (Jurkat cells). Jurkat cells play a significant role in the study of T cell activation, T cell receptor signaling, CAR transduction, as well as cryopreservation of T cells.[31,39,69] Therefore, Jurkat cells were cryopreserved with CS10 in the presence or absence of 2FA or 4ClA to establish the appropriate concentrations for the cryopreservation of T cells. Jurkat cells were obtained from American Type Culture Collection (ATCC), thawed, and cultured in RPMI supplemented with 10% FBS, 100 units/mL penicillin, 100 units/mL streptomycin, and 2 mM L-glutamine for 7 days. Jurkat cells were then frozen in CS10 alone, or in IRI-supplemented CS10 (2FA or 4ClA). The cells were allowed to cool to -80 °C using a Mr. Frosty rate-controlled freezing container (-1°C/min). Jurkat cell samples were then moved to a liquid nitrogen dewar until they were thawed. Post-thaw viability, as well as recovery rate, were assessed using the Trypan blue exclusion assay. The maximum concentrations tested for 2FA and 4ClA depended on their maximum solubility that was observed in CS10, which was found to be 15 mM for 2FA and 5 mM for 4ClA.

Following the establishment of the concentrations of 2FA and 4ClA that improve the post-thaw viability and recovery rate of Jurkat cells, 2FA and 4ClA were further tested

on human-derived T cells and CD19-CAR T cells. In a typical clinical setting, T cells are extracted from cancer patients, followed by activation and then transduction into CAR T cells. T cells and CAR T are grown for 9-14 days prior to transfusion to increase the number of cells per dose.[90] Therefore, we sought to investigate the difference in cryopreservation outcomes on T cells obtained at day 0 (prior to the addition of anti CD3 and CD28 beads), and T cells obtained at the beginning (day 1) or the end of the activation process (day 9) in the presence or absence of IRIs, as depicted in **Figure 5.5**. EGFR- or CD19- transduced CAR T cells were grown for 9 days post transduction, and then were frozen in the presence or absence of IRIs to investigate any improvement in the cryopreservation outcomes when IRI technology is applied (**Figure 5.5**). To assess the efficacy of the cryopreservation protocol being established, post-thaw viability and recovery rates of T cells and CAR T cells, as well as the killing activity of EGFR-CAR T cells were examined.

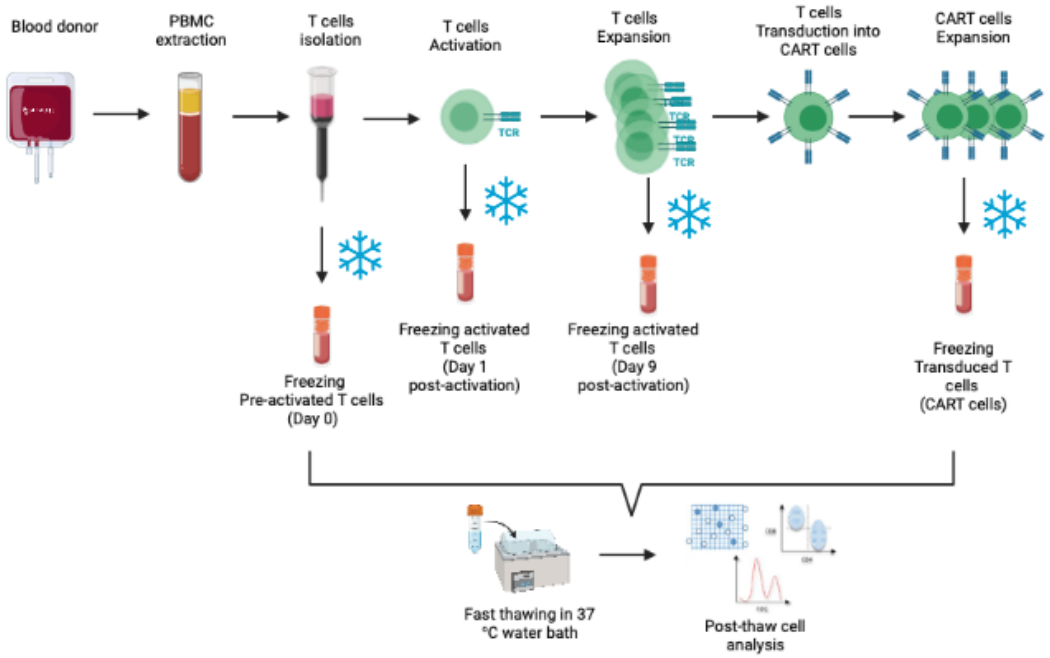

Figure 5.5 Schematic diagram of T cell isolation, activation, transduction, and cryopreservation. T cells were obtained from blood donors and were frozen either at day 0, or at days 1 and 9 post-activation. Figure created using free license from BioRender.

5.3 Assessment of the Post-Thaw Viability and Recovery of 2FA- and 4ClA-Frozen Jurkat Cells, T Cells and CD19-CAR T Cells

Cryopreservation causes cellular injuries that compromise the integrity of the cell membrane, causing cellular components including cytoplasm and nucleus to be susceptible to damage. Many dye-exclusion assays such as Trypan blue or acridine orange and propidium iodide (AO/PI) can be used to determine post-thaw viability/recovery. To explain, live cells have an undamaged cell membrane, and hence, are impermeable, whereas dead/damaged cells are permeable and can absorb the dye.[70-71,79] Post-thaw viability and recovery rates are two of the primary measures that are determined while assessing cryopreservation protocols.[92]

Post-thaw recovery rate refers to the number of live cells post-thaw compared to the total number of cells that were initially frozen. Whereas percent viability refers to the number of live cells compared to the total number of live and dead cells that were counted post-thaw, with the latter tending to give higher values than the former.[92] Both measurements are crucial for the initial stages of establishing a cryopreservation protocol because they offer a preliminary indication on how different cell lines or primary cells respond to cryopreservation.[79,92]

5.3.1 Analysis of the Post-Thaw Viability and Recovery rate of IRI-Frozen Jurkat Cells

Jurkat cells were cultured in complete RPMI medium for 7 days; they were then frozen in triplicate in either CS10 or CS10-formulated with 2FA or 4ClA (**Figure 5.4**). The concentrations of 2FA and 4ClA were selected depending on their maximum solubility in CS10 that was established previously in iPSCs and iPSC-Ns.[93] 2FA was formulated in CS10 at 15 mM, 10 mM, and 5 mM, while 4ClA was formulated in CS10 at 5 mM and 0.5

mM. Jurkat cells were thawed approximately 7 days after cryopreservation. Immediate post-thaw viability and recovery rate were quantified using the Trypan blue exclusion assay.

As shown in **Figure 5.6 A**, the mean post-thaw viability for CS10-, 2FA- and 4ClA-frozen Jurkat cells ranged between 60% and 68% with no statistical difference (n = 3) as suggested by one-way ANOVA with Dunnett's multiple comparison test. However, taking into consideration the number of cells that were frozen initially allowed for the determination of post-thaw recovery (survival rate) for the different freezing conditions. As depicted in **Figure 5.6 B**, the mean recovery rates of 5 mM 2FA- as well as 5 mM 4ClA-frozen Jurkat cells were statistically higher than CS10-frozen ones, with a 1.7-fold increase (n = 3, P value < 0.01). The percent recovery rates were found to be 82.9 ± 4.3 %, 77.7 ± 8.8 % and 46.9 ± 4.6 %, for 5 mM 2FA, 5 mM 4ClA, and CS10-frozen cells, respectively. On the other hand, the difference in mean post-thaw recovery rates between CS10-frozen Jurkat cells and 15 mM 2FA-, 10 mM 2FA-, and 0.5 mM 4ClA-frozen cells was not statistically significant (n = 3, P value > 0.1), where the recovery rates were found to be 51.7 ± 9.9 %, 63.1 ± 13 % and 38.9 ± 5.3 %, respectively (**Figure 5.6 B**).

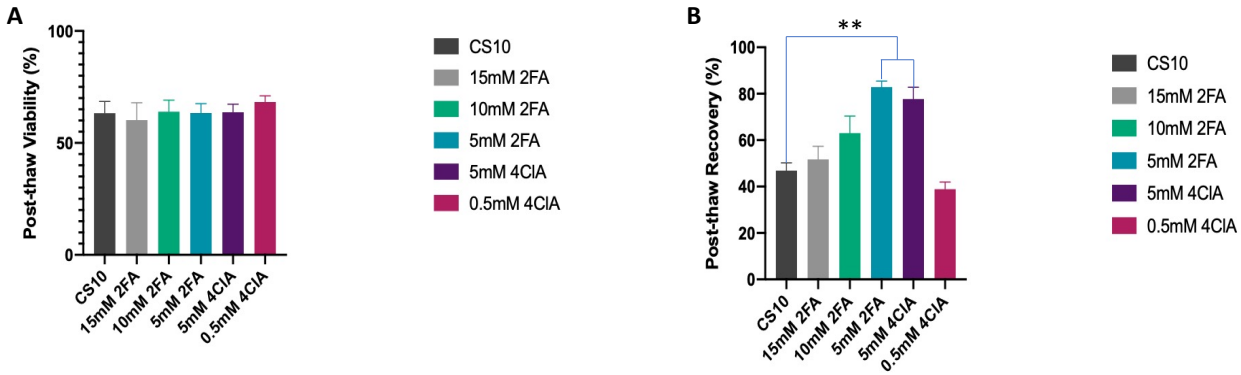

Figure 5.6 Bar graph representing the mean **(A) immediate post-thaw viability** and **(B) immediate post-thaw recovery rate** of Jurkat cells using the Trypan blue exclusion assay. Jurkat cells were cultured in complete RPMI for 7 days and then frozen in **triplicate (n = 3)**. Jurkat cells were cryopreserved in either CS10, or in 2FA- or 4ClA-

supplemented CS10. Error bars represent the standard error of the mean (SEM). One-way ANOVA test suggested that **(A)** there was no statistically significant difference between post-thaw viability of CS10 and the different freezing conditions (P value > 0.1, n=3), however, **(B)** there was a statistically significant difference between the post-thaw recovery of CS10, 5 mM 2FA and 5 mM 4ClA (** = P value < 0.01, n=3).

From these preliminary data, formulation of 5 mM 2FA or 5 mM 4ClA in CS10 results in a higher number of live Jurkat cells compared to CS10-alone, which indicates that protection against ice recrystallization improves the cryopreservation outcome for Jurkat cells. This further implies that 2FA and 4ClA may serve as potential cryo-additives for the cryopreservation of Jurkat cells. Moreover, these data also suggest that the selected concentrations of 2FA and 4ClA are suitable for the preservation of Jurkat cells, and therefore, they may be further applied in the cryopreservation protocol of T cells and CAR T cells.

5.3.2 Determination of the Post-Thaw Viability and Recovery Rate of IRI-Frozen Primary T Cells

T cell-based therapy products represent a distinct approach to the development of innovative immunotherapeutic for cancer treatment, however, their successful application in cell replacement therapies relies on an effective cryopreservation protocol that maintains viable and functional T cells post freezing.[19-22] As mentioned **in section 5.2.1**, several freezing solutions have been proposed for the cryopreservation of primary T cells, however, the presence of animal components, such as FBS, in their formulations limits their application in a clinical setting. Thus, it is vital to develop a GMP-compatible cryo-solution (i.e., CS10) that allows the delivery and use of frozen T cells in clinics. While 10 – 20 % DMSO is essential for the protection of cells from cryoinjuries associated with slow freezing process,[50-52] DMSO fails to mitigate cellular injuries caused by ice recrystallization. Therefore, the two IRIs that were tested on Jurkat cells, 2FA and 4ClA,

were further employed in the cryopreservation protocol of T cells to investigate whether protection against ice recrystallization may increase the number of live T cells post-thaw. IRIs were employed in the freezing process of T cells that were obtained at different stages (i.e., prior or post activation). T cells that were obtained prior to activation/multiplication (i.e., addition of anti CD3, anti CD28) are referred to as day 0-T cells. While T cells that were frozen at day 1 or day 9 post activation/multiplication are referred to as day 1- or day 9-T cells. The purpose of testing the cryopreservation outcome on day 1- and day 9-T cells is to observe and compare any differences in the T cell response to freezing and thawing both at the beginning and end of the activation process.

5.3.2.1 Assessment of the Viability and Recovery Rate of T Cells Frozen on Day 0

Primary T cells are susceptible to cryoinjuries induced by freezing and thawing.[37-38] Therefore, we sought to discover whether employing IRIs while freezing T cells prior to the activation/multiplication process (i.e., day 0-T cells) may assist in maintaining high viability and recovery rate post-thaw. As presented in **section 5.3.1**, formulations of 5 mM of 2FA or 4ClA in CS10 appeared to enhance the survival (recovery) rate of Jurkat cells, and therefore, these two IRIs were further applied on day 0-T cells.

Figure 5.7 represents both the immediate post-thaw viability and recovery rate of primary T cells that were obtained from **donor 85** and frozen on day 0. From **Figure 5.7 A**, it appears that formulating 5 mM 2FA or 4ClA in CS10 resulted in a statistically significant increase in the immediate post-thaw viability compared to CS10-frozen T cells (P value < 0.01 and P value < 0.1, respectively, n = 2), where the mean percentage of the post-thaw viability of 5 mM 2FA, 5 mM 4ClA, and CS10 samples were found to be 81.9 ± 0.6 %, 69.8 ± 0.3 %, and 48.8 %, respectively. On the other hand, formulation of 15 mM

2FA and 10 mM 2FA in CS10 did not appear to increase the post-thaw viability of T cells when they were compared with CS10 using a one-way ANOVA test with Dunnett's multiple comparison (P value > 0.1, n = 2), as shown in **Figure 5.7 A**.

Taking into consideration the total number of cells that were frozen initially, the post-thaw recovery rates of the different freezing conditions were also evaluated and presented in **Figure 5.7 B**. It appeared that formulation of 10 mM and 5 mM of 2FA in CS10 statistically increased the post-thaw recovery rate (P value < 0.01, n = 2) in comparison with CS10 (69.6 ± 8.7 % and 81.1 ± 4.0 % vs 44.1 %, **Figure 5.7 B**). However, the immediate post-thaw survival rate of 15 mM 2FA- and 5 mM 4ClA-frozen cells did not appear to statistically differ than that of CS10-frozen ones (P value > 0.1, n = 2).

The values of the recovery rates are lower than those of the viability percentages because the viability assessment only considers the cells that have damaged membranes and were stained by Trypan blue, while the cell survival analysis takes into consideration all the cells that have severe damaged membranes and were not stained by Trypan blue (cell debris). Overall, 10 mM and 5 mM 2FA increased cell survival which implies that protection against ice recrystallization helps in maintaining a higher number of live T cells which can be beneficial for future clinical applications.

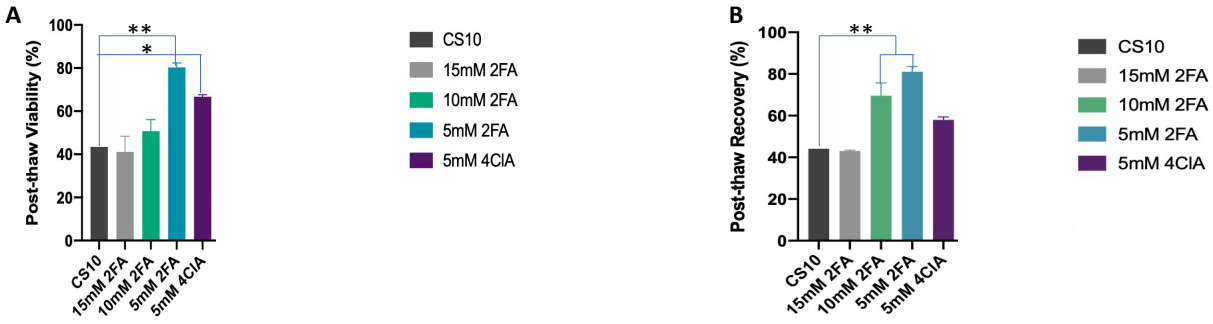

Figure 5.7 Bar graph represents the mean of **(A) the immediate post-thaw viability** and **(B) the immediate post-thaw recovery** of primary T-cells using the Trypan blue exclusion assay**.** Human T-cells were isolated from a blood donor 85. The cells were frozen at **day 0** in **duplicate (n = 2)** for each condition, except Cryostor10 which had one

sample only. Primary T-cells were cryopreserved in a CS10 in the presence or absence of 2FA 4ClA. Error bars represent the standard error of the mean (SEM). Statistical significance marked by asterisks assessed by one-way analysis of variance (ANOVA) for comparison with CS10, where ns = $P > 0.1$, * = $P \leq 0.1$, ** = $P \leq 0.01$, n = 2. One-way ANOVA Test suggests that **(A)** there was a statistically significant difference between the post-thaw viability of CS10, 5 mM 2FA and 5 mM 4ClA, **(B)** whereas only 10 mM and 5 mM 2FA samples showed a statistical significance compared to CS10.

Some 2FA formulations (i.e., 10 mM and 5 mM) showed a significant increase in both viability and recovery rate for T cells obtained on day 0, while 4ClA only resulted in an improvement in the post-thaw viability. Displaying statistically significant changes in both measurements (recovery and viability) is crucial in the process of evaluating the efficacy of any cryopreservation protocols,[92] and therefore, 2FA at concentrations less than 15 mM were further tested on T cells that were obtained on day 0 from two additional different donors (**donor 92 and 97**) to confirm the capacity of 2FA in maintaining high survival rate of T cells.

T cells were extracted from **donors 92 and 97** and were frozen in triplicate for each donor with CS10 in the presence or absence of 10 mM, 5 mM, and 2.5 mM 2FA (n = 3). As presented in **Figure 5.8 A**, there was no statistically significant difference in the immediate post-thaw viability of primary T cells frozen on day 0 with the different 2FA formulations compared to CS10-alone as suggested by one-way ANOVA test (P value > 0.1). On the other hand, the immediate post-thaw recovery rates for 5 mM 2FA and CS10-alone samples were found to be 75.8 ± 11.3 % and 54.1 ± 9.9 %, respectively. Further, it was evident that the formulation of 5 mM 2FA in CS10 significantly enhanced the immediate post-thaw recovery rate compared to CS10-frozen cells (P value < 0.1, n = 6, **Figure 5.8 B**). Overall, the presence of 5 mM 2FA appeared to statistically increase the survival rate of T cells compared to CS10 alone, indicating the importance of preventing

the occurrence of ice recrystallization during cryopreservation for maximizing the number of viable T cells.

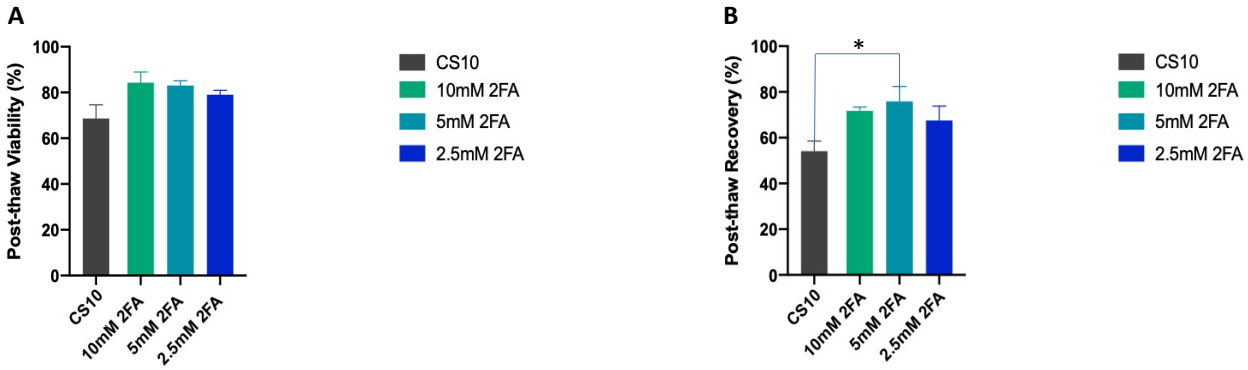

Figure 5.8 Bar graph represents the mean **(A) immediate post-thaw viability** and **(B) immediate post-thaw recovery** of primary T-cells using the Trypan blue exclusion assay**.** Human T-cells were isolated from blood donors 92 and 97. The cells were frozen on **day 0** in **triplicate for each donor (n = 6, in total)**. Primary T-cells were cryopreserved in CS10 in the presence or absence of 2FA (10 mM, 5 mM, and 2.5 mM). Error bars represent the standard error of the mean (SEM). One-way ANOVA test suggests that **(A)** there was no statistically significant difference between the post-thaw viability of the different conditions in comparison with CS10 (P value > 0.1), **(B)** whereas the post-thaw recovery rate of CS10 and 5 mM 2FA showed a statistical difference (* = P value < 0.1, n = 6).

Figures 5.7 and 5.8 suggest that despite the diverse variations present between blood donors (donor 85, 92, and 97), such as age and health, formulation of 5 mM 2FA in CS10 increased the post-thaw recovery rate. This implies that inhibiting ice recrystallization enhances the cryopreservation outcomes on T cells, and consequently, 2FA was further tested on T cells that were obtained on day 1 and day 9 post activation.

5.3.2.2 Analysis of the Viability and Recovery Rate of T Cells Frozen on Day 1 Post Activation

As suggested in **Figure 5.5** primary T cells were extracted, purified, and subjected to activation and expansion prior to freezing or transduction. The activation process of T cells using anti CD3/anti CD28 beads is significant for *in vitro* T cell expansion and for the expression of antigens on the cell surface of T cells.[74,94] In a clinical setting, T cells are

extracted and expanded for 10-14 days before transfusion or cryopreservation.[90] In our experimental model, we sought to investigate the difference in the number of viable cells post-thaw when they were frozen at the beginning (day 1 post activation) and the end (day 9 post activation) of the activation process. Cryopreserved and activated T cells that expand more readily post-thaw are healthy T cells that can be further transduced into CAR T cells. This will serve as an indicator for whether inhibiting ice recrystallization improves the cryopreservation outcomes regardless of the stage at which the cells were frozen.

T cells were extracted from blood **donor 97**, purified, and activated using anti CD3/antiCD28 beads for one day. Cells were then obtained on day 1 post-activation and frozen in triplicate (n = 3) with CS10 in the absence or presence of 2FA (10 mM, 5 mM, and 2.5 mM). Post-thaw viability and recovery rate were assessed using the Trypan blue exclusion assay. From **Figure 5.9 A**, it is evident that 10 mM 2FA improved the immediate post-thaw viability compared to CS10, 79.3 ± 1.0 % vs 62.3 ± 4.6 %, respectively. Moreover, one-way ANOVA test comparing the mean post-thaw viability between 10 mM 2FA and CS10 confirmed that there was a statistically significant increase in the number of live cells (P value < 0.1). However, the mean post-thaw viability of 5 mM and 2.5 mM 2FA-frozen T cells did not show any statistical difference compared to CS10-cryopreserved cells.

The immediate post-thaw recovery rate of the different freezing conditions was evaluated and presented in **Figure 5.9 B**. It appeared that the formulation of 5 mM 2FA in CS10 resulted in a higher cell survival rate compared to CS10 alone, 84.3 ± 1.0 % vs 46.4 ± 4.3 %, respectively (**Figure 5.9 B**). A one-way ANOVA test with Dunnett's multiple comparison also revealed that the difference in the survival rate is statistically significant

for 5 mM 2FA, P values < 0.0001 (n = 3). In contrast, 10 mM, and 2.5 mM 2FA formulations did not show a statistically significant increase in the immediate post-thaw recovery rates compared to CS10 alone (**Figure 5.9 B**).

Comparing the cryopreservation outcomes of the T cells that were frozen prior to activation (day 0, **Figures 5.7 and 5.8**) with the ones frozen on day 1 post activation (**Figure 5.9**), it is apparent that the post-thaw viability percentages vary from one another. Nonetheless, the formulation of 5 mM 2FA in CS10 developed consistent observations in the immediate post-thaw recovery rate of both stages, where the survival rate of 5 mM 2FA-frozen cells appeared to increase significantly in comparison with CS10-frozen ones. This further confirms the importance of employing IRIs in the cryopreservation protocol of T cells which will increase the availability of T cell doses for clinical applications.

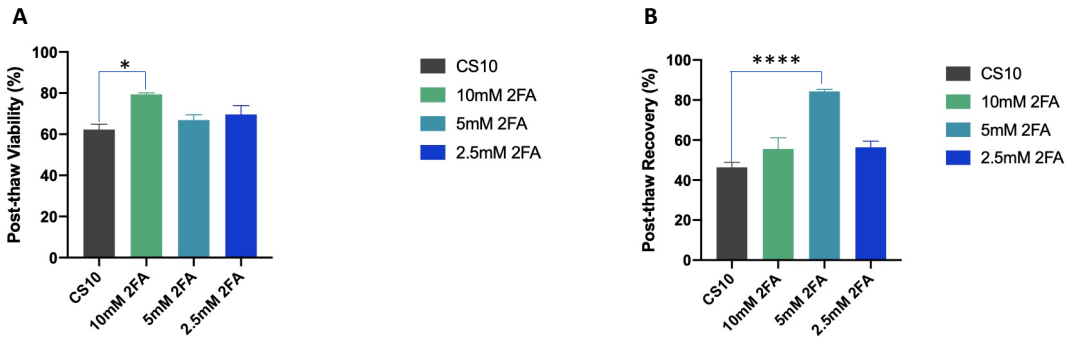

Figure 5.9 Bar graph represents the mean (A) **immediate post-thaw viability** and **(B) immediate post-thaw recovery** of primary T-cells using the Trypan blue exclusion assay**.** Human T-cells were isolated from a blood donor 97. The cells were frozen on **day 1 post-activation** in **triplicate (n = 3)**. Primary T-cells were cryopreserved in CS10 in the absence or presence of 2FA (10 mM, 5 mM, and 2.5 mM). Error bars represent the standard error of the mean (SEM). **(A)** One-way ANNOVA test suggested that there was a statistically significant difference between post-thaw viability percentage of 10 mM 2FA and CS10 (* = P value < 0.1, n = 3), **(B)** whereas the post-thaw recovery of CS10 and 5 mM 2FA showed statistically significant difference (**** = P value < 0.0001, n = 3).

5.3.2.3 Evaluation of the Viability and Recovery Rate of T Cells Frozen on Day 9 Post Activation

T cells can further be manipulated by transduction to express different antigens, such as EGFR and CD19, or can be cryopreserved.[90] 2FA formulations in CS10 showed promising results for improving the recovery rate of T cells that were frozen at day 0 or day 1 post activation, and thus, we sought to further examine any changes in the post-thaw viability or recovery of primary T cells frozen on day 9 post-activation. Freezing of T cells at the end of the activation process will reduce the time required to obtain a high number of active T cells post-thaw, thereby reducing the amount of time for a patient to receive treatment.

The cells were extracted from three different donors (**donor 93, 96, and 97**), and frozen on day 9 post activation in triplicate for each donor with CS10 in the presence or absence of 2FA (10 mM, 5 mM, and 2.5 mM). Viability and recovery rate were assessed using the Trypan blue exclusion assay immediately post-thaw. As presented in **Figure 5.10 A**, the mean immediate post-thaw viability of 5 mM 2FA- and 2.5 mM 2FA-cryopreserved T cells were found to be 73.6 ± 7.4 % and 76.3 ± 5.8 %, respectively, while CS10-frozen T cells had a post-thaw viability of 68.0 ± 4.4 %. A one-way ANOVA test with Dunnett's multiple comparisons revealed that there was a statistically significant increase in the post-thaw viability for 5 mM and 2.5 mM 2FA-frozen cells compared to CS10-frozen cells, P value < 0.1 and P value < 0.01, respectively (n = 9). T cells cryopreserved with 10 mM 2FA did not show any statistical difference in the mean post-thaw viability compared to CS10 ones.

The mean immediate post-thaw recovery rates were also evaluated and are presented in **Figure 5.10 B**. The survival rates were found to be 66.6 ± 7.9 % for 10 mM 2FA, 75.0 ± 8.0 % for 5 mM 2FA, 73.1 ± 7.1 % for 2.5 mM 2FA and 55.7 ± 7.6 % for CS10 alone. Analysis of the post-thaw recovery for the different freezing conditions, and comparison with the control medium (CS10) displayed a statistically significant increase in the recovery rate of 10 mM, 5 mM, and 2.5 mM 2FA cultures when they were compared to CS10, with P values < 0.1, < 0.0001, and < 0.001, respectively (n = 9). The difference in the observations between viability and recovery rate comes from the fact that the latter measurement takes into consideration the damaged cells that were not stained by Trypan blue.

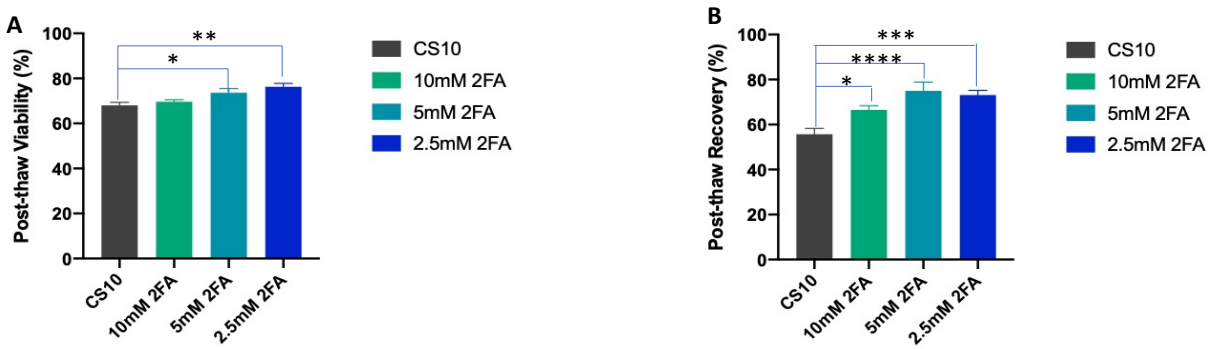

Figure 5.10 Bar graph represents the mean **(A) immediate post-thaw viability** and **(B) immediate post-thaw recovery rate** of primary T-cells using the Trypan blue exclusion assay**.** Human T-cells were isolated from blood donors 93, 96 and 97 and frozen on **day 9 post activation** in **triplicate for each donor (n = 9, in total)**. Primary T-cells were cryopreserved in CS10 in the presence or absence of 2FA (10 mM, 5 mM, and 2.5 mM). Error bars represent the standard error of the mean (SEM). Statistical significance marked by asterisks assessed by one-way analysis of variance (ANOVA) for comparison with CS10, where * = P ≤ 0.1, ** = P ≤ 0.01, *** = P ≤ 0.001 and **** = P ≤ 0.0001 (n = 9). One-way ANOVA Test suggests that **(A)** there is a statistically significant difference between post-thaw viability of 5 mM 2FA and 2.5 mM 2FA in comparison with CS10. **(B)** On the other hand, a statistically significant increase in post-thaw recovery was observed for 10 mM 2FA-, 5 mM 2FA- and 2.5 mM 2FA-frozen cells in comparison with CS10-frozen T cells.

Comparing the results of the post-thaw viability and recovery rates of T cells frozen on day 0, day 1 post activation, and day 9 post activation, it is notable that the formulation

of 5 mM 2FA in CS10 significantly raised the cell survival rate regardless of the stage at which the cells were frozen. Overall, these preliminary data offer evidence that employing IRIs in the cryopreservation protocol of T cells will protect the cells from cryoinjury associated with ice recrystallization, increasing the number of viable cells post-thaw, and thus, increasing the doses of T cell available for cancer patients.

5.3.3 Analysis of the Post-Thaw Viability and Recovery of IRI-Frozen CD19-CAR T Cells

Engineered T cell-based therapies, such as CAR T cells, hold considerable potential as future cancer treatments.[21,75-76] CAR T cells are reprogrammed by overexpressing a specific antigen, such as CD19, on the extracellular domain of T cells. CD19-directed CAR T cells have shown promising clinical results in treating B-cell malignancies and acute lymphocytic leukemia.[21,75-76,95]

The production process of CD19-CAR T cells is lengthy and costly as it requires ~14 days and numerous reagents/materials to produce a sufficient number of doses of CD19-CAR T cells.[90,95] Thus, it is significant to optimize the cryopreservation protocol of CAR T cells to increase the availability of multiple CAR T cell doses for cancer patients. Conventional cryopreservation protocols proposed for CAR T have been reported to reduce the number of viable and functional cells.[76] The post-thaw viability of CAR T cells ranges between 47 to 69 % depending on the cryomedium used for freezing and the quality of the donor cells.[76] Therefore, we sought to investigate whether employing IRI technology in the CAR T cell freezing protocol would improve the post-thaw viability and recovery rate. The IRIs that were tested previously on Jurkat cells and primary T cells (i.e., 2FA and 4ClA) were further applied on CD19-CAR T cells. Frozen CD19-CAR T cells (**donor 1**) were

thawed and grown in complete ImmunoCult™-XF medium (with IL2) for a week. The cells were then cryopreserved in duplicate (n = 2) in CS10 or CS10 formulated with either 4ClA (5 mM, 2.5 mM, and 0.5 mM) or 2FA (15 mM, 10 mM, and 5 mM). As presented in **Figure 5.11 A**, the mean post-thaw viability for the control medium (CS10) and the different formulations ranged between 54.6 % and 66.2 % with no statistically significant difference compared to CS10 alone (one-way ANOVA test, P value > 0.1, n = 2).

The immediate post-thaw recovery rates for the different freezing conditions were assessed and presented in **Figure 5.11 B**. It is evident that the number of viable cells in 5 mM 2FA cultures increased in comparison with CS10-treated cells, 83.9 ± 4.4 % vs 63.0 ± 1.5 %, respectively. Moreover, one-way ANOVA test with multiple comparisons suggested that the difference in the cell survival for 5 mM 2FA-frozen CD19-CAR T cells was statistically significant compared to CS10-frozen ones. The survival rate of the other formulations (15 mM 2FA, 10 mM 2FA, 5 mM 4ClA, 2.5 mM 4ClA, and 0.5 mM 4ClA) ranged between 40 and 60 %, and one-way ANOVA test revealed that there was no statistical difference compared to CS10 (P value > 0.1, n = 2).

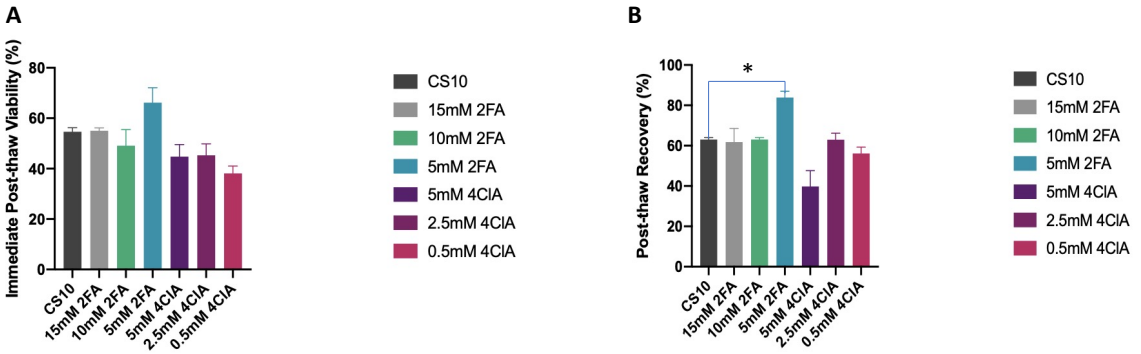

Figure 5.11 Bar graph represents the mean **(A) immediate post-thaw viability** and **(B) immediate post-thaw recovery** of human CD19-CAR T cells of donor 1 using the Trypan Blue exclusion assay**.** Human CD19-CAR T cells were cultured for 7 days in ImmunoCult™-XF supplemented with IL2. The cells were frozen on day 8 **in duplicate** with CS10 in the presence or absence of 2FA or 4ClA. Error bars represent the standard error of the mean (SEM). **(A)** One-way ANOVA test suggested that there was no statistical significance between the post-thaw viability of the different freezing conditions compared to CS10 (P value > 0.1, n=2). **(B)** On the other hand, there was a statistically significant difference between the post-thaw recovery of CS10 and 5 mM 2FA (P value < 0.1, n=2).

Since 4ClA did not show any advantageous effects on the post-thaw recovery rate or viability of CD19-CAR T cells (**Figure 5.11 A-B**), it was dropped from further experiments. 2FA was further tested on CD19-CAR T cells obtained from a different donor (**donor 2**) to account for donor-to-donor variability. 2FA was formulated in CS10 at 15 mM, 10 mM, and 5 mM, and post-thaw recovery and viability were assessed to evaluate and confirm the capacity of 2FA to preserve CD19-CAR T cells.

From **Figures 5.12 A-B**, it is evident that 5 mM 2FA formulations in CS10 improved the post-thaw viability and recovery rates in comparison with the control freezing medium (CS10) for donor 2. The mean immediate post-thaw viability for 5 mM 2FA and CS10 were found to be 74.6 ± 5.7 % and 40.0 ± 4.8 %, respectively. While the mean of the immediate post-thaw recovery rate was 85.8 ± 1.3 % and 62.0 ± 10.8 % for 5 mM 2FA and CS10, respectively. Moreover, a one-way ANOVA test with Dunnett's multiple comparisons revealed that the difference in the post-thaw viability and recovery rate of 5

mM 2FA-frozen cells compared to CS10 ones is statistically significant (P value < 0.1, n = 2). This further confirms that the addition of 5 mM 2FA in CS10 maintains higher number of viable CD19-CAR T cells, similar to what was observed in **Figure 5.11**.

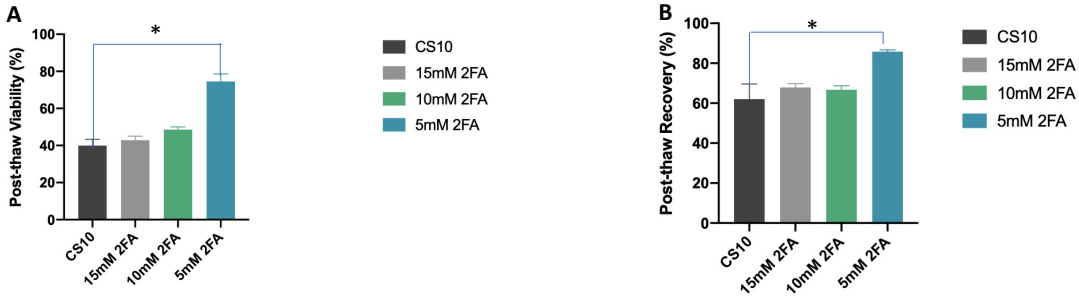

Figure 5.12 Bar graph represents the mean **(A) immediate post-thaw viability** and **(B) immediate post-thaw recovery** of human CD19-CAR T cells of donor 2 using the Trypan blue exclusion assay**.** Human CD19-CAR T cells were cultured for 7 days in ImmunoCult™-XF supplemented with IL2. The cells were frozen on day 8 **in duplicate** with CS10 in the presence or absence of 2FA. Error bars represent the standard error of the mean (SEM). One-way ANOVA test suggested that there was a statistically significant difference in post-thaw viability and recovery of 5 mM 2FA (P value < 0.1, n=2) in comparison with CS10.

The difference in the post-thaw viability between **Figures 5.11 and 5.12 A** can be accounted by for by the variation variables between blood donors (i.e., health condition, age, and gender) as well as the variation in the number of cells lost during cryopreservation processes. Notably, the post-thaw recovery rates of CAR T cells obtained from two different donors were consistent and showed that 5 mM 2FA maximized the number of viable cells in comparison to CS10 alone (**Figures 5.11 B and 5.12 B**). Ultimately, inhibition of ice recrystallization during cryopreservation by employing IRIs in the cryopreservation protocol of CAR T cells appeared to improve the cell survival outcome post-thaw, increasing the number of viable cells, and thus, increasing the availability of CD19-CAR T cell doses for future clinical applications.

5.4 Assessment of Post-Thaw Functionality of 2FA-Frozen T and CAR T Cells

T lymphocytes play a pivotal role in immunity and immunopathology due to their antigen-directed cytotoxicity.[80] The accessibility of T and CAR T cell therapies to patients is greatly dependent on an effective cryopreservation protocol that results in viable and functional T/CAR T cell products post-thaw. As presented in **section 5.3**, employing IRI technology in the cryopreservation protocol leads to a higher survival rate of T and CD19-CAR T cells. Therefore, we sought to further investigate the cryoprotective capacity of an IRI-formulated cryo-solution to maintain the killing activity of T cell products (i.e., MOCK T cells and EGFR-CAR T cells).

5.4.1 The Applicability of MOCK T Cells and EGFR-CAR T Cells in Immunotherapy

The activation process of T lymphocytes is crucial for the expansion of the cells as well as the expression of antigens on the surface of the cells.[74,94] For instance, MOCK cells are $CD4^+$-transduced T cells that utilize T cell receptors (TCRs) to identify peptides from extracellular proteins, allowing the host immune system to start a defense mechanism to fight external antigens.[81-82] Moreover, anti EGFR-CAR T cells are powerful cell-based products in immunotherapy as they treat multiple carcinomas (i.e., lung and gastric carcinomas).[83-86] Therefore, both MOCK T cells and EGFR-CAR T cells were frozen using IRI supplemented cryomedium to monitor their post-thaw functionality.

T cells were isolated from a healthy patient (**donor 116**) and transduced to either MOCK T cells or EGFR-CAR T cells using special viral vectors. MOCK T cells and EGFR-CAR T cells were grown for 8 days in ImmunoCult™-XF with IL2, and then cryopreserved on day 9 post transduction in triplicate (n = 3) in either CS10 or CS10

formulated with 10 mM, 5 mM, or 2.5 mM 2FA. Cells were then thawed, washed with sterile PBS, cultured in complete ImmunoCult medium (with IL2), and assessed for post-thaw viability/recovery using AO/PI dye and a Nexcelom cell counter. MOCK T cells and EGFR-CAR T cells were then co-plated with tumor target cells, SKOV3 and RAJI (ATCC), to test their killing activity post-thaw.

5.4.2 Assessment of the Viability and Recovery of 2FA-Frozen MOCK T Cells and EGFR-CAR T Cells

The viability and recovery rate were two of the first measurements assessed for MOCK T cells and EGFR-CAR T cells. Acridine orange (AO)/propidium iodide (PI) dyes and an automated cell counter (Nexcelom cell counter) were utilized to quantify the number of live and dead cells following cryopreservation. AO dye can penetrate both live and dead cell membranes, staining all nucleated cells and emits a green fluorescent signal. While PI can only penetrate cells with compromised membranes (dead cells) and emits red fluorescent signal. The Nexcelom cell counter allows for automatic counting of the number of live and dead cells based on the detected fluorescent signals from AO and PI.

Assessment of the immediate post-thaw viability of MOCK T cells revealed that there was not a statistically significant increase in the number of viable cells across the different conditions compared to CS10-frozen cells (P value > 0.1, n = 3), presented in **Figure 5.13 A**. The immediate post-thaw viability was found to be 62.9 ± 16.7 %, 75.5 ± 10.1 %, 68.9 ± 10.2 %, 61.5 ± 8.9 % for CS10, 10 mM, 5 mM, and 2.5 mM 2FA, respectively. However, taking into consideration the number of cells that were initially frozen, the recovery rate revealed a significant difference between 5 mM 2FA- and CS10-frozen cells (**Figure 5.13 B**). The immediate post-thaw recovery rate of MOCK T cells was

found to be 48.0 ± 6.1 % and 78.1 ± 5.9 % for CS10 and 5 mM 2FA, respectively. A one-way ANOVA test with Dunnett's multiple comparisons suggest that formulation of 5 mM 2FA in CS10 significantly increased the survival rate of MOCK T cells (P value < 0.001, n = 3, **Figure 5.13 B**), which is consistent with what was observed previously for the cryopreservation outcome of T cells.

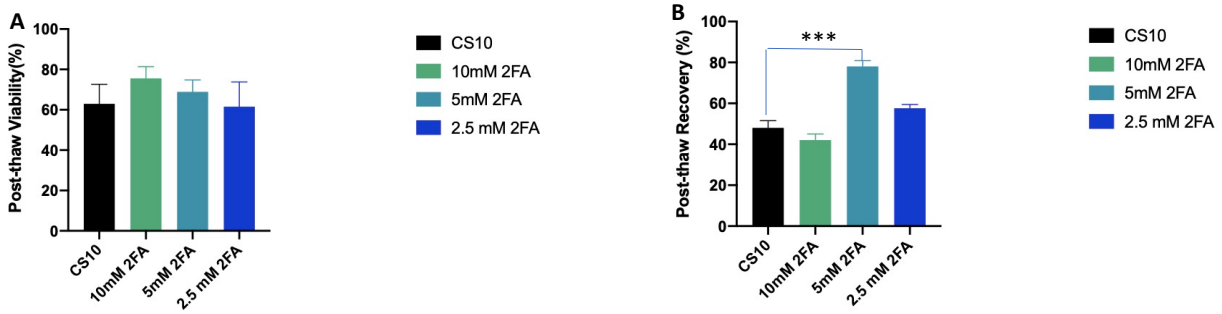

Figure 5.13 Bar graph represents the mean **(A) immediate post-thaw viability** and **(B) immediate post-thaw recovery** of human MOCK T cells of donor 116 using AO/PI dyes and the Nexcelom Cell Counter**.** Human MOCK T cells were cultured for 8 days in ImmunoCult™-XF supplemented with IL2. The cells were frozen on day 9 **in triplicate**. CS10 represents the control freezing medium. 2FA was formulated at different concentrations in CS10. Error bars represent the standard error of the mean (SEM). One-way ANOVA test suggests a statistically significant difference in post-thaw recovery of 5 mM 2FA (P value < 0.001, n = 3) compared to CS10 alone.

Similarly, analysis of the immediate post-thaw viability and recovery of 2FA-frozen EGFR-CAR T cells revealed that a statistically significant difference was found in the survival rate of 5 mM 2FA-frozen cells compared to CS10 alone. The immediate post-thaw viability percentages for CS10, 10 mM, 5 mM, and 2.5 mM 2FA were found to be 78.7 ± 4.3 %, 71.3 ± 8.9 %, 73.1 ± 7.3 %, 55.2 ± 3.9 %, respectively (**Figure 5.14 A**). A one-way ANOVA test with Dunnett's multiple comparisons suggested that there was no significant difference in the post-thaw viability of the different conditions compared to CS10 (P value > 0.1, n = 3, **Figure 5.14 A**). On the other hand, the immediate post-thaw recovery rates of EGFR-CAR T cells were found to be 39.8 ± 4.5 %, 38.7 ± 8.9 %, 70.9 ± 7.3 %, 28.8 ± 11.6 % for CS10-, 10 mM, 5 mM, and 2.5 mM 2FA-frozen cells, respectively

(**Figure 5.14 B**). A one-way ANOVA test comparing the different formulations of 2FA with CS10 revealed that the presence of 5 mM 2FA in CS10 would be beneficial for future clinical applications as it significantly increases the post-thaw recovery rate, allowing for more CAR T cell doses to be available for cancer patients.

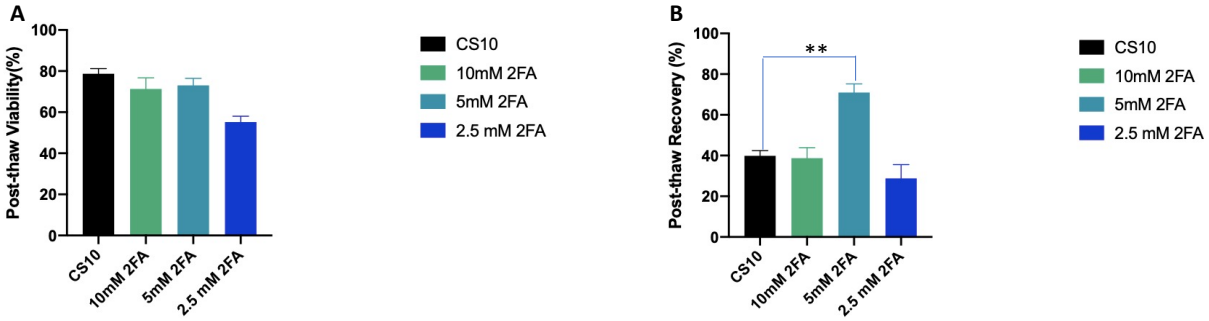

Figure 5.14 Bar graph represents the mean **(A) immediate post-thaw viability** and **(B) immediate post-thaw recovery rate** of human EGFR-CAR T cells of donor 116 using AO/PI dyes and the Nexcelom Cell Counter**.** Human EGFR-CAR T cells were cultured for 8 days in ImmunoCult™-XF supplemented with IL2. The cells were frozen on day 9 **in triplicate**. CS10 represents the control freezing medium. 2FA was formulated at different concentrations in CS10. Error bars represent the standard error of the mean (SEM). One-way ANOVA test suggests that there was a statistically significant difference in the post-thaw recovery of 5 mM 2FA (P value < 0.01, n = 3) compared to CS10 alone.

5.4.3 Evaluation of the Killing Activity of 2FA-Frozen MOCK T Cells and EGFR-CAR T Cells

Since IRI-formulated CS10 appeared to increase the cell survival of T cells and CAR T cells, we further sought to discover the capacity of a CS10 in the presence of IRI to maintain the killing functionality of MOCK T cells and EGFR-CAR T cells post-thaw. Two types of target cells, SKOV3 and RAJI, were utilized to assess the cytotoxic killing activity of both MOCK and EGFR-CAR T cells. SKOV3 are ovarian adenocarcinoma cells that contain high expressions of EGFR antibodies; and therefore, they are highly susceptible to anti EGFR-CAR T cells.[87] On the other hand, RAJI cell lines are human B

lymphoblastoid cells that do not express EGFR antibodies, and thus, they are EGFR-negative targets.[88]

The three different samples of CS10- and 2FA-frozen MOCK T cells and EGFR-CAR T cells were plated with either SKOV3 or RAJI target cells. IncuCyte Live-Cell Analysis system (Sartorius) was then utilized to monitor the red area confluency, a measurement of cell-killing activity based on area (shown in **S. Figures 5.1-5.4**).[89] Red area confluence is indicative of the number of target cells (SKOV3) in the presence of CS10- and 2FA-frozen EGFR-CAR T cells, where a higher red area confluence indicates a greater number of SKOV3 cells present. As presented in **Figure 5.15**, freezing EGFR-CAR T cells in CS10 with or without 2FA did not compromise their killing activity against SKOV3 tumor cells, suggested by the decrease in the mean red area confluence throughout the 136 hours of recording. The number of tumor cells (SKOV3) appeared to increase in the first 28 hours where the red area confluence ranged between 1.2-1.5 % for all conditions (**Figure 5.15**). However, the EGFR-CAR T cells appeared to have reached a sufficient population after 28 hours and started attacking SKOV3 target cells until the red area confluence reached 0 % for all 2FA cultures at 100 hours, implying that the EGFR-CAR T cells were able to kill all expected tumor cells. The red area confluence in CS10 cultures, on the other hand, reached 0.5 % at 100 hours (**Figure 5.15**). A generalized linear model (GLM) analysis revealed that there is a significant difference in the mean of the killing activity of the different treatments at different time points ($P < 0.001$, $n = 3$). The statistical significance in the cytotoxic activity of the frozen cells comes from the difference in the killing activity of 2.5 mM- and 5 mM-frozen EGFR CART cells between 48 and 96 hours. However, comparing 5 mM 2FA-frozen EGFR-CAR T with CS10-frozen cells suggests

that there is not significant difference in their cytotoxic killing activity (P value > 0.1, n = 3), suggesting that employing IRIs in the cryomedium does not compromise the functionality of CAR T cells.

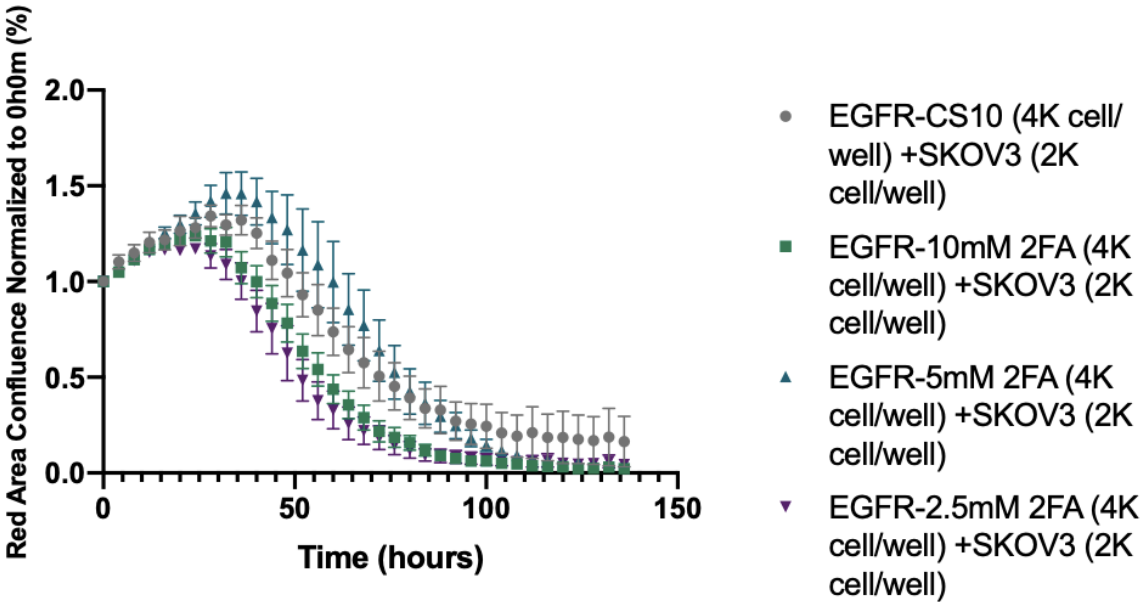

Figure 5.15 Analysis of the red area confluence (normalized to zero hour) as a function of time (hours). Human EGFR-CAR T cells were cultured for 8 days in ImmunoCult™-XF supplemented with IL2. The cells were frozen on day 9 **in triplicate** in CS10 in the presence or absence of 2FA. EGFR-CAR T cells were thawed and plated in duplicate in three different 96-well cells in the presence of SKOV3 target cells to measure the killing activity of EGFR-CAR T cells post-thaw. Red Area Confluence was quantified using the IncuCyte live cell analysis system and plotted against time. A GLM analysis suggests that there is a statistically significant difference in the killing activity of the different treatments at different time points (P value < 0.001, n = 3).

Although formulations of 5 mM-2FA in CS10 appeared to increase the number of viable cells significantly compared to CS10 (shown in **Figures 5.13-5.14**), no significant increase in the post-thaw functionality of EGFR-CAR T cells was observed in comparison with CS10-frozen cells (**Figure 5.15**). Given the fact that supplementing 5 mM 2FA in CS10 resulted in higher yield of viable of EGFR-CAR T cells with sufficient killing activity, 2FA can potentially be used as a cryo-additive for the cryopreservation of CAR T cell products, increasing the number of CAR T doses available for cancer patients.

Moreover, plotting the mean red area confluence of RAJI target cells that were co-plated with CS10- or 2FA-frozen EGFR-CAR T cells further revealed that the presence of 2FA did not compromise the expression of EGFR antigens on CAR T and did not affect their specificity in killing EGFR-positive tumor cells (SKOV3). It is evident that the number of RAJI cells increased over time when they were co-cultured with EGFR-CAR T cells, where the red area confluence reached 4-8% confluence at 136 hours for the different cultures (presented in **Figure 5.16 A)**, while the red area confluence of SKOV3 co-cultures with EGFR-CAR T cells, presented in **Figure 5.16 B,** decreased, and reached 0 % confluence at 136 hours. A GLM analysis revealed that there is a significant difference in the mean of the killing activity of the different treatments at different time points ($P < 0.0001$, $n = 3$). The statistical significance comes from the difference in the growth of RAJI target cells that were co-plated with 2.5 mM-frozen EGFR-CART cells and CS10-frozen cells between 96 and 136 hours.

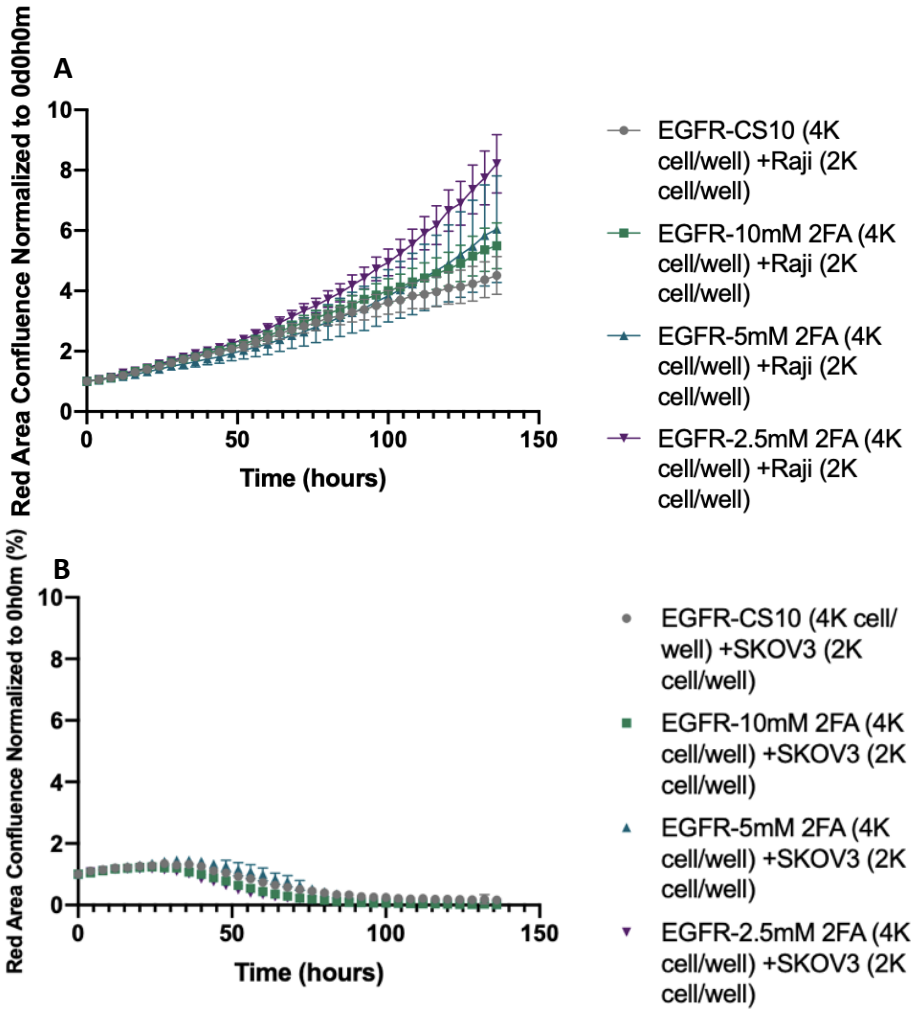

Figure 5.16 Analysis of the red area confluence (normalized to zero hour) of **(A)** EGFR-CAR T cells + Raji **(B)** EGFR-CAR T cells + SKOV3 as a function of time. Red Area Confluence refer to the number of target cells (SKOV3 or RAJI) in the presence of CS10 and 2FA-frozen EGFR-CAR T cells. CS10- and 2FA-frozen EGFR-CAR T cells were co-plated in duplicate in three different 96-well cells in the presence of SKOV3 or RAJI target cells. The red area confluence was quantified using the IncuCyte live cell analysis system and plotted against time. All graphical data refer to the mean red area confluence of each condition against the different time points normalized to 0 hr. Error bars represent the standard error of the mean (SEM). A GLM analysis suggests that there is a statistically significant difference in growth of RAJI target cells in the presence of the different treatments of EGFR-CART cells (P value < 0.0001, n = 3).

$CD4^+$ effector (MOCK) T cells exhibit a cytotoxic killing activity against SKOV3 tumor cells; however, their killing activity is expected to be less effective than that of EGFR-CAR T cells. Therefore, the post-thaw killing activity of EGFR-CAR T cells of the different freezing conditions was compared with their perspective MOCK T cells to

monitor any difference in the cytotoxic activity between $CD4^+$ effector cells (MOCK) and EGFR-specific CAR T cells against SKOV3 target cells. From **Figure 5.17 A-B**, it is evident that EGFR-CAR T frozen cells kill SKOV3 targets faster and more effectively than MOCK T cells, suggesting that the protection against ice recrystallization retains the killing activity of MOCK T and EGFR-CAR T cells. The red area confluence of EGFR-CAR T cells reached 0 % at 136 hours, while it ranged between 2% and 4% for MOCK T cells. This implies that MOCK T cells possess cytotoxic killing activity against EGFR-positive tumors, however, their killing function is less efficient than EGFR-directed CAR T cells. In addition, a GLM analysis confirmed that there was a statistically significant difference in the number of tumor cells for the different treatments at multiple time points. The statistical significance comes from the difference in the killing activity of 2.5 mM as well as 10 mM 2FA-frozen CAR T cells vs 5 mM 2FA- and CS10-frozen cells where the number of target cells (SKOV3) is significantly reduced between 84 and 112 hours (P value < 0.0001, $n = 3$). Overall, employing IRI technology in the cryopreservation protocol of T cell products appeared to increase the number of viable cells without compromising their killing activity against tumor cells.

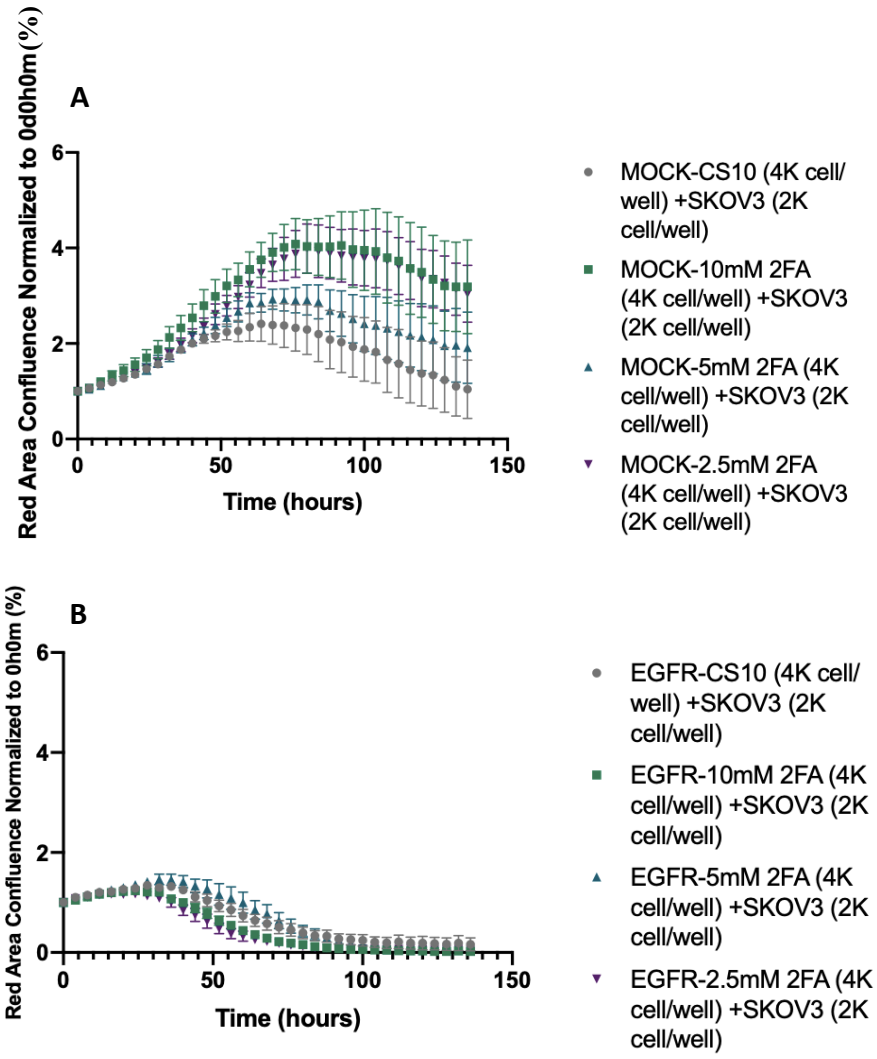

Figure 5.17 Analysis of the red area confluence (normalized to zero hour) of **(A)** MOCK T cells + SKOV3 **(B)** EGFR-CAR T cells as a function of time. Red Area Confluence refer to the number of target cells (SKOV3) in the presence of CS10 and 2FA-frozen EGFR-CAR T cells or MOCK T cells. Cryopreserved EGFR-CAR T and MOCK cells were co-plated in duplicate in three different 96-well cells in the presence of SKOV3 target cells to measure their killing activity post-thaw. Red Area Confluence was quantified using the IncuCyte live cell analysis system and plotted against time. All graphical data refer to the mean red area confluence of each condition against different time points normalized to 0 hr. Error bars represent the standard error of the mean (SEM). A one-way ANOVA test with Dunnett's multiple comparisons suggest that there is a statistically significant difference in the mean killing activity of frozen MOCK cells compared to EGFR-CAR T cells (P value < 0.0001, n = 3).

5.5. Discussion

The production of master T cell banks is a prerequisite for the manufacturing process of CAR T cell therapy and for future clinical applications.[77-78] Moreover, the

preservation of high quality-controlled T cell products requires an optimal cryopreservation protocol.[77-78] Conventional cryopreservation strategies, however, reduce the viability of the frozen T cells and cause an impairment in their proliferation activity, limiting the availability of CAR T cell therapy products for patients as the cryopreserved T cells require time to grow/expand post-thaw.[24,30-32] Although studies have found that the proliferation activity of frozen T cells could be partially recovered by activation post-thaw,[31,39,45] techniques for a robust cryopreservation must be developed to generate an off-the-shelf CAR T cell product. In this study, we report the first comprehensive testing of IRIs in the cryopreservation protocol of T/CAR T cells, in an effort to optimize a GMP-compatible freezing protocol and to maximize the number of viable T and CAR T cells post-thaw, which will facilitate the development of an off-the-shelf CAR T cell product. We hypothesize that employing IRIs in the freezing protocol of T/CAR T cells will protect the cells against the cryoinjury associated with ice recrystallization, which, in turn, will increase the survival rate of T/CAR T cells, maximizing the accessibility of T cell-based therapy products to patients.

T cells are collected from cancer patients, activated, and then transduced into CAR T cells for clinical applications. To increase the number of cells per dose, T cells and CAR T are cultured for 9-14 days before being transfused or cryopreserved.[90] A previous study conducted by MacDonald *et al.* reported that the stage at which the T cells are frozen (i.e., day 1 vs. day 3 post activation) is a crucial factor in the manufacturing protocol of T cell therapy.[97] MacDonald *et al.* demonstrated that cryopreservation of T cells at different time points (i.e., 1-2 days vs. 3-8 days post activation) differ in their recovery rate, viability, and functional properties that would be acceptable for clinical grade cell product upon thawing.

MacDonald *et al.* observed a significant decrease (~ 20-40% reduction) in the cell recovery rate when they were frozen at day 3 and 5 post activation.[97] According to MacDonald *et al.* the decrease in the number of viable cells is influenced by many factors, such as metabolic state, osmotic shock, membrane permeability, and ice recrystallization.[97] Ice recrystallization is one of the major contributors to cell death post-thaw, and therefore, employing IRIs in the freezing medium of T cells may mitigate the cryoinjury associated with ice recrystallization, maximizing the number of viable T/CAR T cells post-thaw. To our knowledge, the essential effect of inhibiting ice recrystallization during the cryopreservation of T cells frozen at different time points has never been described, and therefore, we sought to assess the post-thaw survival rate of T cells that were frozen prior to activation, at day 1 post activation, at day 9 post activation, as well as CAR T cells. Freezing T cells near the end of the activation phase (day 9) or when they are transduced to CAR T cells reduces the time it takes cancer patients to receive treatment.

A clinically relevant cryomedium, CS10, was utilized as control; CS10 was also formulated with an active IRI, 2FA, that has shown to enhance the post-thaw viability and functionality of HSC [56] and iPSC-Ns (chapter 4). Primary T cells that were obtained and frozen prior to activation, at day 1 post activation and at day 9 post activation, as well as transduced T cells (i.e., CAR T cells) showed a statistically significant increase in the survival rate when 5 mM 2FA was formulated in CS10 compared to CS10 alone. This implies that the formulation of 5 mM 2FA in CS10 prevents the occurrence of the cryoinjury associated with ice recrystallization, increasing the number of viable T/CAR T cells. This also indicates that 2FA protects T cells regardless of the time point at which they were frozen (i.e., day 1, day 9 post activation, or CAR T cells), unlike what

MacDonald *et al.* reported previously.[97] Furthermore, the cytotoxic killing activity of 2FA-frozen EGFR-CAR T and activated T cells (i.e., MOCK T cells) did not appear to be compromised post-thaw, where both cells were able to kill SKOV3 tumor cells efficiently over 136 hours post-thaw. These preliminary results suggest that protection against ice recrystallization during cryopreservation processes is a vital parameter that must be accounted for in the freezing protocol of T cells, to produce high quality-controlled T/CAR T cell therapy products.

Although supplementation of IRIs in the CS10 appeared to enhance the number of viable T/CAR T cells post-thaw, further studies are required to determine the underlying mechanism by which 2FA enhances the survival rate and to assess the applicability of IRIs in clinics by conducting *in vivo* studies. One limitation of our studies is that the Trypan blue exclusion assay only considers cells that have damaged cell membrane and are permeable to the dye. However, there are other factors, such as free radical production and accumulation, cytoskeleton disassembly, and protein denaturation, that cause cryopreservation-induced cell death and may not stain the cells by the dye exclusion assay.[96] Therefore, further metabolomic and proteomic studies will need to be conducted on frozen T cell products to better finetune the cryopreservation protocol. Other factors should also be considered to better optimize the cryopreservation protocol are the use of rate-controlled freezers during freezing and the decrease of DMSO concentration in the cryo-solution formulation. Overall, the development of technologies that assist the optimization of the cryopreservation protocol of cell-based therapies is critical for the successful production of an off-the-shelf CAR T cell therapy product.

5.6 Chapter Summary

T cells and their cellular products, such as chimeric antigen receptor (CAR) T cells, hold promising potential for the treatment of various cancer types. The applicability of T cell immunotherapies is highly dependent on an efficacious cryopreservation protocol that maintains viable and functional cells post-thaw. As mentioned in section 5.3.4, employing IRI technology with a clinically relevant cryomedium increased the post-thaw survival rate of primary T cells and CD19-CAR T cells. Further studies were conducted to assess any changes in the post-thaw cytotoxic killing activity of two different T cell products, MOCK and EGFR-CAR T cells. 5 mM 2FA formulations in CS10 were shown to increase the post-thaw recovery rate of both MOCK and EGFR-CAR T cells, assessed by AO/PI staining with the Nexcelom cell counter. We further evaluated the cytotoxic killing activity of both MOCK and EGFR-CAR T cells by co-plating the cells with SKOV3 and RAJI target cells. Notably, no statistically significant changes in the mean red area confluence were observed when 2FA formulations were compared with CS10 alone, suggesting that 5 mM 2FA increased the number of viable MOCK and EGFR-CAR T cells without compromising their killing functionality. Further *in vivo* studies will be conducted in the future to investigate the potential applicability of IRI technology for clinical use. Overall, application of IRIs in the cryopreservation protocol of T cell products protects the cells against the cryoinjury associated with ice recrystallization and maximizes the availability of efficacious T cell products for patients.

5.7 Experimental Procedures

5.7.1 Jurkat Cell Culture

Jurkat cells were acquired from American Type Culture Collection (ATCC, Clone E6-1, TIB-152™). Jurkat cells were cultured in T75 culture flasks (Thermo Fisher Scientific) in RPMI-1640 medium (Sigma Aldrich, catalogue number: R8758). Culture media was supplemented with 10% FBS (Sigma-Aldrich, C8056), and gentamicin. A total of 1E6 of Jurkat cells were seeded in T75 flasks containing 30 mL of culture medium and incubated in a 5% CO2 atmosphere in humidified incubator at 37˚C. Culture media was changed every other day until a sufficient number (~ 22E6) of Jurkat cells was obtained to freeze.

5.7.2 PBMC Collection and T Cell Isolation

Blood samples were collected from healthy donors (Ottawa Hospital Research Institute). Fresh peripheral blood mononuclear cells (PBMCs) were isolated from blood samples using SOP 00.T.26 (confidential, NRC). T cells were then isolated from PBMCs using a T cell isolation kit (SOP 00.T.27, confidential, NRC). The collected T cells were either frozen at this stage (prior to activation) or were further activated/expanded.

5.7.3 T Cell Activation

Freshly isolated T cells were activated using specific beads according to SOP 00.T.31 (confidential, NRC). Activated T cells were then plated with specific antibodies. At day 1 post-activation, T cells are supplemented with interleukin 2 (IL2). At this stage, activated T cells were either frozen (day 1 post-activation), or further expanded for 8 days. Activated T cells obtained at day 9 post-activation were then frozen.

5.7.4 MOCK T Cell, CD19-, and EGFR-CAR T Cell Transduction

T lymphocytes obtained post-activation were further transduced into MOCK, CD19-CAR T or EGFR-CAR T cells using lentiviral transduction procedure (SOP 00.T.28, confidential, NRC). Transduced T cells were further expanded or frozen.

5.7.5 Freezing and Thawing Protocol

A. Freezing

Cryostor®10 was obtained from STEMCELL Technologies (catalogue number: 07930). *N*-2-fluorophenyl-D-gluconamide (2FA) and *N*-4-chlorophenyl-D-gluconamide (4ClA) were synthesized and purified as previously described (Ben Laboratory, University of Ottawa).[57] 2FA and 4ClA were supplemented in CS10 at different concentrations (15 mM, 10 mM, 5 mM, or 2.5 mM for 2FA; 5 mM, 2.5 mM, or 0.5 mM for 4ClA). Cells were counted using AO/PI (catalogue number: CS2-0106) and the Nexcelom Cellometer (Nexcelom Bioscience) (SOP 00.E.141, confidential, NRC). Cells were then washed with sterile PBS (5 mL) and centrifuged at 300g for 5 minutes. The supernatant was removed and cell pellets were resuspended at a concentration of 1E6 cell/mL with either CS10 alone or CS10 supplemented with 2FA or 4ClA. Cells were transferred to 1 mL cryovials. Cryovials were placed in Mr. Frosty rate-controlled freezing container (-1˚C/min) which was then placed in a -80 ˚C freezer for 24 hours. The cryovials were then transferred to a liquid nitrogen (LN2) dewar for long-term storage.

B. Thawing

Cryovials were obtained from the liquid nitrogen dewar and quickly thawed in a 37 ˚C water bath for approximately 3 minutes. Cells were then washed with 2 mL of sterile PBS and centrifuged at 300g for 5 minutes. Cell pellets were then resuspended in 1 mL of fresh

Complete RPMI culture medium for **Jurkat cells** or in 1 mL of ImmunoCult™-XF with IL2 (with a final concentration of 20 IU/mL for IL2) for **T or CAR T cells**.

5.7.6 Viability and Recovery Assessment

Immediate post-thaw viability and recovery were assessed by counting the number of live and dead cells per sample. Trypan blue (0.4% liquid, catalogue number: T8154) and hemacytometer or AO/PI (catalogue number: CS2-0106) and the Nexcelom Cellometer (Nexcelom Bioscience) were used to stain live/dead cells. Immediate post-thaw viability was calculated using the formula $Number\ of\ Live\ Cells⁄Number\ of\ Live + Dead\ cells$, whereas post-thaw recovery rate was calculated using the formula $Number\ of\ Live\ cells⁄Total\ number\ of\ frozen\ cells\ (1xE6)$. Statistical analysis was completed using One-Way ANOVA™ (multiple comparisons) in GraphPad Prism.

5.7.7 Cytotoxicity Killing Assay

SKOV3 (HTB-77) and RAJI (CCL-86) target cells were obtained from ATCC. Cytotoxicity killing assay was conducted following protocol MP5-40 (NRC). Thawed MOCK T cells and EGFR-CAR T cells were plated in duplicate in three 96-well plates at concentrations of 4K cell/well or 1K cell/well. RAJI or SKOV3 target cells were then co-plated at a concentration of 2K cell/well. The 96-well plates were then placed in IncuCyte (in a 5% CO2 atmosphere in humidified incubator at 37 ˚C). The IncuCyte (Sartorius) device was set to image the plates every 4 hours for 6 days. The plates were left in IncuCyte for 136 hours to monitor the cell's killing activity against SKOV3 and RAJI tumor cells. Red Area Confluence was obtained for the different plates from IncuCyte software using the setup analysis template to quantify the number of target cells (Nuclight-Red+). The red area confluence of the different wells was then analyzed using GraphPad Prism.

5.8 Supplementary Figures

CS10- frozen EGFR (4K cell/well) with SKOV3 (2K cell/well)

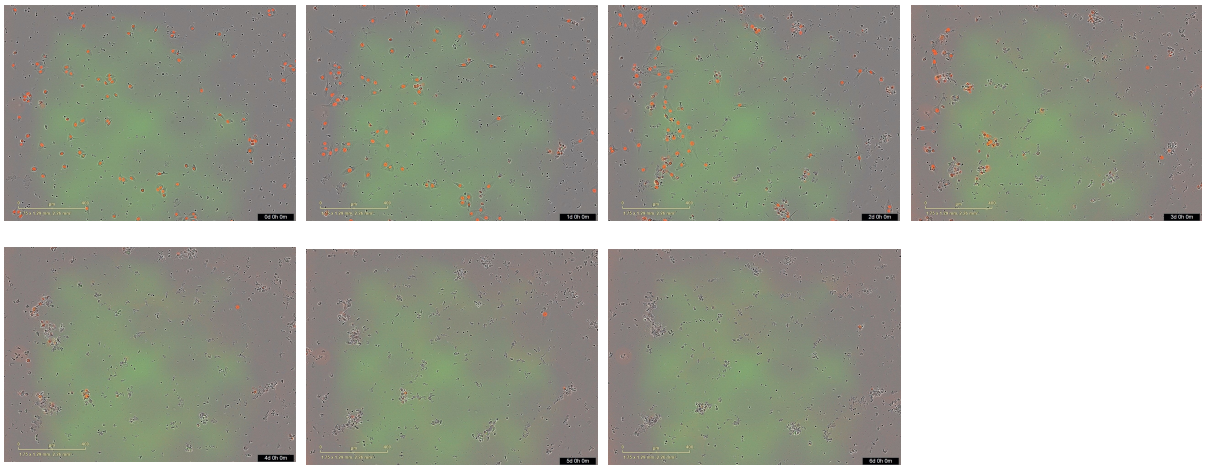

S. Figure 5.1 Pictures extracted from IncuCyte live cell analysis system showing red area confluence in the presence of CS10-frozen EGFR-CAR T cells at 0 hr, day 1, day 2, day 3, day 4, day 5, and day 6 post-thaw.

10mM 2FA- frozen EGFR (4K cell/well) with SKOV3 (2K cell/well)

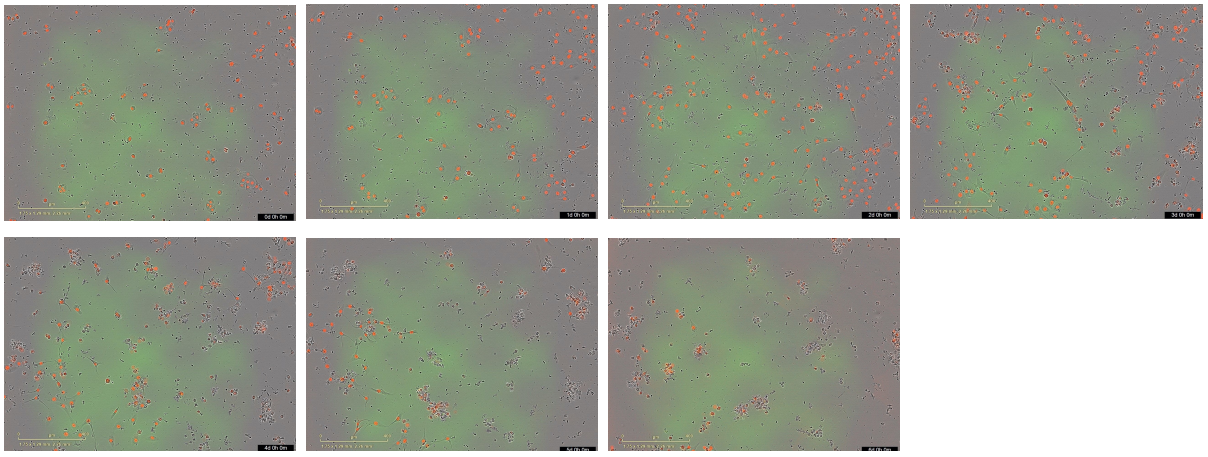

S. Figure 5.2 Pictures extracted from IncuCyte live cell analysis system showing red area confluence in the presence of 10 mM 2FA-frozen EGFR-CAR T cells at 0 hr, day 1, day 2, day 3, day 4, day 5, and day 6 post-thaw.

5mM 2FA- frozen EGFR (4K cell/well) with SKOV3 (2K cell/well)

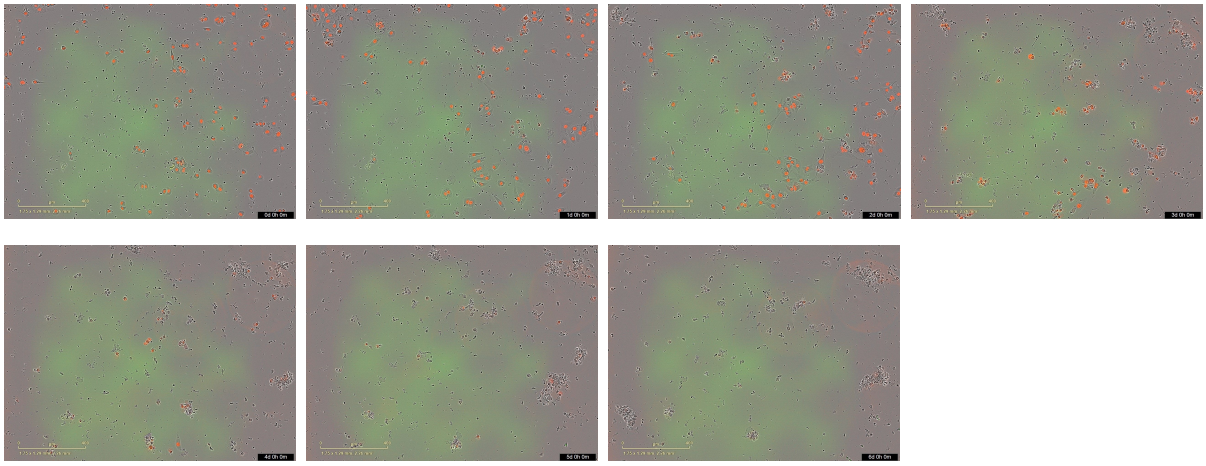

S. Figure 5.3 Pictures extracted from IncuCyte live cell analysis system showing red area confluence in the presence of 5 mM 2FA-frozen EGFR-CAR T cells at 0 hr, day 1, day 2, day 3, day 4, day 5, and day 6 post-thaw.

2.5mM 2FA- frozen EGFR (4K cell/well) with SKOV3 (2K cell/well)

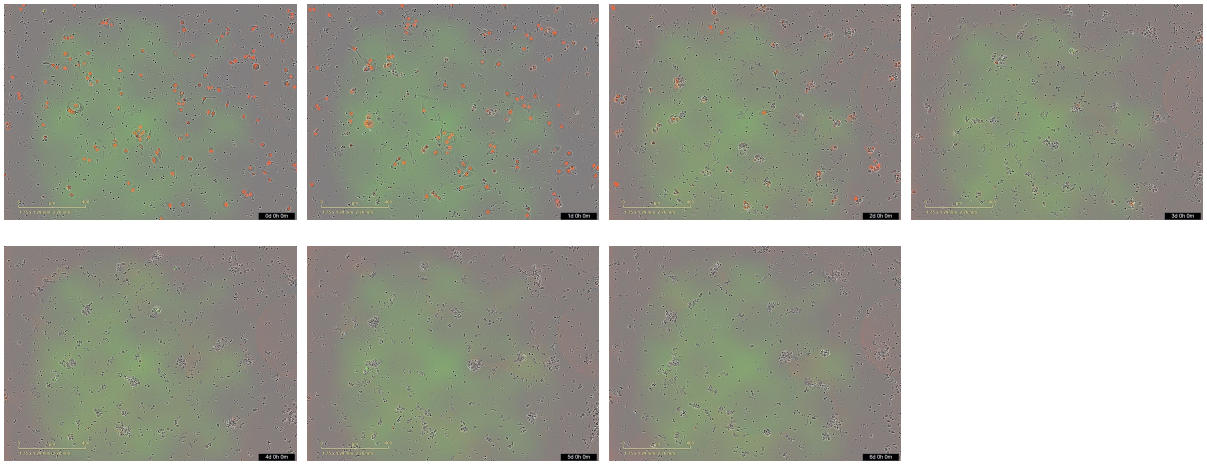

S. Figure 5.4 Pictures extracted from IncuCyte live cell analysis system showing red area confluence in the presence of 2.5 mM 2FA-frozen EGFR-CAR T cells at 0 hr, day 1, day 2, day 3, day 4, day 5, and day 6 post-thaw.

5.9 References

(1) Cancer statistics at a glance http://www.cancer.ca/en/cancer-information/cancer-101/cancer-statistics-at-a-glance/?region=on.

(2) Galon, J.; Fridman, W. H.; Pages, F. The Adaptive Immunologic Microenvironment in Colorectal Cancer: A Novel Perspective. *Cancer Res.* **2007**, *67* (5), 1883–1886. https://doi.org/10.1158/0008-5472.CAN-06-4806.

(3) Pagès, F.; Galon, J.; Fridman, W. H. The Essential Role of the in Situ Immune Reaction in Human Colorectal Cancer. *J. Leukoc. Biol.* **2008**, *84* (4), 981–987. https://doi.org/10.1189/jlb.1107773.

(4) Fridman, W. .; Galon, J.; Dieu-Nosjean, M. C.; Cremer, I.; Fisson, S.; Damotte, D.; Page`s, F.; Tartour, E.; Saute`s-Fridman, C.; Contents. *Immune Infiltration in Human Cancer: Prognostic Significance and Disease Control*; 1977; Vol. 344. https://doi.org/10.1016/0026-265x(77)90137-0.

(5) Jäger, E.; Jäger, D.; Knuth, A. Antigen-Specific Immunotherapy and Cancer Vaccines. *Int. J. Cancer* **2003**, *106* (6), 817–820. https://doi.org/10.1002/ijc.11292.

(6) Van der Bruggen, P.; Zhang, Y.; Chaux, P.; Stroobant, V.; Panichelli, C.; Schultz, E. S.; Chapiro, J.; Van den Eynde, B. J.; Brasseur, F.; Boon, T. Tumor-Specific Shared Antigenic Peptides Recognized by Human T Cells. *Immunol. Rev.* **2002**, *188*, 51–64. https://doi.org/10.1034/j.1600-065X.2002.18806.x.

(7) Miliotou, A. N.; Papadopoulou, L. C. CAR T-Cell Therapy: A New Era in Cancer Immunotherapy. *Curr. Pharm. Biotechnol.* **2018**, *19* (1), 5–18. https://doi.org/10.2174/1389201019666180418095526.

(8) Yee, C.; Thompson, J. A.; Byrd, D.; Riddell, S. R.; Roche, P.; Celis, E.; Greenberg, P. D. Adoptive T Cell Therapy Using Antigen-Specific CD8+ T Cell Clones for the Treatment of Patients with Metastatic Melanoma: In Vivo Persistence, Migration, and Antitumor Effect of Transferred T Cells. *Proc. Natl. Acad. Sci. U. S. A.* **2002**, *99* (25), 16168–16173. https://doi.org/10.1073/pnas.242600099.

(9) Walsh, S. R.; Simovic, B.; Chen, L.; Bastin, D.; Nguyen, A.; Stephenson, K.; Mandur, T. S.; Bramson, J. L.; Lichty, B. D.; Wan, Y. Endogenous T Cells Prevent Tumor Immune Escape Following Adoptive T Cell Therapy. *J. Clin. Invest.* **2019**, *129* (12), 5400–5410. https://doi.org/10.1172/JCI126199.

(10) June, C. H.; Riddell, S. R.; Schumacher, T. N. Adoptive Cellular Therapy: A Race to the Finish Line. *Sci. Transl. Med.* **2015**, *7* (280), 1–9. https://doi.org/10.1126/scitranslmed.aaa3643.

(11) Fesnak, A. D.; June, C. H.; Levine, B. L. Engineered T Cells: The Promise and Challenges of Cancer Immunotherapy. *Nat. Rev. Cancer* **2016**, *16* (9), 566–581. https://doi.org/10.1038/nrc.2016.97.

(12) Payne, K. K.; Bear, H. D.; Manjili, M. H. Adoptive Cellular Therapy of Cancer: Exploring Innate and Adaptive Cellular Crosstalk to Improve Anti-Tumor Efficacy. *Futur. Oncol.* **2014**, *10* (10), 1779–1794. https://doi.org/10.2217/fon.14.0.

(13) Rapoport, A. P.; Stadtmauer, E. A.; Binder-Scholl, G. K.; Goloubeva, O.; Vogl, D. T.; Lacey, S. F.; Badros, A. Z.; Garfall, A.; Weiss, B.; Finklestein, J.; Kulikovskaya, I.; Sinha, S. K.; Kronsberg, S.; Gupta, M.; Bond, S.; Melchiori, L.; Brewer, J. E.; Bennett, A. D.; Gerry, A. B.; Pumphrey, N. J.; Williams, D.; Tayton-Martin, H. K.; Ribeiro, L.; Holdich, T.; Yanovich, S.; Hardy, N.; Yared, J.; Kerr, N.; Philip, S.; Westphal, S.; Siegel, D. L.; Levine, B. L.; Jakobsen, B. K.; Kalos, M.; June, C. H. NY-ESO-1-Specific TCR-Engineered T Cells Mediate Sustained Antigen-Specific Antitumor Effects in Myeloma. *Nat. Med.* **2015**, *21* (8), 914–921. https://doi.org/10.1038/nm.3910.

(14) Robbins, P. F.; Morgan, R. A.; Feldman, S. A.; Yang, J. C.; Sherry, R. M.; Dudley, M. E.; Wunderlich, J. R.; Nahvi, A. V.; Helman, L. J.; Mackall, C. L.; Kammula, U. S.; Hughes, M. S.; Restifo, N. P.; Raffeld, M.; Lee, C. C. R.; Levy, C. L.; Li, Y. F.; El-Gamil, M.; Schwarz, S. L.; Laurencot, C.; Rosenberg, S. A. Tumor Regression in Patients with Metastatic Synovial Cell Sarcoma and Melanoma Using Genetically Engineered Lymphocytes Reactive with NY-ESO-1. *J. Clin. Oncol.* **2011**, *29* (7), 917–924. https://doi.org/10.1200/JCO.2010.32.2537.

(15) Beavis, P. A.; Slaney, C. Y.; Kershaw, M. H.; Gyorki, D.; Neeson, P. J.; Darcy, P. K. Reprogramming the Tumor Microenvironment to Enhance Adoptive Cellular Therapy. *Semin. Immunol.* **2016**, *28* (1), 64–72. https://doi.org/10.1016/j.smim.2015.11.003.

(16) Gill, S.; Maus, M. V.; Porter, D. L. Chimeric Antigen Receptor T Cell Therapy: 25 Years in the Making. *Blood Rev.* **2016**, *30* (3), 157–167.

https://doi.org/10.1016/j.blre.2015.10.003.

(17) Ogba, N.; Arwood, N. M.; Bartlett, N. L.; Bloom, M.; Brown, P.; Brown, C.; Budde, E. L.; Carlson, R.; Farnia, S.; Fry, T. J.; Garber, M.; Gardner, R. A.; Gurschick, L.; Kropf, P.; Reitan, J. J.; Sauter, C.; Shah, B.; Shpall, E. J.; Rosen, S. T. Chimeric Antigen Receptor T-Cell Therapy. *JNCCN J. Natl. Compr. Cancer Netw.* **2018**, *16* (9), 1093–1106. https://doi.org/10.6004/jnccn.2018.0073.

(18) Geyer, M. B.; Brentjens, R. J. Review: Current Clinical Applications of Chimeric Antigen Receptor (CAR) Modified T Cells. *Cytotherapy* **2016**, *18* (11), 1393–1409. https://doi.org/10.1016/j.jcyt.2016.07.003.

(19) Newick, K.; Moon, E.; Albelda, S. M. Chimeric Antigen Receptor T-Cell Therapy for Solid Tumors. *Mol. Ther. - Oncolytics* **2016**, *3* (October 2015), 16006. https://doi.org/10.1038/mto.2016.6.

(20) Elahi, R.; Khosh, E.; Tahmasebi, S.; Esmaeilzadeh, A. Immune Cell Hacking: Challenges and Clinical Approaches to Create Smarter Generations of Chimeric Antigen Receptor T Cells. *Front. Immunol.* **2018**, *9* (July), 1717. https://doi.org/10.3389/fimmu.2018.01717.

(21) Cappell, K. M.; Sherry, R. M.; Yang, J. C.; Goff, S. L.; Vanasse, D. A.; McIntyre, L.; Rosenberg, S. A.; Kochenderfer, J. N. Long-Term Follow-Up of Anti-CD19 Chimeric Antigen Receptor T-Cell Therapy. *J. Clin. Oncol.* **2020**, *38* (32), 3805–3815. https://doi.org/10.1200/JCO.20.01467.

(22) Kochenderfer, J. N.; Somerville, R. P. T.; Lu, T.; Yang, J. C.; Sherry, R. M.; Feldman, S. A.; McIntyre, L.; Bot, A.; Rossi, J.; Lam, N.; Rosenberg, S. A. Long-Duration Complete Remissions of Diffuse Large B Cell Lymphoma after Anti-CD19 Chimeric Antigen Receptor T Cell Therapy. *Mol. Ther.* **2017**, *25* (10), 2245–2253. https://doi.org/10.1016/j.ymthe.2017.07.004.

(23) Raju, R.; Bryant, S. J.; Wilkinson, B. L.; Bryant, G. The Need for Novel Cryoprotectants and Cryopreservation Protocols: Insights into the Importance of Biophysical Investigation and Cell Permeability. *Biochim. Biophys. Acta - Gen. Subj.* **2021**, *1865* (1), 129749. https://doi.org/10.1016/j.bbagen.2020.129749.

(24) Stacey, G. N.; Masters, J. R. Cryopreservation and Banking of Mammalian Cell Lines. *Nat. Protoc.* **2008**, *3* (12), 1981–1989.

https://doi.org/10.1038/nprot.2008.190.

(25) Giwa, S.; Lewis, J. K.; Alvarez, L.; Langer, R.; Roth, A. E.; Church, G. M.; Markmann, J. F.; Sachs, D. H.; Chandraker, A.; Wertheim, J. A.; Rothblatt, M.; Boyden, E. S.; Eidbo, E.; Lee, W. P. A.; Pomahac, B.; Brandacher, G.; Weinstock, D. M.; Elliott, G.; Nelson, D.; Acker, J. P.; Uygun, K.; Schmalz, B.; Weegman, B. P.; Tocchio, A.; Fahy, G. M.; Storey, K. B.; Rubinsky, B.; Bischof, J.; Elliott, J. A. W.; Woodruff, T. K.; Morris, G. J.; Demirci, U.; Brockbank, K. G. M.; Woods, E. J.; Ben, R. N.; Baust, J. G.; Gao, D.; Fuller, B.; Rabin, Y.; Kravitz, D. C.; Taylor, M. J.; Toner, M. The Promise of Organ and Tissue Preservation to Transform Medicine. *Nat. Biotechnol.* **2017**, *35* (6), 530–542. https://doi.org/10.1038/nbt.3889.

(26) Bakhach, J. The Cryopreservation of Composite Tissues: Principles and Recent Advancement on Cryopreservation of Different Type of Tissues. *Organogenesis* **2009**, *5* (3), 119–126. https://doi.org/10.4161/org.5.3.9583.

(27) Baust, J. G.; Gao, D.; Baust, J. M. Cryopreservation: An Emerging Paradigm Change. *Organogenesis* **2009**, *5* (3), 90–96. https://doi.org/10.4161/org.5.3.10021.

(28) Scott, K. L.; Lecak, J.; Acker, J. P. Biopreservation of Red Blood Cells: Past, Present, and Future. *Transfus. Med. Rev.* **2005**, *19* (2), 127–142. https://doi.org/10.1016/j.tmrv.2004.11.004.

(29) Barry J. Fuller, Nick Lane, and Erica E. Benson, E. Life in the Frozen State. Boca. *Boca Raton, Florida CRC Press* **2004**, *83* (3), 696. https://doi.org/10.1016/j.fertnstert.2004.10.025.

(30) Abazari, A.; Hawkins, B. J.; Mathew, A. J. *Cryopreservation Critical Process Parameters: Impact on Post-Thaw Recovery of Cellular Product*; 2019.

(31) Abraham, R. T.; Weiss, A. Jurkat T Cells and Development of the T-Cell Receptor Signalling Paradigm. *Nat. Rev. Immunol.* **2004**, *4*, 1–8.

(32) Meneghel, J.; Kilbride, P.; Morris, J. G.; Fonseca, F. Physical Events Occurring during the Cryopreservation of Immortalized Human T Cells. *PLoS One* **2019**, *14* (5), 1–14. https://doi.org/10.1371/journal.pone.0217304.

(33) Berz, D.; McCormack, E. M.; Winer, E. S.; Colvin, G. A.; Quesenberry, P. J. Cryopreservation of Hematopoietic Stem Cells. *Am. J. Hematol.* **2007**, *82* (6), 463–472. https://doi.org/10.1002/ajh.20707.

(34) Gao, D.; Critser, J. K. Mechanisms of Cryoinjury in Living Cells. *ILAR J.* **2000**, *41* (4), 187–196. https://doi.org/10.1093/ilar.41.4.187.

(35) Lovelock, J. E.; Bishop, M. W. . Prevention of Freezing Damage to Living Cells by Dimethyl Sulphoxide. *Nature* **1959**, *183* (1), 1394–1395.

(36) Pi, C. H.; Hornberger, K.; Dosa, P.; Hubel, A. Understanding the Freezing Responses of T Cells and Other Subsets of Human Peripheral Blood Mononuclear Cells Using DSMO-Free Cryoprotectants. *Cytotherapy* **2020**, *22* (5), 291–300. https://doi.org/10.1016/j.jcyt.2020.01.013.

(37) Wang, S. Y.; Hsu, M. L.; Tzeng, C. H.; Hsu, H. C.; Ho, C. K. The Influence of Cryopreservation on Cytokine Production by Human T Lymphocytes. *Cryobiology* **1998**, *37* (1), 22–29. https://doi.org/10.1006/cryo.1998.2094.

(38) Pollock, K.; Budenske, J. W.; McKenna, D. H.; Dosa, P. I.; Hubel, A. Algorithm-Driven Optimization of Cryopreservation Protocols for Transfusion Model Cell Types Including Jurkat Cells and Mesenchymal Stem Cells. *J. Tissue Eng. Regen. Med.* **2017**, *11* (10), 2806–2815. https://doi.org/10.1002/term.2175.

(39) Yang, T.; Peng, J.; Shu, Z.; Sekar, P. K.; Li, S.; Gao, D. Determination of the Membrane Transport Properties of Jurkat Cells with a Microfluidic Device. *Micromachines* **2019**, *10* (12), 1–13. https://doi.org/10.3390/mi10120832.

(40) Owen, R. E.; Sinclair, E.; Emu, B.; Heitman, J. W.; Hirschkorn, D. F.; Epling, C. L.; Tan, Q. X.; Custer, B.; Harris, J. M.; Jacobson, M. A.; McCune, J. M.; Martin, J. N.; Hecht, F. M.; Deeks, S. G.; Norris, P. J. Loss of T Cell Responses Following Long-Term Cryopreservation. *J. Immunol. Methods* **2007**, *326* (1–2), 93–115. https://doi.org/10.1016/j.jim.2007.07.012.

(41) Baboo, J.; Kilbride, P.; Delahaye, M.; Milne, S.; Fonseca, F.; Blanco, M.; Meneghel, J.; Nancekievill, A.; Gaddum, N.; Morris, G. J. The Impact of Varying Cooling and Thawing Rates on the Quality of Cryopreserved Human Peripheral Blood T Cells. *Sci. Rep.* **2019**, *9* (1), 1–13. https://doi.org/10.1038/s41598-019-39957-x.

(42) Weinberg, A.; Song, L. Y.; Wilkening, C.; Sevin, A.; Blais, B.; Louzao, R.; Stein, D.; Defechereux, P.; Durand, D.; Riedel, E.; Raftery, N.; Jesser, R.; Brown, B.; Keller, M. F.; Dickover, R.; McFarland, E.; Fenton, T. Optimization and Limitations of Use of Cryopreserved Peripheral Blood Mononuclear Cells for Functional and

Phenotypic T-Cell Characterization. *Clin. Vaccine Immunol.* **2009**, *16* (8), 1176–1186. https://doi.org/10.1128/CVI.00342-08.

(43) Luo, Y.; Wang, P.; Liu, H.; Zhu, Z.; Li, C.; Gao, Y. The State of T Cells before Cryopreservation: Effects on Post-Thaw Proliferation and Function. *Cryobiology* **2017**, *79*, 65–70. https://doi.org/10.1016/j.cryobiol.2017.08.008.

(44) Jeurink, P. V.; Vissers, Y. M.; Rappard, B.; Savelkoul, H. F. J. T Cell Responses in Fresh and Cryopreserved Peripheral Blood Mononuclear Cells: Kinetics of Cell Viability, Cellular Subsets, Proliferation, and Cytokine Production. *Cryobiology* **2008**, *57* (2), 91–103. https://doi.org/10.1016/j.cryobiol.2008.06.002.

(45) Zhang, Z.; Qiu, S.; Zhang, X.; Chen, W. Optimized DNA Electroporation for Primary Human T Cell Engineering. *BMC Biotechnol.* **2018**, *18* (1), 1–9. https://doi.org/10.1186/s12896-018-0419-0.

(46) Venkataraman, M.; Westerman, M. P. Susceptibility of Human T Cells, T-Cell Subsets, and B Cells to Cryopreservation. *Cryobiology* **1986**, *23* (3), 199–208. https://doi.org/10.1016/0011-2240(86)90045-3.

(47) WANG, L. E. I.; GONG, W.; WANG, S.; NEUBER, B.; SELLNER, L.; SCHUBERT, M. L.; HÜCKELHOVEN-KRAUSS, A.; KUNZ, A.; GERN, U.; MICHELS, B.; HINKELBEIN, M.; MECHLER, S.; RICHTER, P.; MÜLLER-TIDOW, C.; SCHMITT, M.; SCHMITT, A. Improvement of in Vitro Potency Assays by a Resting Step for Clinical-Grade Chimeric Antigen Receptor Engineered T Cells. *Cytotherapy* **2019**, *21* (5), 566–578. https://doi.org/10.1016/j.jcyt.2019.02.013.

(48) Kety Pratt Riccio, E.; Neves, I.; Maria Banic, D.; Corte-Real, S.; Das Graças Alecrim, M.; Morgado, M.; Daniel-Ribeiro, C. T.; De Fátima Ferreira-Da-Cruz, M. Cryopreservation of Peripheral Blood Mononuclear Cells Does Not Significantly Affect the Levels of Spontaneous Apoptosis after 24-h Culture. *Cryobiology* **2002**, *45* (2), 127–134. https://doi.org/10.1016/S0011-2240(02)00121-9.

(49) Elavia, N.; McManus, A.; Highfill, S. L.; Ren, J.; Shah, N. N.; Fry, T. J.; Brudno, J.; Kochenderfer, J. N.; Stroncek, D.; Panch, S. R. *The Post-Thaw Recovery of Cryopreserved Chimeric Antigen Receptor (CAR) T-Cells during Manufacture Is Better Than That of Cryopreserved Peripheral Blood CD3+ Cells*; American

Society of Hematology, 2017; Vol. 130. https://doi.org/10.1182/blood.V130.Suppl.

(50) Bakar, B.; Kose, E. A.; Sonal, S.; Alhan, A.; Kilinc, K.; Keskil, I. S. Evaluation of the Neurotoxicity of DMSO Infused into the Carotid Artery of Rat. *Injury* **2012**, *43* (3), 315–322. https://doi.org/10.1016/j.injury.2011.08.021.

(51) Fahy, G. M. The Relevance of Cryoprotectant "Toxicity" to Cryobiology. *Cryobiology* **1986**, *23* (1), 1–13. https://doi.org/10.1016/0011-2240(86)90013-1.

(52) Fahy, G. M.; Lilley, T. H.; Linsdell, H.; Douglas, M. S. J.; Meryman, H. T. Cryoprotectant Toxicity and Cryoprotectant Toxicity Reduction: In Search of Molecular Mechanisms. *Cryobiology* **1990**, *27* (3), 247–268. https://doi.org/10.1016/0011-2240(90)90025-Y.

(53) Farrant, J. Water Transport and Cell Survival in Cryobiological Procedures. *Philos. Trans. R. Soc. Lond. B. Biol. Sci.* **1977**, *278* (959), 191–205. https://doi.org/10.1098/rstb.1977.0037.

(54) Matsumoto, S.; Matsusita, M.; Morita, T.; Kamachi, H.; Tsukiyama, S.; Furukawa, Y.; Koshida, S.; Tachibana, Y.; Nishimura, S. I.; Todo, S. Effects of Synthetic Antifreeze Glycoprotein Analogue on Islet Cell Survival and Function during Cryopreservation. *Cryobiology* **2006**, *52* (1), 90–98. https://doi.org/10.1016/j.cryobiol.2005.10.010.

(55) Capicciotti, C. J.; Mancini, R. S.; Turner, T. R.; Koyama, T.; Alteen, M. G.; Doshi, M.; Inada, T.; Acker, J. P.; Ben, R. N. O-Aryl-Glycoside Ice Recrystallization Inhibitors as Novel Cryoprotectants: A Structure-Function Study. *ACS Omega* **2016**, *1* (4), 656–662. https://doi.org/10.1021/acsomega.6b00163.

(56) Briard, J. G.; Jahan, S.; Chandran, P.; Allan, D.; Pineault, N.; Ben, R. N. Small-Molecule Ice Recrystallization Inhibitors Improve the Post-Thaw Function of Hematopoietic Stem and Progenitor Cells. *ACS Omega* **2016**, *1* (5), 1010–1018. https://doi.org/10.1021/acsomega.6b00178.

(57) Briard, J. G. The Rational Design and Use of Novel Small-Molecule Ice Recrystallization Inhibitors for the Cryopreservation of Hematopoietic Stem Cells and Red Blood Cells. *(Doctoral Diss. Univ. d'Ottawa/University Ottawa* **2016**, 235.

(58) Siegel, R. L.; Miller, K. D.; Jemal, A. Cancer Statistics, 2016. *CA. Cancer J. Clin.* **2016**, *66* (1), 7–30. https://doi.org/10.3322/caac.21332.

(59) Rosenberg, J.; Huang, J. CD8+ T Cells and NK Cells: Parallel and Complementary Soldiers of Immunotherapy. *Curr. Opin. Chem. Eng.* **2018**, *19*, 9–20. https://doi.org/10.1016/j.coche.2017.11.006.

(60) Calmels, B.; Mfarrej, B.; Chabannon, C. From Clinical Proof-of-Concept to Commercialization of CAR T Cells. *Drug Discov. Today* **2018**, *23* (4), 758–762. https://doi.org/10.1016/j.drudis.2018.01.024.

(61) Majzner, R. G.; Mackall, C. L. Clinical Lessons Learned from the First Leg of the CAR T Cell Journey. *Nat. Med.* **2019**, *25* (9), 1341–1355. https://doi.org/10.1038/s41591-019-0564-6.

(62) Pantuck, M.; McDermott, D.; Drakaki, A. To Treat or Not to Treat: Patient Exclusion in Immune Oncology Clinical Trials Due to Preexisting Autoimmune Disease. *Cancer* **2019**, *125* (20), 3506–3513. https://doi.org/10.1002/cncr.32326.

(63) Melero, I.; Rouzaut, A.; Motz, G. T.; Coukos, G. T-Cell and NK-Cell Infiltration into Solid Tumors: A Key Limiting Factor for Efficacious Cancer Immunotherapy. *Cancer Discov.* **2014**, *4* (5), 522–526. https://doi.org/10.1158/2159-8290.CD-13-0985.

(64) Turtle, C. J.; Hanafi, L.; Berger, C.; Riddell, S. R.; Maloney, D. G.; Turtle, C. J.; Gooley, T. A.; Cherian, S.; Hudecek, M.; Sommermeyer, D.; Melville, K.; Pender, B.; Budiarto, T. M.; Robinson, E.; Steevens, N. N.; Chaney, C.; Soma, L.; Chen, X.; Yeung, C.; Wood, B.; Li, D.; Cao, J.; Heimfeld, S.; Jensen, M. C.; Riddell, S. R.; Maloney, D. G. CD19 CAR – T Cells of Defined CD4 + : CD8 + Composition in Adult B Cell ALL Patients Find the Latest Version : CD19 CAR – T Cells of Defined CD4 + : CD8 + Composition in Adult B Cell ALL Patients. *J. Clin. Invest.* **2016**, *126* (6), 2123–2138. https://doi.org/10.1172/JCI85309.modified.

(65) Zhang, L.; Tian, L.; Dai, X.; Yu, H.; Wang, J.; Lei, A.; Zhao, Z.; Zhu, Y.; Sun, Z.; Zhang, H.; Church, G. .; Huang, H.; Weng, J.; Zhang, J. Induced Pluripotent Stem Cell-Derived CAR-Macrophage Cells with Antigen-Dependent Anti-Cancer Cell Functions for Liquid and Solid Tumors. *bioRxiv* **2020**, *49* (1), 1–32. https://doi.org/10.11392/jsao.49.40.

(66) Wu, S. M.; Hochedlinger, K. Harnessing the Potential of Induced Pluripotent Stem Cells for Regenerative Medicine. *Nat. Publ. Gr.* **2011**, *13* (5), 497–505.

https://doi.org/10.1038/ncb0511-497.

(67) Kim, J. H.; Auerbach, J. M.; Rodríguez-Gómez, J. A.; Velasco, I.; Gavin, D.; Lumelsky, N.; Lee, S. H.; Nguyen, J.; Sánchez-Pernaute, R.; Bankiewicz, K.; McKay, R. Dopamine Neurons Derived from Embryonic Stem Cells Function in an Animal Model of Parkinson's Disease. *Nature* **2002**, *418* (6893), 50–56. https://doi.org/10.1038/nature00900.

(68) Madeleine K., A. Improving the Engraftment Activities of Cryopreserved Human Umbilical Cord Blood Through the Development of Novel Glyco(Peptide)-Based Aryl Ice Recrystallization Inhibitors. *(Doctoral Diss. Univ. d'Ottawa/University Ottawa* **2020**.

(69) Bloemberg, D.; Nguyen, T.; Maclean, S.; Zafer, A.; Gadoury, C.; Gurnani, K.; Chattopadhyay, A.; Ash, J.; Lippens, J.; Harcus, D.; Pagé, M.; Pon, R. A.; Gilbert, R.; Marcil, A.; Weeratna, R. D.; Mccomb, S. A Modular High-Throughput Screening Platform for Chimeric Antigen Receptor (CAR) Development.

(70) Strober, W. Trypan Blue Exclusion Test of Cell Viability. *Curr. Protoc. Immunol.* **2001**, *Appendix 3*, 2–3. https://doi.org/10.1002/0471142735.ima03bs21.

(71) 7-Amino Actinomycin D (7-AAD) Cell Viability Flow Cytometry Protocol https://www.rndsystems.com/resources/protocols/analysis-cell-viability-using-7-amino-actinomycin-d-7-aad.

(72) Montano, M. Model Systems. In *Translational Biology in Medicine*; 2014; pp 9–33. https://doi.org/10.1533/9781908818652.9.

(73) Kawiak, J. W.; Granicka, L. H.; Weryński, A.; Wójcicki, J. M. Capillary Devices for Therapy. In *Artificial Cells, Cell Engineering and Therapy*; 2007; pp 292–318. https://doi.org/10.1533/9781845693077.3.292.

(74) Cavanagh, M. *T-Cell Activation*; 2007. https://doi.org/10.1016/B978-008055232-3.60244-2.

(75) Bloemberg, D.; McComb, S.; Weeratna, R. Building a Better CAR: Emerging High-Throughput in Vitro Tools for CAR Selection and Optimization. *Cell Gene Ther. Insights* **2019**, *5* (7), 681–692. https://doi.org/10.18609/cgti.2019.078.

(76) Hanley, P. J. Fresh versus Frozen: Effects of Cryopreservation on CAR T Cells. *Mol. Ther.* **2019**, *27* (7), 1213–1214. https://doi.org/10.1016/j.ymthe.2019.06.001.

(77) Yu, S.; Li, A.; Liu, Q.; Li, T.; Yuan, X.; Han, X.; Wu, K. Chimeric Antigen Receptor T Cells: A Novel Therapy for Solid Tumors. *J. Hematol. Oncol.* **2017**, *10* (1), 1–13. https://doi.org/10.1186/s13045-017-0444-9.

(78) Schuler, P. J.; Boeckers, P.; Engers, R.; Boelke, E.; Bas, M.; Greve, J.; Dumitru, C. A.; Lehnerdt, G. F.; Ferris, R. L.; Andrade Filho, P. A.; Brandau, S.; Lang, S.; Whiteside, T. L.; Hoffmann, T. K. EGFR-Specific T Cell Frequencies Correlate with EGFR Expression in Head and Neck Squamous Cell Carcinoma. *J. Transl. Med.* **2011**, *9*, 168. https://doi.org/10.1186/1479-5876-9-168.

(79) Nexcelom. AO / PI Viability.

(80) Zhan, Y.; Carrington, E. M.; Zhang, Y.; Heinzel, S.; Lew, A. M. Life and Death of Activated T Cells: How Are They Different from Naïve T Cells? *Front. Immunol.* **2017**, *8* (DEC), 1–9. https://doi.org/10.3389/fimmu.2017.01809.

(81) Tubo, N. J.; Jenkins, M. K. CD4+ T Cells: Guardians of the Phagosome. *Clin. Microbiol. Rev.* **2014**, *27* (2), 200–213. https://doi.org/10.1128/CMR.00097-13.

(82) Gacerez, A. T.; Sentman, C. L. T-Bet Promotes Potent Antitumor Activity of CD4+ CAR T Cells. *Cancer Gene Ther.* **2018**, *25* (5–6), 117–128. https://doi.org/10.1038/s41417-018-0012-7.

(83) Lozano, T.; Chocarro, S.; Martin, C.; Lasarte-Cia, A.; del Valle, C.; Gorraiz, M.; Sarrión, P.; Ruiz de Galarreta, M.; Lujambio, A.; Hervás-Stubbs, S.; Sarobe, P.; Casares, N.; Lasarte, J. J. Genetic Modification of CD8+ T Cells to Express EGFR: Potential Application for Adoptive T Cell Therapies. *Front. Immunol.* **2019**, *10* (December), 1–12. https://doi.org/10.3389/fimmu.2019.02990.

(84) Li, F.; Lizee, G.; Hwu, P.; Du, X.; Deng, L.; Talukder, A.; Katailiha, A.; Zou, Q.; Roszik, J.; Hawke, D.; Jackson, K.; Bradley, S.; Wang, Y.; Ataullakhanov, R.; Bagaev, A.; Kotlov, N.; Svekolkin, V.; Miheecheva, N.; Frenkel, F.; Sonnemann, H. The Role of EGFR Inhibitor (EGFRi) in Immune Cell Infiltration and CD8+ T-Cell Activation in EGFR Mutant Lung Cancer. *Ann. Oncol.* **2019**, *30* (October), v2. https://doi.org/10.1093/annonc/mdz238.004.

(85) Kumai, T.; Matsuda, Y.; Oikawa, K.; Aoki, N.; Kimura, S.; Harabuchi, Y.; Celis, E.; Kobayashi, H. EGFR Inhibitors Augment Antitumour Helper T-Cell Responses of HER Family-Specific Immunotherapy. *Br. J. Cancer* **2013**, *109* (8), 2155–2166.

https://doi.org/10.1038/bjc.2013.577.

(86) Zeboudj, L.; Maître, M.; Guyonnet, L.; Laurans, L.; Joffre, J.; Lemarie, J.; Bourcier, S.; Nour-Eldine, W.; Guérin, C.; Friard, J.; Wakkach, A.; Fabre, E.; Tedgui, A.; Mallat, Z.; Tharaux, P. L.; Ait-Oufella, H. Selective EGF-Receptor Inhibition in CD4 + T Cells Induces Anergy and Limits Atherosclerosis. *J. Am. Coll. Cardiol.* **2018**, *71* (2), 160–172. https://doi.org/10.1016/j.jacc.2017.10.084.

(87) Gottschalk, N.; Kimmig, R.; Lang, S.; Singh, M.; Brandau, S. Anti-Epidermal Growth Factor Receptor (EGFR) Antibodies Overcome Resistance of Ovarian Cancer Cells to Targeted Therapy and Natural Cytotoxicity. *Int. J. Mol. Sci.* **2012**, *13* (9), 12000–12016. https://doi.org/10.3390/ijms130912000.

(88) Ravanpay, A. C.; Gust, J.; Johnson, A. J.; Rolczynski, L. S.; Cecchini, M.; Chang, C. A.; Hoglund, V. J.; Mukherjee, R.; Vitanza, N. A.; Orentas, R. J.; Jensen, M. C. EGFR806-CAR T Cells Selectively Target a Tumor-Restricted EGFR Epitope in Glioblastoma. *Oncotarget* **2019**, *10* (66), 7080–7095. https://doi.org/10.18632/oncotarget.27389.

(89) Sartorius. *Live-Cell Analysis Handbook - A Guide to Real-Time Live-Cell Imaging and Analysis*; 2019; Vol. 3rd.

(90) June, C. H.; O'Connor, R. S.; Kawalekar, O. U.; Ghassemi, S.; Milone, M. C. CAR T Cell Immunotherapy for Human Cancer. *Science (80-.).* **2018**, *359* (6382), 1361–1365. https://doi.org/10.1126/science.aar6711.

(91) Bachmann, M. F.; Oxenius, A. Interleukin 2: From Immunostimulation to Immunoregulation and Back Again. *EMBO Rep.* **2007**, *8* (12), 1142–1148. https://doi.org/10.1038/sj.embor.7401099.

(92) Murray, K. A.; Gibson, M. I. Post-Thaw Culture and Measurement of Total Cell Recovery Is Crucial in the Evaluation of New Macromolecular Cryoprotectants. *Biomacromolecules* **2020**, *21* (7), 2864–2873. https://doi.org/10.1021/acs.biomac.0c00591.

(93) Chopra, K. Improved Cryopreservation of Induced Pluripotent Stem Cells Using N-Aryl Glycosidic Small Molecule Ice Recrystallization Inhibitors. *(Master's Diss. Univ. d'Ottawa/University Ottawa* **2020**.

(94) Tsoukas, C. D.; Landgraf, B.; Bentin, J.; Valentine, M.; Lotz, M.; Vaughan, J. H.;

Carson, D. A. Activation of Resting T Lymphocytes by Anti-CD3 (T3) Antibodies in the Absence of Monocytes. *J. Immunol.* **1985**, *135*, 1719–1723.

(95) Miller, B. C.; Maus, M. V. CD19-Targeted CAR T Cells: A New Tool in the Fight against B Cell Malignancies. *Oncol. Res. Treat.* **2015**, *38* (12), 683–690. https://doi.org/10.1159/000442170.

(96) Bissoyi, A.; Nayak, B.; Pramanik, K.; Sarangi, S. K. Targeting Cryopreservation-Induced Cell Death: A Review. *Biopreserv. Biobank.* **2014**, *12* (1), 23–34. https://doi.org/10.1089/bio.2013.0032.

(97) MacDonald, K.N., Ivison, S., Hippen, K.L., Hoeppli, R.E., Hall, M.G., Zheng, G., Dijke, I.E., Gandhi, S., West, L., Piret, J.M., Blazar, B.R., Leving, M.K. Cryopreservation timing is a critical process parameter in a thymic Treg cell therapy manufacturing protocol. *Cryotherapy*. 2019, *21* (12), 1216-1233. https://doi.org/10.1016/j.jcyt.2019.10.011.

Chapter 6: Investigating the Potential of Small Molecule Ice Recrystallization Inhibitors in Improving Cryopreservation of Primary Natural Killer (pNK) Cells

6.1 Introduction: Primary Natural Killer (pNK) Cells and Chimeric Antigen Receptor (CAR)-NK Cells as the Future Cell-Based Therapy for Immuno-Oncology Diseases

Cancer is one of the major public health problems that impacts individuals all around the world.[1-2] However, continuous research in the immuno-oncology field has led to advanced cancer treatments based on stimulation of the immune system to recognize and fight tumor cells.[3-6] As mentioned in **chapter 5**, adoptive T cell therapy (ACT) has been found as a promising treatment option for various types of malignancies. ACT treatments, such as chimeric antigen receptor (CAR) T cell therapy, rely on enhancing antigen-specific immunity by introducing modified T cells engineered with specific antigens/receptors to a weakened immune system, allowing them to target specific tumor antigens and kill cancer cells.[7-10] Despite these achievements, the clinical effect of ACT has been confined to a small group of patients and tumor types.[3,7-11] CAR T cell therapy treatments are also accompanied by cytokine released syndrome, graft versus host disease, and neurological toxicities, implying the need for new effective off-the-shelf CAR therapy products.[3,7-11]

One novel strategy is to activate innate immunity by recruiting cytotoxic natural killer (NK) cells to increase immune responses against tumor cells.[3,11] pNK cells are the future of cellular immunotherapy because of their natural cytotoxic characteristics against numerous kinds of tumor cells and the lack of graft-versus-host reactions in patients

receiving allogenic NK cell transfusions.[12-16] NK cells serve as a potential efficacious allogenic solution for treating several kinds of cancer, such as acute myeloid leukemia (AML) and neuroblastoma.[12-16] Moreover, CAR technology has been applied to NK cells because they can be more easily fine-tuned to prevent treatment-related toxicity and immune-mediated adverse events.[7-16] As a result, NK cells are being explored as an alternative platform for CAR engineering and are becoming recognized as important players in the next generation of off-the-shelf cellular therapies targeting cancer.[7-11]

In the allogenic setting, NK cells can be derived from human peripheral blood mononuclear cells (PBMCs) or cord blood (CB), as shown in **Figure 6.1**, which consist of 10-15% and 25% NK cells, respectively.[17-19] The derivation and expansion of NK cells from PBMCs and CB leads to long production times, as well as donor-to-donor variability.[20-21] Moreover, the need to develop clinically applicable procedures for producing higher numbers of fully functional NK cells has increased, and therefore, recent research has shown that $CD34^+$ stem cells from cord blood and induced pluripotent stem cells (iPSCs) can be differentiated into pNK and CAR-NK cells, as shown in **Figure 6.1**.[18,20-26] Developing NK cell-based immunotherapies from iPSCs circumvents the time and scalability constraints while providing off-the-shelf capabilities.[20,24]

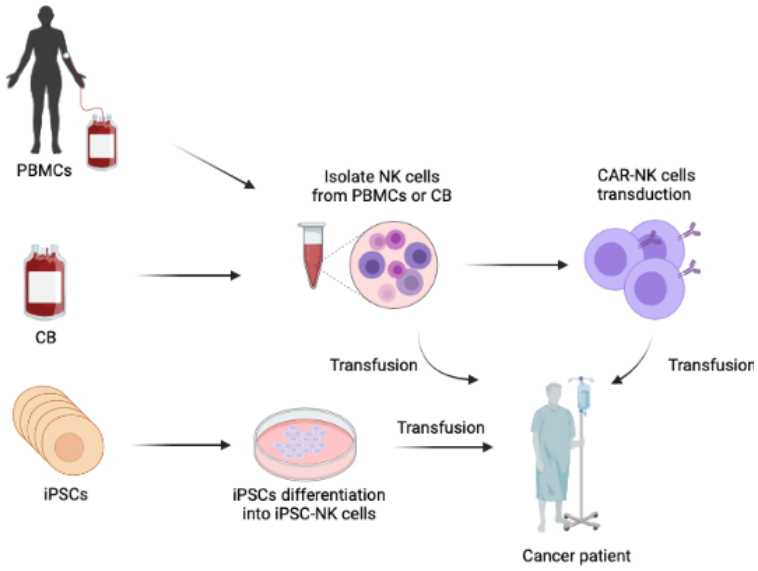

Figure 6.1 Schematic diagram of the different NK cell sources, isolation, transduction, and transfusion of NK and CAR-NK cells. Figure created using free license from BioRender.

Given the substantial potential of CAR-NK cell treatments, fundamental challenges must be resolved to expand their use in clinics and hospitals.[65] Because NK cells are known to be sensitive to the freezing and thawing processes, one of these challenges is the development of an effective cryopreservation protocol.[65-66] In order to bring NK cell immunotherapy to clinics, it's critical that NK cell products can be cryopreserved and thawed without losing their tumor killing function, and that they have the same activity as freshly isolated NK cells.[65-66] Therefore, efforts have been drawn toward establishing an effective freezing protocol that maintains viable and functional NK cells.[18-21]

6.2 The Cryopreservation Protocol of NK Cell-Based Therapy Products

Cryopreservation is essential for the production of off-the-shelf cell therapy products where cellular products are stored for months or years and used as multiple doses.[28-29] However, various parameters, such as freezing and thawing rates, have a major impact on the cells viability and functionality following cryopreservation.[28] DMSO and glycerol are examples of conventional CPAs that have been used to mitigate cryoinjuries

associated with freezing; however, they are unsuccessful at protecting the cells from the cryoinjury associated with ice recrystallization.[30-34] Consequently, it is necessary to improve current cryopreservation protocols to account for cryoinjuries associated with both the freezing and thawing processes.

6.2.1 Conventional Cryopreservation Protocol for NK cells

The development of an efficacious NK cell-based therapy is dependent on cryopreservation to extend their usage in hospitals and clinics.[65-66] Conventional cryopreservation protocols utilized to store NK cell-based therapy products result in a severe reduction in the viability and activity of NK cells immediately after thawing.[67-68] Because NK cells are more susceptible to freezing and thawing cycles compared to other lymphocytes, most conventional cryopreservation protocols depend on freezing the sources of NK cells such as PBMCs and CB. However, the NK cell population within PBMC/CB are quite low, and therefore, enriching NK cells and freezing expanded populations at meaningful concentrations is key.[35,37] Recent studies have reported the successful freezing of NK cells directly using different formulations of cryomedia.[18,36-37] In both cases, cells are cooled to -80 °C using a controlled freezing container (-1 °C/min), followed by the transfer of cryovials into a liquid nitrogen dewar (- 196 °C) for long-term storage.[35-37]

In order to optimize the cryopreservation protocol and media used to freeze pNK cells and CAR NK cells, an immortalized lymphocyte cell line (i.e., NK-92 cells) is often used to test the efficacy of the cryopreservation technique being constructed.[39,54] NK-92 cells are an interleukin-2 (IL-2) dependent natural killer cell line obtained from the PBMCs of a 50-year old male with fast progressing non-Hodgkin's lymphoma.[39,41] the NK-92 cell line has been extensively utilized to generate immunotherapies and to study the cytotoxic

functionality of pNK cells.[62-63] Some of the formulations that have been proposed for the cryopreservation of NK-92 cells are 10% DMSO in fetal bovine serum (FBS), as well as 5% dextran and 7.5% carbonylated ε-poly-L-lysine in DMEM.[41] The cryopreservation of NK-92 cells with FBS and DMSO results in a 65.5 ± 1.2 % post-thaw viability, whereas the dextran-containing cryomedium results in a 73.3 ± 5.3% post-thaw viability.[41] The post-thaw cytotoxic killing activity of NK-92 cells frozen with these cryomedia against tumor target cells (i.e., K562) appeared to decrease compared to unfrozen NK-92 cells.[41]

Several formulations of cryomedia have been described for freezing pNK cells and their sources, such as PBMCs and CB. For example, culture media (i.e., RPMI) with 20% DMSO has been used for cryopreserving PBMCs, resulting in 88% of viable PBMCs, however, the viability of the NK subpopulation is very low (~ 6%).[35] Another cryomedium described for freezing PBMCs is human serum albumin with 25% DMSO and 8% glucose, which results in 99% viable PBMCs.[39] Nonetheless, the post-thaw viability of the pNK subpopulation remains low at 19%, and pNK cells frozen with albumin containing DMSO and glucose suffer a significant decrease in their cytotoxic killing functionality.[38-39] Due to the low abundance of NK cells in their cryopreserved sources and the impairment of their cytotoxic killing functionality, interest has risen in developing suitable cryomedia for cryopreserving pNK cells directly.[21,27,36-44] For instance, some of the formulations proposed for the cryopreservation of pNK cells derived from CB are human AB serum (serum collected from donors with AB blood type) with 10% DMSO, and DMEM with 10% human AB serum and 10% DMSO, which have been found to result in recovery rates of 44% and 25%, respectively.[42] This suggests that lowering the concentration of AB serum decreases the number of viable and functional NK cells.[42] Damodhara *et al*. have also

reported a 79% post-thaw viability of pNK cells using PlasmaLyte with 40% human AB serum and 10% DMSO. However, the post-thaw recovery rate of pNK cells frozen with this solution has been found to decrease to ~ 22%.[43] Formulation of RPMI1640 with 20% albumin, 25% dextran and 5% DMSO has also been found effective for maintaining viable and functional PBMC-derived pNK cells.[35-36] The post-thaw viability of cells frozen with this solution was found to be 90% and the functionality of the cryopreserved NK cells did not appear to decrease post-thaw,[36] however, this high viability rate has not been robustly reproduced in the literature. Commercially available cryomedia, such as Cryostor®10 (CS10), have also been proposed as clinically relevant cryo-solutions that preserve iPSC-derived NK cells.[21] The post-thaw viability of iPSC-NK cells frozen with CS10 was found to be 40%.[21] However, the viability of iPSC-NK cells decreased significantly 2 days post-thaw where it reached 20%, suggesting the occurrence of delayed cell death.[21]

Most of the conventional cryomedia utilized for preserving NK-92 and pNK cells contain high concentrations of DMSO (10 – 20 %) which has been linked to a variety of neurotoxic effects when not washed or diluted prior to therapeutic usage.[45-47] In addition, the presence of animal components in some of the formulations of conventional cryomedia, such as FBS, limits the use of frozen NK cell products in clinics and hospitals. Most cryo-solutions described previously also result in an impairment in the cytotoxic killing activity of NK-92 and pNK cells.[21,36,41] Furthermore, none of the proposed cryomedia account for the cryoinjury associated with ice recrystallization and prolonged ice exposure.[48-50] Consequently, we sought to employ ice recrystallization inhibitors (IRIs) in the clinically relevant cryo-solution, CS10, to examine their potential in maintaining a high number of

viable and functional NK cell products, which will assist in developing an off-the-shelf NK cell products for future clinical use.

6.2.2 IRI-Supplemented Cryomedia as the Next Generation of CPAs

Molecules that inhibit ice recrystallization (i.e., IRIs) have emerged as the next generation of cryoadditives.[48-51] For example, it has been found that an active IRI, *N*-2-fluorophenyl-D-gluconamide (2FA, **Figure 6.2**), from the *N*-aryl-D-gluconamide class of IRIs (**Figure 6.2**) can enhance the post-thaw viability and functionality of HSCs,[50] iPSCs, iPSC-Ns (**chapter 4**), T-cells and CAR-T cells (**Chapters 5**). Consequently, we sought to further discover the cryoprotective characteristic of 2FA on pNK cells.

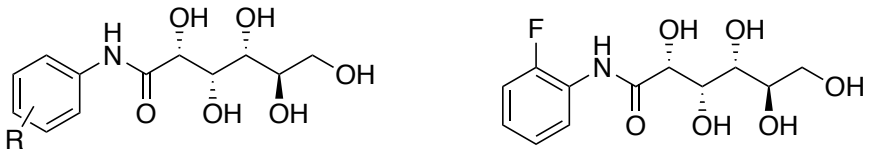

***N*-aryl-D-gluconamides** ***N*-2-fluorophenyl-D-gluconamide (2FA)**

Figure 6.2 General structure of *N*-aryl-D-gluconamide IRIs and *N*-2-fluorophenyl-D-gluconamide (2FA).

6.2.2.1 Optimizing the Cryomedia Utilized for pNK Cells

Several studies have been conducted to optimize the cryomedium used to freeze NK-92, pNK and CAR-NK cells, as mentioned in section 6.2.1. However, most of the proposed formulations contain animal components which limits the use of cryopreserved NK cells for future clinical applications. Therefore, it is significant to develop a GMP-compatible cryomedia (i.e., CS10) that improves the post-thaw viability and functionality of NK-92 and pNK cells. As a consequence, we examined the cryoprotective properties of CS10 on NK-92 and pNK cells by comparing the post-thaw viability and recovery rate of CS10-frozen cells with three different non-GMP formulations of cryomedia, as shown in

Figure 6.3. The three cryo-solution formulations that were chosen were RMPI 1640 with 10% DMSO (RP10), FBS with 10% DMSO (FBS10), and RMPI1640 with 20% albumin, 25% dextran, and 5% DMSO (RP5).

Since pNK cells are sensitive to cryopreservation, the NK-92 cell line was first used to investigate the cryopreservation capacity of the four different cryomedia. Wildtype (Wt)- and CAR-NK-92 cells were obtained from Dr. Lee's laboratory (Department of Biochemistry, Microbiology, and Immunology, University of Ottawa), cultured in complete RPMI 1640 media for 13 days, and frozen in the proposed cryomedia in triplicate at day 14. PBMC-derived NK cells were then frozen in the four cryo-solutions (**Figure 6.3**) to further investigate changes in the cryopreservation outcomes that were observed for NK-92 cells (i.e., post-thaw viability and recovery rates)

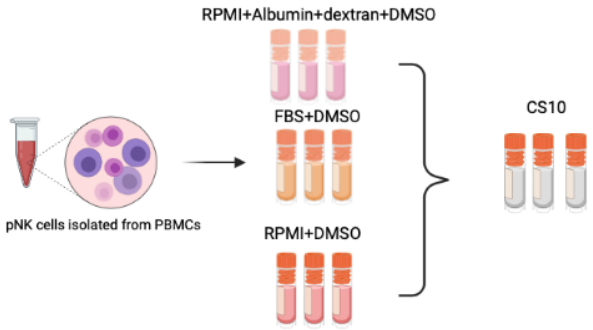

Figure 6.3 Illustration of the different cryomedia formulations used to freeze NK92 and pNK cells in comparison with CS10. Figure created using free license from BioRender.

Following the establishment of CS10's capacity to cryopreserve NK-92 and pNK cells, 2FA was then formulated in CS10 at different concentrations (10 mM, 5 mM, and 2.5 mM) to examine its potential in preserving pNK cells. Fresh PBMCs were isolated from blood donors, followed by NK cell enrichment, and *ex-vivo* expansion using feeder cells for 14 days. Cells were then frozen at day 14 with CS10 or 2FA-formulated CS10 in triplicate. Frozen pNK cells were allowed to cool to - 80 °C overnight using a Mr. Frosty

container (- 1 °C/min) which was then followed by the transfer the cryovials to liquid nitrogen (- 196 °C) for 7 to 14 days, as illustrated in **Figure 6.4 A**. In parallel, freshly isolated pNK cells were objectified to a cytotoxicity assay to assess and compare any changes in their killing functionality after cryopreservation. Frozen pNK cells were thawed using a fast-warming process by submerging cryovials in a 37 °C water bath, depicted in **Figure 6.4 B**. Cryopreserved pNK cells were then cultured in complete culture medium (RPMI 1640 with L-glutamine was supplemented with 1 mM Hepes, 10% FBS, 55 mM mercaptoethanol, 100X Pen/Strep, and 100 U/mL IL2). Cryopreserved pNK cells were expanded using feeder cells for 6 days, followed by an *in vitro* cytotoxicity assay to assess their post-thaw killing activity compared to the killing functionality of fresh cells, shown in **Figure 6.4 B**.

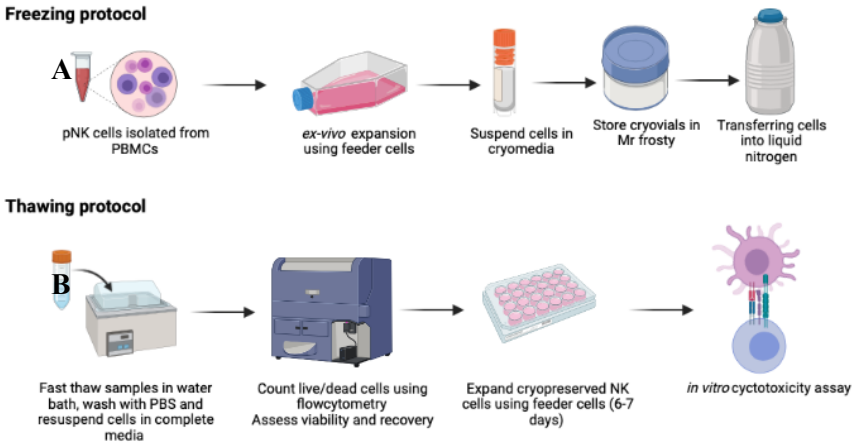

Figure 6.4 Illustration of **(A)** freezing and **(B)** thawing protocols used for the cryopreservation of pNK cells. Figure created using free license from BioRender.

6.3 Assessing the Viability and Recovery Rate of NK cells Frozen with Four Cryo-solutions

Viability and recovery rates are the initial parameters that can be quantified following the thawing process.[64] Post-thaw viability refers to the percentage of cells that

survived cryopreservation over the total number of live and dead cells, whereas recovery rate measures the number of live compared to the total number of cells that were frozen initially.[64] Viability and recovery rates can be determined using dye exclusion assays, such as with Trypan blue or live/dead fixable Near-IR stains.[52-53] Dye exclusion assays allow for the staining of dead cells while viable cells remain unstained due to the presence of intact cell membrane, permitting the assessment of both live and dead cell numbers.[52-53]

6.3.1 The Post-Thaw Viability and Recovery Rate of Wt-NK-92 and CAR-NK-92 Cells Frozen in Four Different Cryomedia

NK-92 cells are an immortalized NK lymphocyte cell line, and are invaluable tools for conducting cytotoxicity functionality assays and for optimizing the cryopreservation protocol of NK cells.[39,41,62-63] The NK-92 cell line has also been used as a robust alternative for pNKs in the immunotherapeutic field.[54] Wildtype (Wt) and chimeric antigen receptor (CAR)-transduced NK-92 cells were grown in complete RPMI 1640 media with 100 U/mL IL2 for 13 days. Wt-NK-92 and CAR-NK-92 cells were then frozen on day 14 in triplicate in the proposed cryomedia: Cryostor®10 (CS10), RMPI 1640 with 10% DMSO (RP10), FBS with 10% DMSO (FBS10), and RMPI 1640 with 20% albumin, 25% dextran and 5% DMSO (RP5).[35-36,41] In this set of experiments, Wt-NK-92 and CAR-NK-92 cells were thawed 4 days after cryopreservation; immediate and 48 hr-post-thaw viability and recovery rates were determined using the Trypan blue exclusion assay.

6.3.1.1 Analysis of the Cryopreservation Outcomes on Wt-NK-92 Cells

As depicted in **Figure 6.5 A**, the average immediate post-thaw viability for Wt-NK-92 cells frozen with CS10, FBS10, RP10 and RP5 were found to be 69.4 ± 4.8 %, 69.5 ± 4.9 %, 61.1 ± 5.6 %, 50.0 ± 0.1 %, respectively. While the average recovery rates

immediately post-thaw for CS10-, FBS10-, RP10-, and RP5-frozen Wt-NK-92 cells were found to be 38.8 ± 9.6 %, 34.7 ± 2.4 %, 30.5 ± 4.8 %, 25 ± 0.2 %, respectively (**Figure 6.5 B**). A one-way ANOVA test with Dunnett's multiple comparisons suggested that there was a statistically significant decrease in the immediate post-thaw viability and recovery of RP5-frozen Wt-NK-92 cells in comparison with CS10-frozen cells (P value < 0.01, and < 0.1, respectively, n = 3). Notably, the post-thaw viability and recovery rates of FBS10- and RP10-frozen cells did not show a significant difference compared to CS10-frozen cells (P value > 0.1, n = 3), implying that CS10 can be used to cryopreserve Wt-NK-92 cells.

Delayed cell death is one of the common factors that results in a decrease in cell viability and functionality 24-48 hours post-thaw. Therefore, we sought to examine any changes in the viability and recovery rates 48 hours post-thaw using the Trypan blue exclusion assay. As shown in **Figures 6.5 A-B**, CS10 resulted in similar or higher viability and recovery immediately post-thaw compared to the other cryomedia formulations, moreover, CS10-frozen Wt-NK-92 cells maintained similar viability and recovery rates 48 hours post-thaw compared to the immediate post-thaw values, at 64.4 ± 3.9 % and 39.8 ± 5.8 %, respectively (**Figures 6.5 C-D**). On the other hand, the number of live cells 48 hours post-thaw increased for FBS10-, RP10-, and RP5-frozen cells, which could be detected by the increase in viability and recovery rates. 48-hr post-thaw viability of cells frozen with FBS10-, RP10-, and RP5 were 73.8 ± 8.0 %, 72.7 ± 6.7 % and 55.6 ± 9.6 %, respectively (**Figure 6.5 C**), while 48-hr post-thaw recovery rate were 50.6 ± 5.9 %, 36.9 ± 4.3 %, 41.7 ± 14.4 %, respectively (**Figure 6.5 D**). A one-way ANOVA test with multiple comparisons suggested that there is no statistical difference in the 48-hr post-thaw viability and recovery rate of the three formulated cryomedia (FBS10, RP10, and RP5) compared to CS10. The

values of 48-hr post-thaw viability and recovery rate were expected to increase compared to the values of the immediate post-thaw viability and recovery because the cells would have started to proliferate and grow. However, there was no increase in the viability and recovery rate of CS10-frozen cells 48 hours post-thaw compared to FBS10-, RP10, and RP5-frozen cells, indicating that CS10 may not protect cells from delayed cryoinjuries or cell death, affecting their growth rate.

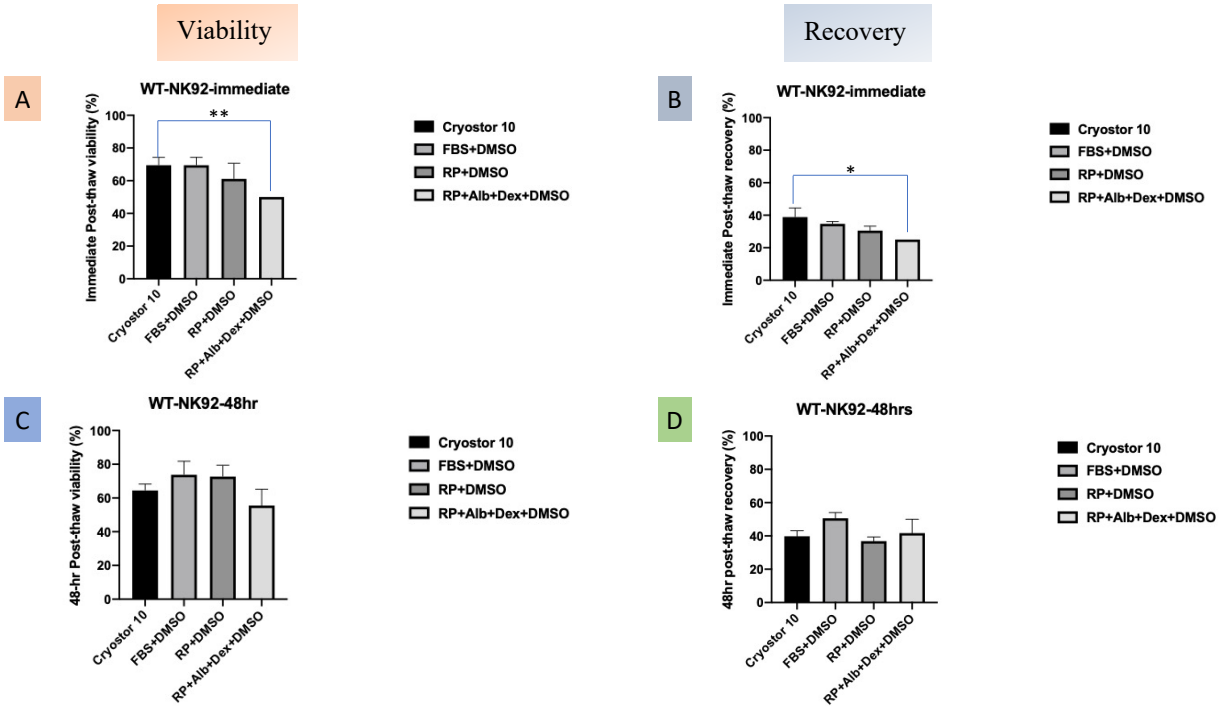

Figure 6.5 Bar graphs represent the mean (A-B) immediate post-thaw viability and recovery rate of Wt-NK-92 cells, respectively, while (C-D) correspond to the 48-hour post-thaw viability and recovery rate of Wt-NK-92 cells, respectively. Post-thaw viability and recovery were assessed using the Trypan Blue exclusion Assay immediately or 48 hours post-thaw. WT-NK-92 cells were cultured for 13 days, and frozen in triplicate with CS10, FBS 10, RP10, and RP5 at day 14. Error bars represent the standard error of the mean (SEM). Asterisks represent a statistically significant difference compared to CS10 which was determined by one-way ANOVA test, where *** = P < 0.1, ** = P < 0.01, and ns = P > 0.1** (n = 3).

6.3.1.2 Analysis of the Cryopreservation Outcomes on CAR-NK-92 Cells

NK cells can be engineered to express a chimeric antigen receptor (CAR) with a specific tumor targeting domain such as B-cell maturation antigen (BCMA), yielding

BCMA-CAR-NK cells which can be used to eradicate multiple myeloma.[54-55] Conventional cryomedia utilized for the preservation of CAR-NK cell products have been shown to decrease their viability and killing activity post-thaw.[35,38,41] Therefore, we further investigated the capacity of the GMP-compatible cryomedium, CS10, to cryopreserve CAR-NK-92 cells, by comparing the immediate and 48-hr post-thaw viability and recovery rates with the other cryomedia formulations. **Figure 6.6 A** represents the average post-thaw viability percentages of CAR-NK-92 cells frozen with CS10, FBS10, RP10 and RP5 which were found to be 85.0 ± 2.9 %, 74.7 ± 5.3 %, 74.6 ± 3.0 %, and 63.7 ± 4.2 %, respectively. A one-way ANOVA test with Dunnett's multiple comparisons suggested that there was a statistically significant increase in the immediate post-thaw viability of CS10-frozen cells compared to the other formulations (P value < 0.1, and < 0.001, n = 3). On the other hand, the immediate post-thaw recovery rates of CAR-NK cells frozen in the four different cryomedia were found to be 65.0 ± 9.0 %, 53.4 ± 2.9 %, 46.7 ± 7.6 %, and 47.1 ± 7.5 % for CS10, FBS10, RP10, and RP5, respectively (**Figure 6.6 B**). A statistically significant increase in the recovery rate was observed for CS10-frozen cells compared to RP10 and RP5- frozen ones (one-way ANOVA test, P value < 0.1, n = 3), as shown in **Figure 6.6 B**, demonstrating the capacity of CS10 to successfully cryopreserve CAR-NK-92 cells.

Although CS10 resulted in increased viability and recovery rate immediately post-thaw, it failed to protect the cells from delayed cell death/cryoinjury, which is indicated by the decrease in the 48-hr post-thaw viability and recovery rate (**Figures 6.6 C-D**). It is evident that 48-hr post-thaw viability of CS10-frozen cells decreased to 58.9 ± 10.3 %, while the number of live cells maintained the same or increased in FBS10, RP10, and RP5 cell cultures where viability was determined to be 76.5 ± 1.5 %, 76.7 ± 0.8 %, and 71.7 ±

4.1 %, respectively. A one-way ANOVA test also suggested that there was a statistically significant decrease in CS10 post-thaw viability compared to RP10 and RP5 ($P < 0.1$, $n = 3$), shown in **Figure 6.6 C**. Similarly, the 48-hr post-thaw recovery rate of CS10-frozen CAR-NK-92 cells appeared to decrease to 45.7 ± 10.1 % (**Figure 6.6 D**), whereas the recovery rates of FBS10-, RP10-, and RP5- were found to either maintain the same or increase (51.7 ± 7.8 %, 47.7 ± 13.1 %, 51.3 ± 53 %, respectively), signifying that CS10 cannot prevent the occurrence of delayed cellular death.

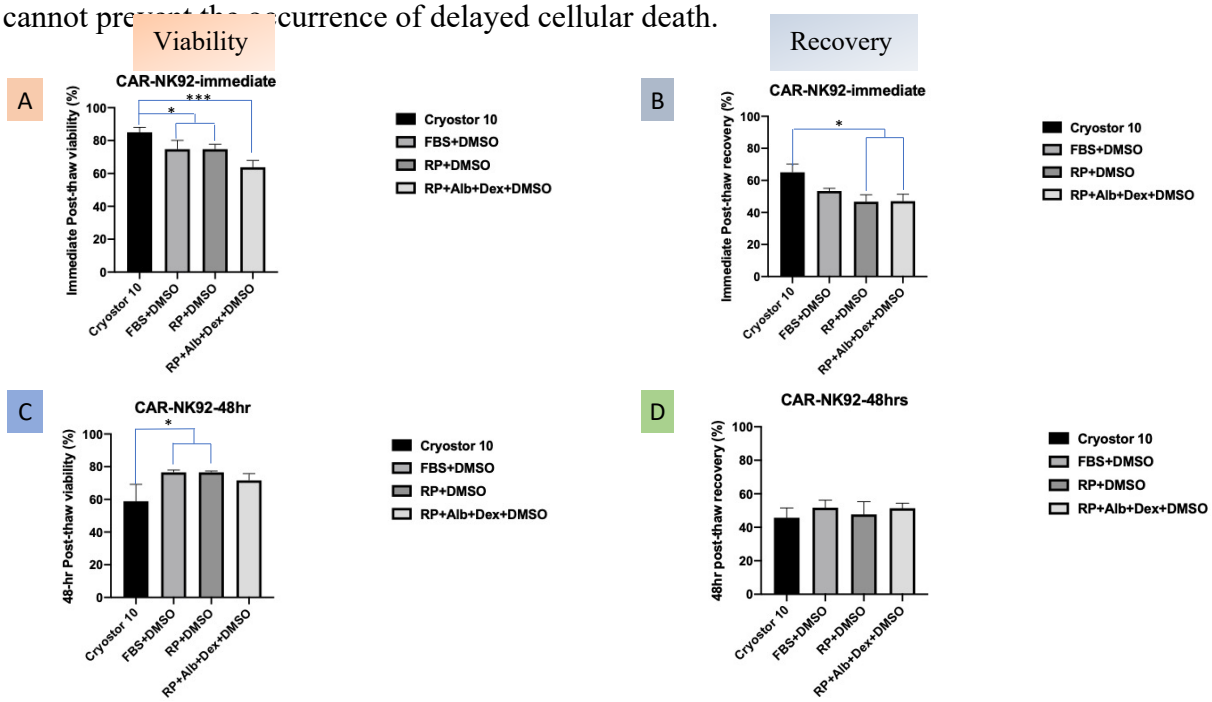

Figure 6.6 Bar graphs represent the mean of **(A-B)** immediate post-thaw viability and recovery of CAR-NK92 cells, respectively, while **(C-D)** correspond to 48-hour post-thaw viability and recovery of CAR-NK92 cells, respectively. Post-thaw viability and recovery were assessed using Trypan Blue exclusion Assay immediately or 48 hours post-thaw. CAR-NK92 cells were cultured for 17 days and frozen in triplicate with Cryostor® 10, FBS + 10% DMSO, RMPI+10% DMSO and RPMI+20% Albumin+25% Dextran+5% DMSO for 4 days. Error bars represent the standard error of the mean (SEM). Asterisks represent a statistically significant difference compared to CS10 which was determined by One-Way ANOVA test, where ****= P < 0.1 and ***= P < 0.001 and ns= P > 0.1 (n = 3)**.

From these preliminary data, it is evident that the capacity of CS10 to cryopreserve NK-92 cells is higher than FBS10, RP10 and RP5 formulations, suggested by the increase in immediate post-thaw viability and recovery rates for both Wt- and CAR-NK-92 cells.

However, CS10 failed to protect both types of the cryopreserved NK-92 cells from the delayed cryoinjuries associated with freezing and thawing processes, suggested by the decreased 48-hr post-thaw viability and recovery rate assessments compared to the other cryomedia formulations. We, therefore, set to examine the cryopreservation outcomes on pNK cells using the GMP-compatible cryo-solution, CS10, and the previously described non-GMP-compatible cryomedia formulations.

6.3.2 The Post-Thaw Viability and Recovery Rate of pNK Cells Frozen in the Four Proposed Cryomedia

pNK cells were derived from PBMCs of blood donor, cultured in complete RPMI 1640 medium, and expanded using feeder cells for 13 days in Dr. Lee's laboratory (Department of Biochemistry, Microbiology, and Immunology, University of Ottawa). Cells were then frozen in triplicate using the four cryomedia described previously (CS10, FBS10, RP10, and RP5). Cells were thawed after four days and cultured in complete RPMI 1640 medium, without the addition of feeder cells, to test the capacity of the cryopreserved pNK cells to grow/expand without the help of feeder cells. The number of live/dead cells were determined immediately and 48 hours post-thaw using the Trypan blue exclusion assay. Viability and recovery rates were then calculated to examine the capacity of each cryomedium to protect pNK cells from cryoinjuries associated with freezing and thawing.

Figure 6.7 A represents the immediate post-thaw viability for cells frozen in CS10, FBS10, RP10, and RP5, which were found to be 79.2 ± 3.8 %, 73.8 ± 3.7 %, 84.5 ± 2.1 %, and 68.7 ± 4.7 %, respectively. A one-way ANOVA test suggested that there was a significant increase in the immediate post-thaw viability of CS10-frozen pNK cells compared to RP5 (P value < 0.1, $n = 3$). On the other hand, no significant difference was

found when cells were frozen in FBS10 or RP10 (P value > 0.1, n = 3) compared to CS10. The immediate post-thaw recovery across the different media was found to be 66.1 ± 9.0%, 79.4 ± 2.9 %, 63.1 ± 3.6 %, and 53.5 ± 7.5 % for CS10, FBS10, RP10, and RP5, respectively, with no statistically significant differences compared to CS10 (P value > 0.1, n = 3), as shown in **Figure 6.7 B**.

Moreover, determination of the 48-hr post-thaw viability and recovery rates allowed for the detection of the occurrence of delayed cell death, where the number of live cells decreases progressively post-thaw. As shown in **Figures 6.7 C-D**, it is apparent that delayed cryoinjuries which can be related to ice formation and recrystallization occurred in CS10-frozen cell cultures where the post-thaw viability and recovery rates decreased to 59.9 ± 7.8 % and 41.7 ± 5.2 %, respectively. Contrastingly, the 48-hr post-thaw viability of FBS10, RP10, and RP5-frozen pNK cells appeared to be similar to the immediate post-thaw viability, which were found to be 73.6 ± 3.1 %, 72.9 ± 5.0 %, and 65.3 ± 0.7%, respectively, shown in **Figure 6.7 C**. In addition, a one-way ANOVA test suggested that there was a statistically significant decrease in the viability of CS10-frozen pNK cells compared to FBS10 and RP10. As depicted in **Figure 6.7 D**, the 48-hr post-thaw recovery rates of CS10-, FBS10, RP10-, and RP5- frozen pNK cells were found to be 41.7 ± 5.2 %, 67.1 ± 8.1 %, 57.5 ±15.3 %, and 55.4 ± 11.6 %, respectively. A one-way ANOVA test with Dunnett's multiple comparisons suggested that there was a significant decrease in the number of live cells in CS10-frozen cell cultures (P value < 0.01, n = 3). From both **Figures 6.7 C-D**, it is observed that the number of live cells did not increase across the different cultures, implying that the growth rate of pNK cells may be impaired in all four cryomedia tested.

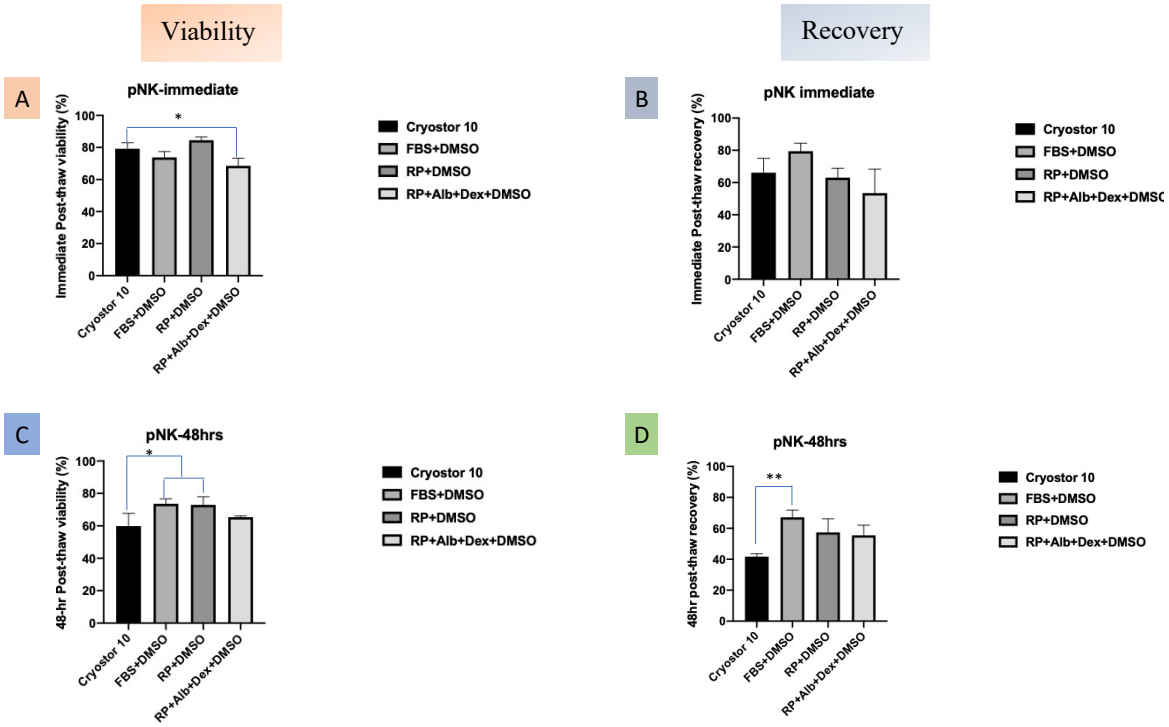

Figure 6.7 Bar graphs represents the mean (A-B) immediate post-thaw viability and recovery of pNK cells, respectively, while (C-D) correspond to the 48-hour post-thaw viability and recovery of pNK cells, respectively. The post-thaw viability and recovery were assessed using the Trypan Blue exclusion Assay immediately or 48 hours post-thaw. pNK cells were isolated from PBMCs of Donor 1, cultured in complete RMPI 1640 medium for 13 days at Dr. Lee's laboratory. Cells were obtained at day 14 and frozen in triplicate with CS10, FBS10, RP10, and RP5 for 4 days. Error bars represent the standard error of the mean (SEM). Asterisks represent a statistically significant difference compared to CS10 which was determined by one-way ANOVA test, where *** = P < 0.1 and ** = P < 0.01 and ns = P > 0.1** (n = 3).

CS10 appeared to increase the immediate post-thaw viability and recovery rate of pNK cells compared to other cryomedia formulations (i.e., RP5), however, it is evident that there was a significant decrease in the viability and recovery rate in CS10 cultures after 48 hours post-thaw, which can be related to delayed cell death/cryoinjury. Moreover, the cryopreserved pNK cells were cultured in complete RMPI-1640 with IL-2 for 48 hours post-thaw without the addition of feeder cells, which are important for the growth and expansion of pNK cells post cryopreservation. This may be another reason to the decrease in the number of viable cells 48 hours post-thaw. In a clinical setting, frozen pNK cells are

thawed and injected into patients without expansion with feeder cells, and therefore, feeder cells were not added in the pNK cultures post-thaw to monitor their capacity in growing and expanding without the help of feeder cells, which will assist in determining the applicability of the cryopreservation protocol in clinical settings. In the next set of experiments, we sought to employ an IRI, 2FA, in the GMP-compatible cryomedium (CS10) to investigate the outcome of inhibiting ice recrystallization during the cryopreservation of pNK cells in the presence of feeder cells post-thaw.

6.4 Evaluating the Post-Thaw Viability, Recovery, and Functionality of pNK Cells Frozen with an IRI-Supplemented Cryo-solution

NK cells are the first line of defense against different malignancies in the innate immune system.[3-5] NK cells, unlike T cells, do not need to be pre-sensitized (i.e., expressing antigen-specific receptors) to produce cytotoxicity and do not cause graft-versus-host diseases.[12,36] The killing activity of NK cells is dependent on cytokine production such as interferon (IFN)-γ and tumor necrosis factor (TNF)-α.[12-13] Interest in producing and cryopreserving NK cells from different sources has risen to produce high quality and off-the-shelf NK cell products..[21,27,35-44]

In **section 6.3**, we tested three different cryomedia formulations: RMPI 1640 with 10% DMSO (RP10), FBS with 10% DMSO (FBS10), and RMPI 1640 with 20% albumin, 25% dextran and 5% DMSO (RP5). The post-thaw viability and recovery rate of the three different formulations were compared with the ones that were frozen with CS10.[35-36,41] From the results presented in **section 6.3**, it was evident that cryopreservation of WT-NK-92 and CART-NK-92, as well as pNK cells in CS10 yields a higher number of viable cells than the three other formulations immediately post-thaw. However, the growth of CS10-

frozen cells decreased over 48 hours post-thaw, which may be a result of delayed cell death/cryoinjury or the absence of feeder cells in the NK cell cultures post-thaw. Thus, we sought to discover whether protecting against ice recrystallization by employing IRI technology would enhance the long-term recovery outcome (i.e., the 48-hr post-thaw recovery rate) of pNK cells cryopreserved in the GMP-compatible cryomedium, CS10, in the presence of feeder cells. pNK cells were isolated from PBMCs, cultured in IL2-supplemented in complete RPMI1640 medium, and expanded using K562-mbIL21-4-1BBL feeder cells for 14 days by an undergraduate student, Bryan Marr, at Dr. Lee's laboratory (Department of Biochemistry, Microbiology, and Immunology, University of Ottawa). The cells were then counted using flowcytometry, washed with sterile PBS, and frozen with either CS10 alone or CS10 supplemented with 10 mM, 5 mM, and 2.5 mM 2FA. A month later, the samples were thawed, counted, and cultured in 12-well plate with feeder cells for 7 days. The thawed pNK cells were then subjected to a functionality assay where they were co-plated with K562 tumor target cells to measure their cytotoxic killing activity post-thaw.

6.4.1 Analysis of the Viability and Recovery Rate of pNK Cells Frozen with 2FA

pNK cells were derived from PBMCs of blood donor 2 and grown for 13 days. Cells were then frozen in triplicate in either CS10 or CS10 formulated with 10 mM, 5 mM, or 2.5 mM 2FA. Samples were thawed and cultured in complete RPMI 1640 medium. The number of live/dead cells was determined immediately and 3 hours post-thaw using flowcytometry to measure the viability and recovery rate of each freezing condition. The forward and side scatter (FSC and SSC) plots with a gate to detect CS10- and 2FA-frozen pNK cells are presented in **S. Figures 6.1-6.4**. From **Figure 6.8 A**, the immediate post-

thaw viability based on live/dead cells with FSC/SSC of NK cells that were frozen with CS10-alone, 10 mM 2FA, 5 mM 2FA, and 2.5 mM 2FA were found to be 95.1 ± 1.2 %, 95.3 ± 0.6 %, 96.0 ± 0.5 %, and 95.2 ± 0.6 %, respectively. On the other hand, the immediate post-thaw recovery rate was found to be 56.8 ± 14.9 %, 57.4 ± 3.6 %, 49.9 ± 3.7 %, and 42.5 ± 4.2 % for CS10, 10 mM 2FA, 5 mM 2FA, and 2.5 mM 2FA, respectively, presented in **Figure 6.8 B**. A one-way ANOVA test with Dunnett's multiple comparisons suggested that there was no statistically significant increase in the immediate post-thaw viability and recovery rate of 2FA-frozen pNK cells compared to cells frozen with CS10 alone, indicating that inhibition of ice recrystallization by formulating 2FA in CS10 does not increase the number of viable NK cells.

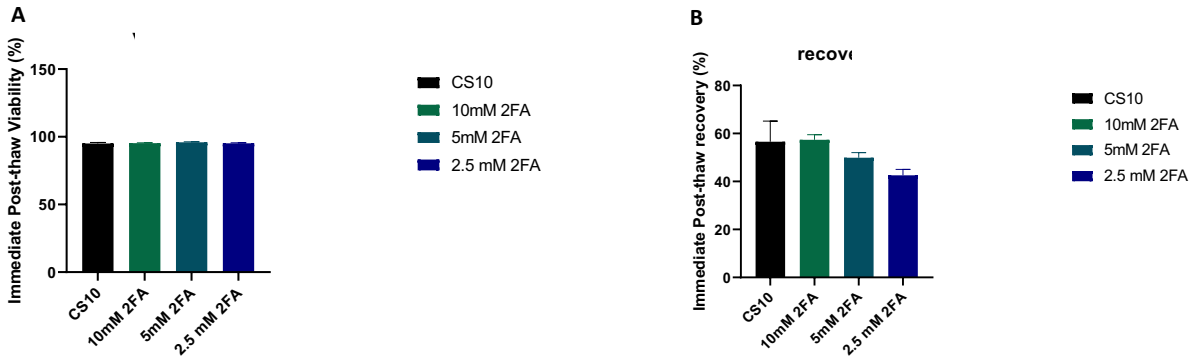

Figure 6.8 Bar graphs represent the mean **(A) immediate post-thaw viability** and **(B) recovery of pNK cells**. Immediate post-thaw viability and recovery were assessed using flowcytometry. pNK cells were isolated from PBMCs of donor 2, cultured in complete RMPI 1640 medium with IL2 for 13 days at Dr. Lee's laboratory. Cells were frozen at day 14 in triplicate with CS10 in the presence or absence of 10 mM 2FA, 5 mM 2FA, and 2.5 mM 2FA. Error bars represent the standard error of the mean (SEM). A one-way ANOVA test with Dunnett's multiple comparisons suggested that there was no significant difference in post-thaw viability and recovery rates amongst different conditions (ns = $P > 0.1$, n = 3).

Moreover, the post-thaw viability and recovery rate were measured prior to adding feeder cells (3 hours post-thaw) to examine any change in the number of viable cells before stimulating expansion of pNK cells. **Figure 6.9 A** represents the mean viability 3 hours post-thaw for CS10, 10 mM 2FA, 5 mM 2FA, 2.5 mM 2FA based on live/dead cells with

FSC/SSC of NK cells; the viabilities were found to be 95.6 ± 2.4 %, 96.8 ± 1.43 %, 97.3 ± 1.68 %, and 97.9 ± 0.19 %, respectively. It is evident that the viability 3 hours post-thaw is very similar to the values that were calculated immediately post-thaw. Notably, the recovery rate of CS10, 10 mM 2FA, 5 mM 2FA, and 2.5 mM 2FA 3 hours post-thaw were higher than the ones that were measured immediately, which were found to be 66.5 ± 16.5 %, 70.9 ± 1.42 %, 65.5 ± 4.6 %, and 63.1 ± 5.1 %, respectively, as shown in **Figure 6.9 B**. The increase in the values of 3-hr post-thaw recovery rates suggest that the pNK cells started to grow, however, there was no significant difference compared to the values of the immediate post-thaw recovery rate. Important to note, however, there appeared to be a slight increase in the number of viable pNK cells when 2FA was formulated at 10 mM in CS10 when compared with CS10-alone frozen cells (71% vs 66%). However, a one-way ANOVA test with Dunnett's multiple comparisons revealed that there was no significant difference in the 3-hr-post-thaw recovery rate nor viability of 2FA-frozen cells compared to the cells frozen with CS10 alone (P value > 0.1, n = 3)

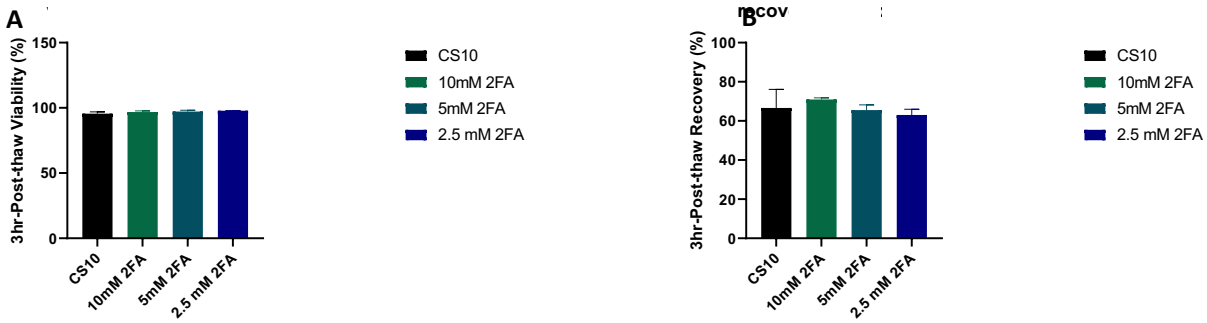

Figure 6.9 Bar graphs represent the 3-hr post-thaw **(A)** viability and **(B)** recovery of pNK cells. 3-hr post-thaw viability and recovery were assessed using flowcytometry, prior to the addition of feeder cells. pNK cells were isolated from PBMCs of donor 2, cultured in complete RMPI 1640 medium with IL2 for 13 days. Cells were then frozen at day 14 in triplicate with CS10 in the presence or absence of 10 mM 2FA, 5 mM 2FA, and 2.5 mM 2FA. Error bars represent the standard error of the mean (SEM). A one-way ANOVA test with Dunnett's multiple comparisons suggested that there was no statistically significant increase in the post-thaw viability and recovery rate amongst the different freezing conditions (**ns = P > 0.1, n = 3)**.

6.4.2 Assessing the Post-Thaw Activity of 2FA-Frozen pNK Cells

The cytotoxicity function of pNK cells comes from natural killer cell stimulatory factor (NKSF) that induces the secretion of IFN-γ and TFN-α, which play a significant role in the *in vivo* resistance to tumor growth.[56-57] Cryopreservation of NK cell therapy products often result in increased cell death, delayed cell growth, and loss of cytotoxic killing activity.[39,41] In this section, we evaluated the capacity of CS10 in the presence or absence of 2FA to maintain the killing capacity of pNK cells post-thaw. The cryopreserved pNK cells were co-cultured with K562 target tumor cells to measure their killing activity.[59] K562 are a human erythroleukemic or myelogenous leukemia cell line with low human leukocyte antigen (HLA) expressions and high levels of activatory NK receptor ligands, making them vulnerable to NK cell-mediated cytotoxicity.[59-61]

CS10- and 2FA-frozen pNK cells were cultured in complete RPMI 1640 medium with IL2 for 7 days post-thaw in the presence of feeder cells. pNK cells were counted at days 4 and 6 post-thaw, prior to the functionality assay, using flowcytometry to determine the growth and number of live pNK cells. As depicted in **Figure 6.10**, the average number of live cells for CS10-, 10 mM 2FA-, 5 mM 2FA-, and 2.5 mM 2FA-frozen cells prior to feeder cells addition were 6.7E5 ± 9.5E4 cells/mL, 7.1E5 ± 8.2E3 cells/mL, 6.6E5 ± 2.7E4 cells/mL, and 6.3E5 ± 2.9E4 cells/mL, respectively, with no statistically significant difference between the different conditions (two-way ANOVA test with multiple comparisons test, P value > 0.1). The average number of live cells post feeder cells addition, at day 4, were found to be similar for CS10-, 10 mM 2FA-, and 5 mM 2FA-frozen cells: 9.3E5 ± 2.4E4 cells/mL, 9.2E5 ± 7.7E4 cells/mL, 8.8E5 ± 4.2E4 cells/mL, respectively. However, the growth of 2.5 mM 2FA-frozen cells appeared to be much lower

than the other conditions with an average number of live cells of 5.5E5 ± 8.1E4 cell/mL. The average number of live cells for the different conditions at day 6 was found to be: 2.6E6 ± 1.7E5 cells/mL for CS10, 2.0E6 ± 1.1E5 cells/mL for 10 mM 2FA, 1.8E6 ± 7.0E3 cells/mL for 5 mM 2FA, 1.4E6 ± 1.8E5 cells/mL for 2.5 mM 2FA. A generalized linear model (GLM) analysis revealed that there was a statistically significant difference in the growth of frozen pNK cells at different times points ($P < 0.1$, 0.001, and 0.0001, $n = 3$). The statistical significance comes from 2.5 mM 2FA-frozen pNK cells at day 4 vs the other treatments where there is ~1.7 folds decrease in the growth of 2.5 mM 2FA-frozen cells. In addition, the growth of 2.5 mM, 5 mM and 10 mM 2FA-frozen cells at day 6 appeared to be significantly lower than that of CS10-frozen ones, as shown in **Figure 6.10**.

Although inhibition of ice recrystallization (i.e., 2FA cell cultures) did not appear to increase the number of viable cells, it is apparent that the addition of feeder cells in all cultures resulted in cell proliferation/expansion, where the number of live cells increased continuously post-thaw (**Figure 6.10**). This implies that feeder cells are important for the growth of pNK cell cultures post cryopreservation.

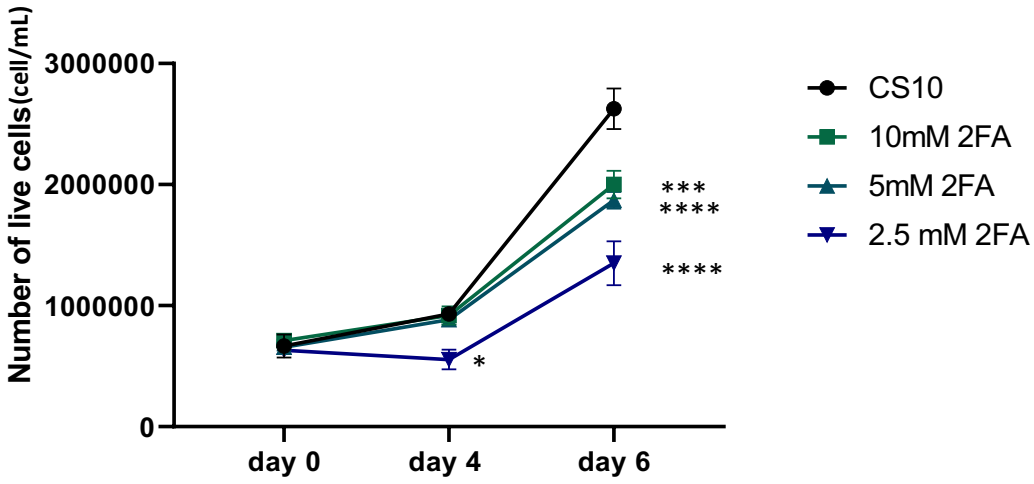

Figure 6.10 Scatter plot representing the number of live pNK cells at 0, 4, and 6 days post-thaw. Analysis of live/dead cells was done using a Live/Dead Fixable near-IR stain kit and flowcytometry. CS10- and 2FA- frozen pNK cells were counted prior to adding

feeder cells (day 0), and after adding feeder cells (day 4 and 6) to measure growth. A GLM analysis suggests that there is a significant difference between the treatments at different time points (* = P value < 0.1, *** = P value < 0.001, **** = P value < 0.0001, n = 3). Error bars represent the standard error of the mean (SEM).

A functionality assay was then conducted on the pNK cells prior to freezing as well as post-thaw following freezing to examine any difference in killing target tumor cells. K562 target cells were co-platted at different ratios with pNK cells (1:1 and 1:3 of pNK:K562 cells) and incubated for 4 hours. Following co-incubation, surface staining (anti CD56, anti CD107, and anti CD16), as well as intracellular staining (anti IFN-γ) were employed to identify pNK cells and dead target cells, respectively. Samples were then analyzed using flowcytometry to measure the percentage of IFN-γ^+ produced by the cryopreserved pNK cells. The scatter plots representing the percentage of IFN-γ^+ in the absence and presence of target cells K562 for the different freezing conditions are represented in **S. Figure 5**. As shown in **Figure 6.11**, The percentage of IFN-γ^+ in 1:1 ratio of pNK:K562 for pre-frozen cells was found to be 24.8%, for CS10-frozen cells was 28.4 ± 5.4%, for 10 mM 2FA-frozen ones was 30.1 ± 7.8%, for 5 mM 2FA-frozen cells was 24.7 ± 0.7%, and for 2.5 mM 2FA-frozen cells was 23.7 ± 2.6%. A two-way ANOVA test comparing the killing activity of (1) pre-frozen cells with frozen cells, and of (2) the different 2FA formulations with CS10-frozen cells suggested that there was no statistically significant change in the cytotoxic activity of pNK when they were co-platted in a 1:1 ratio of pNK:K562 (P value > 0.1, n = 3).

Moreover, K562 target cells were also plated at a higher concentration (1:3 pNK:K562) to further probe the killing capacity of unfrozen and frozen pNK cells. As presented in **Figure 6.11**, the percentage of IFN-γ^+ in 1:3 ratio of pNK:K562 for pre-frozen cells was similar to that of 1:1 ratio, at 29.5%, indicating that the performance of pNK cells

in the presence of high or low concentrations of K562 cells does not differ. This suggests that pNK cells possess a high cytotoxic killing activity against K562 tumor cells and can efficiently destroy tumor cells regardless their number. Moreover, the killing capacity of CS10-, 10 mM 2FA-, 5 mM 2FA-, and 2.5 mM 2FA-frozen cells was found to be 34.7 ± 0.7 %, 37.4 ± 2.6 %, 37.2 ± 0.2 %, and 34.5 ± 2.2 %, respectively. The killing activity of the frozen pNK cells appeared to increase slightly when they were co-incubated with higher concentrations of target tumor cells for the different freezing conditions. Although the percentage of IFN-γ^+ in the presence of unfrozen cells is lower than that of frozen cells, a two-way ANOVA test revealed that there was no significant difference in the killing activity when the different freezing conditions were compared to pre-frozen cells. In addition, a two-way ANOVA comparing 2FA formulations to CS10 alone revealed that there was not a significant difference in the killing activity. From these preliminary data, it is evident that the cytotoxic killing activity of pNK cells does not get compromised upon freezing with CS10 or 2FA formulations. Furthermore, no changes in the cytotoxic functionality of CS10- or 2FA-frozen pNK appeared in the presence of K562 target cells, which may be related to the fact that frozen pNK cells were allowed to expand using feeder cells for 7 days prior to performing the functionality assay.

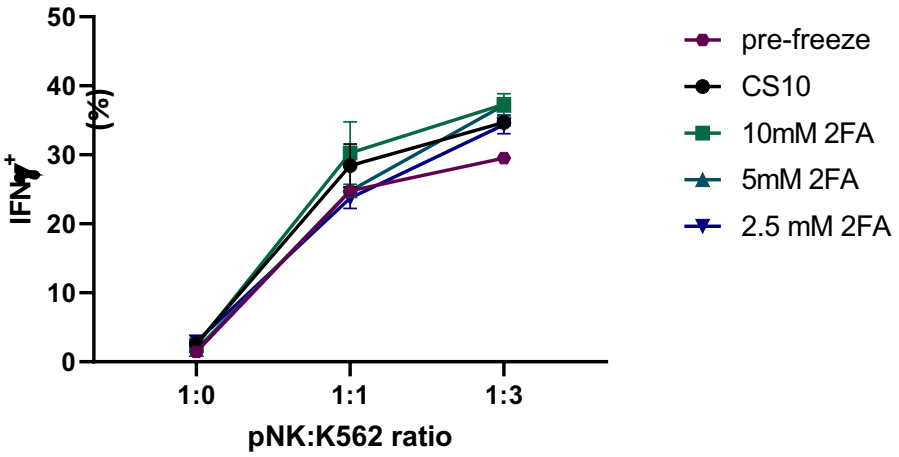

Figure 6.11 Scatter plot representing the percentage of IFN-γ^+ in the absence and presence of target cells K562. Pre-frozen and frozen pNK cells were plated in triplicate for each condition in the absence (1:0 pNK:K562) and presence (1:1 and 1:3 pNK:K562) of target cells. A two-way ANOVA test with multiple comparisons revealed there was no statistically significant difference in the percentage of IFN-γ^+ between pre-frozen cells and the different freezing conditions (P value > 0.1, n = 3). Error bars represent the standard error of the mean (SEM).

Section 6.3 revealed that the absence of feeder cells from the CS10-cryopreserved pNK cultures affected their growth, which was implied by the decrease in the 48-hr post-thaw recovery rate. Moreover, **section 6.4** showed that protection against ice recrystallization and the presence of feeder cells in the frozen pNK cultures retained the growth of the cells post-thaw, which was implied by the increase in the number of live cells at days 4 and 6 post-thaw. Further studies will be conducted to investigate the potential to discard the use of feeder cells post-thaw and examine whether employing IRI technology in the freezing protocol of pNK cells may result in similar or increased growth and functionality outcomes post cryopreservation, which will decrease the timeline required to obtain a high number of viable and functional pNK cells for future clinical applications.

6.5 Discussion

Allogeneic NK cells are being employed as an effective immunotherapy.[12-16] Donor-derived PBMCs are one of the main sources utilized to generate pNK cells and are processed by either NK cell enrichment or NK cell expansion to produce a clinically relevant NK cell densities.[17-19] Due to the variability and scarcity of donor cells, using this production process has limited the availability and scalability of NK cell-based therapies.[17-19] These limitations necessitate the development of a quality-controlled cryopreserved bank of NK cells for the manufacturing process of CAR NK cell therapy and for future clinical applications. However, conventional cryopreservation protocols utilized for preserving NK cell products result in low recovery rates and impairment in their killing functionality, limiting the accessibility of NK cell doses for patients, as the cryopreserved cells require long timeframes to grow and restore their functionality post-thaw.[20-21,65-66]

Human-derived NK cells have been subjected to cryopreservation in several studies, and several cryo-solutions have been proposed for their cryopreservation.[21,35-43] This series of studies demonstrated that the number of viable and functional NK cells decreases post-thaw.[35-43] To date, There have been no studies that objectively compare freezing protocols in the presence or absence of IRIs, and no guidelines controlling the preservation of pNK cells for clinical application have been published. In order to increase the yield of viable and functional pNK cells, we applied an IRI in a clinically related cryopreservation solution (CS10) to examine the efficacy of the cryopreservation protocol in the presence of IRIs. Since freezing and thawing of pNK cells result in a significant cell loss, we expect that protecting the cells from ice recrystallization will improve cell survival and post-thaw killing activity of pNKs.

Zeng *et al.* attempted to implement a GMP-compatible cryopreservation protocol for iPSC-NK cells, where they utilized CS10 as the freezing medium.[21] They reported that the immediate post-thaw viability was 40%, moreover, the viability appeared to decrease ~ 20% when it was evaluated 48 hours post-thaw.[21] Moreover, other studies revealed that the post-thaw recovery rate of pNK cells ranges between 20 to 40%, depending on the cryomedia formulation used.[21,27,35-44] Our study revealed that employing CS10 in the cryopreservation protocol of pNK cells resulted in a ~ 20% decrease in the recovery rate when the cryopreserved pNK cells were counted immediately and 48-hr post-thaw. This indicates that current GMP-compatible cryo-solution formulations significantly reduce the viability of cryopreserved NK cells, regardless of their source (i.e., PBMCs or iPSCs). Zeng *et al.* proposed that expanding of the cryopreserved NK cells using feeder cells would allow for the generation of the required cell densities for clinical application.[21] However, this limits the number of doses available for patients and increases the time needed to produce NK cell therapies.

Ice recrystallization is one of the major causes of cell death during cryopreservation, and therefore, IRIs are promising cryoprotective additives that have been shown to improve the survival and functionality of a variety of cell types, including iPSC-Ns, and T/CAR T cells, after they have been frozen (**Chapters 4** & **5**). Consequently, we sought to examine the efficacy of the cryopreservation solution used to freeze NK cells, CS10, in the absence and presence of an active IRI, 2FA by analyzing the post-thaw viability, recovery rate and killing activity. The viability and recovery rate of frozen pNK cells were assessed using Live/Dead near IR stain and flowcytometry immediately and 3 hours post-thaw. No significant difference was observed in the immediate nor 3-hr post-

thaw viability and recovery rate of pNK cells when 2FA was formulated in CS10 compared to CS10 alone. Assessment of the post-thaw cytotoxic killing functionality of 2FA-frozen pNK cells against tumor cells in comparison with CS10-frozen cells, as well as non-frozen cells, further confirmed that employing IRIs in the cryopreservation protocol of pNK cells did not compromise their functionality post-thaw. These preliminary data suggest that IRI supplementation in a GMP-compatible cryo-solutions, CS10, may enable the production of scalable and quality controlled pNK cell-based therapy which will help in its translation into off-the-shelf immunotherapy and will facilitate its accessibility for cancer patients.

One variation in our study comes from the assays utilized to count the number of live/dead cells. In the previous set of experiments, the Trypan blue exclusion assay was utilized, where all frozen cells with a damaged cell membrane (i.e., frozen NK cells and feeder cells that may have remained from the expansion prior to freezing) were stained blue and counted as dead cells, where the immediate and 48-hr post-thaw viabilities varied between 60 and 80%. On the other hand, flowcytometry requires gating specifically for NK cells to complete the assessment of live/dead cells; this process discards any feeder cells that may have remained in the NK cell cultures prior to freezing, where the immediate and 48-hr post-thaw viabilities were observed to be 90%. One of the limitations in our studies is that feeder cells were added to the cryopreserved cultures of pNK cells prior to the assessment of their post-thaw killing activity, which may have compromised the growth rate and killing activity of the different freezing conditions (i.e., CS10 alone vs 2FA in CS10). Therefore, further studies will be conducted on frozen NK cell products where feeder cells will be eliminated from the NK cell cultures post-thaw to examine any difference in the growth rate and killing activity of pNK cells. Furthermore, the use of rate-

controlled freezers during freezing is another element that should be explored to better fine-tune the cryopreservation protocol of pNK cells. Ultimately, the development of technologies that assist in the optimization of the freezing and thawing protocol of cell-based therapeutics is crucial for the effective creation of an off-the-shelf NK cell therapy.

6.6 Chapter Summary

NK cells are an important component of the innate immune system and have become promising candidates for CAR-based immunotherapies targeting a variety of cancers. Given their promise as off-the-shelf therapies, cryopreservation is a vital component in the availability of NK cells for allogeneic therapy, in addition to the need for the growth of NK cells to achieve clinically effective cell densities. NK cells are extremely sensitive to freezing and thawing, therefore, we sought to investigate different reported formulations of cryomedia (FBS10, RP10, and RP5) and a GMP-compatible cryo-solution (CS10) to examine their ability to cryopreserve NK cells while maintaining high viability and recovery rates. Most of the conventional cryopreservation media described for freezing pNK cells contain animal components, such as FBS, limiting their clinical translation. As such, we focused our efforts to optimize a GMP-compatuble cryomedium (i.e., CS10), supplemented with IRIs, as a novel cryo-formulation to improve the post-thaw recovery rates using clinically relevant reagents.

As mentioned in sections 6.3.1 and 6.3.2, cryopreservation of NK-92 and pNK cells with CS10 resulted in high NK-92 and pNK yields, similar to the three non-GMP grade cryomedia formulations, FBS10, RP10, and RP5. Immediate post-thaw viability of the four cryomedia ranged between 70% to 80%, while recovery ranges between 40% to 70%. Notably, the recovery rate of CS10-frozen NK-92 and pNK cells decreased after 48 hours

post-thaw, implying that CS10 does not protect the cells from delayed cell death/cryoinjury that may be driven by ice formation and recrystallization during the thawing process.

IRI technology was, therefore, employed in CS10 to explore whether protecting against ice recrystallization may improve the cryopreservation outcomes. 2FA is one of the most active IRIs that the Ben lab has developed that has been shown to enhance the functionality and recovery of multiple cell types such as HSCs,[50-51] iPSCs, iPSC-Ns, and T cells. Thus, 2FA was formulated in CS10 and tested on pNK cells. Formulations of 2FA in CS10 did not appear to increase the immediate post-thaw recovery rate, suggested by a one-way ANOVA test. However, it was evident that the 2FA-frozen pNK cells retained their proliferation activity 3 hours post-thaw, prior to the addition of feeder cell, where the number of live cells appeared to increase in comparison with the immediate post-thaw recovery rate. However, the 3-hr post-thaw recovery rate of 2FA-frozen cells did not appear to be significantly different than CS10-alone frozen cells. It was also apparent that the killing activity of pNK cells did not get compromised when they were frozen in the presence of 2FA, as mentioned in section 6.4.2. No statistically significant increase in the cytotoxic killing activity of pNK cells against K562 tumor cells was observed across the different freezing conditions, which may be related to the fact that thawed pNK cells were able to recover and expand in the presence of feeder cells prior to testing with the functionality assay.

While 2FA appeared to significantly increase the number of T/CAR T cells post-thaw in comparison with CS10 alone (Chapter 5), it may not have similar outcome on pNK cells as the two lymphocytes, the former being part of adoptive immune system while the latter is part of the innate immune system, differ in their characteristics which may result

in a difference in their response to cryopreservation. Further studies will be conducted to test higher concentrations of 2FA (i.e., 15 mM and 20 mM), and to investigate the proliferation of pNK cells 24 hr and 48 hr post-thaw in the absence of feeder cells, to verify any changes in the growth of 2FA- and CS10-alone frozen cells. This will establish whether cryopreservation of pNK with IRIs may assist frozen pNK cells to proliferate and expand without the presence of feeder cells which will be beneficial for the translation of pNK and CAR-NK cell-based therapies into clinics and hospitals. Also, a panel of IRIs will be tested on pNK cells to investigate the potential of any new IRI in increasing the post-thaw recovery rate of pNK cells, which will assist in increasing the availability of pNK and CAR-NK cell doses in clinics.

6.7 Experimental Procedures

6.7.1 NK-92 Cell Line Culture

Wt-NK-92 and CAR-NK-92 cells were acquired from American Type Culture Collection (ATCC), Burlington, Ontario, Canada (Clone E6-1, TIB-152™). Wt- and CAR-NK-92 cells were cultured in T50 culture flasks (Thermo Fisher Scientific, Nepean, Ontario, Canada) using complete RPMI-1640 culture medium with Glutamine (Sigma Aldrich, catalogue number: R8758). Complete RPMI medium was supplemented with 1 mM Hepes (Thermo Fisher Scientific, 15630080), 10% FBS (Sigma-Aldrich, C8056), 55 mM mercaptoethanol (Thermo Fisher Scientific, 31350010), 100X Pen/Strep (Thermo Fisher Scientific, 15070063), and 200 U/mL IL2. A total of 1E6 Wt- or CAR-NK-92 cells were seeded in T50 flasks containing 30 mL of culture medium and incubated in a 5% CO_2 atmosphere in humidified incubator at 37˚C. Culture media was changed every other day for 12 days until they were frozen.

6.7.2 pNK Cells Isolation

pNK cells were isolated from PBMCs of healthy donors (Ottawa Hospital Research Institute) using a Mojosort human NK cells isolation kit. PBMCs were counted, washed with RPMI+10% FBS, spun at 400g for 5 minutes. The cell pellet was then resuspended in 10E6 cell per 100 µL of sorting buffer. 20 µL of an antibody cocktail was then added to the cell suspension and vortexed. The mixture was incubated on ice for 20 minutes, followed by centrifugation at 400g for 5 minutes. The cell pellet was then resuspended with 100 µL of sorting buffer, followed by the addition of 20 µL of beads to the 10E6 cell suspension. The mixture was then vortexed and incubated on ice for 20 minutes. 1 mL of sorting buffer was then added, mixed gently and the mixture was transferred into 15-mL falcon tube. The tube was then inserted into a magnetic rack and incubated for 10 minutes at room temperature. The unbound portion of the solution was then transferred into a new 15-mL tube, and a 5 mL of RPMI+10% FBS was added. Cells were then counted and spun down at 400g for 5 minutes. The cell pellet was then resuspended at 500K cells/mL using RPMI+10% FBS with 500 U/mL IL-2. Cells were then plated, and feeder cells were added at a concentration of 2X to each well.

6.7.3 pNK Cell Expansion

Isolated pNK cells were plated with 2X feeder cells (using K562-mbIL21-4-1BBL feeder cells). The feeder cells were received by Dr. Lee's laboratory from the Research Institute at Nationwide Children's Hospital on behalf of Cytosen under a Material Transfer Agreement. On day 3 and 5, half of the media was changed (RMPI + 10% FBS + 500 u/mL IL-2). On day 7, cells were collected, counted, and spun at 410g for 5 minutes. The cell pellet was resuspended in complete media at 250K cell/mL. Cells were then stimulated

with 1:1 pNK:feeder cells. On day 9, cells were collected, counted, and spun at 410g for 5 minutes. The cell pellet was resuspended in complete media at 500K to 1E6 cell/mL, and stimulated with 1:1 pNK:feeder cells. Steps were repeated on days 11 and 13.

6.7.4 Cryopreservation of Wt-NK-92, CAR-NK-92 and pNK Cells

A. Freezing

Cryostor®10 was obtained from Stem Cell Technologies (Vancouver, BC, Canada, 07930). *N*-2-fluorophenyl-D-gluconamide (2FA) was synthesized and purified as previously described (Ben Laboratory, University of Ottawa, ON., Canada).[50-51] 2FA was supplemented in CS10 at different concentrations (10 mM, 5 mM, or 2.5 mM). Cell count was done using either the Trypan blue exclusion assay (for NK-92 cells) or flowcytometry (pNK cells). Cells were then washed with sterile PBS (5 mL) and centrifuged at 400g for 5 minutes. Supernatant was removed and the cell pellets were resuspended at a concentration of 1E6 cell/0.5 mL with either CS10 alone or CS10 supplemented with 2FA. Cells were transferred to 1 mL cryovials. Cryovials were placed in a Mr. Frosty rate-controlled freezing container (-1 ˚C/min) which was then placed in -80˚C freezer for 24 hours. The cryovials were then transferred to a liquid nitrogen (LN2) dewar (-196 ˚C) for long-term storage.

B. Thawing

Cryovials were obtained from the LN2 dewar and quickly thawed in a 37 ˚C water bath for approximately 3 min. Cells were then washed with 5 mL of sterile PBS and centrifuged at 400g for 5 minutes. Cell pellets were then resuspended in 1 mL of fresh complete RPMI culture medium with 500 U/mL IL2.

6.7.5 Flowcytometry

To 6000 µL of staining buffer (SB), 12 µL of anti CD56, 24 µL of anti CD16, and 12 µL of Live/Dead near IR stains were added. For each condition, add 15 µL of cell suspension to 50 µL of staining mixture in a 96-well plate. The cells were then incubated in the dark at 4 ºC for 15 minutes, followed by two washes with 100 µL of staining buffer. Cells were spun at 400g for 5 minutes, and cell pellets were resuspended in 200 µL of staining buffer. The 96-well plate was acquired using flowcytometry machine.

6.7.6 Viability and Recovery Rate Assessment

Immediate post-thaw viability and recovery were assessed by counting the number of live and dead cells per sample. The Trypan blue exclusion assay or flowcytometry were used to stain live/dead cells. Post-thaw viability was obtained using the formula $Number\ of\ Live\ Cells⁄Number\ of\ Live + Dead\ cells$, whereas post-thaw recovery rate was obtained using $Number\ of\ Live\ cells⁄Total\ number\ of\ frozen\ cells\ (1xE6)$. Statistical analysis was completed using a one-way ANOVA™ (multiple comparisons) in GraphPad Prism.

6.7.7 Cytotoxicity Assay

pNK cells and K562 target cells (ATTC, Burlington, Ontario, Canada) were counted using flowcytometry. For each condition, the amount needed for total of 50K cell/well was added to a 15-mL falcon tube. Cells were then spun at 400g for 5 minutes. Cell pellets were resuspended in 600 µL of complete RMPI with 100 U/mL of IL-2. The amount needed for a total 150K cell/50 µL of K562 target cells for 12 samples was added to a 15 mL-falcon tube. Cells were spun at 400g for 5 minutes and the cell pellet was resuspended in 2.66 mL of complete RMPI with 100 U/mL of IL-2. In a U-bottom 96-well plate, 50 µL of pNK

cells were added to the appropriate wells. 50 µL of target cell suspension was then co-plated with pNK cells in the appropriate 1:3 ratio wells. Target cells were diluted down by adding 1.7 mL of complete RPMI with IL-2. The 50 µL of the diluted K562 cell suspension was then co-platted with pNK cells. BFA was diluted to 1000X using RPMI + 10% FBS medium, and 50 µL of BFA was added to all wells. 50 µL of complete RPMI medium with 100 U/mL IL-2 was then added to the wells with 1:1 pNK:K562 ratio. Cells were mixed very well and incubated for 4 hours in a 5% CO_2 atmosphere in humidified incubator at 37 ˚C.

While the cells were being incubated staining solutions were prepared. To a total of 6000-µL of staining buffer, 120 µL of anti CD56, 120 µL of anti CS107, 240 µL of anti CD16, and 120 µL of Live/Dead near IR stains were added to the surface staining master mix. To a 6000-µL of cytoperm wash buffer, 120 µL of anti IFN-γ was added to prepare the intracellular staining master mix. A compensation plate was also prepared where one well of beads contained one of the four antibodies (CD56, CD107, CD16 and IFN-γ). In each well, 300 µL of staining buffer, 3 µL of beads and 1 µL of antibody were added. Plates was kept in the dark until use.

After incubation, cells were mixed very well and transferred to a U-bottom 96-well plate. Cells were spun at 400g for 4 minutes, washed with 150 µL of staining buffer and centrifuged. Cell pellets were resuspended with 50 µL of surface staining master mixture, incubated at 4 ºC for 25 minutes. Cells were then centrifuged at 400g for 5 minutes, and pellets were resuspended with 100 µL of cytofix/cytoperm. Cells were incubated for 20 minutes at 4 ºC, washed twice with 100 µL of wash buffer. Pellets were resuspended with 50 µL of intracellular staining master mixture and incubated at 4 ºC for 25 minutes. Cells

were washed with wash buffer twice and pellets were resuspended with 200 μL of staining buffer. Plate was then acquired using flowcytometry machine.

6.8 Supplementary Figures:

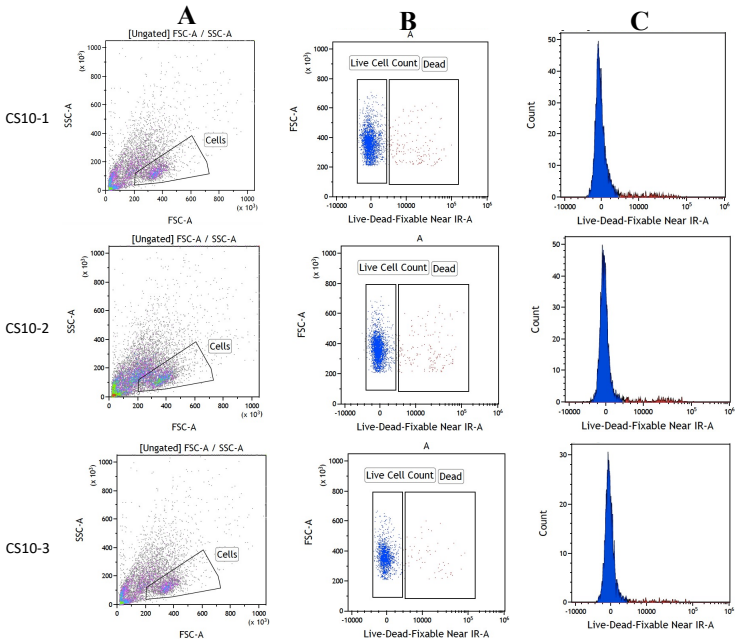

S. Figure 6.1 (A) Forward and side scatter (FSC and SSC) plots with a gate to detect CS10-frozen pNK cells. **(B)** Live and dead CS10- frozen pNK cells were gated in the subsequent Live/Dead fixable near IR-A/FSC plot. **(C)** Representative histogram after staining live/dead cells with Live/Dead fixable near IR.

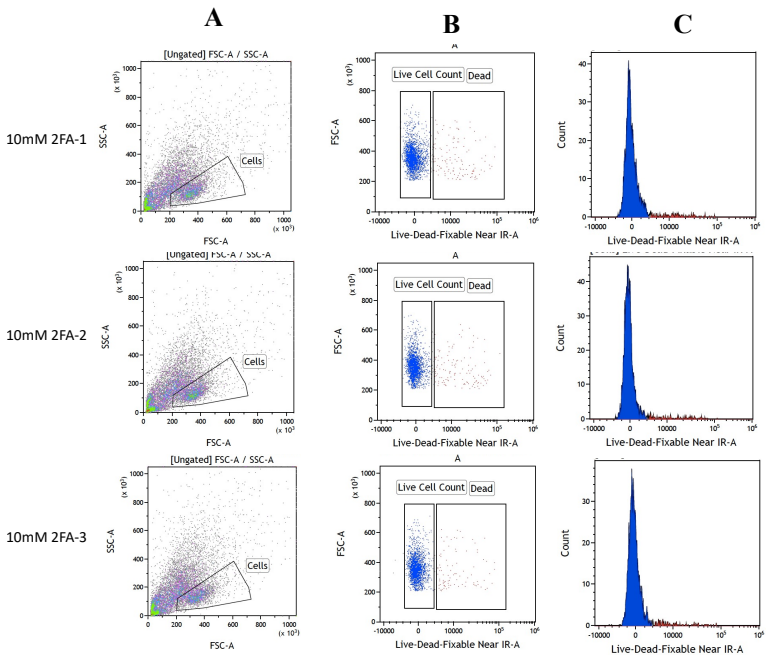

S. Figure 6.2 (A) Forward and side scatter (FSC and SSC) plots with a gate to detect 10 mM 2FA-frozen pNK cells. **(B)** Live and dead 10 mM 2FA-frozen pNK cells were gated in the subsequent Live/Dead fixable near IR-A/FSC plot. **(C)** Representative histogram after staining live/dead cells with Live/Dead fixable near IR.

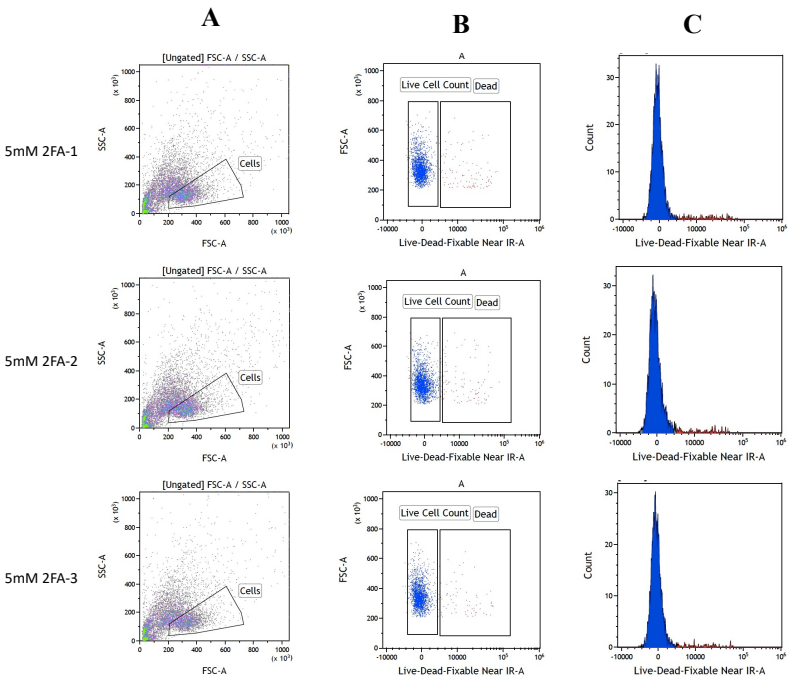

S. Figure 6.3 (A) Forward and side scatter (FSC and SSC) plots with a gate to detect 5 mM 2FA-frozen pNK cells. **(B)** Live and dead 5 mM 2FA-frozen pNK cells were gated in the subsequent Live/Dead fixable near IR-A/FSC plot. **(C)** Representative histogram after staining live/dead cells with Live/Dead fixable near IR.

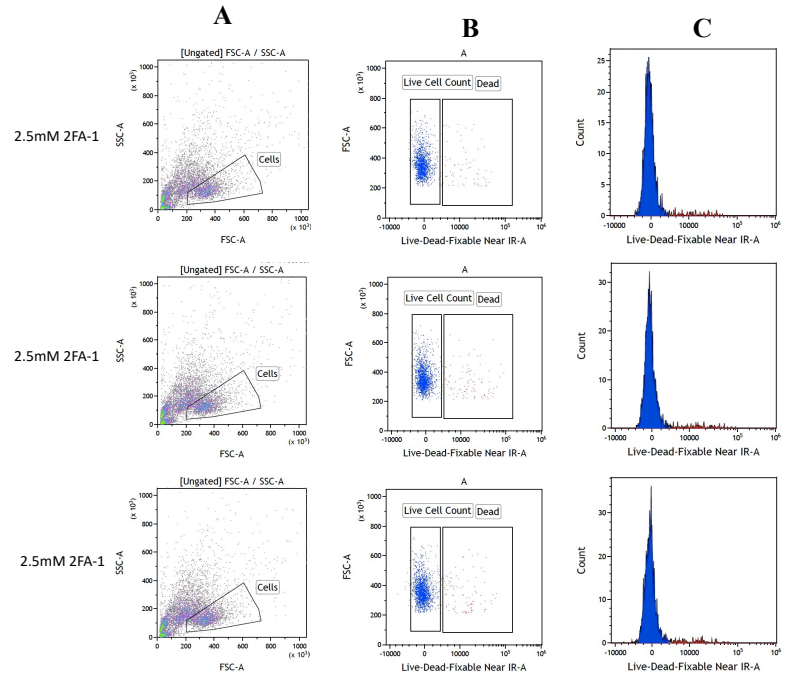

S. Figure 6.4 (A) Forward and side scatter (FSC and SSC) plots with a gate to detect 2.5 mM 2FA-frozen pNK cells. **(B)** Live and dead 2.5 mM 2FA-frozen pNK cells were gated in the subsequent Live/Dead fixable near IR-A/FSC plot. **(C)** Representative histogram after staining live/dead cells with Live/Dead fixable near IR.

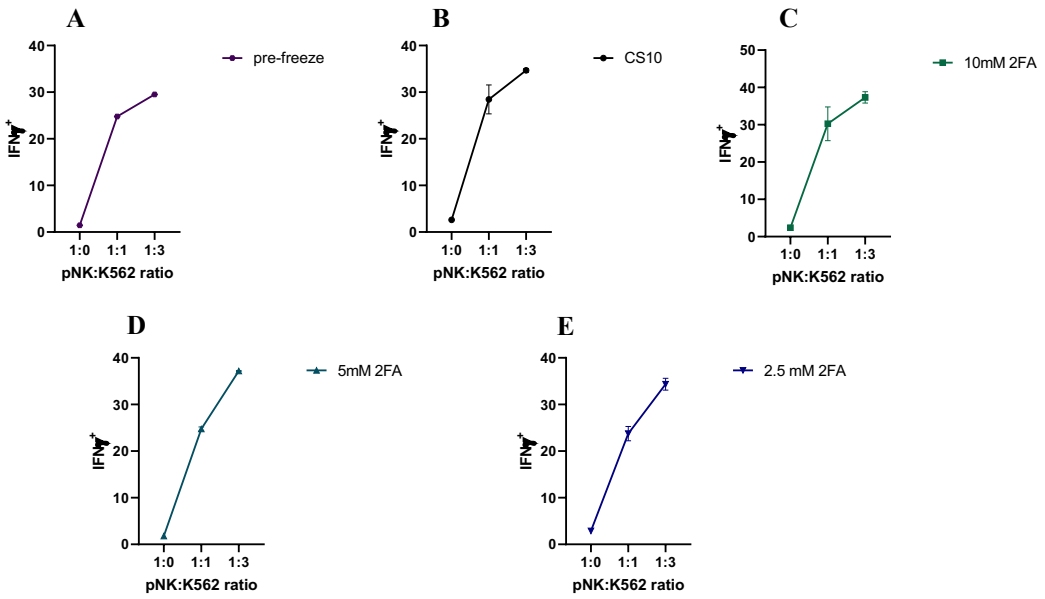

S. Figure 6.5 Scatter plots representing the percentage of IFN-γ^+ in the absence and presence of target cells K562 for **(A)** pre-frozen pNK cells, **(B)** CS10-frozen pNK cells, **(C)** 10 mM 2FA-frozen pNK cells, **(D)** 5 mM 2FA-frozen pNK cells, **(E)** 2.5 mM 2FA-frozen pNK cells.

6.9 References

(1) Cancer statistics at a glance http://www.cancer.ca/en/cancer-information/cancer-101/cancer-statistics-at-a-glance/?region=on.

(2) Galon, J.; Fridman, W. H.; Pages, F. The Adaptive Immunologic Microenvironment in Colorectal Cancer: A Novel Perspective. *Cancer Res.* **2007**, *67* (5), 1883–1886. https://doi.org/10.1158/0008-5472.CAN-06-4806.

(3) Demaria, O.; Gauthier, L.; Debroas, G.; Vivier, E. Natural Killer Cell Engagers in Cancer Immunotherapy: Next Generation of Immuno-Oncology Treatments. *Eur. J. Immunol.* **2021**, *0*, 1–10. https://doi.org/10.1002/eji.202048953.

(4) Jäger, E.; Jäger, D.; Knuth, A. Antigen-Specific Immunotherapy and Cancer Vaccines. *Int. J. Cancer* **2003**, *106* (6), 817–820. https://doi.org/10.1002/ijc.11292.

(5) Van der Bruggen, P.; Zhang, Y.; Chaux, P.; Stroobant, V.; Panichelli, C.; Schultz, E. S.; Chapiro, J.; Van den Eynde, B. J.; Brasseur, F.; Boon, T. Tumor-Specific Shared Antigenic Peptides Recognized by Human T Cells. *Immunol. Rev.* **2002**, *188*, 51–64. https://doi.org/10.1034/j.1600-065X.2002.18806.x.

(6) Melero, I.; Rouzaut, A.; Motz, G. T.; Coukos, G. T-Cell and NK-Cell Infiltration into Solid Tumors: A Key Limiting Factor for Efficacious Cancer Immunotherapy.

Cancer Discov. **2014**, *4* (5), 522–526. https://doi.org/10.1158/2159-8290.CD-13-0985.

(7) Yee, C.; Thompson, J. A.; Byrd, D.; Riddell, S. R.; Roche, P.; Celis, E.; Greenberg, P. D. Adoptive T Cell Therapy Using Antigen-Specific CD8+ T Cell Clones for the Treatment of Patients with Metastatic Melanoma: In Vivo Persistence, Migration, and Antitumor Effect of Transferred T Cells. *Proc. Natl. Acad. Sci. U. S. A.* **2002**, *99* (25), 16168–16173. https://doi.org/10.1073/pnas.242600099.

(8) Walsh, S. R.; Simovic, B.; Chen, L.; Bastin, D.; Nguyen, A.; Stephenson, K.; Mandur, T. S.; Bramson, J. L.; Lichty, B. D.; Wan, Y. Endogenous T Cells Prevent Tumor Immune Escape Following Adoptive T Cell Therapy. *J. Clin. Invest.* **2019**, *129* (12), 5400–5410. https://doi.org/10.1172/JCI126199.

(9) June, C. H.; Riddell, S. R.; Schumacher, T. N. Adoptive Cellular Therapy: A Race to the Finish Line. *Sci. Transl. Med.* **2015**, *7* (280), 1–9. https://doi.org/10.1126/scitranslmed.aaa3643.

(10) Fesnak, A. D.; June, C. H.; Levine, B. L. Engineered T Cells: The Promise and Challenges of Cancer Immunotherapy. *Nat. Rev. Cancer* **2016**, *16* (9), 566–581. https://doi.org/10.1038/nrc.2016.97.

(11) Daher, M.; Rezvani, K. Next Generation Natural Killer Cells for Cancer Immunotherapy: The Promise of Genetic Engineering. *Curr. Opin. Immunol.* **2018**, *51*, 146–153. https://doi.org/10.1016/j.coi.2018.03.013.

(12) Mehta, R. S.; Randolph, B.; Daher, M.; Rezvani, K. NK Cell Therapy for Hematologic Malignancies. *Int. J. Hematol.* **2018**, *107* (3), 262–270. https://doi.org/10.1007/s12185-018-2407-5.

(13) Gurney, M.; O'Dwyer, M. Realizing Innate Potential : CAR-NK Cell Therapies for Acute Myeloid Leukemia. *Cancers (Basel).* **2021**, *13*, 1568. https://doi.org//doi.org/10.3390/cancers 13071568 Academic.

(14) Melaiu, O.; Chierici, M.; Lucarini, V.; Jurman, G.; Conti, L. A.; De Vito, R.; Boldrini, R.; Cifaldi, L.; Castellano, A.; Furlanello, C.; Barnaba, V.; Locatelli, F.; Fruci, D. Cellular and Gene Signatures of Tumor-Infiltrating Dendritic Cells and Natural-Killer Cells Predict Prognosis of Neuroblastoma. *Nat. Commun.* **2020**, *11* (1), 1–15. https://doi.org/10.1038/s41467-020-19781-y.

(15) Xie, G.; Dong, H.; Liang, Y.; Ham, J. D.; Rizwan, R.; Chen, J. CAR-NK Cells: A Promising Cellular Immunotherapy for Cancer. *EBioMedicine* **2020**, *59*. https://doi.org/10.1016/j.ebiom.2020.102975.

(16) Locatelli, F.; Moretta, F.; Brescia, L.; Merli, P. Natural Killer Cells in the Treatment of High-Risk Acute Leukaemia. *Semin. Immunol.* **2014**, *26* (2), 173–179. https://doi.org/10.1016/j.smim.2014.02.004.

(17) Kang, S.; Gao, X.; Zhang, L.; Yang, E.; Li, Y.; Yu, L. The Advances and Challenges of Nk Cell-Based Cancer Immunotherapy. *Curr. Oncol.* **2021**, *28* (2), 1077–1093. https://doi.org/10.3390/curroncol28020105.

(18) Fang, F.; Wang, W.; Chen, M.; Tian, Z.; Xiao, W. Technical Advances in NK Cell-Based Cellular Immunotherapy. *Cancer Biol. Med.* **2019**, *16* (4), 647–654. https://doi.org/10.20892/j.issn.2095-3941.2019.0187.

(19) Dalle, J. H.; Menezes, J.; Wagner, É.; Blagdon, M.; Champagne, J.; Champagne, M. A.; Duval, M. Characterization of Cord Blood Natural Killer Cells: Implications for Transplantation and Neonatal Infections. *Pediatr. Res.* **2005**, *57* (5 I), 649–655. https://doi.org/10.1203/01.PDR.0000156501.55431.20.

(20) Li, Y.; Hermanson, D. L.; Moriarity, B. S.; Kaufman, D. S. Human IPSC-Derived Natural Killer Cells Engineered with Chimeric Antigen Receptors Enhance Anti-Tumor Activity. *Cell Stem Cell* **2018**, *23* (2), 181-192.e5. https://doi.org/10.1016/j.stem.2018.06.002.

(21) Zeng, J.; Tang, S. Y.; Toh, L. L.; Wang, S. Generation of "Off-the-Shelf" Natural Killer Cells from Peripheral Blood Cell-Derived Induced Pluripotent Stem Cells. *Stem Cell Reports* **2017**, *9* (6), 1796–1812. https://doi.org/10.1016/j.stemcr.2017.10.020.

(22) Fujisaki, H.; Kakuda, H.; Shimasaki, N.; Imai, C.; Ma, J.; Lockey, T.; Eldridge, P.; Leung, W. H.; Campana, D. Expansion of Highly Cytotoxic Human Natural Killer Cells for Cancer Cell Therapy. *Cancer Res.* **2009**, *69* (9), 4010–4017. https://doi.org/10.1158/0008-5472.CAN-08-3712.

(23) Rezvani, K.; Rouce, R.; Liu, E.; Shpall, E. Engineering Natural Killer Cells for Cancer Immunotherapy. *Mol. Ther.* **2017**, *25* (8), 1769–1781. https://doi.org/10.1016/j.ymthe.2017.06.012.

(24) Cichocki, F.; Bjordahl, R.; Gaidarova, S.; Mahmood, S.; Abujarour, R.; Wang, H.; Tuininga, K.; Felices, M.; Davis, Z. B.; Bendzick, L.; Clarke, R.; Stokely, L.; Rogers, P.; Ge, M.; Robinson, M.; Rezner, B.; Robbins, D. L.; Lee, T. T.; Kaufman, D. S.; Blazar, B. R.; Valamehr, B.; Miller, J. S. IPSC-Derived NK Cells Maintain High Cytotoxicity and Enhance in Vivo Tumor Control in Concert with T Cells and Anti–PD-1 Therapy. *Sci. Transl. Med.* **2020**, *12* (568), 1–6. https://doi.org/10.1126/scitranslmed.aaz5618.

(25) Goldenson, B. H.; Zhu, H.; Wang, Y. Z. M.; Heragu, N.; Bernareggi, D.; Ruiz-Cisneros, A.; Bahena, A.; Ask, E. H.; Hoel, H. J.; Malmberg, K. J.; Kaufman, D. S. Umbilical Cord Blood and IPSC-Derived Natural Killer Cells Demonstrate Key Differences in Cytotoxic Activity and KIR Profiles. *Front. Immunol.* **2020**, *11* (October), 1–14. https://doi.org/10.3389/fimmu.2020.561553.

(26) Zhu, H.; Kaufman, D. S. An Improved Method to Produce Clinical-Scale Natural Killer Cells from Human Pluripotent Stem Cells. *Methods Mol. Biol.* **2019**, *2048*, 107–119. https://doi.org/10.1007/978-1-4939-9728-2_12.

(27) Shankar, K.; Capitini, C. M.; Capitini, C. M.; Saha, K.; Saha, K.; Saha, K. Genome Engineering of Induced Pluripotent Stem Cells to Manufacture Natural Killer Cell Therapies. *Stem Cell Res. Ther.* **2020**, *11* (1), 1–14. https://doi.org/10.1186/s13287-020-01741-4.

(28) Zhu, H.; Blum, R. H.; Bernareggi, D.; Ask, E. H.; Wu, Z.; Hoel, H. J.; Meng, Z.; Wu, C.; Guan, K. L.; Malmberg, K. J.; Kaufman, D. S. Metabolic Reprograming via Deletion of CISH in Human IPSC-Derived NK Cells Promotes In Vivo Persistence and Enhances Anti-Tumor Activity. *Cell Stem Cell* **2020**, *27* (2), 224-237.e6. https://doi.org/10.1016/j.stem.2020.05.008.

(29) Stacey, G. N.; Masters, J. R. Cryopreservation and Banking of Mammalian Cell Lines. *Nat. Protoc.* **2008**, *3* (12), 1981–1989. https://doi.org/10.1038/nprot.2008.190.

(30) Giwa, S.; Lewis, J. K.; Alvarez, L.; Langer, R.; Roth, A. E.; Church, G. M.; Markmann, J. F.; Sachs, D. H.; Chandraker, A.; Wertheim, J. A.; Rothblatt, M.; Boyden, E. S.; Eidbo, E.; Lee, W. P. A.; Pomahac, B.; Brandacher, G.; Weinstock, D. M.; Elliott, G.; Nelson, D.; Acker, J. P.; Uygun, K.; Schmalz, B.; Weegman, B.

P.; Tocchio, A.; Fahy, G. M.; Storey, K. B.; Rubinsky, B.; Bischof, J.; Elliott, J. A. W.; Woodruff, T. K.; Morris, G. J.; Demirci, U.; Brockbank, K. G. M.; Woods, E. J.; Ben, R. N.; Baust, J. G.; Gao, D.; Fuller, B.; Rabin, Y.; Kravitz, D. C.; Taylor, M. J.; Toner, M. The Promise of Organ and Tissue Preservation to Transform Medicine. *Nat. Biotechnol.* **2017**, *35* (6), 530–542. https://doi.org/10.1038/nbt.3889.

(31) Bakhach, J. The Cryopreservation of Composite Tissues: Principles and Recent Advancement on Cryopreservation of Different Type of Tissues. *Organogenesis* **2009**, *5* (3), 119–126. https://doi.org/10.4161/org.5.3.9583.

(32) Scott, K. L.; Lecak, J.; Acker, J. P. Biopreservation of Red Blood Cells: Past, Present, and Future. *Transfus. Med. Rev.* **2005**, *19* (2), 127–142. https://doi.org/10.1016/j.tmrv.2004.11.004.

(33) Baust, J. G.; Gao, D.; Baust, J. M. Cryopreservation: An Emerging Paradigm Change. *Organogenesis* **2009**, *5* (3), 90–96. https://doi.org/10.4161/org.5.3.10021.

(34) Barry J. Fuller, Nick Lane, and Erica E. Benson, E. Life in the Frozen State. Boca. *Boca Raton, Florida CRC Press* **2004**, *83* (3), 696. https://doi.org/10.1016/j.fertnstert.2004.10.025.

(35) Mata, M. M.; Mahmood, F.; Sowell, R. T.; Baum, L. L. Effects of Cryopreservation on Effector Cells for Antibody Dependent Cell-Mediated Cytotoxicity (ADCC) and Natural Killer (NK) Cell Activity in 51Cr-Release and CD107a Assays. *J. Immunol. Methods* **2014**, *406*, 1–9. https://doi.org/10.1016/j.jim.2014.01.017.

(36) Min, B.; Choi, H.; Her, J. H.; Jung, M. Y.; Kim, H. J.; Jung, M. Y.; Lee, E. K.; Cho, S. Y.; Hwang, Y. K.; Shin, E. C. Optimization of Large-Scale Expansion and Cryopreservation of Human Natural Killer Cells for Anti-Tumor Therapy. *Immune Netw.* **2018**, *18* (4), 1–13. https://doi.org/10.4110/in.2018.18.e31.

(37) Cells, N. K.; Antitumor, E.; Yang, B.; Cho, S. Y.; Hwang, Y. K.; Yun, C. Erratum: Cryopreserved Human Natural Killer Cells Exhibit Potent Antitumor Efficacy against Orthotopic Pancreatic Cancer through Efficient Tumor-Homing and Cytolytic Ability (Running Title: Cryopreserved NK Cells Exhibit Antitumor Effect) (Cancers 2019, 1. *Cancers (Basel).* **2020**, *12* (11), 1–2. https://doi.org/10.3390/cancers12113255.

(38) Mark, C.; Czerwinski, T.; Roessner, S.; Mainka, A.; Hörsch, F.; Heublein, L.;

Winterl, A.; Sanokowski, S.; Richter, S.; Bauer, N.; Schuler, G.; Fabry, B.; Voskens, C. J. Cryopreservation Impairs Cytotoxicity and Migration of NK Cells in 3-D Tissue: Implications for Cancer Immunotherapy. *bioRxiv* **2019**. https://doi.org/10.1101/812172.

(39) Mark, C.; Czerwinski, T.; Roessner, S.; Mainka, A.; Hörsch, F.; Heublein, L.; Winterl, A.; Sanokowski, S.; Richter, S.; Bauer, N.; Angelini, T. E.; Schuler, G.; Fabry, B.; Voskens, C. J. Cryopreservation Impairs 3-D Migration and Cytotoxicity of Natural Killer Cells. *Nat. Commun.* **2020**, *11* (1), 1–8. https://doi.org/10.1038/s41467-020-19094-0.

(40) Ichino, Y.; Ishikawa, T. Effects of Cryopreservation on Human Lymphocyte Functions: Comparison of Programmed Freezing Method by a Direct Control System with a Mechanical Freezing Method. *J. Immunol. Methods* **1985**, *77* (2), 283–290. https://doi.org/10.1016/0022-1759(85)90041-9.

(41) El Assal, R.; Abou-Elkacem, L.; Tocchio, A.; Pasley, S.; Matosevic, S.; Kaplan, D. L.; Zylberberg, C.; Demirci, U. Bioinspired Preservation of Natural Killer Cells for Cancer Immunotherapy. *Adv. Sci.* **2019**, *6* (6). https://doi.org/10.1002/advs.201802045.

(42) Domogala, A.; Alejandro Madrigal, J.; Saudemont, A. Cryopreservation Has No Effect on Function of Natural Killer Cells Differentiated in Vitro from Umbilical Cord Blood CD34+ Cells. *Cytotherapy* **2016**, *18* (6), 754–759. https://doi.org/10.1016/j.jcyt.2016.02.008.

(43) Damodharan, S. N.; Walker, K. L.; Forsberg, M. H.; McDowell, K. A.; Bouchlaka, M. N.; Drier, D. A.; Sondel, P. M.; DeSantes, K. B.; Capitini, C. M. Analysis of Ex Vivo Expanded and Activated Clinical-Grade Human NK Cells after Cryopreservation. *Cytotherapy* **2020**, *22* (8), 450–457. https://doi.org/10.1016/j.jcyt.2020.05.001.

(44) Costantini, A.; Mancini, S.; Giuliodoro, S.; Butini, L.; Regnery, C. M.; Silvestri, G.; Montroni, M. Effects of Cryopreservation on Lymphocyte Immunophenotype and Function. *J. Immunol. Methods* **2003**, *278* (1–2), 145–155. https://doi.org/10.1016/S0022-1759(03)00202-3.

(45) Bakar, B.; Kose, E. A.; Sonal, S.; Alhan, A.; Kilinc, K.; Keskil, I. S. Evaluation of

the Neurotoxicity of DMSO Infused into the Carotid Artery of Rat. *Injury* **2012**, *43* (3), 315–322. https://doi.org/10.1016/j.injury.2011.08.021.

(46) Fahy, G. M. The Relevance of Cryoprotectant "Toxicity" to Cryobiology. *Cryobiology* **1986**, *23* (1), 1–13. https://doi.org/10.1016/0011-2240(86)90013-1.

(47) Fahy, G. M.; Lilley, T. H.; Linsdell, H.; Douglas, M. S. J.; Meryman, H. T. Cryoprotectant Toxicity and Cryoprotectant Toxicity Reduction: In Search of Molecular Mechanisms. *Cryobiology* **1990**, *27* (3), 247–268. https://doi.org/10.1016/0011-2240(90)90025-Y.

(48) Matsumoto, S.; Matsusita, M.; Morita, T.; Kamachi, H.; Tsukiyama, S.; Furukawa, Y.; Koshida, S.; Tachibana, Y.; Nishimura, S. I.; Todo, S. Effects of Synthetic Antifreeze Glycoprotein Analogue on Islet Cell Survival and Function during Cryopreservation. *Cryobiology* **2006**, *52* (1), 90–98. https://doi.org/10.1016/j.cryobiol.2005.10.010.

(49) Capicciotti, C. J.; Mancini, R. S.; Turner, T. R.; Koyama, T.; Alteen, M. G.; Doshi, M.; Inada, T.; Acker, J. P.; Ben, R. N. O-Aryl-Glycoside Ice Recrystallization Inhibitors as Novel Cryoprotectants: A Structure-Function Study. *ACS Omega* **2016**, *1* (4), 656–662. https://doi.org/10.1021/acsomega.6b00163.

(50) Briard, J. G.; Jahan, S.; Chandran, P.; Allan, D.; Pineault, N.; Ben, R. N. Small-Molecule Ice Recrystallization Inhibitors Improve the Post-Thaw Function of Hematopoietic Stem and Progenitor Cells. *ACS Omega* **2016**, *1* (5), 1010–1018. https://doi.org/10.1021/acsomega.6b00178.

(51) Briard, J. G. The Rational Design and Use of Novel Small-Molecule Ice Recrystallization Inhibitors for the Cryopreservation of Hematopoietic Stem Cells and Red Blood Cells. *(Doctoral Diss. Univ. d'Ottawa/University Ottawa* **2016**, 235.

(52) Strober, W. Trypan Blue Exclusion Test of Cell Viability. *Curr. Protoc. Immunol.* **2001**, *Appendix 3*, 2–3. https://doi.org/10.1002/0471142735.ima03bs21.

(53) Invitrogen ™ LIVE / DEAD ™ Fixable Near-IR Dead Cell Stain Kit by Thermo Fisher Scientific Why request a quote through SelectScience ?

(54) Pasley, S.; Zylberberg, C.; Matosevic, S. Natural Killer-92 Cells Maintain Cytotoxic Activity after Long-Term Cryopreservation in Novel DMSO-Free Media. *Immunol. Lett.* **2017**, *192*, 35–41. https://doi.org/10.1016/j.imlet.2017.09.012.

(55) Shah, U. A.; Mailankody, S. CAR T and CAR NK Cells in Multiple Myeloma: Expanding the Targets. *Best Pract. Res. Clin. Haematol.* **2020**, *33* (1). https://doi.org/10.1016/j.beha.2020.101141.

(56) Chehimi, J.; Starr, S. E.; Frank, I.; Rengaraju, M.; Jackson, S. J.; Llanes, C.; Kobayashi, M.; Perussia, B.; Young, D.; Nickbarg, E.; Wolf, S. F.; Trinchieri, G. Natural Killer (NK) Cell Stimulatory Factor I11creases the Cytotoxic Activity of NK Cells from Both Healthy Donors and Human Immunodeficiency Virus-Infected Patients. *J. Exp. Med* **1992**, *175*, 789–796.

(57) Herberman, R. B.; Ortaldo, J. R.; Mantovani, A.; Hobbs, D. S.; Kung, H. fu; Pestka, S. Effect of Human Recombinant Interferon on Cytotoxic Activity of Natural Killer (NK) Cells and Monocytes. *Cell. Immunol.* **1982**, *67* (1), 160–167. https://doi.org/10.1016/0008-8749(82)90208-8.

(58) Oh, E.; Min, B.; Li, Y.; Lian, C.; Hong, J.; Park, G. M.; Yang, B.; Cho, S. Y.; Hwang, Y. K.; Yun, C. O. Cryopreserved Human Natural Killer Cells Exhibit Potent Antitumor Efficacy against Orthotopic Pancreatic Cancer through Efficient Tumor-Homing and Cytolytic Ability. *Cancers (Basel).* **2019**, *11* (7). https://doi.org/10.3390/cancers11070966.

(59) Kandarian, F.; Sunga, G. M.; Arango-Saenz, D.; Rossetti, M. A Flow Cytometry-Based Cytotoxicity Assay for the Assessment of Human NK Cell Activity. *J. Vis. Exp.* **2017**, *2017* (126), 1–8. https://doi.org/10.3791/56191.

(60) Tremblay-Mclean, A.; Coenraads, S.; Kiani, Z.; Dupuy, F. P.; Bernard, N. F. Expression of Ligands for Activating Natural Killer Cell Receptors on Cell Lines Commonly Used to Assess Natural Killer Cell Function 11 Medical and Health Sciences 1107 Immunology. *BMC Immunol.* **2019**, *20* (1), 1–13. https://doi.org/10.1186/s12865-018-0272-x.

(61) Zamai, L.; Mariani, A. R.; Zauli, G.; Rodella, L.; Rezzani, R.; Manzoli, F. A.; Vitale, M. Kinetics of in Vitro Natural Killer Activity against K562 Cells as Detected by Flow Cytometry. *Cytometry* **1998**, *32* (4), 280–285. https://doi.org/10.1002/(SICI)1097-0320(19980801)32:4<280::AID-CYTO4>3.0.CO;2-M.

(62) Klingemann, H.; Boissel, L.; Toneguzzo, F. Natural Killer Cells for

Immunotherapy - Advantages of the NK-92 Cell Line over Blood NK Cells. *Front. Immunol.* **2016**, *7* (MAR), 1–7. https://doi.org/10.3389/fimmu.2016.00091.

(63) Bergman, H.; Sissala, N.; Hägerstrand, H.; Lindqvist, C. Human NK-92 Cells Function as Target Cells for Human NK Cells – Implications for CAR NK-92 Therapies. *Anticancer Res.* **2020**, *40* (10), 5355–5359. https://doi.org/10.21873/anticanres.14543.

(64) Murray, K. A.; Gibson, M. I. Post-Thaw Culture and Measurement of Total Cell Recovery Is Crucial in the Evaluation of New Macromolecular Cryoprotectants. *Biomacromolecules* **2020**, *21* (7), 2864–2873. https://doi.org/10.1021/acs.biomac.0c00591.

(65) Wang, W.; Jiang, J.; Wu, C. CAR-NK for Tumor Immunotherapy: Clinical Transformation and Future Prospects. *Cancer Lett.* **2020**, *472*, 175–180. https://doi.org/10.1016/j.canlet.2019.11.033.

(66) Van Ostaijen-Ten Dam, M. M.; Prins, H. J.; Boerman, G. H.; Vervat, C.; Pende, D.; Putter, H.; Lankester, A.; Van Tol, M. J. D.; Zwaginga, J. J.; Schilham, M. W. Preparation of Cytokine-Activated NK Cells for Use in Adoptive Cell Therapy in Cancer Patients: Protocol Optimization and Therapeutic Potential. *J. Immunother.* **2016**, *39* (2), 90–100. https://doi.org/10.1097/CJI.0000000000000110.

(67) Koehl, U.; Brehm, C.; Huenecke, S.; Zimmermann, S. Y.; Kloess, S.; Bremm, M.; Ullrich, E.; Soerensen, J.; Quaiser, A.; Erben, S.; Wunram, C.; Gardlowski, T.; Auth, E.; Tonn, T.; Seidl, C.; Meyer-Monard, S.; Stern, M.; Passweg, J.; Klingebiel, T.; Bader, P.; Schwabe, D.; Esser, R. Clinical Grade Purification and Expansion of NK Cell Products for an Optimized Manufacturing Protocol. *Front. Oncol.* **2013**, *3 MAY* (May), 1–13. https://doi.org/10.3389/fonc.2013.00118.

(68) Lapteva, N.; Durett, A. G.; Sun, J.; Rollins, L. A.; Huye, L. L.; Fang, J.; Dandekar, V.; Mei, Z.; Jackson, K.; Vera, J.; Ando, J.; Ngo, M. C.; Coustan-Smith, E.; Campana, D.; Szmania, S.; Garg, T.; Moreno-Bost, A.; Vanrhee, F.; Gee, A. P.; Rooney, C. M. Large-Scale Ex Vivo Expansion and Characterization of Natural Killer Cells for Clinical Applications. *Cytotherapy* **2012**, *14* (9), 1131–1143. https://doi.org/10.3109/14653249.2012.700767.

Chapter 7: Thesis Conclusions and Future work

7.1 Conclusions

The main objective of this thesis was to develop ice recrystallization inhibitors (IRIs) for use in conventional freezing protocols, to investigate the potential for IRIs to improve the cryopreservation outcomes of different cellular products, such as iPSC-Ns, T/CAR T cells and NK cells. To test this objective, one of the most active IRIs from the *N*-aryl-D-gluconamide class of IRIs is formulated it in a commercially available, GMP-compatible cryomedium (i.e., CS10) to assess the capacity of IRIs to maintain viable and functional cell products post-thaw through live/dead cell analysis and *in vitro* functionality assays. Another objective of this thesis was to study the structure-activity relationship (SAR) between IRI activity and the net polarity of *O*- and *C*-alkyl-linked glucosides by changing the length of the alkyl chain attached to the glucose moiety at the anomeric position, which will assist in the elucidation of key structural properties to direct future IRI development.

Chapter 3 focused on determining structural features required for IRI activity where the effect of changing the length of the hydrophobic moiety (i.e., alkyl chain) and the type of the glycosidic bond (i.e., C-O and C-C bonds) were studied. Testing this effect involved the synthesis of *O*- and *C*-linked alkyl pyranoses with different alkyl chain lengths, followed by assessment of their IRI activity using the modified splat cooling assay to determine their IC_{50} values. Because *O*-linked derivatives of *n*-octyl-β-D-glycosides have previously been described as active IRIs, therefore, the octyl chain was sequentially shortened to a methyl, and the IC_{50} of each derivative was determined. Polar surface area to molecular surface area (PSA/MSA) ratios of the different *O*-linked derivatives were

computed using Marvin Sketch (ChemAxon) software to measure the net polarity of compounds **334 a-g**. A very weak linear correlation was found between the PSA/MSA ratio and the IRI activity of the *O*-linked compounds, with an R^2 value of the linear regression of 0.55, suggesting there was no direct relationship between the net polarity of *O*-linked alkyl glucosides and their IRI activity The *C*-linked derivatives were also synthesized and assessed for their IRI activity (**compounds 339 a-f**). The PSA/MSA ratios of **339 a-f** were then correlated with their IRI activity. The *C*-linked compounds were found to be less IRI active than the *O*-linked ones, and compounds **339 a-f** show no correlation between the values of PSA/MSA ratio and their IRI activity, as suggested by R^2 value of 0.17. The second aspect of this chapter compared the IC_{50} values of *O*- and *C*-linked derivatives to investigate any relationship between *C*-*C* vs *C*-*O* glycosidic linkage and IRI activity. Generally, *O*-linked alkyl pyranoses appeared to be more active than *C*-linked derivatives, suggesting that alteration in the glycosidic bond at the anomeric position may affect the activity of IRI candidates. Although a positive correlation between the IRI activity and PSA/MSA ratios of the *N*-alkyl-D-gluconamide class that differ in the length of their alkyl chain was previously observed, no correlation between the net polarity of the newly synthesized *O*- and *C*-linked alkyl glucosides and their IC_{50} values. This highlights that the modified splat cooling assay utilized to assess the IRI activity results in a different measurement of IRI activity compared to the conventional splat cooling assay (IC_{50} vs %MGS), which may result in different correlations with the net polarity (i.e., PSA/MSA ratio) of the IRI candidates.

Chapters 4, 5 and 6 target the application of IRI technology on different cellular therapy products (iPSC-Ns, T/CAR T cells, and NK cells) to investigate the potential of

small molecule IRIs to enhance the cryopreservation outcomes. In **chapter 4**, the *N*-aryl-D-gluconamide class of IRIs was utilized to examine their capacity in retaining viable and functional iPSC-Ns. Previous work demonstrated that 2FA maintained a high number of live and active of HSCs and iPSCs post-thaw, and therefore, it was further applied on iPSC-Ns. A commercially available and GMP-compatible cryomedium, CS10, was utilized as the control freezing medium in the absence of IRIs. 2FA was formulated at 10 mM, 5 mM, and 2.5 mM in CS10. As presented in section 4.3.2, formulations of 10 mM and 5 mM 2FA in CS10 significantly increased the mean recovery rate of frozen cells compared to CS10 alone (45% and 50% vs 32%, respectively), as suggested by a one-way ANOVA test with Dunnett's multiple comparisons, offering positive results for a potential cryo-additive for the cryopreservation of iPSC-Ns. Moreover, the cryopreserved iPSC-Ns were subjected to immunostaining to monitor any changes in the expression of synaptic- and membrane-associated neuronal markers post-thaw. The iPSC-Ns frozen in 2FA and CS10 displayed distinct cell bodies and neurite extensions and retained the expression of essential neural markers such as β III tubulin, MAP2, and NeuN. Staining of synaptic- and membrane-associated proteins such as synaptophysin and GABA receptor confirmed that formulations of 2FA in CS10 did not compromise the expression of key neuronal proteins and receptors. Moreover, quantification of GABA and glutamine receptors confirmed the presence of 65% of GABAergic neurons and 35% of glutaminergic neurons in the mixed population of iPSC-Ns. The functionality of the cryopreserved iPSC-Ns was also assessed using a microelectrode array (MEA) where the firing and signaling activity of mature iPSC-Ns was monitored over 229 days *in vitro* (DIV). 5 mM 2FA-frozen iPSC-Ns appeared to develop neuronal networks and synchronized synaptic activity earlier than CS10 control (27 DIV

vs 130 DIV). Lastly, the maturity of the neural receptors, such as GABA and NMDAR, was tested by treating the cryopreserved iPSC-Ns with neuropharmacological drugs. The preliminary results showed that 2FA-frozen iPSC-Ns have similar responses to CS10-frozen ones when treating with GABA, muscimol, and a mixture of NBQX and memantine, confirming maintenance of the activity of GABA and NMDA receptors. Moreover, 5 mM 2FA-frozen iPSC-Ns displayed predictable responses when they were treated with acetylcholine receptor agonists, calcium channel antagonists, and sodium channel antagonists. This work demonstrated that 2FA may serve as a potential cryo-additive for the cryopreservation of sensitive post-mitotically differentiated iPSC-Ns, which are invaluable cell products for future clinical applications.

In **chapter 5** and **6**, 2FA was tested on cell-based immunotherapies, T/CAR T and pNK cells, to evaluate its capacity in improving the post-thaw viability and functionality of cells used for vital immunotherapies. 2FA has shown promising results in cryopreserving a high number of viable and functional iPSCs and iPSC-Ns (**chapter 4**), and therefore, we sought to apply 2FA and another IRI from the *N*-aryl-D-gluconamide class, *N*-4-chlorophenyl-D-gluconamide (4ClA), on the Jurkat cell line and T/CAR T cells. In section 5.3, it was demonstrated that the number of live cells post-thaw increased when Jurkat and T/CAR T cells were frozen with 2FA rather than 4ClA. Thus, 2FA was further applied on primary T cells at different stages (pre-activation, day 1 and 9 post-activation) to investigate any variation in the percentage of recovery rate percentages. Previous research has claimed that cryopreservation of activated T cells is challenging and causes loss of a significant number of functional cells. Moreover, to successfully apply T/CAR T therapies in clinics, it is more relevant to freeze cells at days 9-14 post-activation to

decrease the time required for T cell therapy products to be available for patients. It was demonstrated that the mean recovery rate of primary T-cells frozen with 5 mM 2FA in CS10 increased significantly across the different stages at which T cells were cryopreserved in comparison with CS10 alone (~80% vs 50%, respectively). Following the analysis of the post-thaw viability and recovery of T/CAR T cells, assessment of the activity of 2FA-frozen MOCK-T and EGFR-CART cells was conducted to further examine any changes in their cytotoxic killing activity against target tumor cells. As presented in section 5.4.3, the killing functionality of EGFR-CART did not appear to be compromised upon cryopreservation with CS10 in the presence or absence of 2FA. These preliminary results suggest that freezing T cells or CAR T cells with 2FA may increase the number of viable cells and does not affect their killing activity, allowing for the improved delivery of safe and sufficient doses of T cell therapies to clinics.

pNK cells have revolutionized the cell-based immunotherapy field due to their cytotoxic nature and the lack of graft-versus-host reactions. One of the challenges, however, is encountered in the availability of pNK cells for clinical applications. Multiple cryomedia have been described for freezing pNK and CAR-NK cells. Nonetheless, the conventional cryomedia cannot be used in clinicals due to the presence of animal components (i.e., fetal bovine serum, FBS). Therefore, we sought to discover the capacity of a GMP-compatible cryomedium (CS10) compared with three other conventional cryomedia formulations. As presented in section 6.3 of chapter 6, WT- and CAR-NK-92 cells, as well as pNK cells were cryopreserved in four different cryo-solutions. Assessment of the post-thaw viability and recovery revealed that CS10 resulted in a high viability/recovery rate immediately post-thaw, however, the number of live cells appeared

to decrease 48-hours post-thaw which can be related to delayed cell death/cryoinjury. Therefore, CS10 was further tested on pNK cells in the presence or absence of 2FA. The results in section 6.4 demonstrated that there is no significant change in the immediate nor the 3-hr post-thaw recovery rate in the presence or absence of 2FA (the recovery rate ranges from 45 to 50%). Moreover, the post-thaw cytotoxic killing activity assessment revealed that there is no difference in the cytotoxic killing activity of the cells against a specific tumor target, confirming that formulation of IRIs into the cryomedia did not compromise the functionality of pNK cells upon freezing.

Overall, the work presented in this thesis demonstrates that the application of small molecule IRIs on the cryopreservation protocol of multiple cellular products may enhance the cryopreservation outcomes (i.e., recovery rate and functionality). This will assist in developing a master cell bank of the different cell-based therapy products, allowing the access of off-the-shelf, efficacious cell products for patients. Lastly, the SAR studies presented in this thesis highlight the importance of investigating the correlation between the molecular properties (i.e., log P and PSA/MSA ratio) and the activity of existing IRIs (i.e., IC_{50} values), to better understand key molecular features that are significant for future IRI development.

7.2 Future Directions

The first goal of this thesis was to conduct SAR studies on IRIs to elucidate how changes in the length of hydrophobic moieties (i.e., alkyl chain) affect the activity of IRI candidates. Another aim of this thesis was to investigate the potential of IRIs for use as cryoprotective agents for different cell-based therapies (i.e., iPSC-Ns, T/CAR T cells, and NK cells).

The results of the SAR studies demonstrated in this thesis continue to show that pyranoses require a hydrophobic region to be active IRIs. Notably, the length of the alkyl chain, as well as the type of glycosidic bond at the anomeric position were discovered to affect the IRI activity. Therefore, it is significant to conduct additional SAR studies to further understand the structural properties essential for these small compounds to be active, which will assist in the development of new, more effective, small-molecule IRIs. As indicated in **chapter 3**, it is necessary to investigate the relationship between IRI activity and additional modifications to the carbohydrate moiety and other glycosidic bonds (i.e., *N*- or *S*-linked alkyl glucosides). It was demonstrated that long alkyl chains (i.e., an octyl chain) linked by an *O*-glycosidic bond have higher IRI activity and are very soluble compared to the other *O*-linked derivatives, such as the aryl glucosides. In addition to C_1 modifications, further studies must be conducted to explore modifications at C_4 and C_6 which have been previously shown to be important positions for IRI activity. Changes in the glycosidic bond from *C*-*O* to *C*-*C* resulted in less active IRIs, and therefore, it is pertinent to further examine the effect of *C*-*N* and *C*-*S* glycosidic bonds on IRI activity in comparison with the parent *O*-linked compounds. Lastly, it is important to study the difference in correlations between the molecular properties of IRI candidates and the different IRI activity measurements (i.e., IC_{50} and %MGS), to better understand the measurement of IRI activity measurement and its relationship with IRI molecular properties.

Furthermore, the outcomes of cryopreservation of iPSC-Ns (**chapter 4**) with one of the IRIs that belongs to *N*-aryl-D-gluconamide class (2FA) highlighted the importance of the protection against ice recrystallization during cryopreservation. It was demonstrated

that freezing iPSC-Ns in the presence of 2FA yielded a higher number of live cells and improved the post-thaw re-establishment of their synaptic activity. In addition, metabolomic studies were conducted on the cryopreserved iPSC-Ns (unpublished data) to better understand the cell physiology and to monitor any changes in the 2FA-frozen iPSC-Ns. Differentiation of iPSC-Ns is a lengthy process and does not yield high number of fully mature neurons, therefore, the number of samples that were frozen for this experiment was low (n=2). In order to develop an optimal cryopreservation protocol for iPSC-Ns, it is pertinent to increase the sample size ($n \geq 3$). Moreover, *in vivo* studies will be further conducted where IRI-cryopreserved iPSC-Ns will be transplanted into Alzheimer's-modeled mice to examine any degradation in the formation of amyloid plaques. These studies will pave the way for optimizing the cryopreservation protocol for iPSC-Ns which will be beneficial for banking such susceptible cellular products for clinical applications.

Chapter 5 demonstrated the importance of cryopreserving T/CAR T cell therapy to allow their delivery to clinics for the treatment of types of tumors. Conventional cryomedia proposed for freezing T cell products contain animal components (i.e., FBS), and therefore, we sought to discover whether application of IRI technology with a GMP-compatible cryo-solution would improve the cryopreservation outcomes of T/CAR T cell therapy. As presented throughout **chapter 5**, freezing T and CAR T cells in the presence of 2FA led to a higher recovery rate and did not compromise their cytotoxic killing activity against specific tumor cells. Therefore, it is significant to further study any biochemical changes in the cryopreserved T/CAR T cells, such as DNA and membrane integrity. Moreover, *in vivo* functionality assays should be conducted to investigate the capacity of

frozen T/CAR T cells in killing tumor cells which will allow for the translation of IRI technology application to future clinical applications.

In **chapter 6**, efforts were drawn to study the potential of a GMP-compatible cryomedium (CS10) to preserve pNK cells. It was reported that CS10 resulted in a sufficient number of live cells compared to other non-GMP grade formulations of cryomedia, however, a decrease in the 4h-hr post-thaw recovery rate of CS10-frozen pNK cells was observed. Therefore, one of most active IRIs that showed promising results in preserving T/CAR T cells (2FA) was utilized to cryopreserved pNK cells. No significant increase in the recovery rate nor the cytotoxic killing activity was identified in the 2FA-frozen NK cultures compared to CS10-alone frozen cells. This may be related to the fact that the cryopreserved pNK cells were allowed to expand and grow in the presence of feeder cells prior to the application of the functionality assay. However, in clinical displays, frozen pNK cells are transfused directly without expansion, and therefore, it is pertinent to retain a high number of viable and functional pNK cells post-thaw. Future experiments will focus on monitoring any recovery rate changes in the presence or absence of IRIs over 24, 48, and 72 hours without the addition of feeder cells in the cryopreserved cultures of pNK cells. Further *in vivo* will also be conducted to ensure that the killing activity of pNK cells is not compromised upon freezing and thawing with IRIs.

Overall, the discoveries presented in this thesis highlight the potential and benefits of applying IRI technology in the cryopreservation protocols of iPSC-Ns, T/CAR T cells, and NK cells. Efforts to develop new active IRIs has, therefore, risen. A plethora of SAR studies, such as correlations of IRI activity with log P and critical micellization concentration, must be conducted on existing IRIs to understand key structural features

accompanied with IRI activity. Moreover, improvements in post-thaw recovery and functionality of iPSC-Ns, T/CAR T cells, and NK cells are vital for the treatment of neurodegenerative and immune diseases, highlighting the potential of IRIs to serve as cryoprotective agents.

Appendices

Appendix I: Contribution to Original Research

1. Synthesis and analysis of ice recrystallization inhibition (IRI) activity of *O*- and *C*-linked alkyl glucosides (compounds **334 a-g** and **339 a-f**) in chapter 3.
2. Polar surface area-to-molecular surface area (PSA/MSA) ratio analysis of the different compounds (**334 a-g** and **339 a-f**) and correlations with IRI activity using Marvin Sketch and Prism softwares in chapter 3.
3. Assessment of an *N*-aryl-D-gluconamide compound to cryopreserve iPSC-Ns by analyzing the post-thaw viability/recovery rates, as well as well the synaptic activity of cryopreserved iPSC-Ns using MEAs (chapter 4). Cryopreserved iPSC-Ns were also subjected to immunochemistry staining. This work was done with the assistance of Dr. Anna Jezierski, Ewa Baumann, Junzhuo Huang, Dr. Joseph Tauskela, and Amy Aylsworth at National Research Council of Canada (NRC) in Ottawa.
4. Studying the potential of two derivatives from the *N*-aryl-D-gluconamide class of IRIs to cryopreserve T and CART cells (chapter 5). *In vitro* functional analysis of frozen T and CART cells was also conducted using the IncuCyte live cell imaging software. This work was carried with the assistance of Dr. Scott McComb, Dr. Tina

Nguyen, and Ahmed Zaffir at National Research Council of Canada (NRC) in Ottawa.

5. Optimization of the cryomedia utilized for freezing pNK cells was demonstrated in chapter 6. Application of the IRI technology was further tested on pNK cells to assess the capacity of IRIs to maintain viable and functional cells post-thaw. This work was conducted with the assistance of Dr. Seung-Hwan Lee, Bryan Marr, and Donghyeon (Darren) Jo at the Faculty of Medicine, Department of Biochemistry, Microbiology, and Immunology, University of Ottawa.

Appendix II: Thesis and Non-Thesis Related Publications and Presentations

Publications and Presentations Related to Thesis:

Publications

1- Anna Jezierski, **Salma Alasmar**, Junzhuo Huang; Ewa Baumann; Amy Aylsworth; Karishma Chopra; Melissa Hewitt; Jagdeep K. Sandhu; Joseph S. Tauskela; and Robert Ben. Improved cryopreservation of human induced pluripotent stem cell (iPSC) and iPSC derived neurons using ice-recrystallization inhibitors (IRIs). 2022, Manuscript in preparation.

2- Anna Jezierski; Ewa Baumann; Slavisa Corluka; Amy Aylsworth; Umberto Banderali; Caroline Sodja; Maria Ribecco-Lutkiewicz; **Salma Alasmar**; Willard J Costain; Marzia Martina; Joseph S Tauskela. (2021). Electrophysiological- and neuropharmacological based benchmarking of human induced pluripotent stem cell-derived and primary rodent neurons. Stem Cell Reviews and Reports. https://doi.org/10.1007/s12015-021-10263-2.

3- Karishma Chopra, **Salma Alasmar**, Ahmed Zafer, Junzhuo Huang, Anna Jezierski, Scott Mccomb, Ewa Bauman, Robert N. Ben. (2019). Improving the Cryopreservation of Human Induced Pluripotent Stem Cells (iPSCs) And Human T-Cells with Ice Recrystallization Inhibitors (IRIs), Cryobiology, Volume 91, Page 162. (Referred Conference Abstract).

Presentations

1- **Salma Alasmar-Abdou**, Ewa Baumann, Junzhuo Huang, Joseph Tauskela, Anna Jezierski, Robert N. Ben. Small molecule ice recrystallization inhibitors improve post-thaw functionality and network activity of human induced pluripotent stem cell (iPSC)-derived neurons (iNs). Poster, Till and McCulloch Meetings, November 2021 (Ottawa, Ontario).

2- **Salma Alasmar-Abdou**, Karishma Chopra, Ewa Baumann, Junzhuo Huang, Joseph S. Tauskela, Anna Jezierski, Robert N. Ben. Ice Recrystallization Inhibitors (IRIs) as Novel Cryoprotectants for Human Induced Pluripotent Stem Cells (iPSCs) and iPSC-Derived Neurons (iNs). Poster, Society For Cryobiology, July 2021 (Ottawa, Ontario).

3- **Salma Alasmar-Abdou**, Ewa Baumann, Junzhuo Huang, Joseph Tauskela, Anna Jezierski, Robert N. Ben. Small molecule ice recrystallization inhibitors improve post-thaw functionality and network activity of human induced pluripotent stem cell (iPSC)-derived neurons (iNs). Poster, Brain Health Research Day, June 2021 (Ottawa, Ontario).

4- **Salma Alasmar-Abdou**, Ewa Baumann, Junzhuo Huang, Joseph Tauskela, Anna Jezierski, Robert N. Ben. Ice Recrystallization Inhibitors (IRIs) as Novel

Cryoprotectants for Human Induced Pluripotent Stem Cell (iPSC)-Derived Neurons (iNs). Presentation, Extreme Cryo Symposium, March 2021 (Ottawa, Ontario).

5- **Salma Alasmar-Abdou**, Ewa Baumann, Junzhuo Huang, Joseph Tauskela, Anna Jezierski, Robert N. Ben. Improved Cryopreservation of Human Induced Pluripotent Stem Cell (iPSC)-Derived Neurons (iNs) Using Ice Recrystallization Inhibitors (IRIs). Poster, Women In Science Symposium, February 2021 (Ottawa, Ontario).

6- **Salma Alasmar**, Ahmed Zafer, Anna Jezierski, Scott McComb, Robert N. Ben. Assessing the Cryopreservation Potential of Small Molecule Ice Recrystallization Inhibitors on Human T Cells. Poster, Glyconet Symposium, May 2019 (Banff, Alberta).

Non-Thesis Related Publications:

1- Suzana P. Gelova, Kassidy N. Doherty, **Salma Alasmar**, and Kin Chan. Intrinsic base substitution patterns in diverse species reveal links to cancer and metabolism. Manuscript submitted to Communications Biology, 2022.

2- Mahanish J. Thapa, Reena M. Fabros, **Salma Alasmar**, Kin Chan. Analyses of Mutational Patterns Induced by Formaldehyde and Acetaldehyde Reveal Similarity to a Common Mutational Signature in Cancers. 2022, Preprint in BioRxiv.

Appendix III: Experimental Section

Data plotting and statistical analysis

GraphPad Prism 7 software (La Jolla, California, USA; www.graphpad.com) was used to create the data figures. IC_{50} values of the different IRI candidates synthesized and assessed

in chapter 3 were calculated using non-linear regression of the log concentration of IRI vs normalized response. Moreover, Marvin Sketch (ChemAxon) software was utilized to compute PSA and MSA values of the different targets assessed in chapter 3. GraphPad Prism 7 software was further used to correlate PSA/MSA ratios with log IC_{50} values of all compounds reported in chapter 3 by performing a linear regression to fit the data.

GraphPad was also used to conduct statistical analysis of all post-thaw viability, recovery rate, and functionality assays, using a one-way ANOVA test with Dunnett's multiple comparisons (e.g. 95 or 99 percent confidence intervals). P values of less than 0.1 were deemed significant. Data dispersion calculations (i.e., SEM or SD) were carried out in accordance with the Ben laboratory's standard procedures. The standard error of the mean was used to quantify the precision of the mean obtained from studies where applicable.

Experimental Protocols for IRI analysis

The Modified Splat Cooling Assay

Assessment of ice recrystallization inhibition (IRI) activity of the synthesized compounds was done using the modified splat cooling assay after a 5-minute annealing period, as described previously. In summary, 10 μL of the analyte dissolved in phosphate-buffered saline (PBS) was dropped onto a polished aluminum block that had been cooled to -80 °C. The droplet was quickly frozen after being dropped from a height of 2 metres. The wafer was moved to a coverslip (Fisherbrand, 12-545-80) using pre-cooled tools, and then placed in a cryo-stage maintained at -6.4 °C using a programmable Peltier unit (S3 Series 800 temperature controller, Alpha Omega Instruments). The wafer was annealed for 5 minutes before being imaged with a live imaging camera attached to a microscope. "NIS elements D" software (version 5.30.01) was utilized to capture the images. One image from each ice

wafer was then evaluated with ImageJ (Image Processing and Analysis in Java, version 1.51s). Within the image, ice crystals with clearly defined boundaries were circled, and the area of each circled ice crystal was computed using ImageJ.

Quantification of the IRI Activity

A modified splat-cooling assay was used to evaluate ice recrystallization inhibition (IRI) activity to generate IC_{50} curves. Each compound was tested at a minimum of five concentrations. The ice wafer was annealed at -6.4 °C for 5 minutes, as described before for the modified splat cooling assay. Each wafer had one image chosen for further processing using ImageJ software. Within the selected image, ice crystals with well-defined boundaries were circled in the software, and the area of each circled ice crystal was determined. To get an initial rate (v) of ice recrystallization, a binning strategy based on the size of the ice crystal was used. The ice crystal sections were then separated into discrete bins depending on size using Excel (bin size increases in increments of 0.001 mm^2). Due to ice recrystallization, the resulting areas of ice crystals shifted from bin 1 to higher bins. Dividing the sum of areas within a bin by the sum of areas of all crystals in the image yielded the proportionate area of each bin for each wafer. The rate for each tested concentration was calculated and normalized using the rate for the PBS control (zero inhibitor concentration). The normalized rate, v_{norm}, for each inhibitor and their log concentration values were plotted in GraphPad Prism to produce a dose-response curve. The four-parameter sigmoidal curve fit to the data yielded a value for the half-maximal inhibition concentration (IC_{50}). Error bars represent standard deviation (SD).